4/11/94
E8199

NASA Conference Publication 3239

Rotordynamic Instability Problems in High-Performance Turbomachinery 1993

Proceedings of a workshop held at
Texas A&M University
College Station, Texas
May 10–12, 1993

NASA

NASA Conference Publication 3239

Rotordynamic Instability Problems in High-Performance Turbomachinery 1993

Proceedings of a workshop cosponsored by
Texas A&M University, College Station, Texas,
and NASA Lewis Research Center, Cleveland, Ohio,
and held at Texas A&M University
College Station, Texas
May 10–12, 1993

NASA
National Aeronautics and
Space Administration

Office of Management

Scientific and Technical
Information Program

1994

PREFACE

From the first symposium, where little information was available, to the present symposium, continued progress has been made toward an understanding of rotordynamic instability problems. The proceedings of these symposiums are reported in the following NASA documents:

- 1980 Proceedings, NASA CP-2133
- 1982 Proceedings, NASA CP-2250
- 1984 Proceedings, NASA CP-2338
- 1985 Proceedings, NASA CP-2409
- 1986 Proceedings, NASA CP-2443
- 1988 Proceedings, NASA CP-3026
- 1990 Proceedings, NASA CP-3122
- 1993 Proceedings, NASA CP-3239

This proceedings continues to report field experience fluid excitation forces along with laboratory experiments and the theory of seals, dampers, and bearings, but it also includes works on active controls and two-phase flow. These topics are necessary since they are interrelated with current and future seals—such as damper seals, smart seals, feedback controls, and eccentric floating ring seals, as well as theoretical contributions of bearing flows that are, in essence, eccentric seals with modified boundary conditions.

Without wishing to slight any of the contributions, we call your attention to new directives in understanding the effects of variable thermophysical properties and turbulence in seals and bearings and also including two-phase flows and highly compressible fluids as hydrogen at high pressures.

We are confident that you will find the papers presented in this proceedings to be of interest. Please read them carefully and form your own impressions.

These workshops have been organized to continue addressing problems of rotordynamic instabilities by gathering those persons with immediate interest, experience, and knowledge of this subject and providing a forum for information exchange of both past stability problems and present research and development efforts. The intent of the workshop organizers and sponsors is that the workshop and these proceedings provide a continuity of effort and an impetus for an understanding and resolution of these problems.

Chairs:

Dara Childs and John Vance
Turbomachinery Laboratory
Texas A&M University

and

Robert C. Hendricks
NASA Lewis Research Center

Preceding Page Blank

TABLE OF CONTENTS

Session I – Working-Fluid Forces 1

Experimental Investigation of Turbine Blade-Tip Excitation Forces
Manuel Martinez-Sanchez, Belgacem Jaroux, Seung Jin Song, Soomyung Yoo, and Taras Palczynski, Massachusetts Institute of Technology 3

Active Control of Vaneless Diffuser Rotating Stall
Yoshiki Yoshida, Yoshinobu Tsujimoto, and Tomohiro Tateishi, Osaka University, and Hiromu Tsurusaki, Fukuyama University 15

Calculation of Fluid/Structure Interaction at Pump Impeller Shroud Areas Using Finite Difference Techniques
T. Feng and R. Nordmann, University of Kaiserslautern 29

Session II – Seals 47

An Experimental Study on the Static and Dynamic Characteristics of Pump Annular Seals With Two Phase Flow
T. Iwatsubo and T. Nishino, Kobe University 49

Test Results for Rotordynamic Coefficients of Anti-Swirl Self-Injection Seals
C.H. Kim and Y.B. Lee, Korea Institute of Science and Technology 65

Experimental Investigation of Rotordynamic Coefficients of Long Angular Seals in Centrifugal Pumps
T. Neumer, M. Matros, and R. Nordmann, University of Kaiserslautern 75

Eccentricity Effects Upon the Flow Field Inside a Whirling Annular Seal
Gerald L. Morrison, Robert E. DeOtte, Jr., Purandar G. Das, and H. Davis Thames, Texas A&M University 101

Application of an Improved Nelson-Nguyen Analysis to Eccentric, Arbitrary Profile Liquid Annular Seals
Satyasrinivas Padavala and Alan B. Palazzolo, Texas A&M University, and Pat Vallely and Steve Ryan, NASA George C. Marshall Space Flight Center 113

A 3D-CFD Code for Accurate Prediction of Fluid Flows and Fluid Forces in Seals
M.M. Athavale and A.J. Przekwas, CFD Research Corporation, and R.C. Hendricks, NASA Lewis Research Center 137

The Effect of Inlet Swirl on the Dynamics of Long Annular Seals in Centrifugal Pumps
M. Ismail and R.D. Brown, Heriot-Watt University, and D. France, Weir Pumps Ltd. 149

Whirl Measurements on Leakage Flows in Turbomachine Models
A.J. Addlesee, D. Altiparmak, S. Pan, Heriot-Watt University 167

Preceding Page Blank

Rotordynamic Forces in Labyrinth Seals: Theory and Experiment
Knox T. Millsaps and Manuel Martinez-Sanchez, Massachusetts Institute of Technology 179

Calculation and Measurement of the Influence of Flow Parameters on Rotordynamic Coefficients in Labyrinth Seals
K. Kwanka, W. Ortinger, and J. Steckel, Technische Universität Munchen 209

An Experimental Study of Dynamic Characteristics of Labyrinth Seal
Takuzo Iwatsubo, Koji Fukumoto, and Hideyuki Mochida, Kobe University 219

Session III – General 239

Occurrence of Sub-Synchronous Vibration in a Multistage Turbine Pump and Its Prevention
Yanosuke Kanai and Shinobu Saito, Ishikawajima-Harima Heavy Industries Co., Ltd. 241

A Review of Vibration Problems in Power Station Boiler Feed Pumps
David France, Weir Pumps Limited 249

Experimental and Analytical Study on Fluid Whirl and Fluid Whip Modes
Agnes Muszynska, Bently Rotor Dynamics Research Corporation 277

An Investigation of Angular Stiffness and Damping Coefficients of An Axial Spline Coupling in High-Speed Rotating Machinery
C.-P. Roger Ku and James F. Walton, Jr. Mechanical Technology Incorporated, and Jorgen W. Lund, The Technical University of Denmark 293

Stability and Stability Degree of a Cracked Flexible Rotor Supported on Journal Bearings
Meng Guang, Northwestern Polytechnical University, and Robert Gasch, Technical University Berlin 305

Session IV – Bearings and Dampers 325

An Experimental and Theoretical Study of Structural Damping in Compliant Foil Bearings
C.-P. Roger Ku, Mechanical Technology Incorporated 327

Squeeze Film Dampers With Oil Hole Feed
P.Y.P. Chen and E.J. Hahn, The University of New South Wales 339

Hotfire Testing of a SSME HPOTP With an Annular Hydrostatic Bearing
Steven A. Nolan, Robert I. Hibbs, and Gary G. Genge, Rockwell International, and NASA George C. Marshall Space Flight Center 351

Parameter Identification of a Rotor Supported in a Pressurized Bearing Lubricated With Water
John W. Grant, Agnes Muszynska, and Donald E. Bently, Bently Rotor Dynamics Research Corporation 373

Dynamic Force Response of Spherical Hydrostatic Journal Bearing for Cryogenic Applications
Luis San Andres, Texas A&M University 385

A Test Apparatus and Facility to Identify the Rotordynamic Coefficients of High-Speed Hydrostatic Bearings
Dara Childs and Keith Hale, Texas A&M University 403

A Waved Journal Bearing Concept With Improved Steady-State and Dynamic Performance
Florin Dimofte, NASA Lewis Research Center 419

Session I

Working-Fluid Forces

EXPERIMENTAL INVESTIGATION OF TURBINE BLADE-TIP EXCITATION FORCES

Manuel Martinez-Sanchez, Belgacem Jaroux, Seung Jin Song,
Soomyung Yoo, and Taras Palczynski
Massachusetts Institute of Technology
Cambridge, Massachusetts

Abstract

This paper presents results of a program to investigate the magnitude and parametric variations of rotordynamic forces which arise in high power turbines due to blade-tip leakage effects.

Five different unshrouded turbine configurations and one configuration shrouded with a labyrinth seal were tested with static offsets of the turbine shaft. The forces along and perpendicular to the offset were measured directly with a rotating dynamometer. Exploration of casing pressure and flow velocity distributions was used to investigate the force-generating mechanisms. For unshrouded turbines, the cross-forces originate mainly from the classical Alford mechanism (nonuniform work extraction due to varying blade efficiency with tip gap) while the direct forces arise mainly from a slightly skewed pressure pattern.

The Alford coefficient for cross-force was found to vary between 2.4 and 4.0, while the similar direct force coefficient varied from 1.5 to 3.5. The cross-forces are found to increase substantially when the gap is reduced from 3.0% to 1.9% of blade height, probably due to viscous blade-tip effects. The forces also increase when the hub gap between stator and rotor decreases. The force coefficient decreases with operating flow coefficient.

In the case of the shrouded turbine, most of the forces arise from nonuniform seal pressures. This includes about 80% of the transverse forces. The rest appears to come from uneven work extraction (Alford mechanism). Their level is about 50% higher than in the unshrouded cases.

* This work was performed under Contract NAS 8-35018 from NASA, Marshall SFC, Glenn E. Wilmer, Jr., Technical Monitor.

Nomenclature

C_X, C_Y, C_Z	Fluid velocity components along x, y, z
C_θ	same as C_Y
C_{ij}	Fluid Damping Matrix for turbine displacements
e, e_X	Turbine eccentricity
f, f_Y	Tangential force per unit length
F_X	Net force on turbine in direction of offset
F_Y	Net force on turbine perpendicular to offset
H	Blade height
K_{ij}	Fluid stiffness matrix for turbine displacements

Preceding Page Blank

K_O	Structural stiffness for turbine displacements
M	Rotor mass
P, P_t	Pressure, total pressure
Q	Turbine torque
R	Turbine mean radius
U	Turbine wheel speed (wR)
x	Axial coordinate
y	Tangential coordinate
z	Radial coordinate
α_x	Force coefficient along offset (Eq. 8)
α_y	Force coefficient perpendicular to offset (Eq. 8)
β	Sensitivity of tangential force to relative gap, $\beta = -\frac{\partial f_y}{\partial(\delta / H)}$
β_η	Sensitivity of local efficiency to relative gap, $\beta = -\frac{\partial \eta}{\partial(\delta / H)}$
δ	Blade tip gap
ϕ	Flow coefficient, $C_x/\omega R$
ϕ_f, ϕ_p	Phase angles for fluid force (Eq. 10) and wall pressure (Eq. 13)
ρ	Fluid density
θ	Azimuth angle
ω	Angular frequency of turbine spin
Ω	Whirl angular frequency
ζ	Rotor damping factor

1. Introduction

The existing large body of literature on turbomachine tip leakage has been mainly motivated by the substantial contribution of these leakages to losses. H.J. Thomas (1) , in 1958, and J.S. Alford (2), in 1964, independently pointed out that, in a turbine undergoing transverse vibrations (e.g. a whirling motion), the portion of the blading with the smaller tip gap would produce greater tangential driving force than its 180° opposite. Upon integration, this difference in work extraction results in a cross force tending to promote forward whirl, leading to rotordynamic instability.

Both Alford and Thomas showed that, if the tangential force f per unit length is assumed to vary linearly with the ratio δ / H of local tip gap to blade height

$$f = f_o - \beta \frac{\delta}{H} \tag{1}$$

and if the shaft is offset instantaneously by e_x along the o_x direction, then a cross-force F_y equivalent to

$$F_y = \frac{\beta}{2} \frac{Q}{R} \frac{e_x}{H} \tag{2}$$

arises where Q is the turbine torque and R its mean radius. The factor β has become known in the U.S. as the Alford coefficient which is quoted as varying between 0 and 6. The German literature uses a factor called the "excitation coefficient", k_2, which is equivalent to $\beta/2$. Implicit in the Alford/Thomas model is the assumption that the flow remains perfectly uniform up to the offset turbine, as well as downstream of it, so that only the local efficiency, as determined by the local tip gap, is of concern. Two of the consequences of these models are (a) the absence of a direct force component (in the offset direction, and (b) the absence of frequency dependence (no damping).

If only a cross-coupled coefficient (K_{xy}) is generated, it can be easily shown that the damping factor required for stabilization against it would be

$$\zeta_{min} = \frac{1}{2}\frac{K_{xy}}{K_o} = \frac{\beta}{4}\frac{Q}{RH\,K_o} \qquad (3)$$

This can be very substantial in high-pressure turbines. For the SSME H_2 turbopump, Q = 12800 Nm, R = 0.129m, H = 0.023m, and $K_O = M_{ROT}\,\Omega_o^2 = 1.9\text{x}10^8$ Nm, giving $\zeta_{min} = 0.019$, or a log decrement of 12%.

Relatively little work on these forces has been done since the pioneering efforts of Alford and Thomas. Thomas' collaborators at the T.U. Munich produced the most detailed experimental data. Urlichs (3) used a relatively low power facility, with blade Reynolds numbers below 10^5, and measured cross-forces mainly on shrouded turbines, although one unshrouded case was also tested. He identified the shroud seal as the major contributor to the cross-forces. The mechanics of these seal-related forces has been more clearly elucidated since (see for instance Refs. (4), (5), (6)), and is distinct from the uneven work extraction of Alford-Thomas effect. In his unshrouded tests, Urlichs noted a cross-force reduction with increasing mean tip gap, and an increase with axial stator-rotor spacing. The measured forces were roughly compatible with the simple Alford argument. Wohlrab (7), used a larger, pressurized air turbine, capable of stator leaving Reynolds numbers up to $5\text{x}10^5$, but tested only shrouded turbines. Strong non-linearity of force vs. displacement was noted in the cases with smaller forces, which raises questions about accuracy. Limited dynamic testing was accomplished as well. As in Ref. (3), the main mechanism in these tests was through seal pressure effects, rather than through uneven work extraction. Vance and Laudadio (8), did some very low power tests on a fan with statically moveable casing, and reported measured cross-forces, but no aerodynamic data. Ehrich (9) has recently inferred Alford forces from compressor efficiency test data, and argues that these forces become backward-whirling at pressure ratios above the normal operating point.

We have performed extensive force measurements on an unshrouded turbine identical to the first stage of the Shuttle LH turbopump, and also on a shrouded derivative of it. These were supplemented by flow field measurements and theoretical analysis to clarify mechanisms. In this paper, we will describe the test facility (Sec. 2), and present the force and flow data (Sec. 3-6).

2. Experimental Apparatus

The test facility is a pressurized closed loop, filled with Freon 12 gas, and equipped with a gas blower, heat exchanger/cooler, removable test section, power extraction generator and data acquisition system. Nominal operating conditions are 2.0 atm mean pressure and 4.5 Kg/sec flow rate. Flow rate is mainly controlled by a manual series valve, with help from a bypass valve at low flow. Speed is controlled through generator excitation control.

The test section area is shown in Fig. 1. The upper section (12) of the casing can be rotated and carries the stator and the hub, as well as a variety of flow probes. The turbine shaft connects to the turbine via a four-post rotating dynamometer (14), and is supported by two bearings. The bearings are carried in a heavy cylindrical structure which can be translated sideways by means of four stiff rods, two on each side. Static offsets are achieved (to an accuracy of ± 0.5 mil) by insertion or removal of calibrated shims (11). The dynamometer can sense all components of force and torque on the turbine, and the signals from its 9 strain gauge bridges are carried through the shaft to the slip-ring assembly (23). These signals were sampled 32 or 64 times per revolution, on a pattern which was phase-locked to the rotor by means of signals from an auxiliary encoder (18). The data were ensemble-averaged over 128 or 256 revolutions, to reduce low-frequency noise, and were then numerically projected on fixed axes to extract the DC forces of interest (F_X along the displacement axis, F_Y perpendicular to it). Despite sizable second harmonic contamination from the flex joints in the shaft, these DC components were extracted with an accuracy and repeatability of $\pm 0.05\ \ell b_f$ (the forces F_X and F_Y ranged to a few ℓb_f).

The characteristics and design parameters of the unshrouded test turbine are summarized in Table 1. Due to the low pressure ratio, compressibility effects are minimal, and similarity would be ensured by matching flow and work coefficients, and Reynolds number. The first two are indeed matched to the SSME LH turbine. The Reynolds number (based on stator exit velocity and blade height) is 1.4×10^6, compared to 5.6×10^6 in the SSME turbine; since both are well above transition (10^5 -2×10^5) no significant difference is expected. A limited test of this insensitivity was provided by comparison runs at 1 atm and 2 atm loop pressure, in which no difference was detected in the nondimensional cross-force characteristics.

After the unshrouded turbine tests, the same turbine was modified by removing the outer 6.49 mm (out of a blade height of 22.9 mm) and installing a continuous shroud band with a 2-ridge labyrinth seal (as shown in Fig. 2). Due to the partial flow blockage of the unrecessed seal, the optimum flow rate at the design speed of 3440 rpm dropped to 3.16 Kg/sec, the optimum efficiency dropped to 74%, and the corresponding pressure ratio was reduced to 1.14.

The test matrix is summarized in Table 2, with the geometrical notation contained in Fig. 3.

3. Force Data for the Unshrouded Turbine

Typical force vs. displacement plots are shown in Fig. 4, which corresponds to Configuration 1 of Table 2, at its design condition. The plots for Configurations 2-5 are qualitatively similar. In these graphs, the negative F_X slope indicates a restoring direct force, while the positive F_Y slope indicates a forward-whirling cross-force. Each test was repeated three times, and all test results are shown to illustrate the degree of repeatability of the data. The fact that the forces are not exactly zero at zero eccentricity is due to a combination of casing out-of-roundness and positioning error. Despite the relatively large offsets (± 15 mil on a mean gap of 27 mil), the F_Y data show no departure from linearity. By contrast, the F_X data show in all cases a slight s-shaped curvature, with the slope increasing with eccentricity.

As noted in the Introduction, the simple Alford theory would predict $F_X = 0$. However, the data show $|F_X|$ of the same order as $|F_Y|$, and a different mechanism, or a variation on Alford's postulated mechanism, must be involved.

The results of the measurements for all configurations are reported in nondimensional form in Table 3. The coefficients a_x and a_y are obvious generalizations of Alford's b:

$$\alpha_x = \frac{2F_x R}{Q(e/H)} \quad ; \qquad \alpha_y = \frac{2F_y R}{Q(e/H)} \tag{4}$$

where the notation has been changed from b, which is strictly the sensitivity of blade tangential forces to tip gap, to a, which is a measure of the cross-forces, and may or may not be equal to b (indeed, there is no b counterpart to a_x). The forces at e=0 have been subtracted from F_x and F_y in calculating a_x and a_y.

Table 3 indicates a general increase of a_y with speed at a fixed flow rate, or a decrease with the flow coefficient $\phi = C_x/(wR)$. This is displayed in Fig. 5. The theoretical curve shown is from an xz actuator disk theory which will not be discussed in this paper (see Ref. 10).

A second trend in the data is a substantial increase of the force coefficient (both $|a_x|$ and a_y) as the mean radial gap is reduced. This can be seen by comparing Configurations 2 (gap 3% of blade height) and 4 (gap 1.9%), both with the widest axial hub gap d', and also by comparison of Configurations 3 and 5, similarly related, but with a narrower axial hub gap. Averaging over the various speeds, the effect amounts to a 0.6 decrease in a_y (19%) per 1% increase in $\bar{\delta}/H$ (wide axial gap), or a 0.7 (21%) per 1% for the narrow axial gap. Of course, since only two gap values were tested, there is no confirmation of the linearity of this effect. The theory (Ref. 10) predicts a much smaller effect of $\bar{\delta}$ on a_y, and there are some indications from the flow data (Sec. 4) that viscous flow effects in the narrow tip flow passages may be responsible. This trend had been previously reported by Urlichs (3) as well.

Configurations 2 and 3 differ only in the hub axial gap d', while Configuration 1 differs from 2 and 3 in both, d', and the stator-to-rotor blade spacing, d. All three configurations have $\bar{\delta}/H = 3\%$. Thus, if we postulate a linear variation of a_y with d and d', the data in Table 3 can be used to extract the separate sensitivities of a_y to these gap values. Similarly, comparison of Configurations 4 and 5 can yield the d' sensitivity for the cases with a narrow radial tip gap. The results (Table 4) are inconclusive for d, but are unambiguous as to sign and general magnitude for the hub gap d'. We have not been able so far to find a satisfactory explanation for this effect. Opening the gap d' should have the direct effect of reducing the pressure non-uniformity in the stator-rotor space, and to the extent that this nonuniformity contributes to the cross-force (see Sec. 4), this would indeed reduce a_y. On the other hand, these pressure nonuniformities also redistribute the upstream flow in a manner which tends to dampen the Alford effect, as our x-y actuator disk analysis (Ref. 10) makes clear. The net result must then depend on the balance of these two effects. A more complete analysis of the flow data, and additional theoretical development are needed in this area. Urlichs (3) found the opposite trend (a_y increasing with axial gap), but his geometry was such that both d and d' were varied simultaneously.

In addition to the direct force measurements, both upstream and downstream flow fields were explored through a set of static wall pressure taps and directional probes. More details about this instrumentation and flow data can be found in Ref. 10. The surveys upstream of the stator indicated very small departures from tangential uniformity. On the other hand, the wall pressure surveys downstream of the stator do show a well-resolved nonuniformity. Fig. 6 shows the pressure pattern for the inter-blade row region and the rotor blade tip region. For the region between stator and rotor a pressure fluctuation amplitude of about $0.0027P_{to} = 0.22\,\rho C_{xo}^2/2 = 0.028\,\rho(\omega R)^2$ for e/H =

0.019. The pressure minimum is about 25° ahead of the maximum gap location. The pressure nonuniformity increases in amplitude as one moves downstream over the rotor blades, particularly in their narrow-gap sectors, but it then returns downstream to the same level as between rotor and stator. Thus, the turbine eccentricity is felt upstream and downstream of it, through potential effects, with a length scale of the radius R, and, from limited probing data, spanning the passage depth as well.

At 3 chord lengths downstream of the turbine, the velocity data were obtained to a depth of 75% span, using a 3 hole probe. The tangential distribution is shown in Figure 7, where the mean (centered turbine) tangential velocity has been subtracted out. Based on consistency among various probes and also with the dynamometer data, the errors appear to be under 10%. The positive tangential velocity values seen near the bigger gap region (180°) indicate underturning by the rotor blades. The magnitude seems to be uniform in the outer 5% of the span, gradually decreasing towards the hub.

Thus, two main sources of lateral force on the turbine due to the flow properties can be identified: 1) a tangentially non-uniform flow turning which leads to uneven work extraction; and 2) a non-uniform static pressure distribution acting on the turbine hub. Both forces can be integrated around the perimeter to a direct force and a cross force. Integration of the pressure nonuniformity is straightforward. We assumed the pressure acting on the hub is that observed before and after ther rotor, since the excess nonuniformity over the rotor blades appears to be a near-tip effect. For the work-defect forces, we used the Euler turbine equation locally to calculate an azimuth-dependent tangential force per unit length

$$f_y = \int_0^H \rho C_x \Delta C_y dr \qquad (5)$$

where C_x is taken to be the mean axial velocity, and the flow turning ΔC_y is from our velocity surveys.

The results for Configurations 4 and 5 are shown in Table 5 , where we report the separate pressure and work-defect contributions to a_x and a_y, their sum, and for reference, the dynamometer-measured data. Similar results were also obtained (for all configurations) using velocity data at 1.5 chords downstream of the rotor (Ref. 10). Most of the direct force is due to the pressure force while the cross force is caused by both the pressure force and the blade force. The cross force coefficients, a_y, are larger than expected for this low-reaction turbine on the basis of work-defect arguments. Clearly, the pressure component, not previously identified, is an important factor.

All of the data reported here are for static offsets. An attempt at measuring cross forces under dynamic conditions (using an inertial shaker) was unsuccessful due to excessive vibratory noise. The simple theory of Alford predicts zero damping, while a more complete model (Ref. 10) indicates significant damping due to lag in tangential flow redistribution. Given the large magnitude of the statically measured forces, measurements under dynamic conditions should be undertaken in order to complete our understanding of Alford forces.

4. Forces in a Shrouded Turbine

The turbine was modified, as described in Section 2 of this paper, for the shrouded case, and dynamometer and flow data were obtained. As in the unshrouded cases, the forces scale linearly with eccentricity, and a sinusoidal pressure pattern with a large amplitude develops over the shroud band. Table 6 shows the excitation coefficients from the dynamometer data, and the pressure data at the design speed. Compared to the unshrouded cases, the excitation coefficients are larger by a factor ranging from 1.5 to 2.0.

The nonuniform pressure distribution produces both direct and cross forces which are smaller than those measured with the dynamometer. For this configuration, no measurements were taken of the velocity perturbations, because, due to the presence of the unrecessed shroud, the flow was very turbulent downstream of the rotor. If it is assumed that the work defect mechanism contributes primarily to the cross force as in the unshrouded cases, the discrepancy in the direct force excitation coefficient cannot be explained. Furthermore, the small difference in the cross force excitation coefficients for the shrouded case suggests that the pressure effect, instead of the work defect effect, is primarily responsible for the cross force. Lastly, the pressure non-uniformity, which can be detected upstream and downstream of the shroud, shows again a flow redistribution on the scale of the turbine radius.

A linear labyrinth seal model based on the work of Millsaps (6) was extended to include the effects of non-uniformities in the flow both upstream and downstream of the shroud and was used to analyze the shrouded data. It was found that the non-uniformities have a large effect on the model's predictions, essentially doubling the magnitude of both the direct and the cross force, but even after this correction, the model underpredicts the forces by about 40%. No complete theory exists of a seal interacting with the flow field of the turbine blading. Palczynshki (11) discusses, in greater detail, the work on the shrouded turbine.

8. Conclusions

This work has confirmed the existence of the destabilizing forces suggested by Thomas and Alford. The general scaling and order of magnitude are also consistent with their insights. However, some new effects in the unshrouded cases include the following:

1) In addition to a non-uniform work extraction, a non-uniform pressure distribution also exists.

2) The forces increase significantly as the mean tip gap is reduced, confirming an earlier result.

The lateral forces in shrouded turbines can be larger than those in unshrouded turbines. This is due to a large nonuniformity in the seal gland pressure, which now dominates over the work defect contribution.

Alford force measurements under dynamic conditions are recommended in order to investigate the possible existence and magnitude of a damping component of this force.

References

(1) Thomas, H.J., "Instabile Eigenschwingungen von Turbinenlaeufern Angefacht durch die Spaltstroemung in Stopfubuchsen und Bechauchflug (Unstable Natural Vibrations of Turbine Rotors Induced by the Clearance Flows in Glands and Blading)", Bull. de L.A.I.M. 71 NO 11/12, 1958, PP. 1039-1063.

(2) Alford, J.S., "Protecting Turbomachinery from Self-Excited Rotor Whirl", Journal of Engineering for Power, October 1965, pp. 333-334.

(3) Urlichs, K., "Clearance Flow Generated Transverse Forces at the Rotors of Thermal Turbomachines", NASA TM-77292, Translation of Ph.D. Dissertation, Munich Technical University, 1975.

(4) Iwatsubo, T., "Evaluation of Instability Forces of Labyrinth Seals in Turbines or Compressors", NASA CP-2133, 1980, PP. 139-169.

(5) Scharrer, J.K., Childs, D.W., "Theory Versus Experiment for the Rotordynamic Coefficients of Labyrinth Gas Seals: Parts 1 & 2", ASME Journal of Vibration, Acoustics, Stress and Reliability in Design, Vol 110., No. 3, 1989, pp. 270-287.

(6) Millsaps Jr., K.T., "The Impact of Unsteady Swirling Flow in a Single Gland Labyrinth Seal on Rotordynamic Stability: Theory and Experiment", Ph.D.Thesis, Department of Aeronautics and Astronautics, M.I.T., 1992.

(7) Wohlrab, R., "Experimental Determination of Gap Flow Conditioned Forces at the Rotors of Thermal Turbomachnes", NASA TM-77293, Translation of Ph.D. Dissertation, Munich Technical University, 1975.

(8) Vance, J.M., and Laudadio, F.J., "Experimental Measurement of Alford's Force in Axial Flow Turbomachinery", ASME Paper 84-GT-140, June 1984.

(9) Ehrich, F., Unpublished Report, 1992.

(10) Martinez-Sanchez, M., and Jaroux, B., "Turbine Blade Tip and Seal Clearance Excitation Forces", Phase III Report on NASA Contract No. NAS8-35018, May, 1992.

(11) Palczynshki, T.A., "Experimental and Theoretical Investigation of Rotordynamic Instability in a Shrouded Turbine", S.M. Thesis, Department of Aeronautics and Astronautics, M.I.T., 1992.

Table 1
Design Parameters for SSME Fuel Turbopump First Stage
and the Test Facility Turbine

Parameter	SSME Fuel Turbopump First Stage	Test Facility Turbine
Flow coefficient, ϕ	0.58	0.58
Work coefficient, Ψ	1.508	1.508
Stator exit angle	70°	-
Relative rotor inlet angle	43.9°	-
Rotor exit angle	60°	-60°
Absolute exit angle	-3.1°	-3°
Degree of reaction	0.216	0.216
Rotor mean radius, cm (in)	12.88 (5.07)	12.88 (5.07)
Number of rotor blades	63	63
Rotor blade height, cm (in)	2.17 (0.854)	2.17 (0.854)
Rotor blade chord, cm (in)	2.21 (0.870)	2.21 (0.870)
Rotation Rate, rpm	34,560	3440
Axial flow velocity, m/s (in/s)	262 (10,300)	26 (1020)
Mass flow rate, kg/s (slug/s)	71.8 (4.92)	4.48 (0.307)
Inlet pressure, kPa (psi)	34,950 (5069)	224 (32.43)
Inlet temperature	1053 (1436)	300 (80)
Pressure ratio	1.192	1.231
Efficiency	0.821	0.80

Table 2 The Test Matrix

Conf #	t_m/H (%)	d/c (%)	d'/c (%)	Shroud (Y/N)	m/m_{des} (%)	ω/ω_{des} (%)	e/t_m Range (%)
1	3.0	50	38	N	50 100 100 100 100 100 100	100 70 100 110 70 100 110	±67 (e=±.46 mm)
2	3.0	26	15	N	100	70 100 110	±67
3	3.0	26	1.3	N	100	70 100 110	±67
4	1.9	26	15	N	100	70 100 110	±59 (e=±.25 mm)
5	1.9	26	1.3	N	100	70 100 110	±59
6	4.5	26	1.3	Y	100	70 100 110	±59

Table 3
Nondimensional Force Coefficients from Dynamometer

Configuration	ω / ω_{design}	α_x	α_y
1	0.7	-2.12	2.43
1	1.0	-2.81	2.57
1	1.1	-3.42	3.66
2	0.7	-1.54	2.49
2	1.0	-2.14	2.96
2	1.1	-2.46	3.23
3	0.7	-1.47	2.87
3	1.0	-1.87	3.02
3	1.1	-2.04	3.43
4	0.7	-2.93	3.38
4	1.0	-3.42	3.55
4	1.1	-3.65	3.72
5	0.7	-2.82	3.83
5	1.0	-3.47	3.98
5	1.1	-3.50	4.04

Table 4
Sensitivity of Cross-Force to Axial Stator-Rotor Spacing (d) and Hub Axial Gap (d')
(See Figure 6 for definitions)

$\bar{\delta} / H$	ω / ω_{des}	$\partial\alpha_y / \partial(d/c)$	$\partial\alpha_y / \partial(d'/c)$
0.030	0.7	2.42	-2.78
0.030	1.0	-1.21	-0.44
0.030	1.1	-1.00	-1.44
0.019	0.7	-	-3.32
0.019	1.0	-	-3.13
0.019	1.1	-	-2.37

Table 5 Contributions from work defect (wd) and pressure (p) to the force coefficients α_x, α_y at design conditions, and comparison to dynamometer data.

Configuration	$(\alpha_x)_{wd}$	$(\alpha_x)_p$	$(\alpha_x)_{total}$	$(\alpha_x)_{dyn}$
4	- .6	-2.6	-3.2	-3.36
5	- .6	-2.3	-2.9	-3.47

Configuration	$(\alpha_y)_{wd}$	$(\alpha_y)_p$	$(\alpha_y)_{total}$	$(\alpha_y)_{dyn}$
4	2.1	1.6	3.7	3.55
5	1.9	2.2	4.1	3.98

Table 6 Nondimensional force coefficients from the dynamometer and pressure data for the shrouded turbine

Configuration	ω / ω_{design}	α_x	$(\alpha_x)_p$	α_y	$(\alpha_y)_p$
6	0.7	-4.06		5.94	
6	1.0	-5.63	-3.8	6.28	6.0
6	1.1	-6.00		6.37	

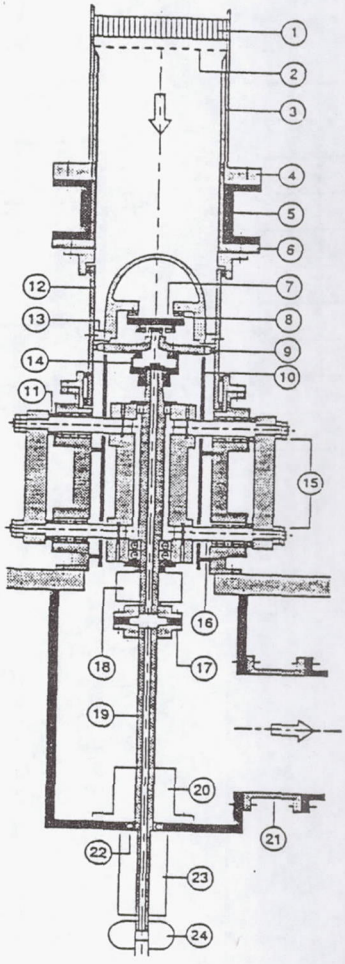

(1) Flow straightener
(2) Screen
(3) Main loop piping
(4) Flange
(5) Flexible insert
(6) Liner
(7) Snubber bearing
(8) Snubber support
(9) Test turbine
(10) Flow-smoothing shield
(11) Shims
(12) Rotatable casing
(13) Stator blades
(14) Rotating dynamometer
(15) Bolts to secure shaft
(16) Turbine-offsetting rods
(17) Upper flex joint
(18) Optical encoder
(19) Intermediate shaft
(20) Double-acting seal
(21) Flexible insert
(22) Pivoting bearing
(23) Slip ring assembly
(24) Lower flex joint

Figure 1: Schematic of the turbine test section.

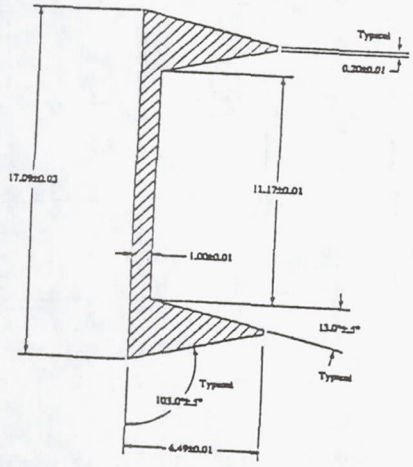

Figure 2: Shroud-seal for turbine. Dimensions in mm.

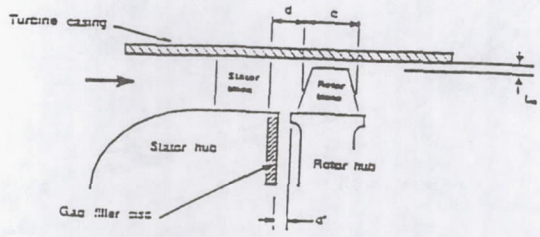

Figure 3: Schematic of turbine's major dimensions of interest.

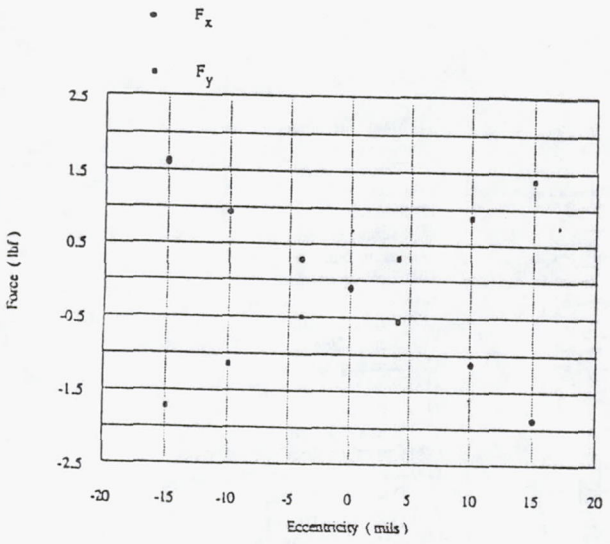

Figure 4: F_X and F_Y versus e
(Conf. 1, $\omega / \omega_D = 1.0$).

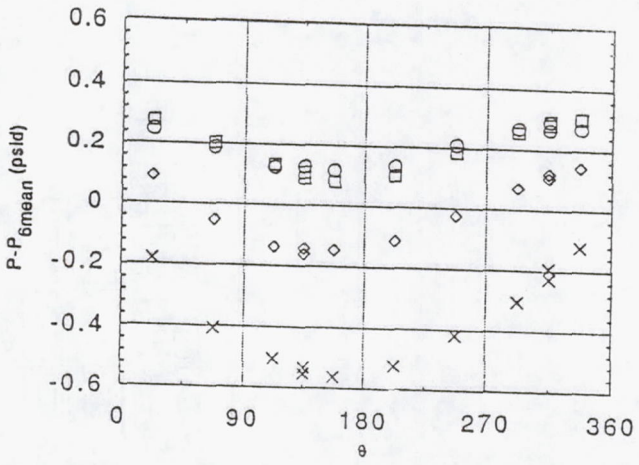

Figure 6: Wall tap pressure between stator and rotor(4) and over the rotor blade tip(5,6, &7)
(Conf. 1, e/H = 0.019).

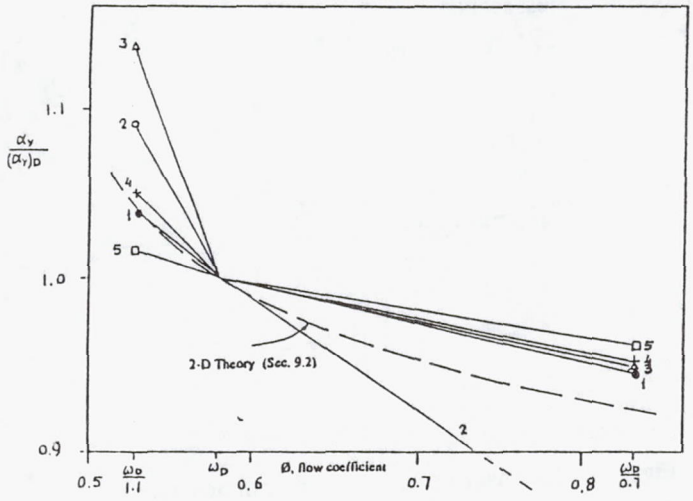

Figure 5: Effect of f on α_Y
(Conf. 1, e/H = 0.019).

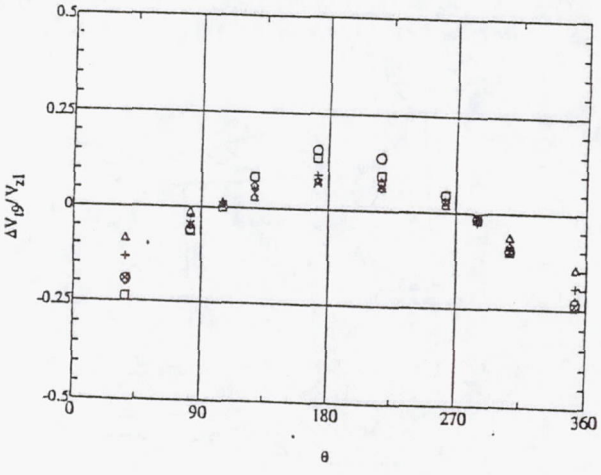

Figure 7: Tangential velocity at station 9
(Conf. 4, e/H = 0.019).

ACTIVE CONTROL OF VANELESS DIFFUSER ROTATING STALL

Yoshiki Yoshida, Yoshinobu Tsujimoto, and Tomohiro Tateishi
Osaka University
Toyonaka, Osaka, Japan

and

Hiromu Tsurusaki
Fukuyama University
Fukuyama, Hiroshima, Japan

SUMMARY

Experiments were carried out to study the feasibility of active stabilization of vaneless diffuser rotating stalls. Pressure fluctuation at the diffuser inlet was monitored and used to control the rotating stall. A.C. control flow, which is produced by a loud speaker, was introduced into the diffuser at the inlet. It is shown that the rotating stall can be suppressed when the phase of the control flow has certain relation with the phase of the rotating stall. By considering the energy flux due to the A.C. control flow, it is shown that the rotating stall is suppressed when the control flow has the phase such that the energy is subtracted out from the diffuser flow. Discussions are made on the relations between the energy flux and the amplitude of the pressure fluctuation due to the rotating stalls.

INTRODUCTION

Rotating stalls in vaneless diffusers of centrifugal compressors set the lower flow limit of stable operation. They cause not only pressure fluctuations but also shaft vibrations [ref.(1)]. Many experiments were carried out to predict the rotating stall onset flow rate [ref.(2),(3)], and to enlarge the flow range of stable operation [ref.(4)].

Compared with experimental works, theoretical studies are few. From a 2-D inviscid irrotational flow analysis, Jansen [ref.(5)] found that outward flow is stable and hence attributed the cause of the rotating stall to local inward flow in the boundary layer on the diffuser wall. Many previous experimental works, such as ref.(2) and (3), are based on this supposition. On the other hand, based on linearized Euler's equation, Abdelhamid [(ref.(6)] and,later, Moor[ref.(7)] have shown that 2-D flow instability can occur even with outward flow. It is

shown by Tsujimoto et al.[ref.(8)], by a 2-D inviscid rotational flow analysis, those flow instabilities are related with the vorticity distribution in the diffuser. Although such theoretical flow models are not fully understood, partly due to the lack of experiments based on those theoretical models.

Recently, attempts are made to apply the active controls to suppress rotating stall and surge: Paduand[ref.(9)] used "wiggling" inlet guide vanes to control rotating stall in the axial compressor and Ffowcs Williams [ref.(10)] controlled surge in the centrifugal compressor.

The purpose of the present study is twofold: to confirm the feasibility of the active stabilization of vaneless diffuser rotating stalls, and to obtain the physical understanding of the rotating stall through studying the response of rotating stall due to external disturbance. The pressure fluctuations at the diffuser inlet are monitored and used to control the stall, by introducing external fluid periodically at the diffuser inlet.

NOMENCLATURE

A.R.: ratio of pressure amplitude [$\triangle p_d$(with control)/$\triangle p_d$ (without control)]
b : impeller width
E : work of control flow [eq.(1)]
G : gain
L : theoretical work of impeller
n : number of rotating stall cells
p : static pressure
q : flow rate of control flow
r : radius
T : periodic time
t : time
u : impeller peripheral speed
$\triangle v$: velocity fluctuation
β : vane angle to circumference
θ : phase angle
ρ : density of fluid
ϕ : flow coefficient [$= Q/2\pi r_1 b_1 u_1$]
ψ : pressure coefficient [$p/\rho u_1^2$]
$\triangle\psi$: pressure fluctuation coefficient [$\triangle p/\rho u_1^2$]
ω : angular frequency of pressure fluctuation
Ω : angular velocity of impeller

subscript
1,2 : impeller inlet and outlet
3,4 : diffuser inlet and outlet
a : air-chamber
d : diffuser

APPARATUS

Fig.1 shows the experimental set up. The flow is introduced into the test impeller⑤ after passing through a flow measuring nozzle①, a booster fan②, a flow control valve③ and a flow straightener④. The straightener and the inlet pressure tap are located at 4.06d and 2.22d upstream of the impeller respectively, where d=40mm is the inner diameter of the inlet pipe. The flow from the diffuser is directly discharged into ambient space. The experimental vaneless diffuser⑥ is equipped with air-chambers⑦ outside the diffuser walls. The inlet portion of the diffuser walls is made with a flat plate with pores. The air-chambers are connected to a loud speaker⑨ (diameter is 300mm) through hardened vinyl tubes⑩. "A.C. control flow", which is produced by the loud speaker, is introduced into the diffuser through the air-chamber and the porous diffuser wall.

Major dimensions of test impeller are given in Table.1. The impeller is two dimensional and has logarithmic vanes, as shown in Fig.2. The rotational speed of the impeller is kept within 3,000±10rpm throughout the present study. Major dimensions of test diffuser are given in Table.2. Fig.3 shows the details around the vaneless diffuser. The air-chambers are composed of six fan-shaped rooms with the depth 5mm. The inlet portion of the diffuser wall(radius ratio r/r_1=1.11～1.31) are made of the flat plate with pores with diameter 0.55mm and pitch 1.1mm. The control flow is introduced into the diffuser through these pores.

For the control of three cells rotating stall, three of six air-chamber rooms are connected to the loud speaker, as shown in Fig.3(a), and the pores of unused air-chambers are covered with vinyl tapes. For the control of two cells rotating stall, two of the air-chamber rooms are used, as shown in Fig.3(b). As shown in Fig.3(c), twelve pressure taps with throat diameter 1mm, are evenly placed at radius ratio r/r_1=1.04 on front diffuser wall. In order to determine the number of rotating stall cells and cell propagation velocity ratio, two pressure transducers are inserted into two of the pressure taps.

CONTROL SYSTEM

The control system used is shown in Fig.4. The diffuser inlet pressure is monitored to detect the phase and magnitude of the rotating stall, which is fed back to the diffuser as a "A.C. control flow" after giving some time lag by the delay controller (Roland SDE-300A). The band pass filter is set to pass the frequency components 1～30Hz, which includes the fundamental component of the diffuser rotating stall. "A.C. control flow" is produced by a loud speaker. The flow rate of the "A.C. control

flow" cannot be measured directly under the operating condition. It is estimated from the air-chamber pressure p_a and the diffuser inlet pressure p_d using the flow coefficient determined quasi-steadily.

The "phase θ" of the air-chamber pressure p_a is defined relative to the diffuser inlet pressure p_d at the peripheral position of the center of the air-chamber. Actually, the diffuser inlet pressure p_d is monitored using a pressure tap apart from the air-chamber, in order to minimize the direct effect of the control flow. The "phase θ" of the above definition is determined by using the frequency and the propagation velocity of the rotating stall.

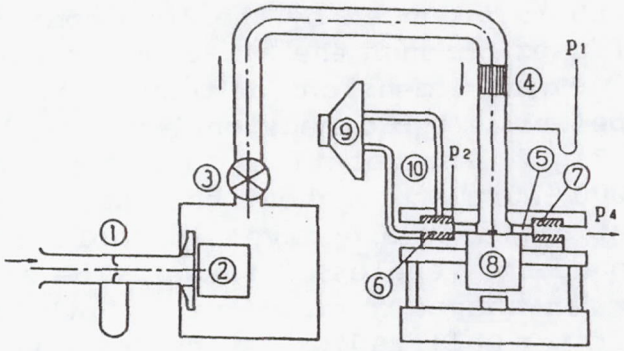

①. Flow measuring nozzle
②. Booster fan
③. Flow control valve
④. Straightener
⑤. Impeller
⑥. Vaneless diffuser
⑦. Air chamber
⑧. Motor
⑨. Loud speaker
⑩. Vinyl tube

Fig.1 Test apparatus

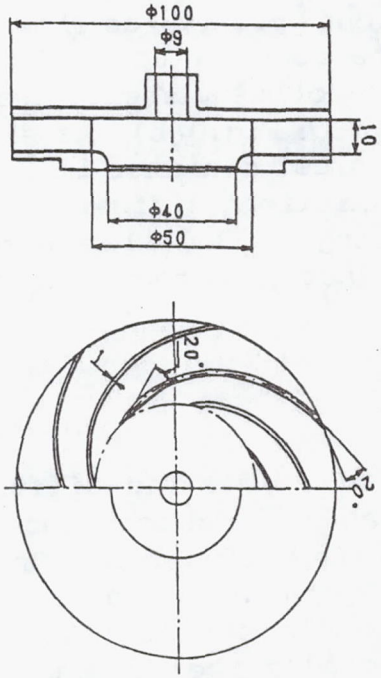

Fig.2 Impeller

Table.1 Dimensions of impeller

Inlet radius	r_1 [mm]	25
Outlet radius	r_2 [mm]	50
Impeller width	b [mm]	10
Vane angle	β [°]	20
Number of vanes	Z	7

Table.2 Dimensions of vaneless diffuser

Inlet radius	r_3 [mm]	50.5
Outlet radius	r_4 [mm]	91
Diffuser width	b [mm]	12

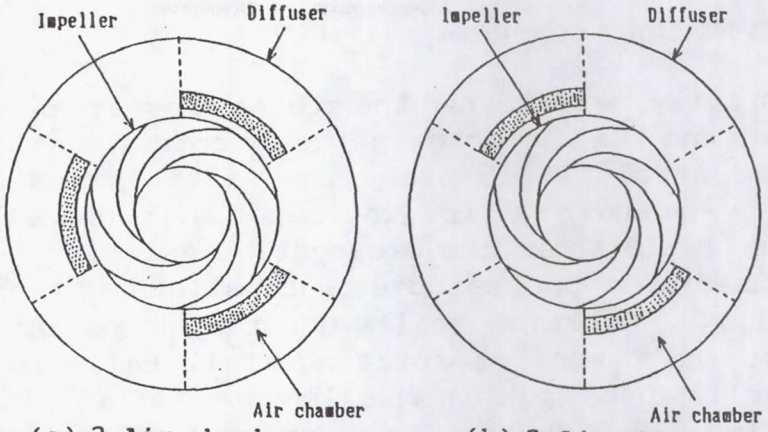

(a) 3-Air chambers (for the case of 3-cells)

(b) 2-Air chambers (for the case of 2-cells)

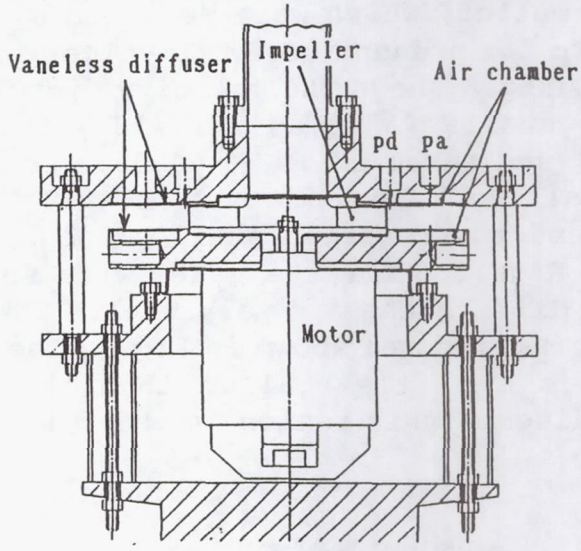

(c) Sectional arrangement

Fig.3 Test apparatus (Detail around the vaneless diffuser)

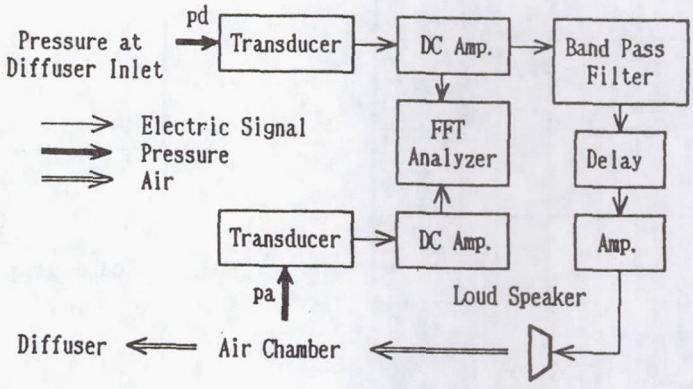

Fig.4 Control and measuring system

RESULTS WITHOUT CONTROL

Firstly, we examined the static pressure performance of the impeller and the characteristics of rotating stalls without the active control. Fig.5 shows the static pressure performance curves p_2-p_1, and p_4-p_1 for the cases with and without the air-chamber. Fig.6 shows the propagation velocity ratio, which are determined from the pressure fluctuations at the diffuser inlet [ref.(11)]. Rotating stalls occur at the flow rate less than $\phi=0.11$. The number of rotating stall cells is two or three: three cells appear within the flow range of $\phi=0.06\sim0.11$, and two cells in $\phi=0.0\sim0.06$. Fig.7 shows the spectra of pressure fluctuations at the diffuser inlet, and velocity fluctuations at the diffuser outlet, which were measured by using the hot wire anemometer. In the present study, impeller rotating stalls were not observed. Fig.8 shows the velocity disturbance field due to the rotating stalls [same as ref.(12)],for the cases of two cells($\phi=0.0$) and three cells ($\phi=0.09$). Cell structure of the rotating stall can be observed clearly. Static pressure performance and the rotating stall propagation velocity ratio are shown in Figs.5,6 for the cases with and without the air-chamber. The differences are very small. The amplitudes of the pressure fluctuation are shown in Fig.9. The amplitude with the air-chamber is a little smaller than that without the air-chamber. We discuss this reason in the following section.

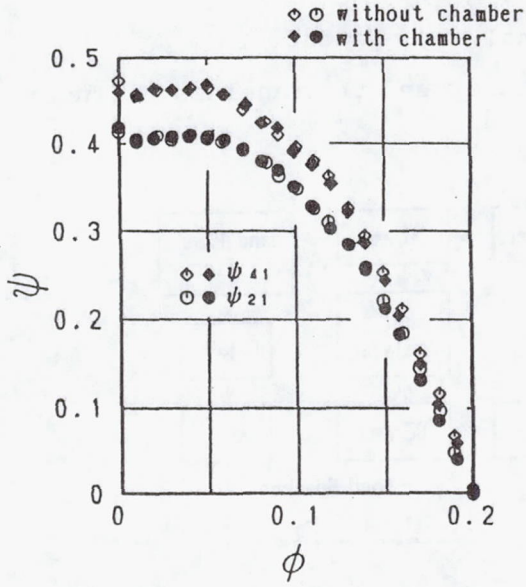

Fig.5 Static pressure performance curves (without control)

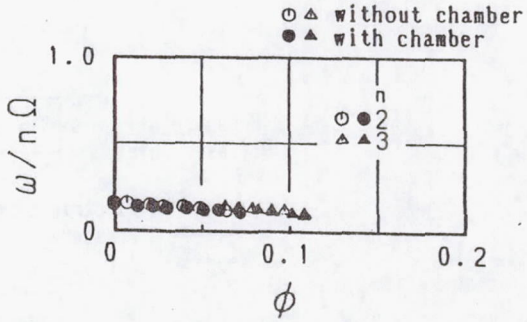

Fig.6 Rotating stall propagation velocity ratio

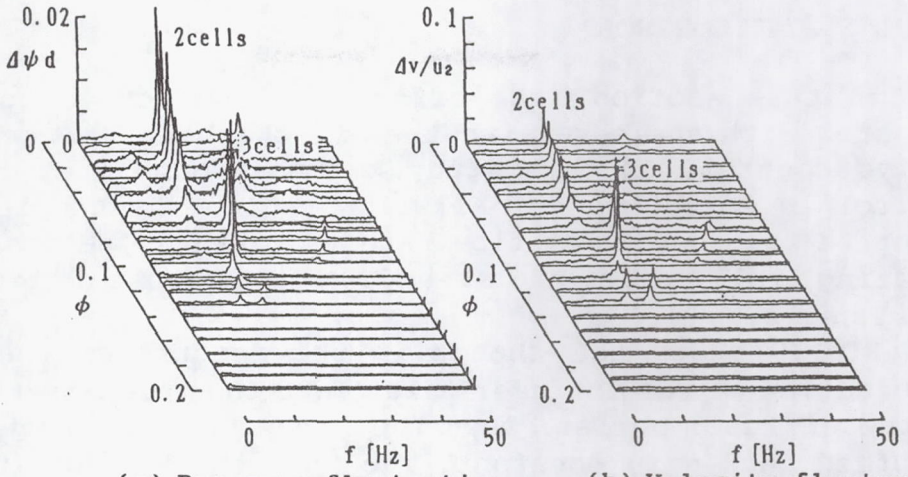

(a) Pressure fluctuation (at the diffuser inlet)

(b) Velocity fluctuation (at the diffuser outlet)

Fig.7 Pressure and velocity spectra(without control)

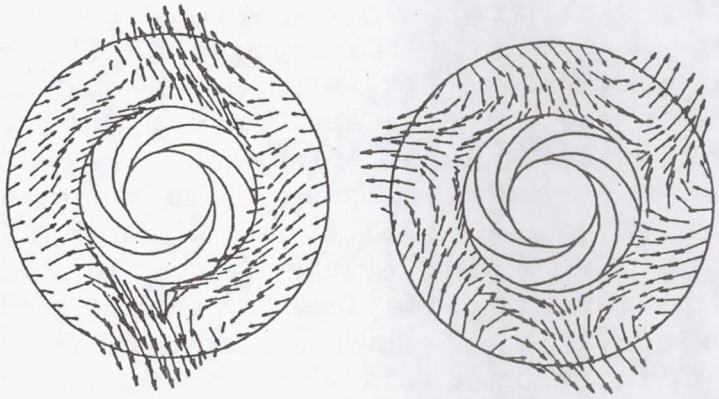

(a) ϕ=0.0

(b) ϕ=0.09

$\longrightarrow$ v/u₂=0.1

$\longrightarrow$ v/u₂=0.1

Fig.8 Velocity disturbance fields (without control)

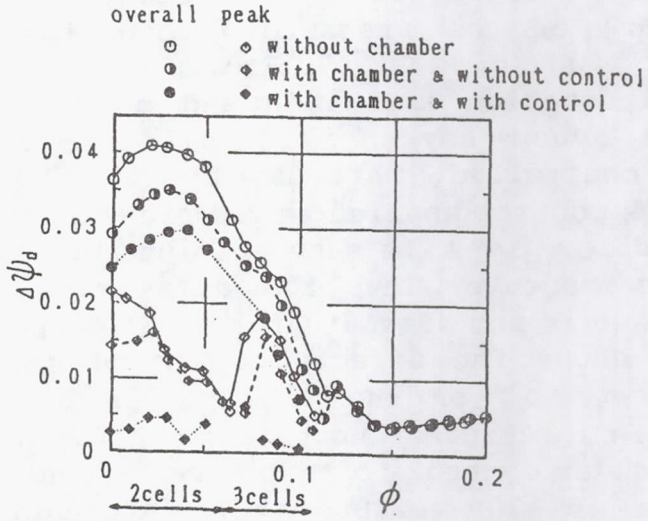

Fig.9 Comparison of the pressure fluctuation amplitudes

RESULTS WITH CONTROL

In this section, the effects of the active control are compared with the case with the air-chambers, but without the active control. In this study, it was found that the active control is effective for all flow region. As sample cases we describe the results at flow rate ϕ=0.09 for the case of three rotating stall cells, and at ϕ=0.0 for the case of two rotating stall cells.

Fig.10 shows the change in the spectra of the pressure fluctuation at the diffuser inlet, and the velocity fluctuation at the diffuser outlet, when the "phase θ" is changed keeping the feed back gain constant. The "phase θ" is defined as the phase of the pressure in the air-chamber relative to the diffuser inlet pressure at the same circumferential location, as mentioned previously. When the phase is $\theta \fallingdotseq 0°$, the amplitude of the rotating stall frequency increases. However, when the phase is θ=-180° ~-240°, the rotating stall is suppressed with decreased peak value. Fig.11 shows the velocity disturbance field due to the rotating stall under the control. From the comparison with Fig.8, we find that the velocity field is controlled all over the diffuser. This means that the decrease in the inlet pressure fluctuation is not caused by the "cancelling", but caused by the control of the rotating stall itself. This is quite different from the noise control by "anti-sound". Figs.12(b),(c) show the spectra of the pressure and the velocity fluctuation at various flow rates with the control. The control is effective in all flow region. However the static pressure performance could not be improved by the control,as shown in Fig.12(a).

As mentioned above, the peak values at the rotating stall frequency could be suppressed excellently, but the over all value(1~50Hz) of the pressure fluctuation did not change remarkably, as shown in Fig.9. From the view point of over-all pressure fluctuation amplitude and of the static pressure recovery we cannot say that the diffuser rotating stall is completely controlled. This may be caused partially by the method of the control applied in the present study. That is, the delay controller gives the same absolute time delay for all the frequency components. Thus the delay time which gives the adequate phase is not adequate for other components.

Fig.13 shows the effects of the phase θ and the gain $G=20\cdot\log_{10}(\triangle p_a/\triangle p_d)$ on the peak values of the spectrum of diffuser inlet pressure fluctuation. A.R. is the ratio of the peak value under control to that without control. A.R.is less than 1.0 for θ=-120° ~-240°. It is interesting that A.R. may become less than 1.0 even for G<0 dB, if the phase θ is appropriate.

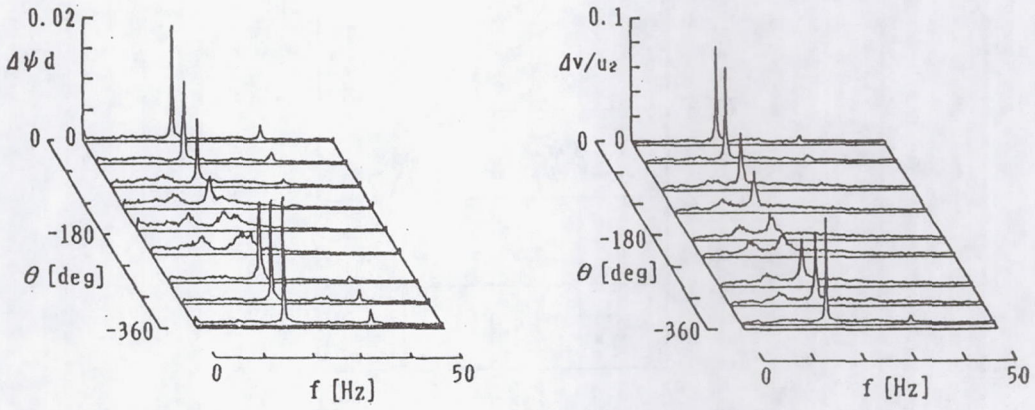

(a) Pressure fluctuation (at the diffuser inlet)

(b) Velocity fluctuation (at the diffuser outlet)

Fig.10 Relation between the pressure, velocity spectra and the phase (ϕ=0.09)

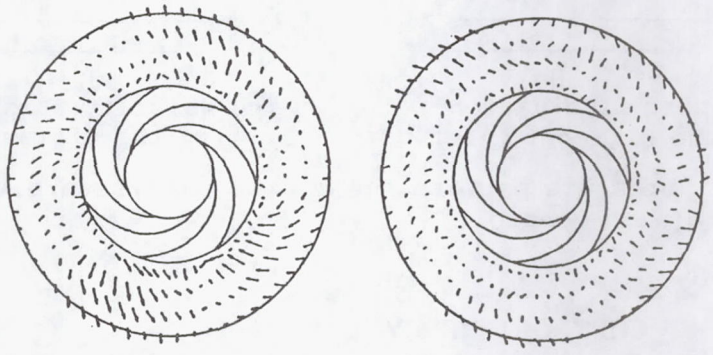

(a) ϕ=0.0 ⟶ v/u2=0.1

(b) ϕ=0.09 ⟶ v/u2=0.1

Fig.11 Velocity disturbance fields (with control)

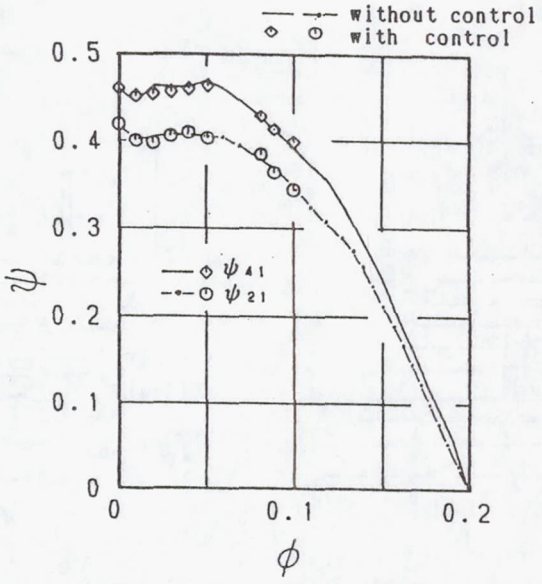

(a) Pressure performance curves

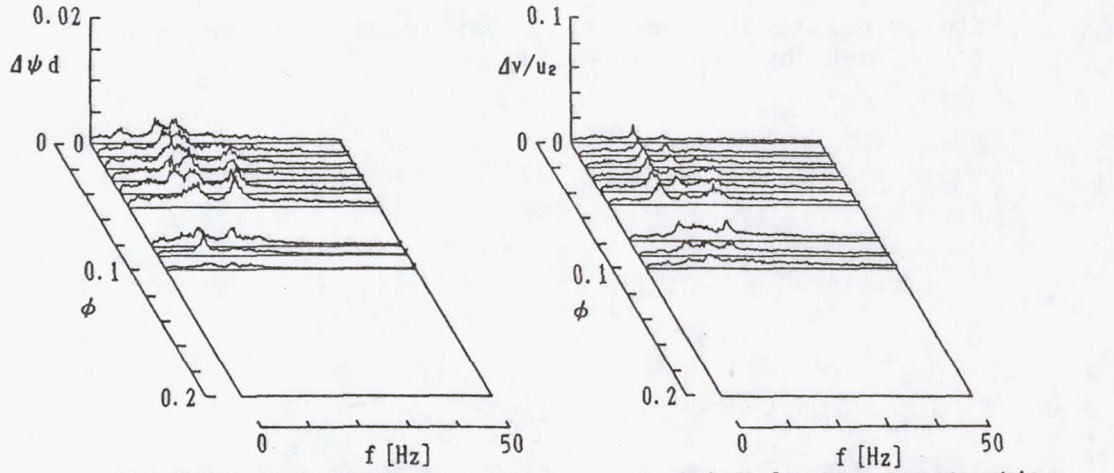

(b) Pressure fluctuation (at the diffuser inlet)

(c) Velocity fluctuation (at the diffuser outlet)

Fig.12 Static pressure performance curves and pressure, velocity spectra(with control)

CONSIDERATION OF CONTROL ENERGY

In this section, we discuss about the mechanisms of the present control. The displacement work done by the control flow on the fluid in the diffuser is given by

$$E = \frac{1}{T}\int_0^T p_d(t) \times q(t)\, dt \qquad \text{---------- (1)}$$

where q(t) is the flow rate of the control flow, and is estimated from the diffuser(p_d) and the air-chamber(p_a) pressure. The phase between the pressure difference and the control flow rate were calibrated dynamically in advance.

In Fig.13, the region with E>0 in the gain-phase plane is shown by hatching. We find that, for the most cases, the peak values of the spectra are increased (A.R.>1) in the region with E>0. Fig.14 shows the quantitative relation between E/L and A.R., where L is the work done by the impeller. We find that the magnitude of the rotating stall can be diminished by extracting a small amount of energy from the diffuser flow, while it requires relatively large amount of energy addition to increase the magnitude. The amplitude of the rotating stall is determine so that the energy supplied to the rotating stall by a certain unknown mechanism is balanced by a energy dissipation. From this point of view, Fig.14 can be looked upon to show the amount of the energy imbalance as a function of the amplitude ratio. The fact that E<0 for A.R.<1 implies the possibility of the passive control of diffuser rotating stalls. In fact, the amplitude of the pressure fluctuation is diminished by the addition of air-chambers without the active control.[ref.(13)] It is worth trying to design passive control systems as well as sophisticating the present active system.

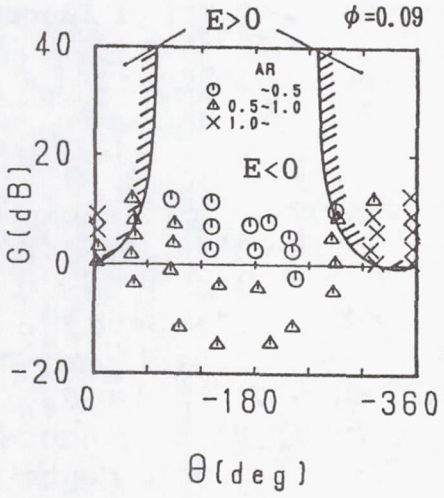

Fig.13 Effects of active control with Gain G and Phase θ

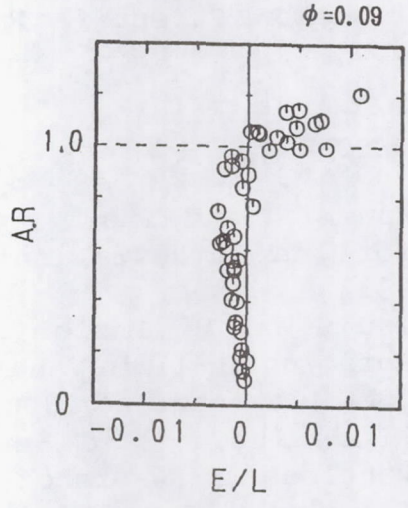

Fig.14 Relation between A.R. and E

(A.R.: ratio of the pressure amplitude
E : work of the control flow)

CONCLUSIONS

Major findings of present study are:

(1) Present active control can suppress the fundamental component of the diffuser rotating stall. The amplitude of the pressure fluctuation at the diffuser inlet can be suppressed about 1/10 of that without control. When the control is effective, the typical velocity disturbance of the rotating stall disappeared.
(2) The over all values of the pressure fluctuation could not be controlled by the present method. In this meaning, the "stall" itself could not be suppressed.
(3) It is made clear that the rotating stall is suppressed when the control flow has the phase such that the energy is subtracted out from the diffuser flow.
(4) From the relation between the energy flux of the control flow and the amplitude of the pressure fluctuation, an important information is obtained concerning the energy supply and dissipation in the vaneless diffuser rotating stall.
(5) The energy imbalance increases largely near the balancing point as the increase of the amplitude of the rotating stall.

Present study was supported by the Grant-In-Aid for Developmental Scientific Research of the Ministry of Education.

REFERENCES

(1) Kaneki, T. and Eino, T., "Centrifugal Carbon Dioxide Compressor for Urea Synthesis Plant", Hitachi Review, 28-6, (1979), pp. 327-332
(2) Tsurusaki, H., Imaichi. K, and Miyake, R., "A Study on the Rotating Stall in Vaneless Diffusers of Centrifugal Fans", JSME International Journal., 30-260(1987), pp. 279-287
(3) Kinoshita, Y. and Seno, Y., "Rotating Stall Induced in Vaneless Diffusers of Very Low Specific Speed Centrifugal Blowers ", Trans. ASME, J. Eng. Gas Turbines Power, 107-2(1985), pp. 514-521
(4) Nishida, H., et al., "A Study on the Stall of Centrifugal Compressors", (in Japanese), Trans. JSME, 54-499, B(1988), pp. 589-594
(5) Jansen, W., "Rotating Stall in Radial Vaneless Diffuser", Trans. ASME, J. Basic. Eng., 86-4(1964), pp. 750-758

(6) Abdelhamid,A.N.,"Analysis of Rotating Stall in Vaneless Diffusers of Centrifugal Compressors",ASME Paper,80-GT-184, (1980)
(7) Moore,F.K.,"Weak Rotating Flow Disturbances in a Centrifugal Compressor with a Vaneless Diffuser", Trans. ASME,J.Turbomach.,111(1989),pp.442-449
(8) Tsujimoto,Y.,Acosta,A.J.,"Theoretical Study of Impeller and/or Vaneless Diffuser Attributed Rotating Stalls and Their Effects on Whirling Instability",Proc.IAHR Work Group on the Behavior of Hydraulic Machinery Under Steady Oscillatory Conditions,1987
(9) Paduand,J.,et al.,"Active Control of Rotating Stall in a Low Speed Axial Compressor", ASME Paper,91-GT-88(1991)
(10) Ffowcs Williams,J.E.,et at.,"Active Stabilization of Compressor Instability and Surge in Working Engine",ASME Paper,92-GT-88(1992)
(11) Yoshida,Y.,et al,"Rotating Stalls in Centrifugal Impeller/ Vaned Diffuser Systems",ASME FED Vol.107(1991), pp.125-130
(12) Tsurusaki,H.,Imaichi,K.and Kajino,Y."Vaneless Diffuser Rotating Stall in Centrifugal Fans",(in Japanese), Turbomachinery,12-6(1984),pp.323-332
(13) Amann,C.A.,Nordenson,G.E.and Skellenger,G.D.,"Casing Modification for Increasing the Surge Margin of a Centrifugal Compressor in an Automotive Turbine Engine", Trans.ASME,J.Eng.Power,97(1975)pp.329-336

CALCULATION OF FLUID/STRUCTURE INTERACTION AT PUMP IMPELLER SHROUD AREAS USING FINITE DIFFERENCE TECHNIQUES

T. Feng and R. Nordmann
University of Kaiserslautern
Kaiserslautern, Germany

1. INTRODUCTION

2. BULK-FLOW MODEL (CHILDS)

3. FD-CALCULATIONS (2D) FOR IMPELLER SHROUD AREA

- SHROUDS WITH ANGULAR WALLS (SULZER)
- EYE-SEAL
- BACK-SEAL (TEST PUMP B/E)

4. NONLINEARITIES

5. DYNAMIC COEFFICIENTS

- DEPENDENCE OF PRESSURE
- DEPENDENCE OF EFFICIENCY

6. PROBLEMS OF CALCULATION

- SIMPLIFICATION OF GEOMETRIES
- BOUNDERY CONDITIONS

7. CONCLUSIONS

Preceding Page Blank

BULK FLOW ANALYSIS

GEOMETRY

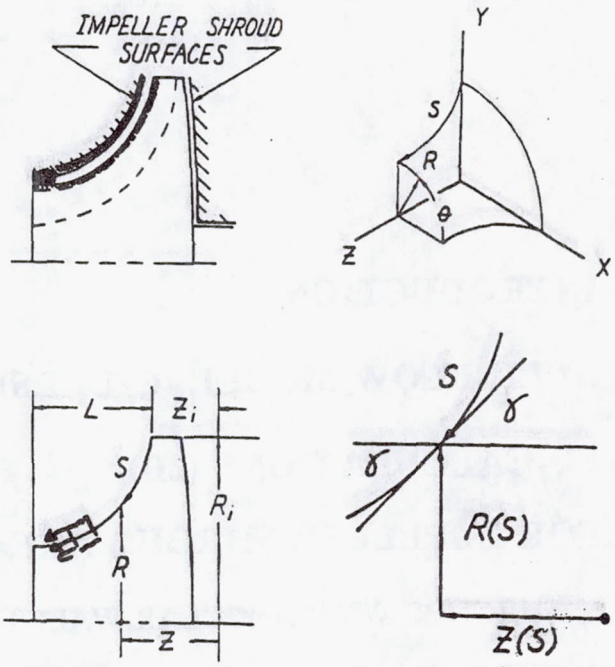

CONTINUITY EQUATION

$$\frac{\partial H}{\partial t} + \frac{\partial}{\partial S}(U_s H) + \frac{1}{R}\frac{\partial}{\partial \theta}(U_\theta H) + \left(\frac{H}{R}\right)\frac{\partial R}{\partial S} U_s = 0$$

PATH MOMENTUM EQUATION

$$-H\frac{\partial P}{\partial S} = -\rho H \frac{U_\theta^2}{R}\frac{dR}{dS} + \tau_{ss} + \tau_{sr} + \rho H\left(\frac{\partial U_s}{\partial t} + \frac{\partial U_s}{\partial \theta}\frac{U_\theta}{R} + \frac{\partial U_s}{\partial S} U_s\right)$$

CIRCUMFERENTIAL-MOMENTUM EQUATION

$$-\frac{H}{R}\frac{\partial P}{\partial \theta} = \tau_{\theta s} + \tau_{\theta r} + \rho H\left(\frac{\partial U_\theta}{\partial t} + \frac{\partial U_\theta}{\partial \theta}\frac{U_\theta}{R} + \frac{\partial U_\theta}{\partial S} U_s + \frac{U_\theta U_s}{R}\frac{\partial R}{\partial S}\right)$$

BULK FLOW ANALYSIS

BULK FLOW MODEL

$$\begin{Bmatrix} F_X \\ F_Y \\ M_Y \\ M_X \end{Bmatrix} = \left[\begin{array}{cc|cc} K & k & K_{\epsilon\alpha} & -k_{\epsilon\alpha} \\ -k & K & -k_{\epsilon\alpha} & -K_{\epsilon\alpha} \\ \hline K_{\alpha\epsilon} & k_{\alpha\epsilon} & K_\alpha & -k_\alpha \\ k_{\alpha\epsilon} & -K_{\alpha\epsilon} & k_\alpha & K_\alpha \end{array}\right] \begin{Bmatrix} X \\ Y \\ \alpha_Y \\ \alpha_X \end{Bmatrix}$$

$$+ \left[\begin{array}{cc|cc} C & c & C_{\epsilon\alpha} & -c_{\epsilon\alpha} \\ -c & C & -c_{\epsilon\alpha} & -C_{\epsilon\alpha} \\ \hline C_{\alpha\epsilon} & c_{\alpha\epsilon} & C_\alpha & -c_\alpha \\ c_{\alpha\epsilon} & -C_{\alpha\epsilon} & c_\alpha & C_\alpha \end{array}\right] \begin{Bmatrix} \dot{X} \\ \dot{Y} \\ \dot{\alpha}_Y \\ \dot{\alpha}_X \end{Bmatrix}$$

$$+ \left[\begin{array}{cc|cc} M & m & M_{\epsilon\alpha} & -m_{\epsilon\alpha} \\ -m & M & -m_{\epsilon\alpha} & -M_{\epsilon\alpha} \\ \hline M_{\alpha\epsilon} & m_{\alpha\epsilon} & M_\alpha & -m_\alpha \\ m_{\alpha\epsilon} & -M_{\alpha\epsilon} & m_\alpha & M_\alpha \end{array}\right] \begin{Bmatrix} \ddot{X} \\ \ddot{Y} \\ \ddot{\alpha}_Y \\ \ddot{\alpha}_X \end{Bmatrix}$$

FINITE DIFFERENCE METHOD

Navier-Stokes-Equations

a) Axial Momentum Equation
b) Radial Momentum Equation
c) Circumferential Momentum Equation

$$\frac{\partial U_i}{\partial t} + U_j \frac{\partial U_i}{\partial x_j} = -\frac{1}{\rho}\frac{\partial P}{\partial x_i} + \frac{\mu}{\rho}\frac{\partial^2 U_i}{\partial x_j \partial x_j}$$

Continuity Equation

$$\frac{\partial U_i}{\partial x_i} = 0$$

To solve by finite difference method

FINITE DIFFERENCE METHOD

The time-averaged NS-Equations

Actual quantity = Mean value + Random fluctuation.

$u = \bar{u} + u'$

$v = \bar{v} + v'$

$w = \bar{w} + w'$

$p = \bar{p} + p'$

Definition:

$$\bar{u} := \frac{1}{\tau}\int_0^{\tau} u(t)dt$$

=> NS Equations

$$\frac{\partial \bar{u}_i}{\partial t} + \bar{u}_j \frac{\partial \bar{u}_i}{\partial x_j} = -\frac{1}{\rho}\frac{\partial \bar{p}}{\partial x_i} + \frac{1}{\rho}\frac{\partial}{\partial x_j}\left\{\frac{\partial u_i}{\partial x_j} - \rho\overline{u'_i u'_j}\right\}$$

Continuity Equation

$$\frac{\partial \bar{u}_i}{\partial x_i} = 0$$

Problem:

$\rho\overline{u'_i u'_j}$ **unknown**

FINITE DIFFERENCE METHOD

Boussinesq Approximation:

$$\rho\overline{v'u'} = -\mu_t\left\{\frac{\partial\bar{u}}{\partial r}+\frac{\partial\bar{v}}{\partial x}\right\}$$

where μ_t is the turbulent viscosity (isotropic)

Similar to laminar flow: (Newton's Flow)

$$\tau_{rx} = \mu_l\left\{\frac{\partial\bar{u}}{\partial r}+\frac{\partial\bar{v}}{\partial x}\right\}$$

Turbulence Model (Effective viscosity):

$$\mu_t = c_\mu\rho\frac{k^2}{\varepsilon}$$

k => Turbulence Energy

ε => Turbulent Energy Dissipation

Viscosity: (effective = laminar + turbulent)

$$\tau_{rx} = \rho\overline{v'u'} = \mu_e\left\{\frac{\partial\bar{u}}{\partial r}+\frac{\partial\bar{v}}{\partial x}\right\}$$

$$\tau_{rx_e} = \tau_{rx_l} + \tau_{rx_t} = (\mu_l + \mu_t)\left\{\frac{\partial\bar{u}}{\partial r}+\frac{\partial\bar{v}}{\partial x}\right\}$$

Impeller / Casing

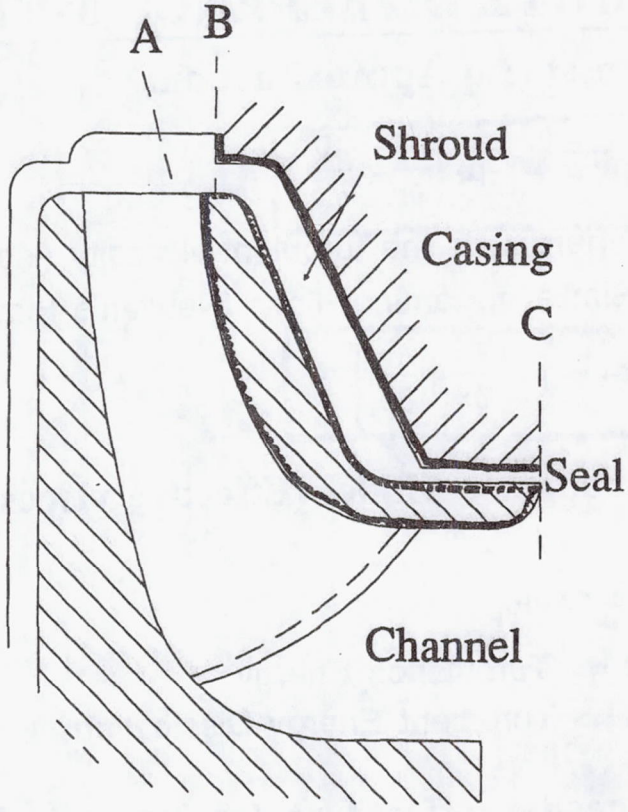

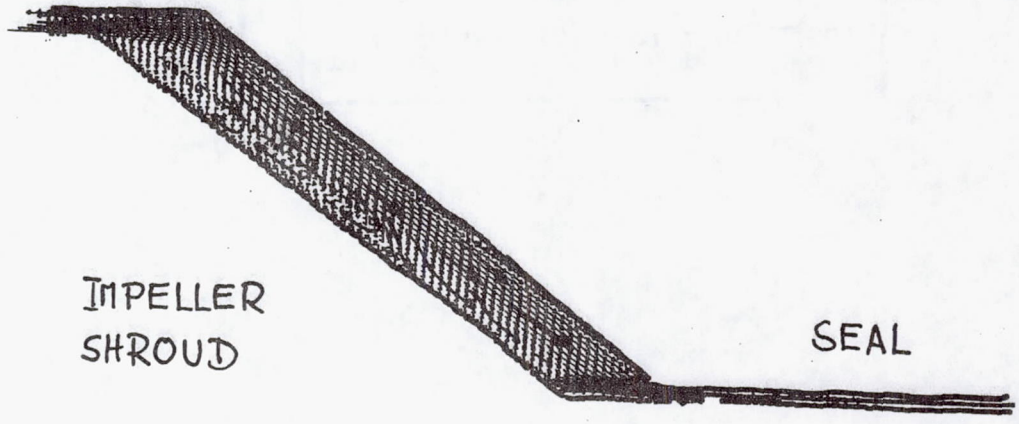

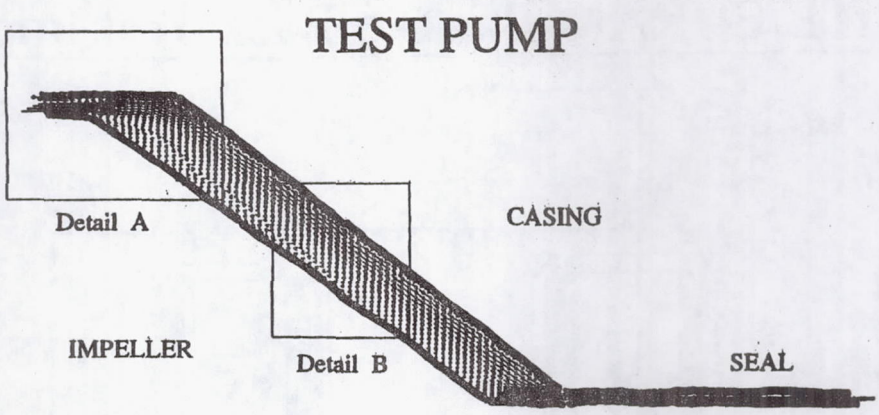
TEST PUMP
Detail A
CASING
IMPELLER
Detail B
SEAL

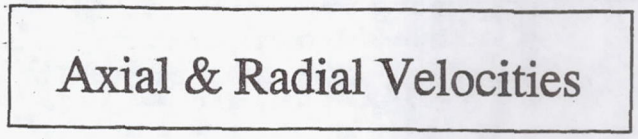
Axial & Radial Velocities

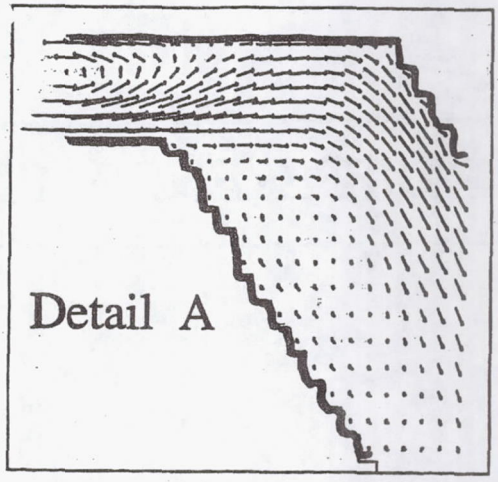
Detail A

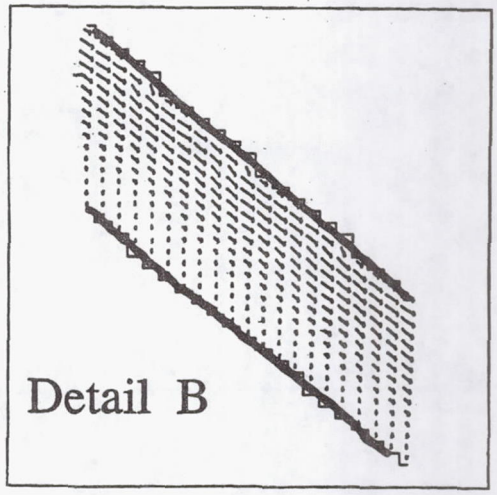
Detail B

BRITE/EURAM Back to Back Test Impeller

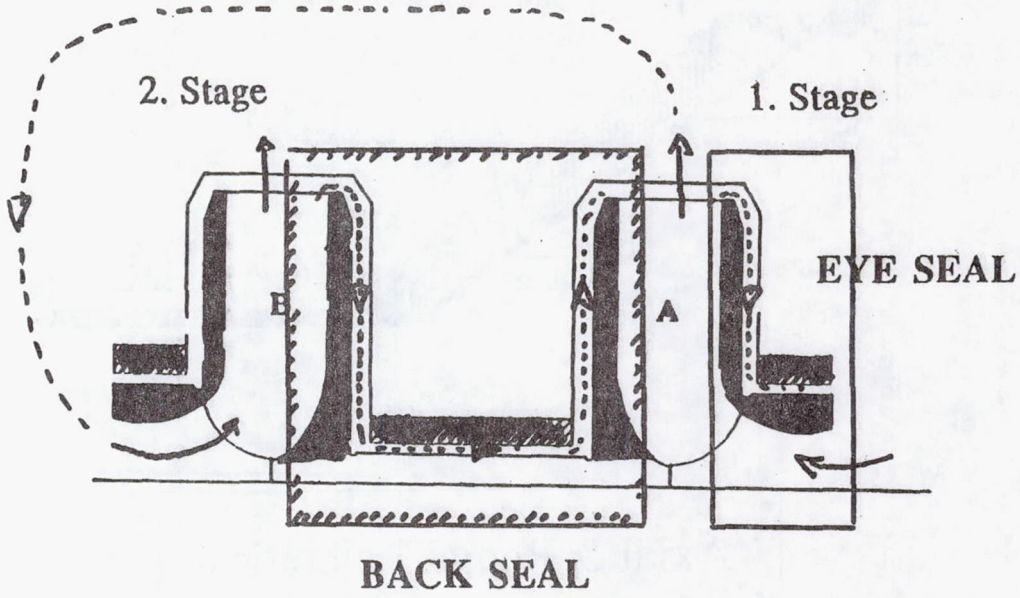

FINITE DIFFERENCE METHOD

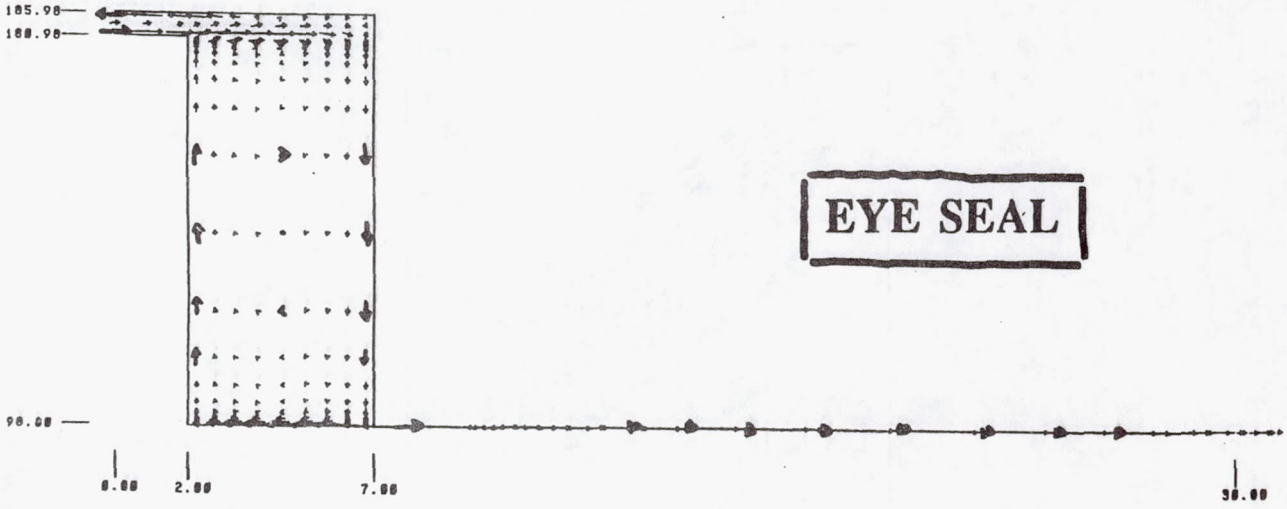

EYE SEAL

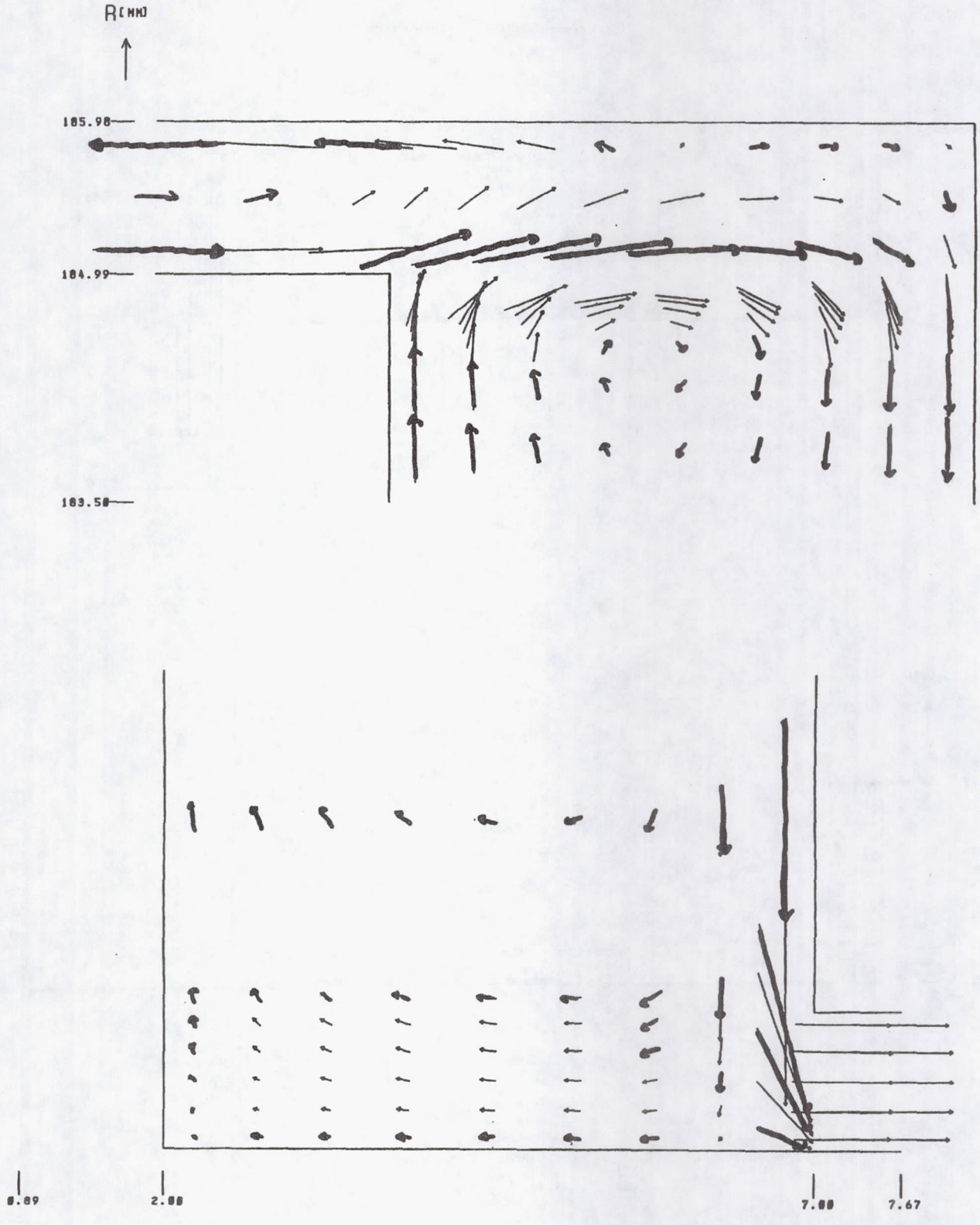
R[mm]
185.98
184.99
183.50
0.89
2.88
7.88
7.67

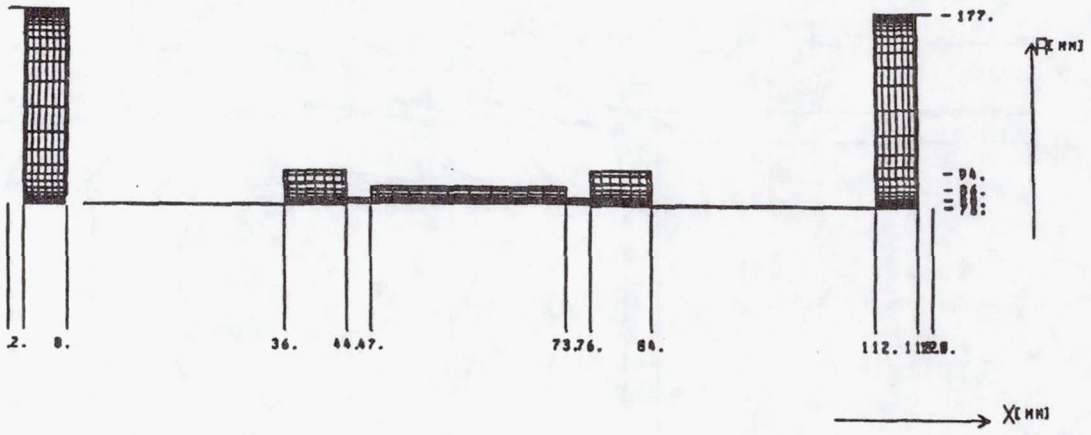
177.
R[MM]
94.
.2.
8.
36.
44.47.
73.76.
84.
112.
X[MM]

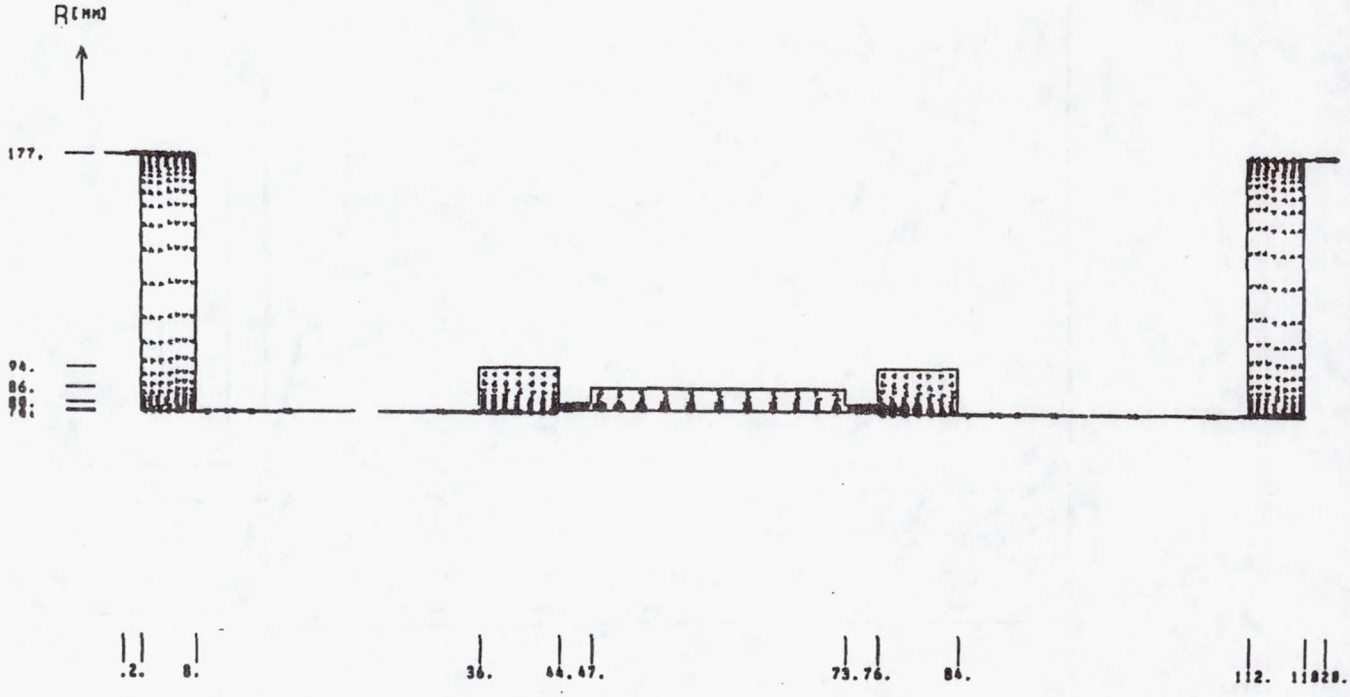
R[MM]
177.
94.
86.
.2.
8.
36.
44.47.
73.76.
84.
112.

AXIAL & RADIAL VELOCITIES

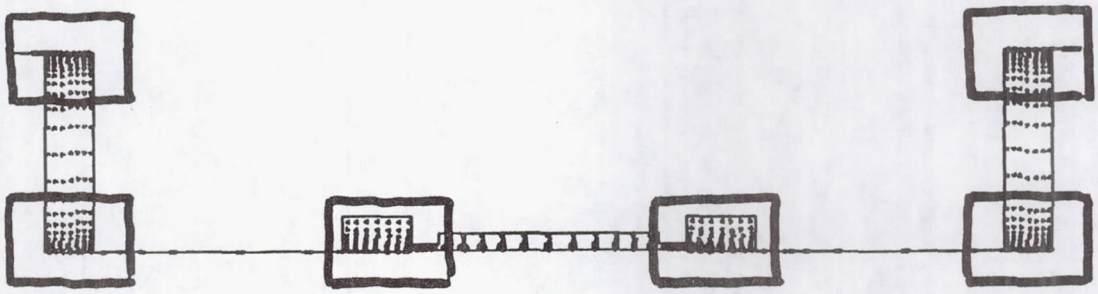

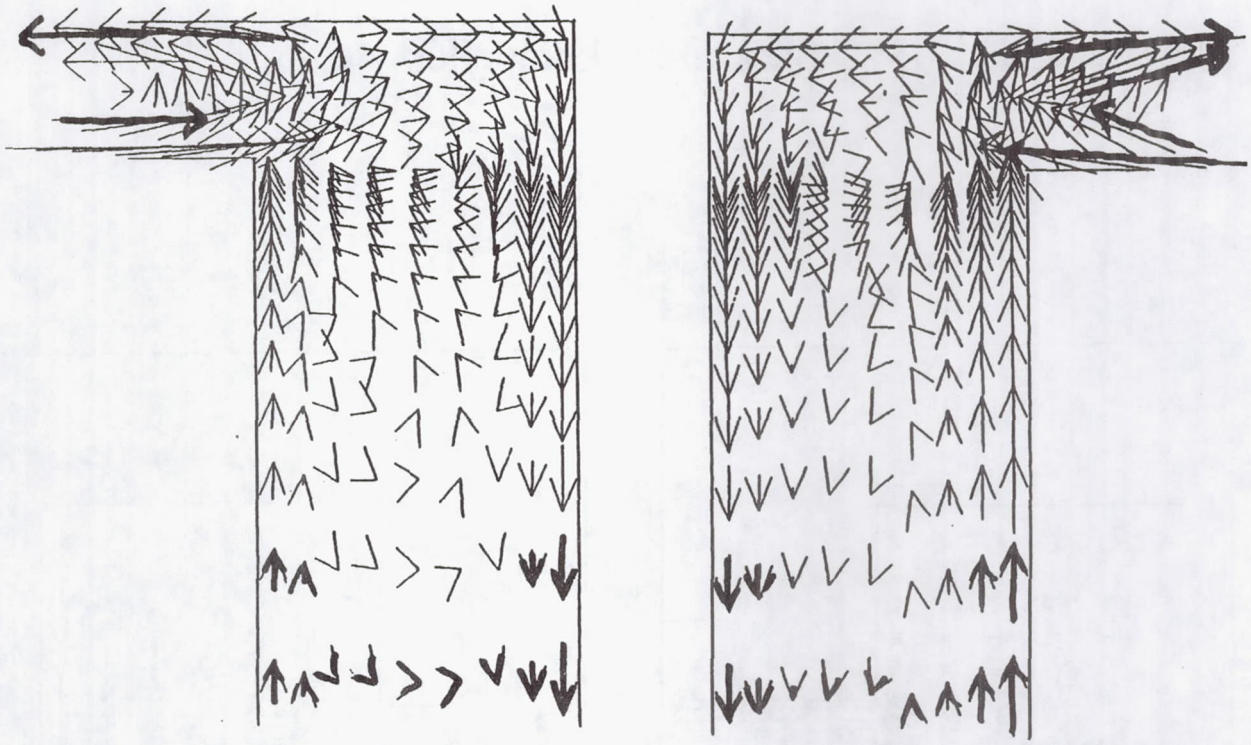

Rotating speed = 2950 rpm

Back to back impeller

Axial & Radial Velocities

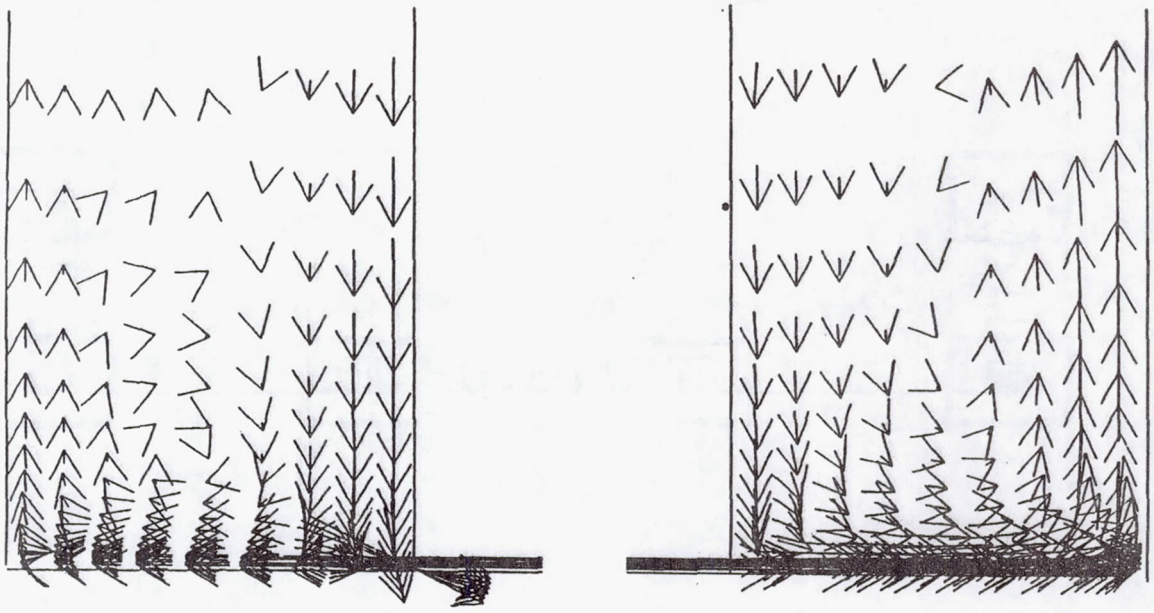

Rotating speed = 2950 rpm

Back to back impeller

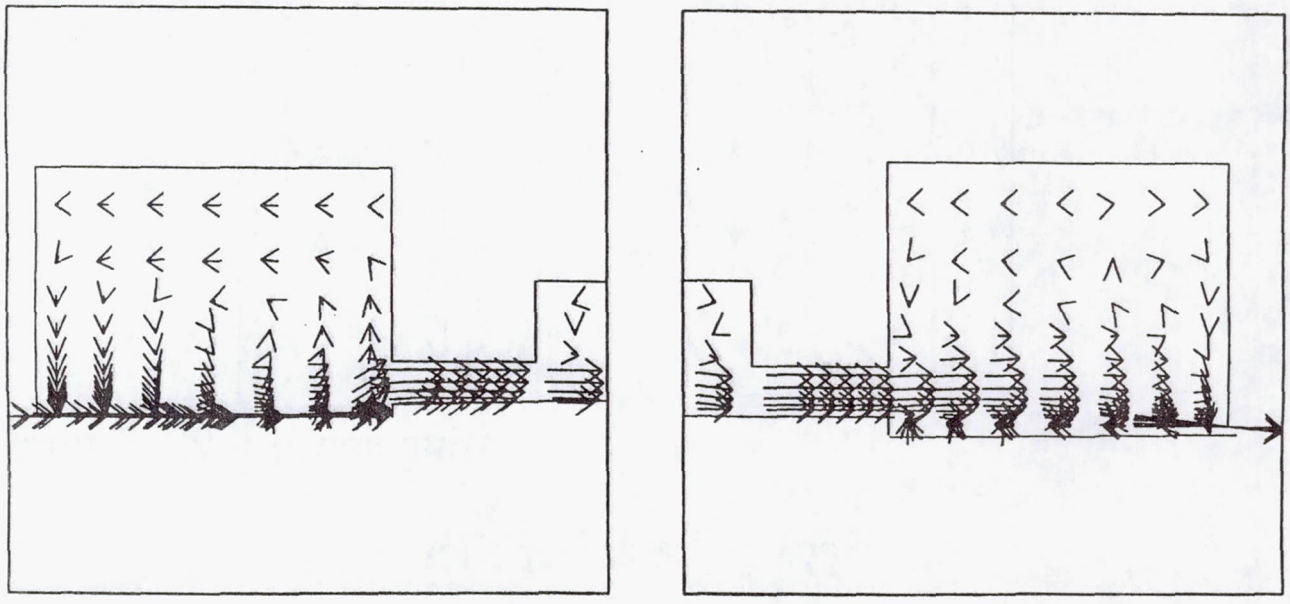

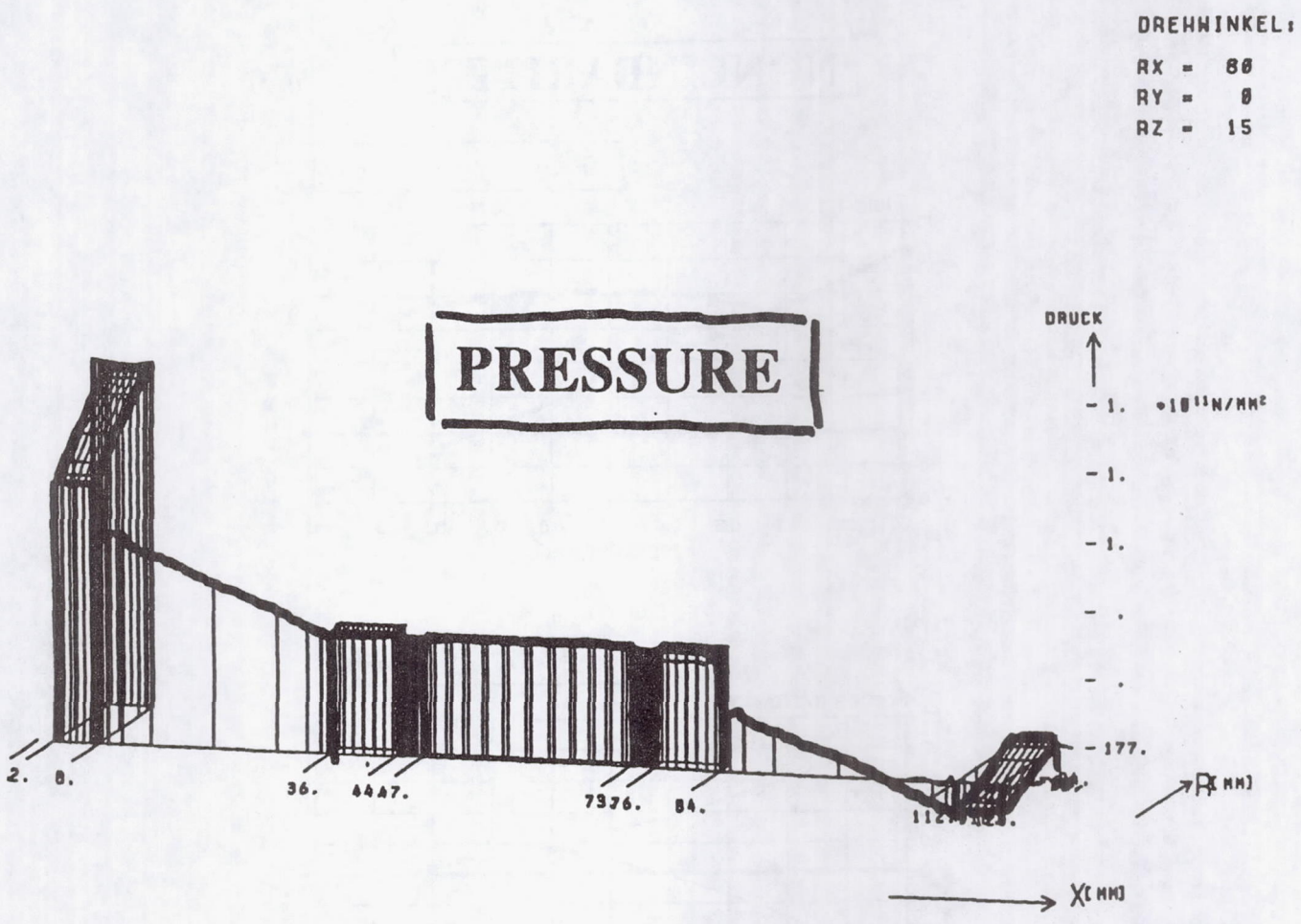
DREHWINKEL:
RX = 80
RY = 0
RZ = 15
PRESSURE
DRUCK
- 1. *10**11N/MM**2
- 1.
- 1.
- .
- .
- 177.
2.
8.
36.
4447.
7976.
84.
X[MM]

NONLINEARITIES

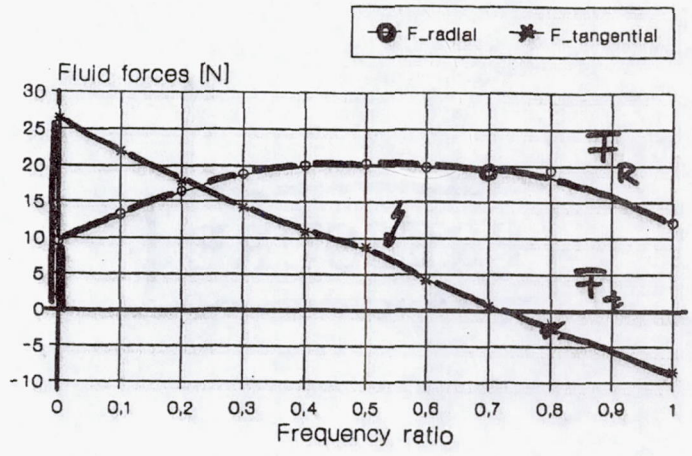

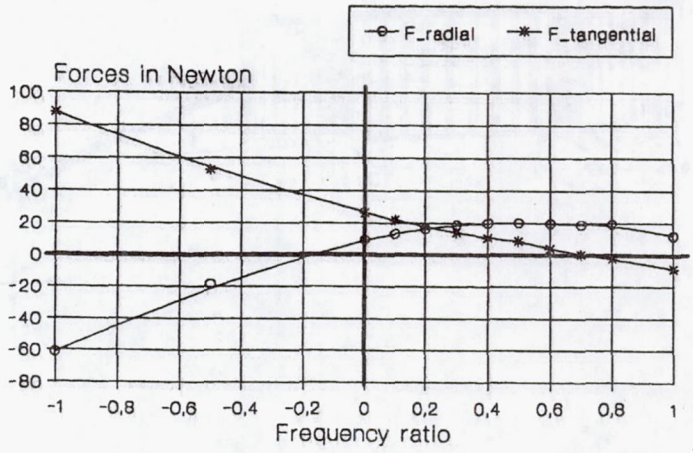

Coefficients (eye seal)

case	BEP	Δp	swirl	K [N/m]	k [N/m]	C [Ns/m]	c [Ns/m]	M [kg]
1	40%	9.63	0.683	0.3910E7	0.2161E7	9079.0	740.8	2.62
2	70%	9.28	0.626	0.3771E7	0.2061E7	8924.5	775.9	2.74
3	100%	8.89	0.569	0.3607E7	0.1952E7	8654.5	816.7	2.82
4	120%	8.62	0.531	0.3490E7	0.1874E7	8370.0	860.2	2.86

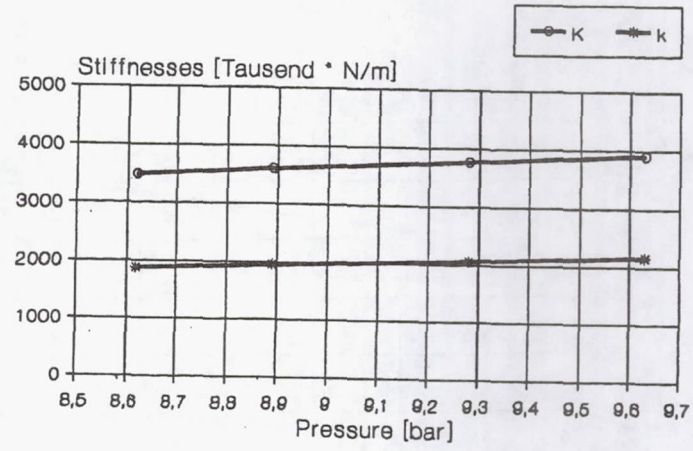

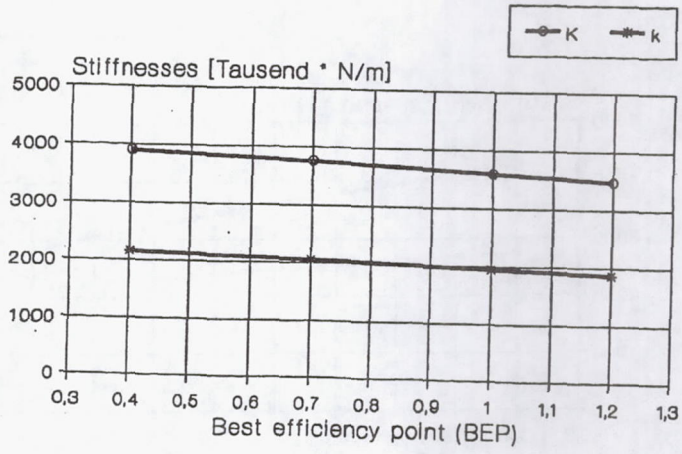

Coefficients (back seal)

case	BEP	Δp [bar]	swirl	K [N/m]	k [N/m]	C [Ns/m]	c [Ns/m]	M [kg]
5	40%	11.88	0.683	0.2852E7	0.2155E7	9998.6	12663.7	47.66
6	70%	11.00	0.626	0.3251E7	0.2339E7	10389.7	13449.3	50.54
7	100%	9.74	0.569	0.3767E7	0.2567E7	10819.1	13117.0	49.24
8	120%	8.76	0.531	0.4131E7	0.2726E7	11194.5	13500.3	50.75

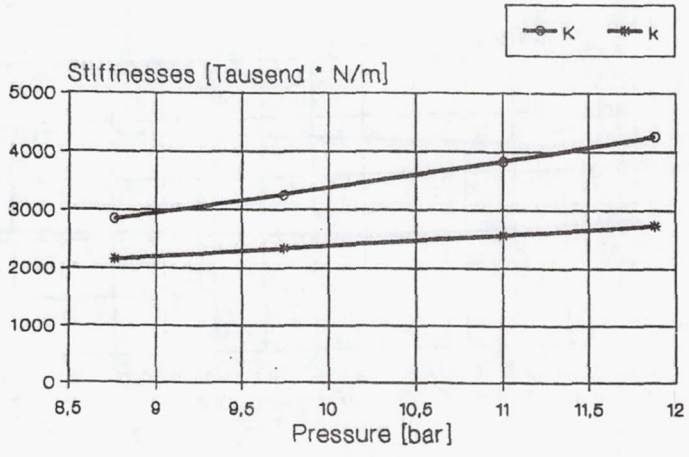

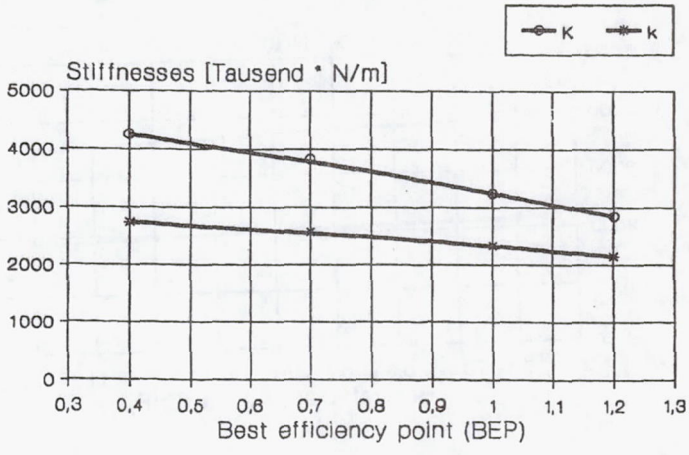

Influence of impeller/casing geometries

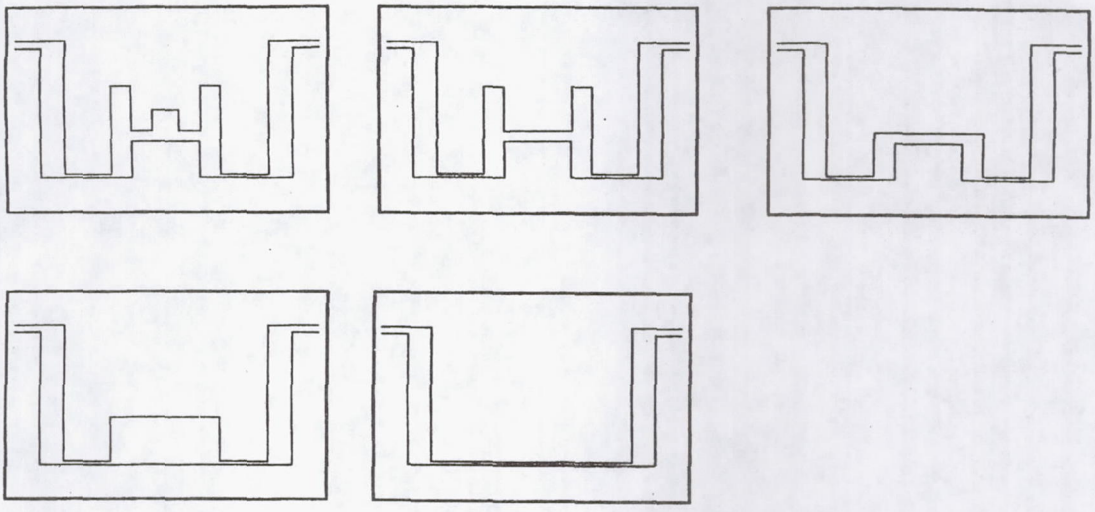

70% BEP 11.bar	case	K	k	D	d	M
	1	0.3831E7	0.2571E7	10902	8754	32.73
	2	0.3864E7	0.2680E7	11207	9868.6	35.62
	3	0.3528E7	0.3172E7	13058	11030	39.60
	4	0.2409E7	0.3017E7	11768	11059	37.30
	5	0.4231E7	0.1760E8	0.1005E6	30467	99.23

Session II

Seals

Preceding Page Blank

AN EXPERIMENTAL STUDY ON THE STATIC AND DYNAMIC CHARACTERISTICS OF PUMP ANNULAR SEALS WITH TWO PHASE FLOW

T. Iwatsubo and T. Nishino
Kobe University, Rokko
Nada, Kobe, Japan

Abstract

A new test apparatus is reconstructed and is applied to investigate static and dynamic characteristics of annular seals leaked by two phase flow (gas and liquid) for turbopumps. The fluid forces acting on the seals are measured for various parameters such as void ratio, the preswirl velocity, the pressure difference between the inlet and outlet of the seal, the whirling amplitude, and the ratio of whirling speed to spinning speed of the rotor. Influence of these parameters on the static and dynamic characteristics is investigated from the experimental results. As a results, with regard to the two phase flow, as the void ratio increases, the flow induced force decreases. Another dynamic characteristics of two phase flow is as almost similer as that of the mono phase flow.

1. Introduction

A turbomachines such as a pump tends to be operated at high speed and high pressure in special sircumstances because of severe performance requirements. In the special sircumstances, the fluid force causes an instability of the rotating machine because of the noncontacting seal. So, it is necessary to make the dynamic behavior of two phase flow clear and to supply accurate data in order to predict and prevent the unstable vibration, and still more necessary to design a stable rotating machine.

Many theoretical and experimental analyses on the characteristics of noncontacting seals are reported for the monophase flow seal. As an experimental research on annular seals, Childs et al. (Refs. 2,3) investigated fluid forces acting on the seals and their characteristics with a test apparatus which has an eccentric rotor. Nordmann (Ref. 4) used an impulse force type test apparatus to carry out an experiment on the characteristics of annular seals. Kaneko et al. (Ref. 7), Kanki et al. (Ref. 8), and Hori et al. (Ref. 9) also reported their test results on the seals. All these results are important for the research on monophase flow annular seals.

The authors also investigated for the many types of seals, that is, annular seal, parallel groove seal, spiral seal and tri angle hale seal and also long annular seal for investigating the effect of moment force. The dynamic characteristics of annular seals leaked by the two phase flow have not been investigated yet in various operating conditions.

This paper shows the experimental results obtained by an experimental apparatus which is newly redesigned to obtain a dynamic characteristics of two phase flow. In the test the fluid force acting on the seals is measured then radial and tangential forces of the seal flow and the stiffness, damping, and inertia coefficients are obtained. Influence

Preceding Page Blank

of the parameters such as whirling amplitude, pressure difference between the inlet and outlet of the seal, preswirl velocity, rotating and whirling speeds, and their directions is investigated. Then the effect of two phase flow on the dynamic characteristics of annular parallel seal is investigated.

2. Nomenclature

F_x, F_y	: Fluid forces in x and y directions
F_r, F_t	: Fluid forces in r and t directions
$K_{xx}, K_{yy}, K_{xy}, K_{yx}$	: Stiffness coefficients
$C_{xx}, C_{yy}, C_{xy}, C_{yx}$	: Damping coefficients
$M_{xx}, M_{yy}, M_{xy}, M_{yx}$	: Inertia coefficient
x, y, z	: Fixed coordinates (z: axial direction)
r, t	: Radial and tangential coordinates
$p(\phi, z)$	: Pressure distribution
$P(\phi)$	: Average pressure in axial direction
P_{in}	: Inlet pressure to the seal
P_{ex}	: Outlet pressure from the seal
ΔP	: Pressure difference between inlet and outlet of the seal
ω	: Spinning angular velocity of the rotor
Ω	: Whirling angular velocity of the rotor
e	: Whirling eccentricity of the rotor
ϕ	: Phase difference between principle force and displacement
R, D	: Rotor radius and diameter, respectively
L	: Seal length
C	: Seal clearance
V_t	: Preswirl velocity
V_{ts}	: Preswirl velocity without a rotating motion
V_a	: Fluid average velocity in axial direction
$\overline{\alpha}$	: mean void ratio
Q_g, Q_l	: flow rate of gas and liquid, respectively
$\overline{P}, P_{atm}$	: average pressure in the seal and outlet pressure

3. Experimental apparatus

3.1 Test seal apparatus

Figs.1 and 2 show assembly of the test apparatus and the layout of the test facility, respectively. In Fig.1, a working fluid, that is, water and gas, is injected through three pairs of swirl passages to accomplish the different inlet swirl velocities shown in cross section B. The water passes through the clearances of the seal and flows to outlets in both sides of the housing. Cool water and gas is continuously supplied to the tanks in

order to maintain constant temperature. The inlet part consists of four tubes connected with swirl passages for injecting the water and gas, and swirl speed is adjusted by a valve for air and two valves for water in order to obtain the arbitrary swirl velocity in the range of 0 - 15.0m/s. These valves are used in order to change the void ratio.

The seal assembly consists of a seal stator and a seal rotor. The seal rotor, of which diameter is 70mm, is connected to the motor by a flexible coupling. The motor is controlled in the speed range 0 - 3500r.p.m. by an electric inverter, which also selects the rotational direction. The seal stator has holes to measure the dynamic pressure in the seal, as shown in cross section C. Both long and short seals have three holes in axial direction and four holes in x and y directions. The dynamic pressure is measured by the strain gauge type pressure gauge shown in cross section C. The fluid dynamic force acting on the stator is also directly measured by the load cells shown in cross section C for comparison with the data of the pressure transducers.

The bearing assembly has two ball bearings to make spinning and whirling motions. To make a whirling motion, an inside sleeve and an outside sleeve, which have a 0.05mm eccentricity to each other, are attached between the two bearings as shown in cross section A of Fig.1. The two eccentric sleeves can be rotated, relatively. So an arbitrary eccentricity can be adjusted in the range of 0 - 0.1mm. The sleeves of both sides are driven by a motor through the timing belts. The motor can also be controlled by an electric inverter in the rotating speed range of 0 - 3500r.p.m., and rotational direction can be selected by an inverter.

The two phase flow is made as shown in Fig.3, where gas is mixed by higher pressure a liquid. The inlet pressure of two phase flow is measured just before the seal.

The void ratio in two phase flow can be changed the pressures of water and gas by of valves and regulator.

3.2 Measuring instruments and methods

The measuring procedure illustrated in Fig.4 consists of four kinds of physical variables: that is, rotating and whirling speed, dynamic pressure in the seal, seal forces and displacement of the rotor. Signals from measuring instruments are recorded by a data recorder and analyzed by a computer.

The rotating and whirling speeds are measured by eddycurrent type pulse sensors and digital counters.

Dynamic fluid force can be directly measured by a load cell as shown in Fig.5. The force measured by the load cell is calibrated to revise the influence of the O - rings and the inertia of the seal.

An eddycurrent type displacement sensor is used to measure the displacement and this displacement is used as a reference signal to obtain the phase difference between the displacement and the flow induced force.

The test data are recorded by a data recorder and sent to the computer through an A/D converter. In the computer the pressure values are integrated in the circumferential direction to obtain the fluid force, then the characteristic coefficients are calculated.

A special pitot tube set is used to measure the preswirl velocity in the seal inlet, as shown in Fig.6. The static and total pressures are measured by the pressure transducers instead of the usual U - tube.

Axial flow velocity in seal is determined from the outlet flow velocity directly mea-

sured by a pitot tube.

The flux of water and gas is obtaind by measuring the leakage of unit period by cylinder.

The void ratio in the two phase flow is decided as average value between inlet and outlet of seal. Here, it is supposed that air is ideal gas and slip ratio between water and gas is 1 because the seal is set horizontally . At this time, we obtain flowing equation from the flux of water and gas and the pressure which averages one of inlet and outlet.

$$\overline{\alpha} = \frac{P_{atm} Q_g}{\overline{P}\left(Q_l + \frac{P_{atm}}{\overline{P}} Q_g\right)} \tag{1}$$

Seal dimensions that is used for the test and experimental conditions are shown in the table 1,2.

3.3 Calibration and measuring error

As a preliminary test, the static and the dynamic characteristics of measuring instruments, i.e. the pressure transducer, the load cell and the pitot tube, are calibrated.

Dynamic calibration of the load cell was done in various working conditions. A periodic force was excited on the seal by a shaker, and the force was simultaneously measured by strain gauges attached to the shaking rod and by the load cell fixed on the other side. These data were used to calibrate the measured data in the real test.

A pitot tube set was used to measure the inlet preswirl velocity. Its pitot tube coefficient for calibration was determined by means of a standard pitot tube.

4. Calculation of fluid force and characteristic coefficients

It is assumed that the motion equation of the rotor system is represented as follows

$$[m]\{\ddot{x}\} + [C]\{\dot{x}\} + [K]\{x\} = \{f(t)\} - \{F\}$$

where [M], [C], [K] are the mass, the damping, and the stiffness matrix and { F(t) } is the force vecter. { F } = { F_x F_y}^{t} is the fluid reaction force acting on a rotor and is represented as a linear function of rotor displacement, velocity and acceleration, as follows.

$$-\begin{Bmatrix} F_x \\ F_y \end{Bmatrix} = \begin{bmatrix} M_{xx} & M_{xy} \\ M_{yx} & M_{yy} \end{bmatrix} \begin{Bmatrix} \ddot{x} \\ \ddot{y} \end{Bmatrix} + \begin{bmatrix} C_{xx} & C_{xy} \\ C_{yx} & C_{yy} \end{bmatrix} \begin{Bmatrix} \dot{x} \\ \dot{y} \end{Bmatrix} + \begin{bmatrix} K_{xx} & K_{xy} \\ K_{yx} & K_{yy} \end{bmatrix} \begin{Bmatrix} x \\ y \end{Bmatrix} \tag{2}$$

For a small whirling motion about a center position, the relation of the coefficients may be expressed by

$$M_{xx} = M_{yy}, \quad M_{yx} = M_{xy} = 0, \quad C_{xx} = C_{yy},$$
$$C_{yx} = -C_{xy}, \quad K_{xx} = K_{yy}, \quad K_{yx} = -K_{xy} \tag{3}$$

where the cross-coupled inertia coefficient is neglected because it is negligible small.

A rotating coordinate system rotating with the rotor is adopted to analyze the fluid force easily. The relation between a fixed coordinate system and a rotating coordinate system is illustrated in Fig.7, where F_x and F_y are represented by the radial force F_r and the tangential force F_t. Details to obtain the fluid force is shown in (Ref.11), so these are not written here.

5. Experimental results and discussions

5.1 Visualization

We visualize a flow patteern of two phase flow in the part of seal made of acryle. As a result, we can observe that bubble of air in two phase flow is fine and two phase flow is homogeneous bubbly flow because of high rotating speed of the rotor.

5.2 Relative Uncertainly

Since the discrepancy of the fluid forces measured by the pressure transducer and load cell are very few, for the void ratio $\overline{\alpha}$=0 as shown in Fig.8, it is decided that the accuracy of the test data is very good. So in this test the fluid force measured by the load cell is used as the experimental results in this discussion.

Fig.9 show the time history of fluid force measured by the load cell for mean void ratio $\overline{\alpha}$=0 and 0.45. From these data it is known that the two phase flow has inherent random noise.

In the measuring process as the void ratio was increased, random vibration due to the two phase flow became very large. So the variance of the measured vibration data become large, but these are not the measurement error.

5.3 Effect of inlet pressure

Fig.10 shows the effect of inlet pressure on the radial and tangential forces. From these data it is known that the flow induced force increases with increasing the inlet pressure and its tendency is not change with increasing the void ratio. From this result it is known that the experiment can be done by constant inlet pressure to investigate the effect of void ratio on the flow induced force.

5.4 Effect of spinning speed

Figs.11(a) to (d) show the effect of spinning speed on F_r/e and F_t/e for different void ratio. Fig.(a) shows for void ratio zero in order to compare the result with another void ratio. Figs.(b) to (d) show F_r/e and F_t/e for the void ratio $\overline{\alpha}$=0.25, 0.45 and 0.7 in the case of various spinning speeds. From these results it is known that the fluid force decreases with the increase of void ratio. The variation of radial force increases with increase of void ratio. These phenomena are seemed to be occurred by the compressibility of the gas. For the tendency of the tangential and radial forces for rotating speed is same, and as rotating speed is increased, the fluid force increases.

Fig.12 shows the equivalent spring coefficients and damping coefficients and added mass. From these figures it is known that as the void ratio is increased, the spring coefficients and damping coefficients decrease as discussed in the result of F_r/e and F_t/e. Fig.13 shows the whirl frequency ratio,

$$f = K_{xy}/C_{xx}\Omega \tag{4}$$

and fluid force F/e, which is important to evaluate the instability force ;

$$F/e = \frac{1}{e}\sqrt{F_r^2 + F_t^2} \tag{5}$$

From this figure it is known that the whirl frequency ratio decreases at $\overline{\alpha}$=0.25 and then increases for increase the void ratio. The whirl frequency ratio has large difference at $\overline{\alpha}$=0.7, because the variation of force due to two phase flow becomes large and the error of amplitude and phase may be large. In this void ratio region the fluid force F/e becomes small, then it seemed to be small effect on the rotor system. Conventionaly, the pump rotor is supported by bearings and seals in the operational condition, and the seal force act as a stabilizing force in the rotor system. In order to demonstrate the effect of two phase flow, we assume that a rotor system is stable and in this system the bearings act to unstable and the seals act to stable. In this case, if the seal force is decreased by the two phase flow as shown in Fig.13, this stabilizing seal force decreases and the rotor system may become unstable.

5.5 Effect of preswirl velocity

Figs.14(a) to (c) shows the effect of the whirl ratio ω/Ω on F_r/e and F_t/e for various preswirl velocities. In this case preswirl velocity ratio is 1.6 for ω=2500rpm. The results illustrate that the effect of preswirl on the fluid force is same tendency as the case of void ratio $\overline{\alpha}$=0 but it decreases as the void ratio increases.

Fig.15 shows the whirl frequency ratio versus preswirl velocity. It is known from this figure that the effect of preswirl velocity decreases as the void ratio increases. Therefore two phase flow of high void ratio does not affect on instability of rotor system.

6. Conclusions

The two phase flow induced force through annular seal are experimentally investigated for setting the parameter void ratio, rotating speed, whirl/spin ratio, preswirl velocity, inlet pressure. Then the following results are obtained,

(1) The void ratio is increased, random vibration due to the two phase flow becomes very large.

(2) The fluid force increases with increasing the inlet pressure and its tendency is not change with increasing the void ratio.

(3) The fluid force decreases with the increase of void ratio. These phenomena is occurred by the compressibility of the gas.

(4) Whirl frequency ratio which is proposed by D. Childs decreases a little at $\overline{\alpha}$=0.25, but in practical, it is not so much changed and as the fluid force decreases in high void ratio, instability force decreases.

(5) The effect of preswirl velocity decreases as the void ratio increases, so this effect dose not act as instability.

(6) Since the seal force is decreased by the two phase flow, this stabilizing seal force decrease, and rotor system may become unstable.

References

1. Black, H. F., Calculation of Forced Whirling and Stability of Centrifugal Pump Rotor System, Trans. ASME. J. Eng. Ind., (1974), 1076.

2. Childs, D. W., and Kim, C. H., Analysis and Testing for Rotordynamic Coefficient of Turbulent Annular Seal With Different, Directionally Homogeneous Surface-Roughness Treatment for Rotor and Stator Elements, NASA. Conf. Pub., (1982), 313.

3. Childs, D. W., Dynamic Analysis of Turbulent Annular Seal Based on Hirs' Lubrication Equation, Trans. ASME No.82-Lub-41.

4. Nordmann, R., and Massmann, H., Identification of Stiffness, Damping and Mass Coefficients for Annular Seals, I. Mech. E., (1984), 167.

5. Iwatsubo, T., Evalution of Instability Forces of Labyrinth Seal in Turbine or Compressors, NASA. Conf. Pub., (1980), 139.

6. Yang, B. C., Iwatsubo, T., and Kawai, R., A study on the Dynamic Characteristics of Pump Seal, (1st Report, In Case of Annular Seal with Eccentricity), Trans. JSME, Vol.49, No.445, (1983), 1636.

7. Kaneko, H., Iino, T., and Takagi, M., An Experimental Research on Dynamic Dharacteristics of Annular Pump Seals, (1st Report, Dynamic Characteristics in Case of Concentricity), Proc. JSME, No.820-3, (1982), 25.

8. Kanki, H., and Kawakami, T., Experimental Study on the Dynamic Characteristics of Pump Annular Seals, I. Mech. E., (1984), 159.

9. Kaneko, S., Hori, Y., and Tanaka, M., Static and Dynamic Characteristics of Annular Plain Seals, I. Mech. E., (1984), 205.

10. Kanemori, Y., and Iwatsubo, T., Experimental Study of Dynamic Characteristics of Long Annular Seal, Proc. 2nd China-Japan Joint Conf., Xi-an, (1987), 143.

11. T. Iwatsubo, et. al., The Experimental Study of on the Static and Dynamic Characteristics of Pump Annular Seals, NASA Conf. Pub., 3026, 1988, PP.229.

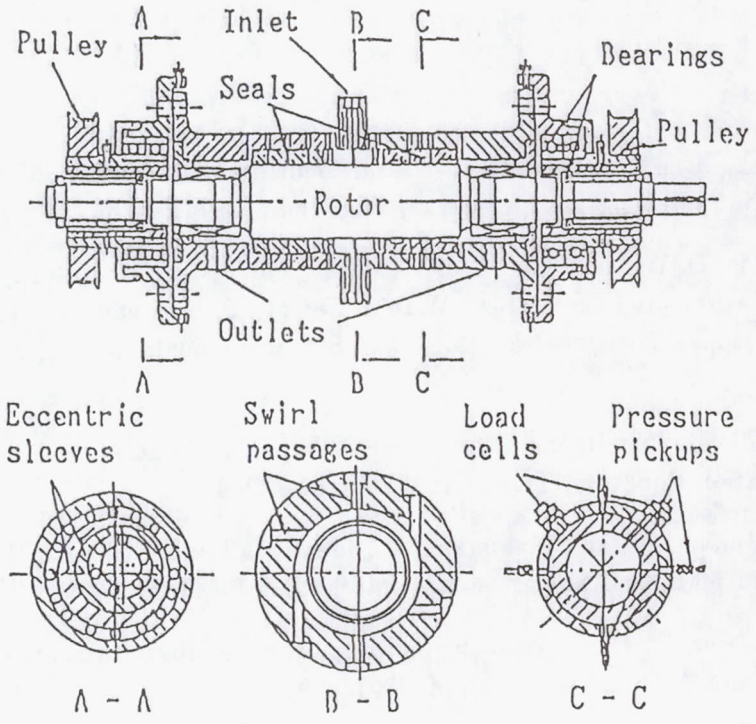

Fig.1 Test apparatus assembly

Table 1 Seal dimension

	Length (mm)	Diameter (mm)	L/D	Clearance (mm)
Plain Seal	70	70	1	0.5

Table 2 Experimental condition

Rotating speed	ω(rpm)	500 ~ 3500
Whirling speed	Ω(rpm)	±600 ~ ±2400
Whirling amplituide	$e(\mu m)$	50
Preswirl velocity without a rotating motion	Vts	-15 ~ 15
Temperature of water	T(°C)	19

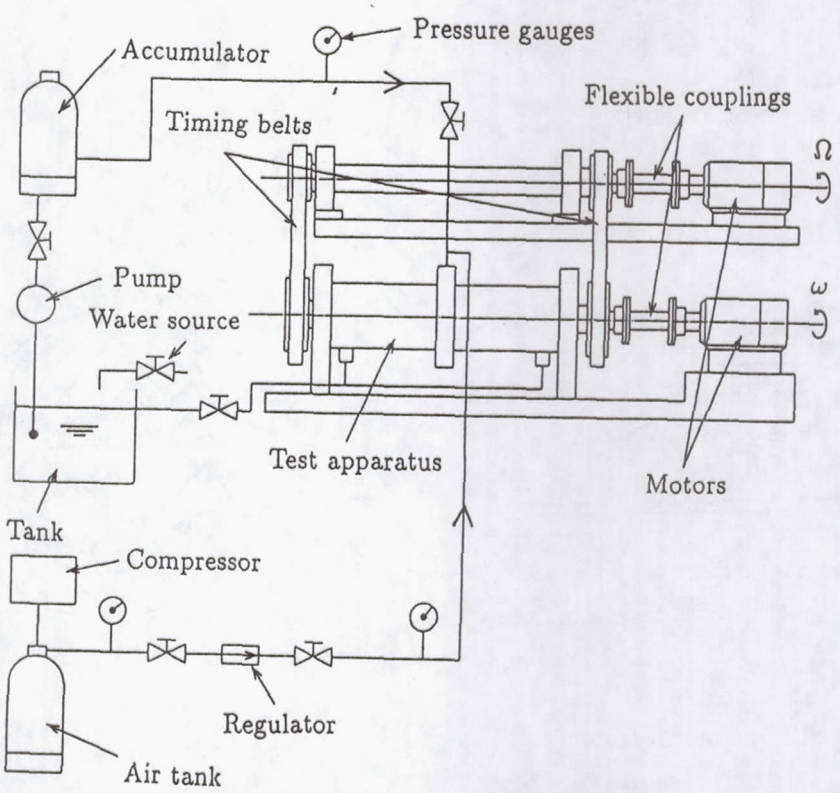

Fig.2 Test facility layout

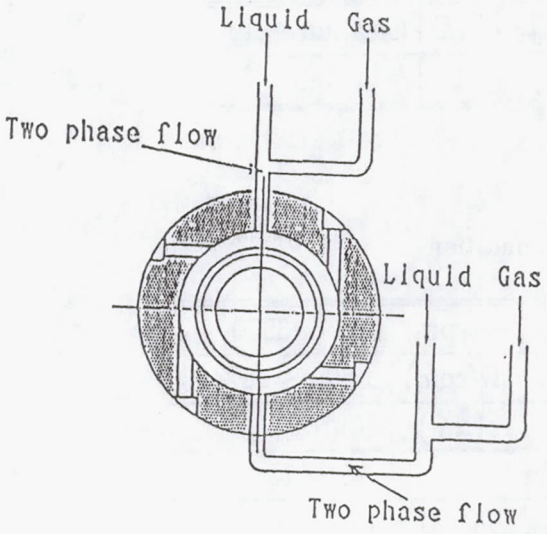

Fig.3 Detail of gas-liquid mixing device

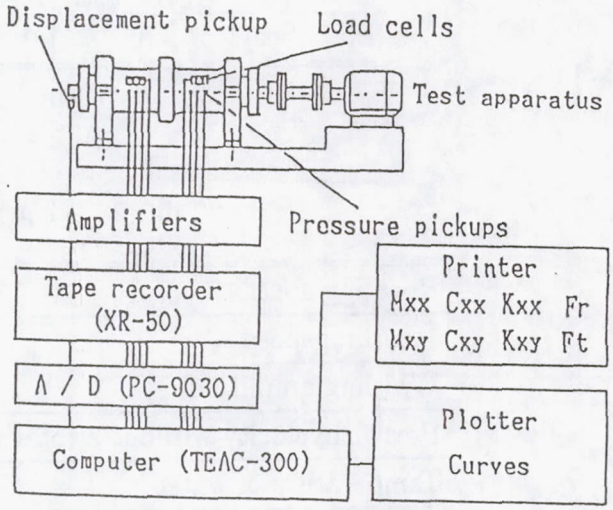

Fig.4 Analysis procedure

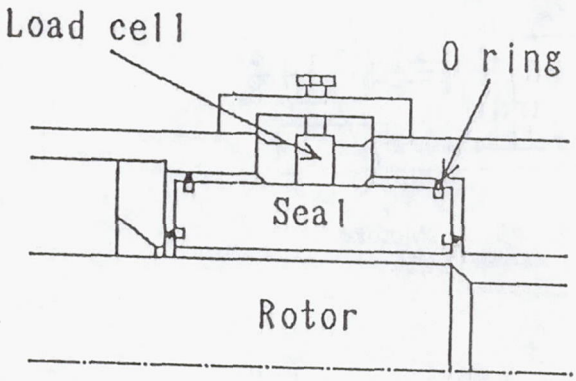

Fig.5 Detail of force measurement

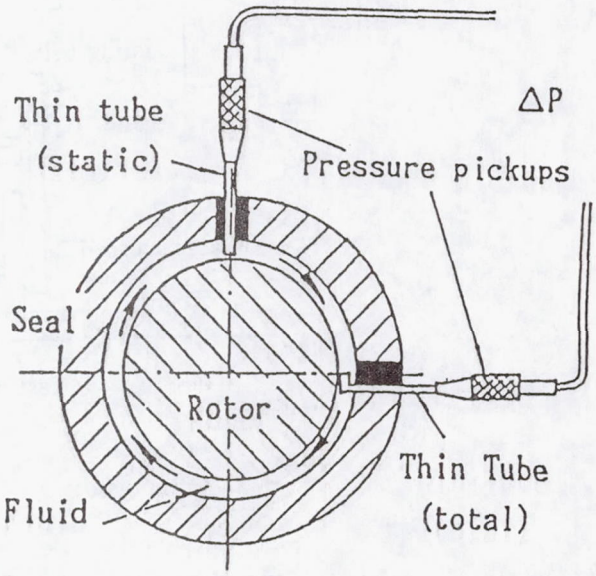

Fig.6 Detail of swirl velocity measurement

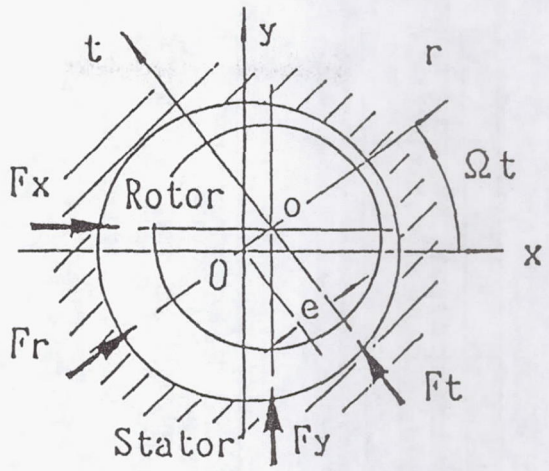

Fig.7 Model of annular seal

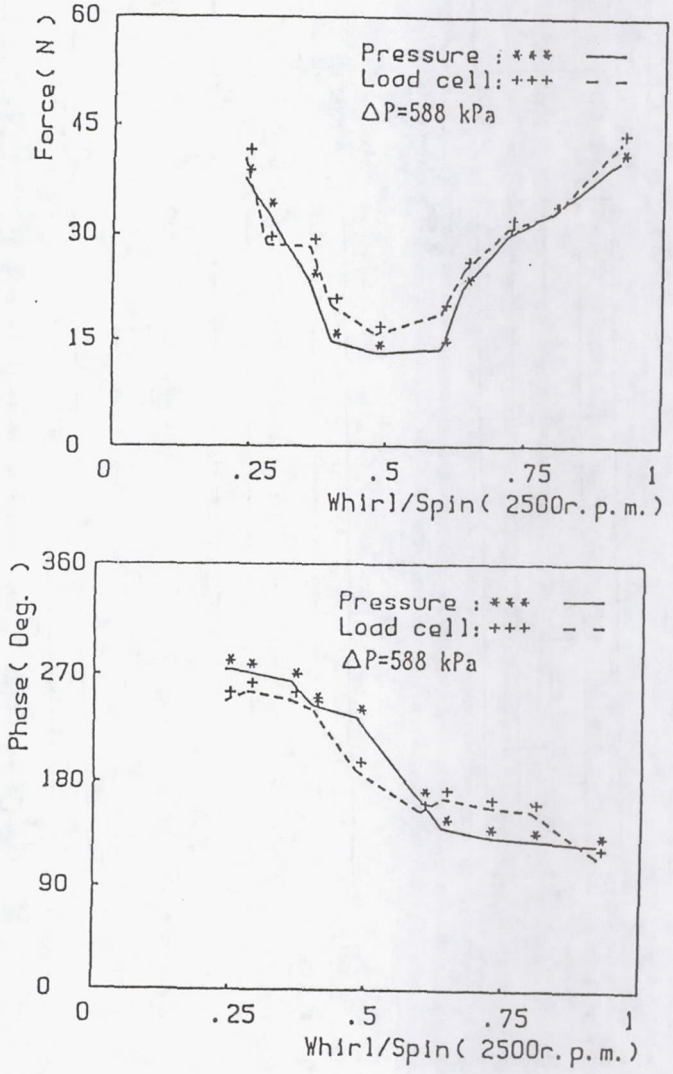

Fig.8 Results measured by two measuring methods

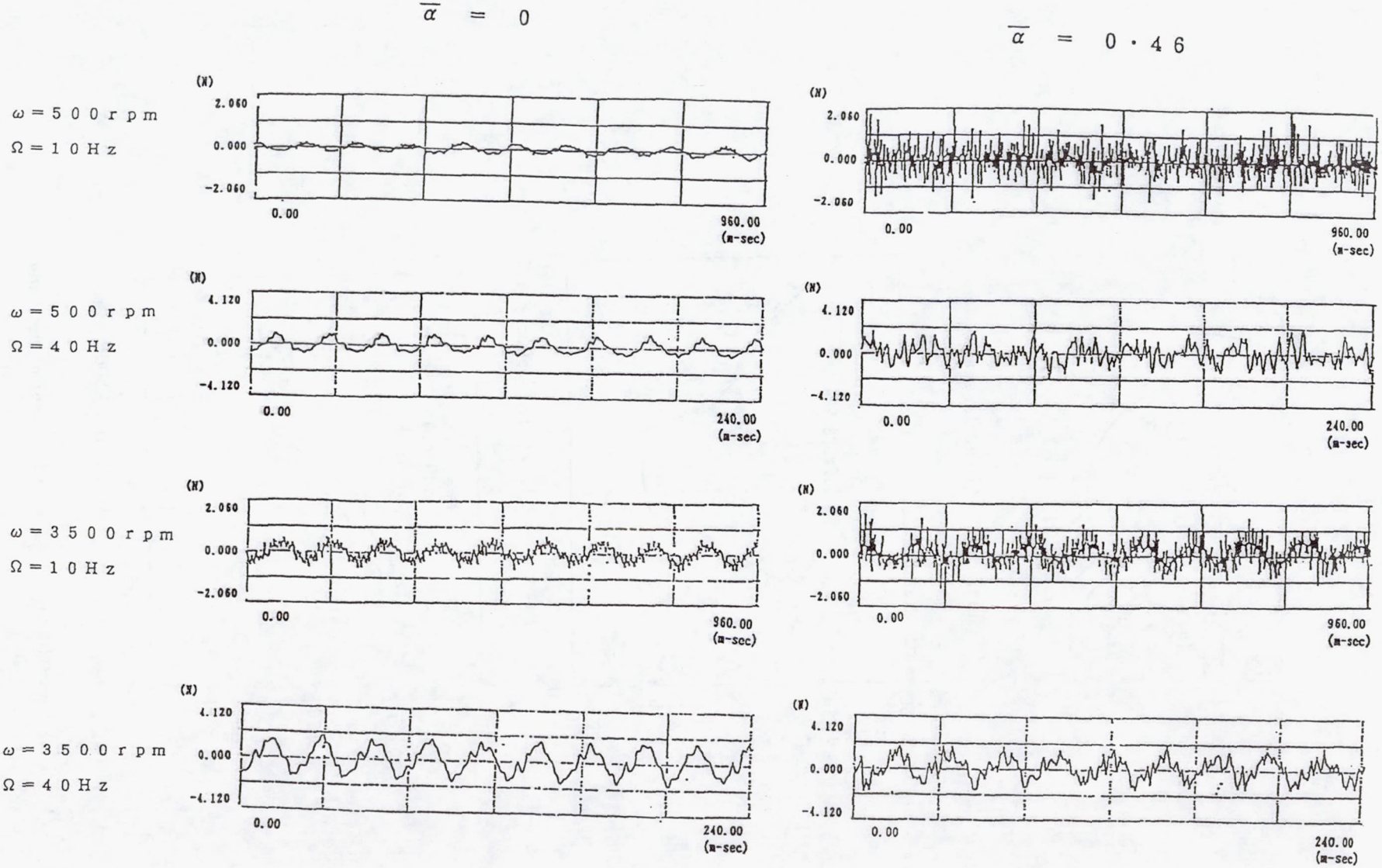

Fig.9 Time history of fluid force

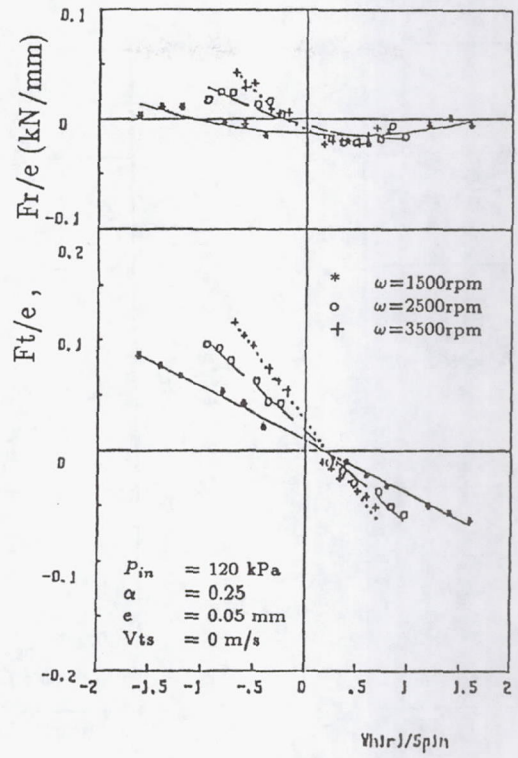

(a) $P_{in} = 120\text{k}P_a$

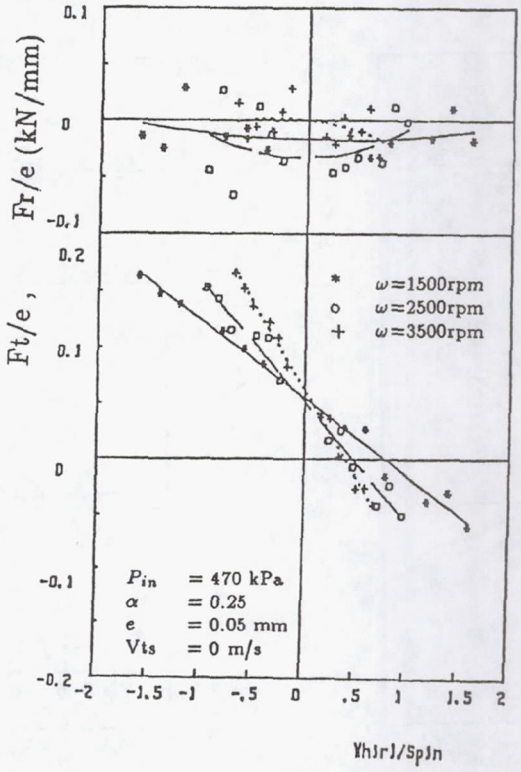

(b) $P_{in} = 470\text{k}P_a$

Fig.10 Radial and tangential forces for the constant void ratio

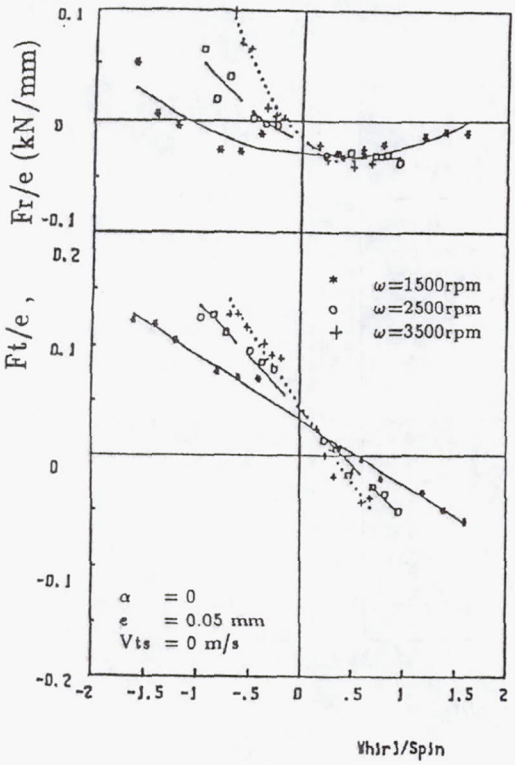

(a) $\bar{\alpha}$=0.0

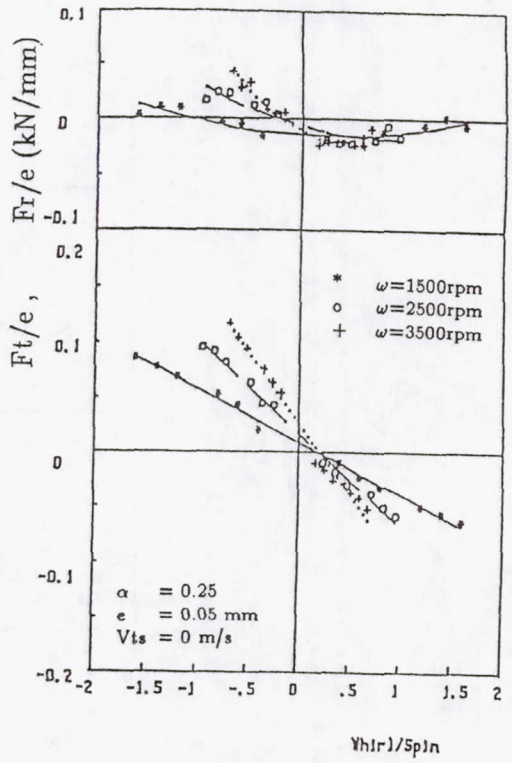

(b) $\bar{\alpha}$=0.25

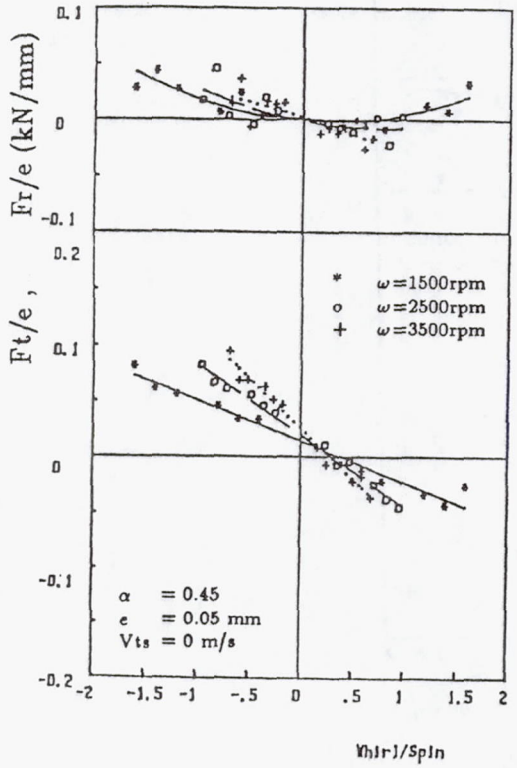

(c) $\bar{\alpha}$ = 0.45

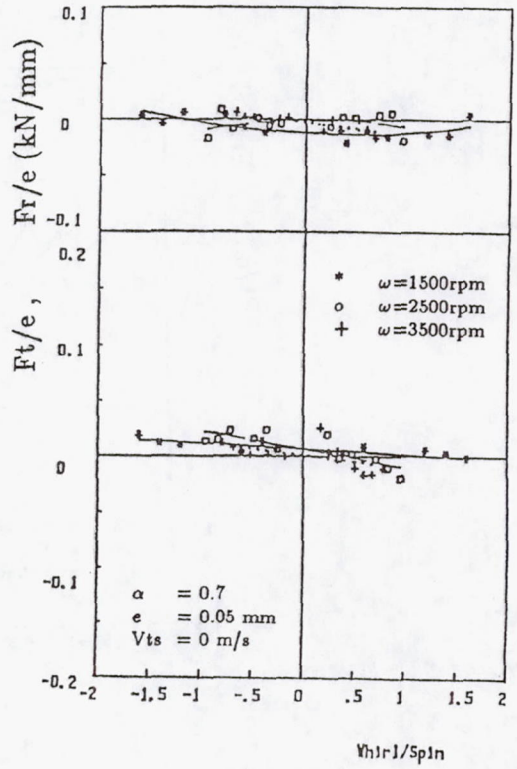

(d) $\bar{\alpha}$=0.7

Fig.11 Radial and tangential fluid forces for void ratios

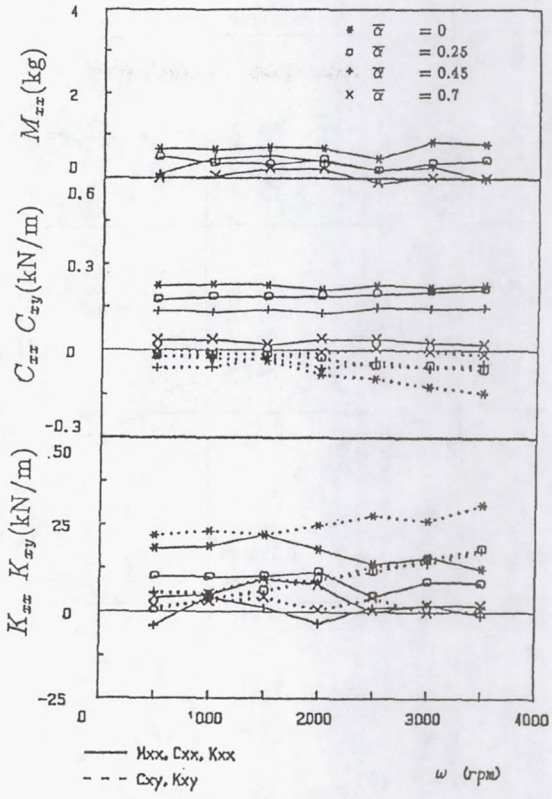

Fig.12 Fluid force cofficients for void ratios

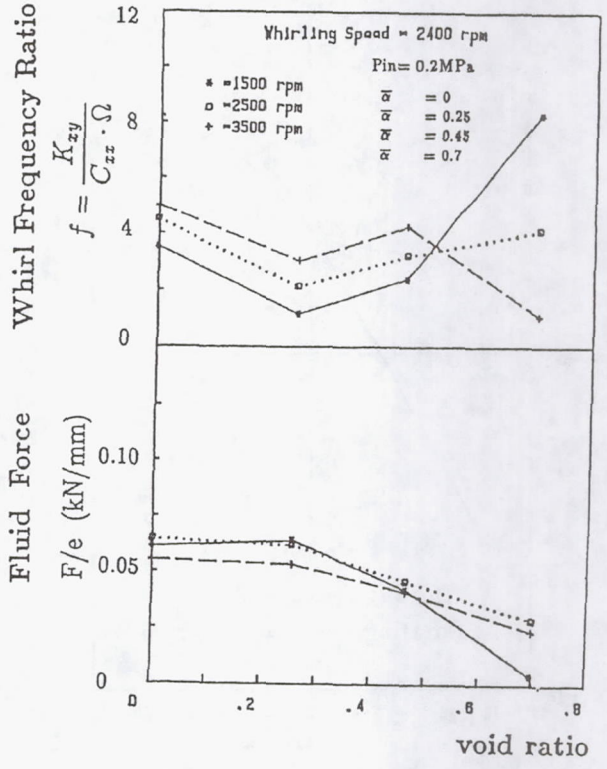

Fig.13 Whril frequency ratio and fluid force versus void ratio

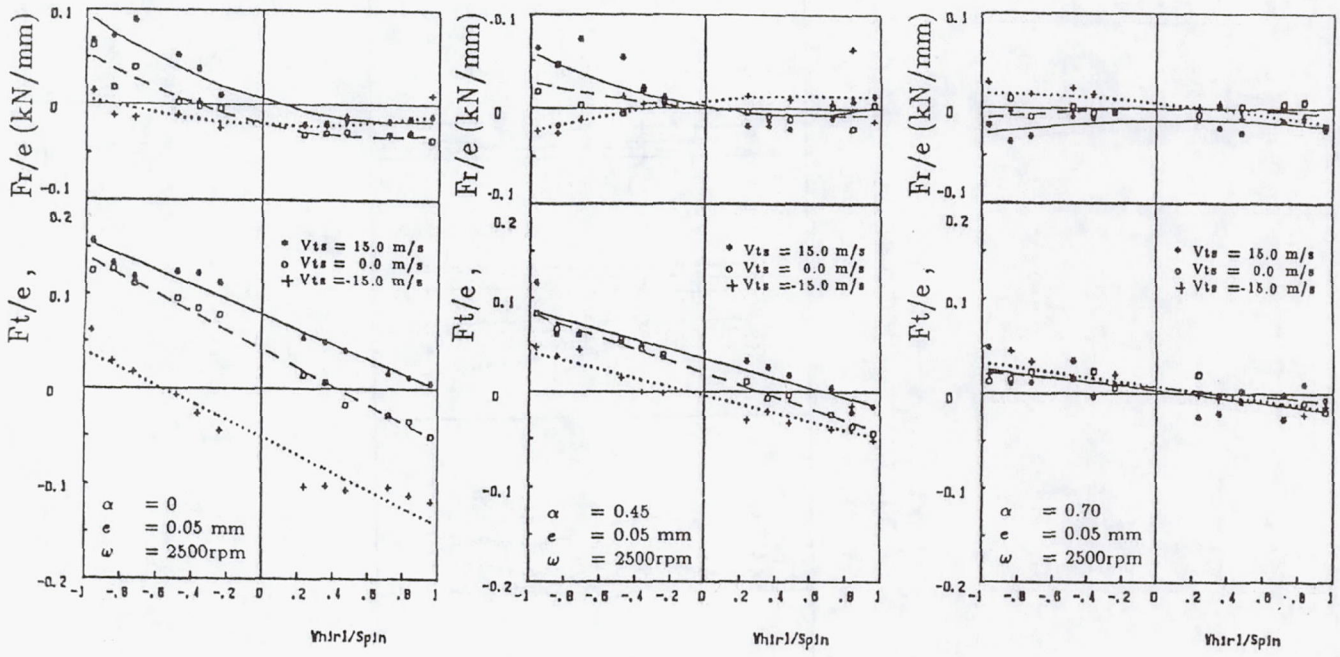

(a) $\overline{\alpha} = 0$ (b) $\overline{\alpha} = 0.45$ (c) $\overline{\alpha} = 0.7$

Fig.14 Radial and tangential forces for preswirl velocity

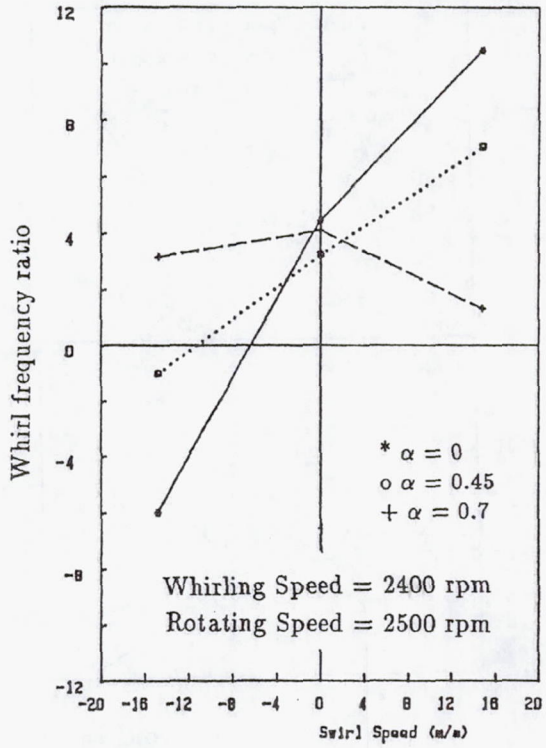

Fig.15 Whirl frequency ratio for void ratios

TEST RESULTS FOR ROTORDYNAMIC COEFFICIENTS OF ANTI-SWIRL SELF-INJECTION SEALS

C.H. Kim and Y.B. Lee
Korea Institute of Science and Technology
Seoul, Korea

ABSTRACT

Test results are presented for rotordynamic coefficients and leakage for three annular seals which use anti-swirl self-injection concept to yield significant improvement in whirl frequency ratios as compared to smooth and damper seals. A new anti-swirl self-injection mechanism is achieved by deliberately machining self-injection holes inside the seal stator to partially divert inlet flow into the anti-swirl direction. The anti-swirl self-injection mechanism is used to achieve effective reduction of the tangential flow which is considered as a prime cause of rotor instability in high performance turbomachinery. Test results show that the self-injection mechanism significantly improves whirl frequency ratios; however, the leakage performance degrades due to the introduction of the self-injection mechanism. Through a series of the test program, an optimum anti-swirl self-injection seal which uses a labyrinth stator surface with anti-axial flow injections is selected to obtain a significant improvement in the whirl frequency ratio as compared to a damper seal, while showing moderate leakage performance.

Best whirl frequency ratio is achieved by an anti-swirl self-injection seal of 12 holes anti-swirl and 6 degree anti-leakage injection with a labyrinth surface configuration. When compared to a damper seal, the optimum configuration outperforms the whirl frequency ratio by a factor of 2.

NOMENCLATURE

$\underline{A}$	Measured frequency response functions, introduced in Eq. (2)
C, c	Direct and cross-coupled damping coefficients, introduced in Eq. (1), (FT/L)
C_d	Leakage coefficient, introduced in Eq. (5)
$\bar{C}$	Radial clearance,(L)
$\underline{E}'$	Identity matrix, introduced in Eq.(2)
F_X, F_Y	Seal reaction-force components, introduced in Eq. (1), (F)
K,k	Direct and cross-coupled stiffness coefficients, introduced in Eq. (1) (F/L)
M	Added-mass coefficient, introduced in Eq.(1), (M)
$\underline{S}'$	Error matrix, introduced in Eq.(2)
X,Y	Seal rotor to stator relative displacement, introduced in Eq.(1), (L)
Ra	Seal axial Reynolds number($2V\bar{C}/\upsilon$)
V	Fluid average axial velocity(L/T)
$\underline{X}$	Unknown coefficients, $\underline{M}$, $\underline{C}$, and $\underline{K}$, introduced in Eq. (2)
f	whirl frequency ratio, introduced in Eq. (4)
ω	rotorational speed, introduced in Eq. (4)
υ	Fluid kinematic viscosity (L /T)
Ω	Impulse hammer frequency

INTRODUCTION

Throughout 1980's , one of the major concerns in seal dynamics is the consequence of a reduction in the tangential velocity inside the seal. Lower tangential velocities yield a reduction in the cross-coupled stiffness coefficient k of the following reaction-force/displacement model for the seal.

$$-\begin{Bmatrix} F_x \\ F_y \end{Bmatrix} = \begin{bmatrix} K & k \\ -k & K \end{bmatrix} \begin{Bmatrix} X \\ Y \end{Bmatrix} + \begin{bmatrix} C & c \\ -c & C \end{bmatrix} \begin{Bmatrix} \dot{X} \\ \dot{Y} \end{Bmatrix} + M \begin{Bmatrix} \ddot{X} \\ \ddot{Y} \end{Bmatrix} \quad (1)$$

This linearized model is assumed to apply for small motion about a centered position and defines the reaction-force components (F_x,F_y) in terms of (X,Y), the components of the displacement vector of the seal rotor relative to its stator. Reducing k reduces the destabilizing forces developed by the seal due to hydrodynamic action and should yield a higher stable operating speed for pumps.

von Pragenau(1982) originally proposed that annular seals for pumps which used rough stators and smooth rotors would lower tangential velocities than conventional seals which use smooth rotors and stators. A reduction of the tangential velocity was realized through damper seals(Childs and Kim, 1985,1986; Iwatsubo and Sheng,1990) which used rough stators and smooth rotors. The surface-roughness pattern retards the generation of the tangential flow inside the seal clearance. While damper seals are adopted in several industrial applications into high performance turbomachinery, a promising alternative in reducing the tangential velocity is introduced and tested, named as " swirl brake". The swirl brake which is used in the inlet section of the seal clearance brakes the inlet swirl inherent inside the seal clearance. The related research effort has been reported with a sucess in the SSME HPOTP turbine interstage seals.(Childs et.al,1990)

In this paper, a 'new' concept in reducing the tangential velocity is proposed and preliminarily tested with a series of the seal. Newly proposed is the anti-swirl self-injection seal which is illustrated in Fig. 1 along with smooth and damper seals for comparisons. Using the inlet high pressure, the inlet flow is partially diverted into holes or slots inside the seal stators and self-injected into the reverse direction of the shaft rotation. This concept can be a more aggressive measure to a reduction of the tangential flow inside the seal clearance. The resultant tangential velocity is presumably reduced, and the consequent improvement in stability can be obtained. This anti-swirl self-injection concept is shown to be a promising alternative to the conventional swirl brake. The present test program examines the process of the concept realization and refinement of the newly proposed seals. The consequence of the anti-swirl self-injection mechanism is tested and the side effect on leakage performance is investigated.

TEST APPARATUS

A new test rig was designed and built, based on the basic design reported in the reference of Massmann and Nordmann(1985). The principle of the test rig is simple but complicated enough to satisfy the current purpose of the test. Fig. 2 illustrates the test rig. The movable housing is flexibly supported by springs and steel bars to the main structure of the test rig. The two identical seal inserts can be exchanged for new test seals. After the seal is inserted into the main housing, the pressure measurement holes are machined and connected to the Scani-valves.With a four stage supply pump and controlled flow rates, the supplied fluid enters the seal section in the middle through two supply holes. The inlet fluid then exits through two seal sections. The magnetic flow meter measures flow rates in the exit pipe line. The pressurized seal generate the seal forces which are the source of the dynamic coefficients. The movement of the main body relative to the rotor was measured by four eddy-current-type proximity probes. As will be explained later, seal coefficients can be measured with dynamic impact tests for each test seal.

The temperatures, flow rates, and pressures are measured and controlled through a personal computer.The temperature of the working fluid, water, was kept constant at 40 °C, using an automatically-controlled cooler inside the water tank. A modification to the apparatus of Massmann and Normann(1985) is the measurement of the static pressure inside the seal clearance through the Scani-valve mechanism illustrated in Fig. 3. The inlet pressure, five pressure readings inside the seal clearance, and the outlet pressure are measured through the Scani-valve mechanism which is connected to a pressure sensor.

With this test rig, a test matrix was set up to vary rotation speeds up to 6000 rpm and supply pressures up to 10 bars. Five seal inserts were sequentially tested for a range of rotation speed and supply pressures.

TEST SEALS

As stated in the preceding section, five seals were tested serially for concept demonstration and refinement of the newly proposed seals. For comparison to conventional seals, a smooth seal and a damper seal were also tested. Fig. 1 shows geometries of a smooth seal, a damper seal, and three anti-swirl self-injection seals. The geometry of the damper seal was adopted from the test results in the reference of Childs and Kim(1986) for a possible optimum damping. For the anti-swirl pattern, a 12 holes injection was considered. Twelve supply holes were drilled into the stator body and then the anti-swirl pattern was realized by drilling holes against the direction of rotation. For leakage reduction, a 6 degree anti-leakage injection and a labyrinth surface were considered. Table 1 shows the configuration of tested seals. All tested seals have the same minimum clearance of 0.2 mm with a smooth rotor. Details are explained in the table. Seal 3 was tested first to see the effect of anti-swirl configurations. The effect of anti-leakage injection was tested in seal 4 with 12 holes of anti-swirl injection. Based on the above series of tested seals, the seal 5 of 12 holes with anti-leakage injection and labyrinth effect was tested.

SEAL PARAMETER IDENTIFICATION

The impulse hammer technique was used for the dynamic testing of the parameter identification in the frequency domain(Massmann and Normann,1985) as illustrated in Fig. 4. As explained in detail in the reference of Massmann and Normann(1985), the instrumental variable method is used. In conjunction with the least square method, the instrumental variable method utilizes the measured frequency response function to iterate the least square algorithm for better curve-fittings.

Utilizing the fact that the product of the mobility matrix and the stiffness matrix should be the identity matrix, a complex equation is arranged into an overdetermined equation system in the case of a broad band excitation of the impulse hammer.

$$\underline{A}\underline{X} = \underline{E}' + \underline{S}' \tag{2}$$

where $\underline{A}$ consists of the measured frequency response functions related to the exciter frequencies Ω , $\underline{X}$ represents the unknown coefficients $\underline{M}$, $\underline{C}$, and $\underline{K}$, $\underline{E}'$ is a modified identity matrix and $\underline{S}'$ is the error matrix. After deriving the loss function with respect to the seal coefficients, the instrumental variable method is applied as shown in Fig. 5. A new matrix $\underline{W}^T$ with instrumental variables is built up, using the initial matrix obtained by the original least square matrix method.

$$\underline{W}^T\underline{A}\underline{X} = \underline{W}^T\underline{E}' \tag{3}$$

As shown in Fig. 5 , this procedure is repeated and after each step the actual estimation is compared with that of the last step. The procedure stops if the correlation is satisfactory. The instrument variable method is less sensitive to noise in the measurement data and reduces the

error of the identified coefficients(Massmann and Normann,1985) as illustrated in Fig.6.

EXPERIMENTAL RESULTS

Dynamic Coefficient and Leakage Test Data

For a given seal configuration, a test matrix is obtained by varying the axial Reynolds number and running speed. The Ra range varies between the maximum flow capacity of the supply pump and minimum ΔP sufficient to generate reasonable transient pressure signal amplitudes. For a given Ra value, the running speed is varied sequentially over the running-speed capacity of the drive motor.

An evaluation of the relative performance of seal configurations is expedited by extracting stiffness, damping, and mass coefficients from the impact force/displacement data in frequency domain. From a stability standpoint, the destabilizing tangential force is of most interst. A positive cross-coupled stiffness k is destabilizing because it drives the forward orbital motion of the rotor. Positive direct damping C and a negative cross-coupled stiffness are stabilizing because they oppose the orbital motion. A convenient measure of seal stability is the whirl frequency ratio of cross-coupled stiffness to direct damping forces with a circular orbit.(Childs et.al,1989)

$$\text{whirl-frequency ratio} = f = \frac{k}{C\omega} \tag{4}$$

The stator inserts are to be evaluated based on k, C, whirl-frequency ratio, and leakage performance. Volumetric seal leakage is defined by

$$\Delta P = C_d \frac{\rho V^2}{2} \tag{5}$$

where the leakage coefficient C_d is a nondimensional relative measure of the leakage to be expected from seals with different radii.

Relative Uncertainty

The uncertainty in the dynamic coefficients can be determined using the method described by Holman(1978). The uncertainty in the force and displacements are 0.5N,0.0016mm, respectively. Before normalization, the nominal calculated uncertainty in stiffness coefficients is 51.53 N/mm(4.67%) and 0.164 N-s/mm(3.82%) for the damping coefficients. These predicted uncertainty values are generally satisfactory in comparison to nominal dynamic coefficients.

Relative Performance of Anti-Swirl Self-Injection Seals

As stated, relative performance of anti-swirl self-injection seals was compared with a smooth seal and a damper seal in terms of leakage and stability. The leakage performance was measured by the leakage coefficient, while the stability was measured by the whirl frequency ratio. The influence of rotor speeds on the direct damping and the cross-coupled coefficients was first examined for an axial Reynolds number 8,000 in Fig. 7. First, as expected, the direct damping is independent to the rotor speeds, while the cross-coupled stiffness is a strong function of the rotor speeds;viz. the current test results follow general trends of other seals as predicted in the previous reports in references of Childs and Kim(1985,1986) and Iwatsubo and Sheng(1990). For the damping coefficient, the damper seal is outstanding ; nearly six times the smooth seal and trifold the anti-swirl self-injection seals. For the cross-coupled stiffness coefficient, seal 5 outperfoms other seals; ten times smaller than the smooth seal and twenty times smaller than the damper seal. The anti-swirl self-injection

seals have much smaller values than conventional seals in the cross-coupled stiffness. These results assure the anti-swirl concept ; the anti-swirl self-injection mechanism retards the tangential flow inside the seal clearance and therefore results in the reduction of cross-coupled stiffnesses.

In Fig. 8, the whirl frequency ratio and leakage coefficients were compared among tested seals. As expected in the measurement of dynamic coefficients, anti-swirl self-injection seals are much better than the smooth seal. Among the anti-swirl self-injection seals, seal 5 is the best; more than six times less than the smooth seal and less than half the damper seal. As far as the leakage performance is concerned, the damper seal outperforms the others. During the test program, seal 3 was tested first and found to have too much leakage as shown in Fig. 8. Therefore, the anti-axial flow pattern was introduced in the seal 4 . Seal 4 improves about 10 % over the seal 3, while showing about the same performance in the whirl frequency ratio. Results show that the anti-axial flow injection is not as attractive as first expected for leakage reduction; maybe because of the limited reverse angle(6 degree) due to the limit of the current test rig installation, or the sharp acute reverse turn make the diverted flow lose too much of its momentum to have a discernible effect on the anti-leakage concept. Finally, in this test series, seal 5 with labyrith effect is tested. The labyrinth effect was introduced to improve the leakage performance; however, it was not enough, compared with the damper seal. More tests are planned for improving the leakage performance. However, more importantly in stability view point, these test results of the anti-swirl self-injection seal concepts clearly show that the anti-swirl concept is very effective in improving the stability .

In Fig. 9, the cross-coupled stiffness and damping coefficients are compared with different pressure differences. As the pressure difference increases, the direct damping increases; this result follows general trends of other seals. The damper seal has the highest damping values. Seal 3 and seal 4 have 30-40% higher damping values than the smooth seal. Seal 5 has about the same damping values as the smooth seal. For the cross-coupled stiffness, the anti-swirl self-injection seals show a clear pattern of reducing cross-coupled stiffnesses: versus the smooth and damper seals which show increased cross-coupled stiffness patterns as the pressure difference is increased. The anti-swirl self-injection seals show decreasing or constant cross-coupled stiffnesses. Again this figure clearly confirms the anti-swirl self-injection concept.

In Fig.10, the whirl frequency ratios and leakage coefficients are compared. As expected from Fig. 9, anti-swirl self-injection seals show clear superiority in stability performance over smooth and damper seals. Among the self-injection seals, seal 5 has the lowest whirl frequency ratio; less than half that of smooth and damper seals. However, the leakage performance can be a drawback. Seal 4 and seal 5 are better than the smooth seal; however, the damper seal leaks 20% less than seal 5. These results show that better designs should be addressed in the anti-swirl self-injection seals . Along with this leakage performance, the dependency of pressure differences and hole numbers for better stability performance should be studied in more details. Current results demonstrate how the anti-swirl self-injection seals perform and introduce the concept of anti-swirl and self-injection mechanisms for annular seals.

CONCLUSIONS

Newly proposed anti-swirl self-injection seals have been tested and compared with smooth and damper seals. Test results show that the anti-swirl self-injection concept can significantly reduce cross-coupled stiffnesses and to show a stability improvement by a factor of 2 in the whirl frequency ratio as compared with a damper seal. A minor drawback identified in this preliminary test is the leakage performance. More detailed tests for the leakage performance based on new designs are planned and could solve this problem.

REFERENCES

Childs, D.W., Baskahrone, E., Ramsey. C., 1990" Test Results for Rotordyanmic Coefficients of the SSME HPOTP Turbine Intersatge Seal with Two Swirl Brakes," NASA

CP 3122, Proceedings of the workshop : Rotordynamic Instability Problems in High Perforamance Turbomachinery held at Texas A&M University, May 21-23, pp165-178

Childs, D.W., Elrod, D. and Hale, K., 1989,"Annular Honeycomb Seals: Test Results for Leakage and Rotordynamic Coeficients; Comparisons to Labyrinth and Smooth Configurations," ASME Trans. Journal of Tribology, Vol. 111, pp293-301

Childs, D.W. and Kim,C.H., 1985,"Analysis and Testing for Rotordyanmic Coefficients of Turbulent Annular Seals with Different, Directionally Homogeneous Surface-Roughness Treatment for Rotor and Stator Elements", ASME Trans. Journal of Tribology,Vol.107, No.3, July , pp296-306.

Childs.D.W. and Kim, C.H., 1986, "Test Results for Round-Hole-Pattern Damper Seals : Optimum Configurations and Dimensions for Maximum Net Damping," ASME Trans. Journal of Tribology, Vol. 108, Oct., pp605-611

Holman,J.P.,1978, Experimental Methods for Engineers, McGraw Hill, pp45

Iwatsubo, T., and Sheng, B.C., 1990,"An Experimental Study on the Static and Dynamic Characteristics of Damper Seals," Proceedings of 3rd International Conference on Rotordynamics, Lyon, France, Sept.10-12,pp99-104

Massmann, H. and Nordmann R., 1985," Some New Results Concerning the Dynamic Behavior of Annular Trubulent Seals," NASA CP 2409, Proceedings of the workshop : Instability in Rotating Machinery held in Carson City, June 10-14, pp179-194

von Pragenau,G.L., 1982,"Damping Seals for Turbomachinery,"NASA Technical Paper 1987

Table 1. Configuration of Test Seals

Test seals	Type	Configuration
seal 1	plain	
seal 2	damper	hole pattern(Childs and Kim,1986)
seal 3	ASIS	12 holes one-line injection
seal 4	ASIS	12 holes one-line with anti-axial flow injection
seal 5	ASIS labyrinth	12 holes one-line with anti-axial flow injection and labyrinth effect

* ASIS : Anti-Swirl Self-Injection Seal

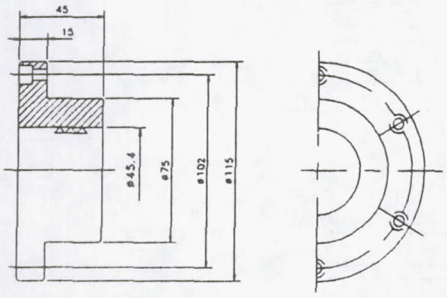

Fig.1(a) Smooth seal insert (seal 1)

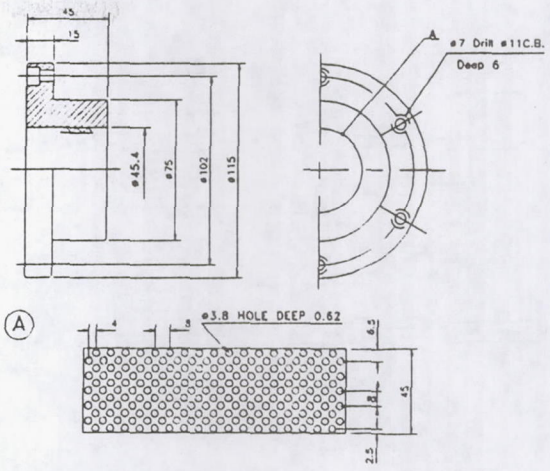

Fig.1(b) Damper seal insert (seal 2)

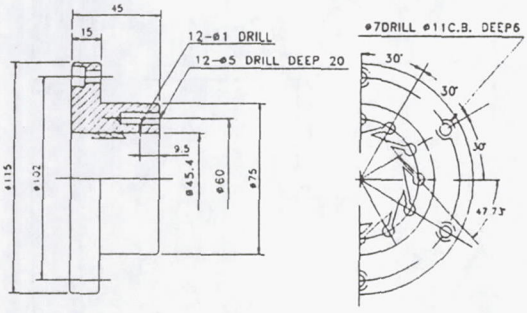

Fig.1(c) Anti-Swirl Self-Injection seal insert (seal 3)

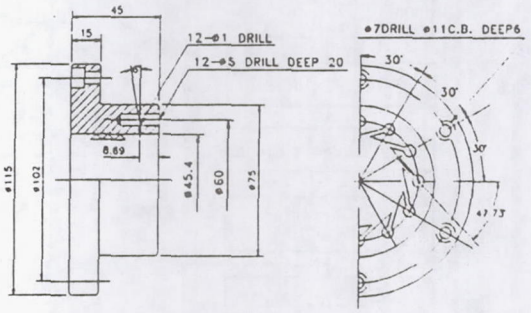

Fig.1(d) Anti-Swirl Self-Injection seal insert with anti-axial flow injection (seal 4)

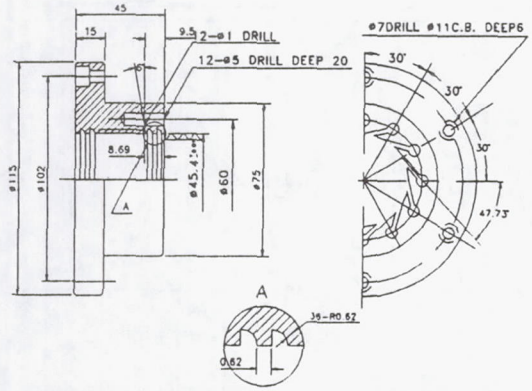

Fig.1(e) Anti-Swirl Self-Injection seal insert with anti-axial flow injection and labyrinth effect (seal 5)

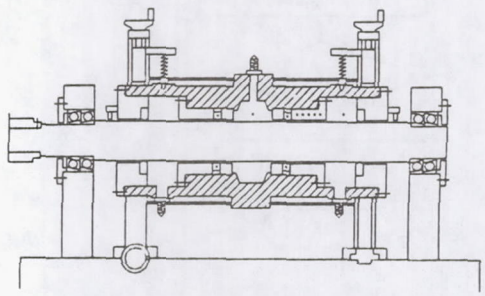

Fig.2 Test apparatus

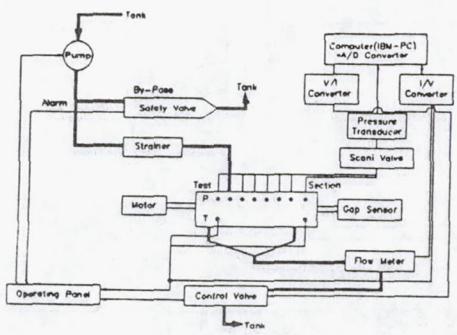

Fig.3 Schematics of the sealing test system

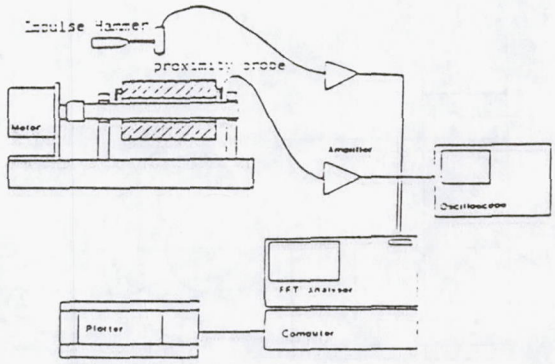

Fig.4 Data acquisition and processing

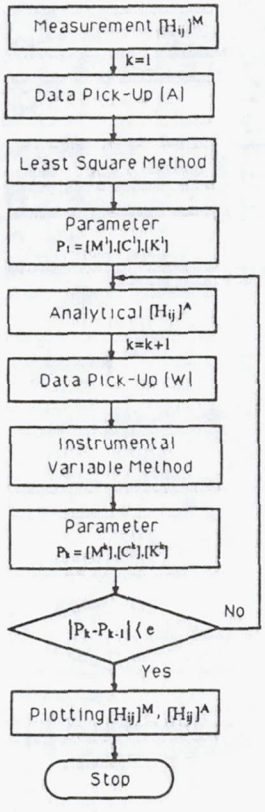

Fig.5 Flow chart of instrumental variable method

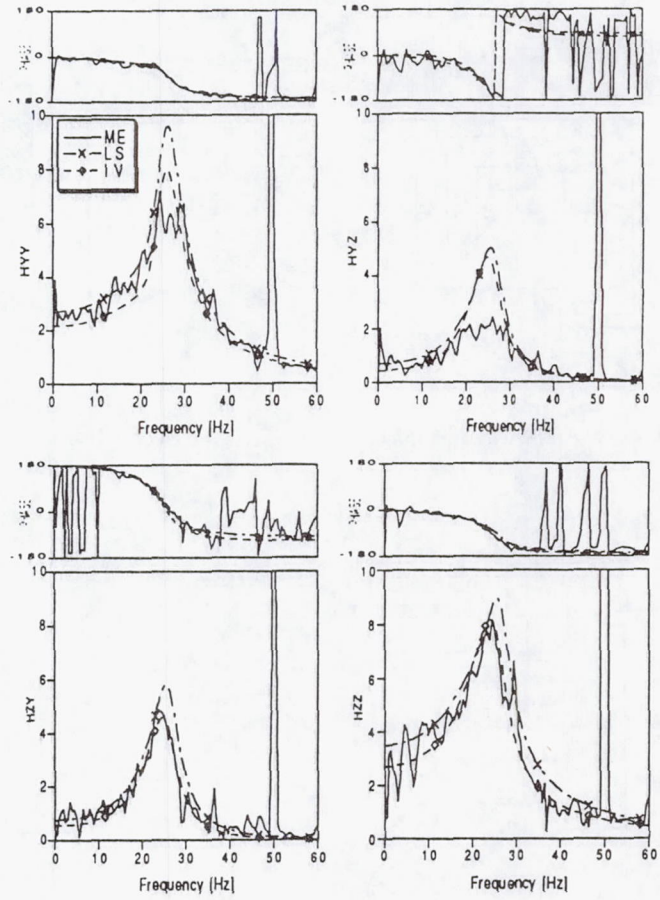

Fig.6 Example of measured and analytical frequency response functions (—— measured(ME), —X— least square(LS), - -◇- - instrumental variable(IV))

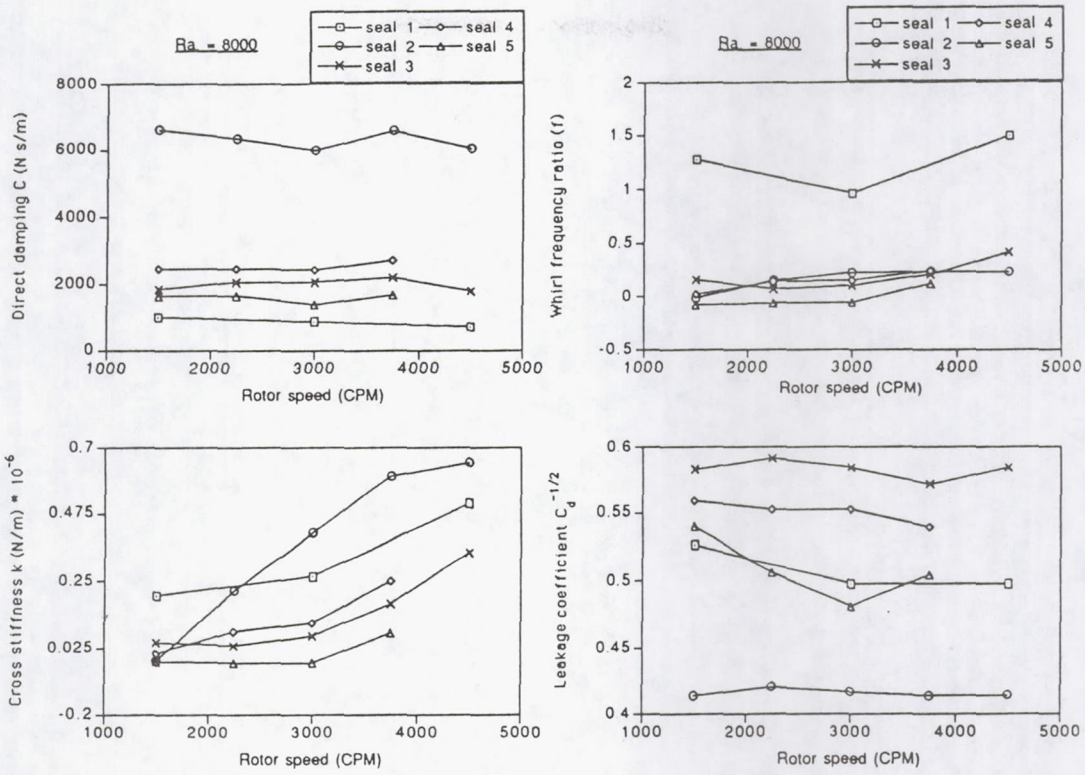

Fig.7 C and k versus CPM for the five seals of Table 1

Fig.8 f and C_d versus CPM for the five seals of Table 1

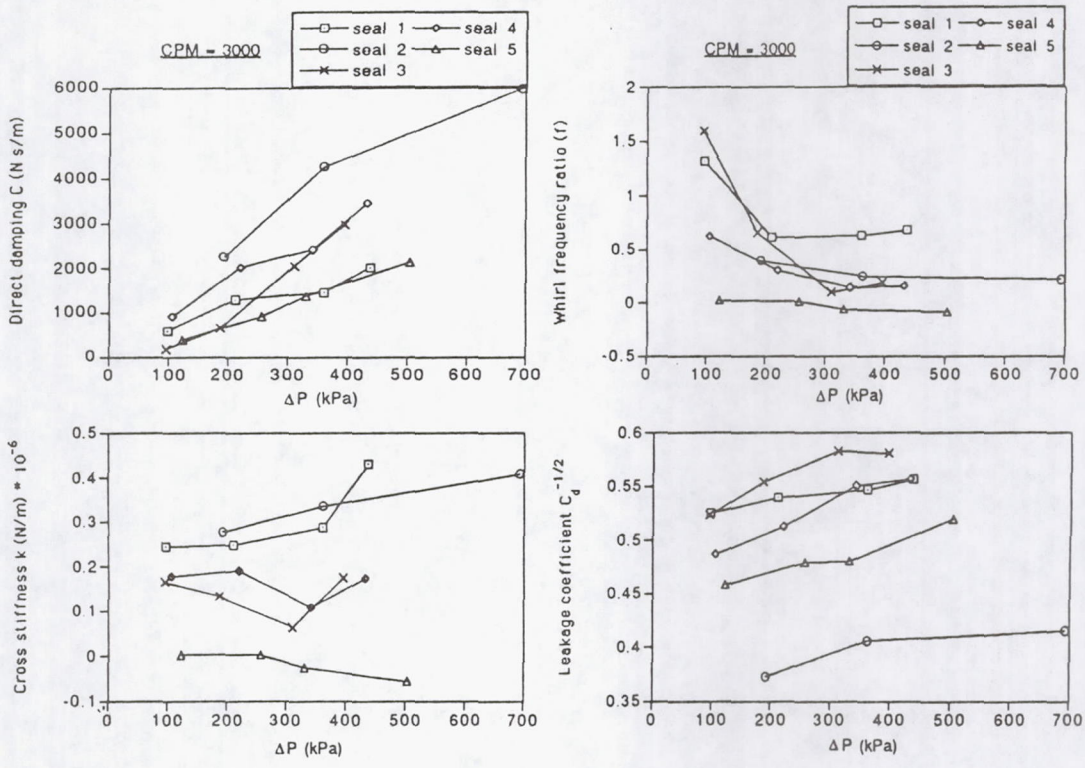

Fig.9 C and k versus ΔP for the five seals of Table 1

Fig.10 f and C_d versus ΔP for the five seals of Table 1

EXPERIMENTAL INVESTIGATION OF ROTORDYNAMIC COEFFICIENTS OF LONG ANNULAR SEALS IN CENTRIFUGAL PUMPS

T. Neumer, M. Matros, and R. Nordmann
University of Kaiserslautern
Kaiserslautern, Germany

Synopsis

1 Introduction

2 State of art

2.1 Fundamentals about fluid-structure-interactions

3 Experimental plant

3.1 Principle of active magnetic bearing support
3.2 Component tester
3.3 Measuring devices

4 Parameter identification

4.1 Fundamentals about identification
4.2 Verification of the measuring chain
4.3 Experimental results for a long annular seal
4.4 Comparison between experiment and calculation

Preceding Page Blank

Tendencies for the Development of Fluid Flow Engines

Requirements:

- variable rotation speed
- increasing power density (rotation speed ↑, weight ↓)
- large availability
- low costs

Physical limitations:

- self exciting mechanisms
- flow separations
- significant circulations
- admissible material stress

Possible conclusions:

- decreasing reserves in stability
- high vibrational amplitudes
- instabilities due to self exciting mechanisms
- period of disuse

Starting problem solution:

- rotordynamic design with consideration of fluid-structure-interactions
- optimization of contour and chosen materials

Dynamic Forces Acting on a Rotor

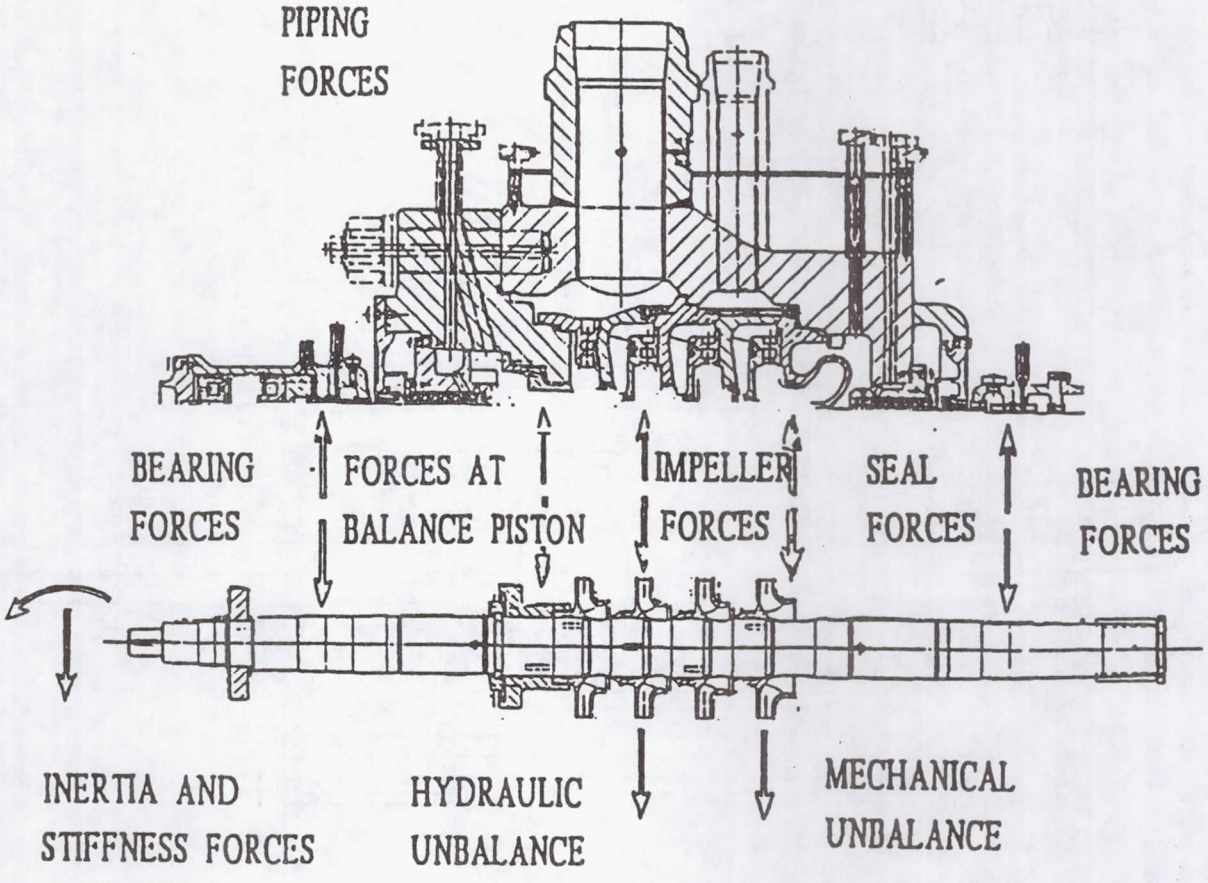

Fluid-Structure-Interactions in Fluid Flow Engines

- Fluid-Structure-Interactions in fluid streamed clearances
  Relative motion leads to motion dependent forces

- Axial flow through clearances in:
  - shaft seal (neck)
  - shaft seal between stages
  - balancing device
  - journal bearings

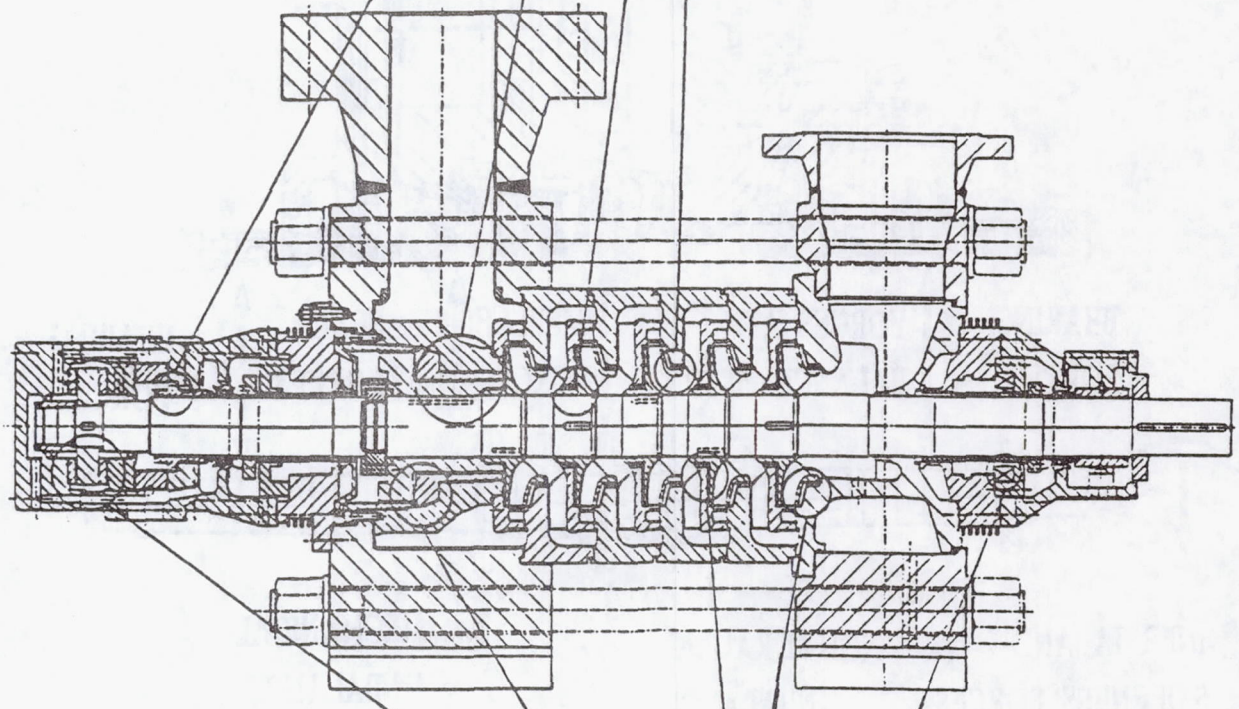

- Radial flow:
  - journal bearings
  - balancing disk
  - impeller back shroud/cover plate
  - mechanical seal

Rotordynamic Description of Fluid Interactions

- In general 6 degrees of freedom

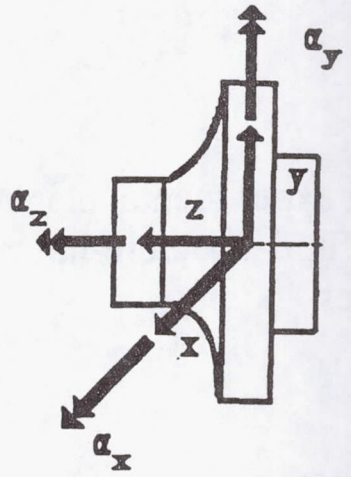

- equations of motion with rotordynamic coefficients with assumption of linear behaviour

$$\begin{bmatrix} m_{11} & m_{12} & m_{13} & m_{14} & m_{15} & m_{16} \\ m_{21} & m_{22} & m_{23} & m_{24} & m_{25} & m_{26} \\ m_{31} & m_{32} & m_{33} & m_{34} & m_{35} & m_{36} \\ m_{41} & m_{42} & m_{43} & m_{44} & m_{45} & m_{46} \\ m_{51} & m_{52} & m_{53} & m_{54} & m_{55} & m_{56} \\ m_{61} & m_{62} & m_{63} & m_{64} & m_{65} & m_{66} \end{bmatrix} \begin{bmatrix} \ddot{x} \\ \ddot{y} \\ \ddot{\alpha}_y \\ \ddot{\alpha}_x \\ \ddot{z} \\ \ddot{\alpha}_z \end{bmatrix} + \begin{bmatrix} d_{11} & d_{12} & d_{13} & d_{14} & d_{15} & d_{16} \\ d_{21} & d_{22} & d_{23} & d_{24} & d_{25} & d_{26} \\ d_{31} & d_{32} & d_{33} & d_{34} & d_{35} & d_{36} \\ d_{41} & d_{42} & d_{43} & d_{44} & d_{45} & d_{46} \\ d_{51} & d_{52} & d_{53} & d_{54} & d_{55} & d_{56} \\ d_{61} & d_{62} & d_{63} & d_{64} & d_{65} & d_{66} \end{bmatrix} \begin{bmatrix} \dot{x} \\ \dot{y} \\ \dot{\alpha}_y \\ \dot{\alpha}_x \\ \dot{z} \\ \dot{\alpha}_z \end{bmatrix}$$

$$+ \begin{bmatrix} k_{11} & k_{12} & k_{13} & k_{14} & k_{15} & k_{16} \\ k_{21} & k_{22} & k_{23} & k_{24} & k_{25} & k_{26} \\ k_{31} & k_{32} & k_{33} & k_{34} & k_{35} & k_{36} \\ k_{41} & k_{42} & k_{43} & k_{44} & k_{45} & k_{46} \\ k_{51} & k_{52} & k_{53} & k_{54} & k_{55} & k_{56} \\ k_{61} & k_{62} & k_{63} & k_{64} & k_{65} & k_{66} \end{bmatrix} \begin{bmatrix} x \\ y \\ \alpha_y \\ \alpha_x \\ z \\ \alpha_z \end{bmatrix} = \begin{bmatrix} F_x \\ F_y \\ M_y \\ M_x \\ F_z \\ M_z \end{bmatrix}$$

Requirements to the Component Tester

Aim:

Development of an experimental plant to investigate motion dependent fluid-structure-interactions in components of fluid flow engines

Requirements:

- Generation of well defined relative motions between rotating and static part of the investigated component
- Rotor motion possible in 5 DOF´s (so far 2 DOF´s)
- Measuring devices (5 DOF´s) to determine the fluid forces and moments as well as the relative displacements
- Possibility of investigation of various components like
  - short and long annular seals
  - impellers
  - mechanical seals
  - journal bearings
- Direct parameter identification following from measured information

Active Magnetic Bearing Used for Parameter Identification

Principle of Function:

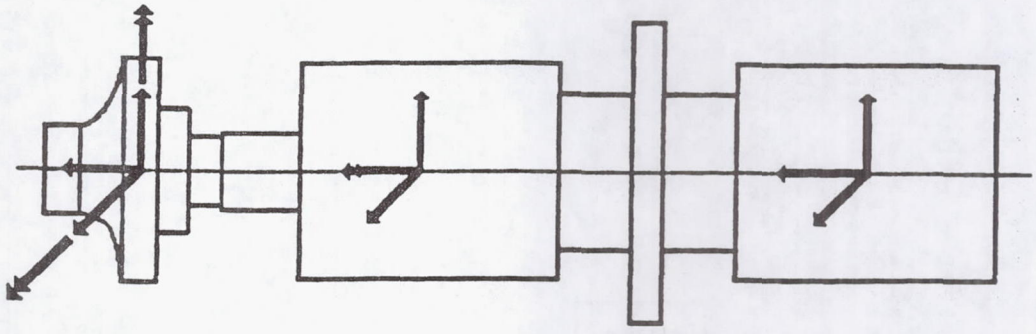

Tested component AMB

- Defined excitation of displacement with magnetic bearings
  → relative motion of the tested component
- Compensation of fluid forces with magnetic bearings
- Non-contact measuring of bearing forces and rotor position with magnetic bearings
- Transformation of the measured variables into the coordinate system of the tested component

Requirements:

- Stiff rotor
- Measuring devices for bearing forces and rotor position
- Rotor decompled from environment ("free-free")

Active Magnetic Bearing with Displacement Excitation

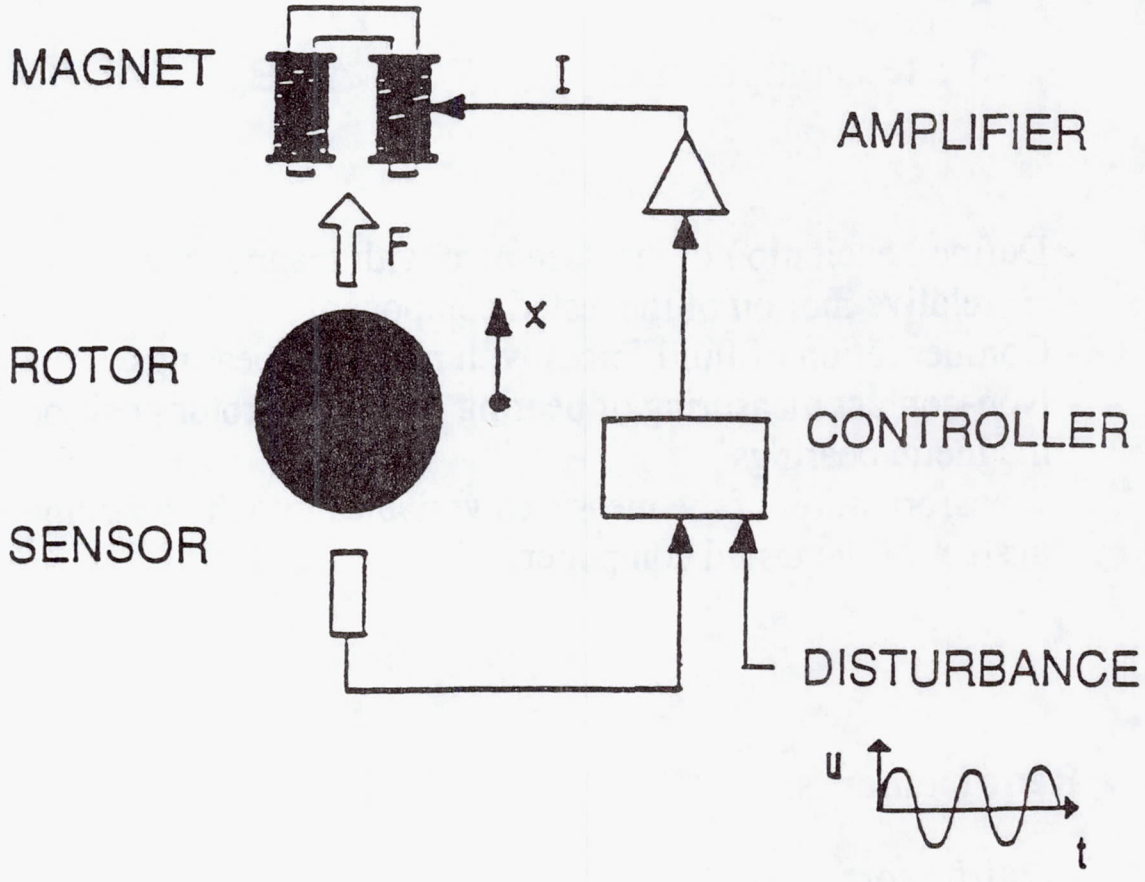

Tracks of Rotor Motions

X_1	X_2	Y_1	Y_2	Z	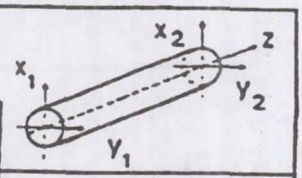
$\hat{a}\sin\Omega t$	$\hat{a}\sin\Omega t$	0	0	0	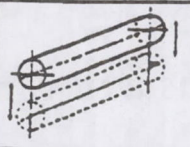
0	0	$\hat{a}\sin\Omega t$	$\hat{a}\sin\Omega t$	0	
$\hat{a}\sin\Omega t$	$\hat{b}\sin\Omega t$	0	0	0	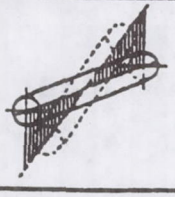
0	0	$\hat{a}\sin\Omega t$	$\hat{b}\sin\Omega t$	0	
$\hat{a}\sin\Omega t$	$\hat{a}\sin\Omega t$	$\hat{a}\cos\Omega t$	$\hat{a}\cos\Omega t$	0	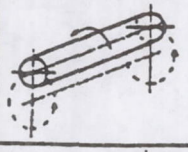
$-\hat{a}\sin\Omega t$	$-\hat{a}\sin\Omega t$	$\hat{a}\cos\Omega t$	$\hat{a}\cos\Omega t$	0	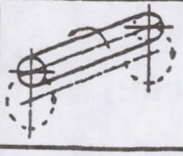
$\hat{a}\sin\Omega t$	$-\hat{a}\sin\Omega t$	$\hat{a}\cos\Omega t$	$-\hat{a}\cos\Omega t$	0	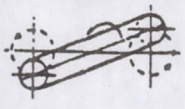
$-\hat{a}\sin\Omega t$	$\hat{a}\sin\Omega t$	$\hat{a}\cos\Omega t$	$-\hat{a}\cos\Omega t$	0	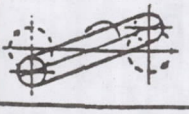
0	0	0	0	$\hat{a}\sin\Omega t$	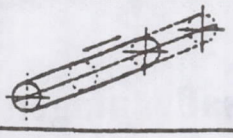

Force Measurement with Magnetic Bearings

Aim: Output signal proportional to bearing force

Measured variables:- Coil currents i
- Rotor position x

Princip: Calculation of the bearing force based on the measured variables

Requirement: Convinient model of magnet, which considers the non-linear force-current-characteristic

$$F_{tot} = KL_o \left[\frac{i_0 + i_x}{\frac{l_{FE}\,\mu_L}{SF\,\mu_{FE}} + 2(x_0 - x)} \right]_o^2 - KL_u \left[\frac{i_0 - i_x}{\frac{l_{FE}\,\mu_L}{SF\,\mu_{FE}} + 2(x_0 + x)} \right]_u^2$$

Problem: Permeability of iron $\mu_{FE} = f(i,x)$

Simplification: $\mu_L >> \mu_{FE}$

$$F_{tot} = KL_o^* \left[\frac{i_0 + i_x}{x_0 - x} \right]_o^2 - KL_u^* \left[\frac{i_0 - i_x}{x_0 + x} \right]_u^2$$

Disadvantage: No consideration of the magnetic saturation in the iron

Rotordynamic Design

Criterias:

- stiff rotor
- determination of mode shapes (position of nodes) to chose position of magnetic bearing
- stability
- rigid body eigenfrequencies in the measurement range

Model:

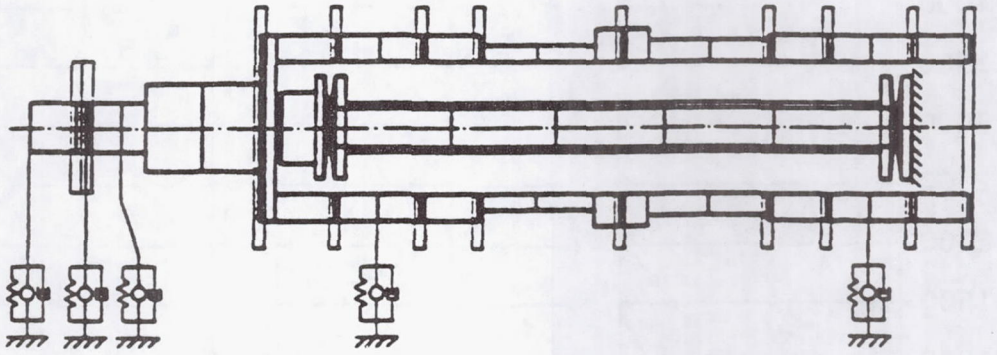

Eigenvalues and Mode Shapes:

EW NR 1 = -0.20 + I * 1.29 HZ

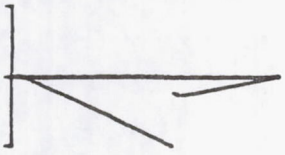

EW NR 2 = 0.18 + I * 2.32 HZ

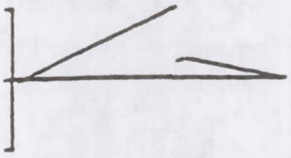

EW NR 3 = -31.45 + I * 47.51 HZ

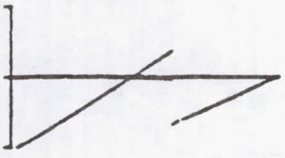

EW NR 4 = -24.08 + I * 53.88 HZ

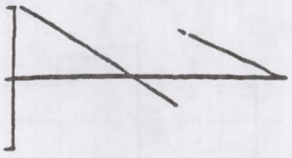

EW NR 5 = -5.02 + I * 367.21 HZ

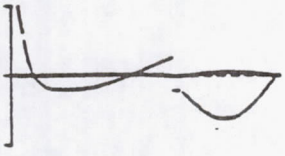

EW NR 6 = -26.52 + I * 384.17 HZ

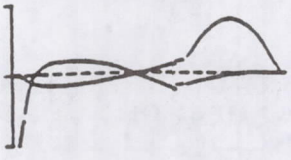

Bearing Forces for Defined Motions of the Rotor

Bearing forces:

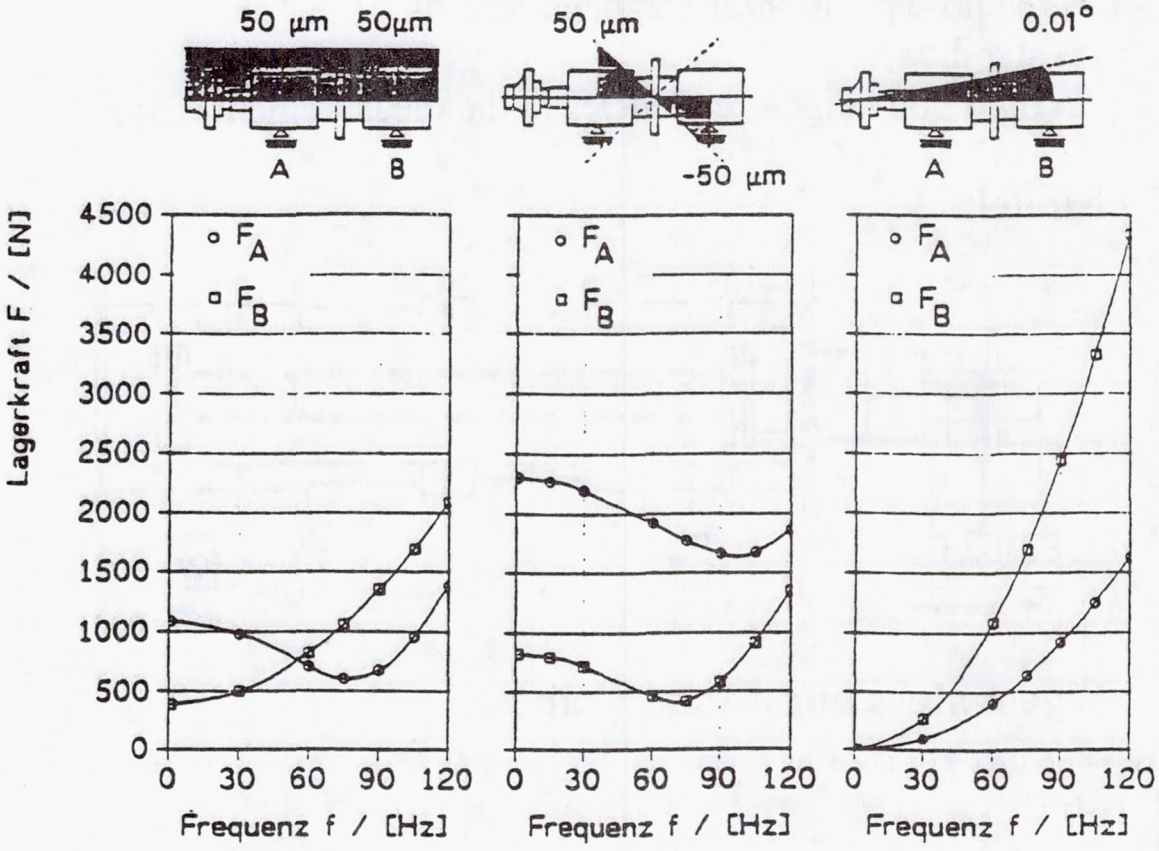

Model:

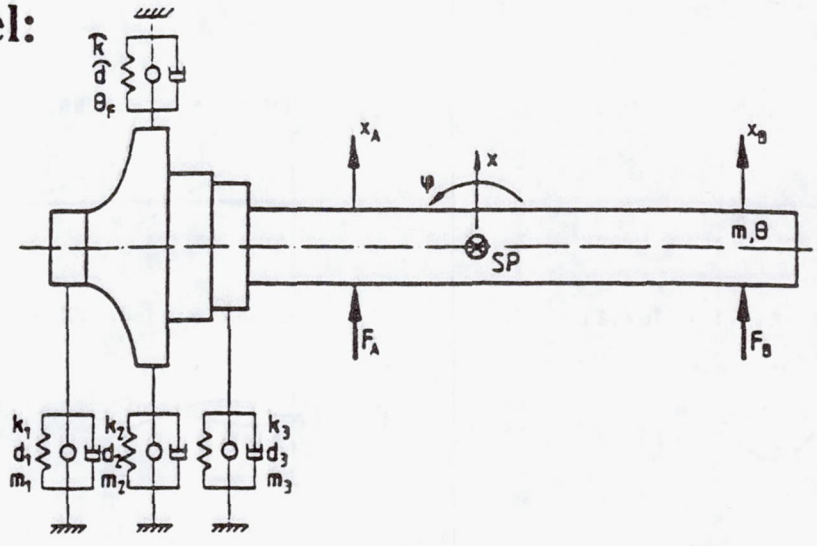

Component Tester

Part-sectioned drawing

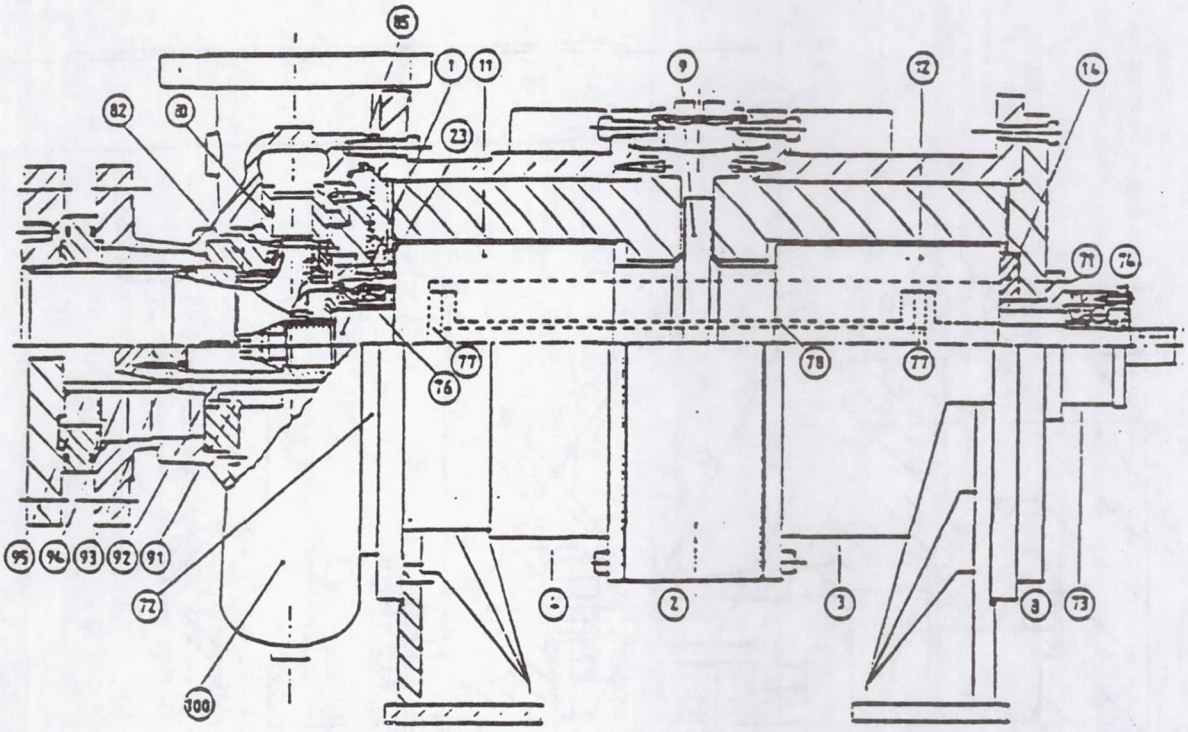

Principle "magnetic bearing supported rotor"

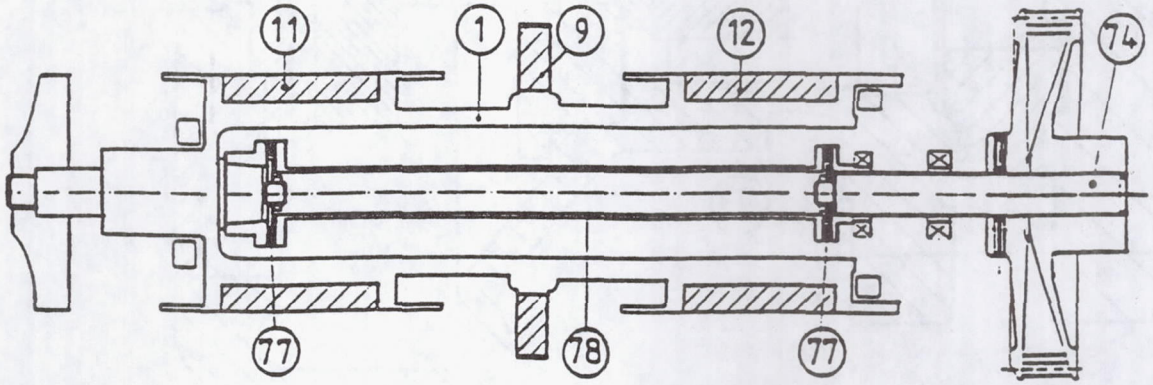

Hydraulic Casing with Long Annular Seal

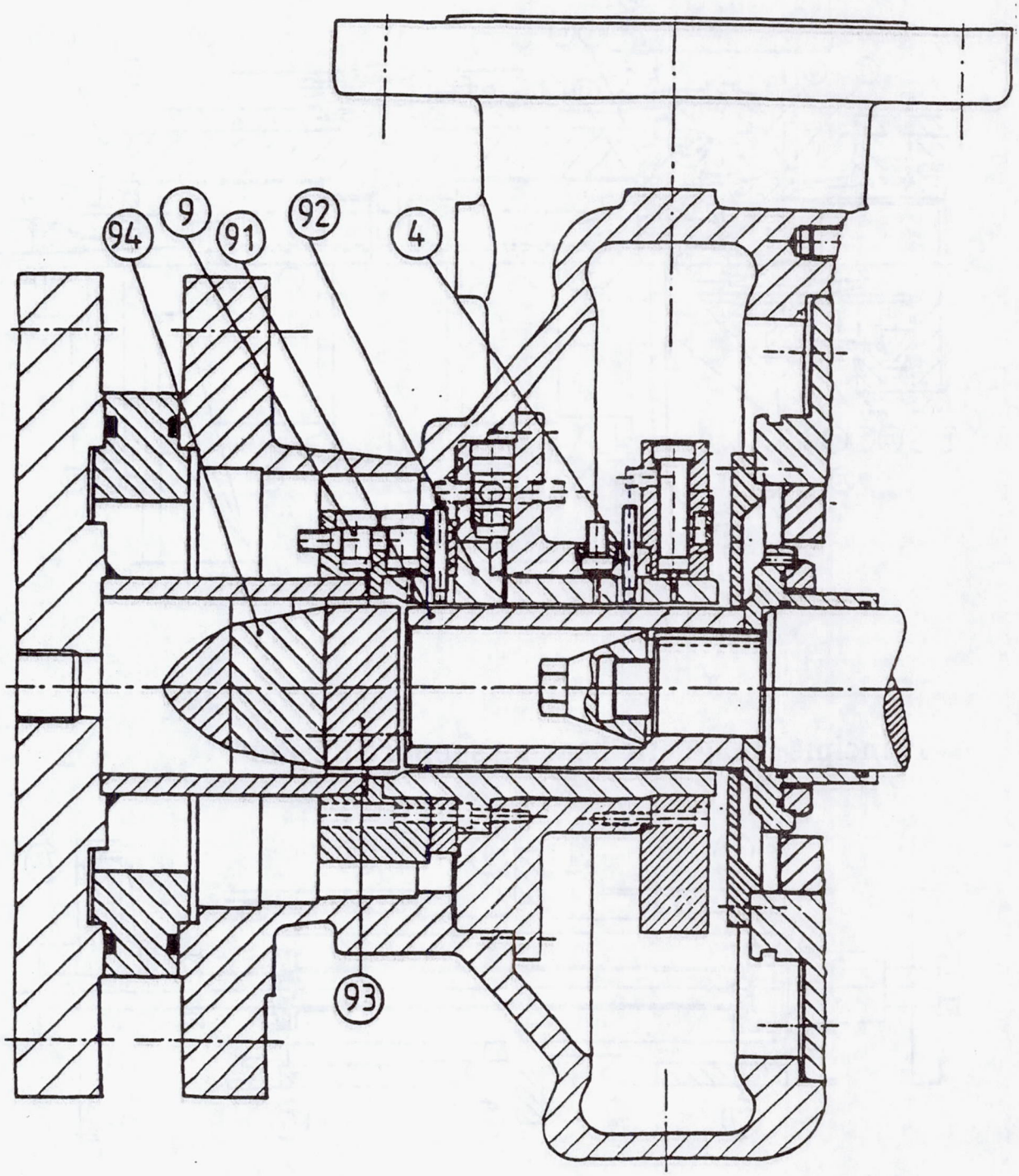

The Testing Plant
Closed Loop

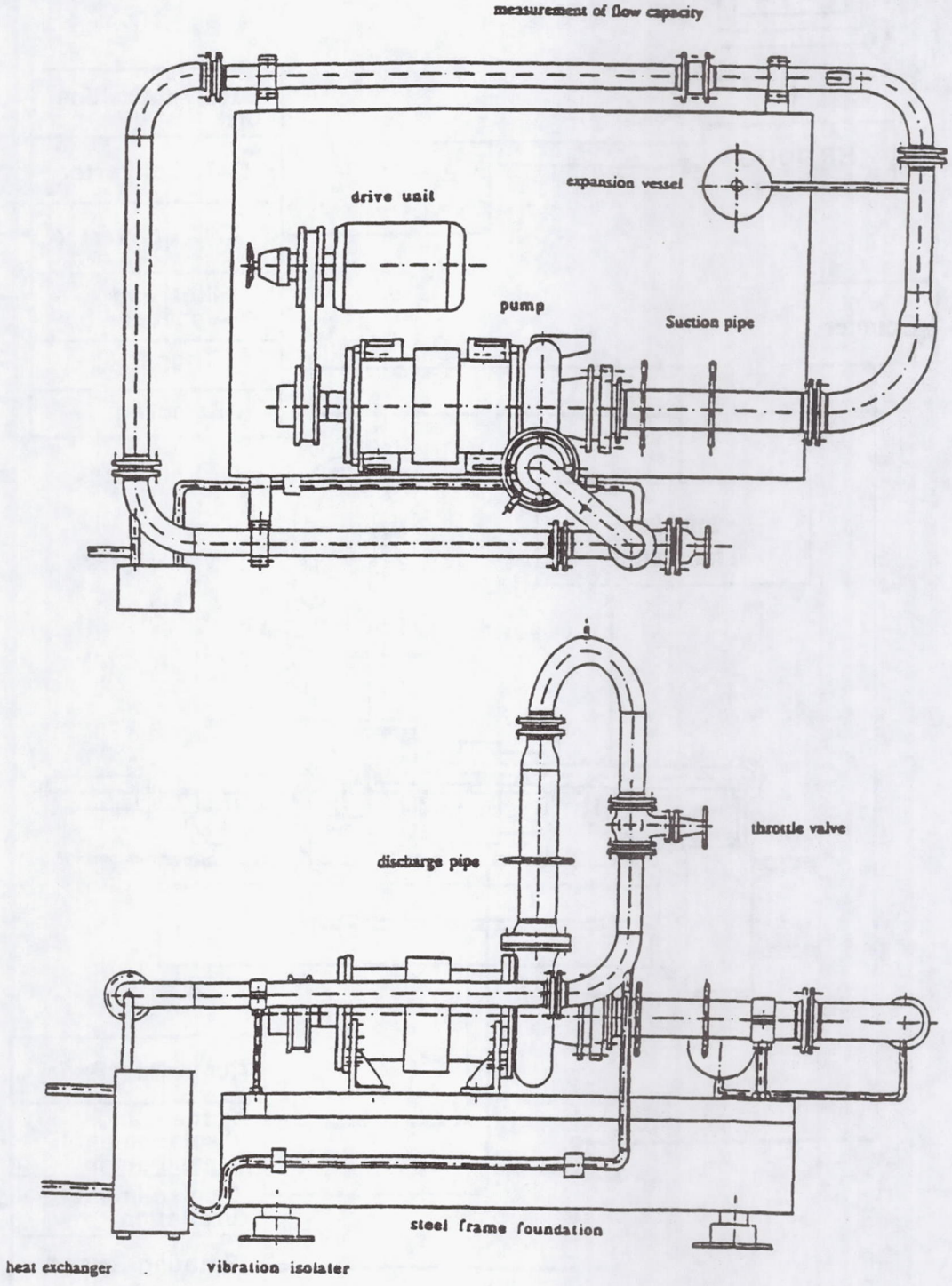

Test Data and their Processing

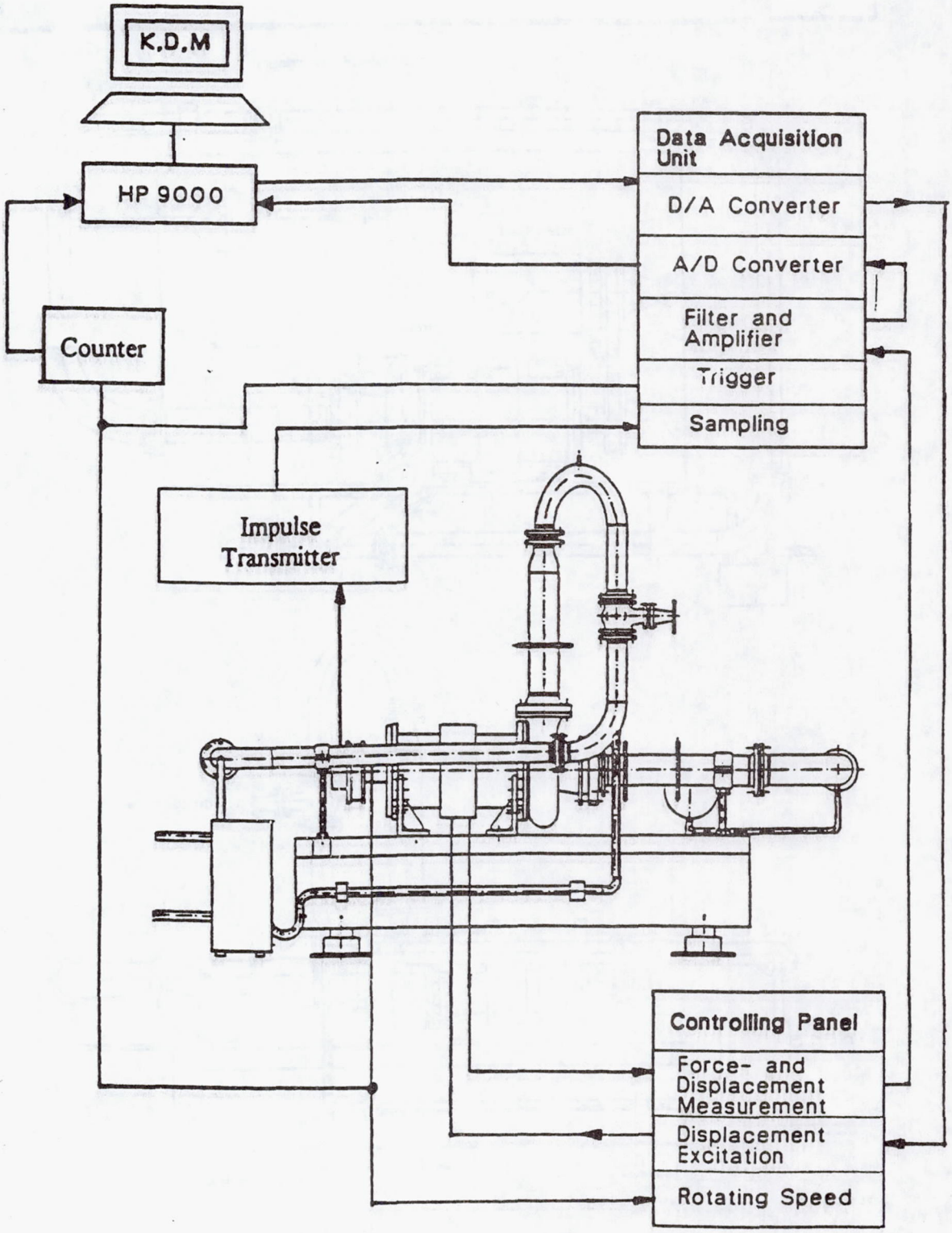

Direct Parameter Identification

Principle:

- Description of fluid interactions by given mechanical model
- Fitting of the model parameters to the according test component
- Identification of the model parameters using measured values

Execution:

- Defined artificial displacement excitation
- Transformation of the bearing data into coordinate system of the tested component
- Calculation of the stiffness frequency response functions
- Curve - fitting for parameter identification

Curve-Fitting

Statement: $y = e^{j\omega t}$ $x = \alpha_y = \alpha_x = 0$

Stiffness frequency response functions:

$$\frac{F_x}{y}(\omega) = (k - m\omega^2) + j\omega d$$

$$\frac{F_y}{y}(\omega) = (K - M\omega^2) + j\omega D$$

$$\frac{M_y}{y}(\omega) = (k_{\alpha\varepsilon} - m_{\alpha\varepsilon}\omega^2) + j\omega d_{\alpha\varepsilon}$$

$$\frac{M_x}{y}(\omega) = (K_{\alpha\varepsilon} - M_{\alpha\varepsilon}\omega^2) + j\omega D_{\alpha\varepsilon}$$

Curve - fitting:

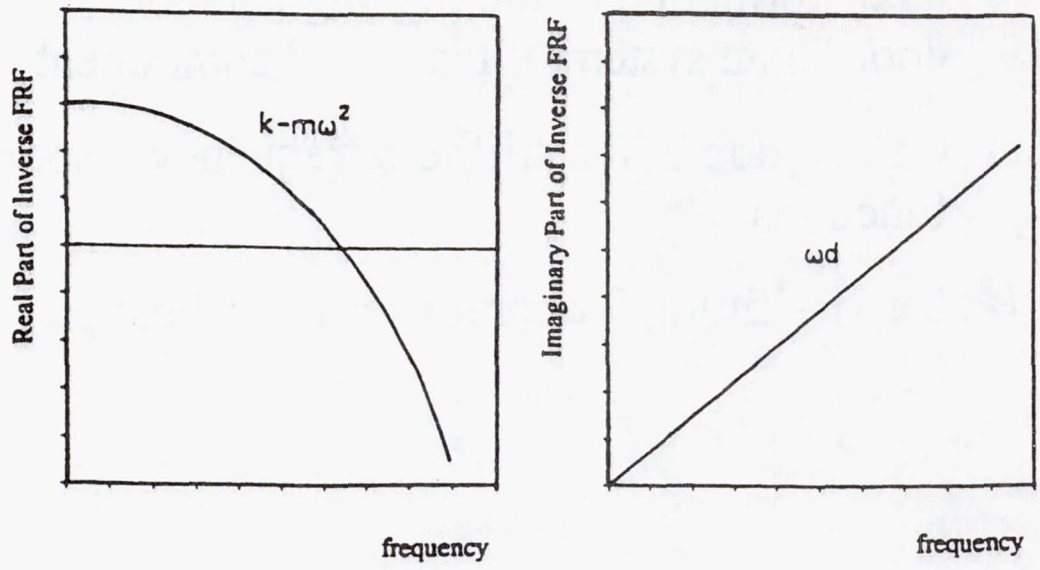

Verification of the Measuring Chain

Idea:

- Identification of well-known physical variables
- Difference between identified and real parameter
  => Information about the accuracy of the complete measuring- and analysing chain

Identification "rotormass":

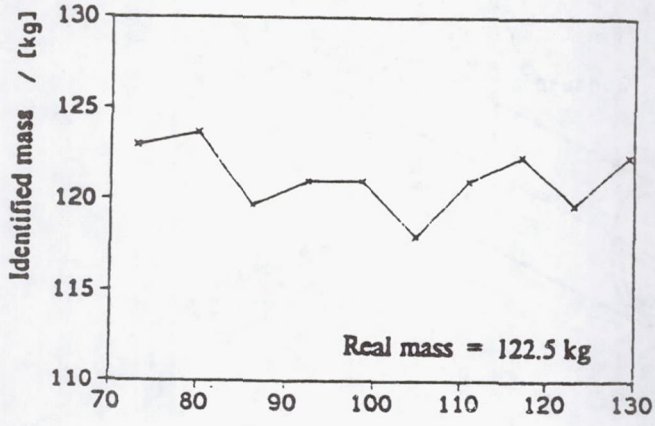

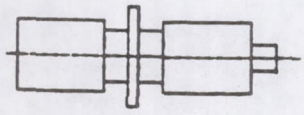

Identification "plate spring":

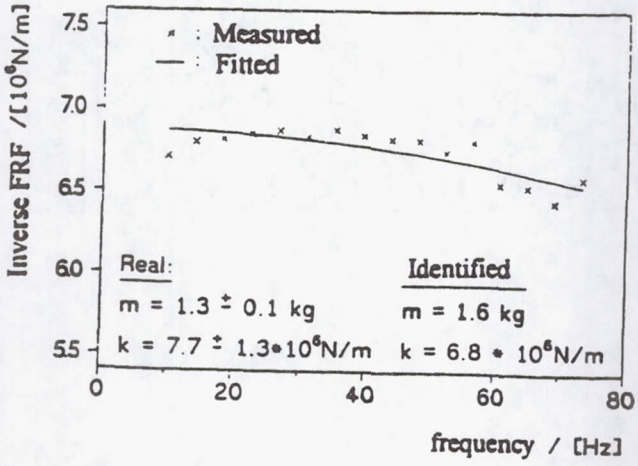

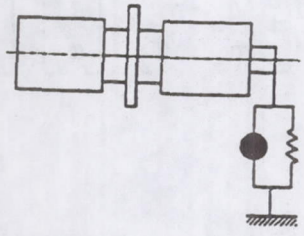

Example Long Annular Seal

- For technical advices only 4 degrees of freedom are of importance

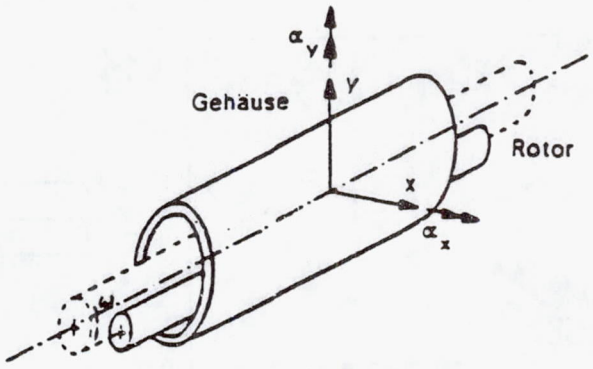

$$\begin{bmatrix} M & m & M_{z\alpha}-m_{z\alpha} \\ -m & M & -m_{z\alpha}-M_{z\alpha} \\ M_{\alpha z} & m_{\alpha z} & M_{\alpha}-m_{\alpha} \\ m_{\alpha z}-M_{\alpha z} & m_{\alpha} & M_{\alpha} \end{bmatrix} \begin{bmatrix} \ddot{x} \\ \ddot{y} \\ \ddot{\alpha}_y \\ \ddot{\alpha}_x \end{bmatrix} + \begin{bmatrix} D & d & D_{z\alpha}-d_{z\alpha} \\ -d & D & -d_{z\alpha}-D_{z\alpha} \\ D_{\alpha z} & d_{\alpha z} & D_{\alpha}-d_{\alpha} \\ d_{\alpha z}-D_{\alpha z} & d_{\alpha} & D_{\alpha} \end{bmatrix} \begin{bmatrix} \dot{x} \\ \dot{y} \\ \dot{\alpha}_y \\ \dot{\alpha}_x \end{bmatrix} + \begin{bmatrix} K & k & K_{z\alpha}-k_{z\alpha} \\ -k & K & -k_{z\alpha}-K_{z\alpha} \\ K_{\alpha z} & k_{\alpha z} & K_{\alpha}-k_{\alpha} \\ k_{\alpha z}-K_{\alpha z} & k_{\alpha} & K_{\alpha} \end{bmatrix} \begin{bmatrix} x \\ y \\ \alpha_y \\ \alpha_x \end{bmatrix} = \begin{bmatrix} F_x \\ F_y \\ M_y \\ M_x \end{bmatrix}$$

Fitted Stiffness Frequency Response Function

$Re = -(K - M\Omega^2)$ $\qquad$ $Im = -\Omega D$

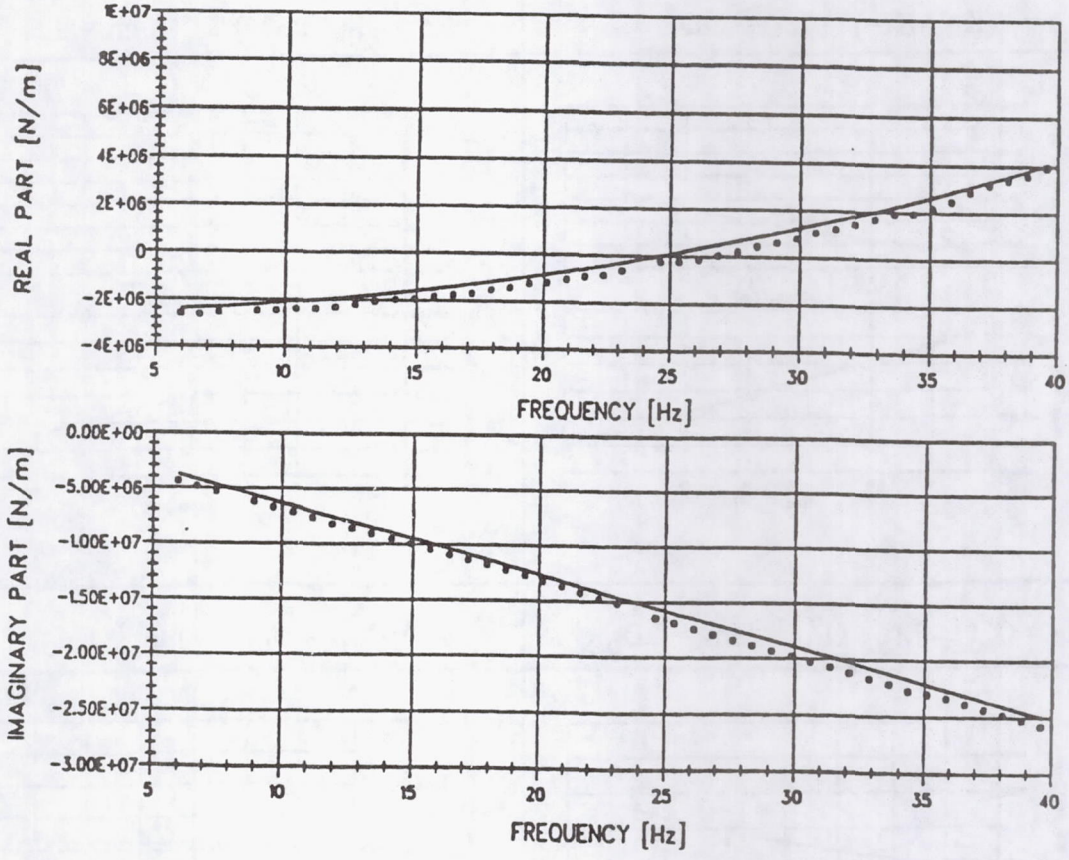

– : Fitted

• : Measured

Fitted Stiffness Frequency Response Functions

Boundary conditions: L/D = 2,0
Δp = 9,5 bar
n = 500 rpm

$Re = -(K - M\Omega^2)$ $Im = -\Omega D$	$Re = -(k - m\Omega^2)$ $Im = -\Omega d$
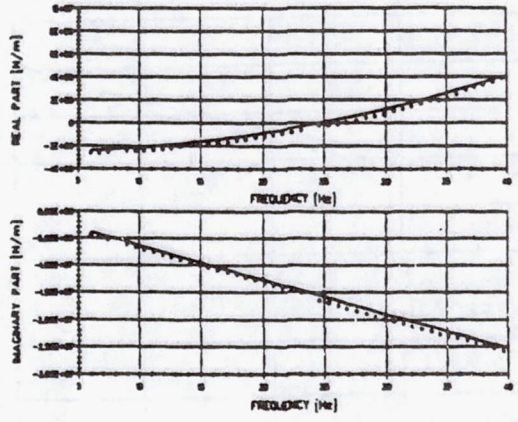	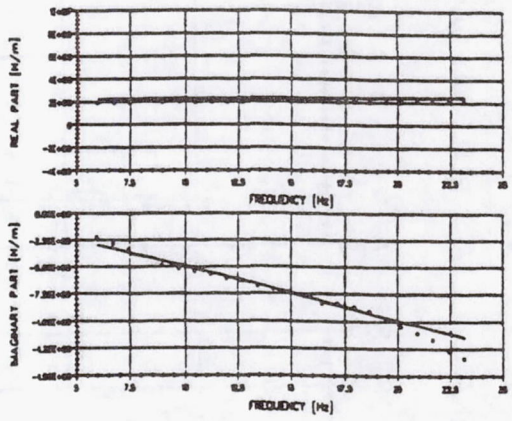
$Re = (K_{\alpha\varepsilon} - M_{\alpha\varepsilon}\,\Omega^2)$ $Im = \Omega D_{\alpha\varepsilon}$	$Re = (k_{\alpha\varepsilon} - m_{\alpha\varepsilon}\,\Omega^2)$ $Im = \Omega d_{\alpha\varepsilon}$
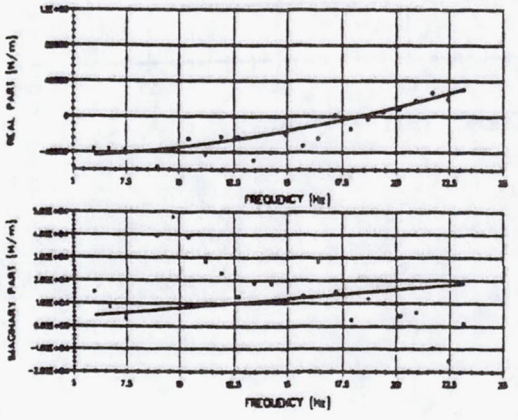	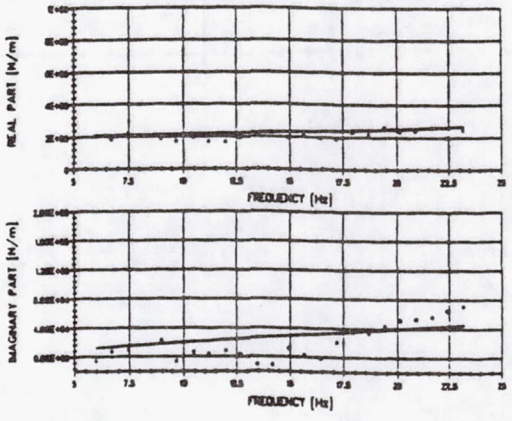

• : Measured — : Fitted

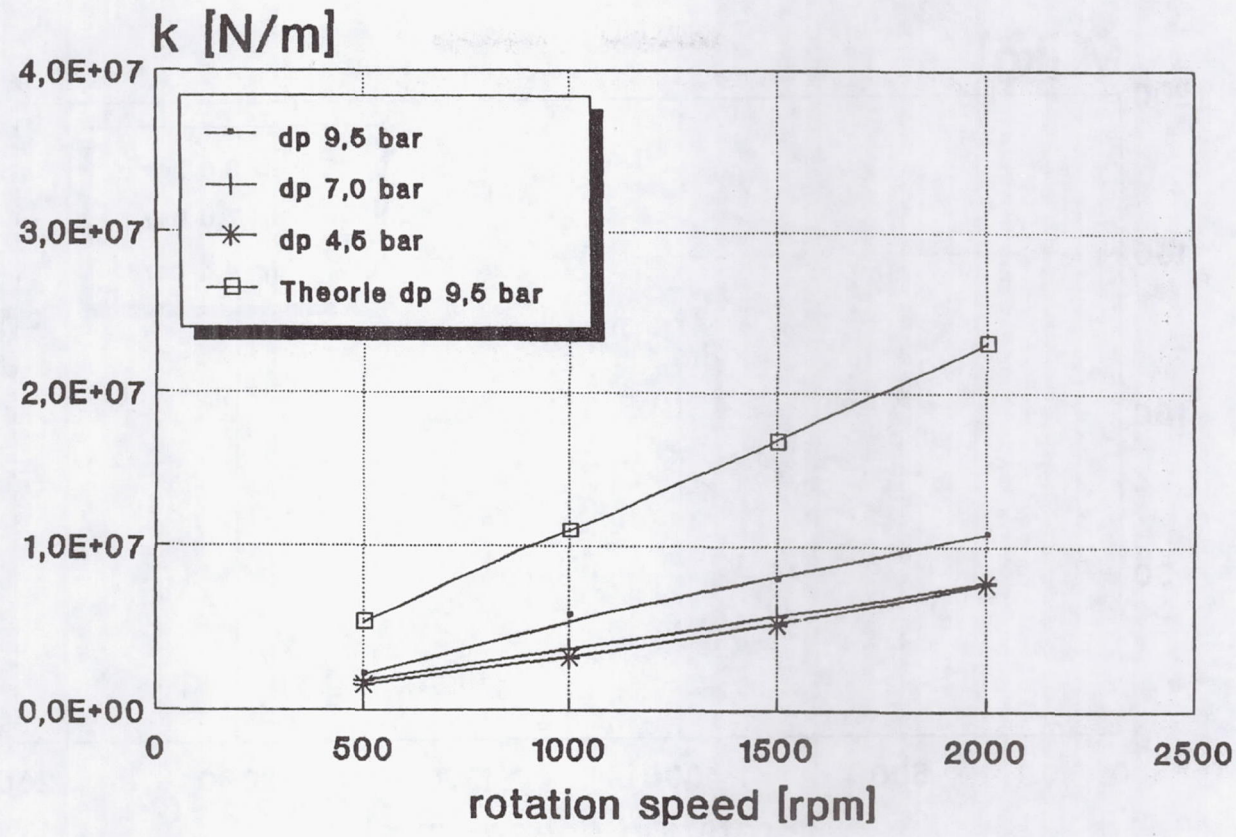
k [N/m]
4,0E+07
3,0E+07
2,0E+07
1,0E+07
0,0E+00
0
500
1000
1500
2000
2500
rotation speed [rpm]
dp 9,5 bar
dp 7,0 bar
dp 4,5 bar
Theorie dp 9,5 bar

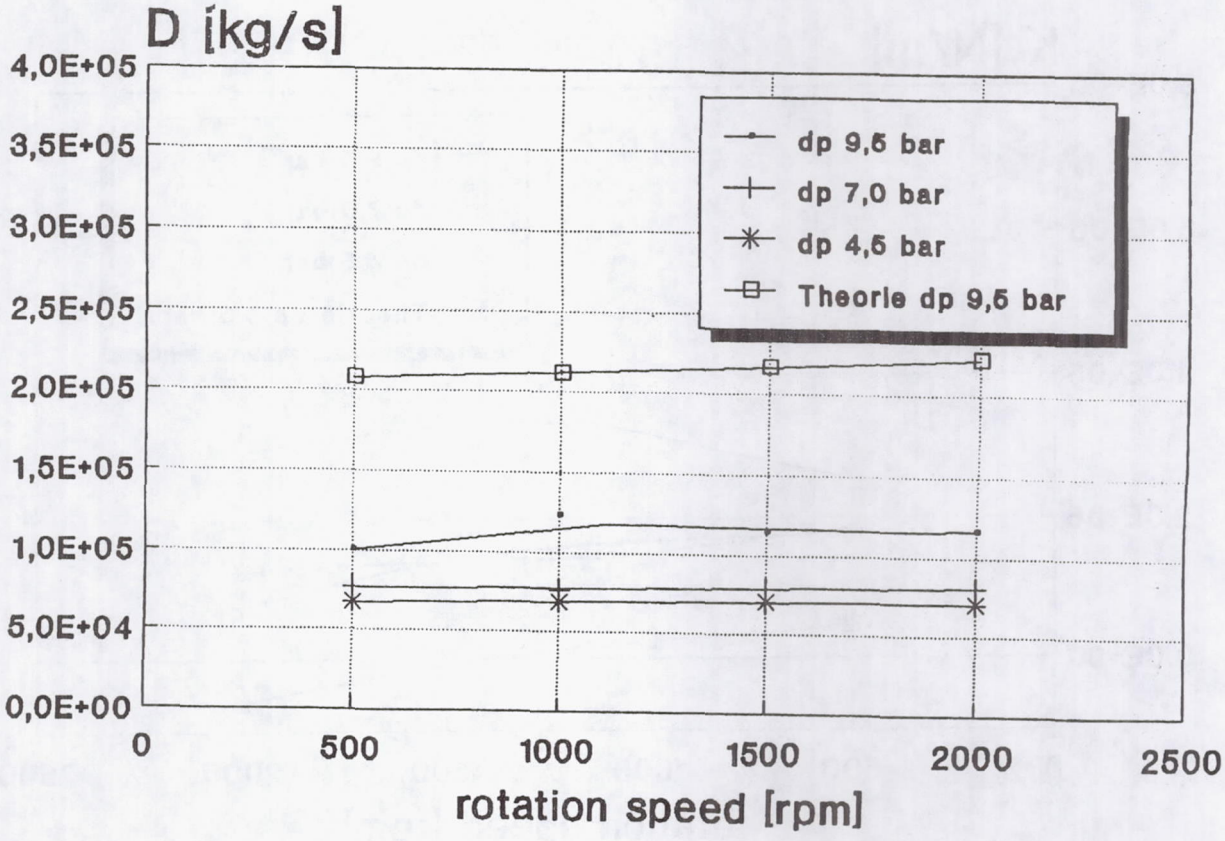
D [kg/s]
4,0E+05
3,5E+05
3,0E+05
2,5E+05
2,0E+05
1,5E+05
1,0E+05
5,0E+04
0,0E+00
0
500
1000
1500
2000
2500
rotation speed [rpm]
dp 9,5 bar
dp 7,0 bar
dp 4,5 bar
Theorie dp 9,5 bar

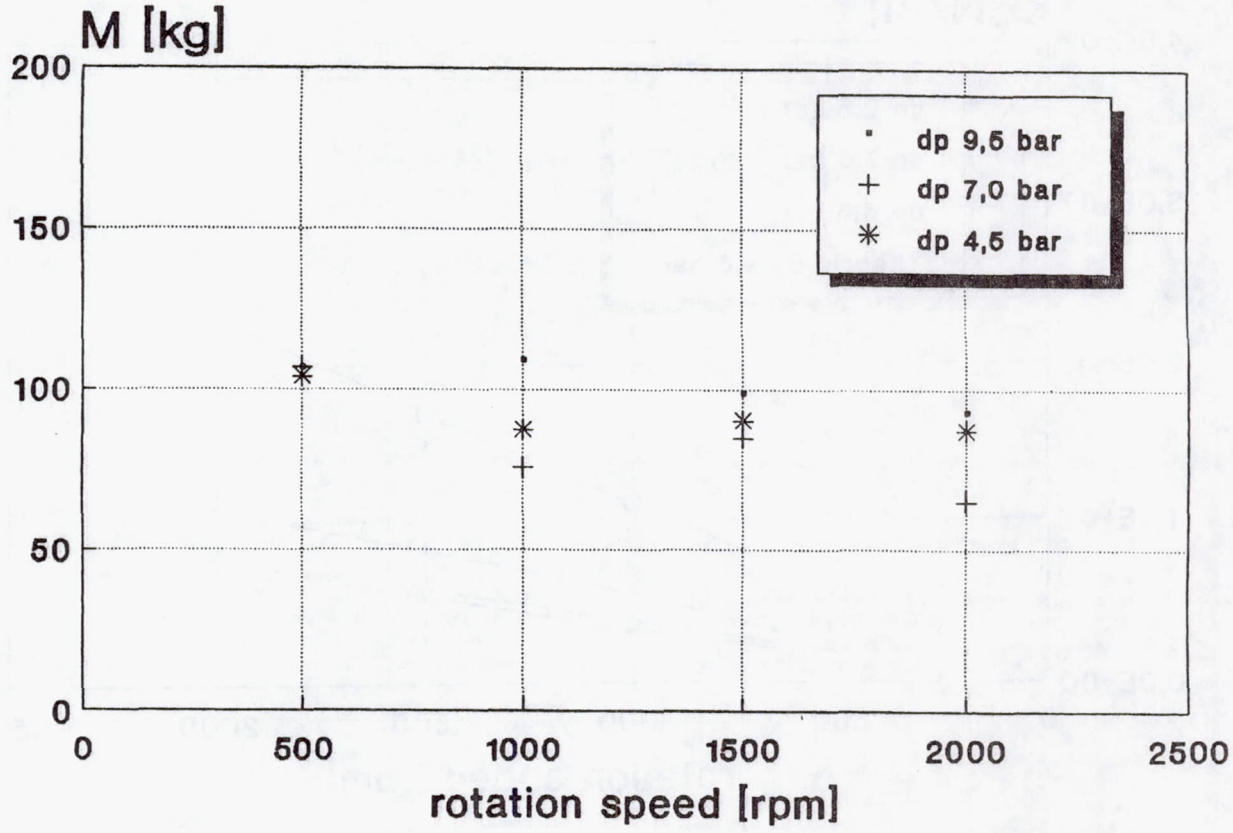
M [kg]
200
150
100
50
0
0
500
1000
1500
2000
2500
rotation speed [rpm]
dp 9,5 bar
dp 7,0 bar
dp 4,5 bar

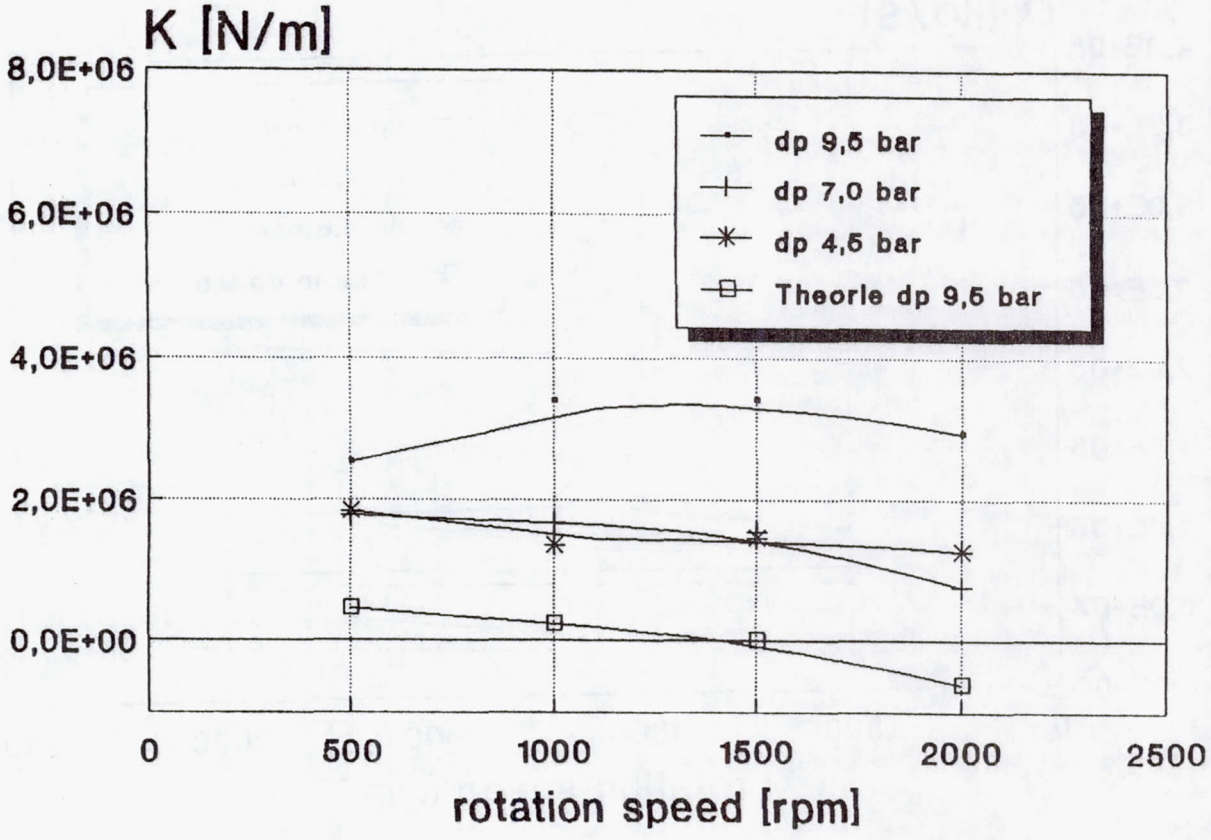
K [N/m]
8,0E+06
6,0E+06
4,0E+06
2,0E+06
0,0E+00
0
500
1000
1500
2000
2500
rotation speed [rpm]
dp 9,5 bar
dp 7,0 bar
dp 4,5 bar
Theorie dp 9,5 bar

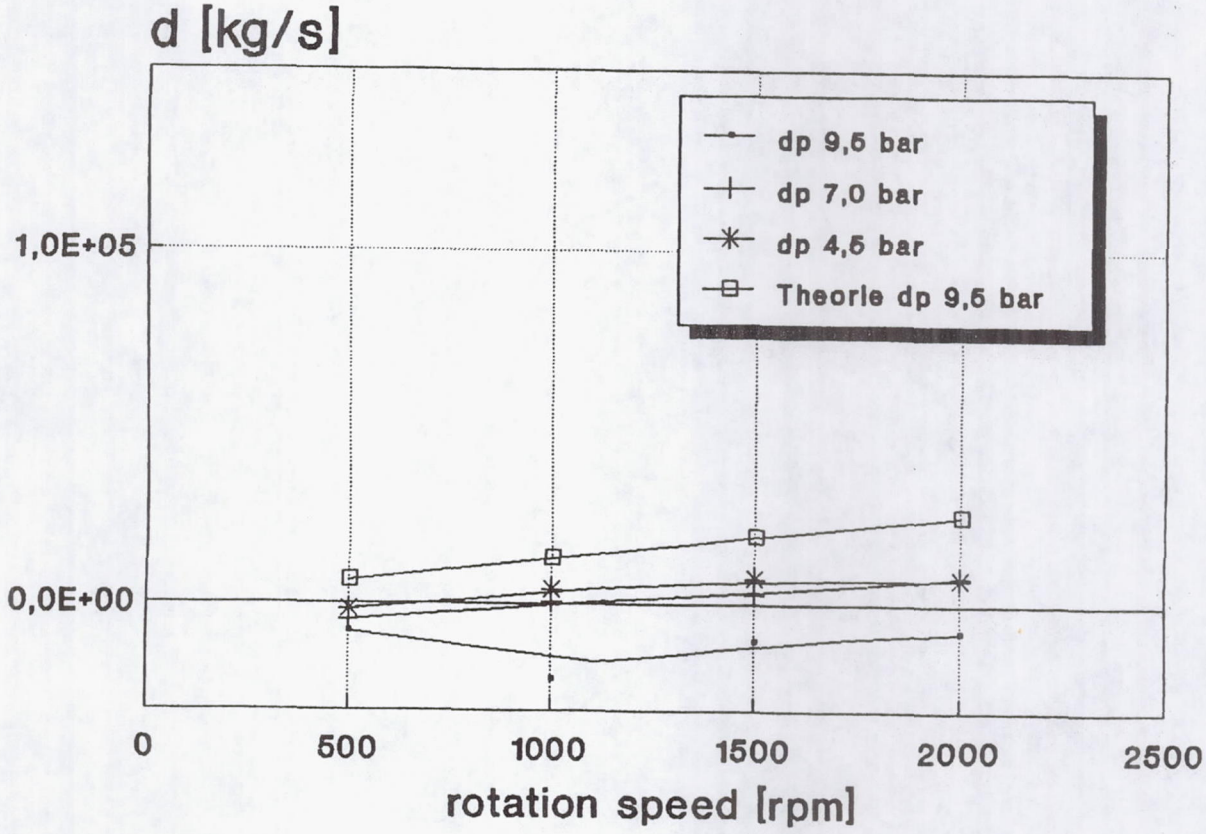
d [kg/s]
dp 9,5 bar
dp 7,0 bar
dp 4,5 bar
Theorie dp 9,5 bar
1,0E+05
0,0E+00
0
500
1000
1500
2000
2500
rotation speed [rpm]

ECCENTRICITY EFFECTS UPON THE FLOW FIELD INSIDE A WHIRLING ANNULAR SEAL

Gerald L. Morrison, Robert E. DeOtte, Jr.,
Purandar G. Das, and H. Davis Thames
Texas A&M University
College Station, Texas

ABSTRACT

The flow field inside a whirling annular seal operating at a Reynolds number of 24,000 and a Taylor number of 6,600 has been measured using a 3-D laser Doppler anemometer system. Two eccentricity ratios were considered, 0.10 and 0.50. The seal has a diameter of 164 mm, is 37.3 mm long and has a clearance of 1.27 mm. The rotor was mounted eccentrically on the shaft such that the whirl ratio is 1.0 and the rotor follows a circular orbit. The mean axial velocity is not uniform around the circumference of the seal; near the inlet a region characterized by high velocity is evident on the pressure side of the seal, but the velocity is relatively uniform by the center plane of the seal. By the exit, another region of high axial velocity has developed, this time on the suction side of the seal. The magnitude and azimuthal distance of the migration increased with increasing whirl amplitude (eccentricity). Throughout the seal length the azimuthal mean velocity varied inversely with the mean axial velocity. Increasing the whirl amplitude did not increase the magnitude of the azimuthal velocity at the seal exit.

NOMENCLATURE

A	Leakage area	W	Tangential mean velocity
c	Mean clearance	$\overline{u'u'}$	Time averaged Reynolds stress
d	Rotor diameter	W_{sh}	Rotor surface speed
e	Eccentricity	Z	Distance from seal inlet
L	Length of the seal	ϵ	Eccentricity ratio, e/c
Q	Leakage flow rate	θ	Azimuthal angle
r	Radial distance from stator centerline	μ	Fluid absolute viscosity
Re	Reynolds number = $2Uc/\nu$	ν	Kinematic viscosity
Ta	Taylor number = $\frac{cW_{sh}}{\nu}\sqrt{\frac{2c}{d}}$	ρ	Fluid density
U	Axial mean velocity	ω	Whirl ratio, ω_p/ω_r
U_{ave}	Bulk mean velocity=Q/A	ω_p	Rotor precession speed
V	Radial mean velocity	ω_r	Rotor speed

INTRODUCTION

A seal, by definition, separates regions of high and low pressure fluids. In some cases, the desire is to prevent leakage, but that is not the general situation. Usually the seals in rotating machinery, such as pumps and compressors, are designed to control but not eliminate the leakage flow which may cool and enhance operating stability by improving vibration damping. Seal design involves balancing considerations of machine efficiency, which is generally higher with lower leakage, with operational stability.

In many applications, the shaft itself plays the part of the seal. The seal clearance is usually less than a tenth of a millimeter. Obtaining accurate measurements in these small regions is, at best, difficult. As a consequence, the database of velocity and turbulence measurements is

[1]Presently a Senior Engineer at BW/IP International, Inc. Pump Division, Vernon, CA.

Preceding Page Blar

very small. Further complicating matters is the turbulent flow found under normal operating conditions. The lack of detailed flow field information hinders the development of accurate seal performance analyses.

Research in this area has been mainly devoted to studying leakage and rotordynamic coefficients. Though quite important for gaining an insight into the behavior of these seals, they alone do not present a complete picture. Velocity measurements have been made in models with clearance ratios (seal clearance to seal diameter) much larger than those found in actual applications. Turbulence measurements, however, are much scarcer. Most of the data available is for seals operating under static conditions and does not provide the knowledge of both the mean velocities and the turbulent quantities necessary for numerical modelling of the flow fields.

Although ideal operating conditions are assumed for seal design and modelling purposes, this is often not the case. During machine operation, shafts become misaligned resulting in the seal spinning eccentric to the center of rotation thus altering the dynamic forces. The flow in such an eccentric seal is different from that in a concentric seal. To provide data applicable to such routine situations, the rotors/seals studied were deliberately spun off center.

One of the important objectives of this study is to help build a database of flow measurements for annular seals over a range of operating conditions. Earlier work done at this lab, Thames[1992], focussed on flow through an eccentric seal with a 0.5 eccentricity ratio. That study represents an extreme case of misalignment. This work compares an annular seal, operating with a 0.1 eccentricity ratio, to the 0.5 eccentricity ratio case operating at the same conditions.

Literature Review

Nelson and Nguyen[1987] working at Texas A & M University, studied the effects of eccentricity on rotordynamic coefficients. They presented a new analysis procedure that solved for flow variables in an eccentric annular seal. The governing equations were based on a turbulent bulk flow model and Moody's friction factor equation. Comparisons with experimental data led them to conclude that this method was more accurate in predicting the rotordynamic coefficients than one which used a finite element analysis procedure. The accuracy of the procedure could be improved significantly if a more accurate friction factor formula for annular seals was found.

Chen and Jackson[1987] studied the influence of eccentricity and misalignment on the performance of high-pressure annular seals. Using existing concentric seal theories they developed a method for the calculation of both seal leakage and dynamic coefficients for short seals with large eccentricities and/or misalignment of the shaft. The Space Shuttle Main Engine High Pressure Fuel Turbopump pump interstage seal was used for calculating the leakage coefficients. From the ensuing predictions they concluded that the effect of eccentricity on the leakage rate was higher in the case of laminar flow than when the flow was turbulent. They also found that as the eccentricity/misalignment ratio (inlet versus outlet) increased the mass flow leakage decreased due to an increase in the passage blockage.

Allaire, et al.[1978], while studying the dynamics of short eccentric plain seals with high axial Reynold's numbers, saw a "Bernoulli" effect in eccentric seals. A bulk flow theory developed by Hirs[1973] was used in the analysis. They found that for a given axial pressure drop across the seal, the axial fluid velocity is greatest in the maximum clearance portion of the seal and least in the minimum clearance portion of the seal. The pressure distribution around the shaft was found to be inversely related to the velocity distribution. This pressure distribution induced a hydrodynamic force which tended to center the shaft. At low Reynold's numbers the pressure differences in the seal were small and mainly due to friction effects. At high Reynold's numbers the friction effects were small and the pressure was constant around and along the seal. In conclusion, they stated that the load capacity of the seal was maximized for a given value of the axial Reynold's number, when the Bernoulli effect was the greatest. At very high Reynold's

numbers, large head losses occurred at the entrance to the seal which induced a constant pressure and diminished the load capacity of the seal.

Tam and et al.[1988] numerically calculated and compared leakage rates and dynamic coefficients for eccentric annular seals. The numerical model was based on a conservative form of the three dimensional Navier-Stokes equations. The analytical model was based on "lumped" fluid parameters. The characteristics of the seal were summarized as strong swirl, high viscosity and a high pressure drop associated with significant wall roughness and small clearances. The turbulence closure was obtained with the zero-equation Prandtl mixing length model. This model was chosen because of its simplicity and the fact that the mixing length can be estimated by the clearance. The eddy viscosity concept was used to compute the Reynold's stresses. The solution was obtained using the SIMPLEST algorithm. The boundary conditions employed included: specified pressure at the flow inlet and outlet, circumferential velocity at the inlet, rotor angular velocity and rotor precessional speed, no slip velocity condition at the rotor and stator walls, fluid shear stresses on the surfaces of the rotor and stator, and cyclic boundary conditions in the circumferential direction. A three dimensional, nonorthogonal, body-fitted computational grid of dimensions 12 X 6 X 16 was employed. The results showed significant changes in the fluid forces along the seal, as well as the presence of secondary recirculation zones, even with large axial pressure drops. It was found that at lower rotational speed and higher perturbation speed, the secondary flow zones were intensified. This, in turn, lowered the average circumferential velocity, enhancing the stability of the rotor. A secondary flow zone occurred just in front of the minimum clearance zone and these zones rotated at the same speed as the shaft. Preswirl, introduced at the inlet end of the seal, influenced the average circumferential velocity. Fluid injection effects were also studied. The fluid was injected radially, both with and against the direction of rotation. Injection in the direction of rotation increased the leakage rate, whereas, a drop of about 7% was observed when the injection was against the direction of rotation. In conclusion, the average leakage rate was found to be most influenced by the axial pressure drop. The effect of rotation and perturbation speed on leakage rate was most pronounced when a low axial pressure drop was assumed.

Simon and Frene[1989] investigated the static and dynamic characteristics of plain annular seals in the turbulent flow regime. They studied a tapered seal mainly with respect to cryogenic applications, considering the effects of swirl, axial acceleration effect of liquid at the inlet and variable fluid properties. Assuming that pressure, viscous, and turbulent stresses rendered the fluid inertial forces negligible they compared their leakage predictions with those of Childs [1986] and obtained good agreement. In conclusion they observed lower leakage rates for a straight seal with constant fluid properties and increasing L/D ratio's of up to a value of 0.2. For tapered seals the leakage was initially found to increase with increasing L/D ratio's up to 0.2, but decreases thereafter.

Kanemori and Iwatsubo [1989] conducted an experimental study of the dynamic forces acting on a long annular seal. They found that their results agreed with Fritz's [1970] theory, which does not make any considerations for axial flow. They suggested that the fluid reaction force in the seal depended on the whirl velocity and that under certain conditions the tangential velocity acted as a de-stabilizing force.

Johnson [1989] and Morrison, et al[1991a] investigated the flow filed inside centered and statically eccentric annular seals using a 3-D Laser Doppler velocimeter. The seal, with a clearance of 0.0127 mm, was operated at a Reynolds number of 27,000 and a Taylor number of 6,600. The mean velocity vector and the entire Reynolds stress tensor at four angular positions (for the eccentric seal) corresponding to the minimum clearance, maximum clearance and two intermediate locations were measured along the entire length of the seal. The different flow cases considered included no pre-swirl, backward pre-swirl, and forward pre-swirl. For the forward swirl case the profile of azimuthal velocity appeared to be reasonably well developed for all

clearances whereas for the no pre-swirl and backward pre-swirl cases, substantial flow development occurred for each clearance. Pre-swirl does have a pronounced effect, although it is not significantly greater for the statically eccentric than the concentric configuration.

Thames [1992] measured the flow field inside a whirling annular seal ($\epsilon=0.5$) using a 3-D Laser Doppler Velocimeter with phase averaging. Two axial flow conditions (Re=12,000 and Re=24,000) were considered. Velocity and Reynolds stress distributions were presented for both flow conditions. The existence of a region of high axial momentum, which at the inlet is on the high pressure side of the seal and migrates to the suction side at the exit of the seal, was identified.

OBJECTIVES

Most studies of seals have been empirical or numerical. The time averaged Navier-Stokes equations were solved by finite difference techniques using a κ-ϵ turbulence closure model. Although the numerical solutions predict the flow field, experimental data is required for verification. This study was undertaken to measure the flow field through eccentrically whirling annular seals. Measurements made were of the instantaneous velocity components in three independent directions. From these, the mean flow velocity in the axial, radial and tangential directions were calculated along with the turbulent kinetic energy and the phase averaged Reynolds stresses.

FACILITIES AND INSTRUMENTATION

The experiments were performed in the seal test facility of the Turbomachinery Laboratory which has been described previously by Morrison, et al.[1991a]. The test section (Figure 1) consists of a 50.8 mm diameter overhung shaft which is rotated by a variable speed electric motor. The rotor is manufactured of acrylic and is mounted onto the shaft via a bushing. For the present study, mounting bushings were made so that the inner hole was eccentric with the outer surface such that eccentricity ratios of 0.1 and 0.5 were obtained. This mounting results in the rotor whirling at the same speed as the shaft, i.e. a whirl ratio of 1.0. The stainless steel stator is mounted concentric with the overhung shaft. For this set of experiments, the internal contoured plug in the plenum (as used by Morrison[1991a]) was not installed leaving the face of the rotor completely exposed to the plenum.

Water is provided to the test section from a 19 m^3 storage tank via a centrifugal pump, throttling valve, and turbine meter. The throttling valve is adjusted to produce the required flowrate through the seal. The water exiting the test section is returned to the storage tank. During the tests, the water temperature remained between 17°C and 23°C.

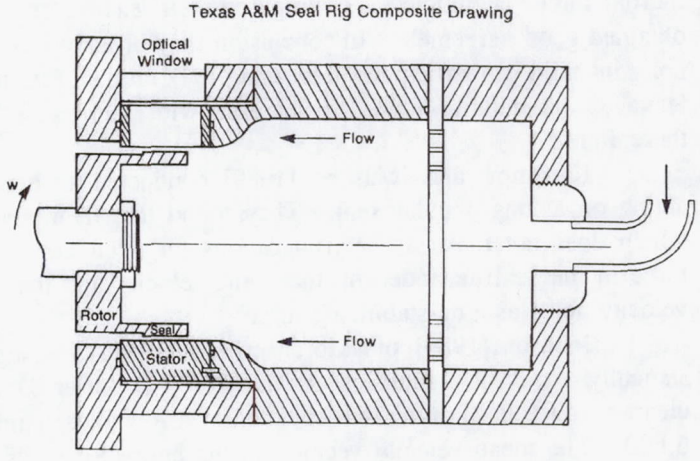

Figure 1. Seal Test Facility.

The velocity field inside the annular seal is measured using a 3-D Laser Doppler Anemometer (LDA) system. This system has been described in detail in Morrison, et al.[1991a] and

Johnson[1989]. The 3-D LDA system uses three colors of laser light to measure three instantaneous non-orthogonal velocity components at one location in space. The composite probe volume is 0.025 X 0.025 X 0.102 mm. The three instantaneous non-orthogonal velocity components are used to calculate the instantaneous velocity vector in the seal coordinates. A rotary encoding system was used to tag each instantaneous velocity measurement with the angle of the rotor when the measurement was obtained. For each spatial location, 90,000 individual instantaneous velocity measurements were made which were then phase averaged (into 18° increments) to determine how the mean velocity varies with rotor position. The phase averaged Reynolds stress tensor was also calculated from the data; however, because of space limitations, only the axial velocity variance will be presented in this paper. Measurements were made across the clearance at 20 different axial locations from slightly upstream of the rotor to the exit plane of the rotor. A complete listing of the data for all angles and axial locations is contained in Thames[1992] and Das[1993]. Morrison, et al[1991b], Thames[1992], and DeOtte, et al[1992] have discussed all the details concerning the accuracy of the measurements made with this system. For the present study, the McLaughlin-Tiederman[1973] velocity bias correction technique was used. The uncertainty of the measurements is as follows: U $\pm$ 0.115 m/s, V $\pm$ 0.432 m/s, W $\pm$ 0.095 m/s, and $\overline{u_x' u_x'} \pm 0.013$ m^2/s^2. Unexpanded polystyrene spheres (6μm in diameter) were used as the seed for the LDA system which possesses a frequency response in excess of 44 kHz in the water.

RESULTS

Axial Velocities

Contour plots of axial mean velocity at axial positions of Z/L = 0.00, 0.21, 0.50. 0.77, and 1.00 in Figure 2 compare the two eccentricity ratios of 0.1 and 0.5. The minimum clearance is at the top of each plot and the rotor is both rotating and whirling in a clockwise direction, i.e. the pressure side of the seal is on the right ($0 \leq \Theta \leq 180°$). For reference, the bulk average velocity (Q/A) is 7.4 m/s. For ϵ=0.1, at the entrance, the mean axial velocity possesses a saddle back profile (velocities higher near the rotor and stator than in the center of the clearance). Such profiles are characteristic of flow encountering an abrupt change in area such as flow through an orifice. The saddle back velocity profile is still present at Z/L = 0.21 but has decreased in severity and by the center of the seal (Z/L=0.5) the saddle back has disappeared. Turbulence generated by shear stresses at the wall diffuses fluctuating momentum radially across the seal which reduces gradients in the mean axial velocity profile. Previous work by Morrison, et al.[1991a] for a non-whirling seal operating at the same Reynolds and Taylor numbers did not show the saddle back profile but in that case a contoured plug was present in the upstream plenum. The plug in conjunction with the stator contour created a nozzle which gently guided the flow into the seal thus eliminating the saddle back profile. At the higher eccentricity ratio (ϵ=0.5) large disturbances caused by the whirling seal overwhelms the influence of the sudden contraction and the saddle back does not occur. In both cases, the azimuthal location of maximum axial velocity is not at the location of maximum clearance at the seal inlet but is located on the pressure side of the seal. The shift away from the maximum clearance location is more pronounced for the larger eccentricity case. Both cases also exhibit the interesting behavior of the migration of the high axial velocity region from the pressure side of the seal at the inlet to the suction side at the exit passing through the maximum clearance at the X/L=0.50. The magnitude of the maximum axial velocity decreased from the entrance to the center of the seal where the axial velocity reaches its most uniform tangential distribution. From the center plane to the exit, the flow concentrated such that a distinct region of higher velocity develops at the exit plane. All of these effects were accentuated by the larger eccentricity. It is hypothesized that the fluid entering the seal preferentially heads towards the location of the maximum clearance. However, since the location is continually changing, the fluid does not reach the rotor before the clearance decreases. The fluid must then either divert

towards the azimuthal location of maximum clearance or accelerate and enter the smaller clearance. Since a smaller acceleration is required in the axial direction than in the tangential direction, the required pressure gradient is smaller and the fluid accelerates axially. Discussion about the migration of the axial momentum to the suction side will be delayed until the azimuthal velocities have been presented.

Radial Velocities

Figure 3 presents contours of the radial mean velocity. The radial velocities are maximum in the inlet plane as the flow adjusts from the large plenum cross sectional area to the substantially smaller clearance area. The radial velocities become negligible past $Z/L=0.21$ as the flow adjusts to the small channel clearance. The flow sweeps into the seal from the stator wall resulting in the large negative velocities at the inlet plane will reach maximum values close to the region where the axial velocities are largest. The whirling of the seal tends to block the flow from entering from the plenum region upstream of the rotor face.

Azimuthal Velocities

The mean azimuthal velocities are shown in Figure 4. Please note that the rotor surface speed is 30.9 m/s. The contour levels were adjusted to show more clearly the fluid velocity. The inlet plane contours illustrate that the rotor induces a significant amount of preswirl into the fluid by the time it reaches the seal inlet. This is more pronounced for the $\epsilon=0.5$ case. The blockage of the incoming fluid due to the large eccentricity results is the higher levels of swirl for this case. For the $\epsilon=0.1$ condition, the azimuthal mean velocity has a saddle back type profile, as did the axial velocity, which is roughly inversely proportional to the axial mean velocity. That is, when the axial velocity is high, the azimuthal velocity is low and when the axial velocity is low the azimuthal velocity is high. This inverse proportionality is also seen at the inlet for $\epsilon=0.5$ with the azimuthal velocities being larger on the suction side and the axial velocities larger on the pressure side. This may be a simple residence time effect with the slower axial velocity increasing the residence time of the fluid which allows the tangential shear produced by the rotor to impart more azimuthal velocity to the fluid. For the $\epsilon=0.5$ case, the inverse proportionality of the axial and azimuthal velocity components continues to the exit plane where the largest azimuthal velocities have migrated to the pressure side and the largest axial velocities are on the suction side. This migration of the maximum axial momentum flux from the pressure side to the suction side is caused over the first half of the seal ($0 \leq Z/L \leq 0.5$) by the fluid expanding from the pressure side with its small clearance to the location of maximum clearance. This is most likely due to an azimuthal pressure gradient. However, it is the azimuthal velocity which becomes increasingly larger on the pressure side pumping additional fluid from the pressure side to the suction side as the flow continues further downstream. The same effect is seen in for the $\epsilon=0.1$ case but to a lesser extent since the effects of the whirl are decreased by the decreased eccentricity. The mean azimuthal velocity approached 10 m/s (32% of the rotor surface speed) at the exit of the seal with very little azimuthal variation for the $\epsilon=0.1$ case but a much greater azimuthal variation for the $\epsilon=0.5$ case. This is larger than the 20% measured by Morrison, et al.[1991a] for a non-whirling annular seal. However, Morrison, et al. also observed inlet azimuthal velocity values of less than 10% of the rotor speed compared to the 13% to 30% observed in the present case. The elimination of the centerline plug in the plenum resulted in significantly higher preswirl for the present study. The fact that the same levels of swirl are present at the seal exit for both the $\epsilon=0.1$ and 0.5 cases show that increased eccentricity (whirl amplitude) does not increase the level of swirl induced by the rotor.

Axial Velocity Variance

The axial velocity variances shown in Figure 5 illustrate that the majority of turbulence production occurs during the first half ($0 \leq Z/L \leq 0.5$) of the seal length. Initially the largest turbulence levels are located near the upstream lip of the rotor where the accelerating fluid comes in contact with the rotor surface resulting in large radial and axial velocity gradients. The shear layer generates large levels of vorticity and produces turbulence. The turbulence production continues along the first quarter of the seal length with the turbulence levels remaining high (exceeding turbulence intensities $\left[\sqrt{\overline{u'u'}} \;/\; U_{ave}\right]$ of 50%) and spreading across the seal clearance. The turbulence level for $\epsilon=0.1$ is significantly larger at $Z/L=0.219$ than for $\epsilon=0.5$. This is a result of the saddle back velocity profiles present only for $\epsilon=0.1$. The saddle back profiles posses larger regions of mean velocity gradient which in turn generate more turbulence. From 0.21 to 0.50 Z/L the turbulence level decreases as the mean flow adapts to the small clearance. The mean velocity gradients (and vorticity) are smaller decreasing the turbulence production. From $Z/L=0.5$ to the exit of the seal the turbulence levels remain relatively constant with only a slight increase near the rotor surface at the exit plane which is caused by the expansion into the region downstream of the seal.

CONCLUSIONS

The complex three dimensionality of the flow through whirling annular seals precludes the use of such quasi-steady state models as that of a statically eccentric seal. Such would predict the maximum axial velocity to be located at the maximum clearance over the entire length of the seal. For both the $\epsilon=0.1$ and 0.5 cases this is not true but instead the maximum axial velocity is on the pressure side of the seal at the inlet and migrates to the suction side at the exit. The larger eccentricity amplified the behavior. The larger eccentricity greatly modified the inlet velocity profiles: the saddle back profiles were eliminated by the rotating blockage effect. The mean azimuthal velocity approached 10 m/s (32% of the rotor surface speed) at the exit of the seal. For the $\epsilon=0.1$ case azimuthal variation was small but is was much greater for the $\epsilon=0.5$ case. The mean radial velocities were largest at the entrance plane due to the flow contracting into the clearance from the plenum but diminished in magnitude rapidly past the entrance. Maximum turbulence production and turbulence levels were present over the first 25% of the seal length with turbulence production and dissipation coming into equilibrium by the center of the seal. Turbulence intensities exceeded 50% $\left[\sqrt{\overline{u'u'}} \;/\; U_{ave}\right]$ in the entrance region. Overall the flowfield is very complex and three dimensional suggesting very complex surface forces.

REFERENCES

Allaire, C.C., Lee, E.J. and Gunter, P.E., 1978, "Dynamics of short eccentric plain seals with high axial Reynolds number.", *J. Space. & Rockets,* Vol. 15, No. 6, pp. 341-347.

Chen, W.C. and Jackson, E.D., 1987, "A general theory for eccentric and misalignment effects in high-pressure annular seals.", *ASLE Transactions,* Vol. 30, No. 3, p. 293-301.

Childs, D.W. and Scharrer J.K., 1986, "An Iwatsubo-based solution for labyrinth seals: comparison to experimental results.", *Transactions ASME Journal of Engineering. Gas Turbines & Power,* Vol. 2, p. 325-331.

Das, P.G., 1993, "3-D LDV Measurements of Eccentric Annular and Labyrinth Seals," Master of Science Thesis, Texas A&M University.

DeOtte, Jr. R.E., Morrison, G.L., and Wiedner, B.G., 1992, "Considerations on the Velocity Bias in Laser Doppler Velocimetry, Presented at the Sixth International Symposium on Applications of Laser Techniques to Fluid Mechanics, Istituto Superior Tecnico, Av. Rovisco Pais, 1096 Lisboa Codes, Portugal.

Fritz, R.J., 1070, "The Effects of an Annular Fluid on the Vibrations of a Long Rotor, Part2-Test.", *Trans. ASME Journal Basic Engineering.*, p. 930.

Hirs, G.G., 1973, "Bulk Flow Lubricant Theory for Turbulence in Lubricant Films," *ASME Journal of Lubricant Technology,* Vol. 110, pp. 137-146.

Johnson, M.C., 1989, "Development of a 3-D Laser Doppler Anemometry System:With Measurements in Annular and Labyrinth Seals.", Ph.D. Dissertation, Texas A&M University.

Kanemori, Y., and Iwatsubo, T., 1989, "Experimental Study of Dynamical Characteristics of a Long Annular Seal," *JSME International Journal Series II,* Vol. 32, pp. 218-224.

Morrison, G. M., Johnson, M.C., and Tatterson, G.B., 1991, "Three Dimensional Laser Doppler Measurements in an Annular Seal," *ASME Journal of Tribolgy,* Vol. 113, pp. 390-396.

McLaughlin, D.K. and Tiederman, W.G., 1973, "Biasing Correction for Individual Realization of Laser Anemometer Turbulent Flows", *The Physics of Fluids,* Vol. 16, pp. 2022-2088.

Morrison, G.L., Johnson, M.C., and Tatterson, G.B., 1991a, "Three Dimensional Laser Doppler Measurements in an Annular Seal," *ASME Journal of Tribolgy,* Vol. 32, pp. 390-396.

Morrison, G.L., Johnson, M.C., Swan, D.H., and DeOtte, Jr., R.E., 1991b, "Advantages of Orthogonal and Non-orthogonal Three-Dimensional Anemometer Systems," *Flow Measurement and Instrumentation*, Vol. 2, pp. 89-97.

Nelson, C.C. and Nguyen, D.T., 1987, "Analysis of Eccentric Annular Incompressible Seals: Part 1. A New Solution Using Fast Fourier Transforms For Determining Hydrodynamic Force." New York, U.S.A., American Society of Mechanical Engineers. ASME paper No. 87-Trib-52.

Simon F., and Freene, J, 1989, "Static and Dynamic Characteristics of Turbulent Annular Eccentric Seals: Effect of Convergent-Tapered Geometry and Variable Fluid Properties," *ASME Journal of Tribology,* Vol. 111, pp. 378-385.

Tam, L.T., Przekwas, A.J., Muszynska, A., Hendricks, R.C., Braun, M.J., and Mullen, R.L., 1988, " Numerical and Analytical Study of Fluid Dynamic Forces in Seals and Bearings," *Journal of Vibration, Acoustics, Stress, and Reliability in Design,* Vol. 110, pp. 315-325.

Thames, H.D., 1992, "Three Dimensional Laser Doppler Measurements of an Annular Seal," Master of Science Thesis, Texas A&M University.

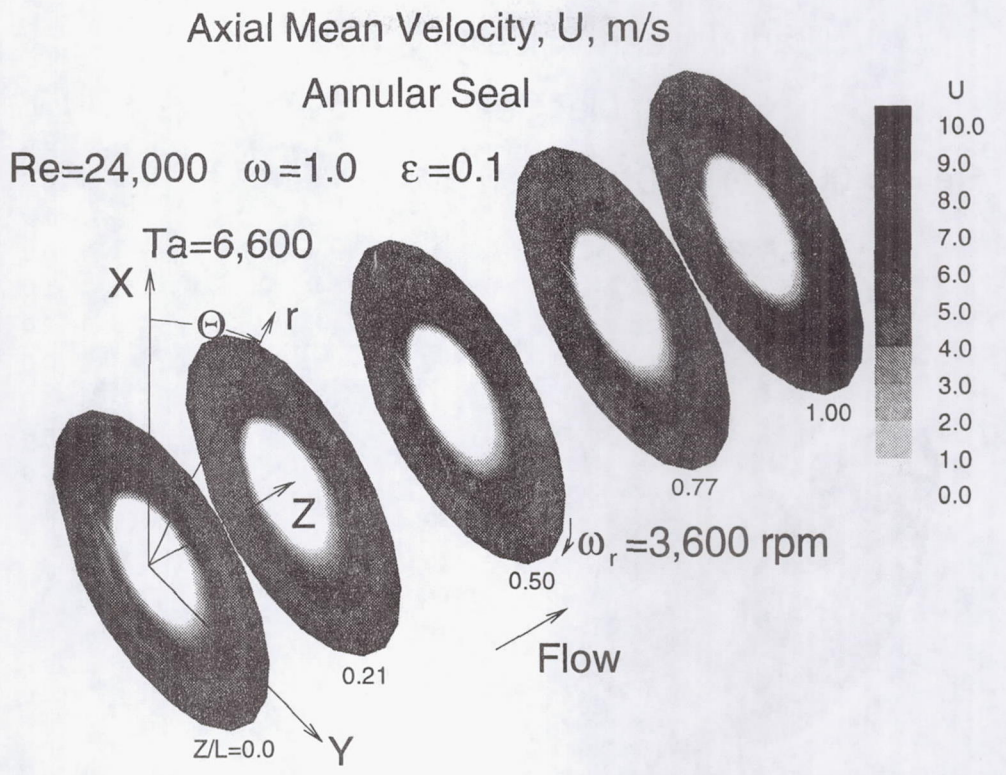

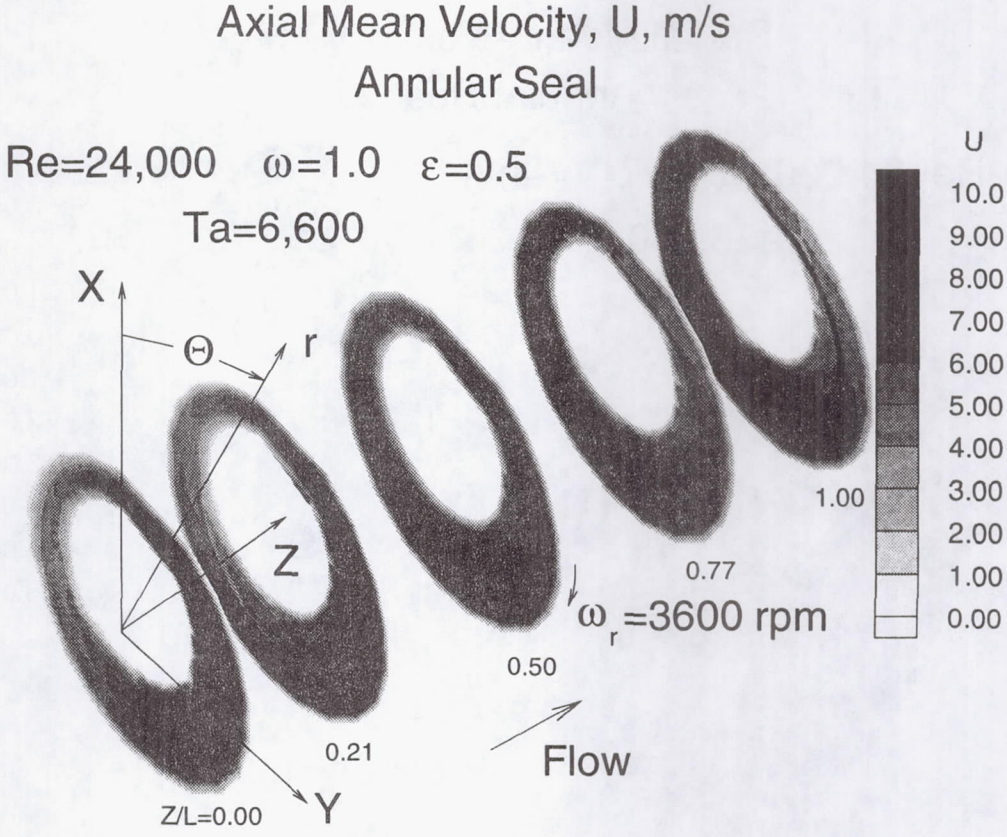

Figure 2. Axial Mean Velocity Contours

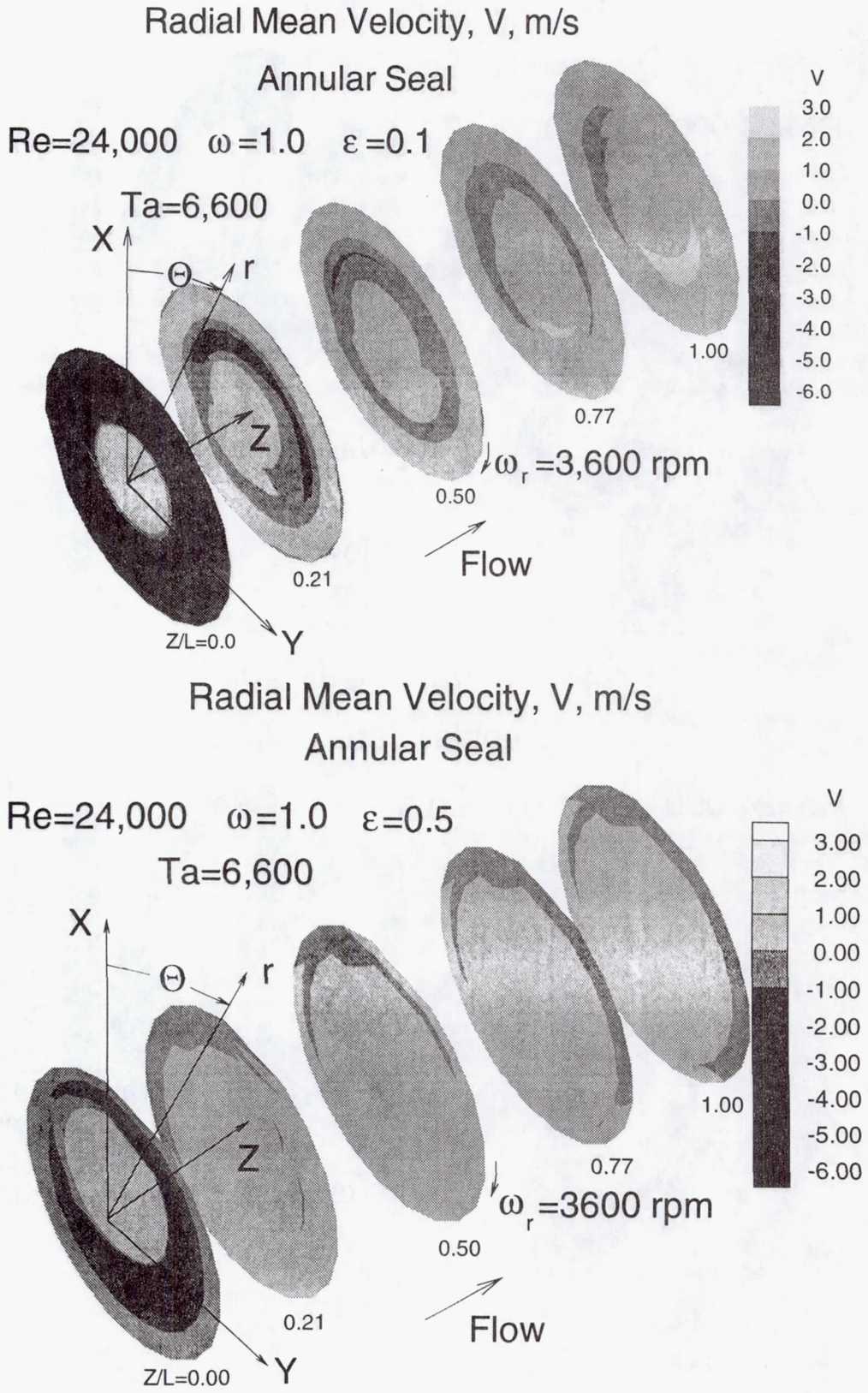

Figure 3. Radial Mean Velocity Contours

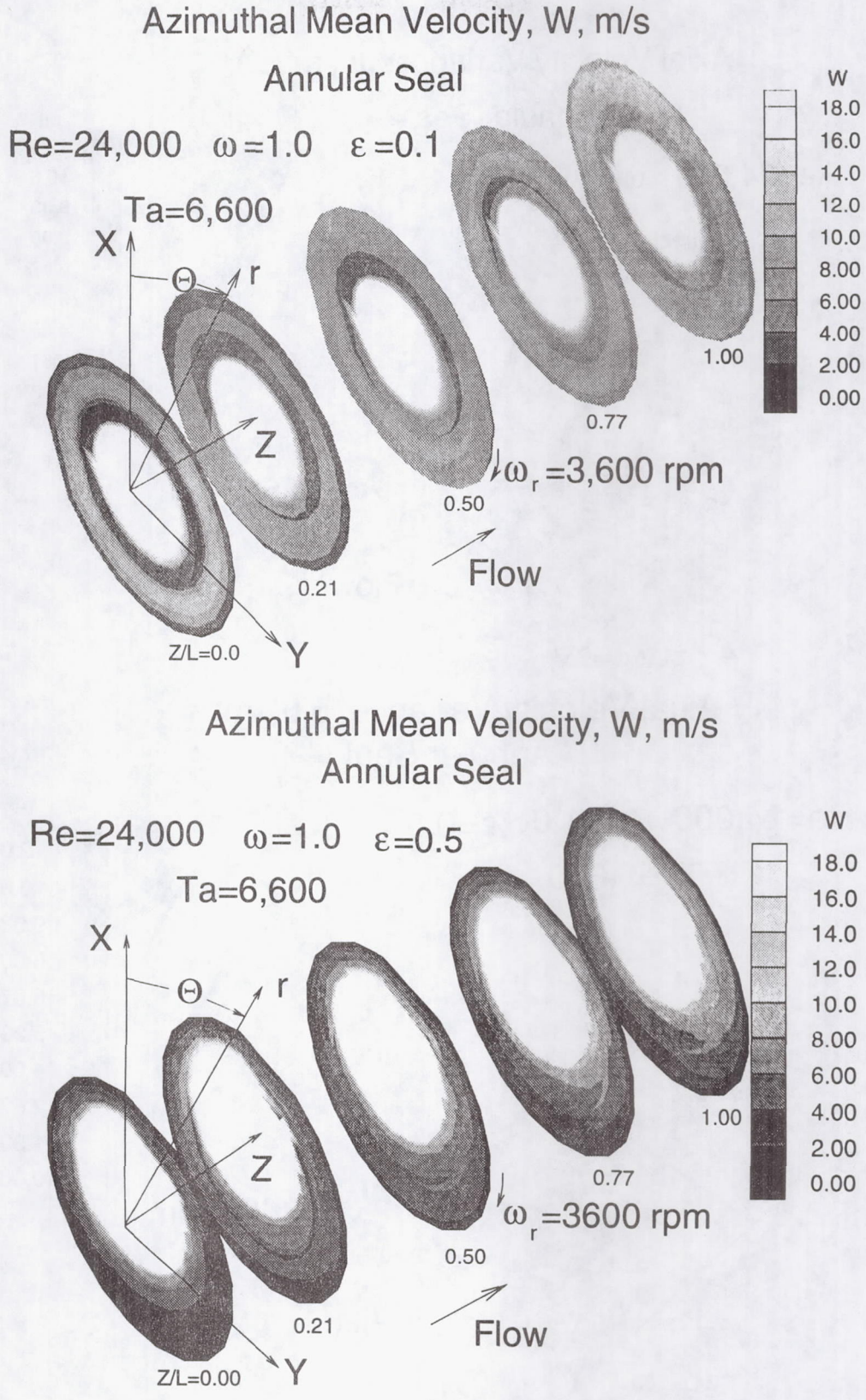

Figure 4. Azimuthal Mean Velocity Contours

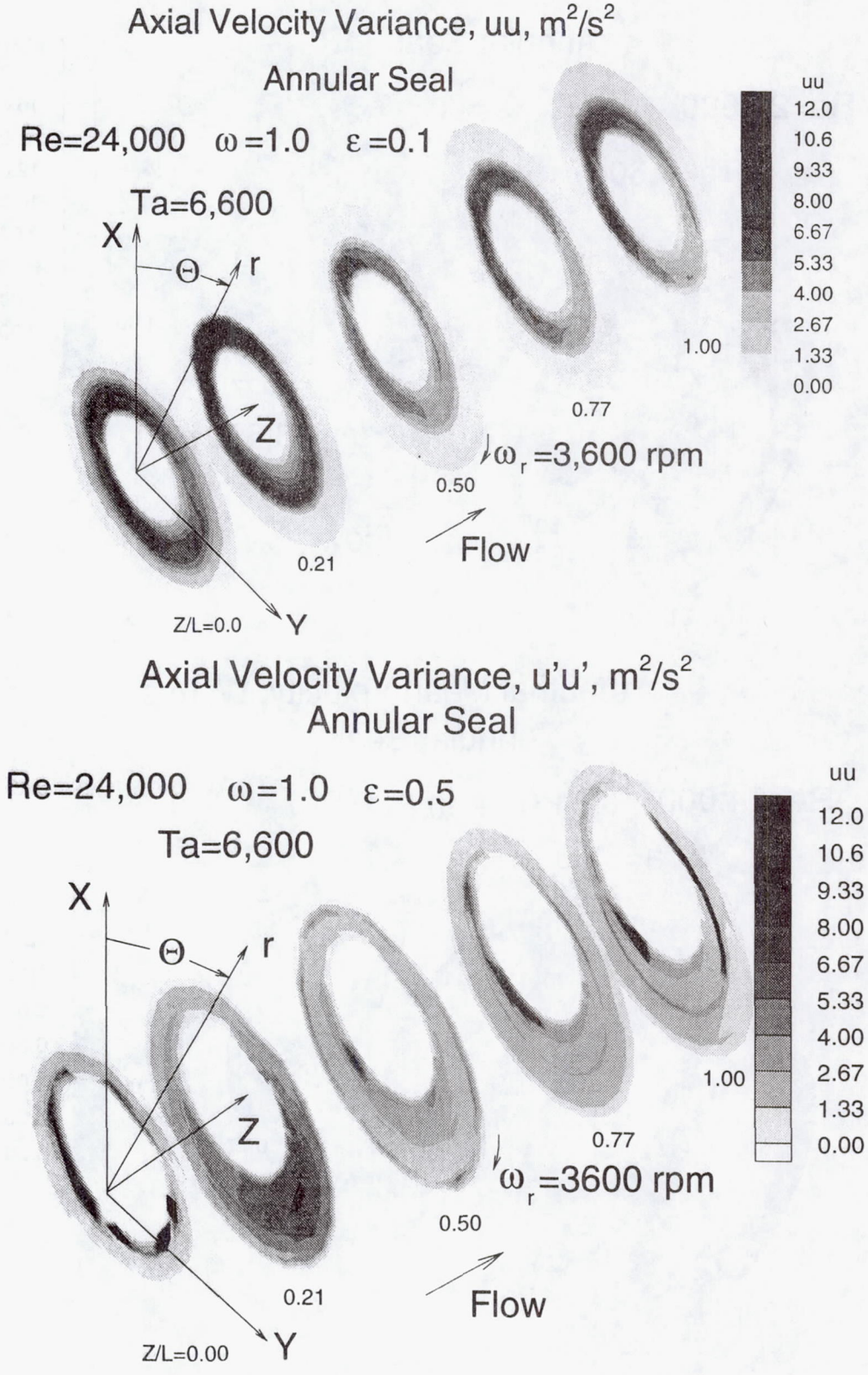

Figure 5. Axial Velocity Variance Contours

APPLICATION OF AN IMPROVED NELSON-NGUYEN ANALYSIS TO ECCENTRIC, ARBITRARY PROFILE LIQUID ANNULAR SEALS

Satyasrinivas Padavala and Alan B. Palazzolo
Texas A&M University
College Station, Texas

and

Pat Vallely and Steve Ryan
NASA George C. Marshall Space Flight Center
Marshall Space Flight Center, Alabama

Abstract

This paper presents an improved dynamic analysis for liquid annular seals with arbitrary profile based on a method, first proposed by Nelson and Nguyen. An improved first order solution that incorporates a continuous interpolation of perturbed quantities in the circumferential direction, is presented. The original method uses an approximation scheme for circumferential gradients, based on Fast Fourier Transforms (FFT). A simpler scheme based on cubic splines is found to be computationally more efficient with better convergence at higher eccentricities. A new approach of computing dynamic coefficients based on external specified load is introduced. This improved analysis is extended to account for arbitrarily varying seal profile in both axial and circumferential directions. An example case of an elliptical seal with varying degrees of axial curvature is analyzed. A case study based on actual operating clearances (6 axial planes with 68 clearances/plane) of an interstage seal of the Space Shuttle Main Engine High Press Oxygen Turbopump (SSME-ATD-HPOTP) is presented.

NOMENCLATURE

a_i, b_i	spatially dependent parts of first order solution
A_u, A_v, A_h	coefficients of the variables of first order axial momentum equation
B_u, B_v, B_h	coefficients of the variables of first order circumferential momentum equation
c_0	nominal clearance (m)
c_i, c_e	inlet and exit clearances (m)
c_x, c_y	x, y axis clearances of elliptical seal (m)
C_{xx}, C_{yy}	direct damping coefficients (N-s/m)
c_{xy}, c_{yx}	cross coupled damping coefficients (N-s/m)
$c(z, \beta)$	clearance function
E_x, E_y	eccentricities along x and y axes (m)
f_{r0}, f_{s0}	friction coefficients (Moody's or Hirs')
F_x, F_y	x and y components of seal force (N)
f_x, f_y	unbalance forces (N)
h_0, u_0, v_0, p_0	variables of zeroth order (steady state) equations
h_1, u_1, v_1, p_1	variables of first order (perturbed) equations
h	film thickness (m)
K_{xx}, K_{yy}	direct stiffness coefficients (N/m)
k_{xy}, k_{yx}	cross coupled stiffness coefficients (N/m)
L	length of the seal (m)
M_{xx}, M_{yy}	direct mass coefficients (kg)
m_{xy}, m_{yx}	cross coupled mass coefficients (kg)
p_{0i}	entrance pressure (Pa)
p_{0e}	exit pressure (Pa)
psr	pre-swirl ratio
R	radius of the rotor (m)
t	time (s)
u, v	axial and tangential velocities (m/s)
w	rotor surface velocity, ωR (m/s)
W	preload
X_0, Y_0	axes of the elliptical whirl orbit
z, β	axial and circumferential coordinates
ρ	density (kg/m^3)
μ	dynamic viscosity (Pa-s)
δ	ellipticity, $(c_x - c_y)/c_x$
$\epsilon, \epsilon_x, \epsilon_y$	eccentricity ratios
ψ	external load angle (rad)
ξ	entrance loss coefficient
ω	angular frequency (rad/s)

INTRODUCTION

Distortions in the interstage seals of the Space Shuttle Main Engine (SSME) High Pressure Oxygen Turbopump (ATD-HPOTP) due to mechanical and thermal loads have been investigated utilizing finite element models of the entire pump. Annular seals, initially designed with either straight or tapered clearance profile have been found to be severely distorted during the course of their operation.

Starting with Black's (1969) analysis of high-pressure seals, followed by Allaire's (1972) eccentric seal analysis and Childs' (1983) Hirs' bulk-flow model for tapered seals there has been a steady improvement in the modeling of annular seals and the agreement of their predicted behavior with experimental results.

The effect of seal distortion on the rotordynamic coefficients was first considered by Sharrer and Nunez (1989). They adapted the analysis of a plain seal to the case of a seal with wavy profile. The distorted seal profile was fitted with a clearance function in the form of a polynomial. Their analysis confirmed a marked change in rotordynamic coefficients due to a change in the seal profile. Similar results for this case were reported by San Andres (1991) using a variable properties model. Scharrer and Nelson (1990), treated a similar problem using a partially tapered seal model.

All the work reported in the literature is limited to distortion along the length of the seal. Detailed thermoelastic studies have revealed seal distortion is not limited to axial direction and a similar distortion occurs along the circumference also. An example of a distorted seal profile is shown in Fig 1. The clearances for this profile were obtained from a thermoelastic analysis.

This paper presents an improved dynamic analysis for an annular seal with arbitrary profile. The arbitrary seal profile may be due to distortion as above, or by design. The analysis used for this purpose is based on an approach, first proposed by Nelson and Nguyen. (1989). The original analysis showed good agreement with experimental results. This analysis is modified by including a more exact first order solution that accounts for the variation of perturbed variables along the circumference with a continuous interpolation.

Typically, seal coefficients are computed in a minimum film thickness coordinate system as a function of eccentricity and then transformed into the user defined coordinate system for actual application. Such a procedure is not valid for an arbitrary profile seal and a method for computing these coefficients directly in a global coordinate system is presented. In addition, a new procedure for computing seal coefficients based on external load specification is also discussed.

An example film thickness analysis for an elliptical seal with varying axial curvature, is discussed. The above improved analysis is employed to analyze a distorted interstage seal of a SSME Turbopump and the results are compared to those of a similar seal with average inlet and exit clearances.

THEORY

Bulk Flow Governing Equations

Mass conservation and force equilibrium considerations in the axial and circumferential directions for the control volumes in figures 2a and 2b yield the following bulk flow continuity, axial momentum and circumferential momentum equations for an incompressible fluid.

$$\frac{1}{R}\frac{\partial(hv)}{\partial\beta} + \frac{\partial(hu)}{\partial z} + \frac{\partial h}{\partial t} = 0 \qquad (1)$$

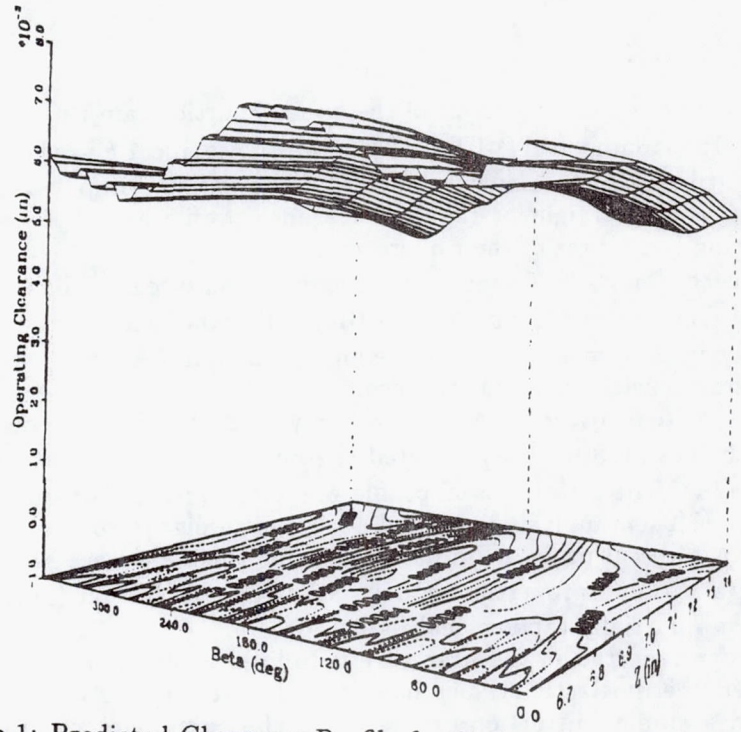

Figure 1: Predicted Clearance Profile for Turbopump Annular Seal

$$-\frac{h}{\rho}\frac{\partial p}{\partial z} = h\{\frac{\partial u}{\partial t} + \frac{v}{R}\frac{\partial u}{\partial \beta} + u\frac{\partial u}{\partial z}\} + \bar{f}_s\frac{u}{2}\sqrt{u^2+v^2} + \bar{f}_r\frac{u}{2}\sqrt{u^2+(v-w)^2} \quad (2)$$

$$-\frac{h}{\rho R}\frac{\partial p}{\partial \beta} = h\{\frac{\partial v}{\partial t} + \frac{v}{R}\frac{\partial v}{\partial \beta} + u\frac{\partial v}{\partial z}\} + \bar{f}_s\frac{v}{2}\sqrt{u^2+v^2} + \bar{f}_r\frac{(v-w)}{2}\sqrt{u^2+(v-w)^2} \quad (3)$$

where the friction factors $\bar{f}_s$ and $\bar{f}_r$ are defined for the Hirs and Moody friction factor models in the appendix.

The boundary conditions at the inlet and exit of the seal are given as,

$$p_{0i} - p_0(0,\beta) = (1+\xi)\frac{1}{2}\rho u_0^2(0,\beta) \quad (4)$$

$$v_0(0,\beta) = psr \times \omega R \quad (5)$$

$$p_0(L,\beta) = p_{0e} \quad (6)$$

where p_{0i} and p_{0e} are the entrance and exit pressures respectively, ξ is the entrance loss coefficient and psr is the pre-swirl ratio.

Film Thickness

The expression for film thickness $h(z,\beta)$ as a function of eccentricity is derived in a fixed coordinate system, instead of a "minimum film thickness" coordinate system. The

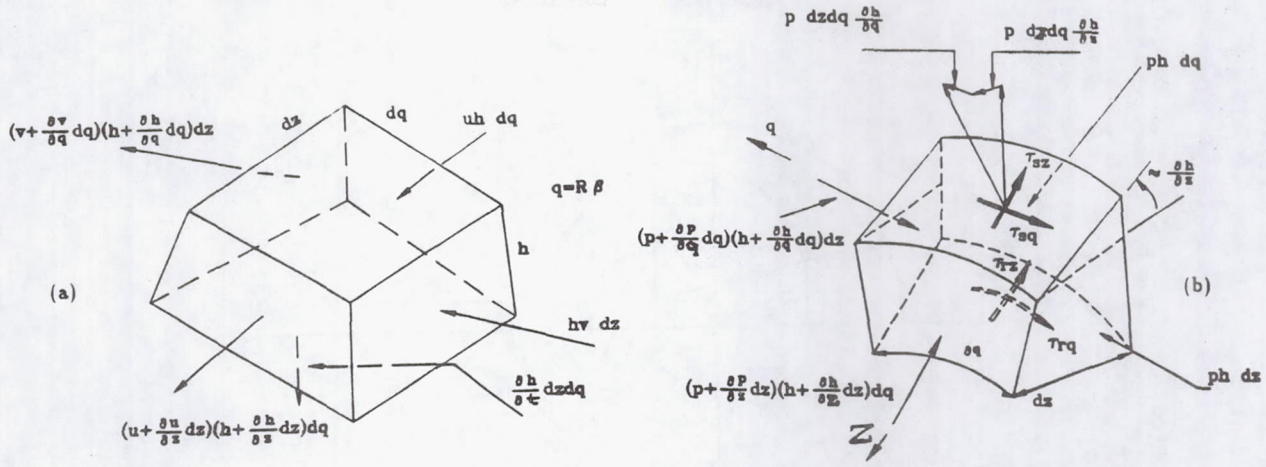

Figure 2: Differential Fluid Volumes, a) Continuity b) Momentum

coordinate system (x, y) shown in Fig. 3, is fixed at the static eccentric position and is oriented parallel to a user defined-global coordinate system. Typically, for eccentric operation of a uniform profile seal such as a straight or tapered seal, the rotordynamic coefficients are computed as a function of eccentricity in a coordinate system aligned with the line of minimum film thickness. The use of these coefficients in an application such as a stability analysis requires their transformation into the user defined coordinate system. This procedure, which is valid for a seal with uniform profile is not applicable for seals with non-uniform profile in the circumferential direction. Such seals require the computation of these coefficients in the user defined coordinate system directly, as these coefficients vary with the angle of minimum film thickness (angle of eccentricity).

The seal geometry is, in general, defined by its clearance function $c(z, \beta)$. A constant c specifies a straight seal, a linear function in z defines a tapered seal and so on. The seal profile will be non-uniform if c varies with β. The film thickness, which varies with eccentricity, is derived as a function of $c(z, \beta)$ and the eccentricity E. The expression for the film thickness and its gradients are given below with reference to Fig. 3. Besides specifying the film thickness in a fixed coordinate system, this general expression is more accurate, particularly at high eccentricities, than the more commonly used approximate form, $h_0 = c - E_x cos\beta - E_y sin\beta$.

$$h_0(z,\beta) = \sqrt{(R+c)^2 - (E_x sin\beta - E_y cos\beta)^2} - (E_x cos\beta + E_y sin\beta) - R \tag{7}$$

$$\frac{\partial h_0}{\partial \beta} = \frac{(R+c)\frac{\partial c}{\partial \beta} - (E_x sin\beta - E_y cos\beta)(E_x cos\beta + E_y sin\beta)}{\sqrt{(R+c)^2 - (E_x sin\beta - E_y cos\beta)^2}} + (E_x sin\beta - E_y cos\beta) \tag{8}$$

$$\frac{\partial h_0}{\partial z} = \frac{(R+c)\frac{\partial c}{\partial z}}{\sqrt{(R+c)^2 - (E_x sin\beta - E_y cos\beta)^2}} \tag{9}$$

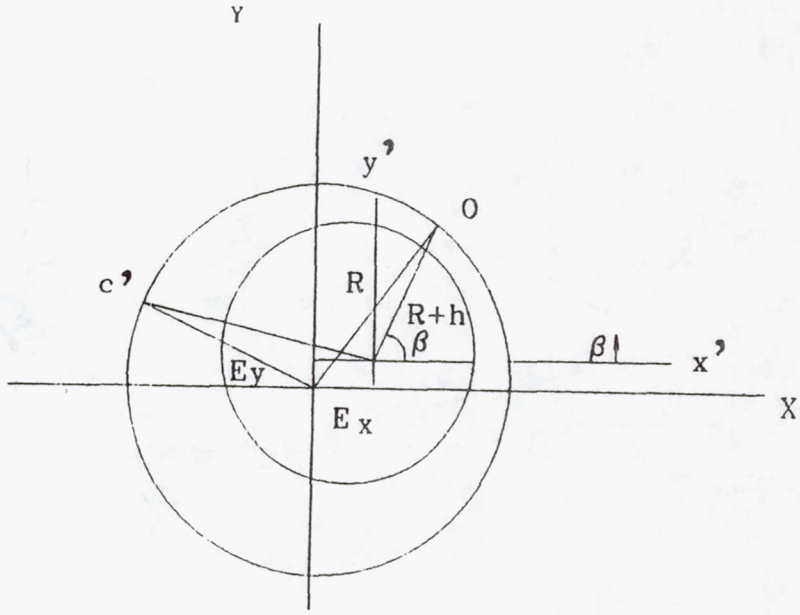

Figure 3: Diagram for Deriving General Clearance Expression

Solution Procedure for Zeroth-Order Equations

The solution for zeroth order equations involves the direct integration of the three coupled nonlinear partial differential equations. Typically, an iterative procedure is used to solve for the pressure distribution. The original analysis of Nelson and Nguyen (1988) proposed a method by which the coupled partial differential equations are reduced to coupled ordinary differential equations by approximating the circumferential gradients of the variables u_0, v_0 and p_0. At each axial step in the iterative procedure, the gradients with respect to β are computed based on the values of the variables at the previous step. An approximation scheme based on *Fast Fourier Transforms (FFT)* was used for this purpose. In the present analysis, a simpler method based on cubic splines is used. This method is more accurate as no truncation error is involved as in the FFT method. Also, convergence at higher eccentricities is achieved with relatively fewer iterations than the FFT method. It is also computationally more efficient as it does not involve the computation of CPU intensive trigonometric functions. A similar approach based on forward differences was reported by Simon and Frene (1992). Figure 4 illustrates typical subdivisions in the axial and circumferential directions. Note that the elliptical seal in Figure 5 represents a special case of the arbitrary profile shown in Figure 4.

The three steady state equations are arranged in the following fashion and integrated from inlet to the exit.

$$\begin{bmatrix} \frac{\partial p_0}{\partial z} \\ \frac{\partial u_0}{\partial z} \\ \frac{\partial v_0}{\partial z} \end{bmatrix} = \begin{bmatrix} g_u(u_0, v_0, p_0, \frac{\partial u_0}{\partial \beta}, \frac{\partial v_0}{\partial \beta}, \frac{\partial p_0}{\partial \beta}) \\ g_v(u_0, v_0, p_0, \frac{\partial u_0}{\partial \beta}, \frac{\partial v_0}{\partial \beta}, \frac{\partial p_0}{\partial \beta}) \\ g_p(u_0, v_0, p_0, \frac{\partial u_0}{\partial \beta}, \frac{\partial v_0}{\partial \beta}, \frac{\partial p_0}{\partial \beta}) \end{bmatrix} \tag{10}$$

The circumference is divided into segments of equal length. The above equations are integrated starting at each circumferential location in the direction of the corresponding point at the next axial step. When this step is reached, all the variables i.e., u_0, v_0 and p_0 are known along the circumference. These values are then used to compute the circumferential gradients for the next step. In other words, at the i-th axial step, the circumferential

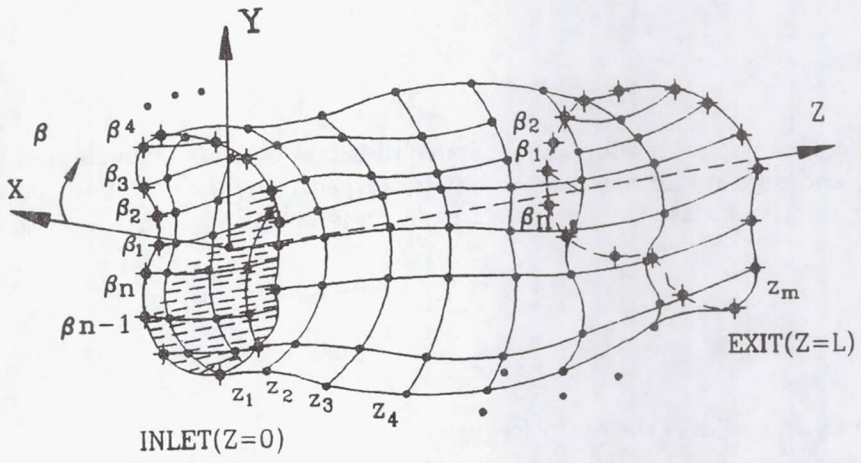

Figure 4: Circumferential and Axial Mesh Points for Numerical Integration

gradients are computed using the values of $u_{0(i-1,j)}$, $v_{0(i-1,j)}$ and $p_{0(i-1,j)}$ .i.e., the values at the previous step. In the current analysis, an approximation scheme based on cubic splines is used to compute these gradients. Nelson and Nguyen used the simple Euler's method for the above numerical integration. For the current work, integration schemes based on 4th and 5th order Runge-Kutta method as well as predictor-corrector methods are used.

First Order Equations

The perturbed or first order equations are obtained for a small motion of the rotor about the steady state eccentric position using the following expressions. $h = h_0 + \epsilon h_1$, $p = p_0 + \epsilon p_1$, $u = u_0 + \epsilon u_1$ and $v = v_0 + \epsilon v_1$.

Substitution of these expressions into equations 1-3 and neglecting second and higher order terms yields the following first order equations.

$$h_0\frac{\partial u_1}{\partial z} + \frac{h_0}{R}\frac{\partial v_1}{\partial \beta} + \frac{\partial h_1}{\partial z}u_1 + \frac{1}{R}\frac{\partial h_1}{\partial \beta}v_1 = -\frac{\partial h_1}{\partial t} - u_0\frac{\partial h_1}{\partial z} - \frac{v_0}{R}\frac{\partial h_1}{\partial \beta} - (\frac{\partial u_0}{\partial z} + \frac{1}{R}\frac{\partial v_0}{\partial \beta})h_1 \tag{11}$$

$$h_0\frac{\partial u_1}{\partial t} + \frac{h_0}{\rho}\frac{\partial p_1}{\partial z} + h_0u_0\frac{\partial u_1}{\partial z} + \frac{h_0v_0}{R}\frac{\partial u_1}{\partial \beta} + A_uu_1 + A_vv_1 = A_hh_1 \tag{12}$$

$$h_0\frac{\partial v_1}{\partial t} + \frac{h_0}{\rho R}\frac{\partial p_1}{\partial \beta} + h_0u_0\frac{\partial v_1}{\partial z} + \frac{h_0v_0}{R}\frac{\partial v_1}{\partial \beta} + B_uu_1 + B_vv_1 = B_hh_1 \tag{13}$$

where A_u, A_v, A_h, B_u, B_v and B_h are functions of steady state variables u_0, v_0, p_0 and their axial and circumferential gradients. These expressions are given in the appendix for both the Hir's and Moody's friction factors models.

The boundary conditions for the first order solution are (Nelson and Nguyen, 1988),

$$p_1(0,\beta) = -(1+\xi)\rho u_0(0,\beta)u_1(0,\beta) \tag{14}$$

$$v_1(0,\beta) = 0 \tag{15}$$

$$p_1(L,\beta) = 0 \tag{16}$$

Assuming that the rotor whirls about its equilibrium position in an elliptical orbit whose semi-major and semi-minor axes are X_0 and Y_0 respectively, then the position of the center of the rotor relative to its static eccentric position is given by,

$$X = X_0 cos\alpha \tag{17}$$

$$Y = Y_0 sin\alpha \tag{18}$$

where $\alpha = \omega t$ and ω is the whirl frequency.
Let $\Delta x = \frac{X_0}{c_0}$, and $\Delta y = \frac{Y_0}{c_0}$ where c_0 is the nominal clearance, and;

$$\epsilon p_1 = \Delta\epsilon_x p_{1x} + \Delta\epsilon_y p_{1y} \tag{19}$$

$$\epsilon u_1 = \Delta\epsilon_x u_{1x} + \Delta\epsilon_y u_{1y} \tag{20}$$

$$\epsilon v_1 = \Delta\epsilon_x v_{1x} + \Delta\epsilon_y v_{1y} \tag{21}$$

$$\epsilon h_1 = \Delta\epsilon_x h_{1x} + \Delta\epsilon_y h_{1y} \tag{22}$$

$$h_{1x} = -c_0 cos\alpha cos\beta \tag{23}$$

$$h_{1y} = -c_0 sin\alpha sin\beta \tag{24}$$

Assume a solution of the form:

$$p_{1x} = a_1(z,\beta)cos\alpha + a_2(z,\beta)sin\alpha \tag{25}$$

$$u_{1x} = a_3(z,\beta)cos\alpha + a_4(z,\beta)sin\alpha \tag{26}$$

$$v_{1x} = a_5(z,\beta)cos\alpha + a_6(z,\beta)sin\alpha \tag{27}$$

$$p_{1y} = b_1(z,\beta)cos\alpha + b_2(z,\beta)sin\alpha \tag{28}$$

$$u_{1y} = b_3(z,\beta)cos\alpha + b_4(z,\beta)sin\alpha \tag{29}$$

$$v_{1y} = b_5(z,\beta)cos\alpha + b_6(z,\beta)sin\alpha \tag{30}$$

Using the above substitutions in the set of first order equations yields 12 coupled linear partial differential equations. The same solution procedure that is used for the zeroth order solution is used to numerically solve for variables a_i and b_i.

The first order boundary conditions are expressed in the assumed solution variables as:

$$a_1(0,\beta) = -(1+\xi)\rho a_3(0,\beta) \tag{31}$$

$$a_2(0,\beta) = -(1+\xi)\rho a_4(0,\beta) \tag{32}$$

$$a_5(0,\beta) = 0 \tag{33}$$

$$a_6(0,\beta) = 0 \tag{34}$$

$$a_1(L,\beta) = 0 \tag{35}$$

$$a_2(L,\beta) = 0 \tag{36}$$

Similar boundary conditions apply to governing equations involving b_i's.

The original analysis assumed these variables to be harmonic and separated them into two auxiliary functions of the form,

$$a_i = f_i(z)cos\beta + g_i(z)sin\beta \tag{37}$$

where f_i and g_i are assumed not to vary with β. Nelson and Nguyen 1988a) thereby apply a second separation of variables substitution to the first order differential equations (eqs. 14-16). While the above form of assumed solution yields results that agree with available experimental results, an examination of the numerical values of the functions $f_i(z)$ and $g_i(z)$ revealed a β dependence, particularly at eccentricities above (0.5). The inclusion of these circumferential gradients should therefore improve the solution at higher eccentricities.

The a_i and b_i in the current analysis are totally general functions of z and β which thereby avoids the mathematical contradiction discussed above. Furthermore, in many cases the results of the current approach show better agreement with experimental results then the earlier results.

The solution procedure for the 12 linear PDE's is exactly the same as that of the zeroth order solution. The solution is performed with 4-th and 5-th order Runge-Kutta method and also with a predictor-corrector method. Both methods almost identical results, the with Runge-Kutta based method being the fastest.

Dynamic Coefficients

The force components acting on the rotor due to its motion about a static eccentric position is given by integrating the first order pressure field, i.e.,

$$-\Delta F_x = \int_0^L \int_0^{2\pi} \epsilon p_1 cos\beta R \, d\beta \, dz \tag{38}$$

$$-\Delta F_y = \int_0^L \int_0^{2\pi} \epsilon p_1 sin\beta R \, d\beta \, dz \tag{39}$$

The following linearized force-motion model is used to define the rotordynamic coefficients. In this equation, X and Y define the relative displacement of the rotor and F_x, F_y are the components of the force due to first order pressure field.

$$-\begin{Bmatrix} \Delta F_x \\ \Delta F_y \end{Bmatrix} = \begin{bmatrix} K_{xx} & k_{xy} \\ -k_{yx} & K_{yy} \end{bmatrix} \begin{Bmatrix} x \\ y \end{Bmatrix} + \begin{bmatrix} C_{xx} & c_{xy} \\ -c_{yx} & C_{yy} \end{bmatrix} \begin{Bmatrix} \dot{x} \\ \dot{y} \end{Bmatrix} + \begin{bmatrix} M_{xx} & m_{xy} \\ -m_{yx} & m_{yy} \end{bmatrix} \begin{Bmatrix} \ddot{x} \\ \ddot{y} \end{Bmatrix} \tag{40}$$

The original analysis discretized the circumference into a number of strips and the function values (f_i, g_i) are assumed to be independent of β over each strip. The current method improves this approach by allowing the a_i and b_i to vary over each strip in obtaining the rotordynamic coefficients.

Substitute eqs. 28–33 into 22–27 and in turn substitute the results into eqs. 43-45. Also substitute eqs. 20 and 21 into 43-45. This yields:

$$K_{xx} - M_{xx}\omega^2 = \frac{1}{c_0}\int_0^L \int_0^{2\pi} a_1 cos\beta R \; d\beta \; dz \tag{41}$$

$$c_{xy}\omega = \frac{1}{c_0}\int_0^L \int_0^{2\pi} b_1 cos\beta R \; d\beta \; dz \tag{42}$$

$$-k_{yx} + m_{yx}\omega^2 = \frac{1}{c_0}\int_0^L \int_0^{2\pi} a_1 sin\beta R \; d\beta \; dz \tag{43}$$

$$C_{yy}\omega = \frac{1}{c_0}\int_0^L \int_0^{2\pi} b_1 sin\beta R \; d\beta \; dz \tag{44}$$

$$-C_{xx}\omega = \frac{1}{c_0}\int_0^L \int_0^{2\pi} a_2 cos\beta R \; d\beta \; dz \tag{45}$$

$$k_{yx} - m_{xy}\omega^2 = \frac{1}{c_0}\int_0^L \int_0^{2\pi} b_2 cos\beta R \; d\beta \; dz \tag{46}$$

$$c_{yx}\omega = \frac{1}{c_0}\int_0^L \int_0^{2\pi} a_2 sin\beta R \; d\beta \; dz \tag{47}$$

$$K_{yy} - m_{yy}\omega^2 = \frac{1}{c_0}\int_0^L \int_0^{2\pi} b_2 sin\beta R \; d\beta \; dz \tag{48}$$

These 8 equations are evaluated for at least two whirl frequencies to obtain solutions for the 12 dynamic coefficients. A least squares approach is employed for this step. The 2D integration performed numerically are an improvement over the average value approach employed by the previous researchers.

Dynamic Coefficients based on External Load Specification

In some cases, it is possible to specify the angle at which external load is supported by the seal during the operation of the turbomachine. This external load is equal and opposite to the resultant seal force. A new method of computing the rotordynamic coefficients based on this load angle is described below.

The static operating position of the rotor is located iteratively such that there is equilibrium between the external specified load and the resultant seal force. The angle at which

the resultant seal force acts is forced to align (180^0) with the specified external load angle. For example, unit 3-01, an experimental seal under design at NASA (results to be discussed later) supports the external load at a constant angle of 290^0 in the rotor coordinate system.

Determination of Steady State Force Equilibrium Position

A modified Newton-Raphson approach is used in two dimensions to locate the operating position. At the steady state equilibrium position,

$$f_x = F_x - W sin\beta = 0$$
$$f_y = F_y - W cos\beta = 0$$

The modified 2-D Newton-Raphson iteration procedure is described below.

$$\Delta x \frac{\partial f_x}{\partial x}|_{xi.yi} + \Delta y \frac{\partial f_x}{\partial y}|_{xi.yi} + f_x|_{x_i.y_i} = 0 \tag{49}$$

$$\Delta x \frac{\partial f_y}{\partial x}|_{xi.yi} + \Delta y \frac{\partial f_y}{\partial y}|_{xi.yi} + f_y|_{x_i.y_i} = 0 \tag{50}$$

The seal forces F_x and F_y are computed using an initial guess of rotor position (x_i, y_i),. The gradients $\frac{\partial f_x}{\partial x}$, $\frac{\partial f_x}{\partial y}$, $\frac{\partial f_y}{\partial x}$ and $\frac{\partial f_y}{\partial y}$ are computed using finite differences about (x_i, y_i). This iterative procedure is repeated until the specified external load is balanced by the resultant seal forces. Once this equilibrium position is attained, the remaining analysis proceeds as before.

Verification Case: Allaire, et. al.

The first illustrative example compares the original and current Nguyen-Nelson approach results to the "short seal" solution employed by Allaire . All three approaches show similar direct stiffness, damping and cross- coupled stiffness vs. eccentricity as seen in figures 6, 7 and 8 respectively.

Seal Parameters for Allaire et al. case	
seal length	40.6 mm (1.60 in)
rotor radius	39.9 mm (1.57 in)
c_i	0.14 mm (0.0055 in)
c_e	0.14 mm (0.0055 in)
c_0	0.14 mm (0.0055 in)
fluid	LO2
density, ρ	57.657 kg/m^3 (3.60 lbm/ft^3)
viscosity, μ	7.4396×10^{-6} Pa–s (1.5538×10^{-7} lb-s/ft^2)
Δ P	7.26 MPa (1050 psi)
rotor speed	23700 rpm
friction factor	Moody's
relative	0.0 (rotor)
roughness,$e/2c_0$	0.000001 (stator)
pre–swirl ratio	0.1
inlet loss, ξ	0.5

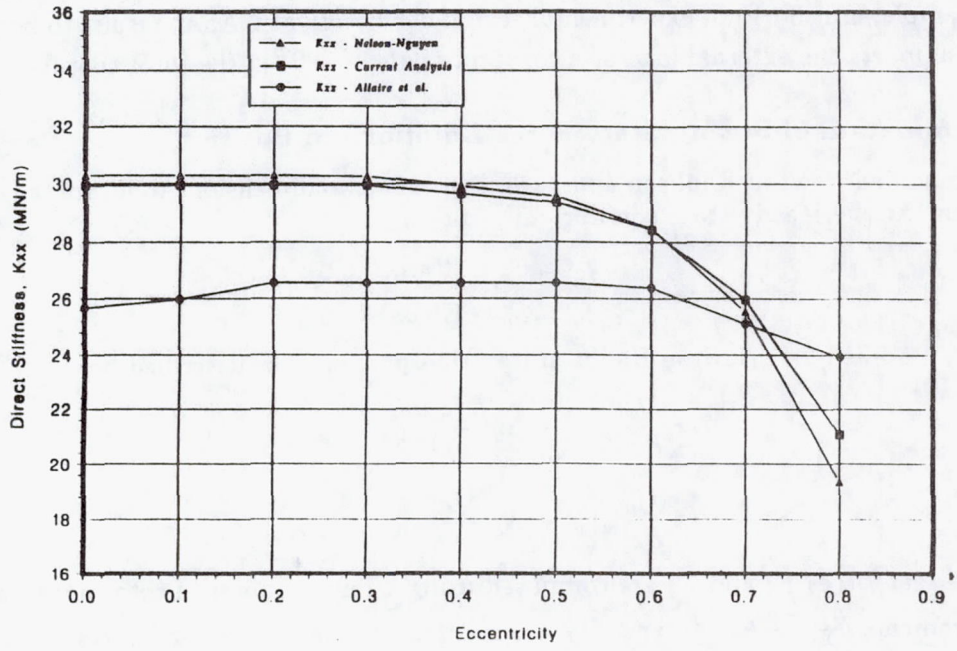

Figure 5: Direct Stiffness .vs. Eccentricity for Allaire Example

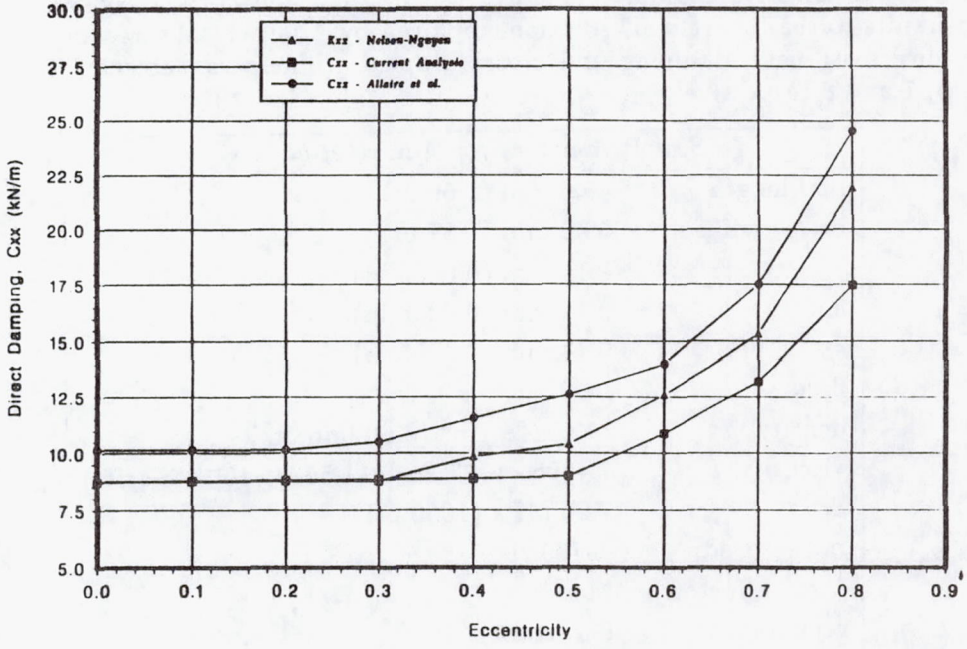

Figure 6: Direct Damping .vs. Eccentricity for Allaire Example

EXAMPLE OF AN ARBITRARY PROFILE SEAL: AN ELLIPTICAL SEAL

The above analysis for an arbitrary profile is applied to the case of an elliptical seal with axially varying curvature. The results for a similar linearly tapered elliptical seal, were initially reported by San Andres (1992). The motivation for this study is two fold. The first is to show the general steps involved in the analysis of arbitrary profile seals and the other is to show, in qualitative terms, the effect of a change in profile on the dynamic coefficients.

Two cases of curvature are considered for this analysis: one with a linear axial profile and the other a quadratic axial profile. For this study, the mid-point clearance of the quadratic profile is made 75% of $(c_i + c_e)/2$, i.e., 0.75 times the mid-point clearance of a linear profile with similar inlet and exit clearances.

The equation of an ellipse is given by,

$$x = a cos\beta \tag{51}$$

$$y = b sin\beta \tag{52}$$

where a and b are the semi-major and semi-minor axes respectively. At any angular position β along the circumference, the radius r of the ellipse is given by,

$$r = \sqrt{(a cos\beta)^2 + (b sin\beta)^2} \tag{53}$$

and the clearance c at this location is given by,

$$c = r - R \tag{54}$$

where R is the radius of the rotor.

If the semi-major and semi-minor axes of the ellipse vary in some functional form along the length of the seal, the clearance is given by,

$$c(z,\beta) = \sqrt{(f_1(z) cos\beta)^2 + (f_2(z) sin\beta)^2} - R \tag{55}$$

where $f_1(z)$ and $f_2(z)$ are the semi-major and semi-minor axes variations along the z-axis. The gradients of this clearance function are given in the appendix.

The ellipticity δ is defined as (Fig. 5),

$$\delta = \frac{c_x - c_y}{c_x} \tag{56}$$

where c_x and c_y are clearances at semi-major and semi-minor axes respectively and,

$$c_x = c_i \quad at \quad inlet$$

$$c_x = c_e \quad at \quad exit$$

and from above,

$$c_y = c_x(1 - \delta) \tag{57}$$

When $\delta = 0$, the ellipse reduces to a circle and for $\delta = 1$, the seal contacts the rotor. The appendix provides the functions $f_1(z)$ and $f_2(z)$ for a linear profile and a quadratic profile, as a function of delta . The results shown are for a centered seal as a function of ellipticity. The dynamic coefficients are normalized with respect to the coefficients for the linear profile case at $\delta = 0$. The values used for this normalization are $K_{xx} = 44975$ kN/m (256883 lb/in), $C_{xx} = 21.78$ kN-s/m (124.4 lb-s/in) and $k_{xy} = 15821$ kN/m (90364 lb/in). The seal parameters for this case are given below.

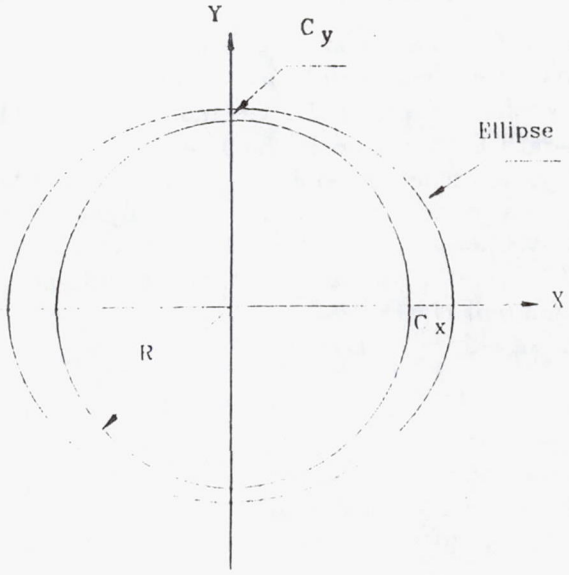

Figure 7: Diagram for Deriving Elliptical Seal Clearance Expression

Seal Parameters for Elliptical Seal	
seal length	16.66 mm (0.656 in)
rotor radius	48.39 mm (1.905 in)
c_i	0.069 mm (0.00273 in)
c_e	0.099 mm (0.00390 in)
c_0	0.069 mm (0.00273 in)
fluid	LO2
density, ρ	1041.7 kg/m^3 (65.03 lbm/ft^3)
viscosity μ	129.6×10^{-6} Pa-s (0.188×10^{-8} lb-s/ft^2)
Δ P	25.39 MPa (3681 psi)
rotor speed	22700 rpm
friction factor	Moody's
relative	0.0 (rotor)
roughness,$e/2c_0$	0.03 (stator)
pre–swirl ratio	0.2
inlet loss, ξ	0.33

The plot for direct stiffness (Fig. 9) shows the effect of a small change in profile on the direct stiffness. For the linear case, there is a complete loss of stiffness at around $\delta = 0.65$. The stiffness for the quadratic profile is almost twice that of the linear profile. Also, it retains its stiffness over a much wider range than the linear profile. The difference in the other coefficients (Figs. 10,11) are relatively small.

CASE STUDY OF A DISTORTED SEAL

The distorted clearance profile for an interstage seal of the Space Shuttle Main Engine High Pressure Oxygen Turbopump (SSME-ATD-HPOTP) is shown in Fig. 1. The distorted

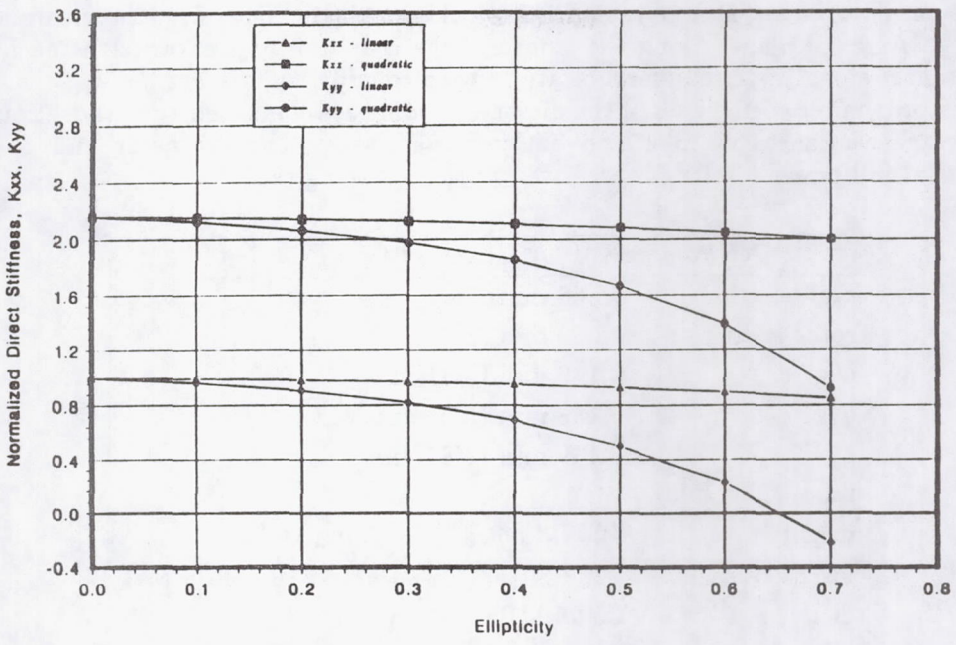

Figure 8: Normalized Direct Stiffness .vs. Ellipticity (Elliptical Seal)

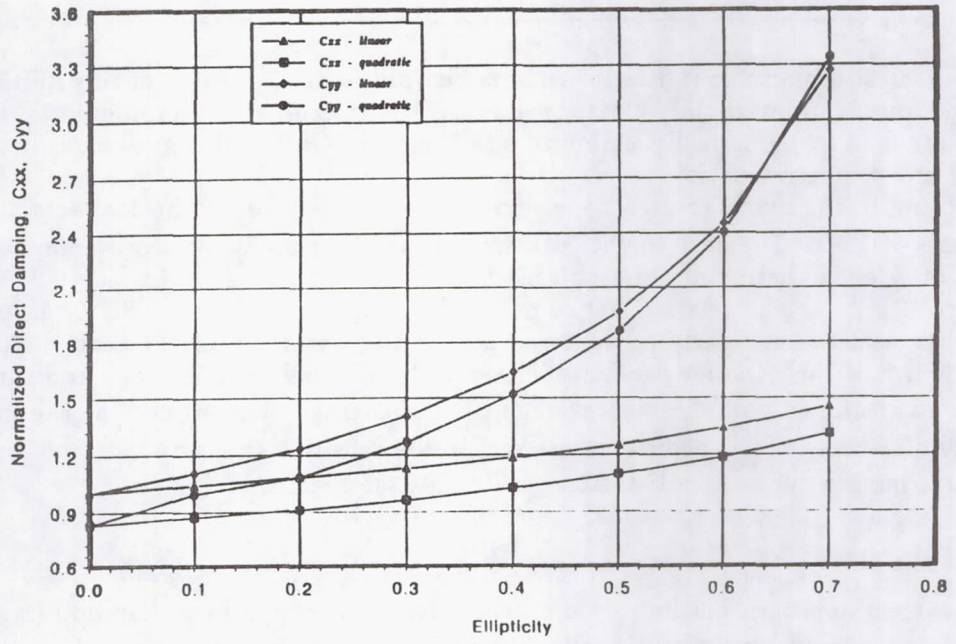

Figure 9: Normalized Direct Damping .vs. Ellipticity (Elliptical Seal)

clearance profile of this seal is obtained from a thermoelastic analysis. The clearances are provided at six axial planes along the length of the seal with 68 clearances at each plane. The clearances along the circumference are located roughly equidistant.

The rotordynamic coefficients of the distorted profile are compared with those computed using average clearances at inlet and outlet respectively. The geometry and operating conditions at full power level FPL are given in the following table.

Seal Parameters for Distorted Seal Unit 3-01	
seal length	16.66 mm (0.656 in)
rotor radius	48.39 mm (1.905 in)
avg. c_i	0.149 mm (5.87 mils)
avg. c_e	0.148 mm (5.81 mils)
c_0	0.149 mm (5.87 mils)
fluid	LO2
density, ρ	1041.7 kg/m^3 (65.03 lbm/ft^3)
viscosity μ	129.6×10^{-6} Pa-s (0.188×10^{-8} lb-s/ft^2)
Δ P	35.25 MPa (5112 psi)
rotor speed	25000 rpm
friction factor	Moody's
relative	0.0 (rotor)
roughness,$e/2c_0$	0.8518 (stator)
pre-swirl ratio	0.2
inlet loss	0.3

The distorted seal profile is fitted with bi-cubic splines. The purpose of this spline fitting is two fold; one is to interpolate clearances at any given axial and circumferential location and the other is to numerically compute axial and circumferential gradients of the seal profile at any required location.

According to the manufacturer's specifications, the side-load on the seal acts at a constant angle of 290^0. The seal coefficients for this variable profile seal are computed as a function of side-load acting at this angle.

Figure 12. shows the relation between seal forces and eccentricity. No load operation requires the seal to be slightly off-centered due to the distortion in the seal. Figs. 13,14 and 15 show how the dynamic coefficients vary with externally applied load and the effects of distorted clearance profile versus average profile (average of clearances at the inlet and exit circumferences). The coefficients are seen to be sensitive to high loads and also show significant changes due to the distorted profile, i.e., see Fig 15.

CONCLUSIONS

The current approach has improved on the original Nelson–Nguyen method (NNM) by;

- (a) Employing a continuous interpolation of the first order variables in the circumferential direction, and
- (b) Utilizing cubic splines instead of Fourier series for the circumferential interpolation of both zeroeth and first order variables.

In addition the current method models seals with arbitrary clearance profiles in the circumferential and axial directions. This capability was demonstrated with the operating seal

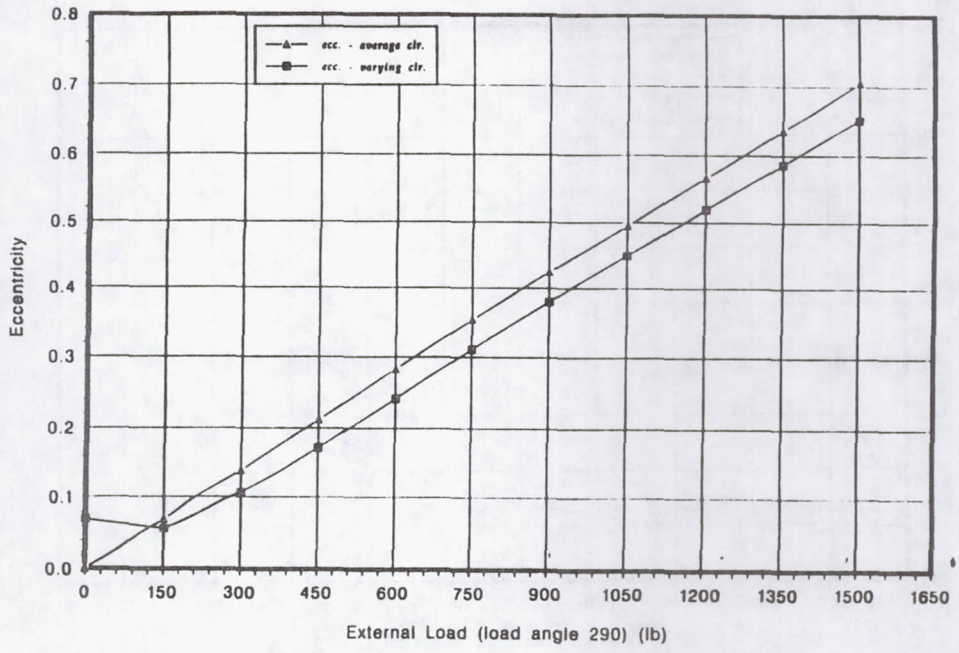

Figure 10: Eccentricity .vs. Preload for Operating Seal Clearance Profile (Fig 1.)

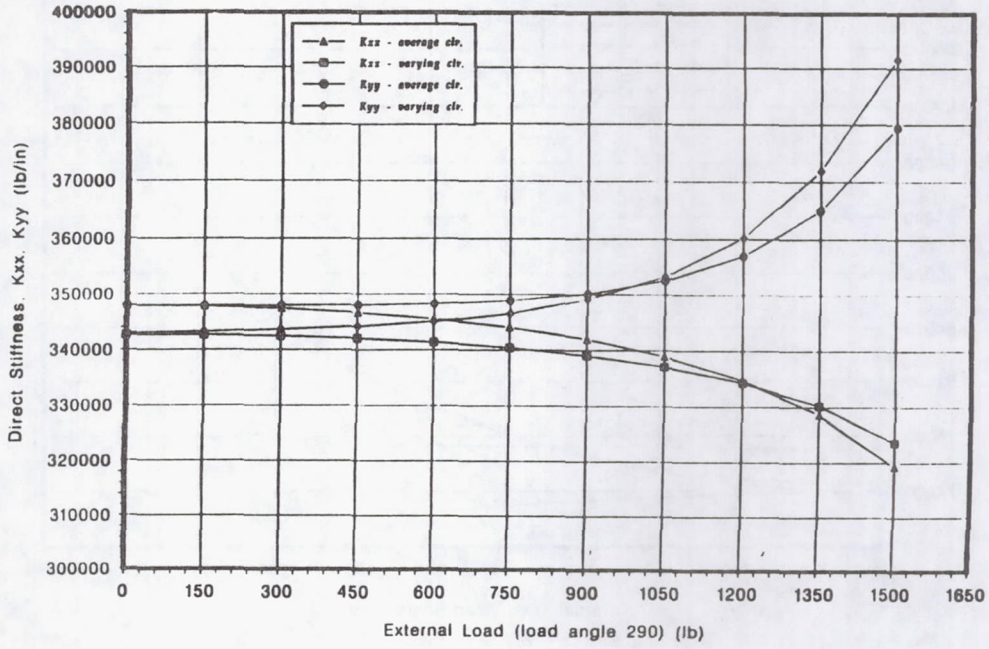

Figure 11: Direct Stiffness .vs. Preload for Operating Seal Clearance Profile (Fig. 1)

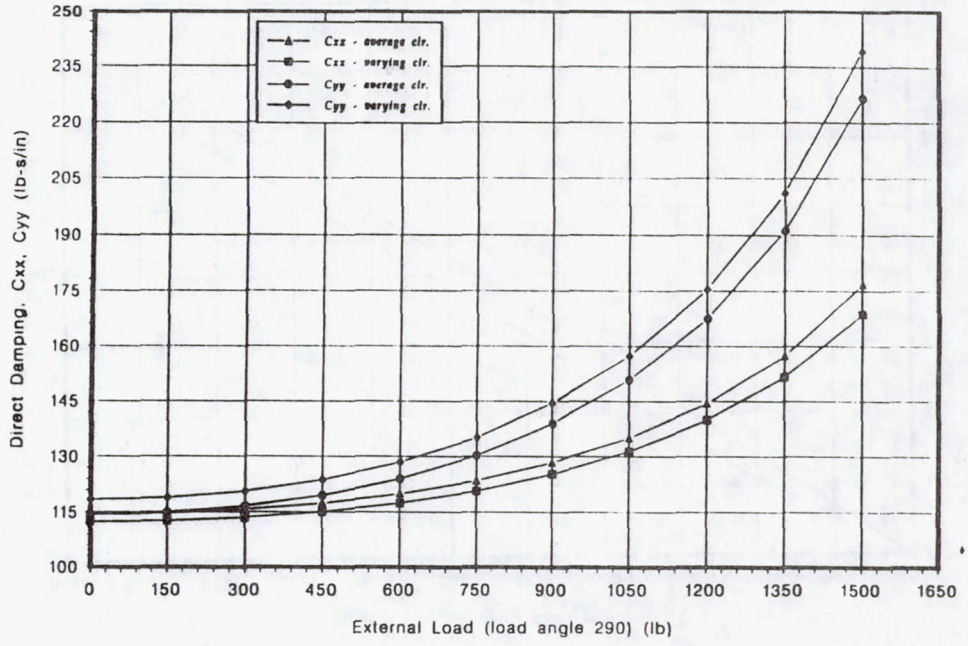

Figure 12: Direct Damping .vs. Preload for Operating Seal Clearance Profile (Fig. 1)

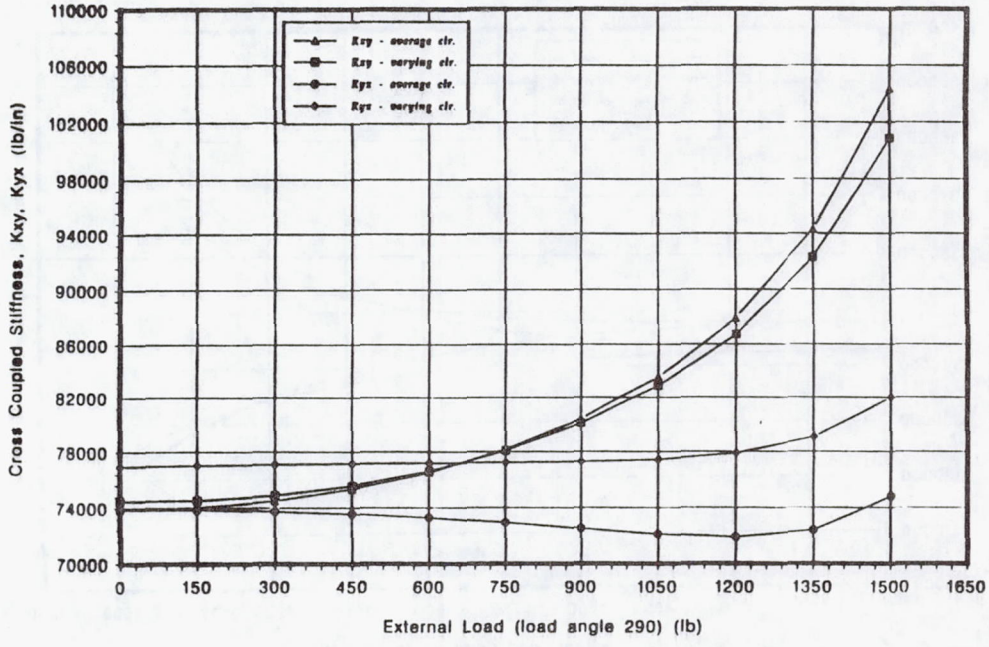

Figure 13: Cross Coupled Stiffness.vs. Preload for Operating Seal Clearance Profile (Fig. 1)

profile of a SSME-HPOTP seal. Finally a procedure is presented for locating the operating equilibrium position of the seal given the preload acting on the seal.

ACKNOWLEDGMENTS

The authors wish to thank NASA Marshall for supporting this research and to acknowledge the technical support provided by Mark Darden, Chip Franks, Kerry Funston, Eric Earhart and Barry Whitsett.

REFERENCES

Allaire,P.E.,et.al., 1978, "Dynamics of Short Eccentric Plain Seals With High Axial Reynolds Numbers," J. Spacecraft, AIAA, Vol.15, No.6, Nov.-Dec.

Black, H.F., Allaire, 1969, "Effects of Hydraulic Forces in Annular Pressure Seals on the Vibrations of Centrifugal Pump Rotors," Journal of Mechanical Engineering Science, Vol. 11, pp. 206–213.

Black, H.F., Allaire, P.E., and L.E. Barrett, 1981, "Inlet Flow Swirl in Short Turbulent Annular Seals," 9–th International Conference on Fluid Sealing, BHRA Fluid Engineering, Leeuwenhorst, The Netherlands, April.

Childs, D.W., 1983a, "Dynamic Analysis of Turbulent Annular Seals Based on Hirs Lubrication Equation," ASME Journal of Lubrication Technology, Vol. 105, pp 429–436.

Childs, D.W., 1983b, "Finite Length Solutions for Rotordynamic Coefficients of Turbulent Annular Seals, "ASME Journal of Lubrication Technology, Vol. 105, pp. 437–444.

Nguyen, D.T., 1988, "Analysis of Eccentric Annular Pressure Seals: A New Solution Procedure for Determining Reactive Force and Rotordynamic Coefficients", Ph.D. Dissertation, Texas A&M University, College Station,TX.

Nelson, C., Nguyen, D.T., 1988a, "Analysis of Eccentric Annular Seals: Part I – A New Solution Using Fast Fourier Transforms for Determining Hydrodynamic Force," ASME Journal of Tribology, Vol 110, pp. 335-360.

Nelson, C., and Nguyen, D.T., 1988b, "Analysis of Eccentric Annular Seals: Part II – Effects of Eccentricity on Rotordynamic Coefficients," ASME Journal of Tribology, Vol. 110, pp. 361-366.

San Andres, L., 1991, "Analysis of Variable Properties Turbulent Annular Seals," ASME Jour. of Tribology, Vol. 113, pp. 694-702.

San Andres, 1992, Personal Communications.

Scharrer, J.K., and D.J. Nunez, 1989, "The SSME HPFTP Wavy Interstage Seal: I – Seal Analysis," Proceedings of the 1989 ASME Vibrations Conference, Machinery Dynamics – Applications and Vibration Control Problems, DE–Vol. 18–2.

Simon, F., and Frene J., 1992, "Analysis of Incompressible Flow in Annular Pressure Seals", STLE/ASME Tribology Conference, St. Louis, MO, 1991.

APPENDIX

The coefficient expressions for the first order equations are defined as

$$A_u = h_0\frac{\partial u_0}{\partial z} + (\frac{F_{so}}{U_{s0}} + \frac{F_{ro}}{U_{r0}}) + (f_s U_{s0} + f_r U_{r0}) \tag{58}$$

$$A_v = \frac{h_0}{R}\frac{\partial u_0}{\partial \beta} + u_0 v_0 \frac{F_{so}}{U_{s0}} + u_0(v_0 - w)\frac{F_{ro}}{U_{r0}} \tag{59}$$

$$A_h = -\frac{1}{\rho}\frac{\partial p_0}{\partial z} - u_0\frac{\partial u_0}{\partial z} - \frac{v_0}{R}\frac{\partial v_0}{\partial \beta} + \frac{u_0}{h_0}(h_{s0}U_{s0} + h_r U_{r0}) \tag{60}$$

$$B_u = h_0\frac{\partial v_0}{\partial z} + u_0 v_0 \frac{F_{so}}{U_{s0}} + u_0(v_0 - w)\frac{F_{ro}}{U_{r0}} \tag{61}$$

$$B_v = \frac{h_0}{R}\frac{\partial v_0}{\partial \beta} + {v_0}^2\frac{F_{so}}{U_{s0}} + (v_0 - w)^2\frac{F_{ro}}{U_{r0}} + f_s U_{s0} + f_r U_{r0} \tag{62}$$

$$B_h = -\frac{1}{\rho}\frac{\partial p_0}{\partial \beta} - u_0\frac{\partial v_0}{\partial z} - \frac{v_0}{R}\frac{\partial v_0}{\partial \beta} + v_0 U_{s0}\frac{h_{s0}}{h_0} + (v_0 - w)U_{r0}\frac{h_r}{h_0} \tag{63}$$

$$\tag{64}$$

with further definitions for Moody's and Hirs' friction models given in the following table:

Moody's Model	*Hirs' Model*
$U_{r0} = ({u_0}^2 + (v_0 - w)^2)^{1/2}$	$U_{r0} = ({u_0}^2 + (v_0 - w)^2)^{1/2}$
$U_{s0} = ({u_0}^2 + {v_0}^2)^{1/2}$	$U_{s0} = ({u_0}^2 + {v_0}^2)^{1/2}$
$R_{r0} = \frac{2\rho h_0}{\mu}(u_0^2 + (v_0 - w)^2)^{1/2}$	$R_{r0} = \frac{2\rho h_0}{\mu}(u_0^2 + (v_0 - w)^2)^{1/2}$
$R_{s0} = \frac{2\rho h_0}{\mu}({u_0}^2 + {v_0}^2)^{1/2}$	$R_{s0} = \frac{2\rho h_0}{\mu}({u_0}^2 + {v_0}^2)^{1/2}$
$f_{r0} = \frac{0.0055}{4}[1 + (10^4\frac{K_r}{h_0} + 10^6\frac{1}{R_{r0}})^{1/3}]$	$f_{r0} = n_r[\frac{2\rho h_0}{\mu}R_{r0}]^{mr}$
$f_{s0} = \frac{0.0055}{4}[1 + (10^4\frac{K_s}{h_0} + 10^6\frac{1}{R_{s0}})^{1/3}]$	$f_{s0} = n_s[\frac{2\rho h_0}{\mu}R_{s0}]^{ms}$
$g_{r0} = \frac{0.0055\times 10^6}{12R_{r0}}(10^4\frac{K_r}{h_0} + \frac{10^6}{R_{r0}})^{-2/3}$	$g_{r0} = -m_r n_r[R_{r0}]^{m_r}$
$g_{s0} = \frac{0.0055\times 10^6}{12R_{s0}}(10^4\frac{K_s}{h_0} + \frac{10^6}{R_{s0}})^{-2/3}$	$g_{s0} = -m_s n_s[R_{s0}]^{m_s}$
$h_{r0} = \frac{0.0055}{12}(10^4\frac{K_r}{h_0} + \frac{10^6}{R_{r0}})^{1/3}$	$h_{r0} = -m_r n_r[R_{r0}]^{m_r}$
$h_{s0} = \frac{0.0055}{12}(10^4\frac{K_s}{h_0} + \frac{10^6}{R_{s0}})^{1/3}$	$h_{s0} = -m_s n_s[R_{s0}]^{m_s}$
$\bar{f}_r = f_{r0}$	$\bar{f}_r = f_{r0}$
$\bar{f}_s = f_{s0}$	$\bar{f}_s = f_{s0}$
$f_r = f_{r0}/2$	$f_r = f_{r0}/2$
$f_s = f_{s0}/2$	$f_s = f_{s0}/2$
$g_r = g_{r0}/2$	$g_r = g_{r0}/2$
$g_s = g_{s0}/2$	$g_s = g_{s0}/2$
$h_r = h_{r0}/2$	$h_r = g_{r0}/2$
$h_s = h_{s0}/2$	$h_s = g_{s0}/2$
$F_{ro} = \frac{f_r - g_r}{2}$	$F_{ro} = \frac{f_r - g_r}{2}$
$F_{so} = \frac{f_s - g_s}{2}$	$F_{so} = \frac{f_s - g_s}{2}$

The first-order governing equations are expressed in terms of the a_i and b_i functions as;

$$\frac{h_0}{\rho}\frac{\partial a_1}{\partial z} + (A_u - u_0\frac{\partial h_0}{\partial z})a_3 + h_0\omega a_4(A_v - \frac{u_0}{R}\frac{\partial h_0}{\partial \beta})a_5 = -\frac{h_0 v_0}{R}\frac{\partial a_3}{\partial \beta} + \frac{h_0 u_0}{R}\frac{\partial a_5}{\partial \beta} - c_0[(A_h + u_0(\frac{\partial u_0}{\partial z} + \frac{1}{R}\frac{\partial v_0}{\partial \beta}))cos\beta - \frac{u_0 v_0}{R}sin\beta] \quad (65)$$

$$\frac{h_0}{\rho}\frac{\partial a_2}{\partial z} - h_0\omega a_3 + (A_u - u_0\frac{\partial h_0}{\partial z})a_4 + (A_v - \frac{u_0}{R}\frac{\partial h_0}{\partial \beta})a_6 = c_0\omega u_0 cos\beta - \frac{h_0 v_0}{R}\frac{\partial a_4}{\partial 3} + \frac{h_0 u_0}{R}\frac{\partial a_6}{\partial \beta} \quad (66)$$

$$h_0\frac{\partial a_3}{\partial z} + \frac{\partial h_0}{\partial z}a_3 + \frac{1}{R}\frac{\partial h_0}{\partial \beta}a_5 = c_0[(\frac{\partial u_0}{\partial z} + \frac{1}{R}\frac{\partial v_0}{\partial \beta})cos\beta - \frac{v_0}{R}sin\beta] - \frac{h_0}{R}\frac{\partial a_5}{\partial \beta} \quad (67)$$

$$h_0\frac{\partial a_4}{\partial z} + \frac{\partial h_0}{\partial z}a_4 + \frac{1}{R}\frac{\partial h_0}{\partial \beta}a_6 = -c_0\omega cos\beta - \frac{h_0}{R}\frac{\partial a_6}{\partial \beta} \quad (68)$$

$$h_0 u_0\frac{\partial a_5}{\partial z} + B_u a_3 + B_v a_5 + h_0\omega a_6 = -c_0 B_h cos\beta - \frac{h_0}{R\rho}\frac{\partial a_1}{\partial \beta} - \frac{h_0 v_0}{R}\frac{\partial a_5}{\partial \beta} \quad (69)$$

$$h_0 u_0\frac{\partial a_6}{\partial z} + B_u a_4 - h_0\omega a_5 + B_v a_6 = -\frac{h_0}{R\rho}\frac{\partial a_2}{\partial \beta} - \frac{h_0 v_0}{R}\frac{\partial a_6}{\partial \beta} \quad (70)$$

$$\frac{h_0}{\rho}\frac{\partial b_1}{\partial z} + (A_u - u_0\frac{\partial h_0}{\partial z})b_3 + h_0\omega b_4 + (A_v - \frac{u_0}{R}\frac{\partial h_0}{\partial \beta})b_5 = -c_0\omega u_0 sin\beta - \frac{h_0 v_0}{R}\frac{\partial b_3}{\partial \beta} + \frac{h_0 u_0}{R}\frac{\partial b_5}{\partial \beta} \quad (71)$$

$$\frac{h_0}{\rho}\frac{\partial b_2}{\partial z} - h_0\omega b_3 + (A_u - u_0\frac{\partial h_0}{\partial z})b_4 + (A_v - \frac{u_0}{R}\frac{\partial h_0}{\partial \beta})b_6 = -c_0[(A_h + u_0(\frac{\partial u_0}{\partial z} + \frac{1}{R}\frac{\partial v_0}{\partial \beta}))sin\beta + \frac{u_0 v_0}{R}cos\beta] - \frac{h_0 v_0}{R}\frac{\partial b_4}{\partial \beta} + \frac{h_0 u_0}{R}\frac{\partial b_6}{\partial \beta} \quad (72)$$

$$h_0\frac{\partial b_3}{\partial z} + \frac{\partial h_0}{\partial z}b_3 + \frac{1}{R}\frac{\partial h_0}{\partial \beta}b_5 = c_0\omega sin\beta - \frac{h_0}{R}\frac{\partial b_5}{\partial \beta} \quad (73)$$

$$h_0\frac{\partial b_4}{\partial z} + \frac{\partial h_0}{\partial z}b_4 + \frac{1}{R}\frac{\partial h_0}{\partial \beta}b_6 = c_0[\frac{v_0}{R}cos\beta + (\frac{\partial u_0}{\partial z} + \frac{1}{R}\frac{\partial v_0}{\partial \beta})sin\beta] - \frac{h_0}{R}\frac{\partial b_6}{\partial \beta} \quad (74)$$

$$h_0 u_0\frac{\partial b_5}{\partial z} + B_u b_3 + B_v b_5 + h_0\omega b_6 = -\frac{h_0}{R\rho}\frac{\partial b_1}{\partial \beta} - \frac{h_0 v_0}{R}\frac{\partial b_5}{\partial \beta} \quad (75)$$

$$h_0 u_0\frac{\partial b_6}{\partial z} + B_u b_4 - h_0\omega b_5 + B_v b_6 = -c_0 B_h sin\beta - \frac{h_0}{R\rho}\frac{\partial b_2}{\partial \beta} - \frac{h_0 v_0}{R}\frac{\partial b_6}{\partial \beta} \quad (76)$$

The clearance functions for the elliptical seal are given in the next table as;

linear taper	*quadratic curve*
$f_1(z) = a_1 + a_2 z$	$f_1(z) = a_1 + a_2 z + a_3 z^2$
$f_2(z) = b_1 + b_2 z$	$f_2(z) = b_1 + b_2 z + b_3 z^2$
$\frac{\partial f_1}{\partial z} = a_2$	$\frac{\partial f_1}{\partial z} = a_2 + 2a_3 z$
$\frac{\partial f_2}{\partial z} = b_2$	$\frac{\partial f_2}{\partial z} = b_2 + 2b_3 z$
$a_1 = R + c_i$	$a_1 = R + c_i$
$a_2 = \frac{1}{L}(c_e - c_i)$	$a_2 = \frac{-1}{L}(c_e - 4c_m + 3c_i)$
	$a_3 = \frac{2}{L^2}(c_e - 2c_m + c_i)$
$b_1 = R + (1-\delta)c_i$	$b_1 = R + (1-\delta)c_i$
$b_2 = \frac{1}{L}(1-\delta)(c_e - c_i)$	$b_2 = \frac{-1}{L}(1-\delta)(c_e - 4c_m + 3c_i)$
	$b_3 = \frac{2}{L}(1-\delta)(c_e - 2c_m + c_i))$

Gradients of the clearance function for elliptical seal are given by;

$$c(z,\beta) = \sqrt{(f_1(z)cos\beta)^2 + (f_2(z)sin\beta)^2} - R \tag{77}$$

$$\frac{\partial c}{\partial z} = \frac{f_1 f_1' cos^2\beta + f_2 f_2' sin^2\beta}{\sqrt{(f_1 cos\beta)^2 + (f_2 sin\beta)^2}} \tag{78}$$

$$\frac{\partial c}{\partial \beta} = \frac{(f_2^2 - f_1^2)cos\beta sin\beta}{\sqrt{(f_1 cos\beta)^2 + (f_2 sin\beta)^2}} \tag{79}$$

A 3D-CFD CODE FOR ACCURATE PREDICTION OF FLUID FLOWS AND FLUID FORCES IN SEALS

M.M. Athavale and A.J. Przekwas
CFD Research Corporation
Huntsville, Alabama

and

R.C. Hendricks
NASA Lewis Research Center
Cleveland, Ohio

ABSTRACT

Current and future turbomachinery requires advanced seal configurations to control leakage, inhibit mixing of incompatible fluids and to control the rotodynamic response. In recognition of a deficiency in the existing predictive methodology for seals, a seven year effort was established in 1990 by NASA's Office of Aeronautics Exploration and Technology, under the Earth-to-Orbit Propulsion program, to develop validated Computational Fluid Dynamics (CFD) concepts, codes and analyses for seals. The effort will provide NASA and the U.S. Aerospace Industry with advanced CFD scientific codes and industrial codes for analyzing and designing turbomachinery seals.

An advanced 3D CFD cylindrical seal code has been developed, incorporating state-of-the-art computational methodology for flow analysis in straight, tapered and stepped seals. Relevant computational features of the code include: stationary/rotating coordinates, cylindrical and general Body Fitted Coordinates (BFC) systems, high order differencing schemes, colocated variable arrangement, advanced turbulence models, incompressible/compressible flows, and moving grids.

This paper presents the current status of code development, code demonstration for predicting rotordynamic coefficients, numerical parametric study of entrance loss coefficients for generic annular seals, and plans for code extensions to labyrinth, damping, and other seal configurations.

INTRODUCTION

Advanced rocket and aircraft engines are aimed to work at progressively higher efficiencies, lower weight-to-thrust ratios, to have greater reliability, and a longer life. Turbomachinery, the most complex engine component, requires advanced seal configurations to control leakage, rotodynamic response, mechanical component tolerances, and to inhibit mixing of incompatible fluids. As all of the above affect engine performance, through parasitic losses or limit cycles, it is important to understand the fundamentals of flow and rotodynamics and their interdependence. As modern turbomachinery becomes lighter and is operated at increasingly higher speeds the influence of seals on the rotodynamic stability becomes an important design concern. Prime examples of the importance of seals are in the Space Shuttle Main Engine (SSME) Fuel and Oxidizer turbopumps where seals performance becomes a critical element for the stable operation of engines. Coordinated seals research efforts of NASA LeRC, MSFC and Texas A&M University have greatly contributed to the Shuttle's reliability and performance. It is realized that accurate prediction of leakage rates and seals rotodynamic coefficients requires advanced computational models. Geometrical complexity and extreme operating conditions of uncommon fluids pushed existing empirical and bulk flow models to their limits. In 1988, Tam, Przekwas, Muszynska, Hendricks, Brown and Mullen[1] demonstrated that CFD can provide new insight into complex flow through seals and can complement the analysis of rotodynamic instability of seals.

Preceding Page Blank

The basic objectives of this program follow.

1. To develop a verified three-dimensional "scientific" CFD code for analyzing seals, representing the state-of-the-art in accuracy of predicting flow fields, rotodynamics and performance of a wide variety of seal configurations. The code will provide insight into flow and dynamics, contribute to the technical data base and provide an accurate standard for less complex "industrial" codes.
2. To compile and generate a set of verified one-, two-, and simplified three-dimensional "industrial" codes that will enable the designer or researcher to expeditiously analyze the wide variety of seals.
3. To develop a modern seal design computational environment with Knowledge Based System (KBS) and links to CAD/CAM packages and scientific data visualization tools.

The project team members include NASA LeRC, Mechanical Technology Incorporated, developing industrial codes and KBS, and CFD Research Corporation developing a scientific CFD seals code. A parallel research effort is being conducted in which the scientific code will contribute to the technical data base and provide an accuracy standard for less complex codes. The industrial codes will provide speedy analysis of seal designs. Graphical User Interface (GUI) and KBS data base will be a unifying mechanism. The technology transfer will be accomplished via annual workshops at which the program workplan will be reviewed and revised.

The aim of the code development effort is to develop a steady/transient 3D CFD code for the analysis of fluid flow for a broad range of seal configurations and for the analysis of the dynamic forces on the seals. The geometrical seal configuration will include cylindrical, labyrinth, honeycomb, damper, brush, face, wave, grooved, tip, contact, and noncontinuous seals. The fluids will range from incompressible liquid, two-phase mixtures, to compressible gases. An existing 3D CFD code, REFLEQS[2], is being adapted for seals by incorporating physical models to test turbulence, non-isotropic wall roughness, phase change, and cavitation. The scientific code was demonstrated at the 1992 annual workshop in August 1992 at NASA LeRC.

CFD CODE ENVIRONMENT

Existing CFD methodology of turbomachinery seals design is an expensive and time consuming process. Geometry definition, grid generation, selection of boundary conditions, numerical parameters selection, post-processing, and analysis of results often require CFD expert involvement. Rapidly advancing computer system software and hardware capabilities allow the automation of the CFD-based design process. In order to develop CFD-based seal design environment integration of CAD/CAM, CFD, structural mechanics, rotodynamics, computer graphics under the Knowledge Based System (KBS) is currently conducted.

The tasks of KBS are to integrate scientific and industrial codes with a consistent database, to provide a user-friendly graphical interface with context-sensitive help and to provide the Expert System to guide the seal design and optimization process. A major component of the KBS environment will be the scientific CFD code. The outline of the structure and brief description of the components of CFD seals code are provided. Technical specifications of the CFD code capabilities are discussed in the next section.

Figure 1 presents a flow chart for the CFD code design environment. The centerpiece of this system is the CFD code and most of the current development effort is dedicated to it. The other major modules CFD GUI-Preprocessor and KBS/GUI are being developed in collaboration with Mechanical Technology, Inc. The remaining components, CAD and Visualization, will be available from commercial vendors and the convenient links to them will

be provided. Comprehensive geometries definition and algebraic grid generation will be provided within GUI-Preprocessor. For more complex geometries, links with a CAD package such as ICEM-CFD, PATRAN, or IDEAS will be available. REFLEQS code, the starting point for the seals code, has already established interfaces with PATRAN and ICEM-CFD codes. Grids in PLOT3D standard format will be used directly without any translation. Similar standards will be adopted for graphical interfaces to scientific visualization tools. PLOT3D format files for grid, vectors, and scalars will be generated for postprocessing with PLOT3D, FAST or other commercial packages, most of which support that standard. The CFD code system can be installed on any UNIX X-window based workstation or on mainframe or mini-supercomputers.

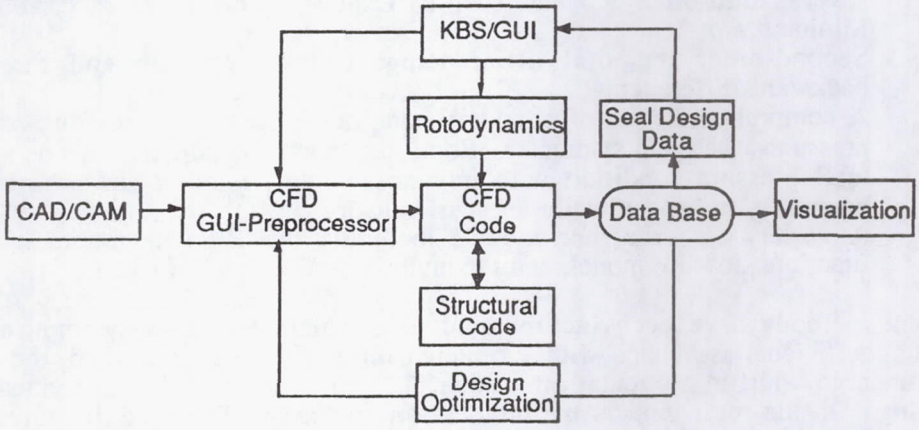

Figure 1. Flow Chart of CFD Code Design Environment: KBS - Knowledge Base System; GUI - Graphical User Interface

CFD CODE CAPABILITIES

The CFD Scientific Code is to be used as an accuracy check for the industrial design codes, and to provide detailed flow information for a variety of seals. It will also be used to predict the details of flow and performance of new seal configurations as well as seals where inadequate testing has been performed. With this in mind, a scientific code must possess following features as a minimum:

1. 3-D Navier-Stokes analysis in generalized body-fitted coordinate grids;
2. Stationary and rotating coordinate frames;
3. Steady-state and time-accurate solution capability;
4. Incompressible and compressible flow solutions;
5. Variable physical properties (viscosity, density, specific heat *etc.*);
6. Cavitation effects;
7. Provision for stepped surfaces and injection ports;
9. Inclusion of viscus dissipation in energy equation;
10. Treatment of sources due to external fields;
11. Variable surface roughness treatment;
12. Provision for effects of pre-swirl and upstream effects;
13. Customized input and output features for seals; and
14. Calculation of rotordynamic coefficients;

The code will use solution procedures that are accurate, efficient and robust when used in the high-aspect ratio computational cells that are typically encountered in seal problems.

As a starting point for the scientific code, REFLEQS[2] (REactive FLow EQuation Solver) code was selected. This code was developed by CFDRC personnel under various NASA and DoD grants as well as IR&D funds. Several modifications were subsequently incorporated in this

code. The current version of the code is a 3-D Navier-Stokes flow solver which uses a pressure-based flow solution method. A finite volume method is used to discretize the solution domains. A colocated arrangement of variables is used, where all flow variables are stored at the cell center. Cartesian components are used as the primary velocity variables, and a strong conservation approach is used to calculate convective fluxes. The momentum and continuity equations are solved sequentially using a variation of the SIMPLEC method. Some of the features of the code are listed below.

1. High-order spatial differencing schemes including central-differencing and several third-order schemes such as Osher-Chakravarthy, Osher, Superbee, Minimod *etc.*
2. Second-order temporal differencing: Crank-Nicholson and three-point backward differencing.
3. A comprehensive set of boundary conditions: specified mass flux, specified pressures, wall and symmetry. Some seal related conditions include specified total pressure condition with inlet loss factor, rotating and whirling wall boundary, and specification of swirl velocity.
4. A variety of turbulence models including the High-Re model with wall functions, low-Re model, and the multiple scale model of Chen.

Two different methods have been incorporated to calculate the skew-symmetric set of rotordynamic coefficients associated with a centered rotor. In the first method, the rotor is assumed to undergo whirl in a circular orbit about the stator center[1]. A transformation to a frame whirling with the rotor renders the problem quasi-steady. The fluid pressures on the rotor are then integrated to provide the fluid restoring forces at several different whirl frequencies. Appropriate polynomials are then fitted to obtain the functional relation between the fluid forces and the whirl frequencies to yield rotordynamic coefficients.

The second method is based on the "external shaker" method used in experimental setups for seal dynamic characteristics[3]. In this method, the rotor center is moved along a straight line in a direction perpendicular to the rotor centerline. A sinusoidal function of time is prescribed for this motion. The resulting time-dependent pressures are integrated to provide the rotordynamic coefficients. Due to the linear rotor motion, the problem is time-dependent, and also involves a time-varying computational domain. A volume-conserving moving grid formulation available in the code is used to compute the flow (the moving grid formulation can also be used for flows where the rotor center describes arbitrary motions). The time-dependent fluid forces are then used to calculate the rotordynamic coefficients. A detailed description of the method is given in Reference 4 . Of the two methods, the first method is faster, but can be used only for the centered rotor coefficients. The moving grid method is more versatile, and can be used to calculate dynamic coefficients for seals with static eccentricity as well as rotor misalignment.

SELECTED RESULTS

Validation of the scientific code is essential for its use in the design environment. It is a time-consuming process, and should be carried out in a step-by-step manner. This process involves computing flow solutions for a variety of test problems, and comparing the numerical results with the corresponding analytical/experimental/numerical results. Four levels of validation problems were suggested by Singhal[5] to be necessary for overall validation of the code, and to ensure code reliability. These are:

1. checkout problems;
2. benchmark problems;
3. validation problems; and
4. field problems.

The CFD scientific code has been put through an extensive array of test problems to assess and ensure the accuracy of the numerical and physical models incorporated in the code. Several checkout problems on relatively simple grids were carried out to ensure mass conservation, invariance of solutions in different reference frames, uniformity of the boundary condition treatment (*i.e.* consistent treatment at all planes), accuracy of the boundary treatment, proper computation of grid metrics, velocities in both orthogonal and non-orthogonal BFC grids, and so on. An exhaustive list of these test cases is too long; instead a selected number of test cases are given below. These cases test the accuracy of numerical and physical models that are directly relevant to seal type problems. Most of the test cases fall into the first three levels of validation outlined in the previous paragraph.

1. Fully-developed and developing flow in pipes, channels, and long narrow annulii.
2. Laminar flow between rotating cylinders, with and without Taylor vortices[6].
3. 2-D driven cavity flow, (Re up to 10,000[7]); 3D driven cavity flow.
4. Couette flow with and without heat transfer; planar wedge flow in a slider bearing[6].
5. Laminar flow over a backstep[8].
6. Laminar flow in a square duct with a 90° bend[9].
7. Turbulent flow in a plane channel[10].
8. Turbulent flow induced by rotating disk in a cavity*[11].
9. Centripetal flow in a stator-rotor configuration*[12].
10. Turbulent flow in an annular seal[13].
11. Turbulent flow in a 7-cavity labyrinth seal[14].
12. Turbulent compressible flow and heat transfer in turbine disk cavities[15].
13. 3-D driven cavity flow with lid clearance and axial pressure gradient and control of flow through vortex imposition[16].
14. Flow in infinite and finite length bearings (without cavitation)[17,18].
15. Rotordynamic coefficient calculations for incompressible flow seals[19,20] and compressible tapered seals[21].

(* Computations performed under NASA MSFC Contract No. NAS8-38101)

Presented below are some of the results described in Item 15. These consist of rotordynamics for a short[19,3] and long[20] incompressible flow seals, and tapered gas seals.[21]

In most of the numerical simulations of seal flows the seal entrance static pressure is linked to the experimentally measured pressures through an entrance loss coefficient. This is expressed as:

$$P_a = P_{in} - 1/2\,(1 + \xi)\,\rho u_a^2$$

where ξ is the loss coefficient, P_{in} the experimentally measured static pressure upstream of the seal, P_a the static pressure that is imposed at the seal entrance and u_a the average axial velocity in the seal. Thus, the entrance loss coefficient is expressed as a fraction of the average dynamic head in the seal, and represents the loss in head as the fluid enters the seal from an upstream region that has a much larger radial width. A series of cases were computed in order to estimate these losses using the present code under different flow and geometry conditions. These results are also described below.

Tapered annular gas seal: This case is described in Nelson *et.al.*[21]. The seal parameters used were: seal radius= 32.5 mm., radial clearances at the inlet and exit = 0.172 and 0.086 mm, inlet pressure = 1.52 MPa, sump pressure = 0.65 Mpa, inlet temperature = 650 K, γ =1.4, dynamic viscosity = 1.8 X 10^{-5} Pa-s, and gas constant=2586 J/Kg-K. The shaft speed was 30,400 rpm, and calculations were performed at three L/D ratios of 0.1, 0.2 and 0.4. The moving grid method also was used in this case. Standard k-ε model was used for turbulence,

and the computational grid used had 12, 6, and 30 cells in the axial, radial and circumferential directions. The results for this case are shown in Table 1. Also shown are the results from bulk flow theory as reported in Reference 21. As seen, the two sets compare reasonably well, including the prediction of flow choking at the exit of the short seal.

Table 1. Tapered Gas Seal Rotordynamic Coefficients

L/D	K N/m	k N/m	C N-s/m	c N-s/m	Exit Mach Number
0.1	948000	19700	11.5	0.016	1.00
	1150000	15429	9.94	0.043	1.00
0.2	1700000	75700	43.9	0.073	0.96
	2125500	60886	38.62	0.09	0.97
0.4	2880000	267000	152	0.27	0.83
	3553200	233820	145.9	0.57	0.83

Nelson, 1985[21] Present Results PA-92-24 11

Incompressible long seal: The seal geometry for this case, as described in Reference 20 is : seal radius = 39.656 mm, clearance = 0.394 mm, length = 240 mm. Properties of water at 20°C were assumed: dynamic viscosity = 1.04 x 10^{-3} Pa-s, density = 998 Kg/m^3. The grid used had 20, 15, and 30 cells in the axial, radial, and circumferential directions, respectively. The low Reynolds number k-ε turbulence model was used in the calculations. The whirling rotor method was used to calculate the rotordynamic coefficients. The calculations were performed at three shaft speeds: 1080, 1980 and 3000 rpm. Six pressure differentials for each speed were used: 20, 50, 10, 250, 500 and 900 KPa. Inlet swirl was specified using the experimental data. Results of these calculations are plotted in Figures 2 through 6. Experimental data from Reference 20 are also plotted on these figures for comparison. The comparison between the experimental and computed values is very good; the negative direct stiffness coefficients at high rpm and/or low pressure differentials are also predicted correctly.

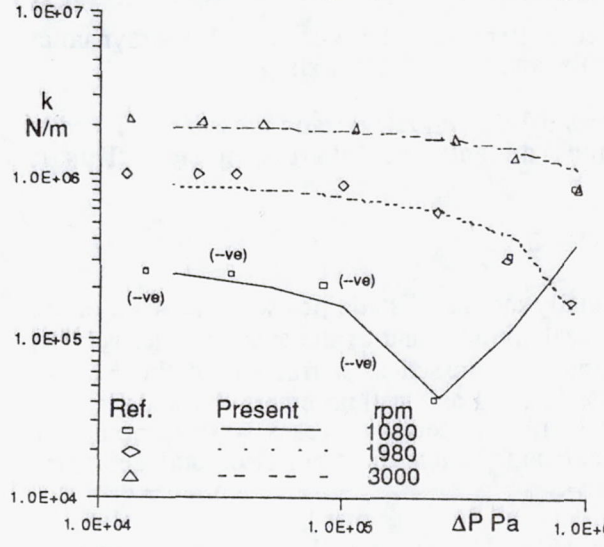

Figure 2. Direct Stiffness Coefficient. Symbols represent experimental data from Reference 20.

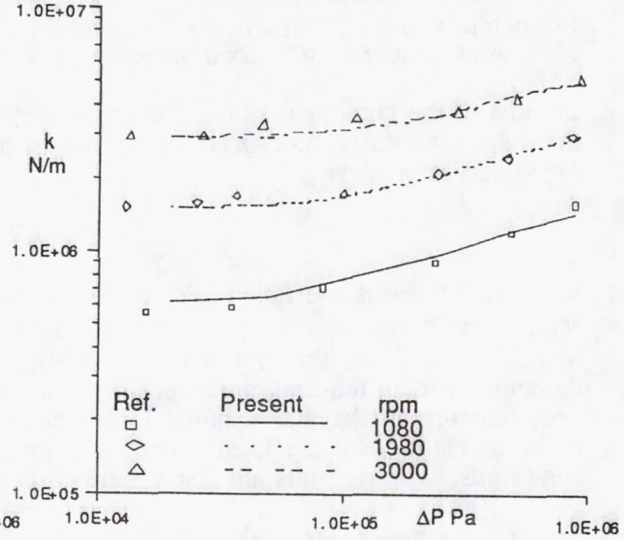

Figure 3. Cross-Coupled Stiffness Coefficient. Symbols represent experimental data from Reference 20.

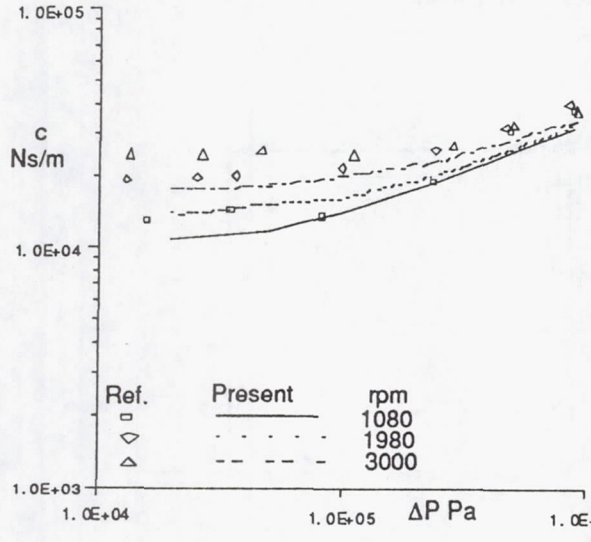

Figure 4. Direct Damping Coefficient. Symbols represent experimental data form Reference 20.

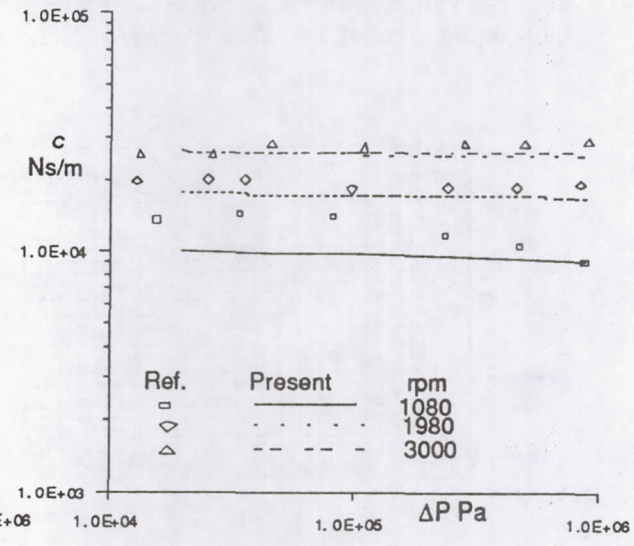

Figure 5. Cross-Coupled Damping Coefficient. Symbols represent experimental data from Reference 20.

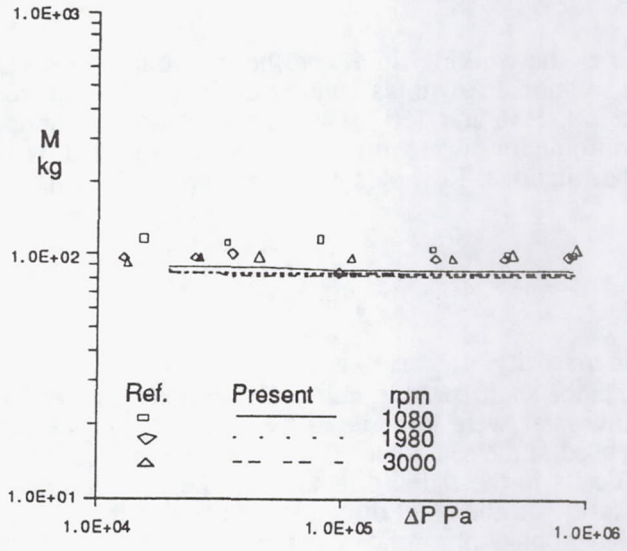

Figure 6. Direct Mass Coefficient. Symbols represent experimental data from Reference 20.

Entrance loss coefficient: As described above, the entrance loss coefficients is an empirical parameter which depends on several factors such as seal entrance geometry, flow rate *etc.* To analyze the effects of some of these parameters on the loss coefficient, a limited parametric study was performed. A generic annular seal geometry was assumed, as shown in Figure 7. The flow was assumed axisymmetric. Effects of three parameters was considered: 1) radius-to-clearance ratio, 2) entrance region radial gap to clearance ratio, and 3) flow rate. The

nominal values were: seal radius = 25 mm, seal length = 25 mm, and the axial length of the inlet region kept at 1.5 times the seal radius.

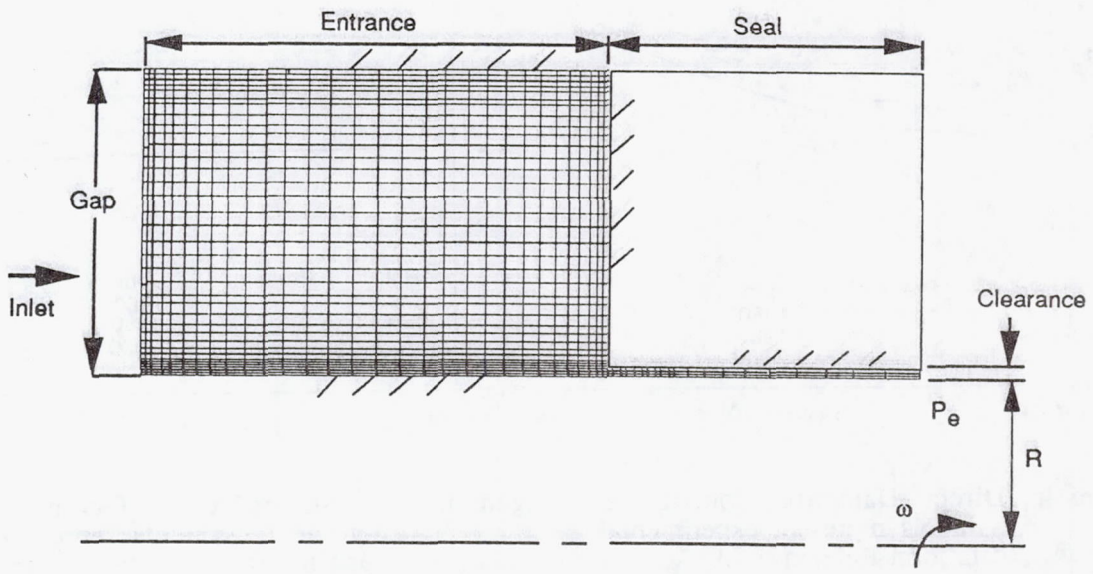

Figure 7. Flow Domain and One of the Grids Used for the Entrance Loss Coefficient Calculations

Water at 20°C was used as the working fluid, and the rotational speed was kept at 3000 rpm, which corresponds to a rotational Reynolds number of 1.88×10^5. Three radius to clearance ratios were considered: 50, 100, and 150. Two gap-to-clearance ratios were used: 50 and 100. Each of these combinations were run at several different flow rates (axial reynolds numbers). The axial and rotational Reynolds numbers were defined as:

$$Re_{ax} = 2 \cdot (CL)u_{ax,m}/\nu$$

and

$$Re_\theta = \omega r^2/\nu$$

where ν is the kinematic viscosity, $u_{ax,m}$ is the mean axial velocity, CL is the seal clearance, r is the seal radius, and ω is the shaft speed in rad/s. The exit pressure of the seal was kept fixed at 0 Pa, and nominal flow rates were imposed at the inlet. A fully-developed turbulent axial velocity profile was imposed at the seal inlet. Computational grids used had 5 cells in the seal clearance, and 30 or 50 cells in the radial directions in the entrance region depending on the radial gap to clearance ratio. In the axial direction 30 cells were used in the entrance region and 20 cells in the seal region. Appropriate clustering was used to resolve the critical flow regions.

To calculate the loss coefficient, the seal entrance pressure is required. Moreover, this pressure should correspond to the value which will generate the specified flow rate in the seal when only the seal is considered. To estimate this, pressures in the downstream part of the seal length were used. The flow becomes fully developed in this region, and the pressure varies linearly with axial length. This slope was calculated and extrapolated to the seal inlet to provide the inlet static pressure. The loss coefficient was then calculated based on this pressure, and the computed pressure at the entrance of the flow domain.

Results of this initial parametric study are given in Tables 2 through 4. A comparison of the results at comparable axial Reynolds numbers reveals several general trends:

1. The radius-to-clearance ratio has the largest effect of the loss coefficient. Increasing the ratio (*i.e.* decreasing the seal clearance) increases the loss coefficient;
2. The loss coefficient also increases with higher entrance region gap to clearance to radius ratio, but the sensitivity is lower;
3. for a fixed geometry, the loss coefficient reduces with higher flow rates.

For the configurations tested, the loss coefficients were between 0.406 to 0.68.

Table 2. Entrance Loss Coefficients, Radius/Clearance = 50

Entrance Gap/Clearance = 50			Entrance Gap/Clearance = 100		
u_{ax} m/s	Re_{ax}	ξ	u_{ax} m/s	Re_{ax}	ξ
10.814	10377	0.471	10.82	10384	0.490
16.232	15484	0.431	10.24	15584	0.488
21.619	20746	0.414	21.66	20785	0.482
26.942	25854	0.406	27.06	25970	0.48

PA-92-24 t2

Table 3. Entrance Loss Coefficients, Radius/Clearance = 100

Entrance Gap/Clearance = 50			Entrance Gap/Clearance = 100		
u_{ax} m/s	Re_{ax}	ξ	u_{ax} m/s	Re_{ax}	ξ
10.80	5181	0.562	10.797	5167	0.567
16.56	7945	0.54	16.176	7761	0.558
21.595	10361	0.526	21.55	10339	0.55
26.67	12796	0.51	26.934	12664	0.54
32.27	15484	0.493	32.24	15469	0.537
43.062	20667	0.478	42.533	20408	0.524

PA-92-24 t3

Table 4. Entrance Loss Coefficients, Radius/Clearance = 150

Entrance Gap/Clearance = 50			Entrance Gap/Clearance = 100		
u_{ax} m/s	Re_{ax}	ξ	u_{ax} m/s	Re_{ax}	ξ
10.82	3461	0.66	10.75	3438	0.68
16.19	5178	0.65	16.09	5146	0.66
21.49	6874	0.647	21.47	6874	0.65
26.74	8553	0.637	26.81	8553	0.648
32.25	10315	0.628	32.176	10292	0.64
48.33	15461	0.606	47.87	15315	0.63
64.487	20630	0.595	64.165	20630	0.624

PA-92-24 t4

CONCLUSION

Advanced, CFD based, turbomachinery seals design environment is being developed. It consists of several major components including a scientific CFD flow solver, and a range of industrial seal design codes. A modern graphical user interface will be integrated with a Knowledge-Based System and will provide links to flow solvers as well as to CAD/CAM and scientific visualization tools. The paper presents a novel concept of integrated CFD design code system under the KBS environment with CFD flow solver as major component. The scientific CFD flow solver incorporating state-of-the-art numerical methods has been developed, validated on a broad range of flow problems and demonstrated for several cylindrical seal flow configurations. The code has also been used to calculate the rotordynamic coefficient of number of test seals and ocmpared with experimental and other analytical/numerical results. Results of validations study show very good agreement with available analytical solutions and with well posed experimental measurements. A short numerical study was conducted to estimate the entrance loss coefficient commonly used in seal calculations. The study indicated that an increase in the seal radius-to-clearance ratio increases the loss coefficient. The ratio of entrance gap to seal clearance and the flow rate also change the loss coefficients, but to a smaller extent.

The present efforts include extending the CFD code to labyrinth and damper seals as well as incorporation of additional physical models and as cavitation. The code will be extended to cover a broad range of seal configurations for fluids ranging from incompressible to compressibel gases in two-phase flow.

ACKNOWLEDGEMENT

This study has been supported by NASA Lewis Research Center under contract No. NAS3-25644, entitled, "Study of Fluid Dynamic Forces in Seals." This support is greatly appreciated.

REFERENCES

1. Tam, L.T., Przekwas, A.J., Muszynska, A., Hendricks, R.C. Braun, M.H., and Mullen, R.L., "Numerical and Analytical Study of Fluid Dynamic Forces in Seals and Bearings," Trans. ASME, *J. or Vibration, Acoustics, Stress, and Reliability in Design,* v. 110, 1988, pp. 315-325.
2. Przekwas, A.J., Habchi, S.D., Yang, H.Q., Avva, R.K., Talpallikar, M.V., and Krishnan, A., "REFLEQS-3D: Computer Program for Turbulent Flows with and Without Chemical Reaction, Vol 1: User's Manual," CFD Research Corporation, GR-89-4-Jan. 1990.
3. Childs, D.W., Nelson, C.E., Nicks, C., Scharrer, J., Elrod, D., and Hale, K., "Theory Versus Experiment for the Rotordynamic Coefficients of Annular Gas Seals: Part 1- Test Facility and Apparatus," *Trans. of ASME, J. of Tribology,* Vol. 108, July 1986, pp.426-432.
4. Athavale, M.M., Przekwas, A.J., and Hendricks, R.C., "A Finite-Volume Numerical Method to Calculate Fluid Forces and Rotordynamic Coefficients in Seals," AIAA-92-3712, AIAA 29th Joint Propulsion Conference, July 1992.
5. Singhal, A.K., "Validation of CFD Codes and Assessment of CFD Simulations," Presented at the Fourth International Symposium on Transport Phenomena and Dynamics of Rotating Machinery (ISROMAC-4), April 5-8, 1992, Honolulu, HI.
6. Schlichting, H., *Boundary Layer Theory,* McGraw-Hill, 1979.
7. Ghia, U., Ghia, K.N., and Shin. C.T., "High-Re Solutions for Incompressible Flow Using the Navier-Stokes Equations and a Multigrid Method," *J. of Comp. Physics,* V.48, 1982, pp.387-411.
8. Armaly, B.F., Durst, F., Pareira, J.C.F., and Schonung, B., "Experimental and Theoretical Investigation of Backward-Facing Step Flow," *J. of Fluid Mech.*, V.127, 1983, pp.473-496.

9. Taylor, A.M.K.P., Whitelaw, J.H., Yianneskis, M., "Measurements of Laminar and Turbulent Flow in a Curved Duct with Thin Inlet Boundary Layers," NASA CR-3367, 1981.
10. Laufer, J., "Investigation of Turbulent Flow in a Two-Dimensional Channel," NACA Report 1053, 1951.
11. Daily, J.W., and Nece, R.E., "Chamber Dimension Effects on Induced Flow and Frictional Resistance of Enclosed Rotating Disks," *Trans. of ASME, J. of Basic Engg.*, V.82, 1960, pp.217-232.
12. Dibelius, G., Rodtke, F., and Ziemann, M, "Experiments on Friction, Velocity, and Pressure Distribution of Rotating Disks," D.E. Metzger and N.H. Afgan Eds., *Heat and Mass Transfer in Rotating Machinery*, 1984, pp.117-136.
13. Morrison, G.L., Johnson, M.C., and Tatterson, G.B., "Three-Dimensional Laser Anemometer measurements in an Annular Seal," *Trans. of ASME, J. of Tribology*, V.113, 1991, pp.421-427.
14. Morrison, G.L., Johnson, M.C., and Tatterson, G.B., "3-D Laser Anemometer measurements in a Labyrinth Seal," *Trans. of ASME, J. of Engg. for Gas Turbines and Power*, V.113, 1991, pp.119-125.
15. Athavale, M.M., Przekwas, A.J., and Hendricks, R.C., "A Numerical Study of the Flow Field in Enclosed Turbine Disk Cavities in Gas Turbine Engines," Presented at the Fourth International Symposium on Transport Phenomena and Dynamics of Rotating Machinery (ISROMAC-4), April 5-8, 1992, Honolulu, HI.
16. Athavale, M.M., Przekwas, A.J., and Hendricks, R.C., "Driven Cavity Simulation of Turbomachinery Blade Flows with Vortex Control," AIAA 31st Aerospace Sciences Meeting and Exhibit, January 1993.
17. Fuller, D.D., *Theory and Practice of Lubrication for Engineers*, pp.364-365, 1984.
18. Cameron, A., *Principles of Lubrication*, Longman's, pp.308-313, 1966.
19. Dietzen, F.J., and Nordmann, R., "Calculating Rotordynamic Coefficients of Seals by Finite-Difference Techniques," *Trans. ASME J. of Tribology*, vol. 109, pp. 388-394, 1987.
20. Kanemori, Y., and Iwatsubu, T., "Experimental Study of Dynamic Fluid Forces and Moments for a Long Annular Seal," *Trans. ASME, J. of Tribology*, v. 114, pp. 773-778, Oct. 1992.
21. Nelson, C.C., "Rotordynamic Coefficients for Compressible Flow in Tapered Annular Seals," *Trans. ASME, J. of Tribology*, v. 107, pp. 318-325, 1985.

THE EFFECT OF INLET SWIRL ON THE DYNAMICS OF LONG ANNULAR SEALS IN CENTRIFUGAL PUMPS

M. Ismail and R.D. Brown
Heriot-Watt University
Edinburgh, United Kingdom

and

D. France
Weir Pumps Ltd.
Glasgow, Scotland

This paper describes additional results from a continuing research program which aims to identify the dynamics of long annular seals in centrifugal pumps. A seal test rig designed at Heriot-Watt University and commissioned at Weir Pumps Research Laboratory in Alloa permits the identification of mass, stiffness, and damping coefficients using a least-squares technique based on the singular value decomposition method. The analysis is carried out in the time domain using a multifrequency forcing function. The experimental method relies on the forced excitation of a flexibly supported stator by two hydraulic shakers. Running through the stator embodying two symmetrical balance drum seals is a rigid rotor supported in rolling element bearings. The only physical connection between shaft and stator is the pair of annular gaps filled with pressurised water discharged axially. The experimental coefficients obtained from the tests are compared with theoretical values.

1. INTRODUCTION

Research conducted in the last decade has shown that the overall rotor dynamic behaviour of centrifugal pumps is dominated by the interaction between the pumped fluid and the pump itself. Experimental evidence suggests that a pump rotor may become dynamically unstable in presence of fluid forces. As a result, the annular clearances inside the pump tend to experience excessive wear which consequently leads to increased vibration amplitude.

To avoid such problems, pump users and manufacturers have begun to adopt new specifications based on accurate prediction of rotor dynamic performance in terms of amplitude response and stability. A complete dynamic analysis of a rotating machine involves calculations of stability, damped natural frequencies and response of the system to excitation forces. Accurate predictions require that all important mechanical components such as bearings and annular seals be represented with regard to their dynamic characteristics.

The dynamic behaviour of neck-ring and interstage seals has been well established using a linear theory. Considerable research has been done with respect to these seals and the theory has been confirmed by experimental data as far as short seals are concerned. However, theoretical models for long seals typical of a balance drum are less satisfactory and there is a dearth of experimental data which is usually obtained from small scale test rigs which do not represent geometric configurations of flow regimes found in modern centrifugal pumps. As a result, the effect of fluid forces in long seals on the performance and dynamic behaviour of centrifugal pumps are not well understood.

The work reported here was supported by S.E.R.C. and Weir Pumps Ltd and aims to identify the dynamics of long annular seals in centrifugal pumps. The detailed design of the test rig was described in (1). A general layout of the test facility including measurement pick-ups is shown in

Preceding Page Blank

figure 1. The test rig situated at Weir Pumps Research Laboratory at Alloa consists of a rigid shaft supported by rolling bearings at both ends and a very rigid housing mounted on coil springs. (initially, the casing was mounted on air bellows). A pair of simulated balance drum test seals is installed in the housing and water is charged from the centre of the casing and discharged from both ends. A significant feature of the flow path is the radial inward motion before entry to the annular clearance space. Two hydraulic actuators offset spatially at 90° are used to apply forces to the middle of the casing. Figure 2 shows a schematic view of the primary test section and figure 3 shows some details of the rotor and seals. The oscillatory motion of the casing, when excited by external forces is modified by the dynamic characteristics of the flow passing through the seals.
A linearised mathematical model is generally the appropriate starting point to study dynamic forces in pump annular seals. Hence the following model was assumed for the seal reaction forces:

$$\begin{Bmatrix} R_x \\ R_y \end{Bmatrix} = \begin{bmatrix} K_{xx} & K_{xy} \\ K_{yx} & K_{yy} \end{bmatrix} \begin{Bmatrix} x \\ y \end{Bmatrix} + \begin{bmatrix} C_{xx} & C_{xy} \\ C_{yx} & C_{yy} \end{bmatrix} \begin{Bmatrix} \dot{x} \\ \dot{y} \end{Bmatrix} + \begin{bmatrix} M_{xx} & 0 \\ 0 & M_{yy} \end{bmatrix} \begin{Bmatrix} \ddot{x} \\ \ddot{y} \end{Bmatrix}$$

Here K, C, and M are the stiffness, damping, and inertia matrices of the fluid as it passes through the clearance space and (x,y) is the instantaneous displacement vector of the seal stator relative to the rotor.
Following the commissioning stage of the test rig, preliminary tests were carried out for moderate pressures and rotor speeds and the obtained results were presented in (2). These results showed good agreement between theoretical and experimental direct and cross-coupled stiffness coefficients. However, experimental direct damping coefficients showed large discrepancies when compared with theoretical values. While the theory predicts an increase in damping with increasing pressure, the experimental results showed no discernible increase in damping. Cross-coupling damping and to a lesser extent fluid inertia could not be estimated accurately. On the other hand, measured radial pressure distributions lead to inlet swirl ratios of about 0.8 to 1.0 as compared to the commonly assumed value of 0.5 .
Now although these preliminary results were seen as very encouraging, the major drawback was that the tests could not be extended to higher pressures and higher rotor speeds. The low stiffness of the casing suspension system resulted in flow induced vibrations which limited the testing range to a rotor speed of about 1600 rpm and a pressure of 4.5 bar. It was clear from the tests that these flow induced vibrations were associated with the rotation of the shaft because of their synchronous nature and there was strong evidence that they were caused by fluid cross-coupled forces in the seals. Using the idea of Massey (3), grooved rings were installed in the axial gap between the back shroud of the simulated impeller and the casing with the expectation that the grooves would result in a lower fluid swirl at seal entry. They were 25 radial grooves of 45 mm length, 6 mm width and 1.5 mm depth. Following this simple modification, a significant reduction in the vibration level was achieved. In fact, with this configuration the rotor could be run up to the maximum achievable speed of 3000 rpm (limited by the DC. motor) at any pressure up to 15.7 bar (limited by the delivery pump) with peak displacements not exceeding 25 μm. It is well known that a reduction of swirl at seal entry results in a reduction of the fluid cross-coupled forces. It is thus obvious that the vibrations experienced without the grooves are a direct result of fluid cross-coupling in the seals. Since the test rig design enabled different test rings to be tested, it was possible to investigate the effect of various groove designs on the dynamic behaviour of the system.

The results presented in this paper are for a pair of seals and are mainly concerned with grooved plates. Modifications to the hardware and software reported in (2) are summarised in section 2. The radial pressure distribution measurements and swirl ratios are discussed in section 3. The measured and theoretical dynamic characteristics of the seals are presented and discussed in section 4.

2. HARDWARE, DATA ACQUISITION AND SOFTWARE

2.1. Hardware

One of the major problems that affected the progress of this work was associated with the hydraulic servo-actuators which provided the exciting forces. The original system worked well at the low speed and pressure limits of the plain test rings. However the system degraded over time, mainly due to the fact the original servo-valves were over-sized and unduly sensitive to wear. In addition the air suspension system was inadequate at the higher speeds made possible by the grooved test rings. The system was modified by changing the casing suspension to a coil spring system , using better quality ball bearings for rotor support and installing servo-valves with a lower flow requirement to suit the very small motions of the casing. The overall stiffness of the coil springs was 900 N/mm considerably less than the expected seal stiffness. The overall behaviour was much improved and it became possible to test throughout the entire range of speed and pressure available.

2.2 . Data Acquisition and signal processing

The instrumentation system detailed in (2) allows for high speed sampling of 12 channels at an overall sampling rate of 30 000 samples/s. These channels consisted of 6 displacement (2 relative), 4 acceleration and 2 force transducers. The absolute accelerations and displacements provide data to confirm that the forced motion of the casing is parallel to the shaft while the relative displacements check that there is no significant movement of the shaft. The forces generated by the hydraulic jacks are controlled by two digital-to-analogue multi-frequency signals which have been synthesised in the computer and stored in the data acquisition unit. In addition to the data sampling, the data acquisition unit is also used to convert the digital forcing signals into analogue ones.
The number of samples recorded for each channel has been increased from 2048 (2) to 15706. As a result a significant reduction in the variance of the estimated coefficients was achieved. Variance is a measure of the scatter in the experimental results.
Worden (12) has shown that estimation of the parameters of a linear system is not possible for single frequency excitation due to linear dependence of the state vectors. However, multi-frequency excitation can yield a large population of state vectors to provide the data set for a least squares optimisation, while avoiding these linear dependencies. In this case the singular value decomposition (SVD) method (2,12,13) was used to assess the significance of any term in the linear model. In order to minimise any contact between shaft and casing a low peak factor algorithm (14) was used to select the phase for the four excitation frequencies of 19, 25, 34 and 43 Hz. The test shaft speeds were chosen so as to avoid these frequencies.
Once a reliable data set had been obtained there was some signal processing involved before the analysis could commence. This consisted of mean removal, band pass filtering and notch filtering to remove any synchronous component. In addition velocity data had to be obtained from a numerical procedure. An estimated velocity vector was formed by integrating the acceleration

values, differentiating the displacement values, and taking the average. The processed data was then used to produce estimates of all the coefficients in the linear model and the appropriate standard errors. A data acquisition and reduction flow chart is shown in figure 4. More details are given by Brown and Ismail (2).

3. SWIRL MEASUREMENTS

3.1. Introduction

The equilibrium equation in the radial direction, in the axial gap h made the simulated impeller and the casing (figure 3) is given by:

$$-V_r \frac{dV_c}{dr} - \frac{V_c^2}{r} = -\frac{1}{\rho}\frac{dp}{dr} + \frac{\tau_{rwall}}{\rho h} \pm \frac{\tau_{rdisk}}{\rho h}$$

Neglecting the radial shear stresses τ_{rwall} and τ_{rdisk} and neglecting the change in radial velocity, the above equation becomes:

$$\frac{dp}{dr} = \frac{\rho V_c^2}{r} = \rho r \omega^2$$

where ω is the fluid angular velocity at radius r. Stepanoff (4) gives results of the integration of the above equation for a velocity distribution given by an equation of the form:

$$\omega = Cr^m$$

where C and m are constants, m = 2 for a free vortex and m = 0 for a forced vortex. The well known free and forced vortex are special cases of vortex motion.
The fluid angular velocity at seal inlet is obtained from the measured radial pressure distribution. For instance, in the case of a forced vortex we have:

$$p(r) = \int dp = \rho\omega^2 \int r dr$$

If the pressure is known at a radius r_1 and at seal inlet (r=R), integration of the above equations yields the fluid angular velocity at seal inlet

$$\omega = \sqrt{\frac{2}{\rho}\frac{p(R) - p(r_1)}{R^2 - r_1^2}}$$

3.2. Radial pressure distribution and fluid swirl at inlet : Results and discussion

The study of the radial pressure distribution of the flow in the gap between the back of the simulated impeller and the casing involved the measurement of the differential pressure at five radial positions (figure 3) for various flow rates and shaft speeds. A non dimensional flow coefficient C_q defined as :

$$Cq = \frac{Q}{\Omega R_2^2 h}$$

was used to analyse the results.

A comparison of swirl measurement results obtained in this work with those directly measured by Addlesee et al (5) for both the plain and the grooved plates is shown in figure 5. Addlesee et al used a Laser Doppler Anemometer to measure the velocity distribution in the gap between two coaxial disks simulating the entrance region of a balance drum seal. Figure 5 shows close agreement between the results obtained from the two different methods although the LDA measurements gave lower swirl values for the plain plates and higher swirl values with the grooves. This difference could be due to a different gap width and is consistent with further measurements (5) which showed that larger gaps lead to a decrease in swirl for the plain plates and an increase in swirl for the grooved plates. Hence, it can be argued that as the gap width increases the grooves become less effective. But it is obvious that the grooves reduce the swirl considerably, about 50 % for low values of C_q that is for high shaft speeds. It is also clear that higher leakage leads to higher swirl implied by a greater fluid total velocity.

4. DYNAMIC COEFFICIENTS

4.1. System coefficients without water

As the test rig only allowed total coefficients to be extracted, the stiffness and damping of the system without water had to be measured. For the grooved plate configuration the overall stiffness was 1.45 MN/m, slightly more than the stiffness of the coil springs alone. This is probably due a combined effect of the lateral stiffness of the springs and the supply hoses. Impact testing using a force hammer gave decay traces which were analysed. The damping coefficient was about 5000 Ns/m, about 10% of the seal direct damping.

4.2. Seal dynamic coefficients

The dynamic coefficients of the test seals were measured at four different flow rates and six shaft speeds, covering a range of 720 to about 3000 rpm. The axial Reynolds number varied from about 6900 to 12100 and the circumferential Reynolds number varied from about 1200 to 6000. In addition to the dynamic tests, some static and impact tests were also carried out in order to check the validity of the data. The experimental coefficients are compared to theoretical values based on Black's theory (9-11). The cross-coupled stiffness is calculated using the measured swirl as explained in (2).

4.2.1 Direct stiffness coefficients

After allowing for the stiffness of the system without water, the experimental direct stiffness coefficients of the seals are plotted in figure 6.a and 6.b . The theoretical coefficients are also plotted for comparison with the experiment. From these figures, it can be clearly seen that the major effect is an increase of stiffness with increasing axial Reynolds number. The theory predicts a symmetric stiffness for a centred seal but the experimental data shows some scatter. This is probably due to small eccentricities since the sampled data corresponds to small displacements around a centred position. The figures also show that while the theory predicts a decrease in stiffness with increasing shaft speed, the test data indicates that the direct stiffness is independent on shaft speed. There is some scatter in the test data but no discernible trend can be observed. The theoretical stiffness is given by the following expression:

$$K = \frac{\pi R \Delta p}{\lambda}\left(\mu o - \frac{1}{4}\mu_2 \Omega^2 T^2\right)$$

If the shaft speed is increased while the flow rate is kept constant, the change in stiffness in the above expression is mainly influenced by the second term which contains μ_2, that is the fluid inertia coefficient. However, published experimental work has shown that this term is generally over-estimated by the theory. The plotted data also shows that the theory under-estimates the stiffness by about 20 to 25%. A direct measurement (static test) of stiffness for no rotation is shown in Figure 6.c . It is clear that the values are comparable with the identified stiffness.

4.2.2. Cross-coupled stiffness coefficients

The theoretical and experimental cross-coupled stiffness coefficients are shown in figure 7. As predicted by the theory, the experimental coefficients increase linearly with the shaft speed. The sign of the coefficients is also detected accurately. There is good agreement between theory and experiment at low axial Reynolds number, figure 7.a, the theory overpredicting the coefficients by about 10%. But when the axial Reynolds number increases the agreement deteriorates. The theory predicts larger coefficients than the experimental ones especially at high shaft speeds, figure 7.b. For this case, the predicted coefficients are about twice as large as the experimental ones. In order to explain this discrepancy some of the theoretical assumptions were reviewed.

The theoretical stiffness expression is based on a model that assumes that (i) the seal is concentric, (ii) the rotating and stationary walls of the seal have the same surface roughness and (iii) the circumferential fluid velocity starts from an arbitrary initial swirl and asymptotically approaches $0.5R\Omega$ as it proceeds axially along the seal. In (6), Childs and Kim used a combined analytical-computational method to predict the fluid circumferential velocity in seals which may have different surface roughness treatments on the stator or rotor seal elements. They predicted that the circumferential velocity solution in a seal with the same rotor and stator roughness converges asymptotically towards $0.5R\Omega$ irrespective of whether both wall surfaces are smooth or rough. However, they predicted an asymptote less than $0.5R\Omega$ if the stator is rougher than the rotor and greater than $0.5R\Omega$ if the rotor is rougher than the stator. Further evidence that the fluid circumferential velocity inside a seal can be different from $0.5R\Omega$ was provided by Addlesee et al (5). Addlesee et al used a specially designed test rig to study the distribution of fluid velocity at different axial positions in a rotating annulus utilising an LDA technique. The test results reported in (5) suggest that the fluid circumferential velocity is strongly dependent on the inlet swirl. Specifically, strong inlet swirl gave high circumferential velocities (greater than $0.5\ R\Omega$) and weak inlet swirl gave low circumferential velocities (less than $0.5\ R\Omega$). On the other hand, the fluid cross-coupled stiffness varies proportionally with the fluid circumferential velocity. Since the inlet swirl in this work can be considered as weak and that the stator surface roughness is greater than the rotor surface roughness (1.5 μm and 0.5 μm), it can be argued that the discrepancy between theoretical and experimental cross-coupled stiffness coefficients is the result of a combined effect of a rougher stator and a reduced fluid circumferential velocity. This view was supported by a good correlation between predicted and measured cross-coupled stiffness coefficients when smaller values of fluid circumferential velocities were assumed. Larger discrepancies between predicted and measured cross-coupled stiffness coefficients at the higher speeds are consistent with flow measurements which showed that higher speeds lead to smaller inlet swirl ratios, resulting in

smaller values for the fluid circumferential velocity. An other factor that contributes to the reduction in fluid circumferential velocity is the axial velocity of the flow. When the fluid enters the seal with an initial swirl, the axial pressure drop imposes an axial velocity component on the flow which then proceeds in the seal with a combined peripheral and axial motion. But as the axial velocity increases, the passage time T becomes smaller and the fluid motion becomes dominated by the axial velocity. As a result, a fluid particle entering the seal with some initial swirl may exit it with little peripheral motion or more specifically with a weaker peripheral motion than in the case of a larger passage time.

4.2.3 Direct damping coefficients

The experimental and theoretical direct damping coefficients are shown in figure 8 for R_a values of 6950 and 12 120. As predicted by the theory, the direct damping does not vary with shaft speed. The theoretical and experimental coefficients coincide at low axial Reynolds number but disagree at high axial Reynolds number. The experimental data indicates that the damping is almost insensitive to changes in Reynolds number, which is in contradiction with the theory. It is worthwhile noting that similar discrepancies between theoretical and experimental direct damping coefficients were also reported by Childs et al in (6), (7) and (8). In (6), Childs and Kim reported that measured damping coefficients were smaller than the theoretical ones at low axial Reynolds number but as the Reynolds number increased the agreement between theory and experiment improved.

4.2.4 Overall dynamic behaviour

The linear modelling of the complete system was tested by comparing the simulated exciting forces from the linear model with the experimentally measured forces from the two hydraulic jacks. As can be seen from figure 9 the comparison demonstrates that an overall RMS error of 16% gives a very good reproduction of the forces acting on the casing. Thus the linear model is shown to be capable of predicting vibration response accurately.

5. CONCLUSIONS

Extensive testing with the grooved plates allowed a constructive critical review of the theoretical model to be made. Reassessment of the theoretical assumptions was made possible by carrying out tests covering the span of the flow rate range permitted by the supply pump. Testing at different flow rate values allowed some of the flow underlying phenomena to be unravelled. The obtained results are summarised in the following section:

- The inlet swirl ratio ω/Ω increases with the flow rate and decreases with the shaft speed, the sensitivity to flow rate being smaller in the high speed range.
- Radial pressure measurements in the gap between the back of the simulated impeller and the casing show pressure distributions which suggest the occurrence of a forced vortex motion, especially at high shaft speeds which is typical of modern centrifugal pumps.
- The use of radial grooves of 1.5 mm depth at the entrance to the balance drum resulted in a significant reduction in inlet swirl.
- The measurements show that only the direct stiffness, cross-coupled stiffness and direct damping coefficients are important. The cross-coupled damping coefficients were found to be insignificant as the least-squares technique gave standard errors which are larger than the

coefficients themselves. The inertia terms were identified but the scatter was large. These terms were found to lie in the range 35 to 150 Kg as compared to the theoretical value of 87 Kg. The plotted data showed no identifiable trend.

- Evidence of the beneficial effect of the grooves was noticed early when the dynamic instability experienced with the plain plates was completely suppressed. Later, experimental measurements of the dynamic characteristics of the seals showed a significant decrease in cross-coupled stiffness with the 1.5 mm deep grooved plates.
- The cross-coupled stiffness coefficients were fairly well predicted by the theory at low flow rates and small groove depth but the agreement between theory and experiment deteriorated with the increase of flow rate and groove depth. The theoretical model was reassessed by assuming that the fluid circumferential velocity in the seal is much smaller than half shaft speed.
- The direct stiffness coefficients were found to be under-predicted by the theory by about 20 to 30% in general and were found to be insensitive to swirl reductions. The measured coefficients are supported by those obtained from direct static tests.
- The measured direct damping coefficients were found to be insensitive to shaft speed, flow rate and swirl reductions. This is in serious discrepancy with the theory which predicts an increase in damping with increasing flow rate. However, impact tests carried out at the highest flow rate showed extremely good agreement with the identified damping.

Finally, it is to be noted that all identified coefficients except the cross-coupled damping terms were identified with small standard errors. The calculated root-mean square errors (RMSE) between the measured forces and those obtained by fitting the experimental data to a ten-coefficient model were of the order of 8 to 20%. The RMSE is defined as

$$RMSE(f) = 100 \times \left[\sum_{i=1}^{N} \sqrt{\frac{\left(f_i - \hat{f}_i\right)^2}{N \sigma_f^2}} \right]$$

where f is the measured force vector, $\hat{f}$ the force vector predicted by the model, σ_f the standard deviation of the measured force and N is the number of sample points in the data records. The RMSE provides a measure of the goodness of fit between the experimental data and the theoretical model.

6. REFERENCES

(1) Brown, R. D., Ismail M. and Abdulrazzak, M. Fluid forces in the annular seals of high performance centrifugal pumps, IMechE seminar, "Vibrations in centrifugal pumps", London, December 11, 1990.

(2) Brown, R. D. and Ismail M. Dynamic characteristics of long annular seals in centrifugal pumps, IMechE 5th International Conference , Vibrations in Rotating Machinery, paper C432/112, Bath, September 7-10, 1992.

(3) Massey, I. C. Sub-synchronous vibration problems in high-speed, multi-stage centrifugal pumps, Proceedings of the 14th turbomachinery symposium, turbomachinery laboratories, Texas A&M University, pp. 11-16, College Station, Texas, 1985.

(4) Stepanoff A. J. Centrifugal and Axial Flow Pumps, John Wiley and Sons, INC., 1957.
(5) Addlesee, A. J., Altiparmak, D. and Pan, S. Whirl measurements on leakage flows in turbomachine models, 7th Workshop on Rotor Instability, Texas A&M University, May, 1993.
(6) Childs, D. W. and Kim, Chang-Ho Analysis and testing for rotordynamic coefficients of turbulent annular seals with different, directionally-homogeneous surface roughness treatment for rotor and stator elements, Transaction of the ASME, Vol. 107, July, 1985, pp. 296-306.
(7) Childs, S. B. and Childs, D. W. Estimation of seal bearing stiffness and damping parameters from experimental data, NASA C.P 2133, 1980.
(8) Childs, D. W. and Dressman, J. Testing of turbulent seals for rotordynamic coefficients. Proceedings of EPRI Symposium in Power Plant Feed Pumps, CHERRY HILL, NJ, June 1982 (ICPR 1984).
(9) Black, H. F. and Jenssen, D. N. Dynamic hybrid properties of annular pressure seals, Proceedings of the Journal of Mechanical Engineering, Vol. 184, 1970.
(10) Black, H. F. and Jenssen, D. N. Effects of high pressure ring seals on pump rotor vibration, Transactions of the ASME, Paper No. 71-WA/FF-38, 1971.
(11) Black, H. F., Allaire, P. E. and Barret, L. E. Inlet flow swirl in short turbulent seal dynamics, 9th International conference on Fluid sealing, Leeewenhorst, Netherlands, April 1-3, 1981.
(12) Worden, K. Parametric and non-parametric identification of nonlinearity in Structural Dynamics, Ph.D. Thesis, 1989, Department of Mechanical Engineering, Heriot-Watt University, Edinburgh.
(13) Press, W. H., Flannery, B. P., Tenkolsky, S. A. and Vettering, W. T. Numerical Recipes, The Art of Scientific Computing, Fortran Version, Cambridge University Press, Cambridge, 1989.
(14) Schroeder, M. R. Synthesis of low-peak factor signals and binary sequences with low autocorrelation, IEEE Trans. on Information Theory, pp. 85-89, January, 1970.

NOTATION

L , c , h	seal length, seal radial clearance, axial gap between wall and rotating disk
r , R , R_d ,	radial position, seal radius, simulated impeller radius
F_x , F_y	components of the external force vector in x and y directions
R_x , R_y	seal restoring forces in x and y directions
V , V_r	average fluid axial velocity, average fluid radial velocity
v_c , v_o	fluid circumferential velocity, fluid circumferential velocity at seal entrance
T	time (L/V)
K, C, m	stiffness, damping and inertia coefficients
P , Q , C_q	pressure, flow rate, flow coefficient
R_a	average axial Reynolds number, $2\rho Vc/\mu$
R_r	average circumferential Reynolds number, $\rho\Omega Rc/\mu$
λ , σ	friction factor, $\sigma = \lambda L/c$
μ , ρ	fluid Viscosity, fluid density
ΔP , ξ	pressure drop across seal, inlet loss coefficient
Ω , ω	shaft angular speed, fluid angular velocity,
τ_{rwall} , τ_{rdisk}	radial wall shear stress, radial shear stress on rotating disk

DISCUSSION

Professor Childs raised a comment concerning the acceleration terms in the equations of motions. The equations of motion for the stator mass M_S can be written as

$$\begin{Bmatrix} F_x - M_s \ddot{x}_s \\ F_y - M_s \ddot{y}_s \end{Bmatrix} = \begin{bmatrix} K_{xx} & K_{xy} \\ K_{yx} & K_{yy} \end{bmatrix} \begin{Bmatrix} \Delta x \\ \Delta y \end{Bmatrix} + \begin{bmatrix} C_{xx} & C_{xy} \\ C_{yx} & C_{yy} \end{bmatrix} \begin{Bmatrix} \Delta \dot{x} \\ \Delta \dot{y} \end{Bmatrix} + \begin{bmatrix} M_{xx} & 0 \\ 0 & M_{yy} \end{bmatrix} \begin{Bmatrix} \Delta \ddot{x} \\ \Delta \ddot{y} \end{Bmatrix}$$

Here, (F_x, F_y) are the measured components of the input forces, $(\ddot{x}_s, \ddot{y}_s)$ are the measured components of the stator acceleration and $(\Delta x, \Delta y)$ are defined bellow:

$$\Delta x = x_s - x_r$$
$$\Delta y = y_s - y_r$$

where the subscripts s and r identify the stator and rotor respectively. We measure the absolute stator displacements (x_s, y_s) and the relative displacements $(\Delta x, \Delta y)$. The measured displacements show that when the synchronous noise is removed from the data we have

$$\Delta x \approx x_s$$
$$\Delta y \approx y_s$$

and hence the use of absolute accelerations is justified. The above condition is implied by the rigid rotor design used. Should this condition not be satisfied one can use a numerical procedure to obtain the relative accelerations from the measured relative displacements $(\Delta x, \Delta y)$. In fact this procedure is currently being adopted for the high pressure tests.

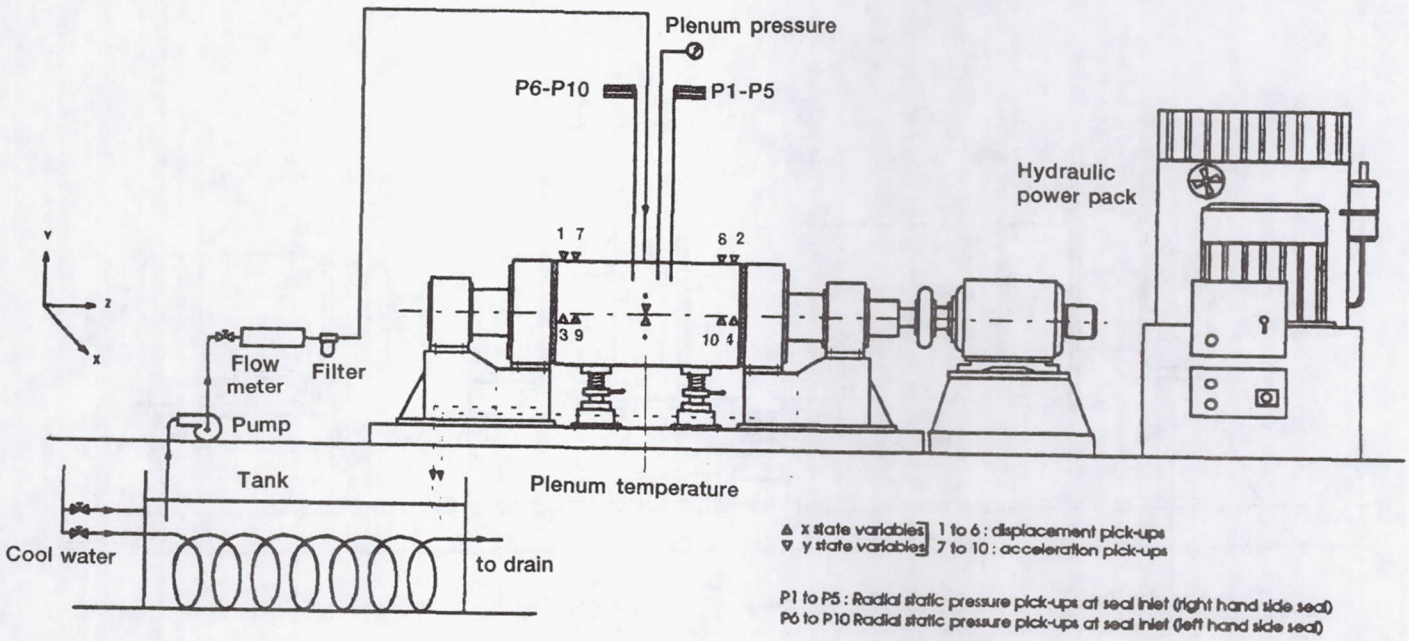

Figure 1 Test rig layout; instrumentation and hydraulic shakers not shown

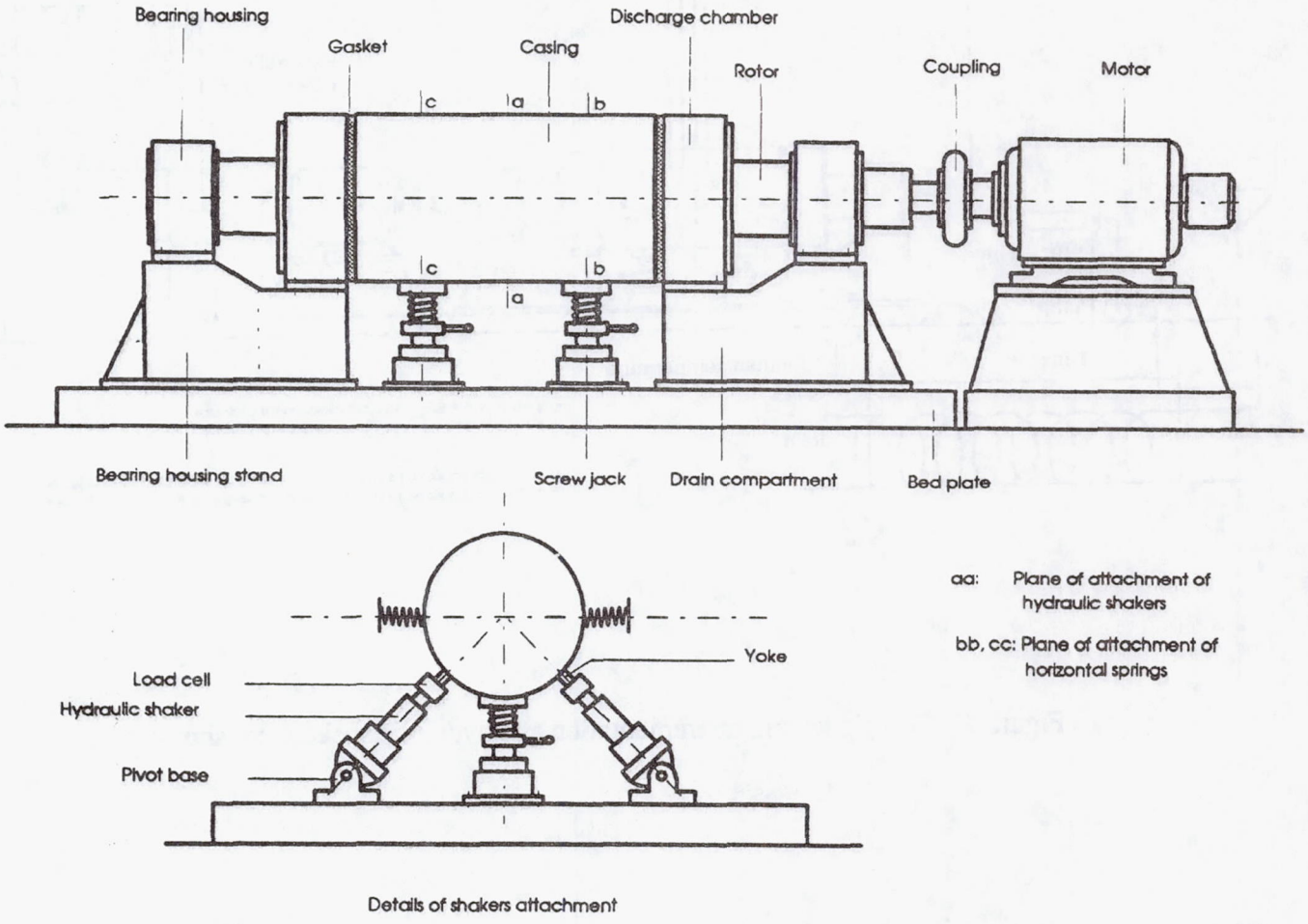

Figure 2 Schematic view of primary test section

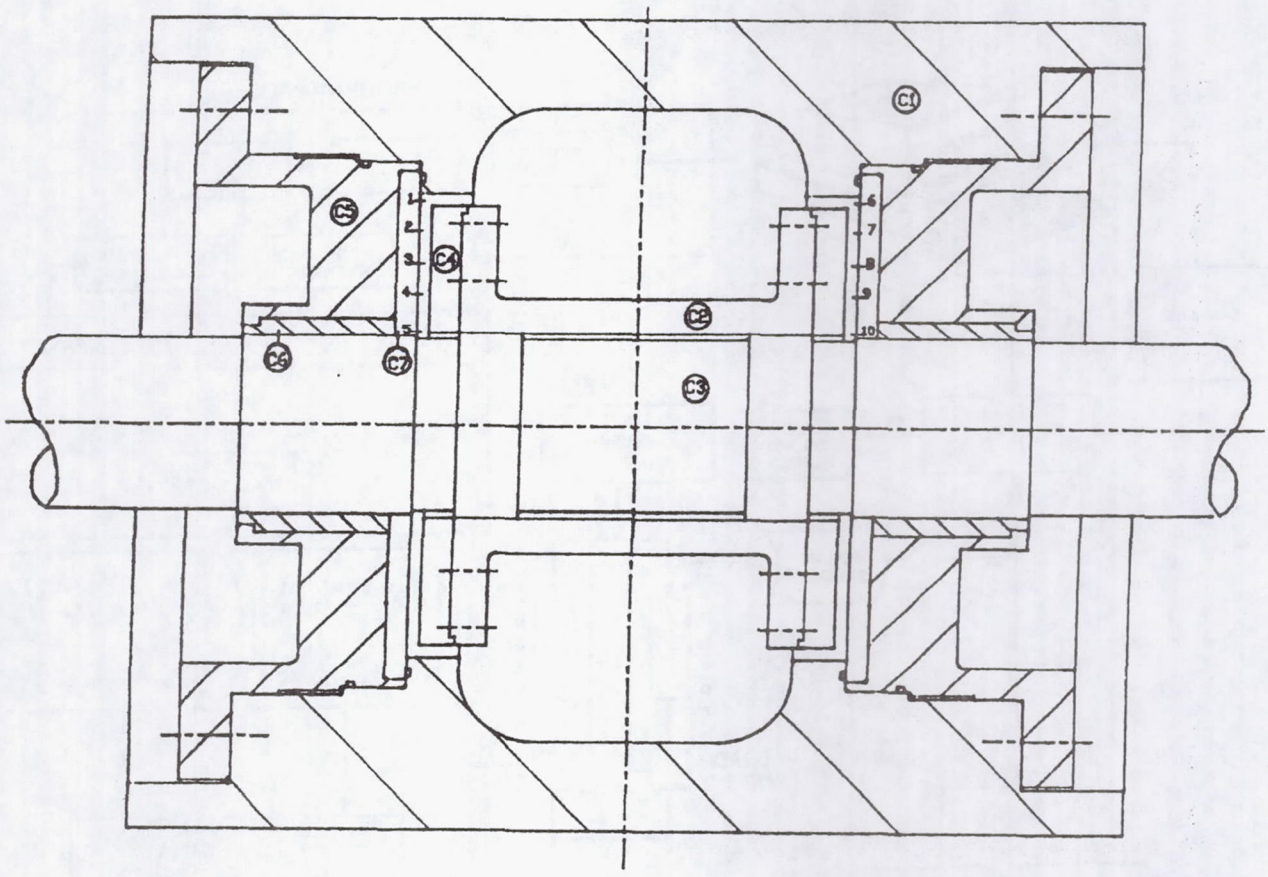

1–10 Static pressure tappings

C1 Casing
C2 Simulated impeller
C3 Rotor
C4 Plate for axial gap control
C5 Seal carrier
C6 Bronze sleeve
C7 anti-swirl plate

Figure 3 Cross-section of test seals

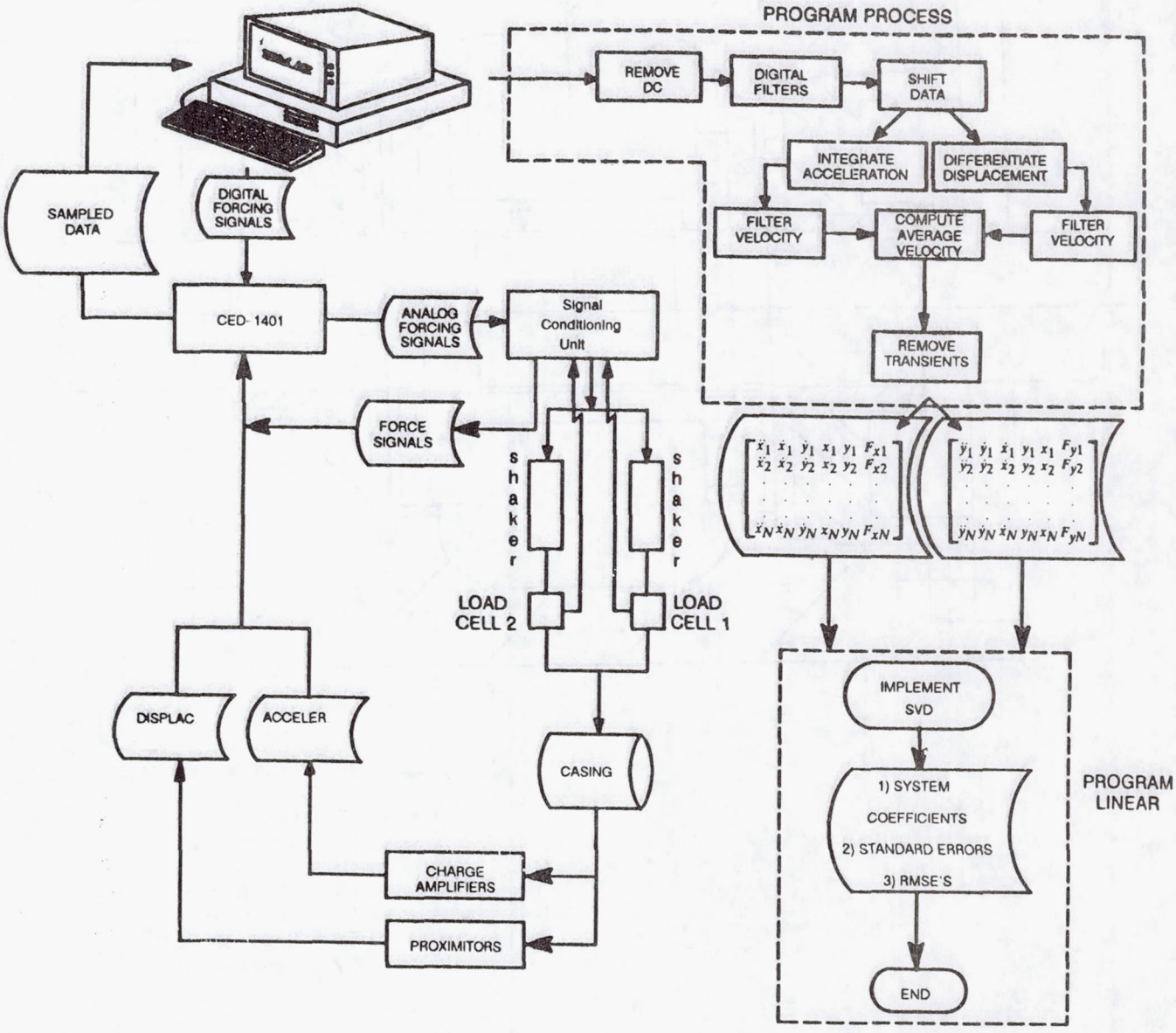

Figure 4 Data acquisition and reduction flow chart

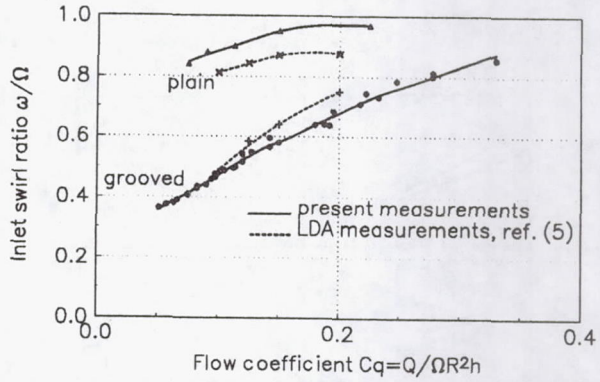

Figure 5 Inlet swirl ratio versus flow coefficient C_q

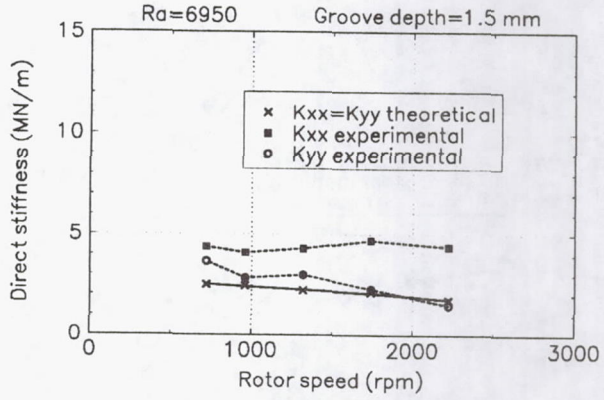

Figure 6.a Direct stiffness coefficients at R_a=6950

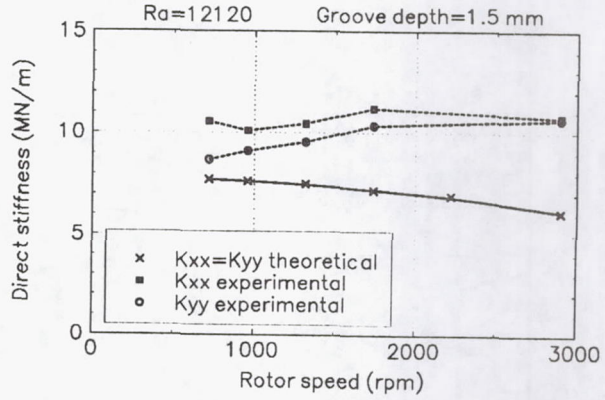

Figure 6.b Direct stiffness coefficients at R_a=12120

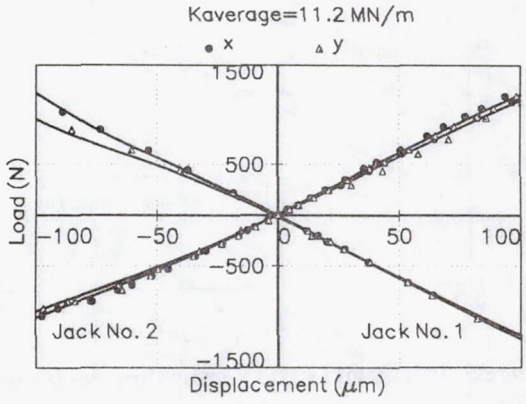

Figure 6.c Static stiffness of system at R_a=12100 and N=0 rpm

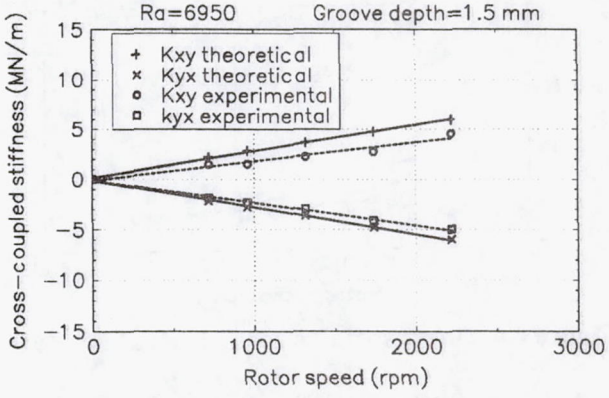

Figure 7.a Cross-coupled stiffness coefficients at R_a=6950

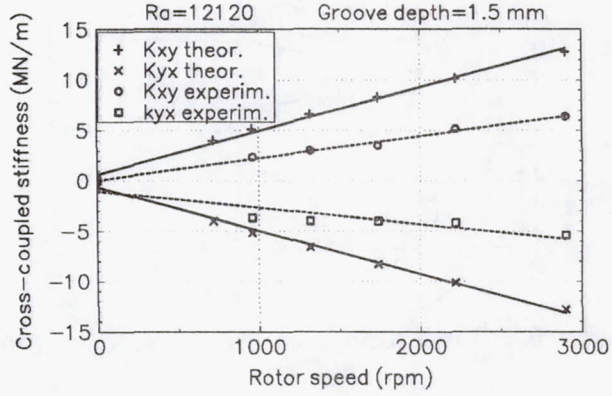

Figure 7.b Cross-coupled stiffness coefficients at R_a=12120

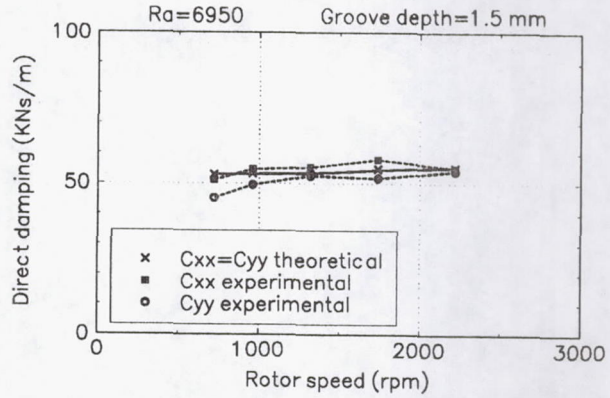

Figure 8.a Direct damping coefficients at R_a=6950

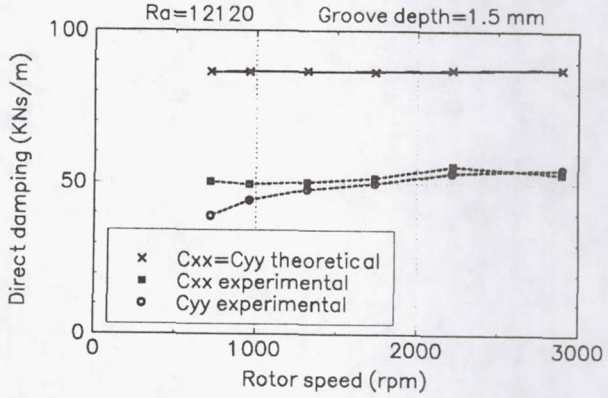

Figure 8.b Direct damping coefficients at R_a=12120

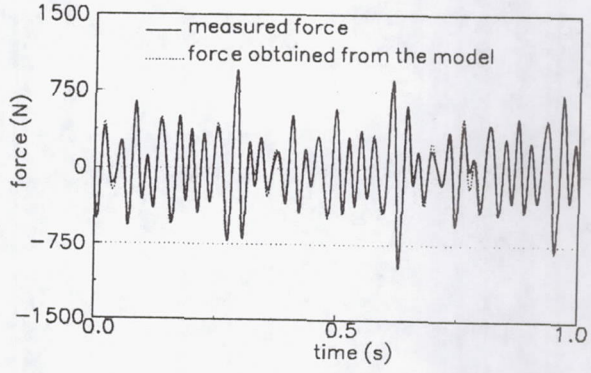

Figure 9 Comparison of measured and modelled forces

WHIRL MEASUREMENTS ON LEAKAGE FLOWS IN TURBOMACHINE MODELS*

A.J. Addlesee, D. Altiparmak, and S. Pan
Heriot-Watt University
Edinburgh, United Kingdom

The beneficial effects claimed for whirl control devices demonstrate that the dynamic behaviour of rotors is influenced by the fluid whirl in shaft and balance drum seals. The present paper reports results from two series of experiments, the first on the factors affecting the whirl at the seal inlet, and the second on the variation of whirl velocity along the seal. In both cases the LDA measurement technique required the clearance between the fixed and rotating parts of the models to be substantially greater than occurs in real machines, but the results are indicative nevertheless. Experimental and theoretical results are given for the radial distribution of whirl velocity in the gap between impeller shroud and pump casing. Results of tests with modified stator surfaces are also shown. This work leads naturally into the second series of experiments where some preliminary measurements of velocity distribution in the clearance between a fixed stator and a rotating shaft are reported for a range of inlet whirl conditions.

NOTATION

C_Q	Flow parameter $Q/\Omega R^2 h$
f	Friction factor
h	Clearance gap size
k	Constant
Q	Leakage flow towards axis
R	Impeller radius
r	Radial coordinate
t	Time
U	Mean axial velocity in annulus
v	Tangential velocity
v_f	Friction velocity
z	Axial coordinate
ε	Eddy kinematic viscosity
ν	Kinematic viscosity
ρ	Fluid density
τ	Shear stress
Ω	Angular velocity of impeller
ω	Angular velocity of fluid

Suffices

1	Impeller shroud surface
2	Surface opposite to impeller shroud
D	Edge of balance drum
R	Edge of impeller
S	Shaft surface

* The work reported here was partially supported by Weir Pumps Ltd.

Preceding Page Blank

INTRODUCTION

The part played by fluid whirl in determining the stiffness characteristics of shaft and balance drum seals is widely acknowledged (1,2,3,4). The present report applies particularly to the situation at the high pressure end of a multi-stage centrifugal pump, where a small fraction of the flow leaving the last impeller leaks away through the shaft or balance drum seal. The diameters of shaft, drum and impeller are typically in the ratios 1:2:3 and the leakage path is shown schematically in Fig.1.

For both experimental and analytical purposes the arrangement shown in Fig.1 can be conveniently investigated in two obvious sections, firstly the whirling radial inflow between the impeller shroud and the casing, and secondly the whirling axial outflow through the seal. The stiffness characteristics are determined by events in the seal, but the radial flow in the gap between shroud and casing is important because it influences the whirl of the leakage flow at entry to the annular seal. A number of whirl control devices have been found to have beneficial effects on rotor stability (5,6,7), thus demonstrating the inaccuracy of earlier theories in which the flow entering the seal was supposed to acquire instantly a whirl velocity independent of the entry value.

When a rotor surrounded by fluid in a small clearance gap moves off-centre, it experiences a force which depends on both the position and the translation velocity of the shaft centre, and which has both radial and tangential components. In particular, Black et al (1) showed that a radial displacement produced a tangential force component dependent on the fluid whirl velocity. The interaction between rotor and fluid is clearly extremely complex, and one way to simplify the problem of computing rotor motion is to make some plausible assumption about the variation of whirl along the seal. The force on the shaft is then obtained by integration of the contributions from all the axial elements of the seal, each depending on the assumed local whirl velocity of the fluid. The proposal of Black and co-workers for an asymptotic approach towards a limiting value of whirl appears to be a useful development beyond the discredited step change at entry mentioned above.

Obvious difficulties arise with this approach when the rotor and seal do not have a concentric equilibrium position and fluid particles experience different conditions on their passage through the seal. In some cases the short bearing assumption may be invoked to justify treating the whirl velocity as independent of angular position, but experimental evidence is hard to find.

IMPELLER/CASING FLOW

The angular velocity of the flow leaving the impeller and entering the gap between shroud and casing is typically about half that of the shaft, although it can be much higher under low flow conditions. The clearance gap is several millimetres wide and the situation may be regarded as a steady axi-symmetric flow provided that shaft misalignment and bending do not cause significant angular or temporal variations in the clearance. The flow will be

virtually unaffected by very small amplitude orbital motion of the shaft and, although a number of recent papers have applied CFD technology to the problem (8,9,10), a simple one-dimensional analysis of the flow provides considerable insight.

The Reynolds number ($\Omega rh/\nu$) is typically in excess of 5000 in the seal and at least an order of magnitude higher at the edge of the impeller. At these levels it is reasonable to treat the angular velocity ω as a function of radius r only, although it must in fact reach Ω on the impeller shroud and zero on the casing. The boundary layer thickness on the walls is assumed to be thin and the velocity step adjacent to the wall is combined with a friction factor to approximate the shear stress transmitted to the fluid. The variation of ω with r which results from such an analysis may be regarded as as a balance between extreme cases.

At one extreme, if friction is negligible the angular momentum of the fluid will be conserved as it approaches the axis. In this case:

$$\omega \cdot r^2 = \text{constant} = \omega_R \cdot R^2 \qquad (1)$$

and, using the typical values mentioned above, the angular velocity at the entry to a drum seal would be:

$$\omega \simeq (\Omega/2) \cdot (3/2)^2 > \Omega. \qquad (2)$$

The value would of course be much higher for a shaft seal of smaller diameter.

An alternative extreme form of behaviour would result if wall friction dominated the flow instead of being negligible, so that at all radii:

$$f_1 \cdot (\Omega_1 - \omega)^2 = f_2 \cdot (\omega - \Omega_2)^2. \qquad (3)$$

Here suffix 1 refers to the impeller shroud so that Ω_1 equals the shaft speed Ω, and suffix 2 refers to the opposite surface. Where surface 2 is the casing, Ω_2 is zero and equation (3) becomes:

$$f_1 \cdot (\Omega - \omega)^2 = f_2 \cdot \omega^2 \qquad (4)$$

whence:

$$\omega = \Omega/(1+(f_2/f_1)^{0.5}) \qquad (5)$$

and, if the friction factors are equal, the outcome is half-speed whirl. For the section of the gap where the opposite surface is the end of the balance drum:

$$\omega = \Omega_1 = \Omega_2 = \Omega.$$

These two extreme cases of angular velocity distribution are illustrated in Fig.2, where it is worth noting that in the dominant friction case the influence of the inlet whirl is confined to a region very close to the impeller edge. As observed in (10), the situation may occur where the high shear stresses, produced by high relative velocities near the outer edge of the impeller shroud, drive the angular velocity close to half-speed whirl (for equal friction factors). But closer to the seal entry where the relative velocities are lower and the fluid residence time is shorter, the tendency to conserve angular momemtum can be expected to assert itself with a consequent rapid rise in whirl velocity. This event is shown as a dashed line on Fig.2.

The whirl profile occurring in any real case is modified by further effects which theoretical work may need to account for. Two mechanisms tend to reduce variations of angular velocity. The first operates by the action of viscosity which produces tangential shear stress between adjacent annular elements of fluid, and the second is the turbulent momentum exchange between elements usually described as Reynolds shear stress. Viscous stress is neglected in the present analysis.

A further effect arises from the secondary flows adjacent to the boundaries. The whirl approaches Ω in the thin fluid layer next to the impeller shroud and, as this is normally faster than the main flow at the same radius, the faster moving fluid tends to move outwards. Similarly the slow-moving fluid next to the fixed boundary tends to move inwards. In cases where the leakage flow is zero or small, these secondary flows can be an important means of transporting angular momentum in the radial direction. The transport is always outwards, whatever the gradient of the main whirl profile. The effect of secondary flows will be small at higher leakage rates except where the net radial flow is zero, in the region :

$$r_s < r < r_D.$$

RADIAL FLOW RIG

Fig.3 shows the arrangement of the test rig used to investigate radial inwards flow. The vertical shaft carries two discs, one 200mm diameter representing the impeller shroud, and a smaller one representing the end of the balance drum. The inlet to the seal is represented by the clearance between the edge of the small disc and an annular plate representing the pump casing. Spacers on the shaft can be changed to vary the effective shaft diameter and the gap between the discs. The test liquid is water and the valves on two pumped loops are used to control the simulated leakage flow and its whirl as it enters the gap at the edge of the large disc. The whirl is induced by the outflow from a whirl chamber with a number of tangential inlets.

The flow is viewed through the sides of the glass-walled containing tank. Velocity measurements are made by forward scatter laser doppler anemometry with the optical axis of the LDA system passing horizontally through the gap between the discs. The beam intersection can be moved on three axes, but direct measurement of the whirl component of velocity by placing the optical axis along a disc diameter is unfortunately obstructed by the shaft. Velocity components have to be computed from measurements at off-diameter positions of the optical axis.

RADIAL FLOW RESULTS

Typical velocity distributions of whirl across the gap width are shown in Fig.4, where the angular velocity is virtually uniform except for thin layers on the walls. These findings provide justification for restricting most further measurements to the mid-plane of the gap and also for a one-dimensional analysis. The Reynolds numbers given on the figures are values of $\Omega R^2/\nu$.

Whirl profiles for a series of tests in which only the flow

rate Q was varied are shown in Fig.5. Increasing the flow rate alters the balance between frictional and inertial effects by increasing the rate at which angular momentum is convected into the gap. The result is a general increase in whirl velocity.

Fig.6 shows the effect on the whirl profile of modifying the stator surface with other controlled variables held constant. The highest line is the standard nominally smooth surface and the dashed line shows the effect of a replacement surface with blind holes 3mm dia × 3mm deep on a 7mm pitch. The other two curves were obtained for stators with twenty-four radial slots 6mm wide extending out to 0.76 × impeller radius. It may be seen that these last results diverge significantly from the smooth surface result only downstream of this radius.

RADIAL FLOW THEORY

A one-dimensional computer model was written to solve the whirl profile, based on the angular momentum equation for an annular element of axial height h and infinitesimal radial extent:

$$r^3 \cdot \partial\omega/\partial t = Q/2\pi h \cdot \partial(r^2\omega)/\partial r + r^2(\tau_2-\tau_1)/\rho h - \partial(r^2\tau/\rho)/\partial r. \qquad (6)$$

Shear stresses τ_1 and τ_2 are applied to the flow by the opposing walls:

$$\tau_1/\rho = f_1 \cdot r^2(\Omega_1-\omega)(\Omega_1\sim\omega)/2 \qquad (7)$$

$$\text{and} \quad \tau_2/\rho = f_2 \cdot r^2(\omega-\Omega_2)(\omega\sim\Omega_2)/2 \qquad (8)$$

where "~" denotes the positive difference between two quantities. The Reynolds stress τ, acting on the interface between adjacent elements can be written as the product of an effective viscosity and the velocity gradient:

$$\tau = -\rho\varepsilon r \cdot \partial\omega/\partial r. \qquad (9)$$

In reality ε will vary across the gap in some way such as:

$$\varepsilon = k(v_{f1} + v_{f2}) \cdot z(h-z)/h \qquad (10)$$

which at least ensures that it is zero on both walls and gives a mean value for use in eq.(9) as:

$$\bar{\varepsilon} = (kh)(v_{f1} + v_{f2})/6. \qquad (11)$$

Each friction velocity can be related to the friction factor on the corresponding wall and the relative velocity. Thus, considering rotational velocities only:

$$v_{f1}^2 = (f_1/2)[(\Omega_1\sim\omega)r]^2 \quad \text{and} \quad v_{f2}^2 = (f_2/2)[(\omega\sim\Omega_2)r]^2 \qquad (12)$$

which allows $\bar{\varepsilon}$ to be written as:

$$\bar{\varepsilon} = kh/6 \cdot \Omega r(f/2)^{0.5} \quad \text{where} \quad f^{0.5}\Omega = f_1^{0.5}(\Omega_1\sim\omega) + f_2^{0.5}(\omega\sim\Omega_2). \qquad (13)$$

The friction factors may be treated as constants or as functions of a local Reynolds number.

Using equation (6) to follow the progress of the transient from an arbitrary initial whirl profile can be made the basis of a numerical solution method. The accuracy of following the transient does not affect the steady-state solution. The equation can be

conveniently made dimensionless by using R and Ω as reference quantities so that ω/Ω becomes ω, r/R becomes r, and Ωt becomes the shaft rotation angle from the start of the transient. If differentiation is denoted by a dash for radius and a dot for angle, equation (6) can be written in dimensionless form as:

$$r^3\dot{\omega} = (Q/2\pi\Omega R^2 h)\cdot(r^2\omega)' - r^2\cdot(\tau_2-\tau_1)/\rho\Omega^2 Rh - (r^2\cdot\tau/\rho\Omega^2 R^2)'. \quad (14)$$

The upper limit on the angular step required to avoid numerical instability in the discretised form of this equation with 20-30 radial steps is typically 5-30 degrees. There is a rapid approach to within a few per cent of the steady state solution in the region where $r>r_D$, but further progress is then limited by slow convergence in the diffusion-controlled region near the shaft where $r<r_D$.

Figs. (7,8) are whirl predictions typical of actual machines and the test rig, which show similar behaviour to the experimental results. A feature observed in some of the test flows is a region of positive ω' near the edge of the balance drum, even though the fluid whirl is below shaft speed. This cannot be accounted for in the one-dimensional model and must be attributed to the two-dimensional character of the flow as it turns into the annular seal.

ANNULUS FLOW

As previously discussed, some rotor dynamicists have used an assumed whirl profile along the seal clearance, and one the main objectives of the present work was to investigate the form of the actual profile. Initial experiments were therefore carried out in a concentric system with and without shaft rotation, and with and without inlet whirl. The assumption of a whirl profile with no angular variation can be strictly true only in the concentric case, but it has been extended to eccentric cases where the short bearing theory could normally be justified. The second aim of the work was to test the validity of this extension by measuring the tangential and axial velocity components at a large number of points in the eccentric annulus.

ANNULUS TEST RIG

Fig. 9 shows the test rig used to study the behaviour of whirling flow in an annulus. The arrangements for controlling the leakage flow rate and the inlet whirl are broadly similar to those used in the radial flow rig, but access to the flow for LDA measurements is more troublesome. A narrow window was fitted along the length of the plain stator and a precision glass tube mounted in roller bearings was used to represent the shaft. It was driven at one end, leaving the other end open for an angled mirror to be inserted. Thus the optical axis is folded, with the transmission radial and the collection axial. A frequency shifter was used to resolve low velocities. The rotor diameter is 92mm and measurements were made over 140mm axial length. The mean radial clearance is 10mm which is clearly very large in comparison with real seals but the Reynolds number and the inlet whirl ratio are however comparable with values

in actual machines.

Two series of tests have been carried out, one series with the rotor and stator concentric, and the other at 50% eccentricity. Measurements were made at six angular positions in the eccentric cases.

RESULTS

Results from some concentric tests are shown in Figs.10 and 11 where measures of tangential velocity are plotted against axial position along the annulus for fixed flow rates. The data for Fig.10 was obtained with the shaft stationary, so the tangential velocity is usefully expressed in terms of the mean axial velocity U for a number of inlet whirl conditions which are quantified by the ratio of the flow passing through the swirl inducer Qs to the total flow Q_T. The axial Reynolds number ($2Uh/\nu$) is 3150. The curves for higher whirl show the expected trend downwards towards zero. The apparent rise along parts of the lower curves is almost certainly due to radial shift of the maximum in the whirl distribution which has been measured in detail in some of the tests.

In Fig.11 the whirl ratio is plotted for a series of tests in which the inlet whirl was varied while the shaft speed was held at 295rev/min and the axial Reynolds number was 2650. The data can be simply tested for exponential behaviour by supposing that it can be described by the equation:

$$(\omega_x - \omega_\infty)/(\omega_0 - \omega_\infty) = \exp(-ax) \qquad (15)$$

where ω_∞ is the limiting angular velocity as x tends to infinity. Taking x as the test section length L, equation (15) can be written as:

$$\omega_L = C\omega_0 + (1-C)\omega_\infty \quad \text{where} \quad C = \exp(-aL). \qquad (16)$$

When data from Fig.11 is plotted as ω_L/Ω against ω_0/Ω, the points lie closely about a straight line from which estimates of C and ω_∞ can be derived:

$$\omega_\infty/\Omega = 0.4 \quad \text{and} \quad C = 0.42.$$

A limiting whirl ratio below 0.5 fits the fact that the stator surface is rougher than the good optical finish on the glass rotor. The value of C implies that, in the present case, departures from the limiting whirl ratio would decrease by a factor of ten for each 300mm of axial length.

Results for the eccentric cases are not yet fully analysed, but early indications are that the distributions of whirl and axial velocity are rather complex.

CONCLUSIONS

It has been demonstrated experimentally that the leakage flow between impeller shroud and pump casing can result in a whirl velocity at the seal inlet much greater than half shaft speed. A one-dimensional theory can model the general behaviour of the flow with empirically determined friction factors.

Different stator surface modifications were tested and radial grooves were found to be an effective whirl-control device. However, one effect of reducing the whirl of the radial inflow will be to increase the pressure at the seal entry. The leakage will therefore tend to increase and the whirl will consequently increase. This self-compensating effect of attempts to reduce the whirl can be minimised by concentrating efforts to modify the flow in the region just before the flow enters the seal.

In the concentric annulus flows so far tested, the influence of the inlet whirl persisted along the length of the test section and could be described quite well by an exponential approach to a limiting value.

REFERENCES

(1) Black HF, Allaire PE & Barrett LE
Inlet flow swirl in short turbulent annular seal dynamics.
9th Int Conf on Fluid Sealing, 141-152, BHRA 1981.

(2) Ehrich F & Childs D
Self-excited vibration in high-performance turbomachinery.
Mechanical Engineering, 66-79, May 1984.

(3) Kirk RG
A method for calculating seal inlet swirl velocity.
Rotating Machinery Dynamics, vol 2, ASME DE-vol 2, 1987.

(4) Kirk RG, Hustak JF & Schoeneck KA
Evaluation of liquid and gas seals for improved design of turbomachinery.
Proc Int Conf on Vibrations in Rotating Machinery, 387-394, IMechE 1988.

(5) Benckert H & Wachter J
Flow-induced spring coefficients of labyrinth seals for application in rotor dynamics.
NASA CP 2133, Proc of Wkshp at Texas A&M Univ, Rotordynamic problems of high performance turbomachinery, May 1980, 189-212.

(6) Hart JA & Brown RD
The use of fluid swirl to control the vibration behaviour of rotating machines.
Proc Int Conf on Vibrations in Rotating Machinery, 69-75, IMechE September 1988.

(7) Childs DW & Ramsey C
Seal-rotordynamic-coefficient test results for a model SSME ADT-HPFTP turbine interstage seal with and without a swirl brake.
NASA CP 3122, Proc of Wkshp at Texas A&M Univ, Rotordynamic instability problems in high performance turbomachinery, May 1990, 179-190.

(8) Tam LT, Przekwas AJ, Muszynska A, Hendricks RC, Braun MJ & Mullen RL
Numerical and analytical study of fluid dynamic forces in seals and bearings.
J Vibration and Acoustics, Stress and Reliability in Design, 315-325, vol 110, July 1988.

(9) Baskharone EA & Hensel SJ
A new model for leakage prediction in shrouded-impeller turbopumps.
Trans ASME, Vol 111, 118-122, June 1989.

(10) Williams M, Chen WC, Baché G & Eastland A
An analysis methodology for internal swirling flowsystems with a rotating wall.
J of Turbomachinery,83-90,vol 113, Jan 1991 Trans ASME

(11) Addlesee AJ & Altiparmak D
Factors influencing whirl at entry to balance drum seals in pumps.
Proc of Conf on Vibrations in Centrifugal Pumps, IMechE 1990, 33-40.

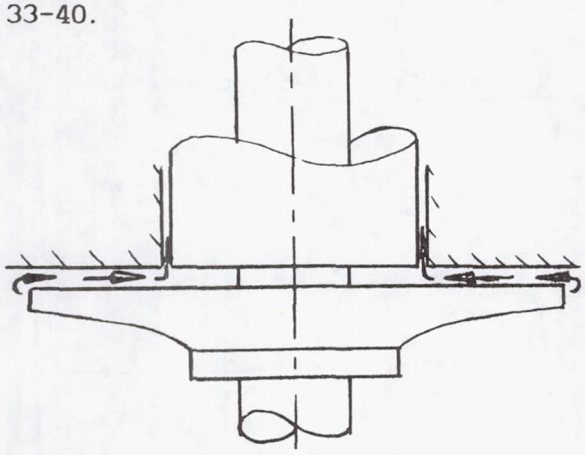

Fig.1 Diagram of leakage path.

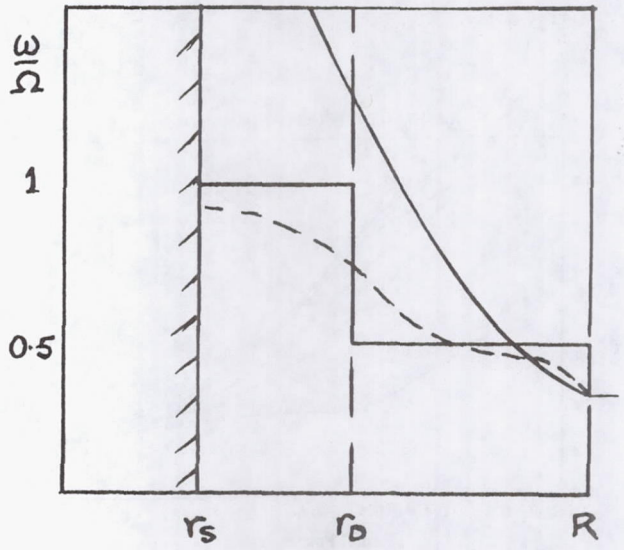

Fig.2 Types of whirl profile.

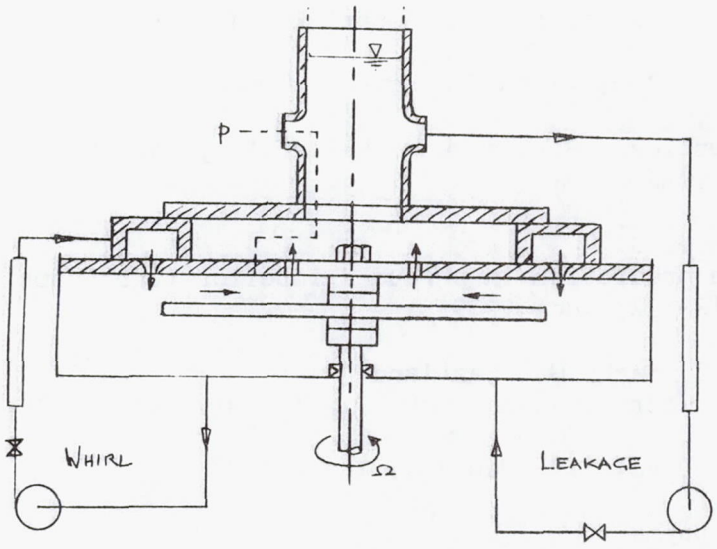

Fig.3 Radial flow rig.

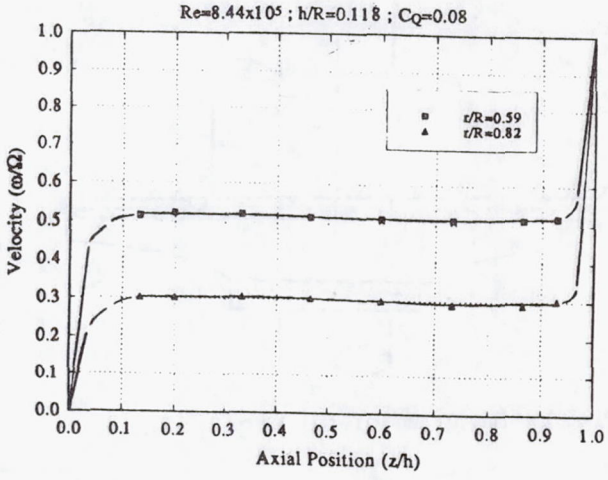

Fig.4 Axial variation of whirl.

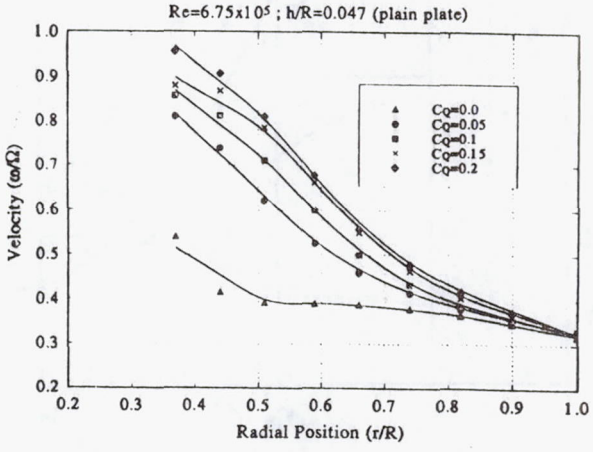

Fig.5 Radial variation of whirl.

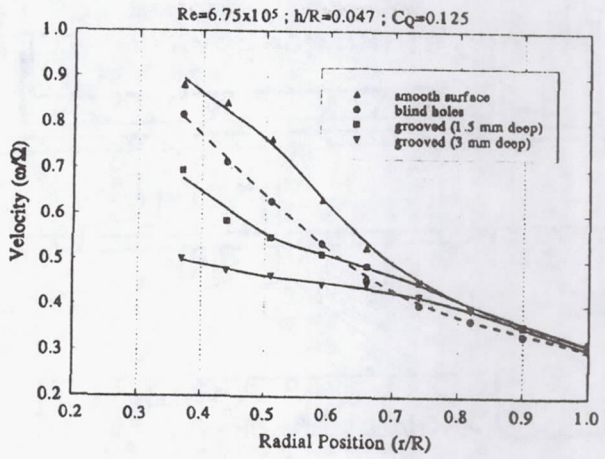

Fig.6 Whirl profiles for different stator surfaces.

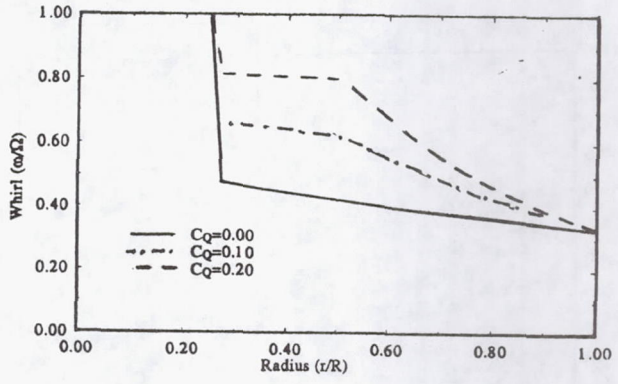

Fig.7 Theoretical whirl profiles for test rig.

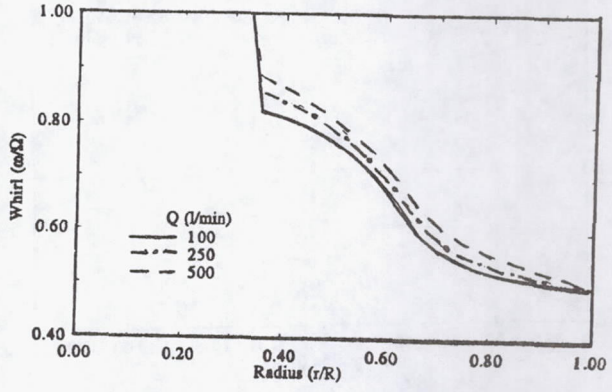

Fig.8 Theoretical whirl profiles for pump.

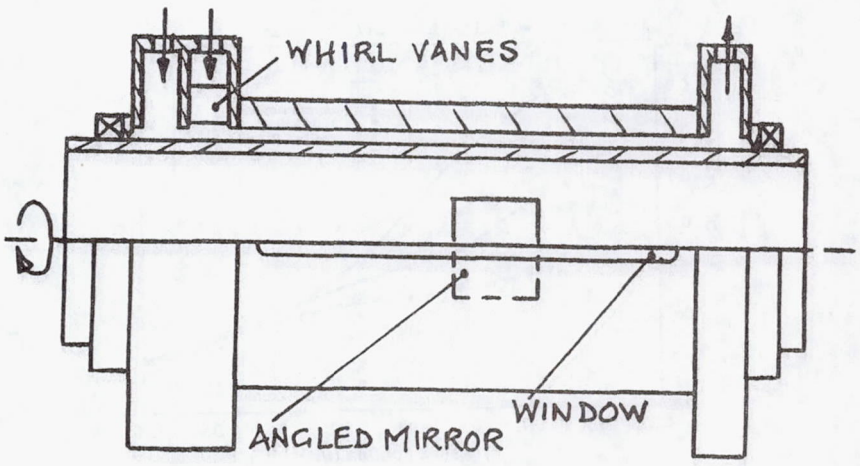

Fig. 9 Annulus test rig.

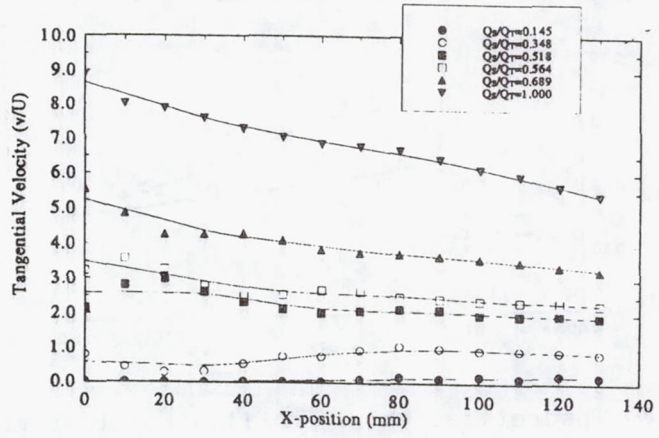

Fig. 10 Tangential velocity variation along a fixed annulus.

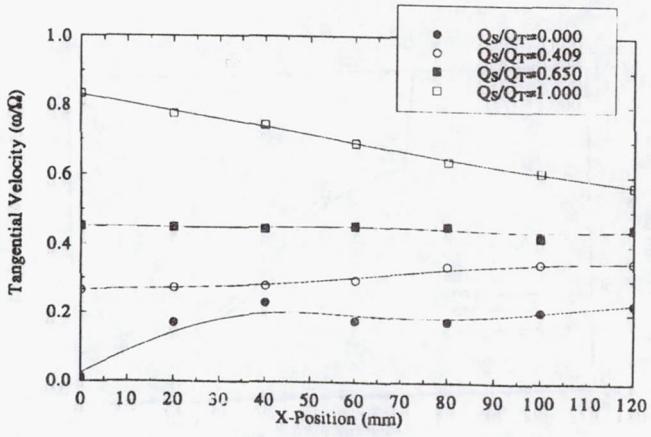

Fig. 11 Whirl variation along annulus with rotating shaft.

ROTORDYNAMIC FORCES IN LABYRINTH SEALS: THEORY AND EXPERIMENT

Knox T. Millsaps* and Manuel Martinez-Sanchez
Massachusetts Institute of Technology
Cambridge, Massachusetts

ABSTRACT

A theoretical and experimental investigation of the aerodynamic forces generated by a single gland labyrinth seal executing a simultaneous spinning/whirling motion has been conducted. A lumped parameter model for a single gland seal with coupling to an upstream cavity with leakage is developed along with an appropriate solution technique. From this theory, it is shown that the presence of the upstream cavity can, in some cases, augment the cross-stiffness and direct damping by a factor of four. The parameters that govern the coupling are presented along with predictions on their influence. A simple uncoupled model is used to identify the mechanisms responsible for cross force generation. This reduced system is nondimensionalized and the physical significance of the reduced parameters is discussed. Closed form algebraic formulas are given for some simple limiting cases. It is also shown that the total cross-force predicted by the uncoupled model can be represented as the sum of an ideal component due to an inviscid flow with entry swirl and a viscous part due to the change in swirl created by friction inside the gland. The frequency dependent ideal part is solely responsible for the rotordynamic direct damping. The facility designed and built to measure these frequency dependent forces is described. Experimental data confirm the validity and usefulness of this ideal/viscous decomposition. A method for calculating the damping coefficients based on the force decomposition using only the static measurements is presented. Experimental results supporting the predicted cross force augmentation due to the effect of upstream coupling are presented.

---

* Present address: Naval Postgraduate School, Monterey, CA 93943.

NOMENCLATURE

Symbol	Definition (units, SI)
C_{xx}	Direct damping. (N s/m)
C_{xy}	Cross damping. (N s/m)
$C^{**}_{xx} = \frac{C_{xx}\delta_1^*}{lR_s^2\sqrt{P_i - P_o}}$	Non-dimensional direct damping. [1]
$C^{**}_{xy} = \frac{C_{xy}\delta_1^*}{lR_s^2\sqrt{P_i - P_o}}$	Non-dimensional cross damping. [1]
$D = \delta_1^* / h$	Nondimensional sealing gap. [1]
F_N	Force acting on the rotor in the direction of instantaneous displacement. (N)
F_T	Force acting on rotor in the direction tangent to the instantaneous displacement.(N)
F_Γ	Frictional(viscous) cross force component.(N)
F_σ	Ideal cross force component. (N)
$H = h / R_s$	Nondimensional depth of labyrinth knife. [1]
h	Depth of seal gland. (m)
h_i	Depth of cavity upstream of seal. (m)
$i = \sqrt{-1}$	
$K = \kappa / \mu_2^*$	Normalized energy carry-over factor.[1]
K_{xx}	Direct stiffness. (N/m)
K_{xy}	Cross stiffness. (N/m)
$K^{**}_{xx} = \frac{K_{xx}\delta_1^*}{lR_s(P_i - P_o)}$	Nondimensional direct stiffness. [1]
$K^{**}_{xy} = \frac{K_{xy}\delta_1^*}{lR_s(P_i - P_o)}$	Nondimensional cross stiffness. [1]
$L = l / R_s$	Nondimensional labyrinth sealing pitch. [1]
l	Sealing pitch. (m)
l_i	Axial gap from the vanes to seal inlet. (m)
$P = P^*(1+\xi)$	Static pressure in the labyrinth gland.(Pa)
P_i	Total pressure upstream of first knife. (Pa)
P_o	Static pressure downstream of seal. (Pa)
q_1	Flow rate through first knife/length(kg/m s)
q_2	Flow rate through second knife. (kg/m s)
R_a	Gas constant for air. 287.15 (J/ kg K)
r	Radial displacement of whirling shaft. (m)
$\hat{r}$	Magnitude of radial displacement. (m)
$S = \frac{\omega R_s}{V^*}$	Nondimensional spin rate. [1]
T	Air temperature. (K)
t	Time. (s)
$V = V^*(1+\eta)$	Swirl velocity inside the seal gland. (m/s)
$W = \frac{\Omega R_s}{V^*}$	Nondimensional whirling frequency. [1]

$\alpha = \delta_2^* / \delta_1^*$	Nondimensional divergence. [1]
$\beta = \mu_2 / \mu_1$	Kinetic energy carry-over coefficient. [1]
$\Gamma = 1 - \frac{V_i}{V^*}$	Nondimensional swirl gradient parameter. [1]
$\Delta = \frac{q^*}{\mu_1^* \delta_1^* \rho^* \sqrt{R_a T}}$	Nondimensional seal flow rate. [1]
δ_1, δ_2	Sealing gaps for the sealing knives. (m)
$\varepsilon = r / \delta_1^*$	Nondimensional whirling eccentricity. [1]
λ_r	Darcy friction factor for the stator. [1]
λ_s	Darcy friction factor for the rotor. [1]
$\kappa = -C_c \frac{\partial \beta}{\partial r}\Big\|_{r=0}$	Kinetic energy carry-over sensitivity. (1/m)
μ_1, μ_2	Flow coefficients for the sealing knives. [1]
$\xi = \hat{\xi} e^{i(\theta - \Omega t)}$	Harmonic pressure perturbation. [1]
$\eta = \hat{\eta} e^{i(\theta - \Omega t)}$	Harmonic velocity perturbation. [1]
ρ	Fluid density. (kg/m^3)
$\sigma = \frac{\rho^* \delta_1^* V^*}{q^*}$	Nondimensional swirl parameter. [1]
$\bar{\sigma} = \sigma(1 - W)$	Swirl parameter as observed in whirling reference frame. [1]
Ω	Whirling frequency of the shaft. (1/s)
ω	Shaft rotational speed. (1/s)
$[]^*$	Steady solution for the case of centered rotor.
$[]_1, []_2$	Quantities at the first or second knife respectively.

1. INTRODUCTION

One of the major sources of rotordynamic instabilities in high power-density turbomachinery is asymmetric pressure distributions in the glands of labyrinth seals which generate cross forces. If the net seal force tangent to the instantaneous whirling displacement is in the direction of this whirl, instability will be promoted.

The possibility of labyrinth seals creating unstable rotor whirl has been known since the 1940's as reported by Den Hartog [1]. Alford [2] and Thomas [3] were the first to propose analytical models for the prediction of labyrinth seal forces. However, neither of these models is particularly useful, because the influence of the inlet swirl, which is known to dominate in the generation of cross forces, was neglected by both authors. A lumped parameter model that couples the axial flow over the knives to one-dimensional continuity and momentum equations inside the seal gland was developed by Kostyuk [4]. The gland-depth variation with rotor eccentricity was neglected and hence no cross stiffness nor direct damping is predicted from this model for a rotor whirling with a parallel precession. Subsequently, Iwatsubo [5] added the necessary term to account for this variation. Many other authors, including Gans [6], Kurahasi and Inoue [7], Fujikawa, Kameoka and Abe [8], Scharrer and Childs [9], and Martinez and Lee [10], have used similar lumped parameter models to predict the cross forces for a great variety

of geometries and flow conditions. All of these models have assumed constant upstream and downstream boundary conditions.

Analyses that consider variations within each seal gland, by using multi-control volumes within each seal gland, have been conducted [8,11]. However, this approach is cumbersome and the different control volumes must be coupled with ad-hoc assumptions or analysis. No advantages have been clearly shown from such models over the single control volume models.

Computational Fluid Dynamics (CFD) methods have also been used, most notably by Nordmann and Weiser [12], to predict results similar to those obtained by the lumped parameter models. These codes may be very useful in modeling some of the detailed flow fields in the glands, which can be used for the sub-models to predict carry-over coefficient variation, friction factors, etc. However, it appears that the simple lumped parameter models contain the dominant fluid physics, which is asymmetric injection of swirl momentum, necessary to predict destabilizing forces, at least for multi-cavity seals.

All of these analyses have assumed uniform upstream and downstream boundary conditions. These assumptions may not be adequate for the prediction of the rotordynamic forces in short seals, where the end conditions may greatly affect the perturbations in both pressure and the swirl component of velocity.

The first experiments to measure the self-exciting forces in isolated labyrinths were those of Benckert and Wachter [13,14,15], who measured the static pressure distributions around the casing and integrated them to find the direct and cross forces due to a statically offset rotor. Many different geometries were tested over a wide range of flow conditions. They determined the general pressure/inlet kinetic energy scaling parameters for statically offset seals. Brown and Leong [16], Thieleke and Stetter [17], Kanki and Morii [18] and Hisa, Sakakida and Asatu [19], have all made similar measurements yielding a good data base on the displacement dependent rotordynamic coefficients. Experimental investigations on the dynamic characteristics of labyrinths have been conducted by Wright [20], Kanemitsu and Ohsawa [21], Scharrer [22], Scharrer and Childs [23] and Millsaps and Martinez [24].

Kostyuk-type lumped parameter models are capable of predicting the cross-stiffness coefficients for long labyrinth seals (more than 6 chambers) to within 25% of the experimentally obtained values [10]. However, the situation with respect to short seals, and with the dynamic coefficients, especially the direct damping, has been far less satisfactory. The measured cross-stiffness coefficients in two and three gland seals, as measured by Benckert [12], are more than 100% larger than those predicted by theory in most cases. Measured dynamic coefficients for both long and short seals are not well predicted by theory. Discrepancies between the measured and predicted direct damping of nearly 500% are shown by Scharrer [21] for some conditions. While the results from many computations have been reported using the various lumped parameter models, little physical understanding on the mechanisms that generate dynamic forces has been obtained from the models. In particular, no analysis has been presented that clearly delineates the importance of the various geometric and flow related parameters and explains, in physical terms, the origin of the damping forces. The general mechanisms that

generate the static and dynamic force components in a spinning/whirling seal has not been adequately explained.

The purpose of this paper is to introduce a new analytical model which includes the effect of upstream coupling, which is believed to be responsible for the much higher than expected cross stiffness and direct damping obtained experimentally, and to describe the nature and mechanisms of the damping forces in labyrinth seals.

In Section 2, an analytical model is presented that allows for non-uniform flow in the volume upstream of the whirling seal. Coupled continuity and momentum equations are given for both the whirling, single gland seal with the added terms due to the non-uniform inlet, and for the non-whirling, finite volume upstream cavity which has a leakage path to a large center cavity. The addition of the extra leakage flow significantly complicates the solution of this system because it introduces an essential non-linearity. An approximate solution method is presented, based on harmonic averaging, to deal with this difficulty. The parameters that control the augmentation in cross forces are identified. Results from this new model are presented that show a large impact due to the non-uniform upstream flow field due to the coupling with the seal perturbations.

In Section 3 the general nature of cross forces in labyrinth seals is discussed. The mechanisms for the generation of rotordynamic damping will be delineated. All the physical arguments will be developed with uniform inlet conditions to avoid unnecessary algebraic complexity. However, all of the arguments to be presented can be readily generalized to account for the upstream non-uniformities. These reduced equations are nondimensionalized, and formulas for the frequency-dependent direct and cross forces are given. The physical significance of the various parameters is discussed, and the scaling behavior provided. The rotordynamically destabilizing cross force will be shown to be the sum of two distinct components. An "ideal" one due to an inviscid flow, and a "viscous" part due to frictional shear. The damping will be shown to originate entirely from the ideal component. From this decomposition, a method for extracting the damping coefficients from purely static measurements are shown.

In Section 4, the experimental apparatus and measurement methods used to determine these dynamic forces are described. The instrumentation and data analysis procedures are given.

In Section 5, comparisons of the theory to the experimental data will be provided. Although no precise comparison of the coupled model to the experimental data is possible due to the lack of control or measurement of the axial gap of the face seal which vents the upstream pressure perturbations to the center hub plenum. The experimental data support the use of the ideal/viscous decomposition for the determination of direct damping coefficients from purely static stiffness data. Also the theory is compared to the experimental results of Benckert for statically offset two and three chamber seals.

2. MODEL FOR UPSTREAM COUPLING

The experimental and analytical research proceeded initially on the assumption that the boundary conditions for the single gland labyrinth seal were uniform. That is, the whirling eccentric seal is fed by an upstream reservoir where the pressure and tangential velocity is

spatially and temporally uniform, and discharges to a downstream volume at a constant static pressure.

Indications that substantial upstream non-uniformity may exist and be of importance were provided from time resolved pressure measurements in the MIT Labyrinth Seal Test Facility (LSTF) with a whirling seal, just upstream of the first knife, and from steady pressure measurements in the MIT Alford Force Test Facility (AFTF) upstream and downstream of a statically off-set seal, that was attached to a shrouded turbine rotor.

The experimental values of cross stiffness and direct damping measured in the LSTF were consistently 2 to 4 times the values predicted by the lumped parameter model. Several attempts were made to reconcile the simple model with the experiments by parameterically varying the sub-model coefficients such as friction factors, discharge coefficients, kinetic energy carry-over coefficients, etc. It was found that, within reasonable ranges of variation, no combination of these coefficients would yield results in agreement with the experimental data. Therefore, the basic assumptions of the model were investigated. This reassessment led to an extended model where variations in the upstream flow, induced by the flow perturbations in the gland itself are included. This extended theory is capable of predicting the high force levels that were measured.

Before embarking upon algebraic manipulations, it is useful to provide a qualitative description of the coupling mechanisms involved. When the shaft is offset and the sealing gap varies around the seal perimeter, a low pressure area will develop upstream of the seal in the vicinity of the widest gap. Because of this, the velocity magnitude will be higher there, and, in particular, the all-important tangential velocity will have a relative maximum near the widest gap. When the fluid carrying this excess tangential momentum enters the seal cavity and mixes with the swirling seal flow, it will preferentially energize it in this area. The result will be a positive pressure gradient, $(\partial P/\partial\theta)$, in this area, and hence a maximum P in the seal about 90° ahead of this maximum gap. This will then produce a forward whirling force. For a concrete formulation of these effects, consider the geometry of Figure 1. This geometry reflects that of the LSTF and most other test section configurations that have been used to measure rotordynamic forces. The swirl vanes, which are located l_i upstream from the first knife, have an effective radial gap of δ_v. There is some reduction of the effective flow area due the vane metal and boundary layer blockage. These vanes deliver air into the first cavity with an effective swirl angle of α_v, which is the metal angle minus some small turning deviation. The cavity is h_i deep and is sealed from a large center volume by an axial face labyrinth seal with a gap of δ_c. Since there is no net flow into this center cavity, the pressure here is uniform and the same as in the swirl cavity, namely P_i^*. The one-dimensional continuity equation for the upstream cavity (swirl chamber) is

$$\frac{\partial}{\partial t}(\rho_i l_i h_i) + \frac{1}{R_s}\frac{\partial}{\partial\theta}(\rho_i l_i h_i V_i) + q_i - q_v + q_{c,out} - q_{c,in} = 0 \qquad (1)$$

where V_i is no longer constant, q_v is the flow rate per unit length issuing from the swirl vanes and the q_c's are the radial flows in and out of the center cavity, respectively. Incompressible relations are sufficient for treating these flows since the transfer velocities are very low. These flows can be written as

$$q_c = \mu_c \delta_c \sqrt{2\rho_i^* \left(P_i - P_i^*\right)} \tag{2}$$

This relation is fundamentally different from those for q_v, q_1 and q_2 in that there is no flow to or from the center volume when the seal is centered in the casing because $P_i = P_i^*$. This introduces an essential nonlinearity into the analysis and hence must be dealt with in a different manner. Likewise the momentum equation in this cavity is

$$\frac{\partial}{\partial t}\left(\rho_i l_i h_i V_i\right) + \frac{1}{R_s}\frac{\partial}{\partial \theta}\left(\rho_i l_i h_i V_i^2\right) + q_1 V_1 - q_v V_v$$

$$+ q_{c,out} V_i - q_{c,in} V_c + \tau_s\left(2l_i + h_i\right) - \tau_r h_i + \frac{l_i h_i}{R_s}\frac{\partial P_i}{\partial \theta} = 0 \tag{3}$$

where V_c is the swirl velocity inside the center volume. In this cavity the cross sectional area, $l_i h_i$, and the vane gap, δ_v^*, are constant. However, the inlet swirl component of velocity, V_v, is not. The angle of the fluid leaving the vanes, α_v, is constant. Therefore, a drop in the pressure at one location in this cavity will induce a greater mass influx and hence a higher swirl velocity at that location. This is the essence of the mechanism that augments the forces.

The usual 1-D continuity and momentum equations for the seal gland as presented by many Authors [5,6,8,9,10] are still valid within the constraints of the model, except that their linearization will yield additional terms from the upstream pressure and velocity non-uniformities. The continuity equation is

$$\frac{\partial[\rho l(h+\delta_1)]}{\partial t} + \frac{1}{R_s}\frac{\partial}{\partial \theta}[\rho l(h+\delta_1)V] + q_2 - q_1 = 0 \tag{4}$$

and the momentum equation is

$$\frac{\partial[\rho l(h+\delta_1)V]}{\partial t} + \frac{1}{R_s}\frac{\partial}{\partial \theta}[\rho l(h+\delta_1)V^2] + q_2 V - q_1 V_i + \tau_s l - \tau_r(l+2h) + \frac{lh}{R_s}\frac{\partial P}{\partial \theta} = 0 \tag{5}$$

and the q's, other than those to and from the center cavity, are given by

$$q_1 = \frac{\mu_1 \delta_1}{\sqrt{R_a T}}(P_i^2 - P^2)^{\frac{1}{2}} \qquad q_2 = \frac{\mu_2 \delta_2}{\sqrt{R_a T}}(P^2 - P_o^2)^{\frac{1}{2}} \qquad q_v = \frac{\mu_v \delta_v}{\sqrt{R_a T}}(P_\infty^2 - P_i^2)^{\frac{1}{2}} \tag{6}$$

The same linear perturbation solution procedure used for the single gland seal with no upstream coupling can be used when there is no flow into the center cavity. However, as previously stated the nature

of the oscillating flow between the two upstream volumes requires some modifications and careful treatment. This is because these oscillating leakage flows vary as $\sqrt{\tilde{P}_i}$, where $\tilde{P}_i$ is the upstream pressure perturbation, rather than linearly with $\tilde{P}_i$ (first order) or P_i (zeroth order) like the others. Thus, their effect can be disproportionally great at small offset amplitudes.

First the zeroth order solutions are obtained for the centered rotor. The velocity, pressure and density in the upstream swirl cavity will be denoted by V_i^*, P_i^* and ρ_i^* respectively and similarly in the seal gland, V^*, $P^*$and ρ^*. The pressure and velocity in the swirl cavity are expressed as

$$P_i = P_i^*\left(1+\hat{\xi}_i e^{i(\theta-\Omega t)}\right) \qquad V_i = V_i^*\left(1+\hat{\eta}_i e^{i(\theta-\Omega t)}\right) \tag{7}$$

and in the seal gland by

$$P = P^*\left(1+\hat{\xi}\, e^{i(\theta-\Omega t)}\right) \qquad V = V^*\left(1+\hat{\eta}\, e^{i(\theta-\Omega t)}\right) \tag{8}$$

Where it is understood that the real part of all expressions are to be used. The perturbation expressions for $\hat{\xi}_i$, $\hat{\eta}_i$, $\hat{\xi}$ and $\hat{\eta}$ are substituted into the continuity and momentum equations for both the upstream swirl cavity and the seal gland. The nondimensional perturbation leakage flow into the center cavity is

$$\frac{q_c}{q^*} = \frac{\mu_c \delta_c}{\mu_1 \delta_1^*}\sqrt{\frac{2P_i^*}{P_i^* - P^*}}\cdot\left[\mathrm{Re}\left\{\hat{\xi}_i e^{i(\theta-\Omega t)}\right\}\right]^{\frac{1}{2}} \tag{9}$$

The first harmonic component of this function will be extracted by averaging over one period. The first harmonic of the perturbation reduces, after some manipulation, to

$$\left[\mathrm{Re}\left\{\hat{\xi}_i e^{i\Psi}\right\}\right]^{\frac{1}{2}} = \frac{4\sqrt{|\hat{\xi}|}}{\pi}\int_0^{\frac{\pi}{2}}\cos^{\frac{3}{2}}\Psi d\Psi = \frac{4\sqrt{|\hat{\xi}|}}{\pi}\sqrt{2}\cdot B\left(\frac{5}{4},\frac{5}{4}\right) \tag{10}$$

Where B is the beta function. From this the first harmonic of $q_{c,out} - q_{c,in}$ is found to be

$$\frac{\tilde{q}_c}{q^*} = 1.57377\frac{\mu_c^*\delta_c}{\mu_1^*\delta_1^*}\sqrt{\frac{P_i^*}{P_i^* - P^*}}\cdot|\hat{\xi}_i|^{-1/2}\cdot\hat{\xi}_i e^{i(\theta-\Omega t)} \tag{11}$$

Similarly the first harmonic of $q_{c,out}V_1 - q_{c,in}V_c$ is

$$1.57377\frac{\mu_c^*\delta_c}{\mu_1^*\delta_1^*}\sqrt{\frac{2P_i^*}{P_i^* - P^*}}\cdot|\hat{\xi}_i|^{-1/2}\frac{1}{2}\left(V_c^* + V_i^*\right)\hat{\xi}_i e^{i(\theta-\Omega t)} \tag{12}$$

The first harmonic of the perturbation continuity equation for the swirl cavity, after dividing by q^* is

$$\left\{\frac{1.57377\mu_c^*\delta_c}{\mu_1^*\delta_1^*\sqrt{|\hat{\xi}_i|}}\left[\frac{P_i^{*2}}{P_i^{*2}-P^{*2}}\right]^{\frac{1}{2}}+\left[\frac{P_i^{*2}}{P_\infty^{*2}-P_i^{*2}}+\frac{P_i^{*2}}{P_i^{*2}-P^{*2}}\right]+\right\}$$

$$\left\{\frac{\rho_i^* l_i h_i}{\gamma q^*}\left(\frac{V_i^*}{R_s}-\Omega\right)i\right\}\hat{\xi}_i+\left\{\frac{\rho_i^* V_i^* l_i h_i}{R_s q^*}i\right\}\hat{\eta}_i-\left\{\frac{P^{*2}}{P_i^{*2}-P^{*2}}\right\}\hat{\xi}_i=\left\{\frac{1}{\delta_1^*}\right\}\hat{r} \qquad (13)$$

and the swirl cavity momentum equation after dividing by $q^*V_i^*$ is

$$\left\{\frac{0.78688\mu_c^*\delta_c\left(1+\frac{V_c^*}{V_i^*}\right)}{\mu_1^*\delta_1^*\sqrt{|\hat{\xi}_i|}}\left[\frac{P_i^{*2}}{P_i^{*2}-P^{*2}}\right]^{\frac{1}{2}}+\left[\frac{P_i^{*2}}{P_i^{*2}-P^{*2}}\right]+\right\}$$

$$\left(\frac{V_v}{V_i^*}\right)\left(\frac{P_i^{*2}+P_\infty P_i^*}{P_\infty^2-P_i^{*2}}\right)+\frac{\lambda_{si}\rho_i^*(l_i+h_i)V_i^*}{4\gamma q^*}+\left\{\left[\frac{\rho_i^* l_i h_i}{\gamma q^*}\left(\frac{V_i^*}{R_s}-\Omega\right)+\frac{P_i^* l_i h_i}{V_i^* q^* R_s}\right]i\cdot\right\}\hat{\xi}_i+$$

$$\left\{1+\frac{\lambda_{si}\rho_i^*(l_i+h_i)V_i^*}{2\gamma}+\left[\rho_i^* l_i h_i\left(\frac{2V_i^*}{R_s}-\Omega\right)\right]i\right\}\hat{\eta}_i+\left\{\frac{P^{*2}}{P_i^{*2}-P^{*2}}\right\}\hat{\xi}=\left\{\frac{1}{\delta_i^*}\right\}\hat{r} \qquad (14)$$

The nondimensional continuity equation for the seal gland, which includes the effect of the upstream cavity coupling is

$$\left\{\frac{-P_i^{*2}}{P_i^{*2}-P^{*2}}\right\}\hat{\xi}_i+\left\{\left[\frac{P^{*2}}{P^{*2}-P_o^2}+\frac{P^{*2}}{P_i^{*2}-P^{*2}}\right]+\frac{\rho^* lh}{\gamma q^*}\left(\frac{V^*}{R_s}-\Omega\right)i\right\}\hat{\xi}$$

$$\left\{\frac{\rho^* V^* lh}{R_s q^*}i\right\}\hat{\eta}=\left\{\frac{\kappa}{\mu_2^*}+\left(\frac{1}{\delta_2^*}-\frac{1}{\delta_1^*}\right)+\frac{\rho^* l}{q^*}\left(\frac{V^*}{R_s}-\Omega\right)i\right\}\hat{r} \qquad (15)$$

and the coupled momentum equation for the seal gland is

$$\left\{\left(\frac{V_i^*}{V^*}\right)\frac{-P_i^{*2}}{P_i^{*2}-P^{*2}}\right\}\hat{\xi}_i+\left\{\frac{-V_i^*}{V^*}\right\}\hat{\eta}_i+\left\{\frac{P^{*2}}{P^{*2}-P_o^2}+\left(\frac{V_i^*}{V^*}\right)\frac{P^{*2}}{P_i^{*2}-P^{*2}}+\left(\frac{\rho^*}{8\gamma q^* V^*}\right)(\lambda_s l V^{*2}\right\}$$

$$\left\{-\lambda_r(1+2h)(\omega R_s-V^*)^2)+\left[\frac{\rho^* lh}{\gamma q^*}\left(\frac{V^*}{R_s}-\Omega\right)+\frac{\rho^* lh R_a T}{R_s}\right]i\right\}\hat{\xi}$$

$$\left\{1+\frac{\rho^*}{4q^*}\left(\lambda_s l-\lambda_r(1+2h)(V^*-\omega R_s)^2\right)+\rho^* lh\left(\frac{2V^*}{R_s}-\Omega\right)i\right\}\hat{\eta}$$

$$=\left\{\frac{\kappa}{\mu_2^*}+\frac{1}{\delta_2^*}-\frac{V_i^*}{V^*\delta_1^*}+\frac{\rho^* l}{q^*}\left(\frac{V^*}{R_s}-\Omega\right)i\right\}\hat{r} \qquad (16)$$

This can be written compactly in matrix form as

$$\begin{pmatrix} Z_{1,1} & Z_{1,2} & Z_{1,3} & Z_{1,4} \\ Z_{2,1} & Z_{2,2} & Z_{2,3} & Z_{2,4} \\ Z_{3,1} & Z_{3,2} & Z_{3,3} & Z_{3,4} \\ Z_{4,1} & Z_{4,2} & Z_{4,3} & Z_{4,4} \end{pmatrix} \begin{Bmatrix} \hat{\xi}_i \\ \hat{\eta}_i \\ \hat{\xi} \\ \hat{\eta} \end{Bmatrix} = \begin{Bmatrix} R_1 \\ R_2 \\ R_3 \\ R_4 \end{Bmatrix} \hat{r} \tag{17}$$

This is **not** a linear system. The elements $Z_{1,1}$ and $Z_{2,1}$ contain $|\hat{\xi}_i|^{-1/2}$. Of course if $\hat{\xi}_i = \hat{\eta}_i = 0$ the system decouples and the original 2x2 system for the isolated seal with no upstream coupling is recovered. To solve this system a simple iteration scheme was employed. Equation (17) is first solved with $\delta_c = 0$ then from this solution, $\hat{\xi}_i^1$, is used on the left hand side to calculate an updated solution. This iteration procedure continues until a predetermined convergence criterion is satisfied

$$|\hat{\xi}_i^{n+1} - \hat{\xi}_i^n| < \varepsilon \tag{18}$$

Now this model shall be used for predicting the influence of this coupling mechanism. In addition to the parameters that control the generation of rotordynamic forces for an isolated seal, the parameters that characterize the influence of the upstream coupling are

1. The ratio of the swirl cavity area to the seal gland area, $(l_i h_i)/(lh)$.

2. The relative size of the axial sealing gap compared to the radial gap, δ_c / δ_1^*.

3. The swirl velocity inside the center cavity, V_c. This is strongly influenced by rotation of the seal disk.

4. The relative whirl eccentricity, $\hat{r}/\delta_1^*$. This is a purely non-linear effect. For the linear system all of the forces are directly proportional to the whirl eccentricity.

The effects of the cross force augmentation of each parameter will now be considered separately. According to the model, if there is no leakage into the center cavity, the effect of the upstream coupling always acts to increase the magnitude of both the cross stiffness and direct damping, and in the same proportions. Figure 2 shows the ratio of the direct damping from the coupled model, with $\delta_c = 0$, to that of the uncoupled one for various swirl chamber to seal area ratios. As the swirl cavity area approaches zero the predicted force augmentation does not vanish but, approaches a value of 1.62. This residual effect in the absence of the first cavity is due to the condition imposed at the swirl vanes. In the simple model V_i is constant. If instead the vanes are close coupled a reduction in the gland pressure will still bring in more flow and hence will induce a higher swirl component locally. The maximum increase in the cross stiffness and direct damping over the uncoupled model is about 4.42 and occurs at an area ratio, $(l_i h_i)/(lh)$ of 1.35. Even at

an area ratio of 10 the forces are increased by a factor of two. The force predicted by the coupled model asymptotically approaches the uncoupled one as $(l_i h_i)/(lh) \to \infty$. The coupled and uncoupled models match to within 1% for an area ratio of about 80. Well before this value the assumptions of the model probably break down. In particular, significant variations in the perturbation quantities are likely to occur in the axial direction within the swirl cavity.

The presence of the axial clearance between the swirl cavity and the large center volume permits for a ``venting'' that reduces the magnitude of $\hat{\xi}_i$. This effect tends to mitigate the large augmentation of the forces that the upstream cavity may induce. Figure 3 shows the direct and cross force vs. the relative leakage area δ_c/δ_1^*. It is assumed that $V_c = V_i^*$ for simplicity. As δ_c goes from 0 to ∞ both force components go from the fully coupled values to those predicted by the uncoupled model. However, this does not occur when $V_c \neq V_i^*$. The forces are very sensitive to small changes in the axial gap when it is less than δ_1^*. However, when $\delta_c/\delta_1^* > 1$, there is a greatly reduced sensitivity to small changes in axial gap.

The model predicts that the swirl velocity inside the center volume can have a minor impact, on the order of 10-20%, on the seal pressure perturbations. For cases where there is no seal rotation it is probably safe to assume that $V_c = 0$. This is because the tangential momentum feed into the seal is of perturbation order and the shear stresses acting to retard the flow are of order unity. For cases with seal rotation, it would be very difficult to estimate the swirl velocity inside the center cavity. Figure 4 shows the effect that changes in the center cavity swirl velocity have on the forces.

In the absence of the leakage flow non-linearity, the theory predicts that the forces should scale with whirl eccentricity and hence the rotordynamic coefficients, and should be independent of the whirl amplitude. The nonlinearity due to axial leakage is shown in Figure 5, which shows K_{xx} and K_{xy} the relative eccentricity $\hat{r}/\delta_1^*$. The behavior of C_{xx} is the same as for K_{xy}. The direct force is much more sensitive to the whirl amplitude than is the cross force. At large whirl amplitudes, the predicted forces approach those obtained for $\delta_c = 0$ (i.e. the fully coupled case). However, as $r \to 0$ the center leakage flow is able to ``kill'' the swirl cavity pressure perturbation completely. This effectively decouples the whirling seal from the upstream cavity.

3. IDEAL - VISCOUS FORCE DECOMPOSITION

It will now be shown that within the constraints of the lumped parameter model, the total cross force can be separated into two additive components. One of these is the ideal part, due to an inviscid inlet flow with entry swirl, and the other is the viscous part, due to the change in swirl brought about by frictional shear stresses in the gland.

The following development shall be done without consideration of upstream coupling. However, all of the arguments can be readily generalized to account for such coupling.

In order to isolate these two contributions it is useful to nondimensionalize the continuity and momentum equations for the seal

gland. Equations (15) and (16) can be written in terms of the following non-dimensional parameters as

$$\left\{\frac{1}{\Delta^2}+\left(\frac{\alpha\mu_2^*}{\Delta\mu_1^*}\right)^2+\left[\frac{\sigma L}{\gamma D}(1-W)\right]i\right\}\hat{\xi}+\left\{\frac{\sigma L}{D}i\right\}\hat{\eta}=\left\{\left(\frac{1}{\alpha}-1\right)+K+\sigma L(1-W)i\right\}\hat{\varepsilon} \qquad (19)$$

and

$$\left\{\frac{\sigma L}{8\gamma DH}\left(\lambda_s-\lambda_r\left(1+\frac{2H}{L}\right)(S-1)^2\right)-\frac{\Gamma}{\Delta^2}+\left[\frac{\sigma LW}{\gamma D}+\frac{L}{\Delta^2\sigma\mu_1^{*2}D}\right]i\right\}\hat{\xi}$$

$$\left\{1+\frac{\sigma L}{4DH}\left(\lambda_s-\lambda_r\left(1+\frac{2H}{L}\right)(1-S)\right)+\frac{\sigma L}{D}(1-W)i\right\}\hat{\eta}=\Gamma\hat{\varepsilon} \qquad (20)$$

All of these non-dimensional parameters may be categorized as geometric, kinematic or flow related. The geometric ones are

$$\hat{\varepsilon}=\frac{\hat{r}}{\delta_1^*} \qquad \alpha=\frac{\delta_2^*}{\delta_1^*} \qquad D=\frac{\delta_1^*}{h} \qquad H=\frac{h}{R_s} \qquad K=\frac{\delta_1^*\kappa}{\mu_2^*} \qquad L=\frac{l}{R_s} \qquad (21)$$

Note that K has been considered along with the geometric parameters because it is analogous to a convergent/divergent gap (Alford effect) in the effect that it has on the direct and cross forces. The kinematic parameters that specify the motion of the seal are

$$S=\frac{\omega R_s}{V^*} \qquad\qquad W=\frac{\Omega R_s}{V^*} \qquad (22)$$

and the dynamic parameters that indicate the axial flow rate or pressure gradient, the inlet swirl and the change in swirl respectively are

$$\Delta=\frac{q^*}{\mu_1^*\delta_1^*\rho^*\sqrt{R_aT}} \qquad \sigma=\frac{\rho^*\delta_1^*V^*}{q^*} \qquad \Gamma=1-\frac{V_i}{V^*} \qquad (23)$$

There are two combinations of these parameters, $\sigma\Gamma$ and $\sigma(1-W)$, which will be shown to be very important.

Cramer's rule can be used to write an explicit expression for the nondimensional pressure perturbation which, upon integration, yields the forces acting on the rotor. The forces are proportional to $P^*\xi$. In general the shear stresses may also contribute to the forces. However, from the equation solutions it has been shown that the shear forces due to velocity perturbations are small when compared to the forces arising from pressure perturbations [24]. For moderate whirl relative inlet swirl angles, which occurs providing the following condition is satisfied

$$\frac{1+\alpha^2\beta^2}{\Delta^2}>>\frac{\sigma L}{\gamma D}(1-W) \qquad (24)$$

the full expression may be simplified to yield the following real and imaginary parts for the pressure perturbation normalized by both the flow and eccentricity

$$\frac{\hat{\xi}_{\Re}}{\Delta^2\varepsilon} = \frac{K - \left(1 - \frac{1}{\alpha}\right) - \frac{\sigma^2 L^2}{D}(1-W)^2}{1 + \alpha^2\beta^2 + \frac{L^2}{D^2\mu_1^{*2}}} \tag{25}$$

$$\frac{\hat{\xi}_{\Im}}{\Delta^2\varepsilon} = \frac{\frac{\sigma L}{D}\left[\Gamma + (1-W)(-D-K+1-\frac{1}{\alpha})\right]i}{1 + \alpha^2\beta^2 + \frac{L^2}{D^2\mu_1^{*2}}} \tag{26}$$

The first of these is real and therefore is in the direction of the minimum gap and hence is proportional to the direct force. The imaginary part is proportional to the destabilizing cross force. Both forces are proportional to $P^*\Delta^2$. For low inlet-to-exit pressure ratios, this reduces approximately to a simple pressure difference scaling, $P_i - P_o$, as one would expect for an incompressible flow. For this to hold, all of the other nondimensional parameters must be kept constant. In particular, the inlet swirl flow angle as observed from the whirling rotor must be fixed as the pressure difference is changed. As an example, if the axial pressure difference is increased the inlet swirl velocity and whirl speed must also be increased to maintain constant, σ and W, if this scaling is to be used. This is a generalization of the relationship used by Benckert [12] for statically offset seals.

The direct force is mainly due to the kinetic energy carry-over variations and differences in the nominal sealing clearances as seen in Equation (25). These effects generate a direct stiffness. The smaller terms, that are proportional to $\sigma^2(1-W)^2$, generate direct inertia coefficients. It is possible that this direct force may alter the natural frequency of the rotor slightly. Therefore, no further discussion of the direct force will be given due to the small impact it has on rotordynamic stability.

The cross force can be seen from Equation (26) to be the summation of two terms, one proportional to $\sigma(1-W)$ and the other proportional to $\sigma\Gamma$. The nature of these two contributions and their crucial differences are very important and will lead directly to the cross force decomposition to be given. The kinetic energy carry-over term, K, and the "Alford" [2] term due to seal convergence/divergence, $(1-1/\alpha)$, do not generate cross force in the absence of swirl. But do alter this force in the presence of swirl. A convergent seal and/or kinetic energy carry-over will tend to increase the cross force magnitude. This is destabilizing when $W<1$ or equivalently when the whirl frequency is less than V^*/R_s. However, this will enhance stability, in the forward direction, when Ω is greater than V^*/R_s.

The total cross force, F_Γ, will now be split into "ideal" and "viscous" contributions. The ideal or inviscid part, F_σ, is the cross force that would be generated in a purely inviscid fluid with inlet swirl. It is

proportional to $\sigma(1-W)$. The viscous contribution, F_Γ, which is proportional to $\sigma\Gamma$, is due to the frictional forces changing the swirl velocity inside the seal gland. The two forces tend to be of the same magnitude but, the nature of these two contributions is quite different. The ideal component is *dependent* on the rotor whirl frequency and hence will contribute to the direct damping. The viscous component is *independent* of the whirl speed and hence can not contribute to the direct damping. The frequency dependent behavior of a seal in an inviscid fluid can be readily explained by considering a simple change of reference frame. Let the relative inlet swirl, denoted by $\overline{V}_i = V_i - \Omega R_s$, be the inlet swirl velocity as measured by an observer rotating in the whirling frame. The non-dimensional swirl parameter in the whirling frame will be similarly denoted by $\overline{\sigma}$ and is

$$\overline{\sigma} = \sigma(1-W) = \frac{\rho^* \overline{V}^* \delta_1^*}{q^*} \tag{27}$$

The cross force generated by an inviscid flow at an inlet swirl of V_i at a frequency of Ω is identically the same as the cross force that would be generated for a static offset with the associated relative inlet swirl of $\overline{V}_i$. This equivalence can be seen by noting that the governing continuity and momentum equations are invariant under Galilean transformation. As a particular case of this argument, consider a rotor whirling so that the minimum gap is traveling at the same speed as the inlet swirl. Then there is no swirl relative to the rotating frame observer. Therefore the inviscid cross force must be zero when $\Omega = V_i / R_s$, or equivalently when W=1. This behavior is very similar to the quasi-static oscillation of an airfoil. The damping force there is related to the induced angle of attack due to the vertical motion. For the case of the whirling rotor, it is the "induced" inlet swirl angle change, due to the whirling motion, that creates the rotordynamic damping. Figure 6 shows the analogy between these two phenomena.

This simple behavior for both the airfoil and the rotor is limited to the quasi static case. For the rotor, this condition of low reduced frequency, is satisfied when the fluid residence time in the seal is short when compared to the period of oscillation of the rotor. This can be expressed as

$$\frac{\Omega l}{V_x} << 1 \tag{28}$$

where V_x is the axial velocity through the seal. An interesting and useful consequence of this relationship between the static and dynamic forces, is that in the absence of viscosity the direct damping, C_{xx}, can be calculated from purely static measurements of the cross stiffness , K_{xy}, versus the inlet swirl by

$$C_{xx} = R_s \frac{dK_{xy}(V_i)}{d(V_i)} \tag{29}$$

If the stiffness is a linear function of the inlet swirl, then a single measurement of the cross stiffness is needed to find the damping behavior.

$$C_{xx} = R_s \frac{K_{xy}(V_i)}{V_i} \tag{30}$$

A similar argument can be used to extract the direct damping coefficient from the static coefficient measurements in the presence of viscosity. However, a discussion of this will be reserved until later.

The viscous contribution, F_Γ, which is proportional to $\sigma\Gamma$ and hence the swirl velocity difference $V_i - V^*$, contributes to the cross stiffness only. The physical reason that this force is independent of the whirling frequency is that it depends on a velocity difference which is necessarily independent of any change of reference frame due to the whirl. The mechanism that produces this force is shown Figure 7. The flow enters the offset seal with a higher swirl velocity than exists inside the seal. Less excess momentum enters through the narrow gap on the right than the wider gap to the left. As the flow mixes out, it energizes the fluid inside the gland increasing the static pressure like an ejector pump. The place with the highest pressure will be at the bottom yielding a positive cross force as shown. A simple analysis of this is done by using the following simplified momentum equation

$$\tilde{q}(V - V_i) + \frac{lh}{R_s}\frac{\partial P}{\partial \theta} = 0 \tag{31}$$

this expression can be integrated to yield the viscous cross force

$$F_\Gamma = \frac{i\pi q^* R_s^2 (V_i - V^*)\hat{r}}{h\delta_1^*} \tag{32}$$

From Equation (26) the relative magnitudes of the ideal and viscous contributions are found. Two limiting cases are possible

$$|\Gamma| = |1 - \frac{V_i}{V^*}| << |D| = |\frac{\delta_1^*}{h}| \qquad \text{friction is unimportant} \tag{33}$$

$$|\Gamma| = |1 - \frac{V_i}{V^*}| >> |D| = |\frac{\delta_1^*}{h}| \qquad \text{friction is dominant} \tag{34}$$

However, in real hardware it is more common to have $|\Gamma| \cong |D| \cong 0.05$ and hence, both contributions must be accurately modeled.

Figure 8 shows the cross force vs. the non-dimensional whirling frequency, W for an ideal and real flow. Here increasing viscosity means that the swirl change is becoming more negative through viscous action either through higher friction factors or lower rotational speeds (in the direction of inlet swirl). As stated, the cross force vanishes for an inviscid flow when W=1. That is, when the gap travels at the swirl velocity. When the presence of viscosity is considered the cross force increases the same at all whirl frequencies.

If the swirl speed decreases through the seal, as is typical, then the frequency at which the force becomes negative shifts to a higher W, as shown.

4. EXPERIMENTAL APPARATUS

The Labyrinth Seal Test Facility (LSTF) was designed and built to measure the dynamic forces in a spinning/whirling labyrinth seal. Figure 9 shows a cross section of the hardware. Air from a compressor enters the first plenum and is turned radially outward through eight 1 and 1/2 inch holes having honeycomb plugs. Next the air turns axially and accelerates through a set of replaceable swirl vanes into the swirl plenum. The air flows through the test seals and discharges to the atmosphere. The spinning/whirling motion of the seal is produced by the nested bearing arrangement. Different whirl amplitudes are obtained by adjusting the inner spindle bearing seat eccentricity. The spin motion (+6700rpm to -6700 rpm) is driven by an in-line flexible coupling driven by an electric motor. The speed of the whirling motion, which can be controlled independently, (+3400 rpm to -3400 rpm) is driven by a V-belt attached to another motor. Four equally spaced, flush mounted, high response, Kulite XCS190 differential pressure transducers were placed on the seal land to measure the time resolved gland pressure oscillations created by the seal whirling motion. The back pressure ports were referenced to the gland average pressure to obtain higher sensitivity. Proximeters were used to precisely measure the whirling motion. Measurements of the swirl angle leaving the second knife were made with a hot wire anemometer. The data acquisition system was triggered and clocked with a chopper wheel attached to the whirl producing spindle. Thirty-two phase locked points were taken for each whirl revolution. Records of 64 revolutions were taken. The pressures were composite phase-locked ensemble averaged to find the forces acting on the rotor for each operating condition. A total of five different seal geometries, shown in Table 1, were tested under various operating conditions. The inlet pressure, swirl vane angle, spin velocity, whirl eccentricity and frequency were varied parametrically. Figure 10 shows a typical output trace from one of the Kulites versus data point number. Note the periodicity of 32 data points per cycle as expected. Spectral analysis of these signals showed that virtually all of the energy of the signal is concentrated at the whirl frequency for cases with no seal rotation [24]. For cases including rotation, a small harmonic component, with amplitude of about 5% of the primary component due to whirl, at the spin frequency was present. This was due to very small deviations from circularity of the seal.

5. COMPARISON OF EXPERIMENTS TO THEORY

A strict comparison of the preceding theory with coupling to the LSFT test results is not possible because of the lack of control over the axial leakage gap, δ_c, the importance of which was shown in Section 2. What can be shown, however, is that for the range of likely values of δ_c, the upstream coupling effects increase the cross forces the required amount to explain the very large deviations between experimental data and the simple, uncoupled theory.

The general character of the comparison can be seen from Figure 11, which shows the nondimensional cross stiffness versus the nondimensional inlet swirl. The trends and comparisons for C_{xx} are the same as for K_{xy}, due to the relationships shown in Section 3. The theoretical lines were calculated using the cavity parameters for Build #3. The volume ratio (upstream to seal cavity) was in that case 3.01, whereas it was 4.64 for Build #2. The amplification factors calculated from the coupled theory (for δ_c= 10 mil) are 3.7 for Build #3 and 2.8 for Build #2.

Looking first at the Build #3 data only, we notice a general grouping about the theoretical line for δ_c between 5 and 10 mil. The design value of this gap was 10 mil. We also see that the points appear in groups, each of which is aligned with a somewhat different δ_c line. These groups in fact correspond to the different swirl vane assemblies, and δ_c can be expected to have remained constant within each of them, but perhaps not with exactly the same value from assembly to assembly.

The data for the two outer groups of points for Build #2 are roughly on a line with a slope lower by 1/1.3 than those for Build #3, in accordance with the noted difference between the volume ratios of both cases. The group for the smaller dimensionless inlet swirl is anomalously high, however. In general, for all builds, the data are indeed bracketed between the limits of the uncoupled ($\delta_c \rightarrow \infty$) theory and the fully coupled ($\delta_c = 0$) models.

As a related test of the theory, equations were derived for multi-cavity seals with upstream coupling [9]. This coupled theory for a 2-gland seal, plus the upstream cavity was compared to some 2-gland static seal data of Benckert and Wachter [5], whose facility had the same general upstream configuration as the LSTF. These researchers also failed to keep a careful control of their face seal, for which no value is reported. As noted before, no theoretical calculation had been able to match the higher than expected cross-forces in these short seals. Using the coupled model, the cross forces obtained in all three 2 gland seals that Benckert tested can be matched by the theory with appropriate choices of the axial sealing gap, ($\delta_c = 0$) (a slightly different one for each build). Not only can the total force be predicted, but the relative contributions from each gland can be matched for the one case for which this was reported. The model predicts that the effects of the upstream coupling die exponentially. After a few glands the upstream influence cannot be seen. The data of Benckert support this conclusion.

Table 2 gives the data of Benckert along with several cases from the model. The cross force as predicted with uniform upstream conditions is given. Finally, the value of the axial gap that matches Benckert's data is given for each case. These values are reasonable and show that the strong upstream coupling is the most likely cause for the high cross forces generated in the first gland of a seal.

Figure 12 shows a typical plot of the cross force vs. whirl frequency for five different pressure ratios from Build #4. There is no rotation and the nominal inlet swirl angle is 8.6 degrees. The general frequency dependent behavior of the experimental data is well predicted by the analytical model. In particular, the cross force is a linear function of the whirl speed and the frequency at which the force changes sign matches the theoretically predicted value within

experimental uncertainty. Of course the absolute force levels are much higher as predicted by the coupled theory. Figure 13 shows the cross force vs. whirl frequency for five different spin rates for the same build. It can clearly be seen that the data at different spin rates fall on parallel lines. Similar results were found for all builds at all flow conditions. The narrow implication of this is that changes in rotational speed do not affect the damping. More generally, these data strongly support the general validity of the cross force decomposition into ideal and viscous contributions as presented above.

The method presented above for predicting the dynamic coefficients from inviscid static values can be readily extended to cases with "viscosity" if the frictional component is isolated properly. Probably the best method for removing this frictional "contamination" is to handle it directly in the experiment. If the inlet and exit swirl velocities are measured then for every value of the inlet swirl the seal spin speed should be adjusted to maintain a constant swirl difference, $V_i - V^*$. Hence, the additive frictional component is fixed. For $V_i = V^*$, the viscous component is totally eliminated. For typical designs the spin speed needs to be maintained at about 125% of the inlet swirl velocity to keep $\Gamma = 0$. If this procedure is not followed the measurements of a statically offset seal can still be used to obtain damping data. If static data is taken with no rotation, a correlation of the cross stiffness coefficient, K^*_{xy}, versus swirl parameter, σ, can be obtained. The problem is that as the inlet swirl velocity is increased the total cross force increases due to a higher inlet swirl (inviscid contribution) as well as the frictionally induced change in swirl. The change in the ideal component with inlet swirl, which is equal to the direct damping must be separated. One procedure is to use the static correlation to calculate a total force, $F_T(\Omega_d R_s)$, at an inlet swirl velocity corresponding to a whirl frequency Ω_d. The viscous force, found from theory or correlation, is subtracted form the total force to yield the ideal component. The damping is the rate of change of this force with frequency.

$$C_{xx} = \frac{F_T(\Omega_d R_s) - F_\Gamma(\Omega_d R_s)}{\Omega_d} = \frac{F_\sigma(\Omega_d R_s)}{\Omega_d} \tag{35}$$

The values of the direct damping, C_{xx}, calculated from the static measurement correlations employing this method agree with the values that were directly measured in the dynamic mode to within 13%, 8% and 15% for builds 2,3 and 4 respectively as shown in Table 3. This demonstrates that it is possible to predict the dynamic coefficients with the use of static measurements only. Another method for extracting the dynamic coefficients from static data, based on extrapolation, is presented by Millsaps and Martinez-Sanchez [26].

6. CONCLUSIONS

A new theory was developed that contains the effect of flow coupling. It was shown that this theory is capable of predicting the larger than expected forces found experimentally.

This finding has several important implications for design and analysis of short labyrinth seals, and, by extension, probably for other seal types as well. Data on cross forces from such seals should be

supplemented by a description of the upstream (and also the downstream) configuration of the test device, unless it can be ascertained by auxiliary tests that no coupling exists. As an example of the latter situation, it was verified that the rotordynamic force data were insensitive to the downstream configuration. This was found by blocking parts of the exhaust holes from the downstream chamber. The remaining holes were large enough to equilibrate this chamber with the atmosphere, hence making coupling negligible.

Calculation of seal rotordynamic coefficients, either for design or for rotordynamic diagnostic purposes, should always account for these possible coupling to the external flowfield. Ignoring them may make other refinements, such as more precise 2 or 3-D cavity flow modeling or CFD calculations irrelevant by comparison. Including the upstream and downstream coupling is relatively straightforward for simple geometries, such as the LSTF rig, but no theory currently exists that can be used to predict the non-uniformities ahead of, for example, the seal on a turbine tip shroud, where the tip area interacts strongly with the main turbine through flow. Development of such a theory would seem important. Similar considerations should apply for other seal environments.

In future designs of rotordynamic testing devices, consideration should be given to either minimizing the coupling mechanisms or matching the expected coupling levels that may occur in a real turbomachine. In any case measurements of the flow field upstream and downstream should be done to asses the degree of non-uniformity induced from the offset seal.

The following conclusions on the nature of rotordynamic damping have been drawn from consideration of the analytical model and the supporting experimental data.

1. The total cross force acting on a labyrinth seal at a given whirl frequency can be decomposed into "ideal" and "viscous" components.

2. The ideal component, which is due to an inviscid swirling flow, is a unique function of the inlet swirl relative to the gap variation phase speed. This force component vanishes when the velocity of the traveling gap is equal to the swirl velocity inside the gland. This component is solely responsible for damping.

3. The viscous component does not create nor alter the direct damping. It adds to (if the swirl velocity decreases in the gland) or subtracts from (if the swirl increases) the cross stiffness only.

4. The direct damping can be calculated from measurements of cross stiffness. The importance of this is that difficult and expensive dynamic measurements are not necessary in order to obtain damping coefficients.

REFERENCES

1. Den Hartog, J. P., 1956, Mechanical Vibrations, 4th Edition , McGraw Hill, pp. 319-321.

2. Alford, J. S., 1965, "Protecting Turbomachinery form Self-Excited Rotor Whirl", Journal of Engineering for Power, October, pp. 333-344.

3. Thomas, H. J., 1958, "Instabile Eigenschwing von Turbinelauefern Angefacht durch die Spaltstroemung in Stopfubuchseen und Bechauchflug (Unstable Natural Vibrations of Turbine Rotors Induced by the Clearance Flows in Glands and Blading)", Bull. de L.A.I.M. 71 No. 11-12, pp. 1039-1063.

4. Kostyuk, A. G., 1972, "A Theoretical Analysis of the Aerodynamic Forces in the Labyrinth Glands of Turbomachines, Teploenergetica, Vol. 19, No. 11, pp. 29-33.

5. Iwatsubo, T., 1980, "Evaluation of Instability Forces in Labyrinth seals in Turbines or Compressors", NASA CP-2133, pp. 139-169.

6. Gans, B. E., 1983, Prediction of Aeroelastic Forces in a Labyrinth Type Seal and its Impact on Turbomachinery Stability, Eng. Thesis, Department of Mechanical Engineering, M.I.T.

7. Kurahashi, Y., Inoue, T., 1980, "Spring and Damping Coefficients of Labyrinth Seals", Proceedings of the Institute of Mechanical Engineers.

8. Fujikawa, T., Kameoka, T., Abe, T.,1984, "A Theoretical Approach to Labyrinth Seal Forces., NASA CP-2338, pp. 28-30.

9. Scharrer, J. K., Childs, D. W., 1989, "Theory vs. Experiment for the Rotordynamic Coefficients of Labyrinth Gas Seals", Parts 1&2, ASME Journal of Vibration, Acoustics, Stress and Reliability in Design, Vol. 110, No. 3, pp. 270-287.

10. Martinez-Sanchez, M., Lee, O. W. K., Czajkowski, E., 1984, "Prediction of Force Coefficients in Labyrinth Seals", NASA CP-2338, pp. 235-256.

11. Jenny, R. J., Wyssmann, H. P., Pham, T. C., 1984, "Prediction of Stiffness and Dynamic Coefficients for Centifical Compressor Labyrinth Seals", ASME 84-GT-86, 29th International Gas Turbine Conference, June 4-7, Amsterdam, The Netherlands.

12. Nordman, R., Weiser, P., 1990, "Evaluation of Rotordynamic Coefficients of Look-Through Labyrinths by Means of a Three Volume Bulk Flow Model", Sixth Workshop on Rotordynamic Instability. Texas A&M Univ., May 21-23, pp. 141-157.

13. Benckert, H., 1980, Stromungsbedinte Federkennwerte in Labyrinthdithtungen, Doctoral Dissertation, University of Stuttgart.

14. Benckert, H., Wachter, J., 1978, "Querkrafte aus Spaltdichtungen - Eine Mogliche Ursache fur die Laufunruhe von Turbomachinen, Atomkernenergie, Bd. 32, Lfg. 4, pp. 239-246.

15. Benckert, H., Wachter, J., "Flow Induced Spring Coefficients of Labyrinth Seals for Applications in Rotordynamics", NASA CP-2133, pp. 189-212.

16. Brown, R. D., Leong, Y. M. M. S., 1982, "Circumferential Pressure Distributions in a Model Labyrinth Seal", NASA CP-2133, pp. 222-232.

17. Thielele, G., Stetter, H., 1990, "Experimental Investigation of Exciting Forces in Labyrinth Seals", Sixth Workshop on Rotordynamic Instability. Texas A&M University, May 21-23, pp. 141-157.

18. Kanki, H., Morii, S., 1985, "Destabilizing Forces in Labyrinth Seals", NASA CP-2409, pp. 205-223.

19, Hisa, S., Sakakida, H., Asatu, S. , 1986, "Steam Excited Vibrations in Rotor-Bearing Systems", Proceedings of the International Conference on Rotordynamics", Sept. 14-17, Tokyo, pp. 635-641.

20. Wright, D. V., 1978, "Air Model Tests of Labyrinth Seal Forces on a Whirling Rotor", Journal of Engineering for Power, Series A , Vol. 100, No. 14, October, pp. 533-543.

21. Kanemitsu, Y., Ohsawa, M., 1986, "Experimental Study on Flow Induced Forces of Labyrinth Seals", Proceedings of the IFTOMM Conference on Flow induced Force in Rotating Machinery, Sept. 18-19, Kobe University, Japan, pp. 106-112.

22. Scharrer, J. K., 1987, A Comparison of Experimental and Theoretical Results for Labyrinth Gas Seals, Ph.D. Dissertation, Mechanical Engineering Department, Texas A&M University.

23. Millsaps, K. T., Martinez-Sanchez, M., 1990, "Static and Dynamic Pressure Distributions in a Short Labyrinth Seal", NASA CP-2543., pp. 129-140.

24. Millsaps, K. T., 1992, The Impact of Unsteady Swirling Flow in a Single Gland Labyrinth Seal on Rotordynamic Stability: Theory and Experiment, Ph.D. Dissertation, Department of Aeronautics and Astronautics, M.I.T.

25. Varmes, G., 1960, "A Fluid Mechanics Approach to the Labyrinth Seal Leakage Problem", Journal of Basic Engineering, Transactions of the ASME, Series D, Volume 82, No. 2, pp. 265-275.

26. Millsaps, K. T., Martinez-Sanchez, M., 1993, "Dynamic Forces From Single Gland Labyrinth Seals: Part I - Ideal and Viscous Decomposistion, International Gas Turbine Conference, Cincinnatti, OH.

27. Millsaps, K. T., Martinez-Sanchez, M., 1993, "Dynamic Forces From Single Gland Labyrinth Seals: Part II - Upstream Coupling, International Gas Turbine Conference, Cincinnatti, OH.

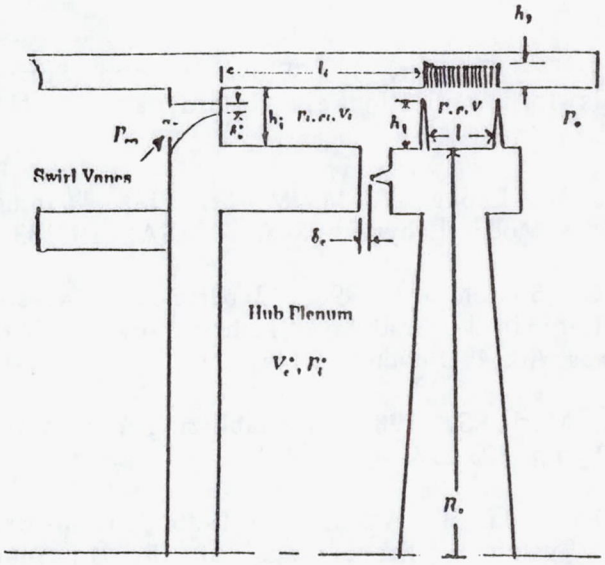

Figure 1. Schematic of Labyrinth Seal Test Facility test section showing upstream swirl cavity and the flows into and out of the center hub plenum.

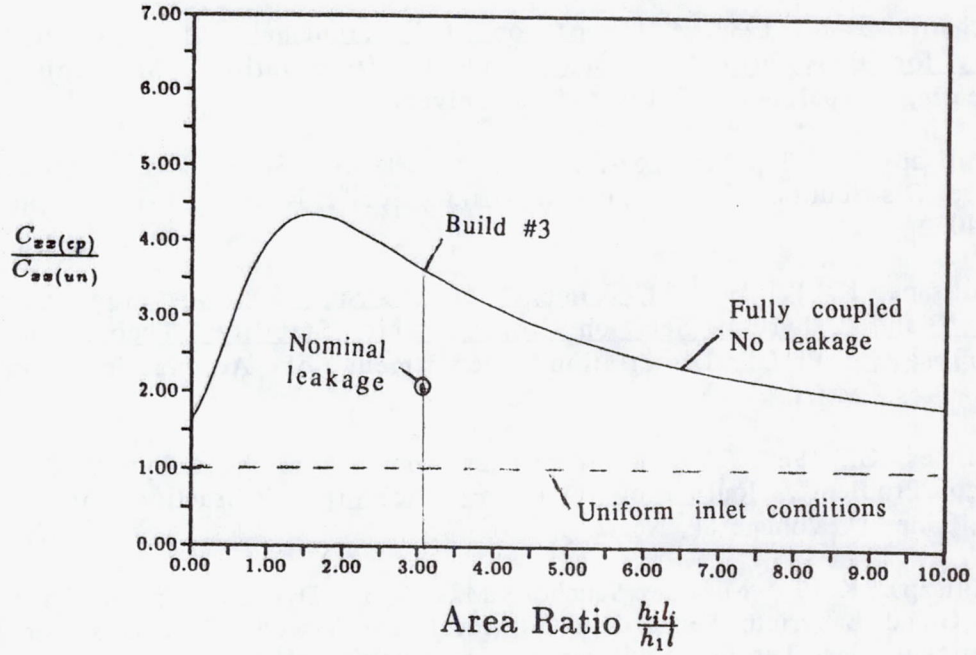

Figure 2. Ratio of rotordynamic damping with upstream coupling to that with no coupling versus swirl cavity to seal gland area ratio.

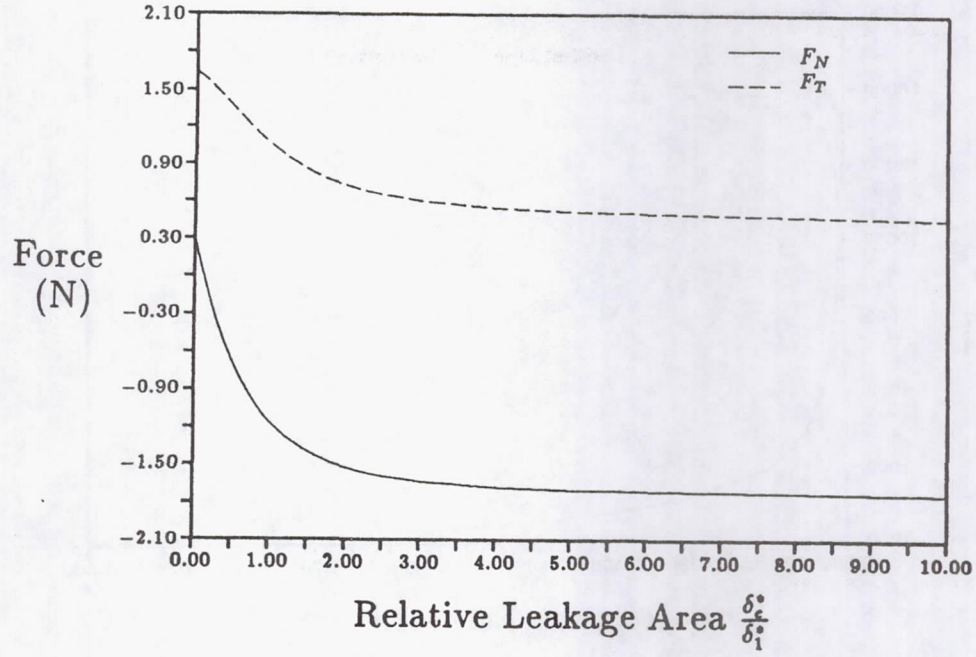

Figure 3. Predicted direct and cross force at $\Omega = 0$ for the coupled model versus the relative axial clearance. The geometry is the same as for build #3. π_s=1.4, α_v = 15 degrees, ε_1=0.1407 and ω=0.

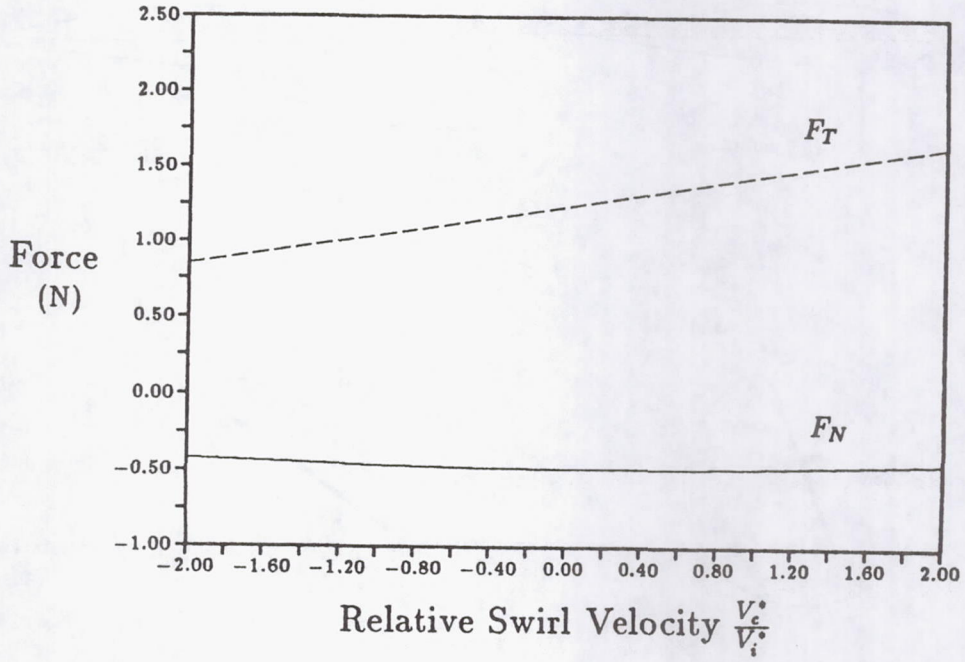

Figure 4. Direct and cross force predicted by the coupled model versus the center cavity swirl velocity. These are for the same conditions as Figure 3.

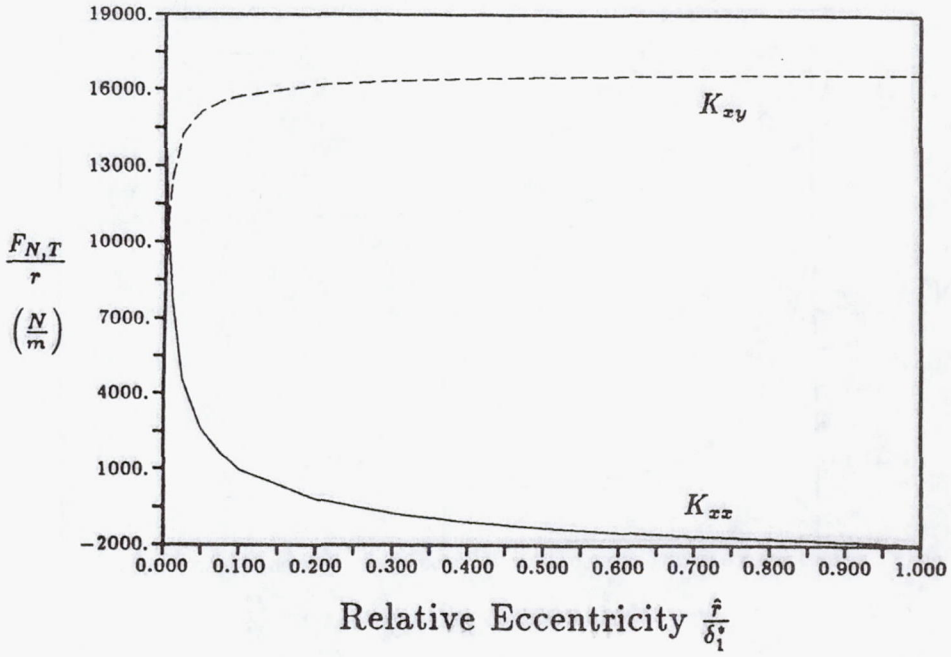

Figure 5. Effect of relative whirl amplitude on the direct and cross stiffness as predicted by the coupled model with hub leakage. Build #3 geometry and $\delta_c / \delta_1^* = 0.19$.

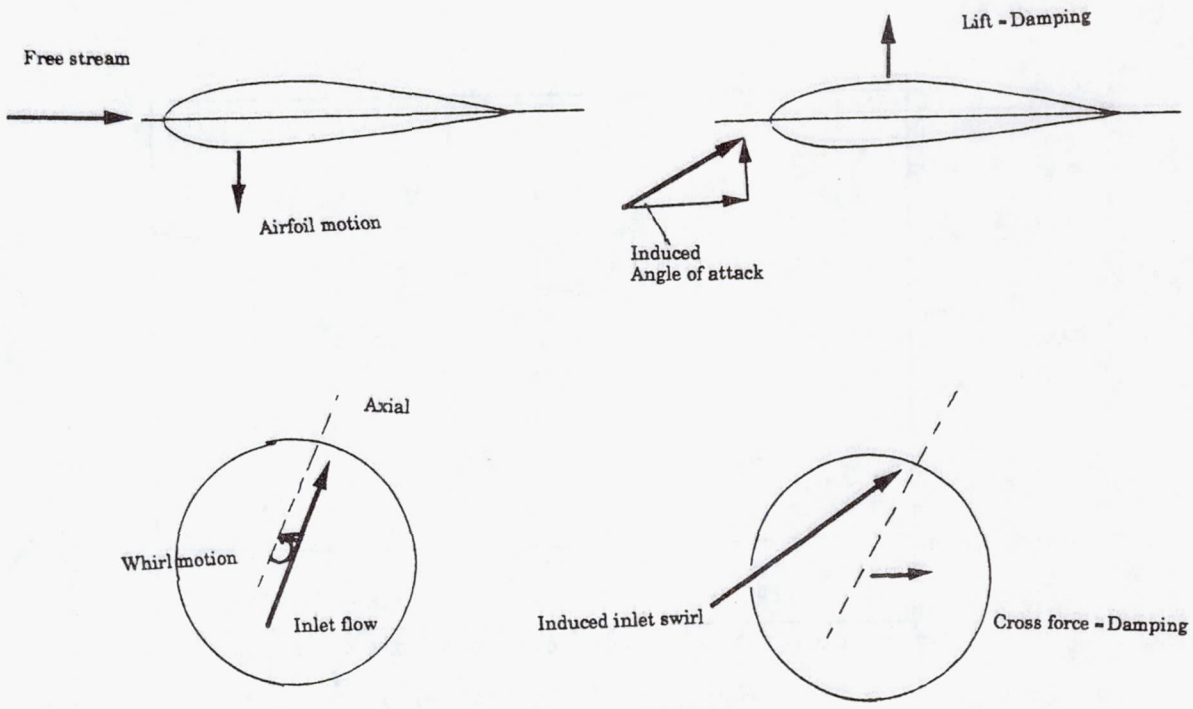

Figure 6. Analogy between quasi-static damping of a translational airfoil generating an induced angle of attack and a whirling seal inducing a inlet swirl component.

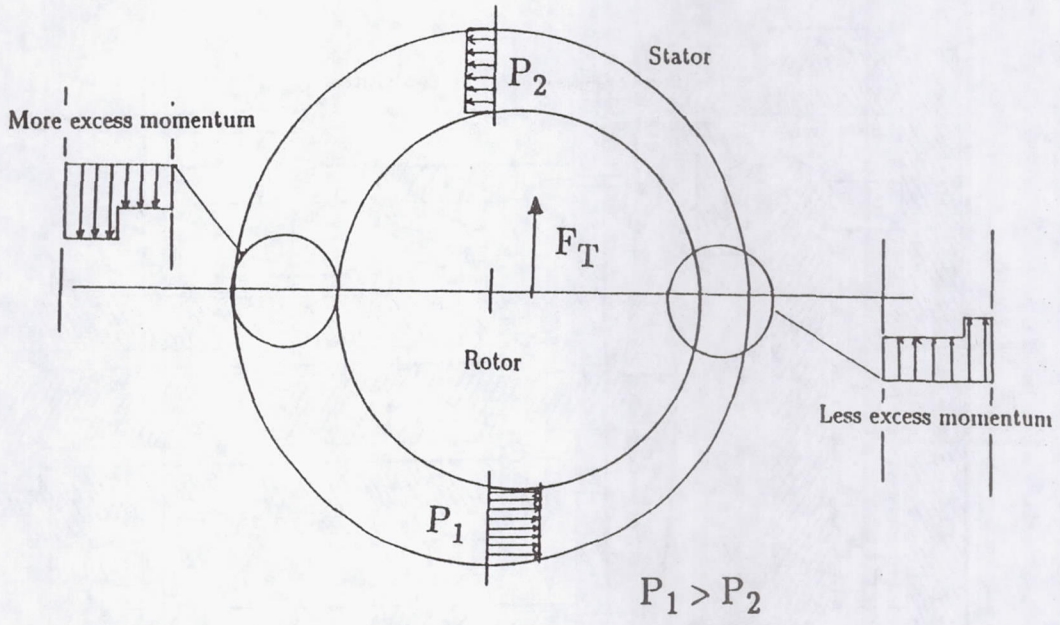

Figure 7. Physical origin of the viscous force. This force is due to a velocity difference and hence is independent of the whirl frequency. Therefore, it does not contribute to the damping.

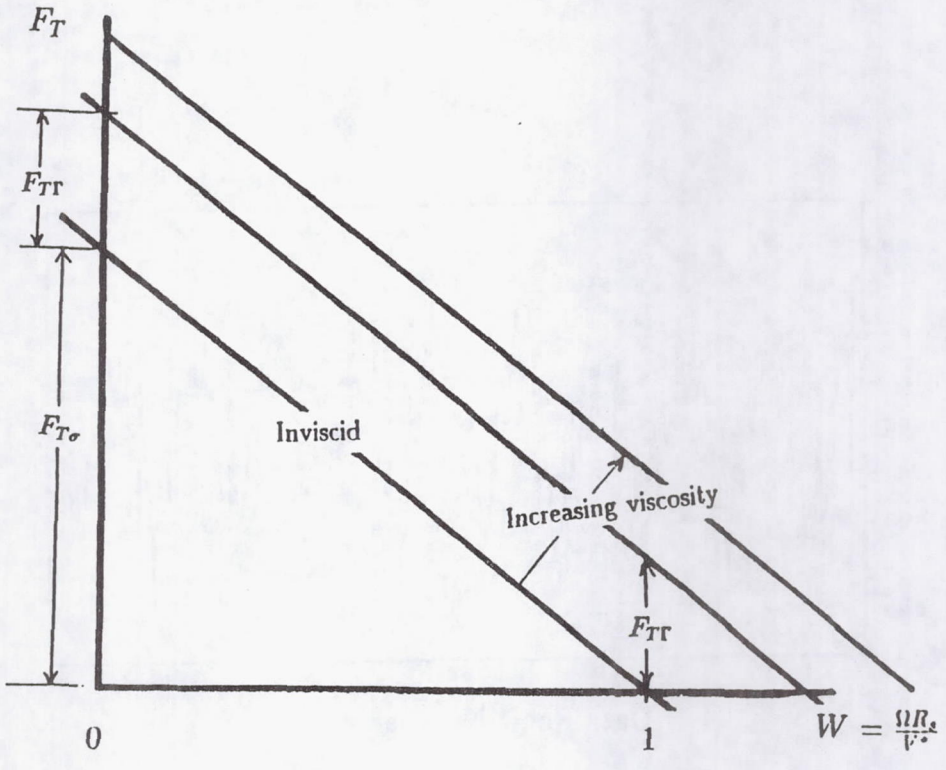

Figure 8. General frequency dependent behavior of the cross force, showing both the ideal and viscous contributions.

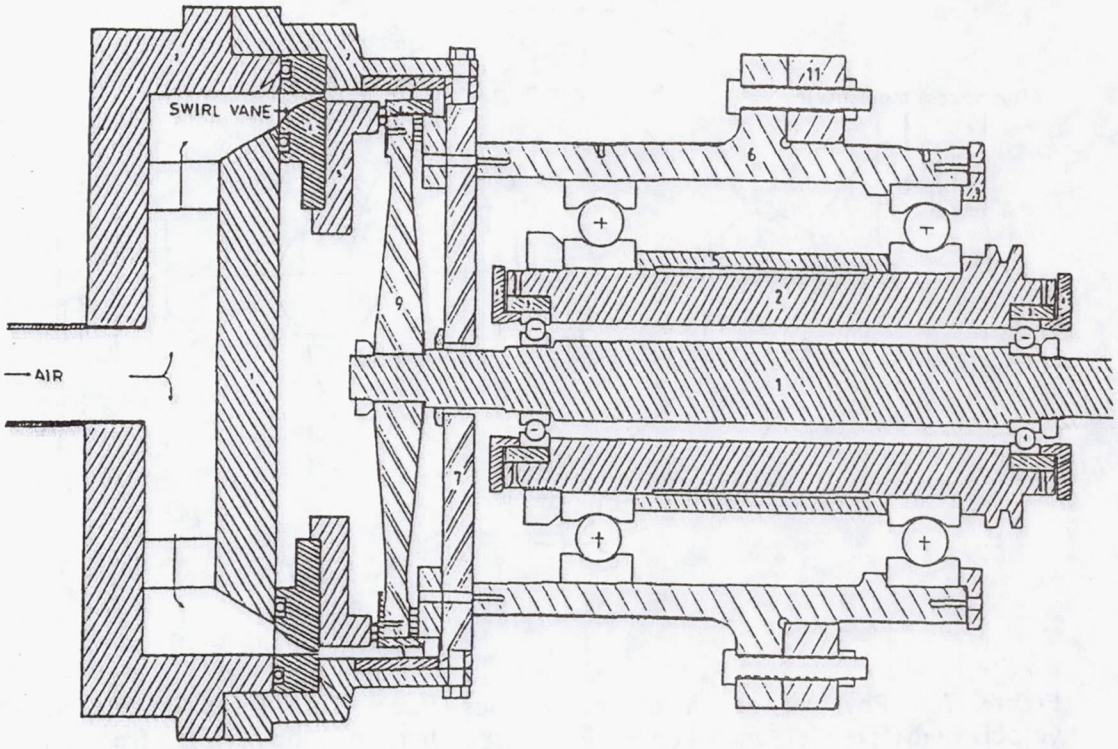

Figure 9. Cross section of the LSTF test section and nested spindle whirl/spin producing rotating machinery.

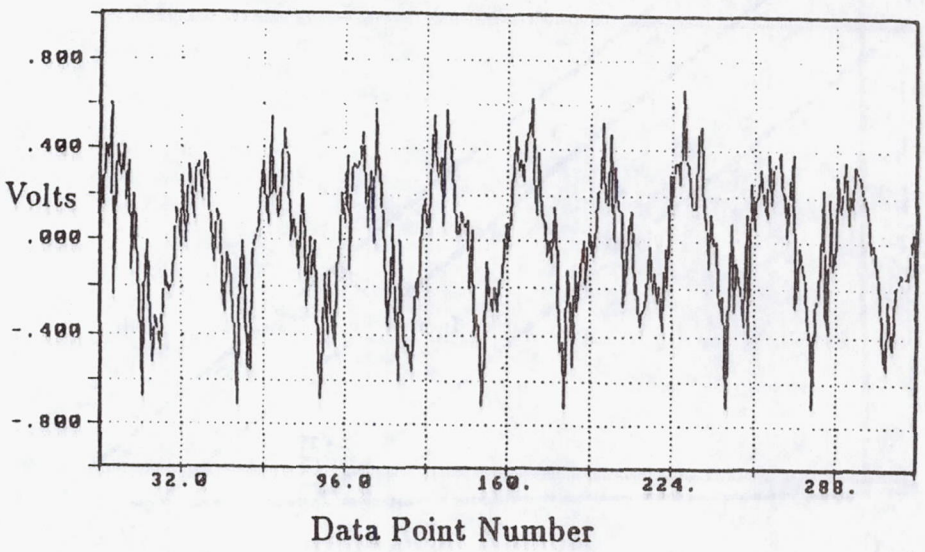

Figure 10. Typical output trace from one of the flush mount pressure transducers. There are 32 data points per whirl revolution.

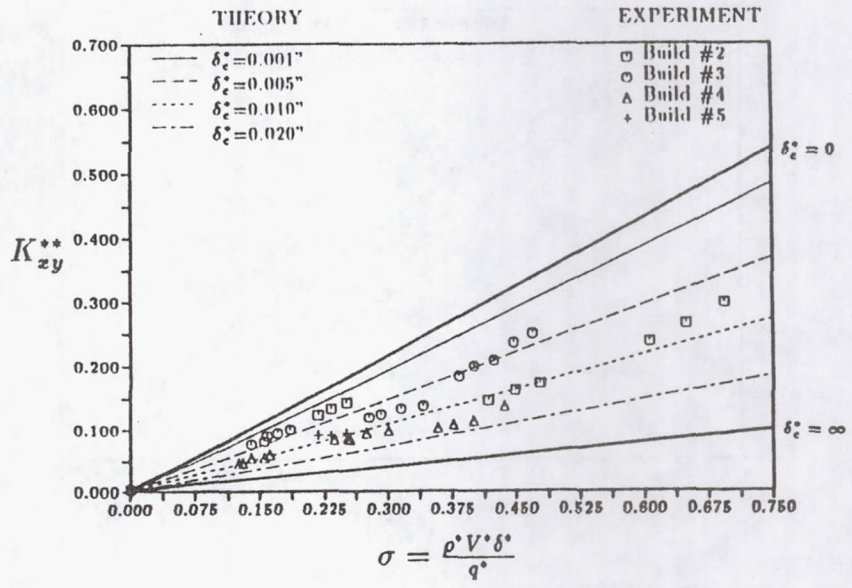

Figure 11. Nondimensional cross stiffness, K_{xy}, versus the swirl parameter, σ, for the experimental data and theory, with the axial gap used as a parameter. All experimental values fall between the theoretical predictions with 0.004" (0.0001m)<δ_c<0.017" (0.0004m). The top thick line is the fully coupled case (i.e. no center leakage) and the bottom on is for uniform inlet conditions (i.e. no coupling). Calculations are for build #3 geometry.

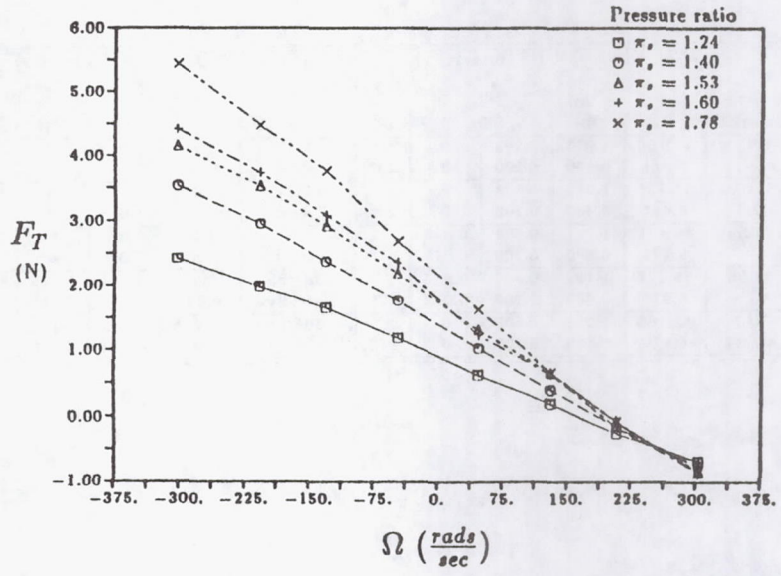

Figure 12. Experimentally obtained cross force versus whirl frequency for five different pressure ratios. These data are from build#4 with 8.6 degrees of inlet swirl and no shaft rotation.

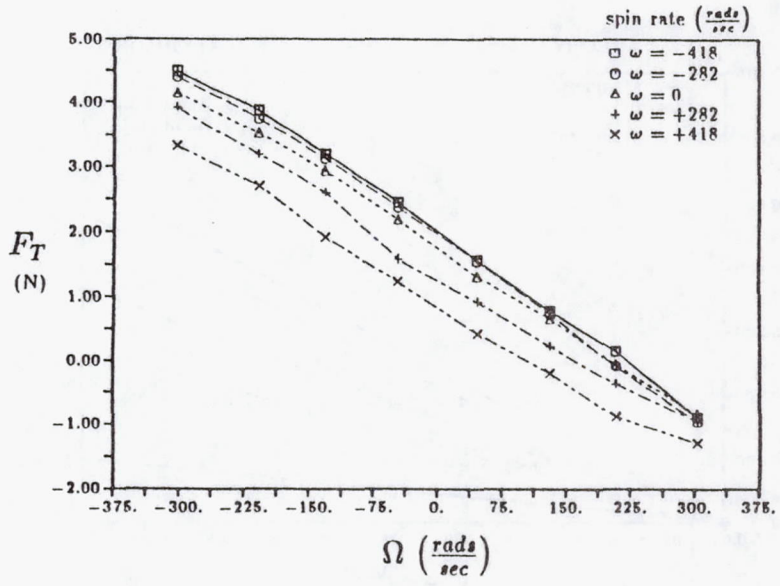

Figure 13. Experimentally obtained cross force versus whirl frequency for five different seal spin rates. These data are from build#4 with 8.6 degrees of inlet swirl and the pressure ratio is 1.47.

Table 1. Geometry for the five seal builds.

BUILD	SEAL DIMENSIONS (rotor) cm in.						LAND DIMENSIONS (stator) cm in.				
	Material	R_s	l	h_1	d	α_s	Material	ϕ_s	h_2	l_s	δ_1^*
	4140	15.166	1.016	0.508	0		1117	15.240	0	0	0.0737
#1	steel	5.971	0.400	0.200	0	20°	steel	6.000	0	0	0.029
	4140	15.166	1.016	0.508	0		1117	15.245	0	0	0.0787
#2	steel	5.971	0.400	0.200	0	20°	steel	6.002	0	0	0.031
	304 SS	15.177	1.727	0.508	0.043		1117	15.245	0	0	0.0686
#3		5.975	0.680	0.200	0.017	17°	steel	6.002	0	0	0.027
	304 SS	15.177	1.727	0.508	0.043		304 SS	15.245	0.483	1.905	0.0686
#4		5.975	0.680	0.200	0.017	17°	HastollyX	6.002	0.190	0.750	0.027
	4140	15.166	1.016	0.508	0		304 SS	15.245	0.483	1.905	0.787
#5	steel	5.970	0.400	0.200	0	17°	HastollyX	6.002	0.190	0.750	0.031

Table 2. Comparison of the static data of and Wachter to the coupled model. The first column shows the experimental value. The second column gives the value predicted with full coupling. The third gives predictions for constant upstream conditions (i.e. no coupling). The last column gives the value of the axial sealing gap needed for the model to match the experimentally obtained value.

CONFIG.	$F_T(meas.)$	$F_T(\delta_c^* = 0)$	$F_T(\delta_c^* = \infty)$	Matched δ_c^*
1	10.21(N)	16.28(N)	4.99(N)	0.008"
2	8.28(N)	16.15(N)	4.25(N)	0.011"
3	11.91(N)	15.51(N)	4.09(N)	0.010"

Table 3. The first column gives the cross stiffness correlation coefficient obtained from static measurements. The next two columns give the total, and frictional force, respectively calculated at a whirl speed of 300 (rads/sec). The last two columns give the calculated and measured direct damping coefficients.

BUILD#	$\frac{\partial K_{xy}^{**}}{\partial \sigma}$	$\frac{F_T(\Omega_d)}{f}$	$\frac{F_{TF}(\Omega_d)}{f}$	C_{xx}^{**}	From Static Correlation $C_{xx}\left(\frac{Ns}{m}\right)$	Measured Directly $C_{xx}\left(\frac{Ns}{m}\right)$
2	0.372	7763	953	0.289	22.70	19.95
3	0.416	27821	3162	0.371	82.19	75.80
4	0.283	20001	3162	0.247	56.13	48.54
5	0.338	7053	953	0.231	20.33	15.81

CALCULATION AND MEASUREMENT OF THE INFLUENCE OF FLOW PARAMETERS ON ROTORDYNAMIC COEFFICIENTS IN LABYRINTH SEALS

K. Kwanka, W. Ortinger, and J. Steckel
Lehrstuhl Thermische Kraftanlagen
Technische Universität München
München, Germany

Abstract

First experimental investigations performed on a new test rig are presented. For a staggered labyrinth seal with fourteen cavities the stiffness coefficient and the leakage flow are measured. The experimental results are compared to calculated results which are obtained by a one-volume bulk-flow theory. A perturbation analysis is made for seven terms. It is found out that the friction factors have great impact on the dynamic coefficients. They are obtained by turbulent flow computation by a finite-volume model with the Reynolds-equations used as basic equations.

Nomenclature

C, E, K	Damping, inertia, stiffness coefficients
F	Force
H	Labyrinth height
U	Part of cavity perimeter
c_f	Friction factor
$c_{u,}$ c_{ax}	Circumferential velocity, axial velocity
e	Eccentricity
f	Cross-sectional area of cavity
$\dot{m}$	Mass flow related to circumference
l	Length of cavity
n	Rotating speed
p	Pressure
R_R	Radius of rotor
δ	Radial clearance
φ	Peripheral angle
κ	Isentropic coefficient
λ	Friction factor
μ	Flow coefficient, dynamic viscosity
τ	Shear stress
$\Psi,\xi, \Lambda, \Xi, \eta, \zeta, \tilde{n}$	Perturbation terms
ω	Angular velocity
ρ	Density

Preceding Page Blank

Introduction

Despite the numerous efforts in the past, there still remain some open questions in understanding tip-clearance excitation and, as a consequence, a lack in modelling and predicting forces and coefficients induced by labyrinth flow. The efforts to increase the efficiency and to minimize the specific costs or the specific weight of a rotor-casing configuration often lead to parameters which are in some cases very close to the stability margin. Beyond the stability limit the rotational energy which is transferred to the rotor bending exceeds the damping that dissipates this energy. As a consequence, self-excited vibration mechanisms impede the scheduled operation regime of the turbomachine. In addition to the labyrinth seal forces several other mechanisms (e.g. oil whip) act on the rotor and an amplification of the excitation may occur [5].

The labyrinth seal forces are usually described in a linearized formulation for small deflections out of the centered position by using dynamic coefficients. These are stiffness, damping and inertia coefficients.

$$\vec{F} = -\begin{pmatrix} K_{xx} & K_{xy} \\ -K_{yx} & K_{yy} \end{pmatrix}\begin{pmatrix} x \\ y \end{pmatrix} - \begin{pmatrix} C_{xx} & C_{xy} \\ -C_{yx} & C_{yy} \end{pmatrix}\begin{pmatrix} \dot{x} \\ \dot{y} \end{pmatrix} - \begin{pmatrix} E_{xx} & E_{xy} \\ -E_{yx} & E_{yy} \end{pmatrix}\begin{pmatrix} \ddot{x} \\ \ddot{y} \end{pmatrix} \qquad (1)$$

Many investigations were performed to estimate the dynamic coefficients on several seal geometries. In the experimental field two procedures are frequently used. First, static measurements were made [4, 2,12] which allow the determination of the direct and cross-coupled stiffness coefficients of the labyrinth seal. Second, dynamic measurements [2, 7], which were carried out to identify the other coefficients in eq. (1).

The experimental results can be used for verification of the various theoretical approaches. The computational effort is low when a bulk-flow theory - either a one-, two- or three-volume model [1, 3, 8]- is used. An increased amount of computational time is needed if the seal geometry is discretized by a grid, and if the local variables are calculated by the finite-difference or the finite-volume method [9]. The forces acting on the rotor are obtained by a final integration.

In this paper a staggered labyrinth seal is investigated. Only few experimental results are published for this geometry in comparison to others. With the help of the static identification method a maximum accuracy for the measured stiffness coefficients is expected. In most cases these coefficients are of outstanding importance for the dynamic behaviour of the rotor.

The calculated results are obtained by a one-volume bulk-flow theory. It is found out that the bulk-flow theory in connection with the perturbation method is highly sensitive to friction factors. In this case they are calculated by means of turbulent flow computation. The Reynolds equations in cylindrical coordinates including the standard k-ε model give the velocity components and the turbulent values. A boundary-layer theory is applied and the friction factors are calculated depending on the axial and circumferential status of the flow.

Test Rig

The test rig is designed with the purpose to measure labyrinth flow induced radial forces on the eccentric rotor. In fig. 1a. a schematic representation of the test rig can be seen. Two identical grooved labyrinth seals with fourteen cavities each are located symmetrically to the inflow region. The inflow region is outlined in fig. 1b. The inlet swirl can be varied by the combination of radial and circumferential flow components.

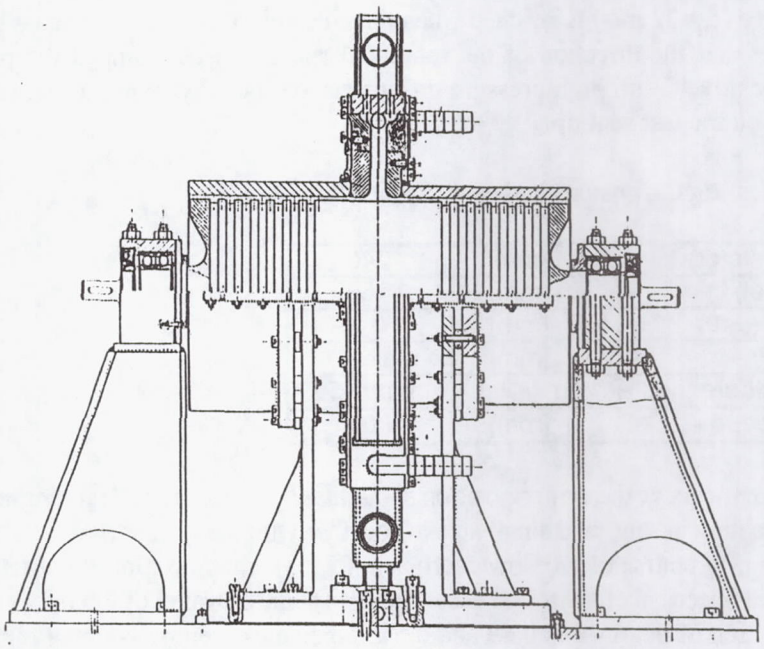

Fig. 1a. Schematic of the test rig

The geometric data of the staggered labyrinth are indicated in fig. 2. At the center position the gap between the rotor and the seal tips attached to the casing is 0.5 mm. The eccentricity can be adjusted in horizontal direction by moving the casing relative to the rotor.
One of the seals is used to measure the pressure distribution in circumferential direction and, as a consequence, the acting force in each cavity and on the whole rotor. Ten pressure lines are located in each cavity. This gives a total of some 160 data points per labyrinth seal unit. The pressure lines are connected to a multifunction pressure measurement rig. The flow field in the cavities and the inlet swirl is determined by using a probe which is located in the second labyrinth seal.

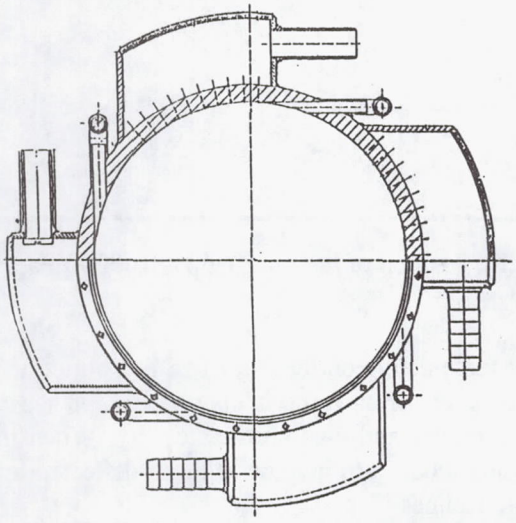

Fig. 1b. Inflow configuration of the test rig

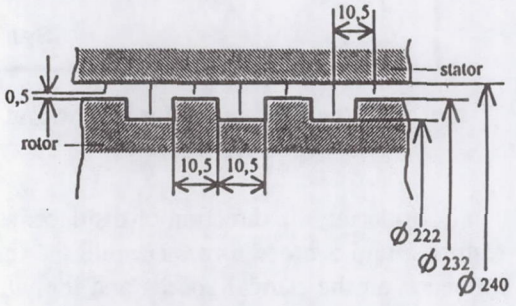

Fig. 2. Geometric data of the labyrinth (dimensions in mm)

Some test rig dimensions and experimental conditions are listed in table 1. The maximum preswirl velocity ($c_u \approx 22$ m/s) is reached when there is an inflow only via the tangential feeders. Due to the fact that the direction of the rotational speed can be changed the preswirl can be negative and positive. With high pressure differences on the labyrinth seal the critical pressure ratio prevailes on the last seal tip.

Table 1. Test rig dimensions and experimental conditions

Diameter (stator)	D [mm]	240
Length (seal)	L [mm]	150
Clearance (e=0)	d [mm]	0,5
Eccentricity	e [mm]	max. 0,4
Pressure difference	Δp [kPa]	max. 450
Rotating speed	n [rpm]	±8000

First measurements at the center position show that the pressure is declining in axial direction, alternately in big and small steps. Together with the geometry dependent flow area this causes a zigzag course of the flow coefficient (fig. 3), which is almost entirely independent on the rotational speed, inlet swirl and eccentricity. The mean value of the flow coefficient in the neutral position of the rotor is 0.69 and 0.675 when the eccentricity is 0.4 mm.

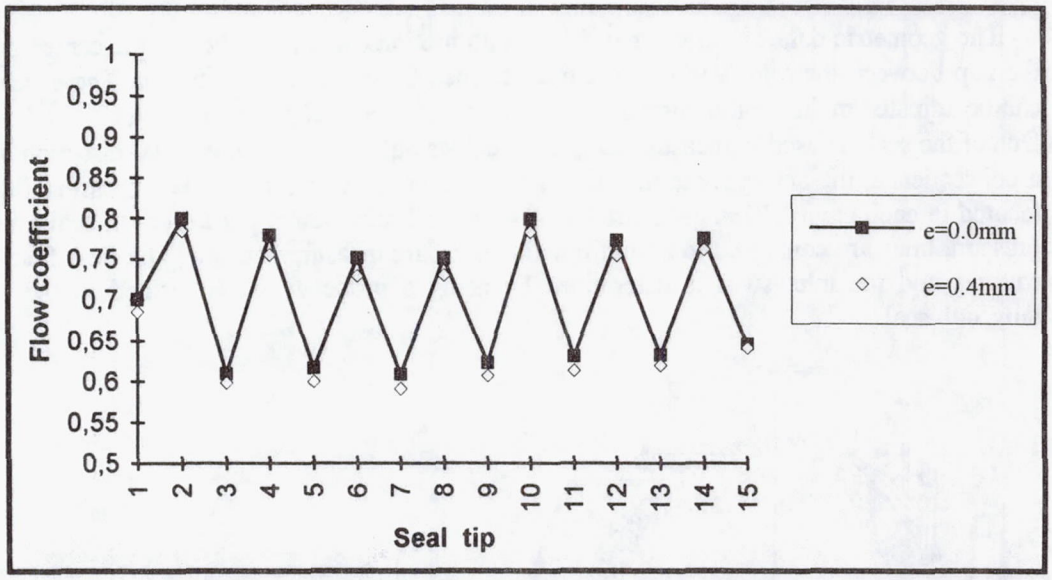

Fig. 3. Flow coefficient for centric and eccentric position of the rotor (Δp = 160000 Pa; n = 4000 rpm)

Considering the direction of displacement, the force acting on the rotor can be splitted in a restoring and a cross force. Despite the fact that the restoring force is conservative it has an influence on the critical speeds and the vibrational modes and thus on the stability. When the restoring force has a decentralized effect the bending modes are in general more deflected and more excited by cross forces, and the stability limit declines.

In center position of the rotor the circumferential pressure distribution in each cavity has shown that almost no resulting force is acting on the rotor and which means that the rotor is well manufactured and exactly alined. At the off-center position of the rotor the restoring force has a zigzag course like the flow coefficient (fig. 4). The resulting force for the whole labyrinth

is decenterizing for all parameters investigated. This behavior of the restoring force can be explained by the change of state of the throttled flow in the alternating large flow areas in the cavity and the small flow areas between the strips and rotor. Only in the gap behind the last seal tip the direction of the force is directed against the deflection as is normally expected for plain seals.

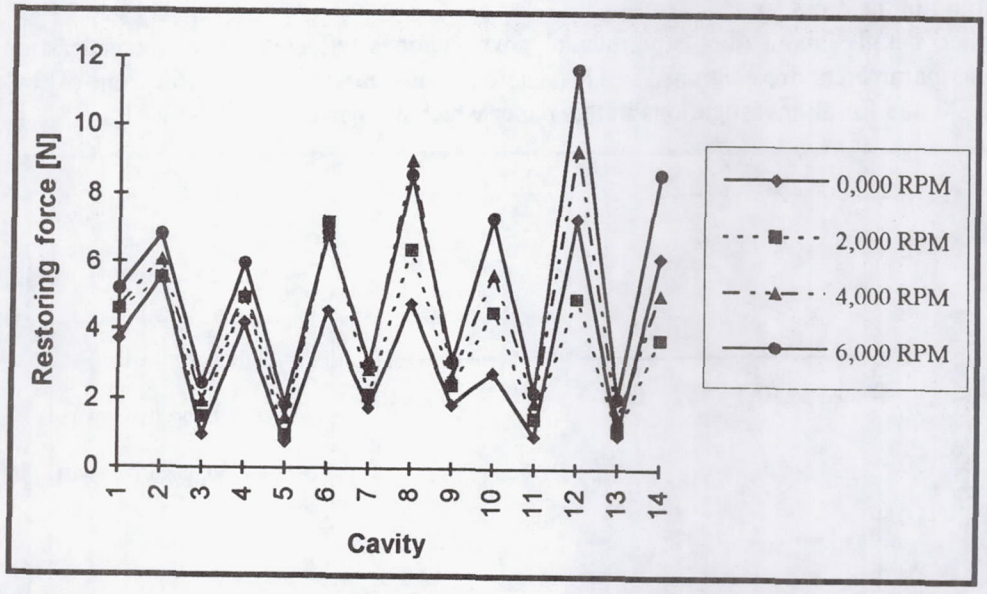

Fig. 4. Restoring force versus cavity in dependence of rotating speed ($\Delta p = 300000$ Pa; $e = 0.4$ mm; $c_u \approx 22$ m/s)

From a maximum in the first cavities the cross force declines towards the end of the labyrinth seal (fig. 5). The influence of the rotational speed on the restoring and the cross force is small. For all investigated parameters the restoring force was higher than the cross force.

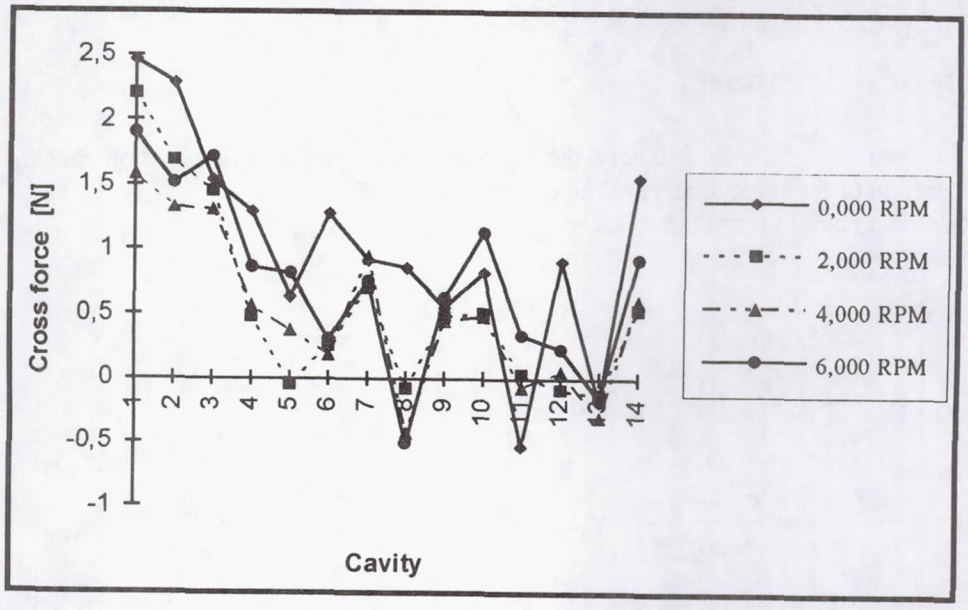

Fig. 5. Cross force versus cavity in dependence of rotating speed ($\Delta p = 300000$ Pa; $e = 0.4$ mm; $c_u \approx 22$ m/s)

The rotational speed and the entry swirl act together and influence the magnitude of the destabilizing force (fig. 6). When the direction of rotation and inlet swirl coincide then the cross force is smaller than in case of counteracting swirl and drag exerted by the rotating surface of the rotor to the flow. The influence of swirl exceeds the influence of rotation. Decisive for the magnitude of the cross force is the change of circumferential velocity and not the absolute value of this velocity. In case of conspiring swirl and drag the circumferencial velocity has the highest values but not the cross force.

Further details about the experimental investigations effected under consideration of numerous parameters are contained in [11].The circumferential velocity c_u in front of the seal is about 20 m/s for all investigations in this paper which are performed with swirl .

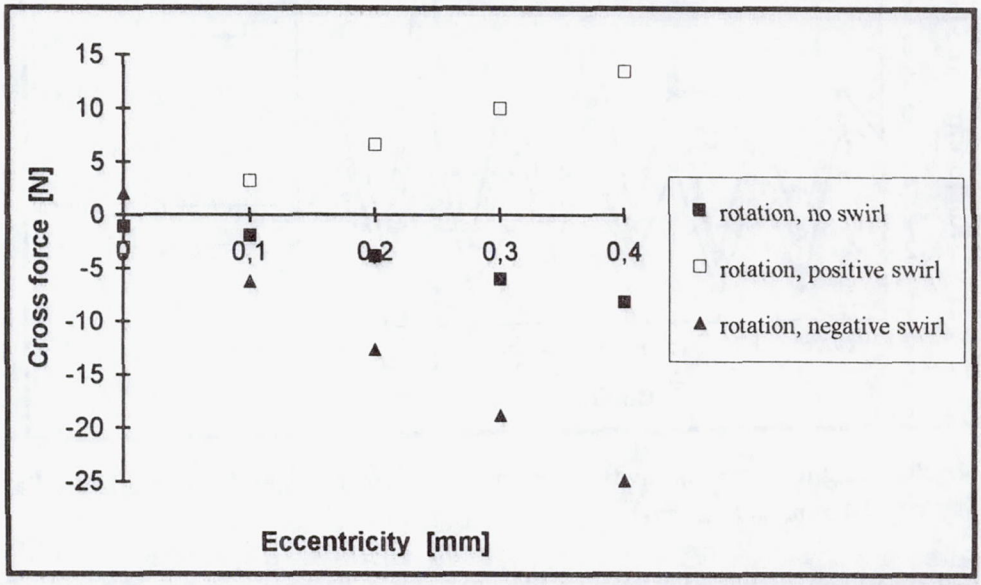

Fig. 6. Influence of entry swirl and rotating speed on the cross force ($\Delta p = 460000$ Pa; n = 4000 rpm)

Theoretical Treatment

With the help of a bulk-flow theory the circumferential pressure distribution due to the eccentric position of the rotor relative to the casing is obtained.

The governing equations are the following:

$$\dot{m}_i = \mu_i \delta_i \sqrt{p_{i-1}^2 - p_i^2}$$

$$\frac{\partial}{\partial t}(\rho_i f_i) + \frac{\partial}{R_R \partial \varphi}(\rho_i c_{ui} f_i) + \dot{m}_{i+1} - \dot{m}_i = 0$$

$$\frac{\partial c_{ui}}{\partial t} + c_{ui}\frac{\partial c_{ui}}{R_R \partial \varphi} + \dot{m}_i \frac{c_{ui} - c_{ui-1}}{\rho_i f_i} + \kappa_{Si} c_{ui}^2 - \kappa_{Ri}\left(R_R\omega - c_{ui}\right)^2 = -\frac{\partial p_i}{\rho_i R_R \partial \varphi} \qquad (2) - (5)$$

$$\kappa_{Si} = \lambda_{Si}\frac{U_{Si}}{2 f_i} sgn(c_{ui}) \quad ; \quad \kappa_{Ri} = \lambda_{Ri}\frac{U_{Ri}}{2 f_i} sgn(R_R\omega - c_{ui})$$

This is the well-known set of partial differential equations. In order to find an analytical solution the differential equation system is linearized by splitting the main variables into an average value (for the centric position) and an additional value for the eccentric position. This perturbation method is applicated for eight terms.

$$\delta = \delta_*(1+\Psi) \qquad f = f_*(1+\Xi) \qquad \dot{m} = \dot{m}_*(1+\zeta)$$
$$p = p_*(1+\xi) \qquad c_u = c_{u*}(1+\eta) \qquad \mu = \mu_*(1+\tilde{n}) \qquad (6)(a\text{-}h)$$
$$\lambda_R = \lambda_{R*}(1+\Lambda_R) \qquad \lambda_S = \lambda_{S*}(1+\Lambda_S)$$

The most important ones are ξ for the pressure distribution and Λ_S, Λ_R for the friction factor.

Eqs. (6) are put in eqs. (2) - (5) and an exponential formulation for the perturbation term leads to the cross force acting on the rotor of the labyrinth seal.

$$F = -R_R l\, p_* \int_0^{2\pi} \xi \sin\varphi d\varphi \qquad (7)$$

With the help of this perturbation method it is possible to calculate the forces in a first step and, in a second step, to obtain the dynamic coefficients of the seal. Details of the calculation method can be seen in [1].

The value of the cross force is influenced by two factors. First, by the difference of the circumferential velocity from chamber to chamber. This leads to methods to control the swirl, for example swirl-brakes or helically grooved seals, a well-known and often discussed phenomenon.

Second, a great influence of the cross forces on the friction factor is found. This can be seen in figure 7. For the given labyrinth geometry in the test rig a great variety of results for the cross forces is obtained by the application of several friction factors for labyrinth seals.

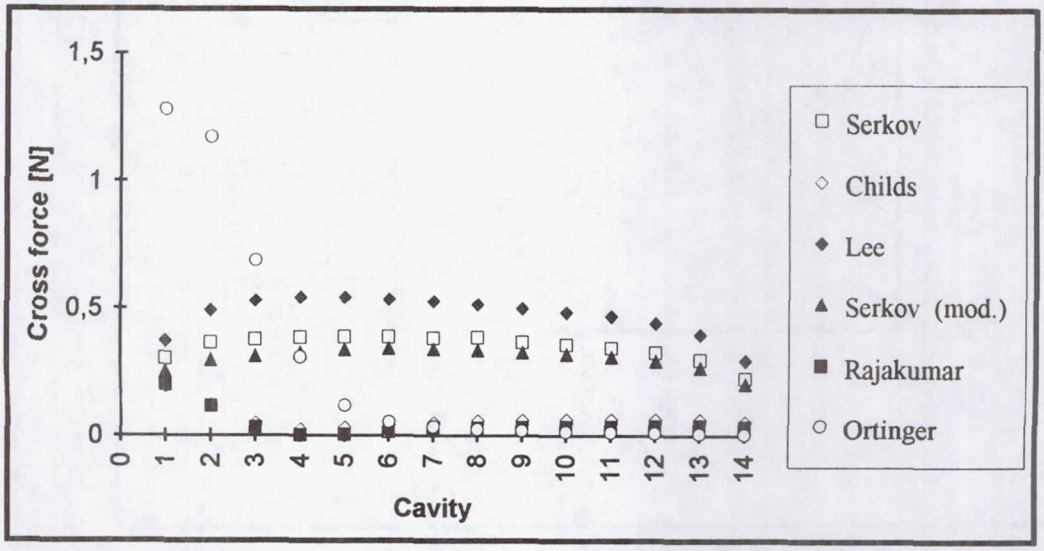

Fig. 7. Cross force in dependence on different methods to calculate the friction factor (Δp = 80000 Pa; n = 4000 rpm)

For the following calculations the friction factor is obtained by computing the turbulent flow field in the labyrinth seal with the Reynolds equations in connection with a k-ε turbulence model. The circumferential velocity near the wall is determined and a theory for the computation of the friction factor is applied.

$$c_f = \frac{\tau_W}{0.5\rho c_u} \qquad \lambda = 4c_f \tag{8}$$

For the shear stress on the labyrinth wall the following formulation is found:

$$\tau_W = \rho u_\tau^2 \tag{9}$$

where the shear stress velocity is dependent on the region where the calculated velocity occurs, i.e. either in the viscous sublayer or the full turbulent layer. Details can be seen in [10].

This theory leads to the friction factor of the seal. The Reynolds number is defined

$$\mathrm{Re} = \frac{\rho c_{ax} H}{2\mu} \tag{10}$$

Results of the calculated friction factor in relation to other methods can be seen in fig. 8.

For all the methods there can be observed a tendency of decreasing friction factors with increasing Reynolds numbers. For the calculated method the friction factor reaches an asymptotic value, whereas in the other cases the factors are still decreasing.

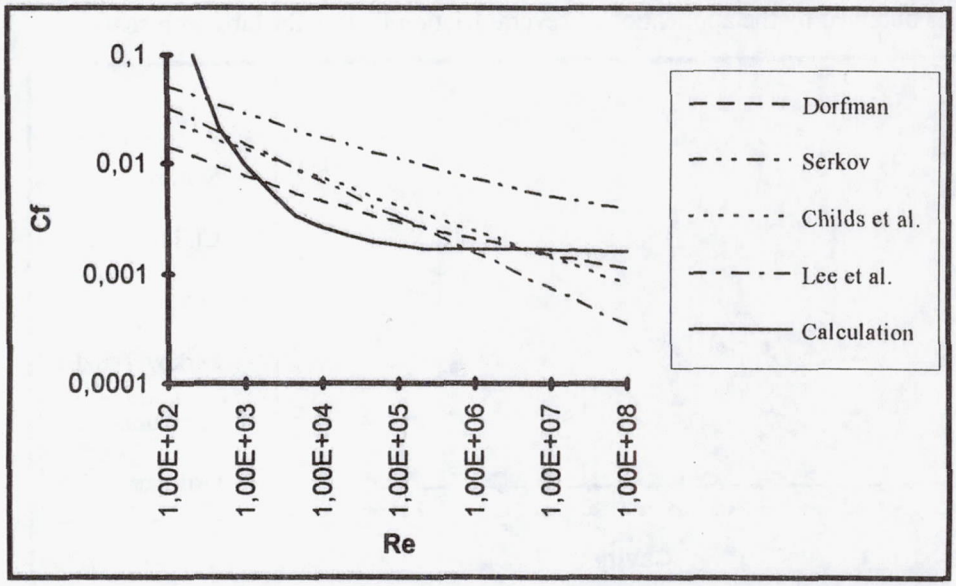

Fig. 8. Comparison of friction factors obtained by various methods and authors.

Comparison between Theory and Experiment

The cross coupled stiffness is an important input value for calculations of the rotordynamic stability limit. For three differencies of inlet and outlet pressure maximum preswirl and constant rotating speed the calculated results are compared to experimental results (fig. 9). The calculated results are obtained by the bulk-flow theory presented before including the friction factors contained in fig. 8.

The calculation exceeds slightly the experiment whereas the tendency is in good agreement. The almost proportional increase of the calculated cross force with the inlet-outlet pressure difference cannot be confirmed totally by experiment. The measured cross force is about linear to eccentricity.

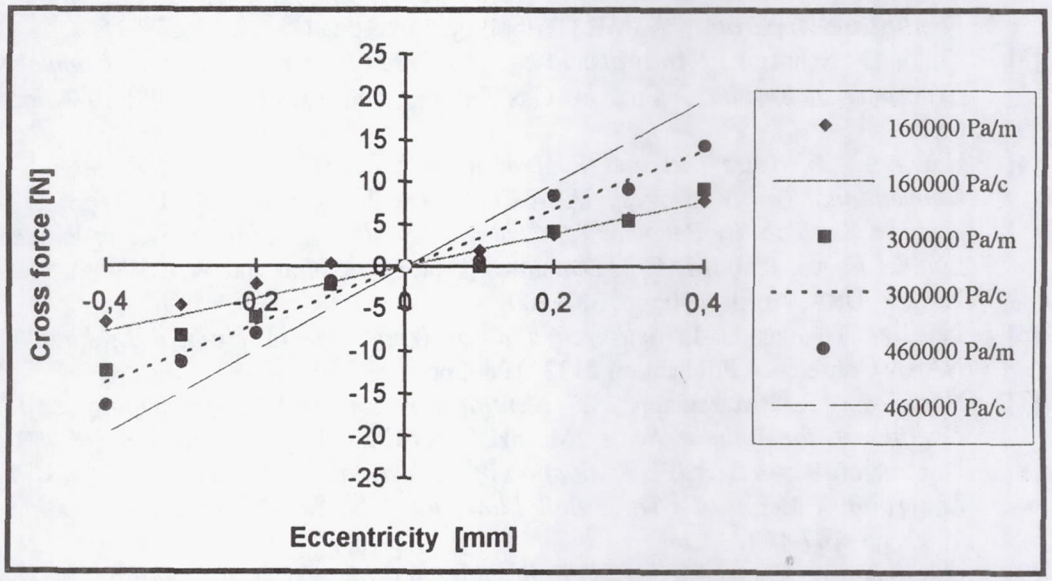

Fig. 9. Comparison of calculation and experiment in dependence of the pressure difference (n = 6000 rpm; m - measurement, c -calculation)

Conclusions

Measured normal and cross forces for a fourteen cavity staggered labyrinth are presented. The forces are obtained by the circumferential pressure distribution in each cavity when the rotor is in an eccentric position relative to the casing. The influence of inlet swirl, pressure ratio and rotor speed has been investigated.

The restoring force acts in direction of eccentricity and can decrease indirectly the stability limit. The cross force is linear to eccentricity and increases with the pressure ratio. Despite the fact that the length of the seal is large the effect of inlet swirl has a higher effect than the rotating speed. The absolute value of circumferential velocity is not decisive for the magnitude of the cross force which, is the highest in the first cavities.

The calculation of the labyrinth forces is very sensitive to friction factors. When the friction factors, which are obtained by turbulent flow computation are used as input quantities in a bulk-flow theory calculation the agreement with experimental data is fairly good.

References

[1] Baumgartner M.: *Evaluation of Exciting Forces in Turbomachinery Induced by Flow in Labyrinth Seals*. ASME Conf. on Mech. Vib. and Noise, Boston, Mass., USA, Sept. 1987, pp. 337-346.

[2] Childs D., Nelson C., Nicks C., Scharrer J., Elrod D., Hale K.: *Theory versus Experiment for the Rotordynamic Coefficients of Annular Gas Seals: Part 1 - Test Facility and Apparatus.* ASME J Tribology, Vol. 108, 1986, pp. 426-432.

[3] Childs D., Scharrer J.: *An Iwatsubo-based Solution for Labyrinth Seals. Comparison to Experimental Results.* J. Eng. for Gas Turbines and Power, Vol. 108, 1986, pp. 599-604.

[4] Hauck L.: *Measurement and Evaluation of Swirl-Tip Flow in Labyrinth Seals of Conventional Turbine Stages.* NASA Conference Publication 2250, 1982, pp. 242-259.

[5] Kwanka K.: *Stability Behavior of a Three Journal Bearing Rotor System Excited by a Lateral Force.* ISROMAC-3, Dynamics (Editor J.H. Kim and W.J. Wang), Honolulu, Hawaii, USA, April 1990, pp. 387-400.

[6] Leie B., Thomas H.-J.: *Self-excited Rotor Whirl Due to Tip-Seal Leakage Forces.* NASA Conference Publication 2133, 1980, pp. 303-316.

[7] Nordmann R., Massmann H.: *Identification of Stiffness, Damping and Mass Coefficients for Annular Seals.* IMechE, Paper C 280/84, 1984, pp. 159-166.

[8] Nordmann, R., Weiser, P.: *Evaluation of Rotordynamic Coefficients of Look- Trough Labyrinth by Means of a Three Bulk Flow Model.* NASA Conference Publication 3122, 1990, pp. 147-163.

[9] Nordmann R., Dietzen, F.: *A 3D Finit-Difference Method for Calculating the Dynamic Coefficients of Seals.* ISROMAC-2, Honolulu, Hawaii, 1988

[10] Ortinger W.: *The Calculation of Friction Factors in a Labyrinth Seal by Means of Turbulent Flow Computation.* ISROMAC - 4, Honolulu, Hawaii, USA, April 1992, pp. 340-349.

[11] Steckel J.: *Experimentelle Untersuchungen zum Durchfluß- und Radialkraftverhalten einer Labyrinthdichtung.* Dissertation TU München, 1993.

[12] Thieleke G., Stetter H.: *Experimental Investigations of Exciting Forces Caused by Flow in Labyrinth Seals.* NASA Conference Publication 3122, 1990, pp. 109-134.

AN EXPERIMENTAL STUDY OF DYNAMIC CHARACTERISTICS OF LABYRINTH SEAL

Takuzo Iwatsubo, Koji Fukumoto, and Hideyuki Mochida
Kobe University
Rokkodai-cho, Nada-ku
Kobe, Japan

Abstract

The fluid force due to labyrinth seal sometimes makes the turbomachineries unstable under higher rotating speed, higher pressure and higher power. Therefore, it is important to predict the magnitude and the direction of the fluid force and to evaluate the stability of the rotor system in design process.

Then, this paper shows the experimental results of the fluid force induced by a straight labyrinth seal and the rotordynamic coefficients calculated from the fluid force. Influences of the number of fins under the rotating speed, whirling speed, inlet pressure, inlet tangential velocity are mainly investigated on a stability of the rotor system.

The results show that increase of the number of fins makes the fluid force small and the rotor system stable, an increase of inlet pressure makes the fluid forces large and an increase of inlet tangential velocity makes the rotor system unstable.

Introduction

Labyrinth seal are used as the non-contact type seals between rotor and stator of the fluid turbomachineries, such as a gas turbine and a compressor. To improve the efficiency of these fluid turbomachineries, inlet pressure of the working fluid and rotating speed of the rotor tend to become higher while the clearance of labyrinth seal is designed narrow to prevent for the leakage flow. As the result of using such a high performance machineries, unstable vibrations of the rotor may occur and they may draw an industrial important problem. The labyrinth seal is considered as one of the cause of these vibration problems.

Unstable vibration induced by the labyrinth seal was first pointed out by Alford[1], and after that it has been studied by many investigators. Among them, Benckert & Wachter[2] had interested in the dynamic characteristics and they measured the hydraulic spring coefficients by using the static method. On the other hand, Wright[3] investigated the instability condition of rotors induced by the labyrinth seal force for two seal strips model under many test conditions and also measured the destabilizing fluid force which included the damping coefficient. Childs & Scharrer[4][5] presented the set of dynamic data in which inlet tangential velocity as well as vibratory frequency were adequately controlled. They reported directly measured force data for 16-tooth on stator seal and on rotor seal, and obtained good correlation to theory on the effect of some of the parameters. Scharrer[6] investigated the effect of the number of fins on the static and dynamic characteristics of labyrinth seals theoretically.

The Influences of the rotating speed, inlet pressure and inlet tangential velocity have been already investigated. But the influence of the number of fins have not been experimentally investigated yet. The purpose of this paper is to investigate the influences of the number of fins under the rotating speed, whirling speed, inlet pressure, inlet tangential velocity on a stability of the rotor system.

The fluid force is measured under the condition of both rotating and whirling motions of the rotor. The rotordynamic coefficients, which represent the flow induced force of labyrinth seal by the function of velocity and displacement, are obtained.

Test Facility

The test facility to measure the fluid force is shown in figure 1. In this figure the rotor is driven by the three-phase motor⑨. The rotor is supported at the left and right sides by the eccentric bearings. The dimensions and directions of both eccentricities are set to be equal. Therefore, the rotor is whirled by the rotation of the eccentric bearing. The eccentric bearings are driven by the three-phase motor⑩ through the timing-belt and pulley⑪. Since the rotor and the eccentric bearing are driven by different motors, the rotor can be whirled in the same direction(forward) and in the opposite direction(backward), and these rotating and whirling speeds are continuously changed from 200(rpm) to 2000(rpm).

The working fluid is compressed by the compressor⑭ and transported from the air-tank⑯ into the test casing through the regulator⑬. The test seals are changeable by changing seal② and③. The detail seal dimension in this test is shown in table 1.

The rotating speed of the rotor is measured by the pulse notched on the coupling. The whirling speed of the rotor is measured by the pulse of the balance weight⑧.

The fluid forces generated in the labyrinth seal are measured by the pressure transducers as shown in figure 2 and six loadcells which directly support the seal as shown in figure 3. By measuring the force with six loadcells it is possible to measure the lateral force and moment. The measured signal current is sent to the AD converter through the D.C. amplifier and is analyzed. Figure 7 shows the data flow chart.

Analysis of Measured Data

Figure 4 shows the definition of displacement, velocity and flow induced forces.

(a) Data analysis of the pressure transducers

Since the data measured by the pressure transducers are the pressure distributions around the rotor, we can obtain the fluid forces by integrating the pressure distributions around and along the rotor.

It is assumed that the circumferential pressure distribution is elliptic and the center of it is O' as shown in figure 5. Thus, the circumferential pressure distribution in the i th chamber $P_i(\theta, t)$ is given as;

$$P_i(\theta, t) = \overline{P}_i + \Delta P_i \cdot \cos(\Omega t - \theta + \phi_i) \tag{1}$$

where $\overline{P}_i$ is the magnitude of steady pressure in the ith chamber, ΔP_i is the magnitude of the pressure fluctuation in the ith chamber and ϕ_i is the phase of the fluid force relative to the rotor displacement. The x and y direction components of the fluid force in the ith chamber are obtained by using Eq.(1) and considering the condition that the eccentric direction of the rotor agrees with x direction, that is, $t = 0$, the folllowing equations are obtained.

$$Fx_i = -\int_0^{2\pi} P_i(\theta, t) \cdot Ptg \cdot Rs \cdot \cos\theta d\theta$$

$$= -\pi \cdot Rs \cdot Ptg \cdot \Delta P_i \cos\phi_i \tag{2}$$

$$Fy_i = -\int_0^{2\pi} P_i(\theta, t) \cdot Ptg \cdot Rs \cdot \sin\theta d\theta$$

$$= -\pi \cdot Rs \cdot Ptg \cdot \Delta P_i \sin\phi_i \tag{3}$$

where Rs is the rotor radius, Ptg is the seal pitch. Then, since the overall fluid forces generated in the labyrinth seal are calculated by adding the fluid force in each chamber, the following equations are obtained.

$$Fx = -\pi \cdot Rs \cdot Ptg \cdot \sum_{i=1}^{n} \Delta P_i \cos\phi_i \tag{4}$$

$$Fy = -\pi \cdot Rs \cdot Ptg \cdot \sum_{i=1}^{n} \Delta P_i \sin\phi_i \tag{5}$$

where n is the number of fins.

(b) Data analysis of the loadcells

The fluid forces are calculated by dividing the each forces f_j measured by six loadcells into x, y components and adding the divided force components in the each direction. That is to say, the fluid forces Fx, Fy is calculated by the following equations;

$$Fx = \frac{2}{3}\sum_{1}^{6} f_j \cdot \cos(\alpha_j) \tag{6}$$

$$Fy = \frac{2}{3}\sum_{1}^{6} f_j \cdot \sin(\alpha_j) \tag{7}$$

where α_j is each loadcell's setting angle.

Then, using these forces measured by loadcells, moment can be calculated.

Figure 6 shows the definition of the moment generated in the labyrinth seal. The moment are defined by Kanemori[9] as following equations;

$$Mx = (Fy_{in} - Fy_{out}) \cdot \frac{L_b}{2} \tag{8}$$

$$My = -(Fx_{in} - Fx_{out}) \cdot \frac{L_b}{2} \tag{9}$$

where Mx, My is the moment with regard to the x and y axes, respectively, Fx_{in}, Fy_{in} are forces in x and y directions measured by inlet side loadcells, Fx_{out}, Fy_{out} are forces in x and y directions measured by outlet side loadcells and L_b is the distance between the inlet side and the outlet side loadcells.

The rotordynamic coefficients are defined by the following equations.

$$-\begin{Bmatrix} Fx \\ Fy \end{Bmatrix} = \begin{bmatrix} K_{xx} & K_{xy} \\ K_{yx} & K_{yy} \end{bmatrix} \begin{Bmatrix} x \\ y \end{Bmatrix} + \begin{bmatrix} C_{xx} & C_{xy} \\ C_{yx} & C_{yy} \end{bmatrix} \begin{Bmatrix} \dot{x} \\ \dot{y} \end{Bmatrix} \tag{10}$$

where (x, y) are the rotor displacement, (F_x, F_y) are the x and y direction components of the reaction force acting on the rotor, and $(K_{xx}, K_{xy}, K_{yx}, K_{yy})$ and $(C_{xx}, C_{xy}, C_{yx}, C_{yy})$ are the stiffness and damping, respectively.

For small motion about a centered position, Eq.(10) is rewritten simpler as follows;

$$-\begin{Bmatrix} Fx \\ Fy \end{Bmatrix} = \begin{bmatrix} K_{xx} & K_{xy} \\ -K_{xy} & K_{xx} \end{bmatrix} \begin{Bmatrix} x \\ y \end{Bmatrix} + \begin{bmatrix} C_{xx} & C_{xy} \\ -C_{xy} & C_{xx} \end{bmatrix} \begin{Bmatrix} \dot{x} \\ \dot{y} \end{Bmatrix} \tag{11}$$

For centered position, the rotor displacement (x, y) are described as;

$$x = e\cos(\Omega t) \tag{12}$$

$$y = e\sin(\Omega t) \tag{13}$$

where e is the eccentricity of the rotor.

Substituting Eq.(12), Eq.(13) into Eq.(11) and considering the condition that the eccentric direction of the rotor agrees with x direction, that is, $t = 0$,the folllowing equations are obtained.

$$-\frac{Fx}{e} = C_{xy}\Omega + K_{xx} \tag{14}$$

$$-\frac{Fy}{e} = C_{xx}\Omega - K_{xy} \tag{15}$$

$$F = \sqrt{Fx^2 + Fy^2} \quad , \quad \phi = \tan^{-1}\left(\frac{Fy}{Fx}\right) \tag{16}$$

where F is the magnitude of the fluid force.

As we obtain the fluid forces for 10 whirling speed Ω in experiments, we can determine the rotordynamic coefficients by the least squares method.

Experimental Results

The range of parameter in this test is shown in table 2. The ratio of inlet tangential velocity to rotor surface velocity (inlet tangential velocity ratio) is shown table 3. Figure 8 shows the comparison of the fluid force versus whirling/ rotating ratio between the loadcell data and the pressure transducer data. This figure also shows the magnitude and the phase of the fluid force measured by two ways almost agree. After this, the data put in this paper are the one measured by the loadcells.

Fluid Forces and Moment Results

Figure 9 shows an effect of the rotating speed on the fluid force changing whirling/rotating speed. The figure shows that the tangential force,Fy, is sensitive to the change of rotating spped. The figure also shows that the radial force,Fx, changes very much from negative to positive with increasing the number of fins and is constant with increasing the rotating speed.

Figure 10 shows an effect of the inlet pressure on the fluid force changing whirling/rotating speed. The figure shows that the tangential force,Fy, increases with increasing inlet pressure and the radial force,Fx, increses the magnitude with increasing inlet pressure. The figure also shows that the tendencies of the tangential force and the radial force to the number of fins is constant.

Figure 11 shows an effect of the inlet tangential velocity on the fluid force changing whirling/
rotating speed. The figure shows that the tangential force,Fy, increases from negative to positive with increasing the inlet tangential velocity from negative to positive and the radial force Fx changes the slope from right-up to right-down with increasing the inlet tangential velocity. As shown in figure 13 which are caluculated results, inlet tangential velocity has a greater influence on the seal which have less seal fins.

Figure 12 shows an effect of the number of fins on the fluid force changing whirling/rotating speed. The figure shows that the tangential force,F_y, is sensitive to inlet tangential velocity with decreasing the number of fins, the radial force,F_x, increases from the negative to positive with increasing the number of fin in every inlet tangential velocity.

Figure 14 shows an effect of rotating speed on the moment changing whirling/rotating speed. The figure shows that the moment with regard to the x axis,Mx, is constant with increasing the rotating speed and the number of fins, the moment with regard to the y axis,My, is constant with increasing the rotating speed and the magnitude of My increases with increasing the number of fins.

Figure 15 shows an effect of the inlet pressure on the moment changing whirling/rotating speed. The figure shows that the moment with regard to the x axis,Mx, is constant with increasing the inlet pressure and the number of fins, the maginitude of moment with regard to the y axis,My, increases with increasing the number of fins.

Figure 16 shows an effect of the inlet tangential velocity on the moment changing whirling/
rotating speed. The figure shows that the moment with regard to the x axis changes negative to positive with increasing the inlet tangential velocity in every seal, the magnitude of moment with regard to the y axis increases with increasing the number of fins.

Figure 17 shows an effect of the number of fins on the moment changing whirling/rotating speed. The figure shows that the moment with regard to the x axis changes negative to positive with increasing the inlet tangential velocity, the moment with regard to the y axis changes very much with increasing the number of fins.

Rotordynamic Coefficients Results

Figure 18 show that an effect of the number of fins on the rotordynamic coefficients changing the inlet pressure.

The figure 18(a) shows that the magnitude of direct stiffness increases with increasing inlet pressure. This figure also shows that direct stiffness changes positive to negative with increasing the number of fins.

The figure 18(b) shows that an increase of inlet pressure makes the magnitude of cross-coupled stiffness large. This figure also shows that the magnitude of cross-coupled stiffness decreases with increasing the number of fin.

The figure 18(c) shows that direct damping increases with increasing inlet pressure.

The figure 18(d) shows that an increase of inlet pressure has no influence on cross-coupled damping. The magnitude of cross-coupled damping increases with increasing the number of fins.

Figure 19 show that an effect of the number of fins on the rotordynamic coefficients changing the inlet tangential velocity.

The figure 19(a) shows that a change of inlet tangential velocity has no influence on direct stifness. The figures also show that direct stiffness changes from positive to negative with increasing the number of fins.

The figure 19(b) shows that cross-coupled stiffness changes from negative to positive with increasing inlet tangential velocity, and the quantity of cross-coupled stiffness fluctuation in this time is greater with decreasing the number of fins.

The figure 19(c) shows that direct damping is constant with increasing inlet tangential velocity.

The figure 19(d) shows that cross-coupled damping changes from negative to positive with increasing inlet tangential velocity and the quantity of cross-coupled damping fluctuation in this time is greater with decreasing the number of fins.

Figure 20 shows that an effect of the number of fins on 'whirl frequency ratio' changing the inlet tangential velocity.

Whirl frequency ratio f is defined by Childs[4] as following equation;

$$f = \frac{K_{xy}}{C_{xx}\Omega}$$

where Ω is rotor whirling frequency, $K_{xy}/C_{xx}\Omega$ is the ratio of the destabilizing influence of the cross-coupled stiffness and the stabilizing influence of direct damping. From viewpoint of stability, a less value of whirl frequency ratio is desireble.

The figure shows that 11 fin's labyrinth seal has a greater whirl ratio than other seals in giving inlet tangential velocity. And this agrees with Scharrer's theoretical results[6].

Conclusion

In this paper, the fluid force, moment and the rotordynamic coefficients are experimentally obtained. The conclusions are as follows;

1. The labyrinth seal which has less seal fins is sensitive to increase of inlet tangential velocity.

2. The labyrinth seal which has less seal fins is not always stable.

3. Tangential fluid force increases with increasing inlet pressure and inlet tangential velocity.

4. Radial fluid force increases the magnitude with increasing inlet pressure.

5. Moment with regard to the x axis is sensitive to the change of inlet tangential velocity.

6. Moment with regard to the y axis increases the magnitude with increasing the number of fins.

7. Cross-coupled damping and stiffness increases from negative to positive with increasing inlet tangential velocity.

8. Direct damping is constant with increasing inlet tangential velocity.

References

1. Alford,J.S. :" Protecting Turbomachinery from Self-Excited Rotor Whirl " Trans. ASME, J. Eng. Power, Oct. 1965, pp. 333-344

2. Benckert,H. ;and Wachter,J :" Flow Induced Spring Coefficients of Labyrinth Seals for Application in Rotor Dynamics " NASA Lewis,Conference Publication 2133, Rotordynamic Instability Problems in High-Performance Turbomachinery, 1980, pp. 189-212

3. Wright,D.V. :" Air Model Tests of Labyrinth Seal Force on Whirling Rotor " Trans. ASME, J. Eng. Power, Oct. 1978, pp. 533-543

4. Childs,D.W.;and Scharrer,J.K. :" Experimental Rotordynamic Coefficient Results for Teeth-on-Rotor and Teeth-on-Stator Labyrinth Gas Seals " Trans. ASME, J. Eng. Gas Turbines Power, Oct. 1986, pp. 599-604

5. Childs,D.W. ;and Scharrer,J.K. : " Theory Versus Experiment for the Rotordynamic Coefficients of Labyrinth Gas Seals:Part 2 – A Comparison to Experiment ", Trans. ASME, J. Vib. Acoust. Stress Reliab. Des., July 1988, pp.281-287

6. Scharrer,J.K. : " Rotordynamic Coefficients for Stepped Labyrinth Gas Seals ", Rotordynamic Instability Problems in High-Performance Turbomachinery 1988, pp.177-195

7. Kanemitsu,Y. ;and Osawa,M. : " Cross-Coupled Aerodynamic Forces on a Whirling Rotor of Labyrinth Seals (Straight-Type Labyrinth Seals) " Trans. JSME, Vol.51, No.472 , Dec. 1985, pp. 3407-3412

8. Kanemitsu,Y. ;and Osawa,M. : " Cross-Coupled Aerodynamic Forces on a Whirling Rotor of Labyrinth Seals (2nd Report, Interlocking-type Seals) " Trans. JSME, Vol.54, No.498 , Feb. 1988, pp. 346-352

9. Kanemori,Y. ;and Iwatsubo,T. : " Expeimental Study of the Dynamic Characteristics of a Long Annular Seal (Fluid Force due to Conical and Cylindrical Whirl) " (in Japanese) Trans. JSME, Vol.56, No.532 , Dec. 1990, pp. 56-64

10. Iwatsubo,T. ;and Sugimaru,N. : " Experiment for Unstable Fluid Force in Labyrinth Seals " (in Japanese) Trans. JSME, No.910-39 Vol.B , Jul. 1991, pp. 202-206

Table.1 Seal Dimension in this study

Seal Clearance	mm	0.5
Fin Height	mm	4.0
Seal Pitch	mm	6.0
Fin Thickness	mm	1.0
Rotor Radius	mm	80.0
Number of Fin		5,11,21
Fin Side		On Stator

Table.2 Experiment Condition

Rotating Speed	ω(rpm)	1000 , 1500 , 2000
Whirling Speed	Ω(rpm)	$\pm$ (0.2 , 0.4 , 0.6 , 0.8 , 1.0) $\times\omega$
Inlet Pressure	P_{in}(MPa)	0.2 , 0.3 , 0.4
Inlet Tangential Velocity	w_{in}(m/s)	-34.0 , 0 , 34.0

Table 3 Preswirl Velocity Ratio

	-34.0(m/s)	0(m/s)	34.0(m/s)
1000(rpm)	-4.06	0.0	4.06
1500(rpm)	-2.70	0.0	2.70
2000(rpm)	-2.03	0.0	2.03

1	Rotor	4	Loadcell
2	Labyrinth Seal (on stator)	5	Swirl Chamber
		6	Air Entrance
3	Labyrinth Seal (on rotor)	7	Air Exit
		8	Balance Weight

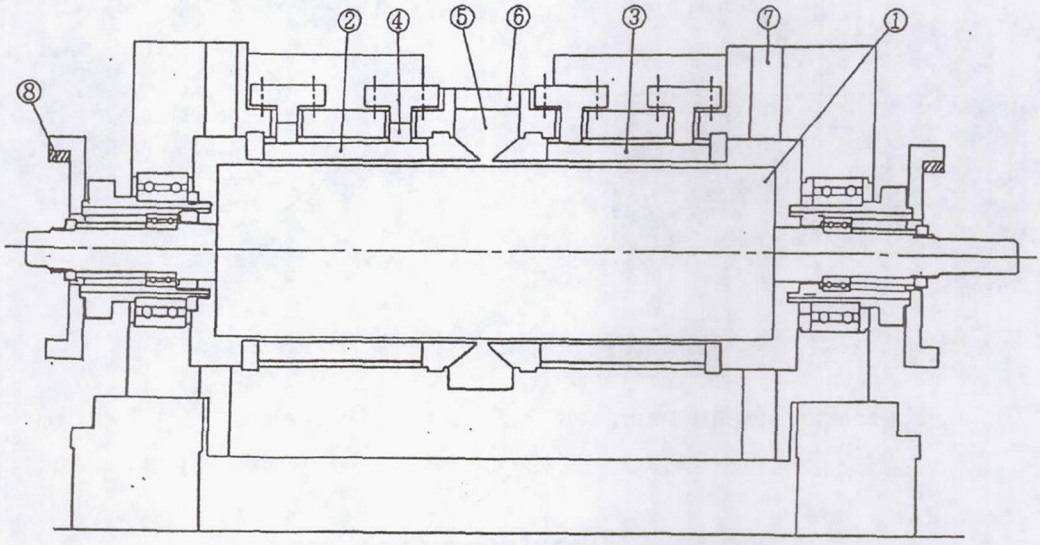

(a) Cross section of test facility

9	Three-phase Motor (for rotation)
10	Three-phase Motor (for whirl)
11	Timing-belt and Pulley
12	Universal Joint
13	Regulator
14	Compressor
15	Valve
16	Air Tank

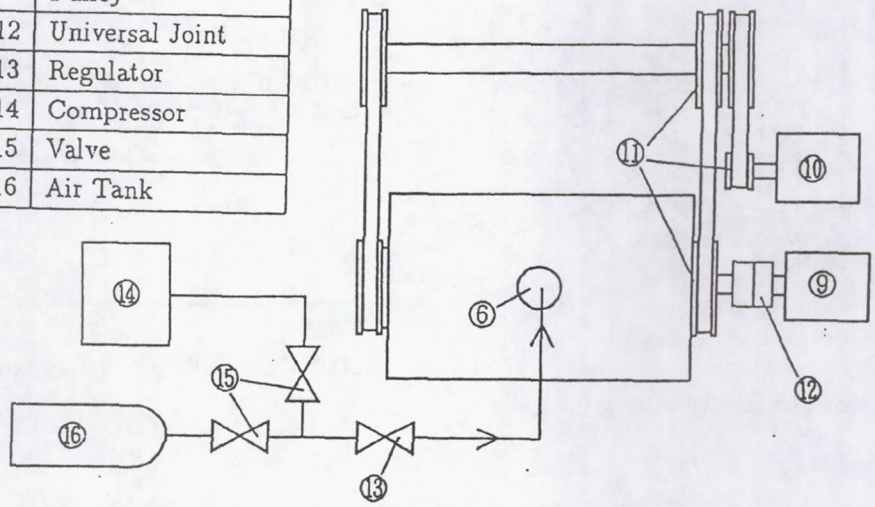

(b) Test facility layout

Fig. 1 Test facility

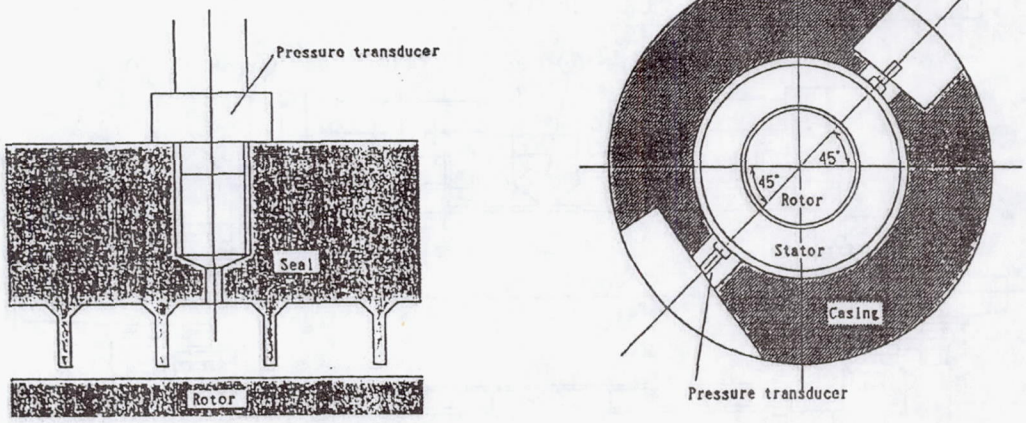

(a) Detail of hole for pressure transducer (b) Cross section of test facility setting pressure transducers

Fig. 2 Setting of pressure transducer

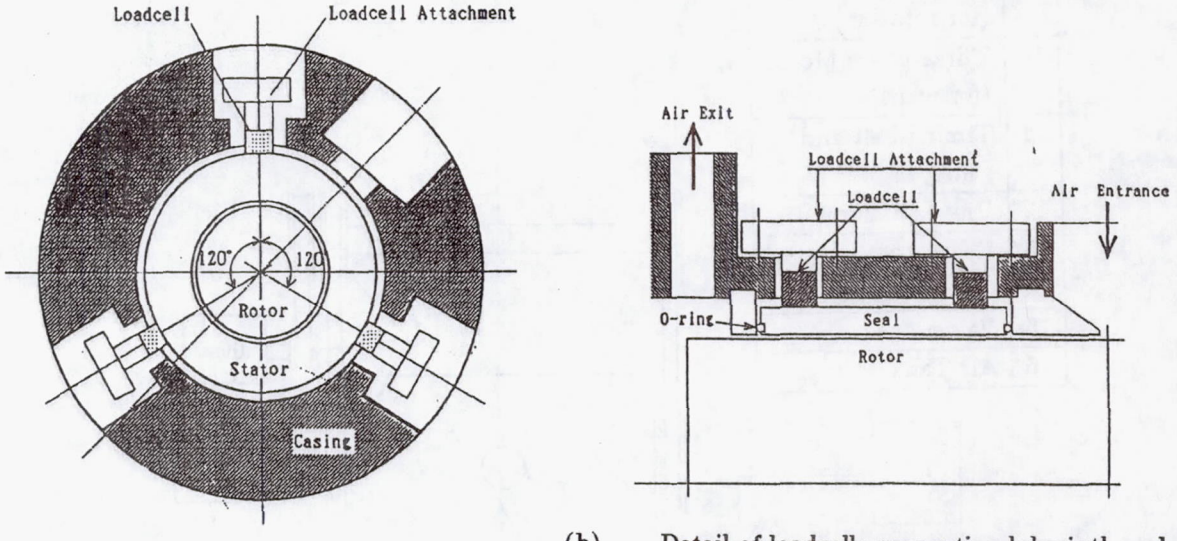

(a) Cross section of test facility setting loadcells (b) Detail of loadcells supporting labyrinth seal

Fig. 3 Setting of loadcells

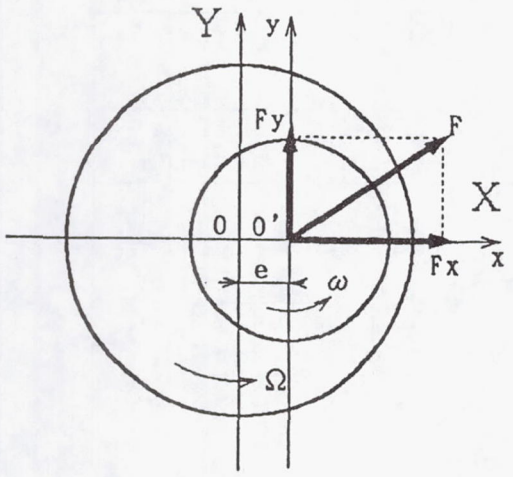

Fig. 4 Definition of displacement, velocity and flow induced force

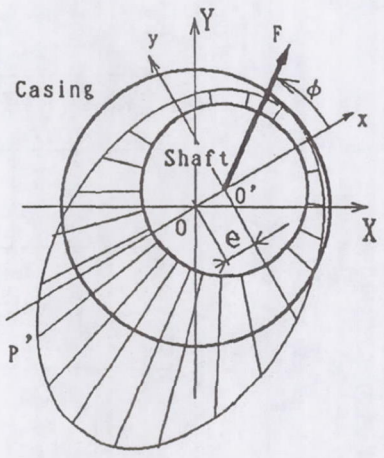

Fig. 5 Pressure distribution around the rotor

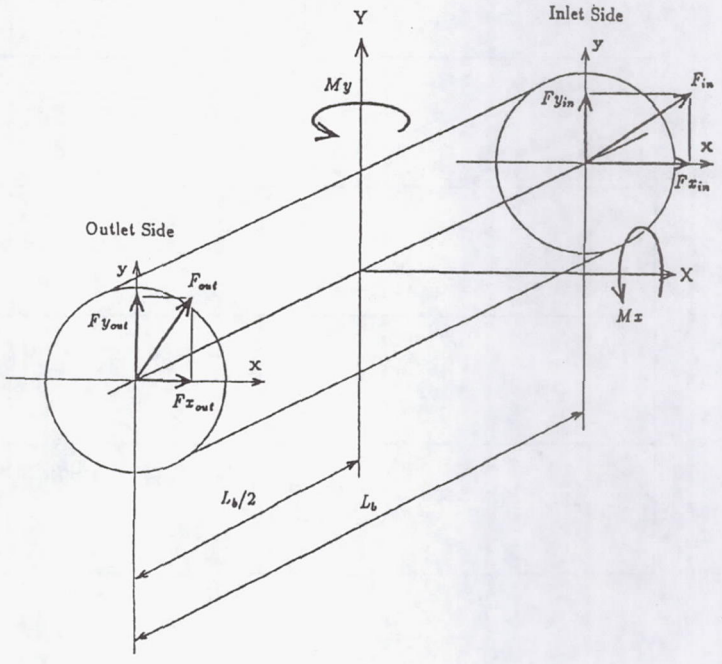

Fig. 6 Definition of flow induced force and moment

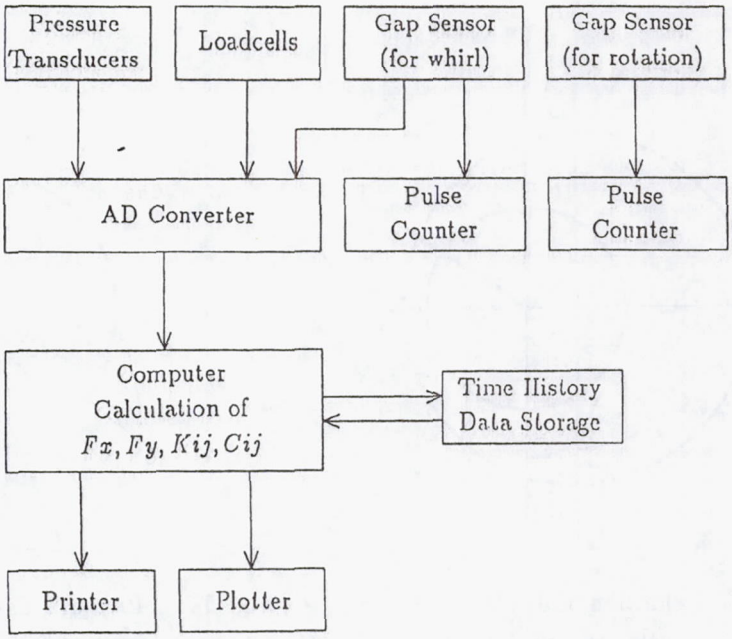

Fig. 7 Data flow chart

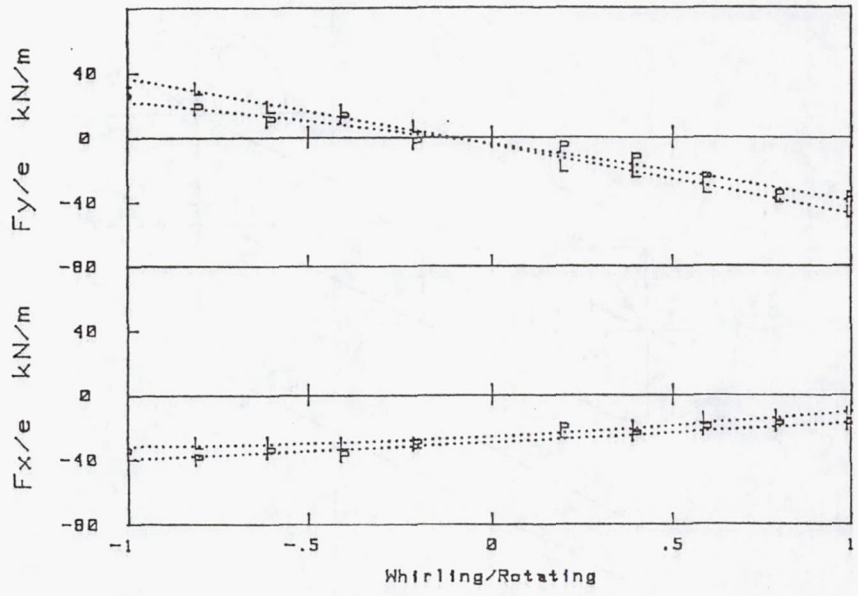

Fig. 8 Comparison of loadcells data and pressure transducers data

$\omega = 2000$ (rpm) , $P_{in} = 0.1$ (MPa) , $w_{in} = 0$ (m/s)

L : Loadcells data

P : Pressure transducers data

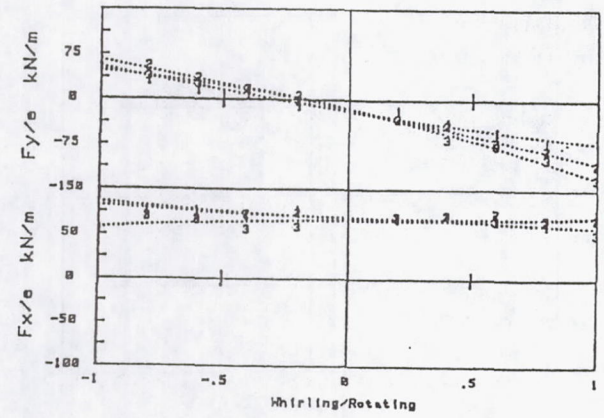

(a) 21 fins

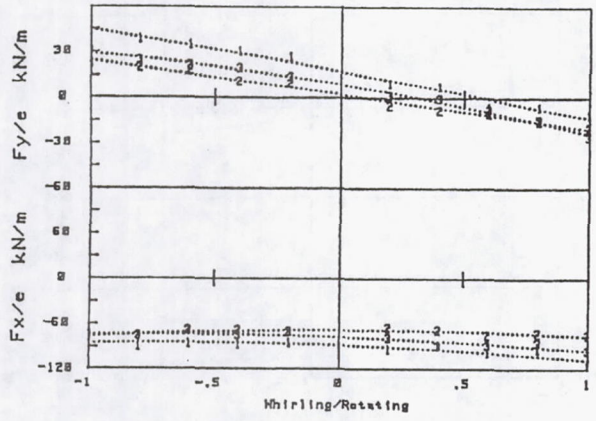

(b) 11 fins

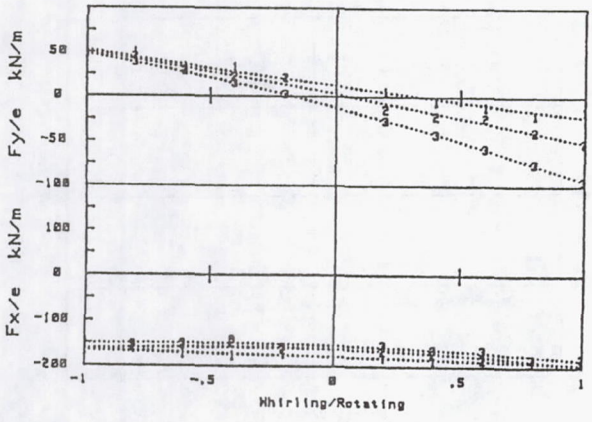

(c) 5 fins

Fig. 9 Fluid force versus whirling/rotating ratio
(Parameter: Rotating speed)
$P_{in} = 0.4$ (MPa) , $w_{in} = 0$ (m/s)

1 : 1000(rpm)
2 : 1500(rpm)
3 : 2000(rpm)

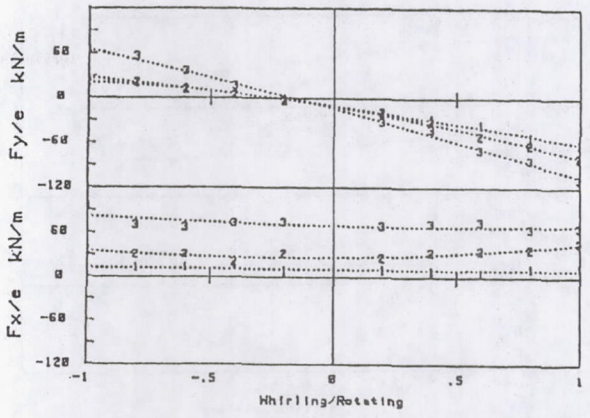

(a) 21 fins

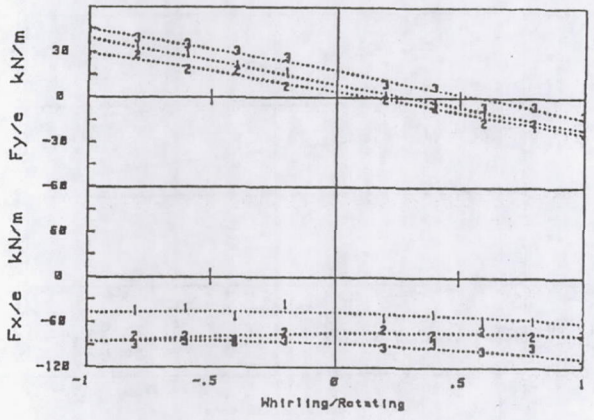

(b) 11 fins

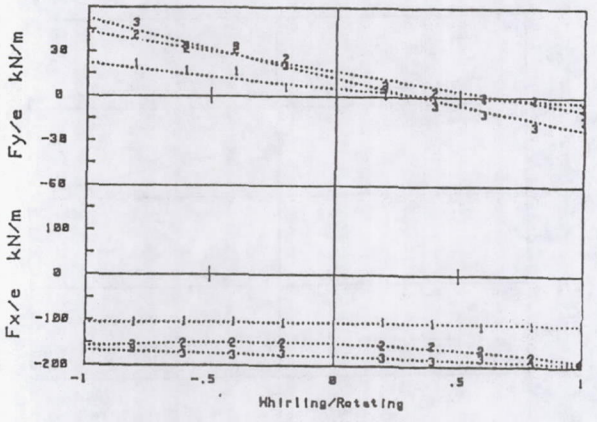

(c) 5 fins

Fig. 10 Fluid force versus whirling/rotating ratio
(Parameter: Inlet Pressure)
$\omega = 1000$ (rpm) , $w_{in} = 0$ (m/s)

1 : 0.2 (MPa)
2 : 0.3 (MPa)
3 : 0.4 (MPa)

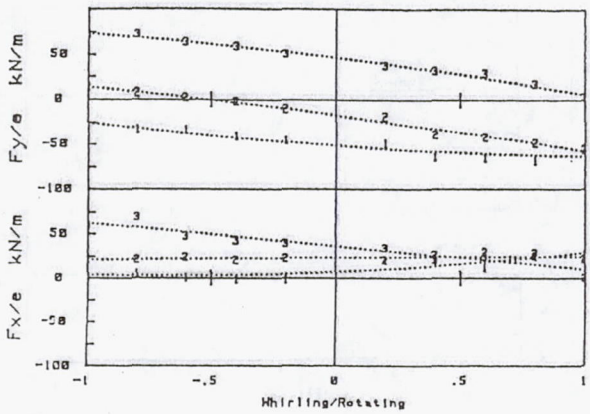

(a) 21 fins

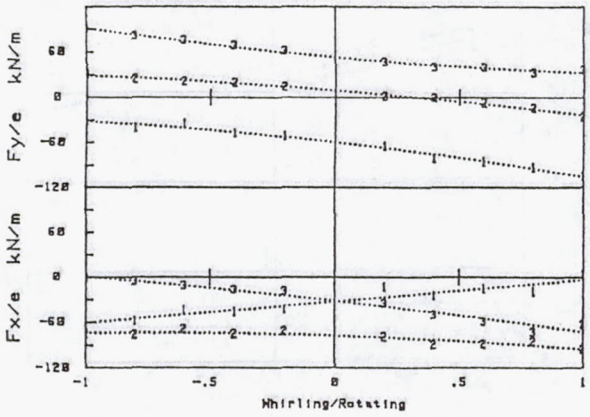

(b) 11 fins

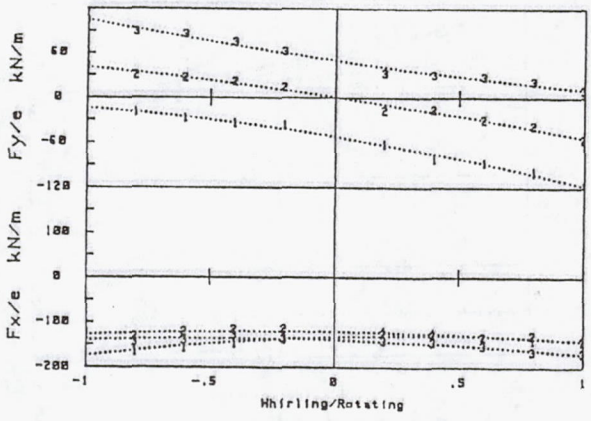

(c) 5 fins

Fig. 11 Fluid force versus whirling/rotating ratio
(Parameter: Inlet tangential velocity)
ω = 2000 (rpm) , P_{in} = 0.2 (MPa)

1 : -34.0 (m/s)
2 : 0.0 (m/s)
3 : 34.0 (m/s)

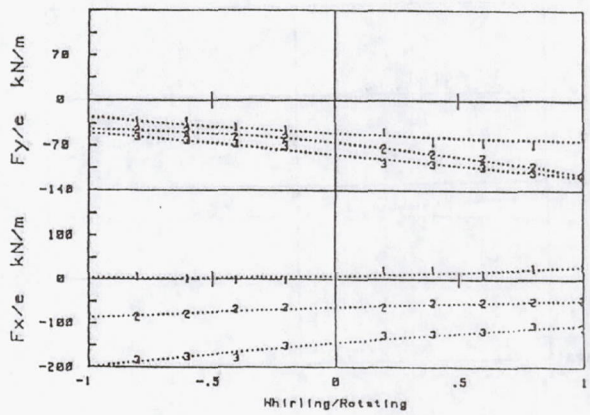

(a) w_{in} = -34.0 (m/s)

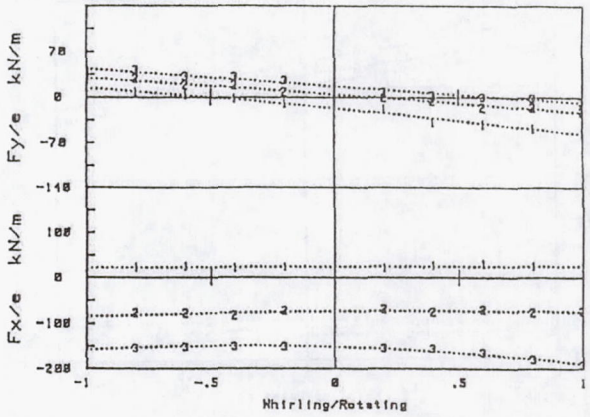

(b) w_{in} = 0.0 (m/s)

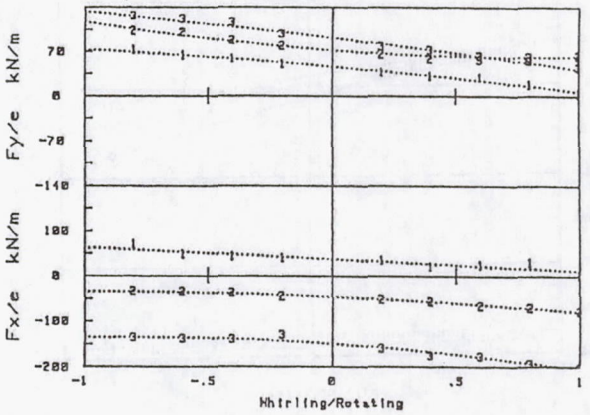

(c) w_{in} = 34.0 (m/s)

Fig. 12 Fluid force versus whirling/rotating ratio
(Parameter: The number of fins)
ω = 1000 (rpm) , P_{in} = 0.3 (MPa)

1 : 21 fins
2 : 11 fins
3 : 5 fins

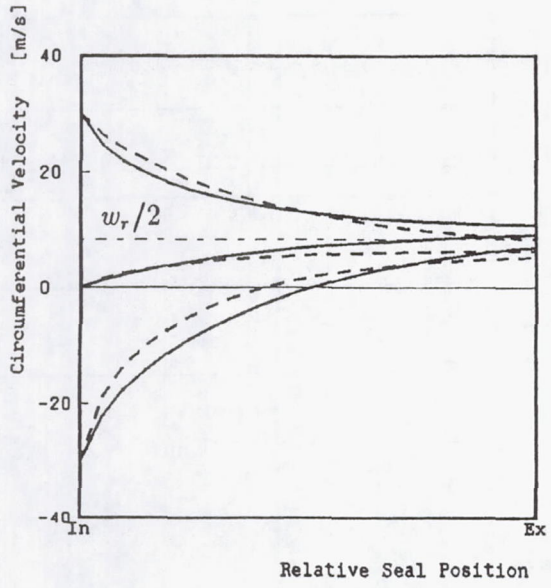

(a) 21 fins

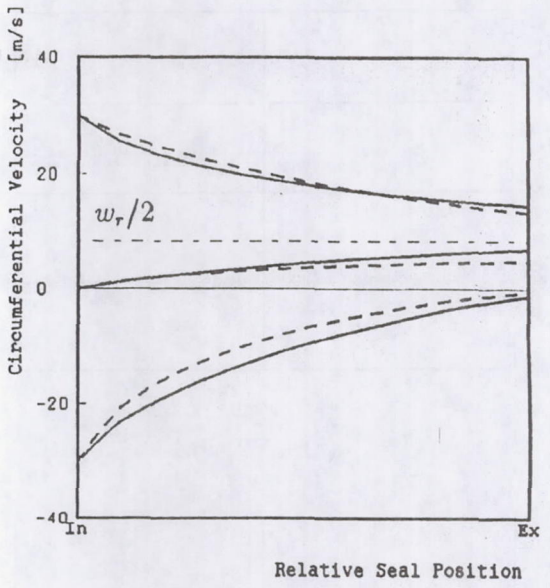

(b) 11 fins

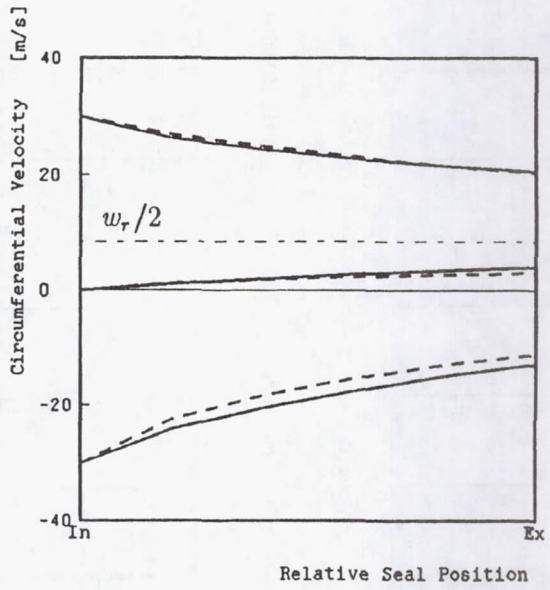

(c) 5 fins

Fig. 13 Circumferential velocity versus seal length
(Parameter: fin side)
ω = 2000 (rpm) , P_{in} = 0.3 (MPa)

——— Teeth on stator
– – – – – Teeth on rotor

w_r : Rotor surface speed

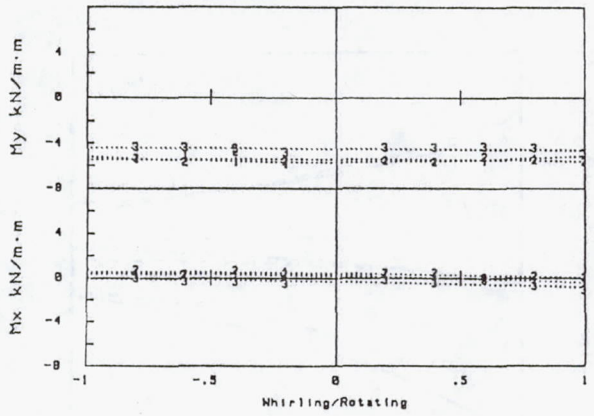

(a) 21 fins

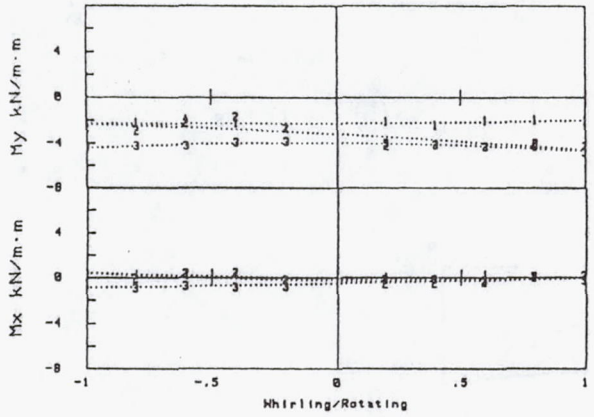

(b) 11 fins

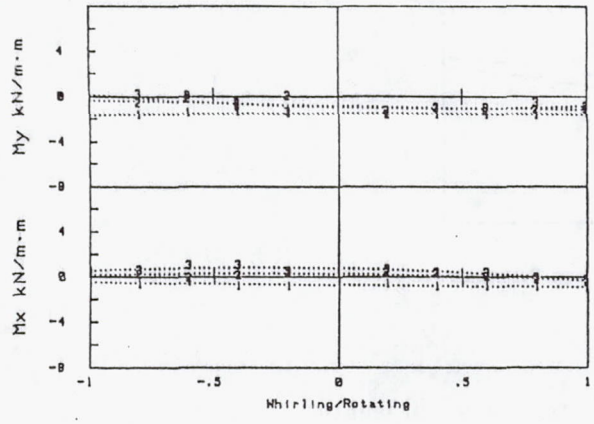

(c) 5 fins

Fig. 14 Moment versus whirling/rotating ratio
(Parameter: Rotating speed)
$P_{in} = 0.3$ (MPa) , $w_{in} = 0$ (m/s)

1 : 1000(rpm)
2 : 1500(rpm)
3 : 2000(rpm)

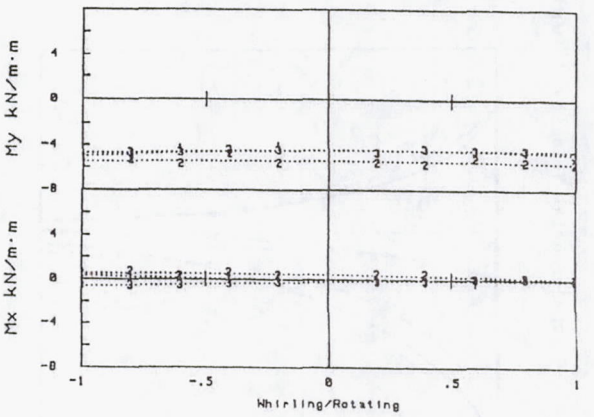

(a) 21 fins

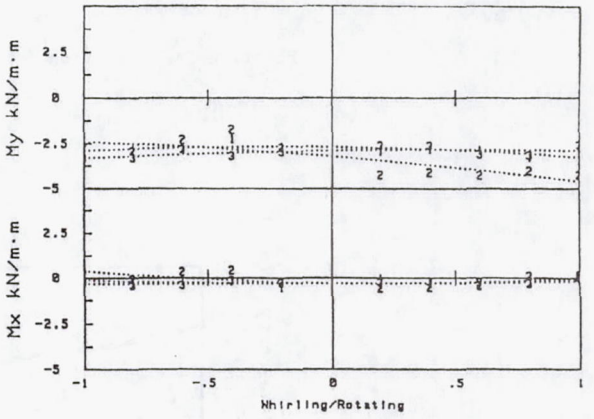

(b) 11 fins

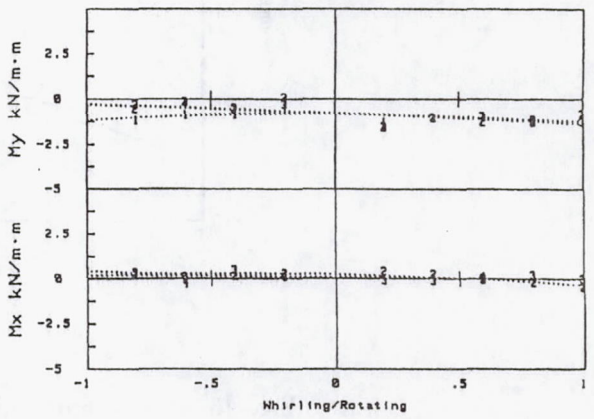

(c) 5 fins

Fig. 15 Moment versus whirling/rotating ratio
(Parameter: Inlet pressure)
$\omega = 1500$ (rpm) , $w_{in} = 0$ (m/s)

1 : 0.2 (MPa)
2 : 0.3 (MPa)
3 : 0.4 (MPa)

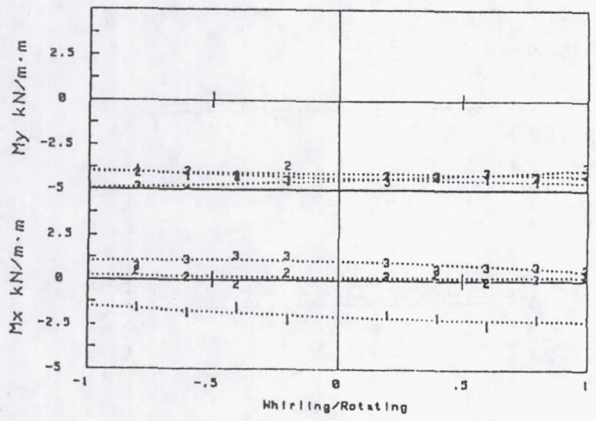

(a) 21 fins

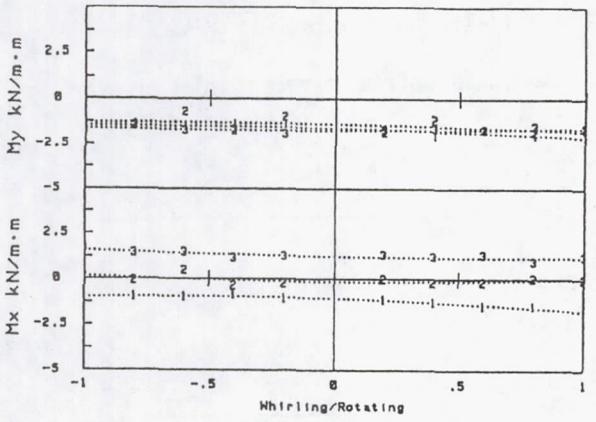

(b) 11 fins

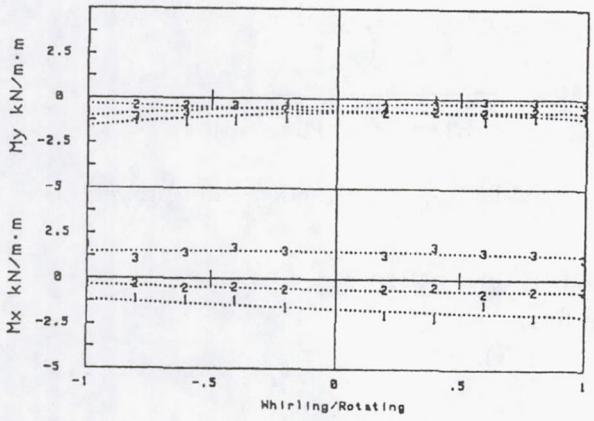

(c) 5 fins

Fig. 16 Moment versus whirling/rotating ratio
(Parameter: Inlet tangential velocity)
ω =1000 (rpm) , P_{in} = 0.2 (MPa)

1 : -34.0 (m/s)
2 : 0.0 (m/s)
3 : 34.0 (m/s)

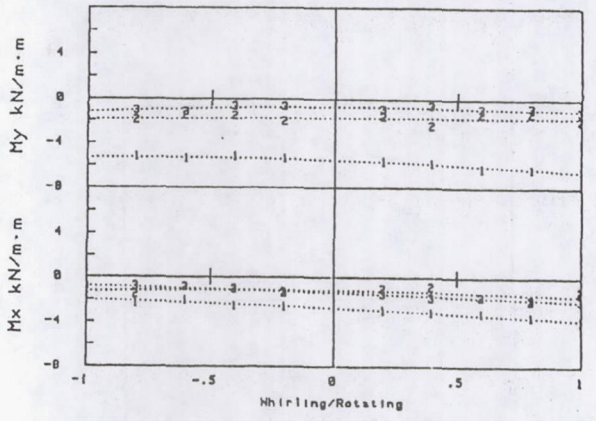

(a) w_{in} = -34.0 (m/s)

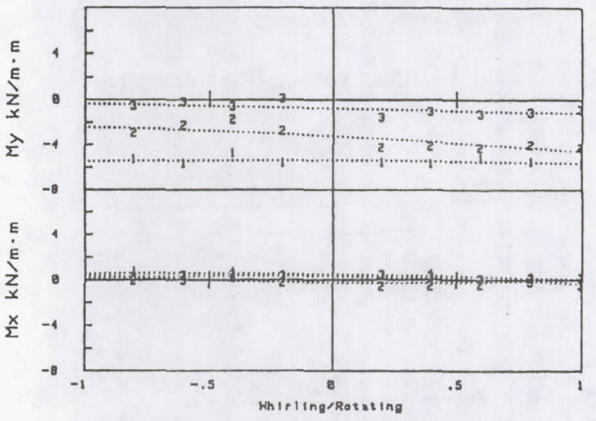

(b) w_{in} = 0.0 (m/s)

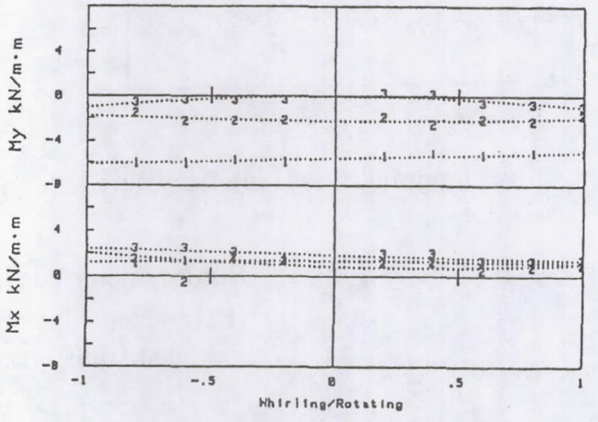

(c) w_{in} = 34.0 (m/s)

Fig. 17 Moment versus whirling/rotating ratio
(Parameter: The number of fins)
ω = 1500 (rpm) , P_{in} = 0.3 (MPa)

1 : 21 fins
2 : 11 fins
3 : 5 fins

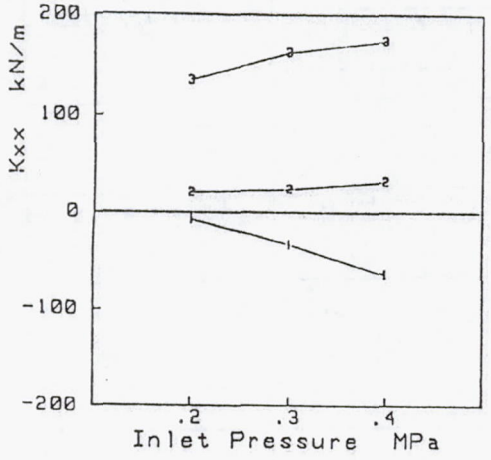

(a) Direct stiffness versus inlet pressure

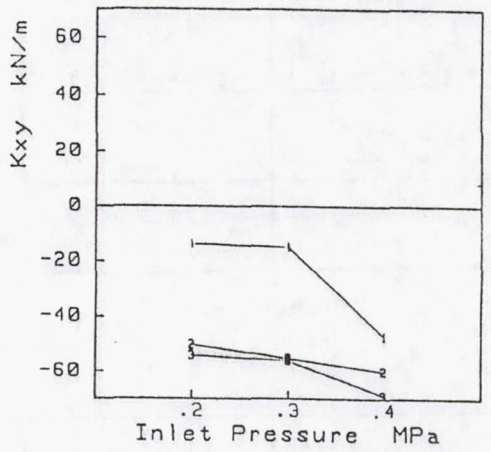

(b) Cross-coupled stiffness versus inlet pressure

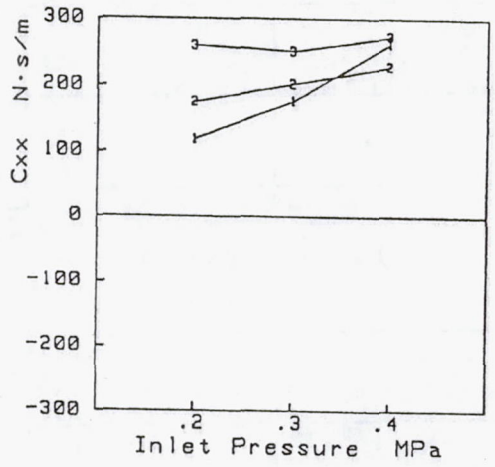

(c) Direct damping versus inlet pressure

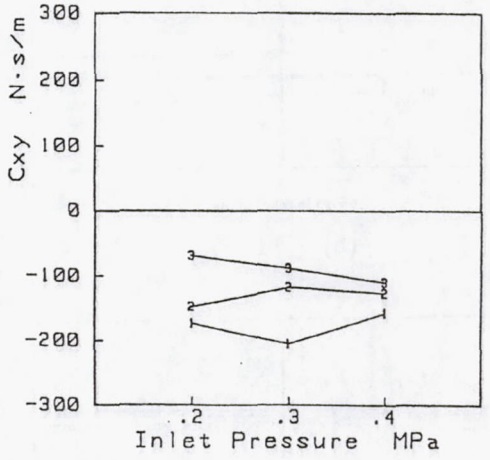

(d) Cross-coupled damping versus inlet pressure

Fig. 18 Rotordynamic coefficients versus inlet pressure
(Parameter: The number of fins)
ω = 2000 (rpm) , w_{in} = -34.0 (m/s)

1 : 21 fins
2 : 11 fins
3 : 5 fins

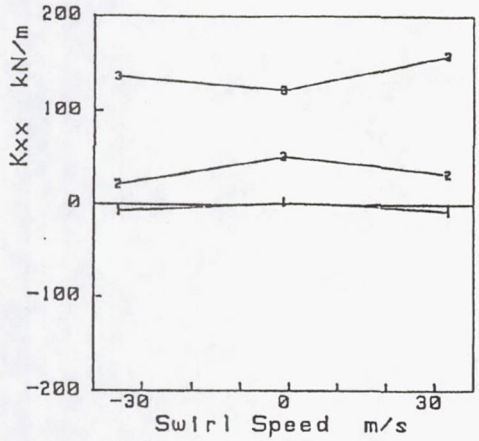

(a) Direct stiffness versus inlet tangential velocity

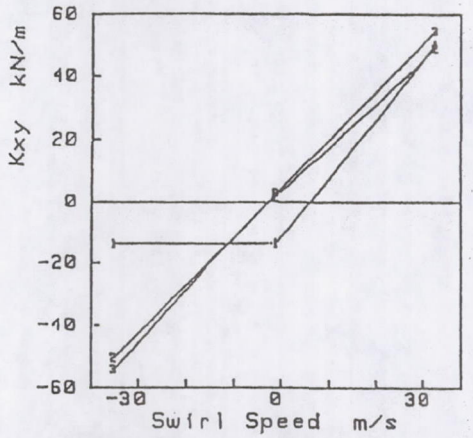

(b) Cross-coupled stiffness versus inlet tangential velocity

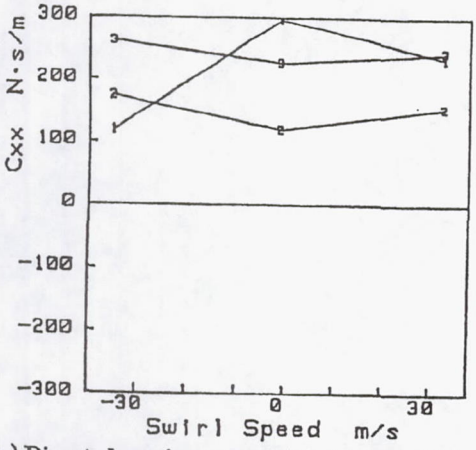

(c) Direct damping versus inlet tangential velocity

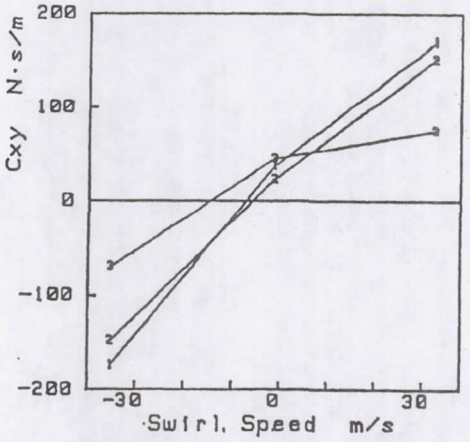

(d) Cross-coupled damping versus inlet tangential velocity

Fig. 19 Rotordynamic coefficients versus inlet tangential velocity
(Parameter: The number of fins)
ω = 2000 (rpm) , P_{in} = 0.2 (MPa)

1 : 21 fins
2 : 11 fins
3 : 5 fins

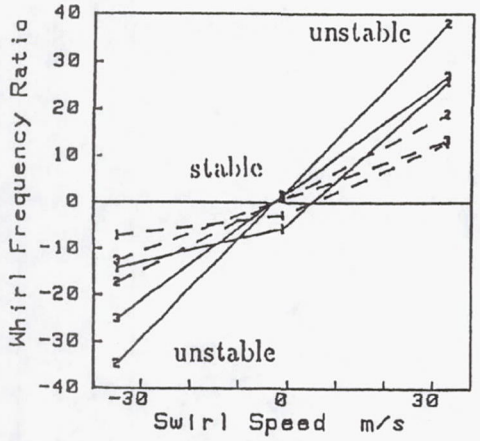

——— Ω = 500 (rpm)
– – – – Ω = 1000 (rpm)

1 : 21 fins
2 : 11 fins
3 : 5 fins

Fig. 20 Whirl frequency ratio versus inlet tangential velocity
(Parameter: The number of fins)
ω = 2000 (rpm) , P_{in} = 0.2 (MPa)

Session III

General

Preceding Page Blank

OCCURRENCE OF SUB-SYNCHRONOUS VIBRATION IN A MULTISTAGE TURBINE PUMP AND ITS PREVENTION

Yanosuke Kanai and Shinobu Saito
Ishikawajima-Harima Heavy Industries Co., Ltd.
Tokyo, Japan

1. Introduction

It is evidently because of the critical importance the prevention of occurrence of vibration for high-load rotary machinery assumes in ensuring reliability of a plant as a whole that so many investigations and studies have been done on the matter. Regarding the sub-synchronous vibration with which we are concerned here, the self-excited vibration such as due to oil whipping, forced vibration such as due to propagating stall, and non-linear vibration such as due to sub-harmonic resonance have been studied quite well. However, we note that the case of self-excited vibration, whose frequency has been found to be generally less than one half the revolution number, is rather complex, because there can be any number of exceptions. For example, when the labyrinth seal is responsible for the self-excited vibration, its frequency is often entirely unrelatable to the machine revolution, and one of us (S. S.) has found for rotating hollow shafts that are partially filled with liquid that the frequency is over one half of the revolution[1].

As for the pump vibration, on the other hand, the vibration due to non-steady fluid force that arises mainly in the partial flow domain[2,3] and the kind that is induced by the fluid force acting within propagating stall are by no means uncommon.

In this paper, we intend to present and discuss a peculiar vibration that we have encountered in a multistage turbine pump. The pump in question was serving an active power plant in a part that was a veritable "heart" of the entire plant, and the major vibration component was of about 80% frequency of the revolution.

At first, the propagating stall was thought to be responsible, but the absence of higher harmonics made this presumption untenable. Or else, even though we were aware of previous reports that dealt with seemingly similar mechanical vibration troubles[4,5], we found these investigations to offer no clear diagnosis nor suggest simple remedial measures.

It is for these reasons that we have attended the problem from the start. Through fundamental tests and experiments, we have been able to gain several insights into the nature of this anomalous vibration, determine whereat the fluid force that caused such a vibration was given rise to[6,7], as well as devise countermeasures that turned out to be quite effective. These are, then, the subjects of the present paper.

2. Service History of the Pump

The pump that gave rise to anomalous vibration was a high pressure multistage turbine pump serving a seven-train, 1,000 MW combined cycle

Preceding Page Blank

power plant. The duty of the pump was to transfer the feedwater from low pressure drum to high pressure drum for the high/low dual line steam generator of the gas turbine waste heat recovery unit. It is illustrated in Fig. 1 in a vertical cross sectional view, and its major specifications are given in Table 1.

Since it was commissioned in 1985, this power plant has served quite well as a "peak shaver" in the entire power network for its ease of rapid start-and-stopping and high efficiency over a wide load range. Therefore, the plant was often shut down when the total power demand was low, e.g., at nights and over weekends, so much so that, even though its annual operation time was no more than about 5,000 hours on average, the number of start-and-stopping amounted to about 100 an year.

This is a rather demanding service condition for any machine to operate under, and for this pump it is particularly so on starting, when the pump suction condition varies from 3 to 5 kgf/cm^2 and 100 to 130°C to 10 to 11 kgf/cm^2 and 180°C in only about one hour of time. To bear up to such a large and fast thermal expansion taking place within the pump, we had a highly skilled worker assemble the shaft seal using a precision formed gland packing made of Graphoil, yet a lifetime of one to one and a half year was all that could be achieved.

To ameliorate on the maintenance work, the shaft seal was changed to mechanical seal in 1988, whereupon the pump ran into a serious vibration trouble: the vibration, which was about 10 μm p-p on modification, became 156 μm p-p in ten days when the pump was forced to shut down. The accumulated operation time to stoppage was 130 h, in which the pump went through four start-and-stops.

The pump was restarted on temporary repair, which consisted in replacing substantially all the parts within the casing, including impellers, shaft, and wearing rings, with the reserves, but the vibration grew with time rapidly as shown in Fig. 2; the vibration level was deemed to have reached the danger lever in a week, after an accumulated running time of about 100 h and eight start-and-stops. The vibration situation at the time of this second shutdown is given in Table 2.

The vibration behaviors and the damage the pump sustained as found on opening inspection are as follows:

1) the main component of vibration was 40 to 42 Hz (i.e., about 80% of the revolution number), and its amplitude was far greater than that of the synchronous component (49.5 Hz);
2) no higher harmonics were found;
3) the amplitude increased with operation time;
4) it grew also with increasing flow rate, and the frequency, too, changed, though slightly; and
5) the stationary wearing rings were seen to have worn greatly, but only in the vicinity of their bottom parts, as illustrated in Fig. 3.

3. Fundamental Shop Testing

Trying to reproduce the accident, we have assembled a pump at a shop on a reserve pump of the identical dimensions with the damaged pump's impellers, shaft, wearing rings, etc., and run a series of vibration tests. From the histories of vibration changes and frequency analyses thus acquired, which are exemplified in Figs. 4 and 5, following observations were made:

1) the same anomalous vibration with about 80% of the synchronous frequency for the main component did also occur in this isolated pump;
2) even though the initial vibration amplitude observed at shop was smaller than that found on the site, this was thought ascribable to the better initial concentricity between the rotor and the casing realized at shop; this advantage was lost rapidly so that the vibration amplitude approached that which was experienced actually within a comparatively short period of time, however;
3) the vibration amplitude increased greatly with the rise of suction temperature, due most probably to aggravation of concentricity between rotor and casing; and
4) for the same suction temperature, the amplitude tended to grow with the elapse of operation time, due most probably to aggravating concentricity under progressive wear.

Based on these observations, we have deducted the following as the major mechanism of vibration:

1) the elimination of the gland packing, which used to work as a bearing to support the shaft also, has brought about increase in the natural deflection of the shaft, which in turn has brought about increase in the bearing pressure on the intermediate wear rings located in between the shaft bearings;
2) the wear rings that are used in the interstage seals are all provided with a groove so as to prevent seizing by foreign matter floating in the feedwater, so that its load bearing capacity was not large enough to start with for a job of hydraulic bearing;
3) for this reason, metallic contact took place at or near the wearing ring bottom to wear them according to the amount of shaft's natural deflection;
4) excessive wear of the wearing ring has resulted in excessive eccentricity between the stationary part and the rotating part; and
5) this brought about increase in the fluid force acting on the rotor, giving rise to self-excited vibration of the about 80% the synchronous frequency in question, which in its turn accelerated the wear, thereby constituting a vicious cycle of events.

The fact that the observed wear was mainly in the direction of static loading as shown clearly in Fig. 3 attests to this theory.

4. Remedial Measures and Their Effects

A) The First Countermeasure Taken

Having analyzed the cause of the anomalous vibration as described above, we have decided to form the wearing rings eccentrically so that their inner diameters should change in alignment with the natural deflection of the shaft, or, in other words, so that no eccentricity may arise between the rotating part and the stationary part at each interstage seal.

The performance of the pump thus modified is shown in Fig. 6-a, where we see that, although the vibration characteristics have been greatly improved as a whole, the 80% synchronous frequency still persists, though now with an amplitude that is much smaller than that of the synchronous component. Also, a tendency, even though slight, for the amplitude to increase with time was noted. For these reasons, we have judged this measure to be insufficient for the long-term operation expected of the pump on the site.

B) The Complementary Measure

It is known that in many cases what induces self-excited vibration for a rotating shaft is swirl of the fluid, and that the vibration caused by labyrinth seal can be prevented most effectively by preventing the swirl from flowing into the seal. Translated into the case at hand, this would mean that it is the swirling flow that leaks back into the suction direction from the tip of an impeller blade presumably at the accelerated peripheral velocity by the impeller shroud that should be reduced.

Thereupon, we have provided each impeller with a swirl breaker at the outer space of its shroud as depicted in Fig. 7. The result was rather remarkable: as shown in Fig. 6-b, the troublesome sub-synchronous vibration has disappeared completely. The pump modified thus and installed for the same duty as before has been working in the plant already for over two years now, giving off no sign of anomalous vibration of any kind.

Even then, we recognize one more point that remains to be clarified; according to Childs, who has analyzed the fluid forces generated outside of the shroud[6,7], such a force does not induce self-excited vibration directly, but his conclusion had the constant concentricity between the rotor and the stator as its base. This may mean that once the concentricity is lost, the same fluid force will become able to induce a self-excited vibration. In fact, we have observed during the shop testing that vibration did indeed grow when the concentricity was degraded on purpose. We intend to continue the study on this matter.

References

1) S. Saito and T. Someya, "Self-Excited Vibration of a Rotating Shaft Partially filled with Liquid," ASME Paper 79-DET-62.

2) P. Hergt and P. Krieger, "Radial Forces in Centrifugal Pumps with Guide Vanes," PIME, 1969-70, p. 101.

3) H. Kanai, Y. Kawata, and t. Kawatani, "Experimental Research on the Hydraulic Excitation Force on the Pump Shaft," ASME Paper 81-DET-71.

4) H. F. Black, "Lateral Stability and Vibrations of High Speed Centrifugal Pump Rotors," IUTAM Symp. on Dynamics of Rotor, Lyngby, Denmark, Aug.., 1974.

5) R. D. Brown, *Vibration Phenomena in Large Centrifugal Pumps*

6) D. W. Childs, "Fluid-Structure Interaction Forces at Pump-Impeller-Shroud Surface for Rotor Dynamic Calculation," ASME Vibration Conf., 1987, p. 263.

7) J. P. Williams and D. W. Childs, "Influence of Impeller Shroud Forces on Turbopump Rotor Dynamics," ASME Vibration Conf., 1989, p. 41.

Table 1 Principal specifications of the pump

Type	Horizontally Split Type Turbine Pump
No.of Stages	9
Capacity	3.63 m3/min
Total Head	930 m
Rotaing Speed	2970 RPM
Moter Output	820 KW
Suction Pressure	2 -- 14 kg/cm2
Suction Temperature	Room Temp. -- 180 Deg.C
Pumping Liquid	Boiler Water
Shaft Seal	Gland Packing (GRAFOIL)

Table 2 Vibration characteristics of the as-damaged pump determined at the bearing housing

Pump Flow Rate (%)	Generator Output (MW per Train)	Pump's Bearing Housing Vibration			
		Synchronous Component		Sub-synchronous Component	
		Freq.(Hz)	Amp(μmP-P)	Freq.(Hz)	Amp.(μmP-P)
45	0	49.5	3.0	41.8	12.0
60	70	49.5	7.2	39.8	28.8
90	150	49.5	5.8	39.3	35.6
100	165	49.5	1.4	39.8	40.0

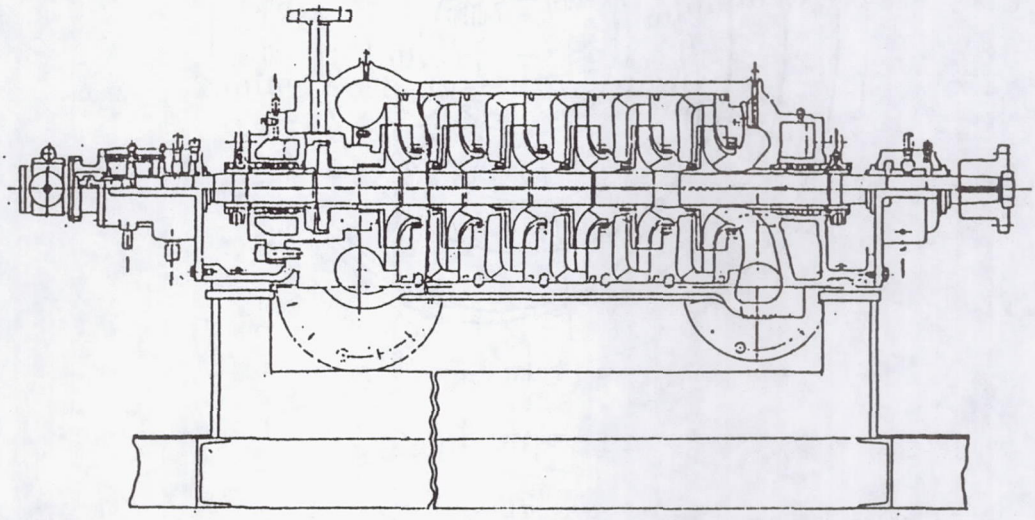

Fig. 1 Multistage turbine pump

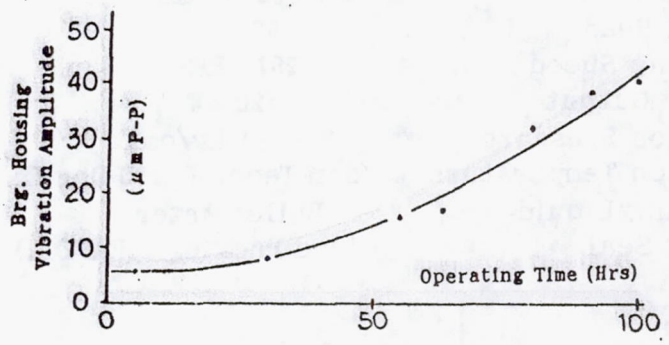

Fig. 2 Growth of vibration

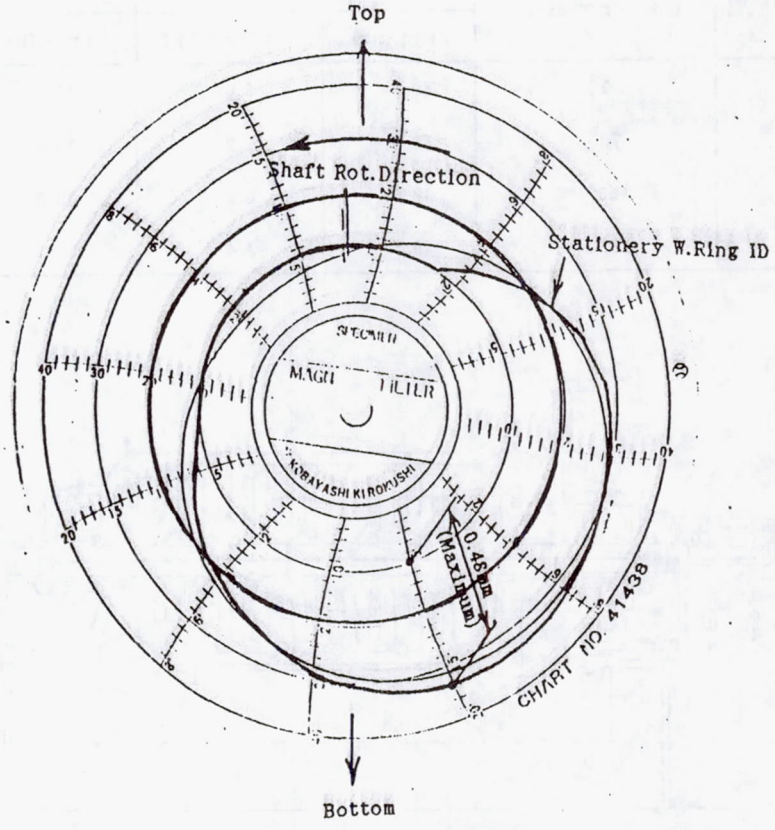

Fig. 3 Profile of a wearing ring as determined on pump shutdown

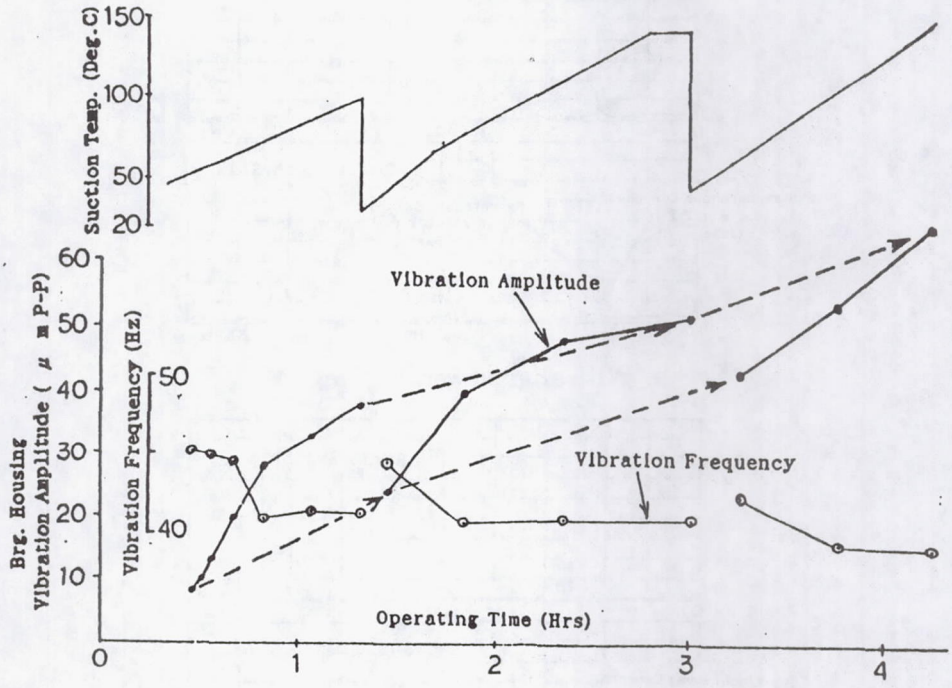

Fig. 4 Growth of sub-synchronous vibration

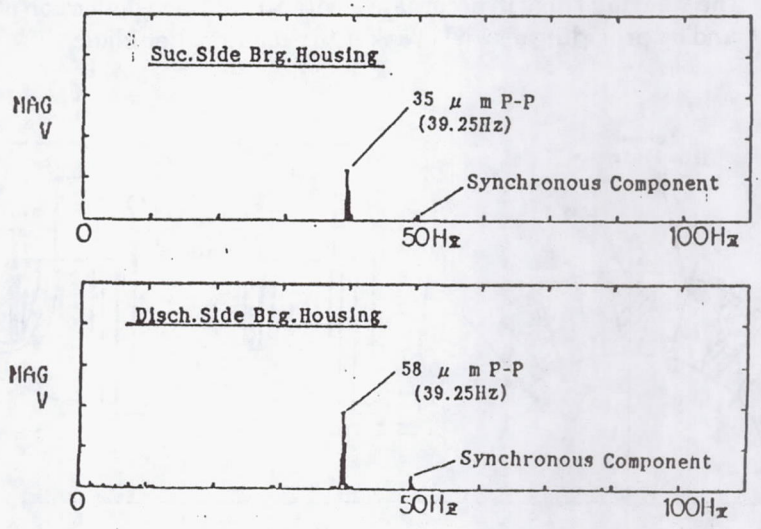

Fig. 5 Power spectrum of the sub-synchronous vibration

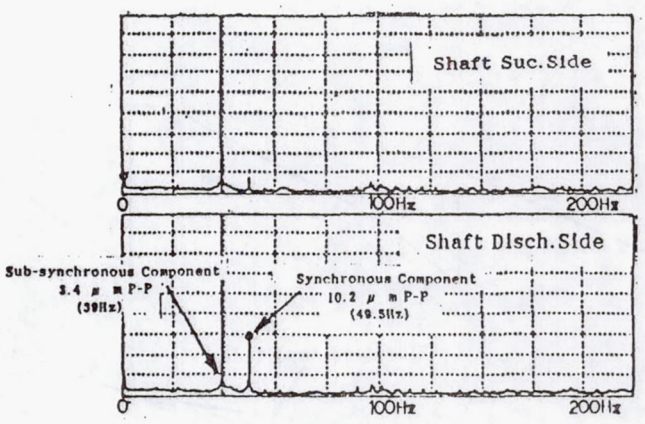

a. With aligned wearing rings

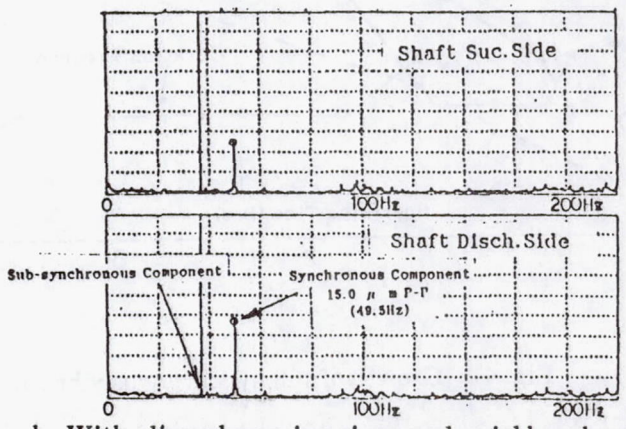

b. With aligned wearing rings and swirl breakers

Fig. 6 Successful suppression of the sub-synchronous vibration by aligning the wearing rings in accordance with the natural deflection of shaft and by providing a swirl breaker to each impeller blade

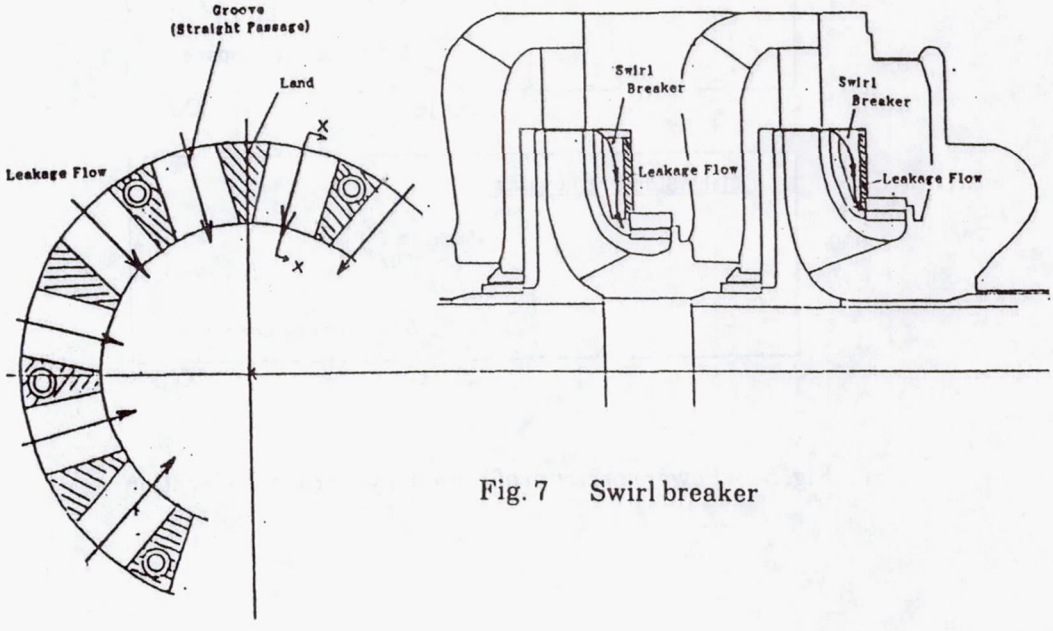

Fig. 7 Swirl breaker

A REVIEW OF VIBRATION PROBLEMS IN POWER STATION BOILER FEED PUMPS

David France
Weir Pumps Limited
Glasgow, Scotland

SYNOPSIS

Boiler Feed Pump reliability and availability is recognised as important to the overall efficiency of power generation. Vibration monitoring is often used as part of planned maintenance. This paper reviews a number of different types of boiler feed pump vibration problems describing some methods of solution in the process. It is hoped that this review may assist both designers and users faced with similar problems.

1.0 INTRODUCTION

The reliability of the boiler feed pump in modern power stations is seen as essential to ensure the overall availability of the power generating plant and is often included in the rotating machinery vibration monitoring programme practised by many power station maintenance departments. The vibration characteristics of a boiler feed pump can be complex and difficult to understand and it is the purpose of this paper to describe typical vibration mechanisms at work to assist those engaged in the diagnosis of problems. Case studies are presented which demonstrate the following types of vibration responses:-

1. Forced
2. Resonant
3. Self excited
4. Transient
5. Cavitation

Some solutions to these are described in the hope that these may assist both designers and users faced with similar problems.

2.0 FORCED VIBRATIONS

Forced vibrations - vibrations which are produced by the application of an external set of oscillatory forces.

Centrifugal pump vibrations are often described as being either synchronous or non-synchronous with respect to its operating speed. Usually synchronous is taken to mean the vibration component at the pump's operating speed although it is often taken to include any harmonic of this. Nonsynchronous covers all other frequency components. Synchronous forcing influences may arise from either mechanical or hydraulic sources of unbalance. Mechanical sources are fairly well understood because of the general similarity in other types of rotating equipment. Hydraulic sources may result from either casting asymmetries or partial

blockage of impeller passageways by, for example, ingress of foreign matter. Generally speaking the magnitude of hydraulic unbalance generated by an impeller is greater than the residual mass unbalance component. A Japanese investigator, ref.1, measured the hydraulic force as a function of flowrate, fig.1. The maximum value of unbalance qualities of G2.5 - G6.3. Practical experience suggests that precision castings for the impellers of high speed feed pumps could offer a hydraulic reduction of possibly an order of magnitude. Nonsynchronous forced responses usually arise at part load operations where hydraulic forces, generated by recirculating flows within the impeller or diffuser, may give rise to irregular or cyclic low frequency excitations. These have been discussed previously by a number of authors, ref.2, 3. A typical example of this can be seen in fig.2, where the shaft displacement increased threefold between the design flowrate and the recirculation flow quantity.

Substantial forces may be generated due to interaction of the impeller blades with guide vanes in either the upstream or downstream flow fields. These forces manifest themselves as vibration at the impeller blade number and blade number harmonics. The main area of concern to any maintenance engineer is undoubtedly the effect that high blade vibration levels may have on the reliability of the pump. Understandably the worry is whether or not this may result in a fatigue failure of impeller or diffuser. General machinery vibration guidelines offer little help in this regard except to suggest that vibration monitoring may help to identify deterioration. Data from the field serve to illustrate the difficulties of interpretation further. For example, blade vibration levels of 15mm/sec rms are not untypical on some of our boiler feed pumps yet these pumps have given many years of trouble free operation. On the other hand, impeller blade or impeller shroud failures have occurred after some 6 months to 2 years into operation yet external levels of blade vibration have been less than 2mm/sec rms. Clearly, therefore, there is not necessarily a one - one relationship between vibration level and the stress levels within the working components. Insight into generation of vibration at blade frequency and blade frequency harmonics results from the studies by Zotov, ref.4. this theory shows that it is possible to select impeller and diffuser blade number combinations to suppress the vibration at the fundamental blade frequency, or if required, at a higher blade frequency harmonic. This is indicated by the values shown in Table I. The table shows the radial vibration force frequency components relative to a unit magnitude radial interaction force between each of the impeller and diffuser blades. It is significant that the vibration of the pump casing can be minimised in this way, but care is needed to ensure that certain blade combinations do not give rise to reinforced pressure fluctuations in the fluid as could be the case with 6 x 9, and 8 x 12 blade combinations. Experimental data obtained from pumps with 7 x 12 and 7 x 13 blade combinations show encouraging correlation with theory, these also are given inTable I. Although blade numbers can have a powerful effect on the distribution of the harmonic content of the resultant blade interaction forces, the stresses induced on the individual blades are not significantly modified by the number of blades between the impeller and diffuser. The magnitude of the interaction forces are influenced by the hydraulic design, the stage power, the impeller to diffuser gap, the operating point relative to the best efficiency point and possibly the inlet guide vane geometry and upstream flow field. It seems fairly well accepted that a minimum tip gap of 3% of impeller radius, (derived empirically by Makay, ref.5.), is sensible to avoid highly stressed components. Some results of research by Weir Pumps Limited into blade combinations and tip gaps give interesting insight into such effects, fig.3a, 3b.

In 1985 an unusual blade vibration phenomenon was identified on a number of boiler feed pumps destined for an East European power station. The pumps are 4 stage boiler feed driven by steam turbines. Pump design duty is $0.36m^3$/sec at 2461m head at 5454 rpm, impeller blade number is 7 and diffuser number is 12. Tip gap is 3%. This should have resulted in low

blade rate vibration levels, yet high vibration levels were experienced on some of the pumps on the drive end bearing housing only. The vibration was only experienced over a narrow range of flow. A typical blade frequency vibration characteristic is shown in fig.4. Each pump showed similar characteristics but the vibration level on some of the pumps was only about 2.0 - 3.0mm/sec rms. Despite many hours of tests and subsequent examinations of components from a number of pumps, it was not possible to ascertain any difference which might explain the variation in vibration level. The only modification done was to eliminate the upstream inlet guide vanes to the first stage impeller, this had no effect on the magnitude of the vibration. The problem source has never properly been identified, yet the vibration levels would appear not to be detrimental to reliability as the pumps have been operating satisfactorily for more than six years.

3.0. RESONANT VIBRATIONS

Resonance - a phenomenon evident when the frequency of the disturbing force equals a natural frequency of the system.

In 1982 a resonance problem was experienced on a four turbine driven variable speed boiler feed pump, installed at Huntly Power Station, (4 x 250MW), New Zealand. The area is seismically active and the design of the pump and turbine support structure reflected the seismic requirements. The pump was centre line mounted on a baseplate which was secured to a large steel table onto which the turbine was also mounted. The steel table was supported from the floor level by a number of tall vertical metal columns, ensuring a low frequency mounting system for the equipment. A schematic is shown if fig.5. High vibration levels, in excess of 20mm/sec peak, at pump shaft frequency, were obtained at generator loading of 200-220MW, corresponding to a pump speed in the range 5300 rpm-5500rpm. Examination of the amplitude phase relationship suggested a resonance was responsible. Excitation tests were carried out with the pump stationary using an air driven rotary out of balance exciter to stimulate the structure into vibration and to examine the mode shape. These tests confirmed there was a natural frequency of the pump, but the mode shape was complex showing motion involving the pump and turbine support structure. Surprisingly, there was little or no deformation of the pump casing and pump supporting baseplate, the whole body appeared to be moving on the flexibility of the steel supports beneath the base plate. A comparison of the on load vibration characteristic compared with the vibration obtained from the air driven exciter is shown in fig.6a. Exciter tests were then carried out with one of the pumps and its baseplate secured to a concrete foundation. No evidence of any natural frequencies in the range 3000cmp - 6000cpm were found indicating that the steel support structure was important in terms of the mode of vibration of concern. A comparison of the responses on the steelwork and on the concrete floor are shown in fig.6b. The next stage of this investigation was to consider how detuning the resonant frequency could be achieved on site. Clearly a solid support for the pump bedplate would have solved the problem but it was impractical to stiffen the support steelwork sufficiently. It was decided to introduce compliance between the pump casing and the bedplate at the pump support feet. As designed the support feed slide relative to the pump baseplate on greased brass pads to accommodate thermal expansion. A modification was made as shown in fig.7, this introduced horizontal flexibility but still allowed the pump support feet to slide. On site a series of exciter experiments was carried out to optimise the flexibility of the detuning element. Once an optimum was found the pump was run up to full load to demonstrate the modification. The vibration levels were found to be a maximum of 5mm/sec peak. A comparison before and after modification is shown in fig.8.

4.0 SELF EXCITED VIBRATIONS

Self excitation - vibrations which are caused by disturbing forces which result from feedback from the motion of the vibrating object itself.

A review of self excited vibrations in centrifugal pumps has been presented in ref.6. This paper discusses a wide variety of types including the "near running speed" nonsynchronous vibrations reported by a number of authors. There have been only a few reported examples with boiler feed pumps, and then mainly outside the UK.

In the late sixties a 0.8 x running speed vibration problem was found on starting and standby boiler feed pumps at Longannet Power Station, Scotland. The high vibrations were seen over a range of operating speed from 3500 rpm - 6000 rpm as shown in fig.9. The pump was found to undergo an almost instantaneous progression from low level synchronous vibration to "foundation shaking" nonsynchronous vibration as pump speed was increased; typical of a classical self excited vibration phenomenon. The problem was related to premature wear out of the pumps internal clearances caused by intermittent low flow operation and consequential reduction in rotor stiffness. The problem was eliminated by increasing the minimum recirculating flow to eliminate the wear out problem; no further research was done at this time on what was believed to a "one off" phenomenon.

In 1978 serious problems were experienced during works testing of three pumps. Performance tests were conducted at full power and fixed speed and near running speed subsynchronous vibration was experienced. These pumps were 7 stage pumps absorbing 2230Kw at 5850 rpm. The problem was first noticed as flowrate was increased from the minimum recirculation quantity to the design flow. Shaft probes were fitted as standard and the transition from synchronous to nonsynchronous vibration was abrupt. It was also established that reducing flowrate could once again stabilise the pump. Shaft displacement levels were 75µm pk-pk at a frequency of 80Hz-84Hz giving a whirl frequency ratio of 0.82-0.86. A typical average spectrum is shown in fig.10. A 24 hour endurance test on the test bed confirmed the severity of the problem when balance drum leakage flowrates doubled and bearing housing vibrations increased fourfold. Initially it was assumed that the problem was a classical rotor instability, i.e. unstable eigenvalue. It was believed that negative stiffness and forward driving cross coupling could arise due to an impeller/diffuser interaction of the type described in (11). However, it seemed unlikely that the problem was due to an unstable eigenvalue as rotordynamic analysis predicted well damped eigenvalues even with generous allowances for impeller/diffuser interaction forces. Nevertheless, both aspects of the problem were examined, the former by a specially instrumented single stage test rig and the latter by conducting variable speed tests on one of the pumps with clearances set at design values (0.5mm) and then twice design (1mm). To assist the problem diagnosis a pair of displacement probes were installed to view the shaft motion at the balance drum as well as the bearings of the pump. The results of these tests are summarised in fig.11a and fig.11b. Tracking of the amplitude and phase of the synchronous component of shaft vibration over a speed range from 4000 rpm - 6500 rpm showed no significant phase or amplitude change which would indicate even a near proximity to a natural frequency. A similar result was obtained for both the design and twice design clearances build configurations. Rotordynamic calculations confirmed the shaft motion and phase measurements at the balance drum and bearings and absence of unstable eigenvalues. Of enormous significance was the fact that the subsynchronous component of vibration bore an almost fixed ratio with respect to speed (.85) for both clearance cases tested. The subsynchronous component was discernible down to the minimum speed tested. The test rig

comprised a single impeller and diffuser stage and was instrumented with shaft motion probes and dynamic pressure transducers to examine distributions of pressure in the diffuser inlet, impeller shroud to casing gaps and near to the impeller eye. Tests were carried out to approximately 80% pump design speed. Sum and difference measurements of two pressures at 180° at impeller eye showed a nonsynchronous frequency component which was out of phase implying a net resultant force on the impeller. This correlated extremely well with the resultant shaft motion as shown in fig.12a and fig.12b and was very similar to that obtained from the pump, fig.10. Tests subsequently confirmed that this was an impeller inlet stall which appeared to rotate relative to the impeller at a frequency equal to the difference of the synchronous and subsynchronous frequencies. The forces involved were quite small and the feedback element which was evidently present with the 7 stage pump was never reproduced on the test rig. In the final event no design changes were made to the pumps, although an impeller with revised inlet geometry had been tested successfully in the single stage test rig. There were however, significant improvements made to the build concentricity of the pump cartridge and a change to the shaft material. Tests confirmed that subsynchronous vibrations were still present but a factor of ten below synchronous amplitude levels. No change in vibration was obtained over a 48 hour endurance test at full load. The pumps have been in service for over twelve years and have given trouble free operation.

During proving tests on the prototype of a new frame size of barrel casing pump in 1987, the opportunity was taken for an in-depth examination of the effects of annular clearance wear and the influence of inlet swirl at the balance drum upon rotor dynamics and, in particular, subsynchronous vibration. The device used to control inlet swirl was similar to that described in (7). The prototype was a six stage pump with radial diffusers and a balance drum with a design maximum running speed of 5000 rpm. The design parameters of this barrel casing pump are set out in Appendix I. The materials chosen for the renewable wearing rings were chosen for their high wear resistance and freedom from galling. To maintain optimum efficiency the recommended renewal clearances are set at 1.5 times the new design clearances. It was decided to study the effects of wear up to a maximum of twice the renewable limits. The tests were carried out in the production test facilities and the pump was installed on a temporary, but substantial, support structure. The prime mover gave a variable speed capability from 3600-5500 rpm, representing 10% above pump design speed. Instrumentation was fitted to the pump to measure, head, flow, speed, loop temperature, bearing metal and oil temperatures, axial thrust, balance return line flow. Dynamic measurements taken were bearing housing vibration, (seismic), shaft to casing radial displacement and pressure fluctuations in the suction, and discharge and balance return lines. The dynamic signals were taped recorded for subsequent analysis off line. During each test discrete points were taken over the performance envelope of the pump together with data from controlled runs varying one parameter at a time and keeping others constant, e.g. varying speed at constant discharge control valve setting. The tests carried out are summarised in Table II and the incidence of subsynchronous vibration during the tests is summarised in Table III. The pump was stable when clearances were within the recommended limits, but became unstable with 2 x design clearances. In contrast inlet flow swirl control delayed unstable behaviour until clearances approached twice the renewable values. When the subsynchronous vibration occurred it had a well defined character. Figure 13 shows a time history and a spectrum of the shaft motion taken during Test 3. The time history shows the typical beating resulting from the presence of two strong vibration signals with frequencies close together. The spectrum shows not only the running speed vibration and the subsynchronous vibration but also the sidebands associated with these frequencies. This spectrum with its strong difference frequency, (running speed - subsynchronous speed), and the similarly displaced sidebands is typical of this phenomenon.

The vibration locked in and dropped out as the speed was varied. On fig.14 a waterfall plot of the shaft vibration on a run up highlights this characteristic. The waterfall was taken by varying the speed against a constant throttle valve setting, approximately equivalent to the best efficiency point at any speed. At this setting the subsynchronous vibration drops out at 3600 rpm. On fig.15 a waterfall plot of shaft vibration on a run down shows that the subsynchronous vibration dropped out at 3600 rpm. The waterfall plots also show that the subsynchronous vibration did not occur at a fixed frequency but varied as a constant proportion of running speed. In Test 3 the subsynchronous whirl frequency ratio 0.84 irrespective of the actual running speed of the pump. This is particularly well illustrated on the run down characteristic. At speeds, where the subsynchronous vibration was well established, the variation of flow had little effect on the character of the vibration. However, at speeds around the stability boundary of the subsynchronous vibration a change of flow caused the phenomenon to 'lock in' or ';drop out'. In general reducing the flow brought on the onset subsynchronous vibration. The effect of flow on the subsynchronous was noticeably less powerful than the effect of speed. Throttling the balance return line to increase the back pressure on the balance drum also delayed the onset of the subsynchronous vibration. Where the subsynchronous motion was well established the shaft vibration appeared to take up virtually the full bearing clearance. Not unsurprisingly this imposed an upper bound to the amplitude of the vibration. The general character of the bearing housing vibration was the same as the character of the shaft vibration. The vibration levels in the frequency range 10-200Hz, were of order 2mm/sec when running normally and up to 7mm/sec when the subsynchronous vibration was present. The vibration at blade rate and twice blade rate showed some modulation at the difference frequency. The pressure fluctuations in the suction and discharge were largely random in character with some contribution at blade rate and twice blade rate but nothing evident at the subsynchronous frequency. The balance return line pressure pulsed strongly at shaft rate and, when present, at the subsynchronous frequency. Impulse tests on the bearing housings showed that the natural frequencies were well away from running speed. The pump rigid body natural frequencies, (on the temporary supports), were about 2500 cpm whilst the characteristics natural frequencies of the pump body and bearing housings were much higher, above 500Hz. The dynamic characteristics obtained during Test 5, i.e. with swirl control, showed stable operation over the complete range of flow and speed available. With clearance opened out to 3x, Test 6, the pump became unstable at a speed of about 4800 rpm and the whirl ratio remained the same as before at 0.84, fig.16. The frequency of the subsynchronous vibration maintained the same relationship to speed up to the test maximum of 5500rpm as had been obtained before (Test 3).

To summarise, the characteristics of the subsynchronous vibration obtained on this pump were:-

1. the vibration appeared at a constant proportion of running speed, whirl ratios being typically 0.85 and was <u>independent</u> of annular seal clearance or actual pump speed.

2. the vibration 'locked in' and 'dropped out' with speed and to a lesser extent flowrate and there was a very rapid growth in amplitude to a limit cycle; typical of a classical self excited oscillation.

3. the vibration contained not only the subsynchronous frequency but also the difference frequency and sidebands.

4. the shaft vibration at the subsynchronous frequency indicated a forward precessing whirl, again typical of a self excited oscillation.

5. there was no evidence to prove that the subsynchronous vibration response was due to a rotor natural frequency (i.e. not an unstable eigenvalue).

6. control of inlet swirl to the balance drum delayed the onset of subsynchronous vibration.

Since the mid 1980's there have been reported several more instances of the "near running speed" nonsynchronous vibration problem, ref 7, 8, 9. In some cases major redesign of the pump has been necessary to solve the problem. Opinions differ regarding the source of the problem, some believe it is the excitation of the natural frequency of the rotor but others believe that hydraulic destabilising forces in the impeller may be the source. Further research and investigation will no doubt ultimately give more insight into such problems.

5.0 TRANSIENT VIBRATIONS

Transient vibrations - vibrations which result from rapidly changing operating conditions and which decay with increasing time.

Transient vibrations in boiler feed pump installations are fairly rare although most modern power stations have probably experienced pipework vibration resulting from either rapid loading or unloading of the pump or from the rapid opening and closing of flow control valves. Disturbed suction conditions can also lead to pipework vibration and vapour locking within the pump causing the pump to eventually run dry. However, there are few documented examples of pump rotor vibrations which result from transient operations. One such problem arose in 1987 on boiler feed pumps installed in a large modern fossil fired power station in South Africa. The incident occurred each time a pump was restarted following a shut down from hot operation. These pumps were fitted with eddy current shaft monitoring equipment and a vibration trip occasionally occurred due to high level shaft displacement during the restart. Normal steady state levels of shaft vibration were typically 30 μm to 50 μm pk-pk raising to 150μm to 175μm during restart. The problem was caused by a thermally induced bow in the pump shaft induced by a temperature differential in the area of the mechanical seal. A typical shaft displacement record is shown in fig.17, where it can be seen that it took between 40 - 50 seconds before the displacement levels have returned to normal following the restart of the pump. From a comprehensive series of tests on site, it was possible to establish the characteristics of the phenomenon in terms of some of the dependent variables. These were:-

1. length of time the pump remained stationary following hot shut down

2. acceleration rate during run up

3. feed temperature

4. journal bearing loading.

In this particular case the 'solution' was simply to operate a vibration inhibit during start up, it being argued from past experience and detailed analysis of the shaft bending forces involved

that the pump would not suffer accelerated wear. It is believed that this phenomenon occurs in most boiler feed pumps fitted with mechanical seals. A review of Weir feed pump installations carried out 1988 showed 127 fully operational pumps with over 1.6 million hours operation. None of these were fitted with shaft displacement monitoring with alarm and trip function. In the absence of shaft monitoring the phenomenon has gone unnoticed with, it would appear, no adverse effect on long term integrity.

6.0 CAVITATION RELATED VIBRATIONS

Cavitation related phenomena are associated with the first stage impeller suction region and may be responsible for many unusual dynamic phenomena in pump and piping systems, ref.10.

The suction stage feed pumps designed by Weir Pumps in the 1970's for CEGB incorporated inducers so that they could cope with the low NPSH transients associated with sudden loss of load. One concern was the susceptibility of these designs to promote surging in the suction pipework in the boiler feed system. Works test are generally unrepresentative of pipework installations on site, particularly as the suction pipework often incorporates a throttle device to control the suction pressure at inlet. This provides considerable damping to the suction pipework, effectively inhibiting the propensity to surge. A series of special tests were carried out in the Weir test facilities to examine the boundary of the surge phenomenon at various flowrates and over a wide range of NPSH values. For these tests a free surface was introduced between the throttle valve and the pump suction. A summary of the cavitation surge band is shown in fig.18. It was comforting to find that although a well defined surge envelope could be defined it occurred at NPSH values below that available during loss of load transient.

In 1988 a cavitation related problem was seen during works testing of pressure stage feed pumps for a Nuclear Power Station. These tests were carried out at rated speed of 5610 rpm and over the full range of flow. Tests however, were carried out without the booster stage pump and the NPSH was less than a half of the site NPSH at rated duty falling to less than a third of the site NPSH at 40% rated flow. Although this was considered acceptable for the hydraulic performance measurements it was found to give unsatisfactory vibration levels as measured on the pump bearing housings compared with the vibration targets. On site the pumps were to meet a vibration level of 2.8mm/sec rms (10Hz-1KHz) at duty flow, 4.5mm/sec rms down to 40% flow and 7.1mm/sec rms at 30%, the recirculation flow quantity. It was desirable to demonstrate these levels during the works test. The measured vibrations were higher than target as characterised in terms of broad band excitation, impeller blade frequency excitation and general unsteady/erratic readings. Figure 19 shows the highest vibration recorded during test at 80m NPSH in terms of the overall level, once per revolution and blade rate frequency components compared with the target. It was suspected that cavitation was responsible for the problem. A review of some visual cavitation tests done on a ½ scale model impeller in our Research Laboratory indicated that sizeable bubble formation could exist 80m NPSH despite the fact that no loss in head had occurred. Typical bubble size data are shown in fig.20 where it can be seen that bubble size in excess of 30mm would be expected at the NPSH used during the test. The NPSH was increased to 145m, still only 50% of the site NPSH at duty flow and 50% at 40% rated flow. The vibration levels were found to be very close to the vibration targets as can been seen in fig.21. Clearly this underlines the need to consider carefully before agreeing to meet tight vibration limits during tests designed primarily to demonstrate hydraulic performance.

7.0 CONCLUDING REMARKS

The paper has provided examples of different types of vibration experienced in boiler feed pumps for Power Station duties. It is likely that other manufacturers can cite similar problems but different solutions may have been adopted. The task of the methods of the pump designer is to try and eliminate the problems in any new designs and, preferably, before site installation. This process is helped if manufacturers and users are encouraged to report on problem areas.

Clearly there are generic problem areas. The subsynchronous vibration problem has generated more interest in the US than in Europe and there are many research projects directed toward investigation of hydraulic destabilising forces and fine clearance seal dynamics. Cavitation and NPSH related dynamic effects offer considerable scope for investigation relating to system and pump rotor stability. Impeller blade frequency vibrations are not completely understood and further research into areas of concern would seem desirable.

8.0 REFERENCES

1. UCHIDA, N. Radial Force on the Impeller of a Centrifugal Pump. Bulletin of the ISME, Vol 14, No.76, 1971.

2. HERGT, P., KREIGER, P. Radial Forces in Centrifugal Pumps with Guide Vanes. Conference on Advanced Class Pumps. I.Mech.E., 1970.

3. BROWN, R.D., FRANCE, D. Vibration Response of Large boiler Feed Pumps. Worthington European Technical Award 1974, Vol III, Hoepli, Milan, 1974.

4. ZOTOV, B.N. Selection of Number of Runner and Guide Mechanism Blades for Centrifugal Pumps. Russian Engineering Journal, Vol LII, No.11.

5. MAKAY, E., SZAMODY, O. Survey of Feed Pump Outages. EPRI Report - 754, 1978.

6. FRANCE, D. Rotor Instability in Centrifugal Pumps. Shock and Vibration Digest, Vol. 18, No.1, 1986.

7. MASSEY, I. Subsynchronous Vibration Problems in High Speed Multi Stage Pumps. Proc. 14th Turbomachinery Symposium, Texas A&M University, 1985.

8. MARSCHER, W.D. Subsyncrhonous Vibration in Boiler Feed Pumps due to Stable Response to Hydraulic Forces at Part Load. I.Mech.E Conference 'Part Load Pumping, Operation, Control and Behaviour', 1988.

9. FRANCE, D., TAYLOR, P.W. Near Running Speed Subsynchronous Vibration in Centrifugal Pumps. Conference on Vibrations in Centrifugal Pumps, I.Mech.E., London, 1990.

10. NG, S.L. and BRENNEN, C. Experiments on the Dynamic Behaviour of Cavitating Pumps. ASME Fluids Engineering, 1978.

11. BLACK, H.F. Lateral Stability and Vibrations of High Speed Centrifugal Pump Rotors. Symposium on the Dynamic of Rotors, Lyngby, Denmark.

TABLE I

RADIAL VIBRATION FORCES

Blade Number	Blade Rate Harmonic										
Imp/Diff	1	2	3	4	5	6	7	8	9	10	11
6/7	1.114	0	0	0	0	0.186	0	0	0	0	0
6/9	0	0	0	0	0	0	0	0	0	0	0
6/13	0	1.035	0	0	0	0	0	0	0	0	0.188
7/9	0	0	0	0.358	0.286	0	0	0	0	0	0
7/12	0	0	0	0	0.382	0	0.273	0	0	0	0
	0	0.13*	0	0	0.27*	0	0	0	0	0	0
7/13	0	1.035	0	0	0	0	0	0	0	0	0.188
	0	1.0*	0	0.4*	0.13*	0	0	0	0	0	0
8/7	1.114	0	0	0	0	0.186	0	0	0	0	0
8/9	1.432	0	0	0	0	0	0	0.179	0	0	0
8/12	0	0	0	0	0	0	0	0	0	0	0
8/13	0	0	0	0	0.414	0	0	0.259	0	0	0
5/7	0	0	.371	.279							
5/8	0	0	.424	0	.255	0	0	0	0	0	0

N.B. *** Measured Normalised Radial Force Values for 7 x 12 and 7 x 13 blade combinations**

TABLE II

Test Conditions Prototype Pump

Test No.	Build	Clearances
1	Standard design	nominal design
2.	Standard design	1.5 x nominal design
3.	Standard design	2.0 x nominal design
4.	Balance drum swirl control	nominal design
5.	Balance drum swirl control	2.0 x nominal design
6.	Balance drum swirl control	3.0 x nominal design

TABLE III

Incidence of Subsynchronous Vibration

Test		Subsynchronous	Whirl Frequency Ratio	Onset Speed
1.	Design, New	No	--	--
2.	Desing, 1.5 x	No	--	--
3.	Design, 2.0 x	Yes	0.84	≥3900 rpm
4.	Controlled, New	No	--	--
5.	Controlled, 2.0 x	No	--	--
6.	Controlled, 3.0 x	Yes	0.84	≥4800 rpm

Fig.1. Shaft Speed Hydraulic Unbalance as a Function of Flow (After Uchida)

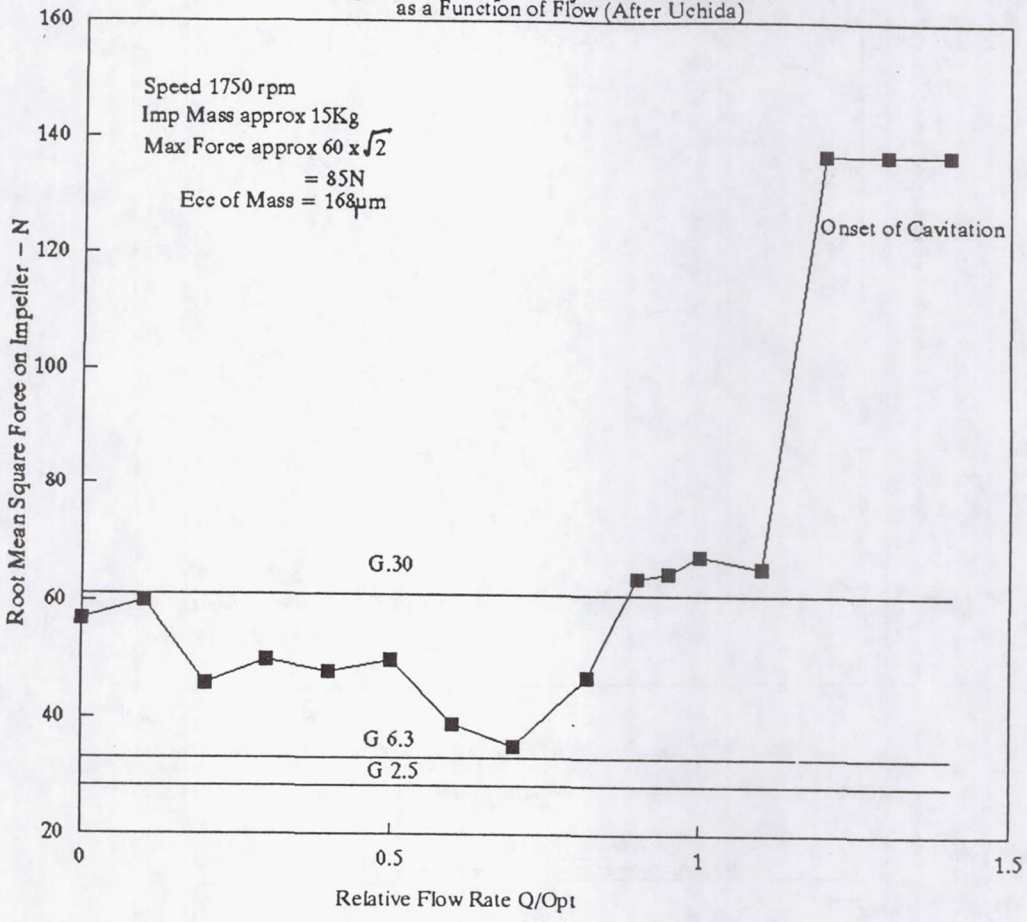

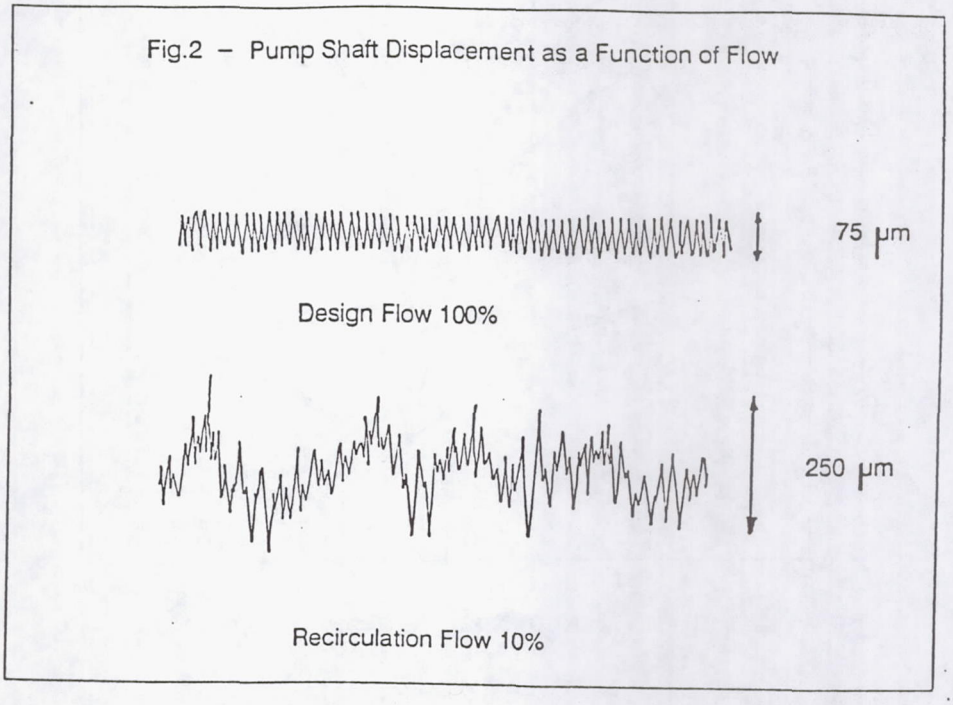

Fig.3a Dynamic Force – Influence of Blade Number and Gap G

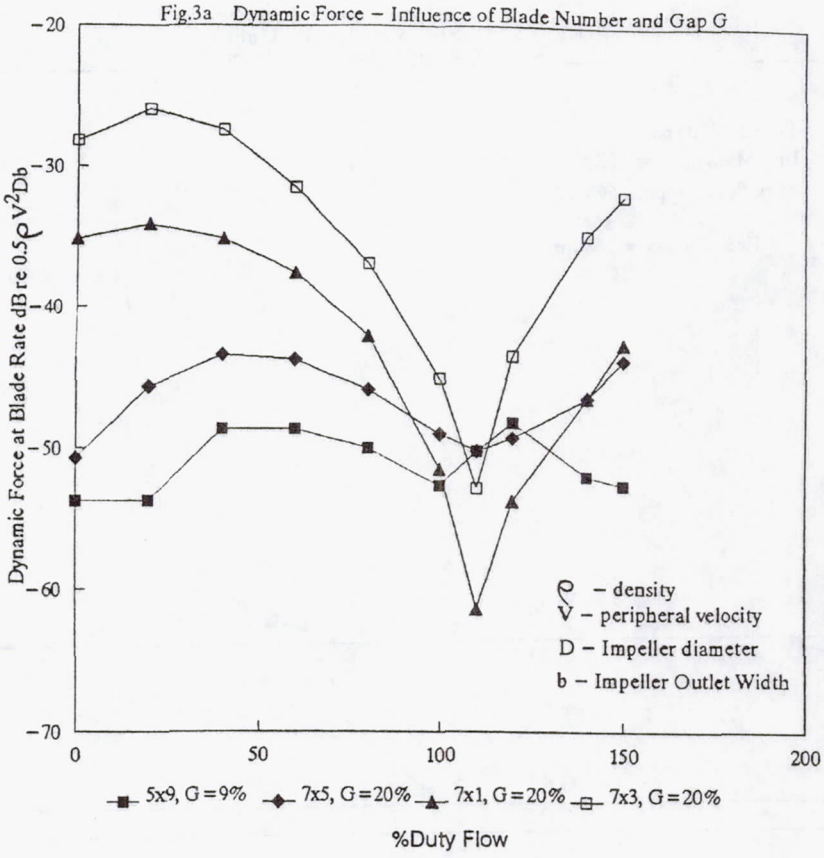

Fig.3b Dynamic Force – Influence of Impeller/Diffuser Gap G

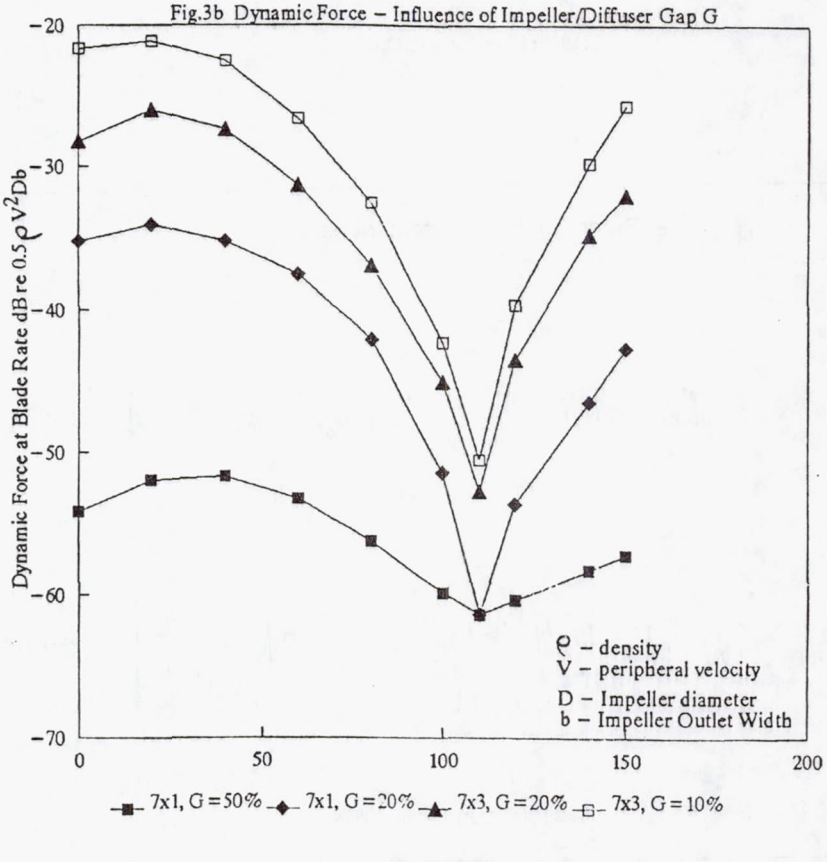

Fig.4 Blade Rate Vibration

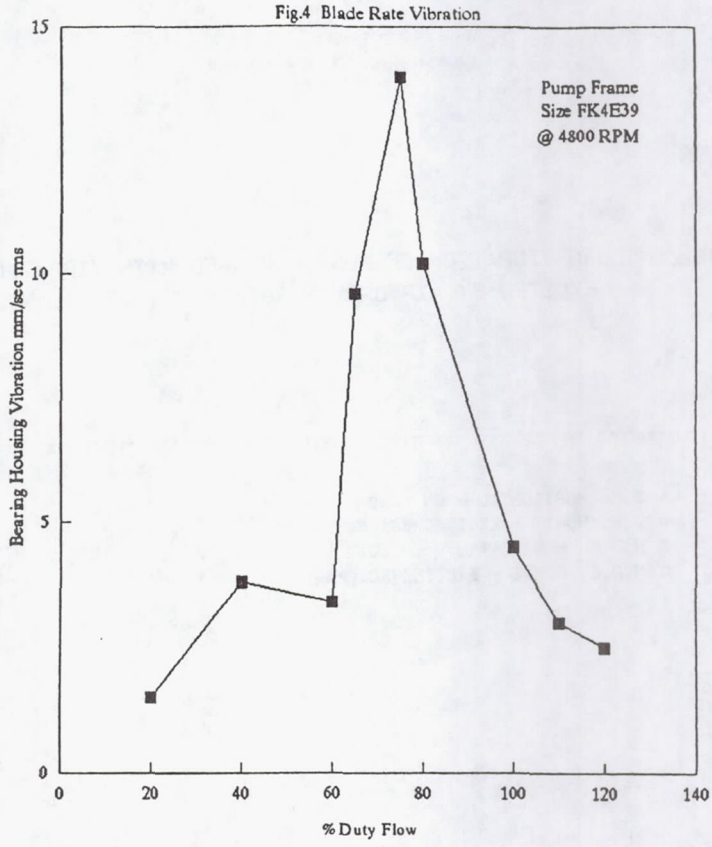

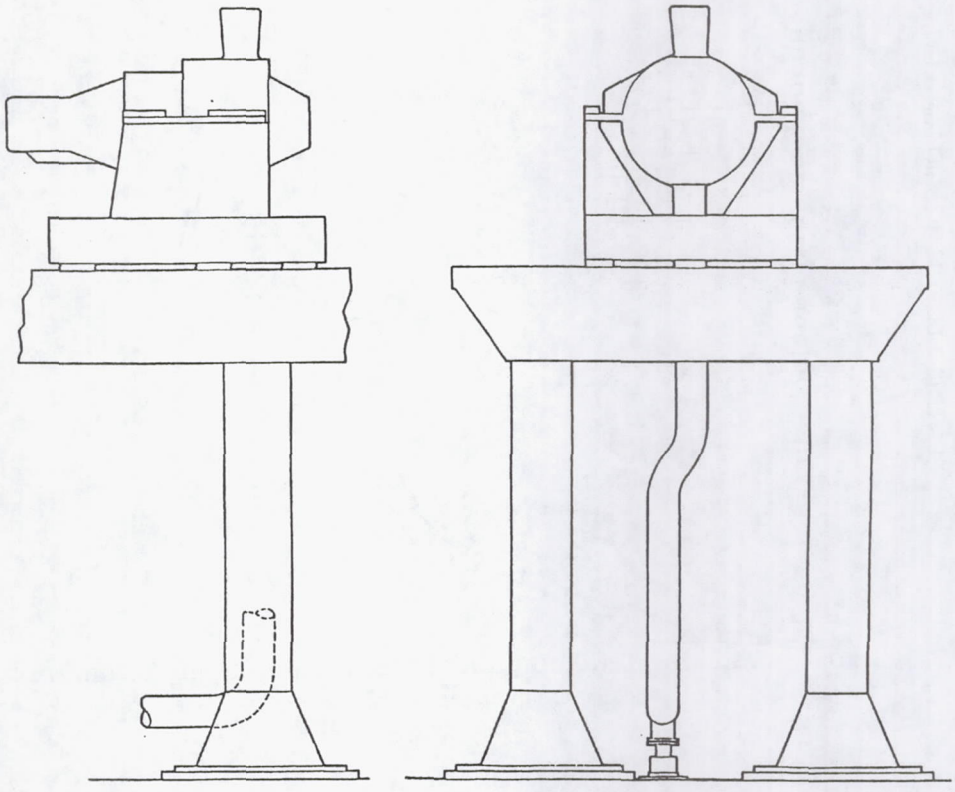

FIG. 5 ARRANGEMENT OF MAIN FEED PUMP AND SUPPORTING STEELWORK

FIG6a ON LOAD VIBRATION OF PUMP COMPARED WITH VIBRATION OF PUMP EXCITED BY AIR DRIVEN ROTARY OUT OF BALANCE DEVICE

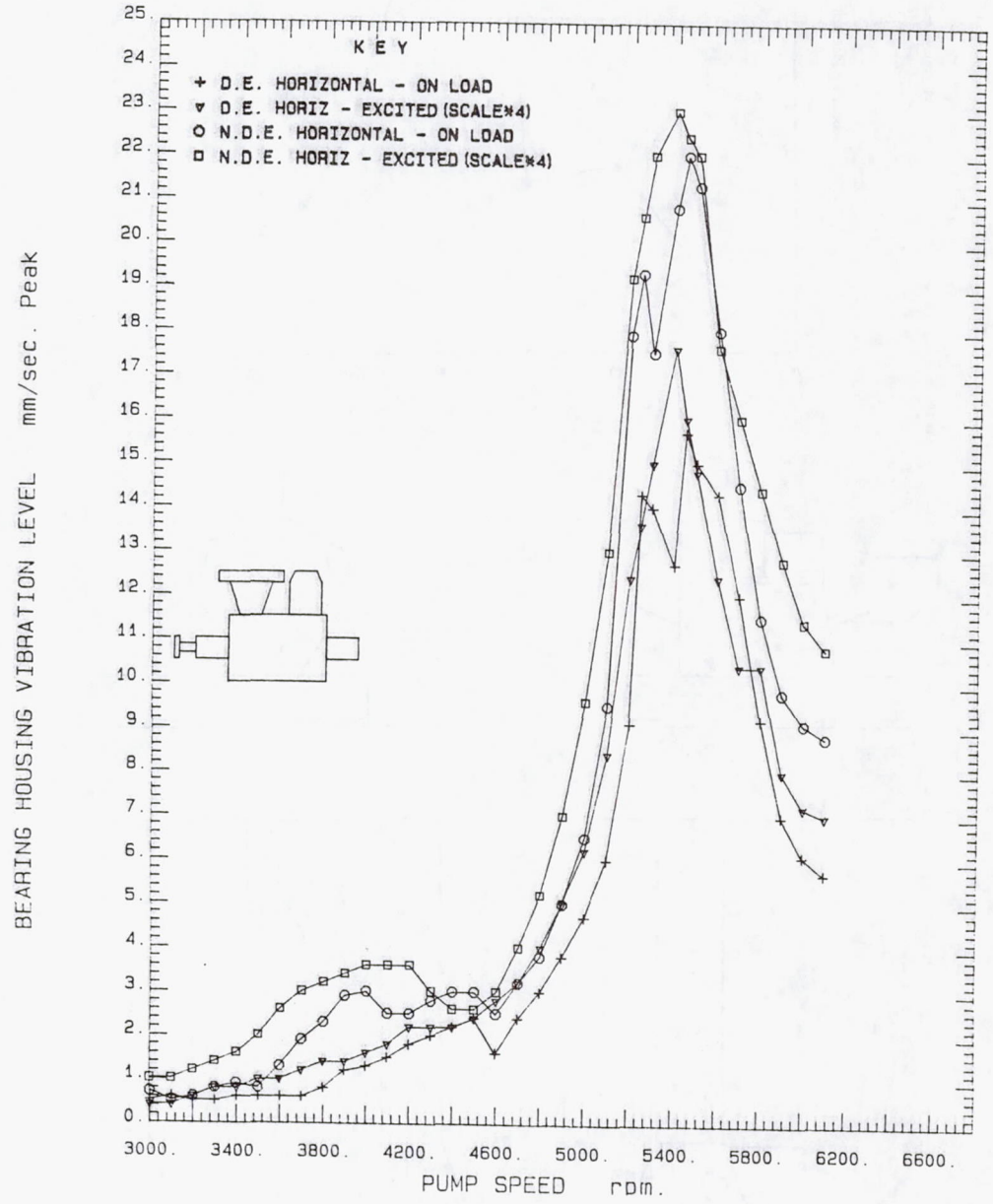

FIG 6b RESPONSE OF PUMP ON STEELWORK COMPARED WITH PUMP ON CONCRETE FLOOR - EXCITED BY ROTARY DEVICE

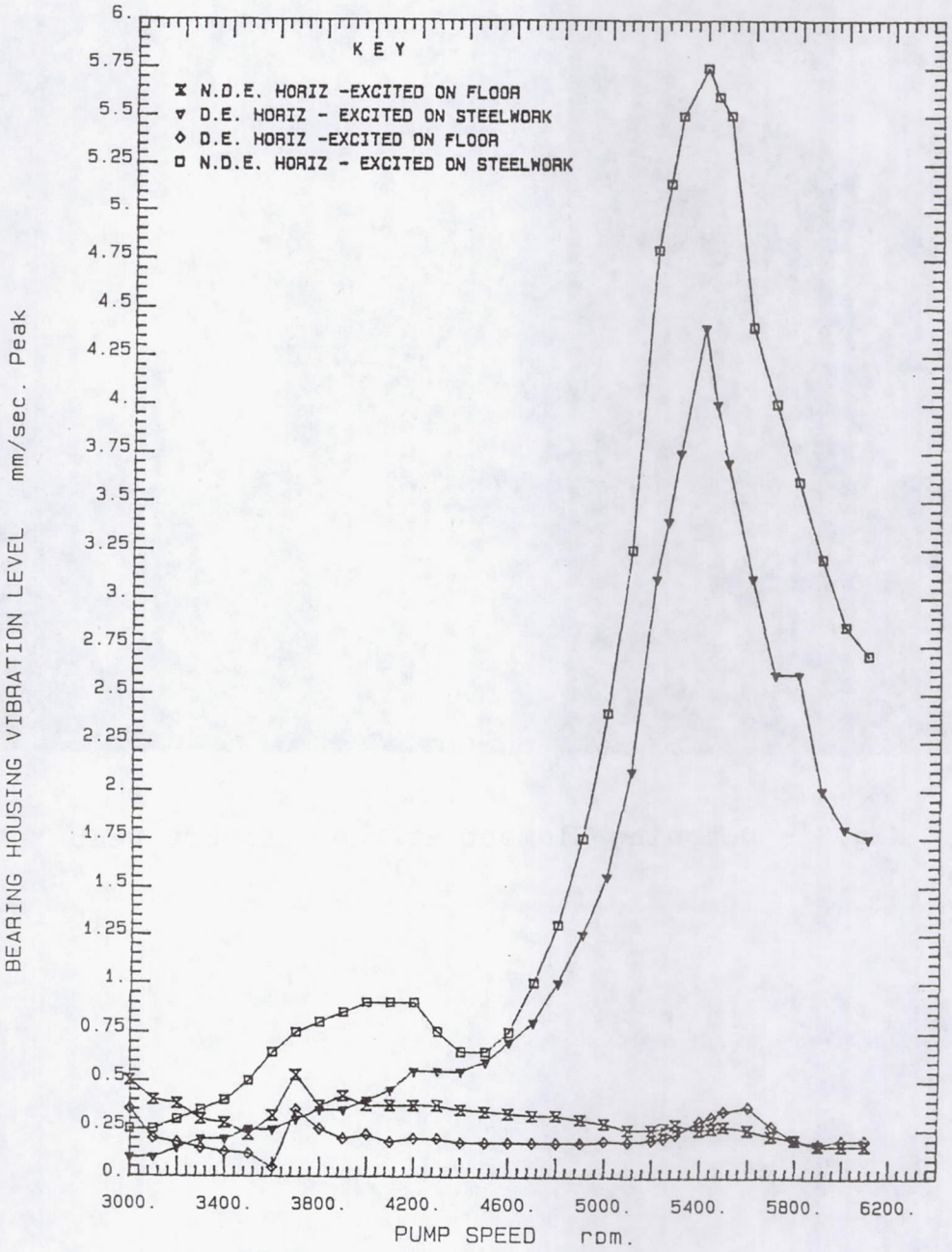

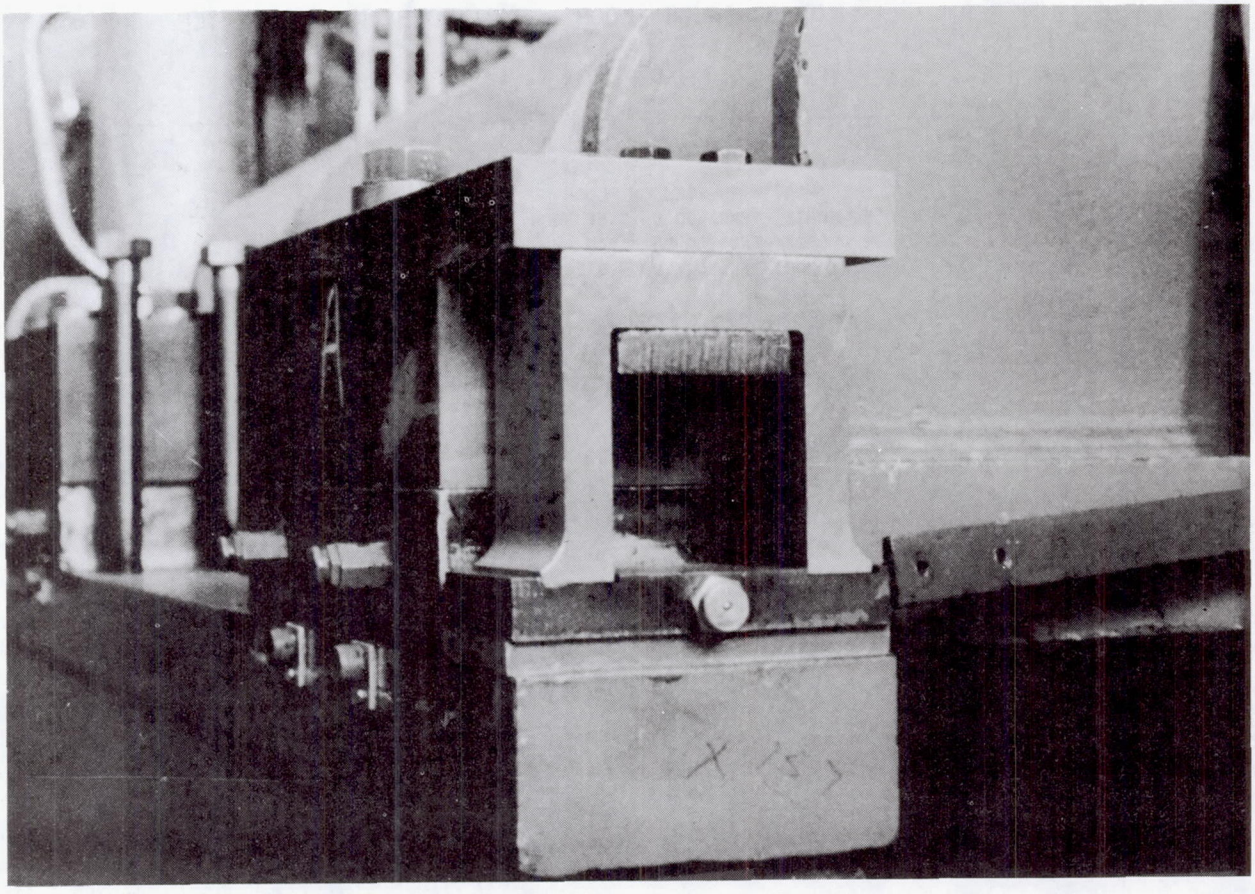

Fig.7 - Detuning Element at Pump Support Feet

FIG 8 ON LOAD VIBRATION RESPONSE OF PUMP FITTED WITH FLEXIBLE DETUNING ELEMENT COMPARED WITH PUMP AS ORIGINALLY INSTALLED

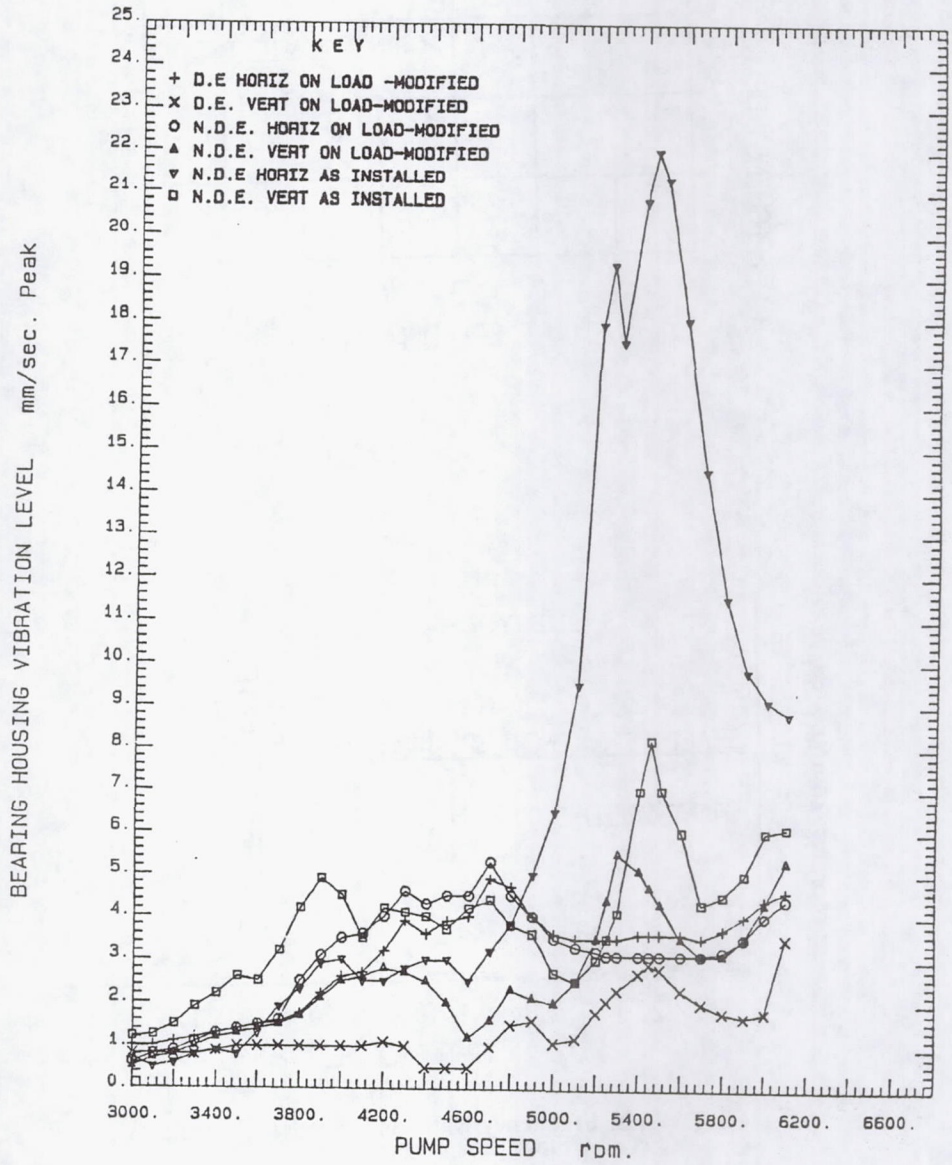

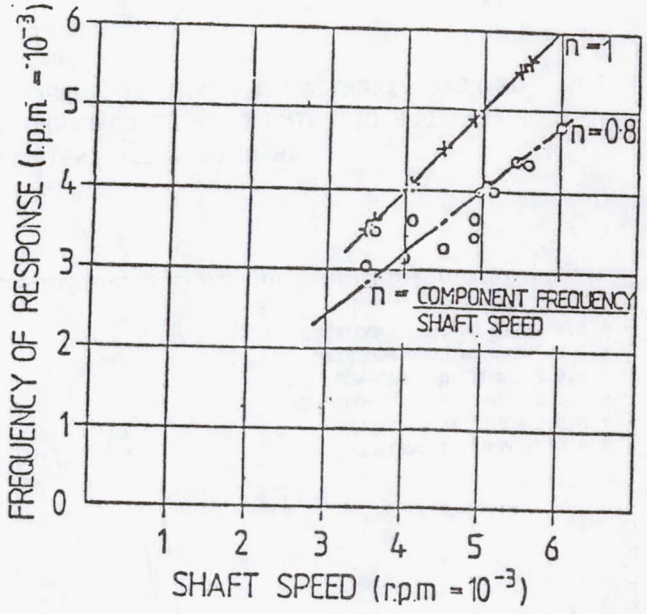

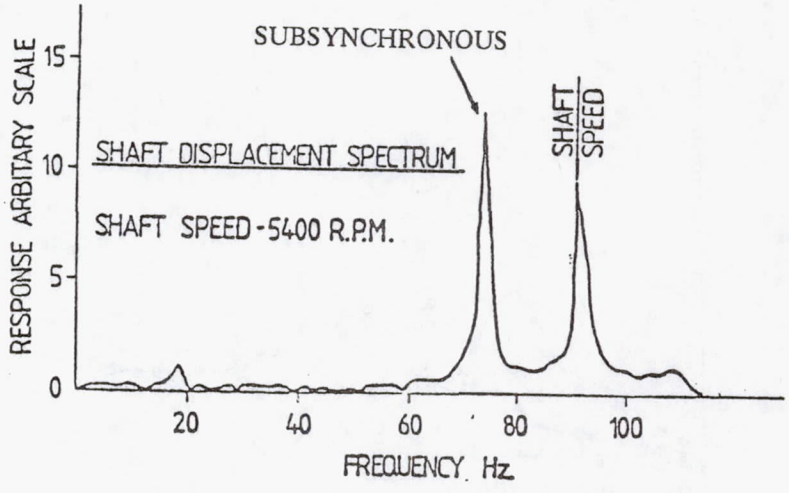

Fig.9. Whirl Frequency Ratio and Frequency Spectrum From 4 Stage Boiler Feed Pump

FIG.10 – Frequency Spectrum taken at Drive End Bearing for 7 Stage Pump with 2 x Design Clearances at 5850 r.p.m.(97.5 Hz)

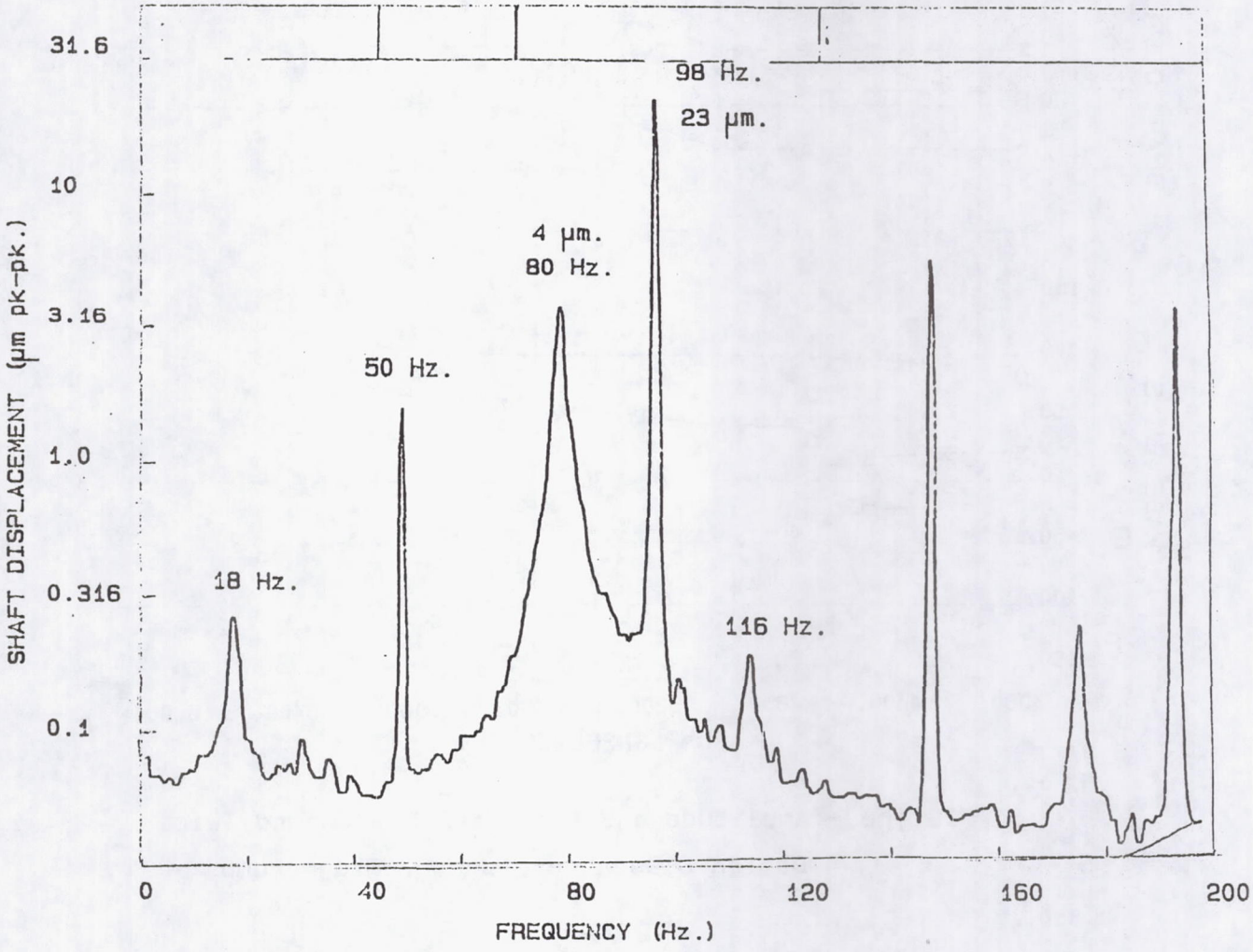

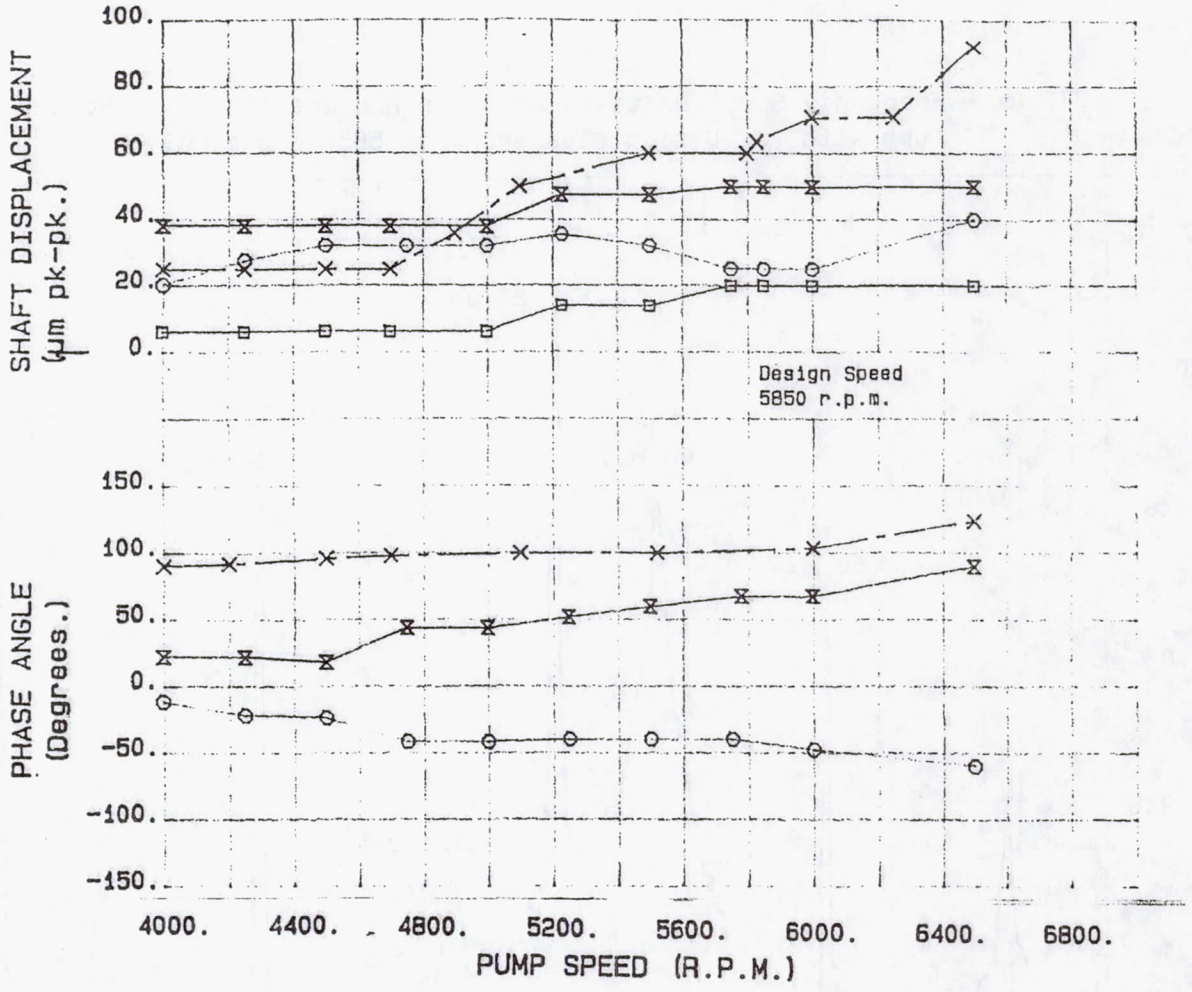

FIG. 11a.- Amplitude and Phase for Design and Twice Design Clearances for a 7 Stage Pump

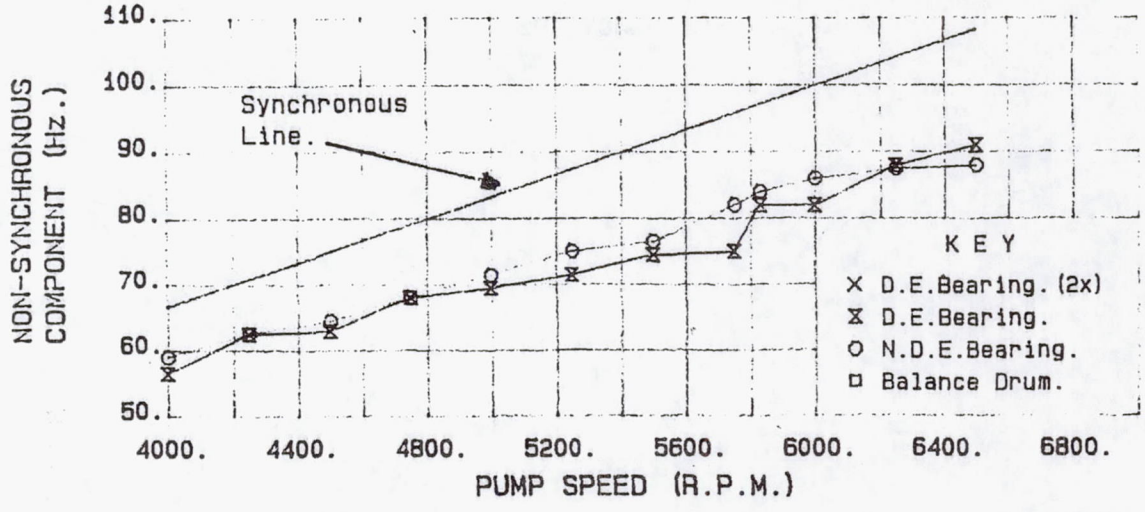

FIG. 11b.- Frequency of Non-synchronous Vibration versus Pump Speed for a 7 Stage Pump

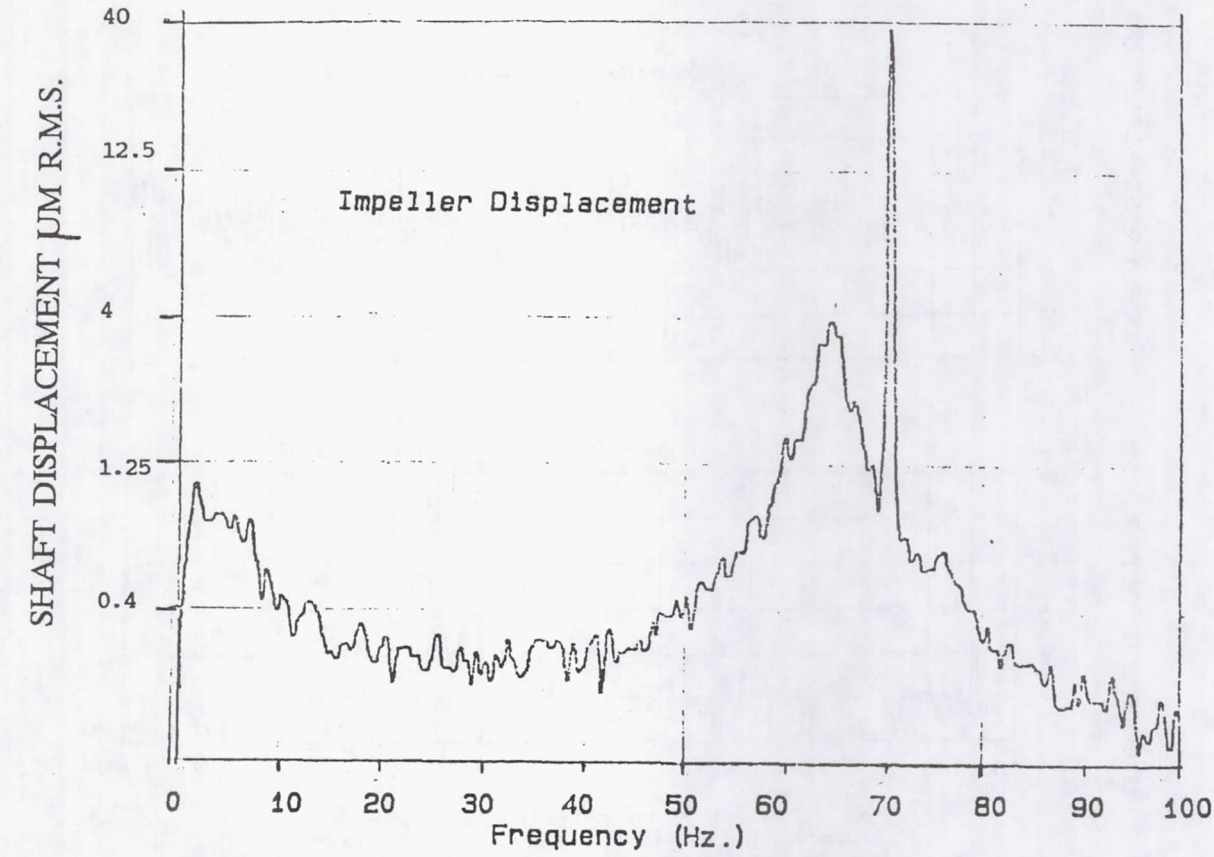

FIG12a - Impeller Displacement From Single Stage Test Rig at 4250 r.p.m. and 65% Best Efficiency Point Flow

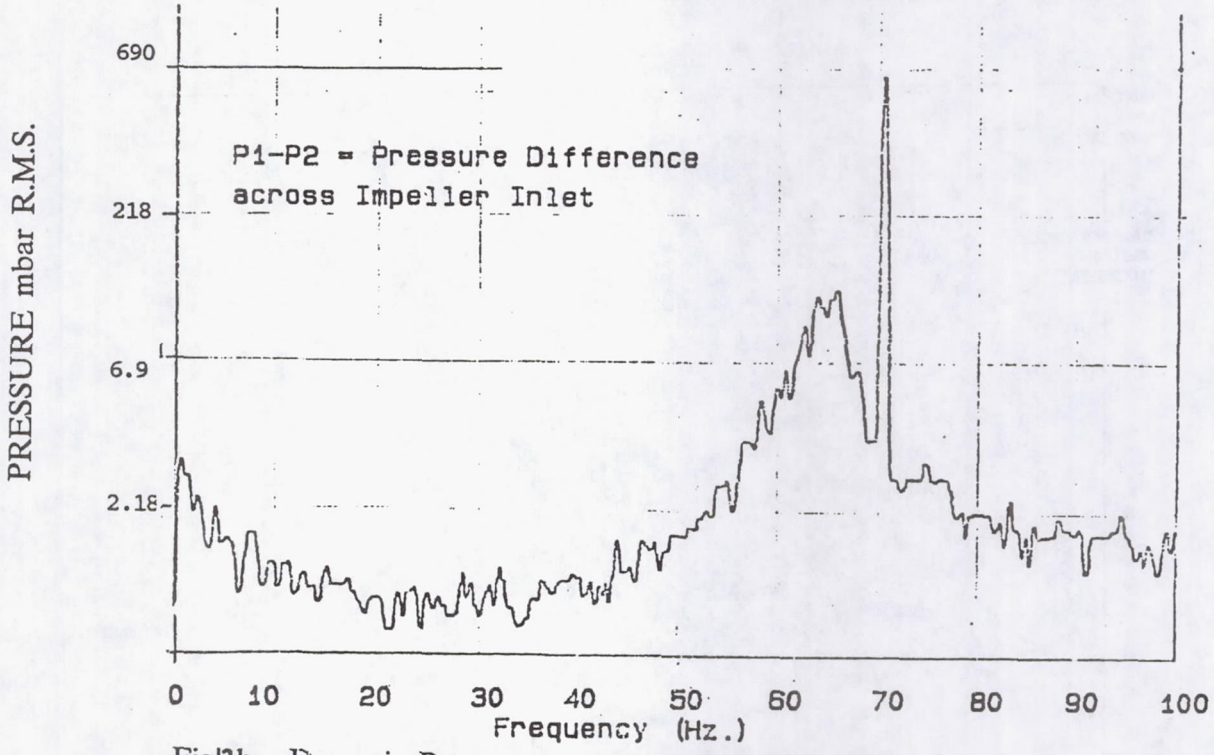

Fig12b - Dynamic Pressure across Impeller Inlet from Single Stage Test Rig at 4250 r.p.m. and 65% Best Efficiency Flow.

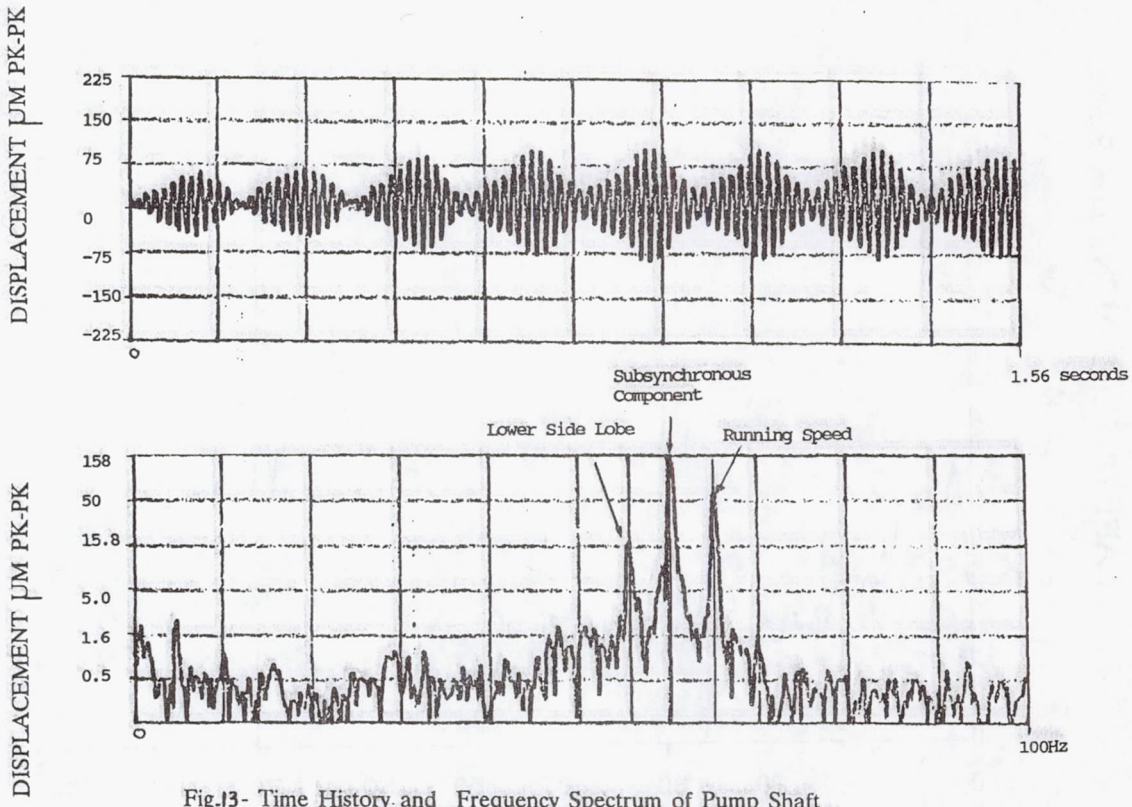

Fig.13- Time History and Frequency Spectrum of Pump Shaft Displacement [Pump Clearances at Twice Design Values - Refer Test 3]

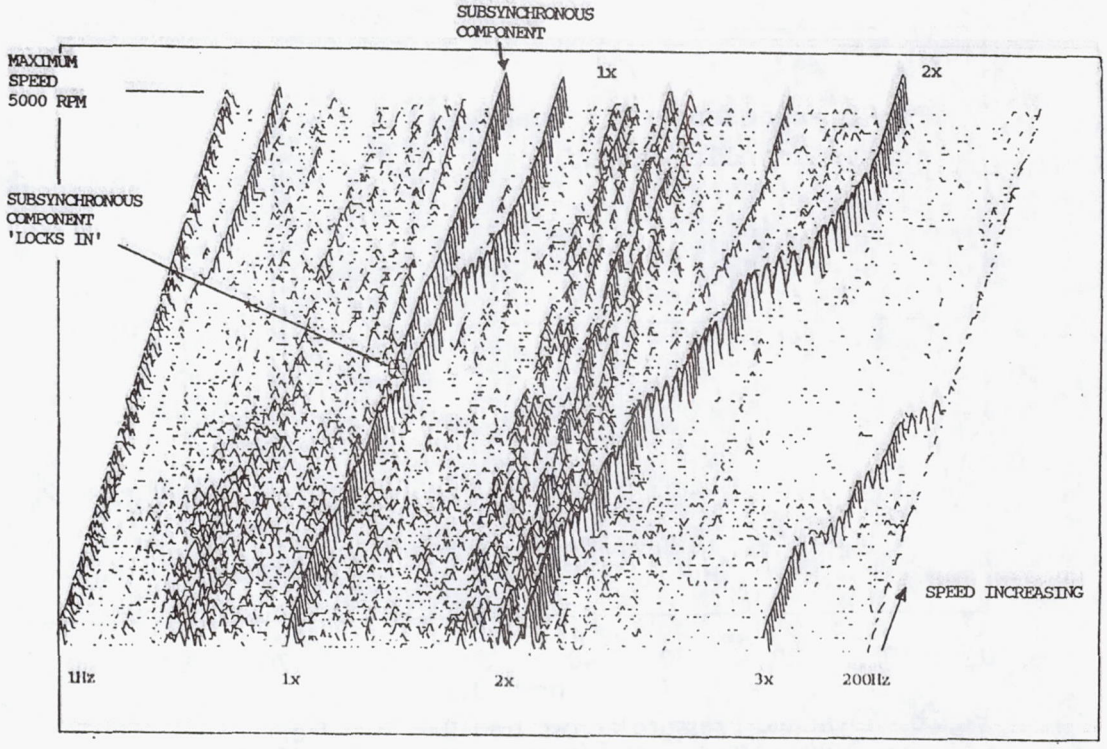

Fig.14- Waterfall Plot of Shaft Motion during controlled speed increase. (Pump Clearances at Twice Design Values)

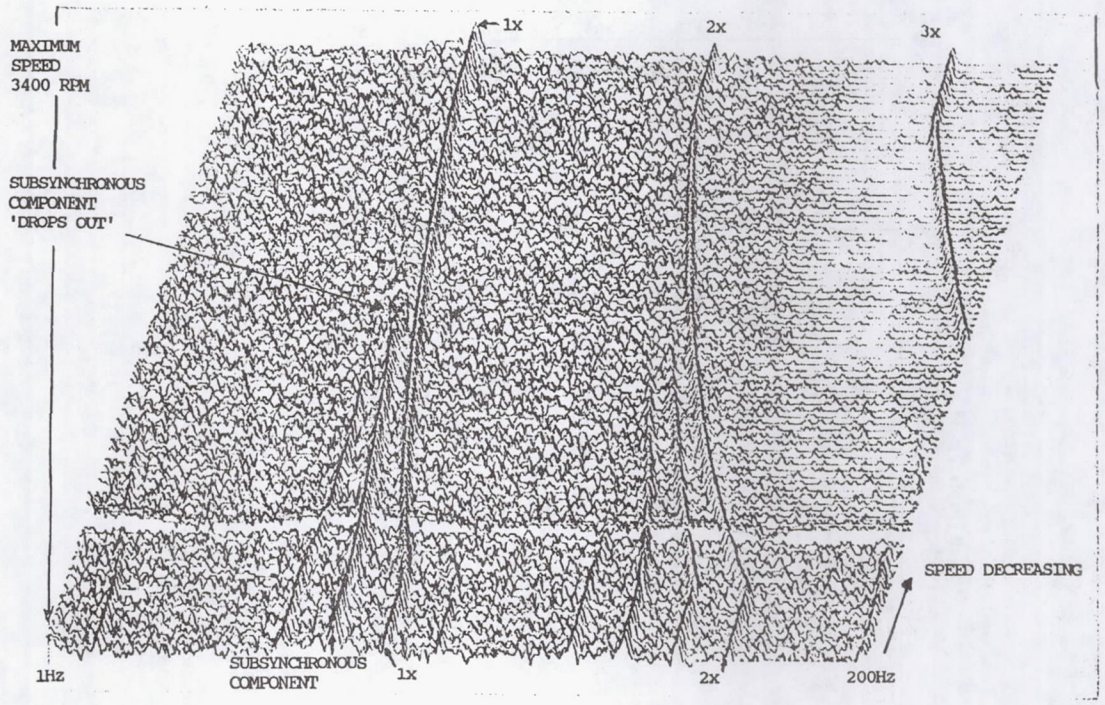

Fig.15 - Waterfall Plot of Shaft Motion during controlled speed reduction.
(Pump Clearances at Twice Design Values)

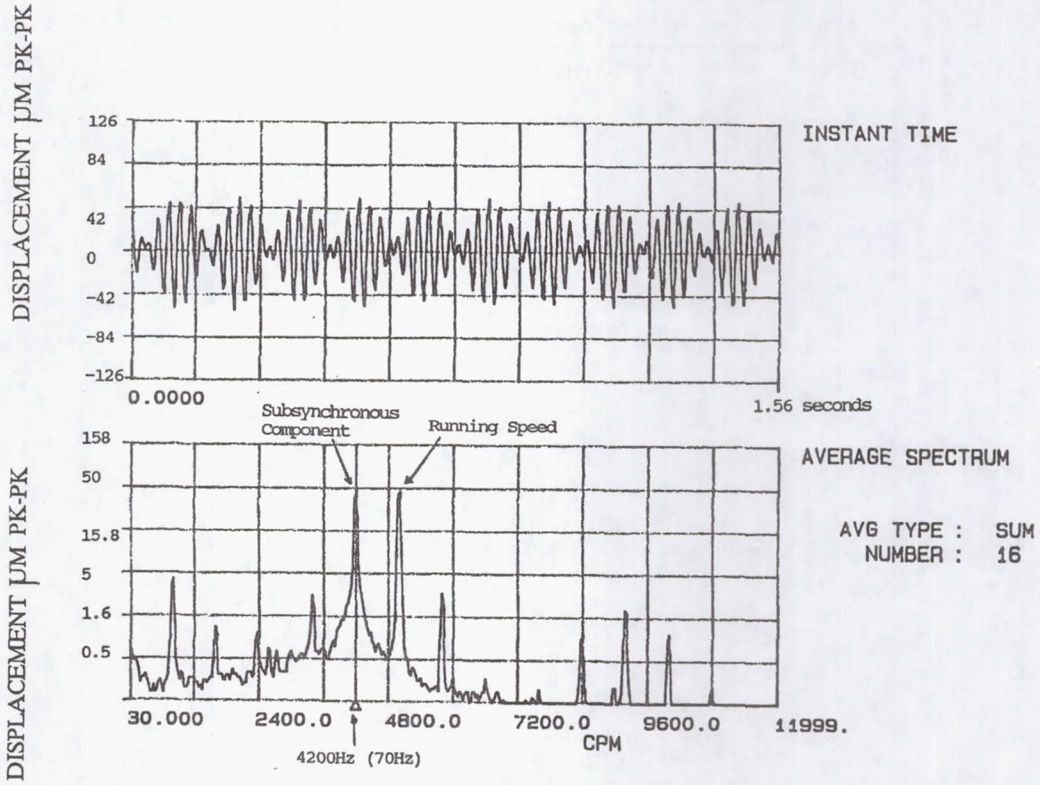

Fig.16 - Time History and Frequency Spectrum of Pump Shaft Displacement [Pump Clearances at 3 x Design, with Swirl Control Test 6]

Fig.17 – Transient Shaft Vibration During Hot Start

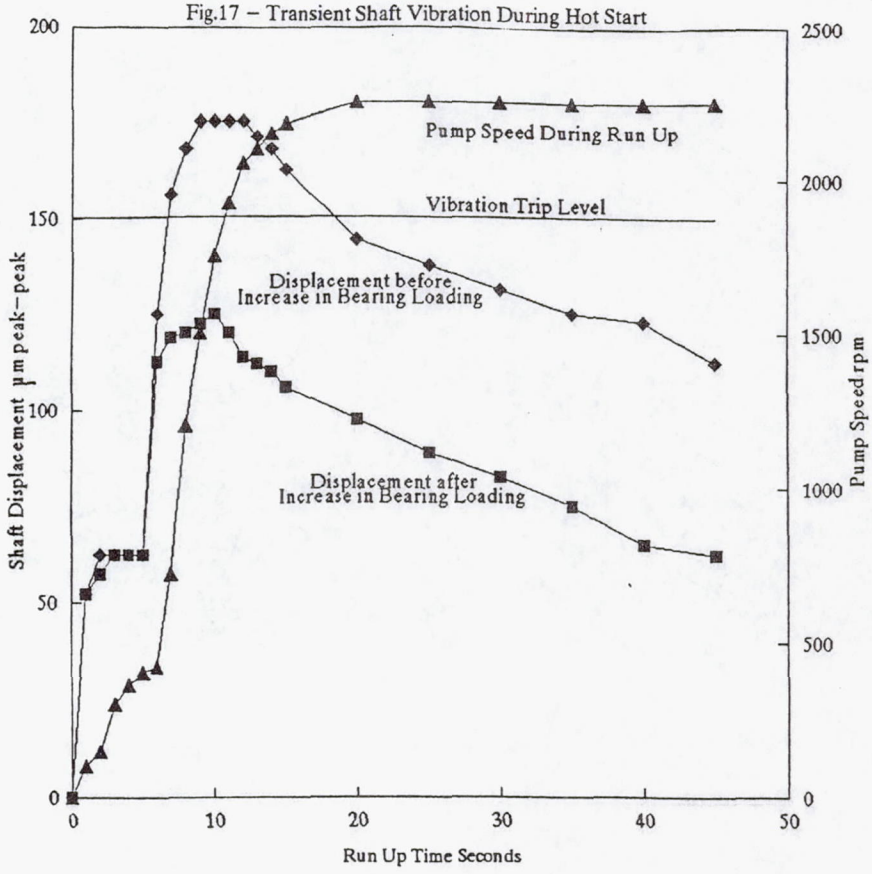

Fig.18 – Cavitation Surge Band on Works Test

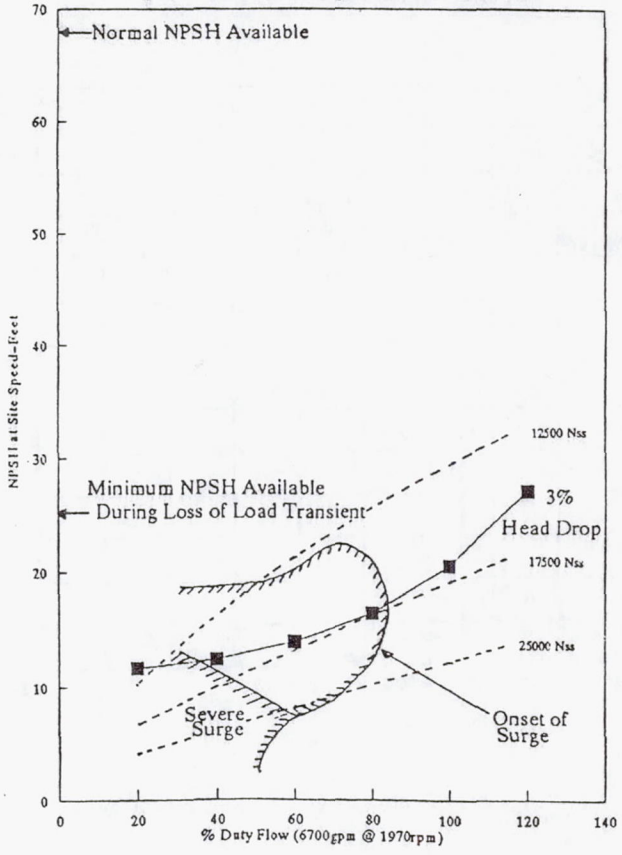

Fig.19 – Pressure Stage Feed Pump Vibration Levels @ 80m NPSH

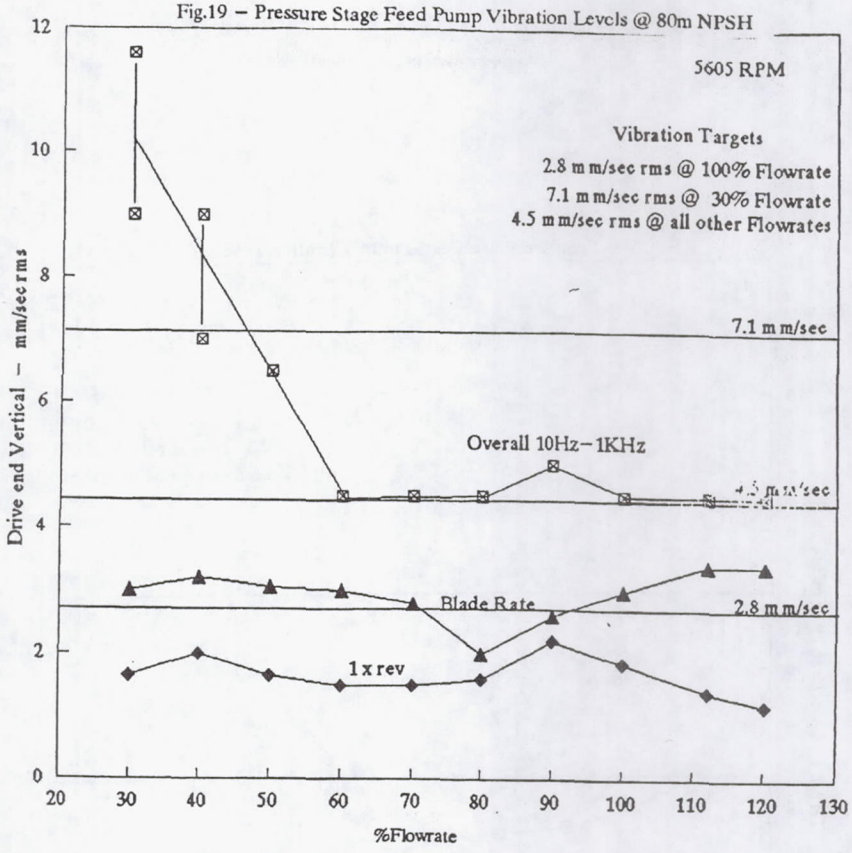

Fig.20 – Scale Model of Cavitation Performance in Cavitation Visualisation Rig vs Site available NPSH

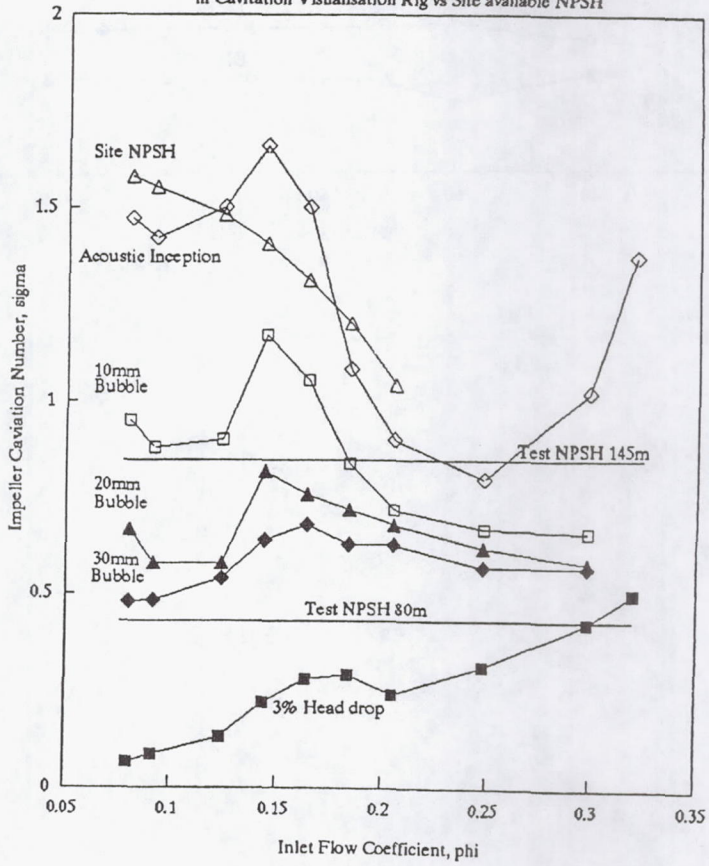

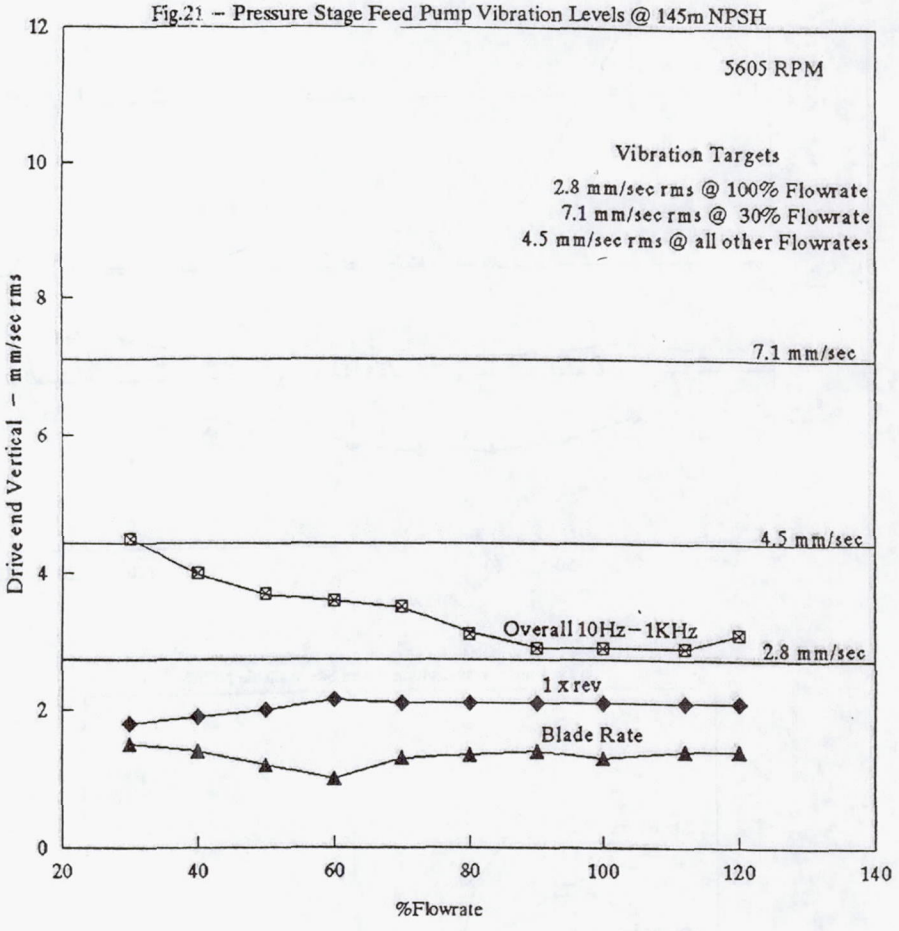
Fig.21 – Pressure Stage Feed Pump Vibration Levels @ 145m NPSH
5605 RPM
Vibration Targets
2.8 mm/sec rms @ 100% Flowrate
7.1 mm/sec rms @ 30% Flowrate
4.5 mm/sec rms @ all other Flowrates
7.1 mm/sec
4.5 mm/sec
2.8 mm/sec
Overall 10Hz – 1KHz
1 x rev
Blade Rate
Drive end Vertical – mm/sec rms
%Flowrate
0
2
4
6
8
10
12
20
40
60
80
100
120
140

EXPERIMENTAL AND ANALYTICAL STUDY ON FLUID WHIRL AND FLUID WHIP MODES

Agnes Muszynska
Bently Rotor Dynamics Research Corporation
Minden, Nevada

ABSTRACT

Fluid whirl and fluid whip are rotor self—excited, lateral vibrations which occur due to rotor interactions with the surrounding fluid. There exist various modes of fluid whirl and fluid whip. These modes are close to rotor modes corresponding to free vibrations (based on the linear model). Small differences are due to nonlinearities in the system. This paper presents experimental and analytical results on the lowest modes of fluid whirl and fluid whip. Examples of rotors supported in fluid lubricated bearings show the variations of rotor deflection amplitudes and phases in the whirl and whip modes with changes of rotative speeds and/or changes in lumped mass locations along the shaft.

1. INTRODUCTION

Dynamic phenomena induced by interaction between the rotor and the surrounding fluid, such as occur in fluid—lubricated bearings and seals of fluid—handling machines, have been recognized for over 60 years. The resulting rotor lateral self—excited vibrations, usually occurring at subsynchronous frequencies, are known as "fluid (oil,..) whirl, "fluid (aerodynamic, steam,..) whip," or simply "rotor instability." The rotor precessional direction of these self—excited vibrations is always forward. Most of the existing literature have documented occurrences of these phenomena in low ranges of rotative speeds [1—6]. Classical literature on fluid—lubricated bearings, which concentrates on lubrication problems rather than rotor instabilities, reports only occurrences of whirl vibrations of rigid rotors. References on rotor instability due to dynamic phenomena occurring in seals report whip type of vibrations only. This leads to an unjustified belief that the whirl and whip phenomena may occur only in dissimilar, uncomparable systems, and are due to different causes.

When the rotating shaft and surrounding fluid involved in motion are considered, however, as one system, it is evident that vibration modes interact. If the fluid—induced, self—excited vibrations of the rotor occur at relatively low rotative speed, the shaft would vibrate as either rigid body (whirl), or at its first lateral mode [7]. With an increase in rotative speed, there is a smooth transition from the whirl to whip of the first mode. It is obvious that both these phenomena are generated by the same source, and thus can be modeled by one algorithm. At higher rotative speed, higher mode whirl or whip vibrations may be induced [8,9]. The modal approach in rotor system modeling allows for clear interpretation of the occurring vibrational phenomena.

This paper is a continuation of the series of papers [7—11] on applications of the improved model of the fluid force for lightly radially loaded shafts rotating in a fluid environment. Following Bolotin [12] and Black [13,14], the fluid force model is based on the strength of the circumferential flow generated mainly by the shaft rotation [15]. This model can be used for lightly radially loaded bearings, as well as seals (with or without preswirls and/or injections). The fluid force model, identified experimentally by using physical perturbation techniques [16,17] and the modal approach in modeling, allow for more adequate prediction of rotor stability

thresholds, and evaluation of the post–stability fluid–induced rotor lateral limit cycle self–excited vibration parameters (whirl and whip).

Using the multi–mode modal approach [8, 17], the linearized rotor system eigenvalue problem is solved, and approximate values of natural frequencies and thresholds of stability are given. It is shown that there exist fluid–generated natural frequencies of the system, and the corresponding sequence of modes. The nonlinear model allows for calculation of the after–threshold, self–excited vibration parameters, including modes of vibration.

2. MATHEMATICAL MODEL OF A TWO–MODE ROTOR WITH ONE SOURCE OF INSTABILITY

Two physical models of rotors on which mathematical models are the same will be discussed in this section. In both cases the rotors carry one source of fluid–induced instability.

Consider a balanced isotropic rotor of a fluid–handling machine supported by two rigid bearings. The rotor rotates concentrically in a seal located at the axial section "S" (Fig. 1a). Consider a balanced isotropic rotor rotating concentrically in one fluid–lubricated and one rigid bearing (Fig. 1b). When using the multi–mode modal approach (mode summation), the mathematical model of the rotor, in both cases, is as follows:

$$
\begin{aligned}
&M_1\ddot{z}_1 + D_1\dot{z}_1 + (K_1+K_2)z_1 - K_2z_2 = 0 \\
&M_2\ddot{z}_2 + D_2\dot{z}_2 + (K_2+K_3)z_2 - K_2z_1 - K_3z_3 = 0 \\
&D(\dot{z}_3 - j\lambda\Omega z_3) + (K_B+K_3+K_4)z_3 + z_3\psi(|z_3|) - K_3z_2 = 0 \\
&z_i(t) = x_i(t) + jy_i(t), \quad i=1,\,2,\,3, \quad |z_3| = \sqrt{x_3^2 + y_3^2}, \quad j=\sqrt{-1}, \quad \cdot = d/dt
\end{aligned}
\tag{1}
$$

where x_i, y_i are rotor horizontal and vertical displacements, M_1, M_2, K_1, K_2, K_3, K_4, D_1, D_2 are two–mode rotor modal masses, stiffnesses, and external damping coefficients, respectively (in case of the fluid–lubricated bearing, the stiffness K_4 either equals zero or represents an external supporting spring (Fig. 1b)). D, K_B, λ are seal or bearing fluid radial damping, radial stiffness and circumferential average velocity ratio, respectively, ψ is fluid nonlinear stiffness function of radial displacement, Ω is rotative speed, t is time.

For clarity of presentation, the unbalance forces, radial side–load forces, external cross damping, fluid inertia effect, and other nonlinear functions are omitted in the model.

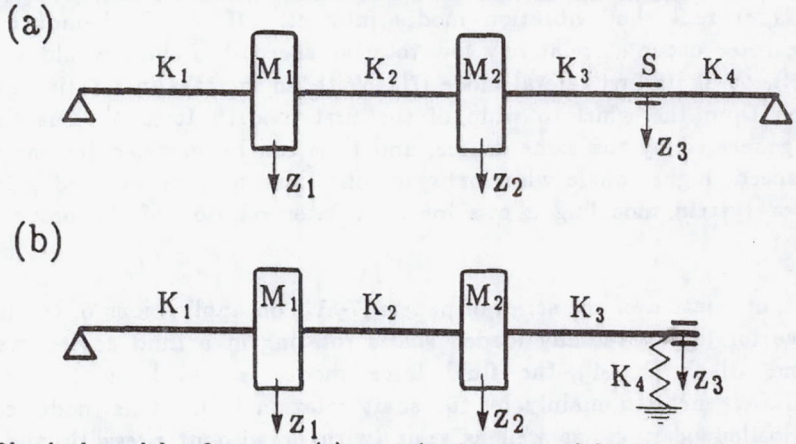

Fig. 1 Physical models of rotors: (a) rotor/seal system, (b) rotor/bearing system.

2.1 Eigenvalue Problem: Natural Frequencies, Thresholds of Stability

The eigenvalue problem for the linearized Eqs. (1) (that is, when ψ=0) provides the following characteristic equation:

$$(\bar{\kappa}_1\bar{\kappa}_2-K_{\frac{2}{3}}^2)[jD(\omega-\lambda\Omega) + K_B + K_3 + K_4] - K_{\frac{2}{3}}^2\bar{\kappa}_1 = 0 \tag{2}$$

where

$$\bar{\kappa}_i = K_i + K_{i+1} + j\omega D_i - M_i\omega^2, \qquad i=1,2 \tag{3}$$

are rotor partial complex dynamic stiffnesses and ω is the complex eigenvalue. Eq. (2) can certainly be solved numerically for specific parameter values. It is the author's intention, however, to show specific qualitative features of this equation solution.

The split of Eq. (2) into real and imaginary parts provides the following equations:

$$D\omega(\omega-\lambda\Omega)(\kappa_1D_2+\kappa_2D_1) - (\kappa_1\kappa_2-K_{\frac{2}{3}}^2-\omega^2D_1D_2)(K_B+K_3+K_4) + K_{\frac{2}{3}}^2\kappa_1 = 0 \tag{4}$$

$$D(\omega-\lambda\Omega)(\kappa_1\kappa_2-K_{\frac{2}{3}}^2-\omega^2D_1D_2) + \omega(\kappa_1D_2+\kappa_2D_1)(K_B+K_3+K_4) - K_{\frac{2}{3}}^2\omega D_1 = 0 \tag{5}$$

where κ_1, κ_2 are direct dynamic stiffnesses, that is the real parts of the complex dynamic stiffnesses (3). The approximate values of the system natural frequencies (real parts of ω) can be calculated from Eq. (5). With damping D_i assumed of the second order of smallness the zero–th approximation establishes $\omega_1 \approx \lambda\Omega$, $\omega_{2,\ldots,5} \approx \pm\omega_{ni}$, i=1,2. The first approximation provides more accurate relationships:

$$\text{FLUID WHIRL FREQUENCY} \equiv \omega_1 \approx \lambda\Omega\left[1 - \right.$$

$$\left. - D_1\frac{[K_2+K_3-M_2\lambda^2\Omega^2+(K_1+K_2-M_1\lambda^2\Omega^2)D_2/D_1](K_B+K_3+K_4)-K_3^2}{D[(K_1+K_2-M_1\lambda^2\Omega^2)(K_2+K_3-M_2\lambda^2\Omega^2) - K_2^2 - \lambda^2\Omega^2D_1D_2]}\right] \tag{6}$$

$$\text{FLUID WHIP FREQUENCIES} = \omega_{2,3} \approx \omega_{ni} -$$

$$- (-1)^iD_1\frac{[K_2+K_3-M_2\omega_{ni}^2+(K_1+K_2-M_1\omega_{ni}^2)D_2/D_1](K_B+K_3+K_4)-K_3^2}{2D(\omega_{ni}-\lambda\Omega)M_1M_2(\omega_{n2}^2-\omega_{n1}^2)}, \quad i=1,2 \tag{7}$$

$$\text{REVERSE MODE FREQUENCIES} = \omega_{4,5} \approx -\omega_{n1,n2} \tag{8}$$

where ω_{n1}, ω_{n2} are solutions of the rotor partial characteristic equation $\kappa_1\kappa_2 - K_{\frac{2}{3}}^2 = 0$:

$$\omega_{ni} = \left\{\frac{K_1+K_2}{2M_1} + \frac{K_2+K_3}{2M_2} + (-1)^i\sqrt{\left[\frac{K_1+K_2}{2M_1} - \frac{K_2+K_3}{2M_2}\right]^2 + \frac{K_{\frac{2}{3}}^2}{M_1M_2}}\right\}^{1/2}, \quad i=1,2 \tag{9}$$

The approximation (7) cannot be applied for the value $\Omega=\omega_{ni}/\lambda$, thus this case should be calculated using Eq. (6).

The fluid whirl frequency ω_1 is almost a linear function of the rotative speed. The fluid whip frequencies $\omega_{2,3}$ are independent from the rotative speed. At the crossing of ω_1 with ω_2 and ω_3

in the plane (Ω, ω_i), i=1,2,3, the straight lines degenerate into hyperbolas (Fig. 2), resulting in a smooth transitions from the whirl—to—whip and whip—to—whirl modes.

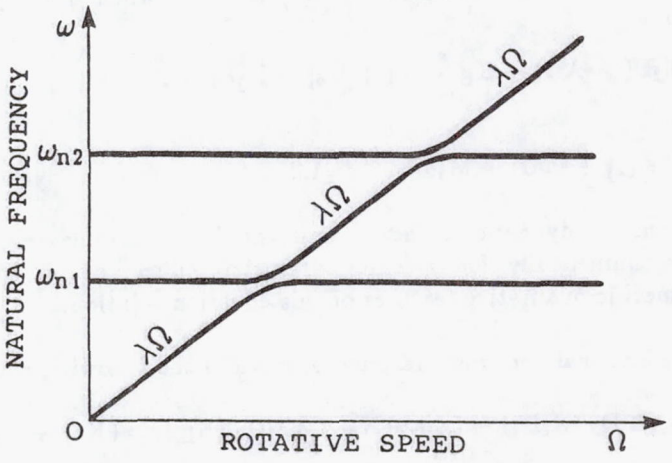

Fig. 2 Natural frequencies versus rotative speed.

Eq. (4) provides the approximate values for stability thresholds. For the whirl onset, ω in Eq. (4) is substituted by $\lambda\Omega_{ST}$ (the zero—th approximation (6) with D_1=D_2=0). The resulting quadratic equation for Ω_{ST}^2 establishes:

$$\Omega_{ST\,i} = \frac{1}{\lambda}\left\{\frac{K_1+K_2}{2M_1} + \frac{K_2}{2M_2} + \frac{K_3(K_B+K_4)}{2M_2(K_3+K_B+K_4)} + \right.$$

$$\left. + (-1)^i \sqrt{\left[\frac{K_1+K_2}{2M_1} - \frac{K_2}{2M_2} - \frac{K_3(K_B+K_4)}{2M_2(K_3+K_B+K_4)}\right]^2 + \frac{K_2^2}{M_1 M_2}}\right\}^{1/2}, \qquad i=1,2 \quad (10)$$

There exist, therefore, two instability onsets leading to the fluid whirl instability. For the whip cessations, ω in Eq. (4) is substituted by ω_{ni}, i=1,2 (the zero—th approximation (7) with D_1 = D_2 = 0), and Ω is substituted by $\Omega_{ST\,i+2}$:

$$\Omega_{ST\,i+2} = \frac{1}{\lambda}\left\{\omega_{ni} + \frac{K_3^2}{D\omega_{ni}[D_2+D_1(K_2+K_3-M_2\omega_{ni}^2)^2/K_2^2]}\right\}, \qquad i=1,2 \qquad (11)$$

Note that all stability thresholds are inversely proportional to the fluid circumferential velocity ratio λ . The onsets (10) do not depend on damping, while the cessations (11) do: larger damping, lowers the cessation rotative speed, thus narrowing the range where the instability occurs. Practically, the cessations seldom occur at rotative speeds (11), because the rotor is already in the self—excited vibration condition, and the system parameters differ from the linear ones. (The first order approximation (11) does not show dependence on K_B, thus no dependence on ψ ; it is necessary to consider higher approximations).

In the rotor/seal system case, the fluid radial stiffness K_B is usually smaller than the stiffness K_4, thus the third term in Eq. (10), and the third term under the radical in Eq. (10), are approximately the stiffnesses of the rotor right portion, combined by two elements in sequence: $K_3K_4/(K_3+K_4)$ (Fig. 1a). The expressions in large parentheses of Eq. (10) represent, therefore,

the natural frequencies of the entire shaft. The stability onset expressed as the $1/\lambda$ fraction of the natural frequency (which for the most often used value λ=0.5 equals 2) is well known in rotor/seal dynamics. At the rotative speed as high as double the first natural frequency, only whip type of instability may occur. That is why very often only whip, and no whirl vibrations, are associated to rotor/seal dynamics. As Eq. (10) indicates, however, the multiplier $1/\lambda$ is not necessarily equal to 2 (which it very seldom is), but depends on the actual circumferential flow conditions in the seal. Swirl brakes or anti–swirl injections can significantly modify λ [11]. Additionally, the fluid radial stiffness may modify the instability onset (10): the larger K_B, the higher the instability onset. (A larger fluid radial stiffness results, for instance, from a higher external pressure of the fluid.) The onset (10) also depends on the location of the seal along the rotor, thus on the values of stiffnesses K_3 and K_4.* The highest values of the onsets (10) occur where the stiffness K_3 is equal to $K_B + K_4$, that is, when the seal is located approximately in the middle between the second modal mass and the right–side bearing.

The function $f_1 = \kappa_1\kappa_2 - K_{\frac{1}{2}}^2$, which provides the whip frequencies ω_{ni}, Eq. (9), and the functions $f_2 = (\kappa_1\kappa_2 - K_{\frac{1}{2}}^2)/\kappa_1$, $f_3 = K_{\frac{1}{2}}^2/(K_B+K_3+K_4)$, which provide onsets of instability, Eq. (10), can be investigated graphically in the plane (ω^2, f_ν), ν=1,2,3. The result is presented in Figure 3. The instability onsets can be found on intersections of the hyperbola f_2 and the straight line f_3 . Now it is easy to discuss the effect of the stiffnesses K_3, K_4, K_B on the instability onsets. If the stiffness K_4 is low (rotor/bearing model), then the line f_3 is higher, and the resulting stability onsets occur at lower rotative speeds, thus, very often in the whirl instability range. An increase of the stiffness K_3 (mass M_2 closer to the instability source) results, again, in a decrease of the instability onset. An increase of the fluid radial stiffness K_B provides a stability improvement by moving the instability onsets toward higher rotative speeds. In all cases, however, the onsets occur at the speeds $\Omega_{ST\,i}$ which are lower than ω_{ni}/λ, i=1,2.

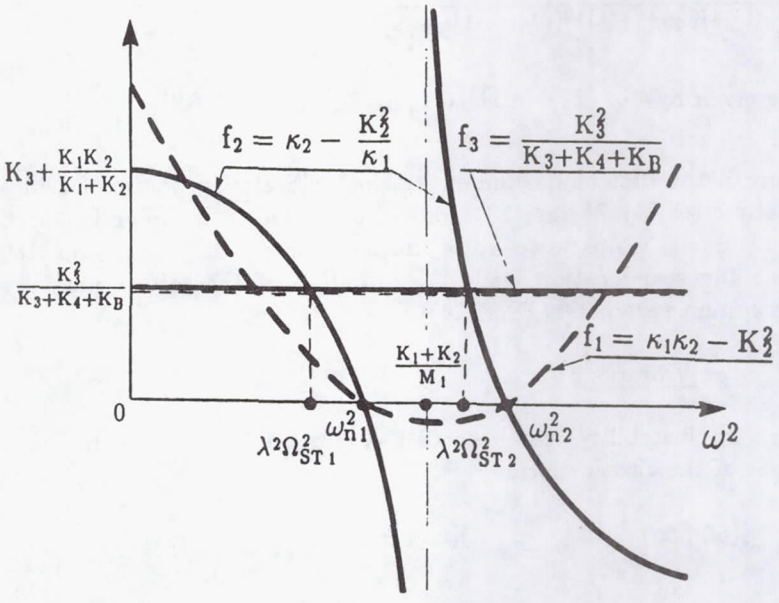

Fig. 3 Graphical solution of Eqs. (4) and (5) showing whip frequencies (9) and onsets of instability (10).

*In this study the seal location is chosen outside the modal masses; a similar analysis can be performed for a case where the seal is located between the modal masses, that is being closer to the second mode nodal point.

2.2 Rotor Modes

The complex modal functions that are calculated from the linear part of Eqs. (1) are as follows:

$$\bar{\phi}_{1\nu} = 1, \quad \bar{\phi}_{2\nu} = 1 + \frac{K_1+D_1 j\omega-M_1\omega^2}{K_2}, \quad \bar{\phi}_{3\nu} = \frac{K_3(K_1+K_2+D_1 j\omega-M_1\omega^2)}{K_2[Dj(\omega-\lambda\Omega)+K_B+K_3+K_4]} \tag{12}$$

Using the natural frequencies (6) and (7), the approximate modal functions at stability thresholds are obtained. The modal functions of the first and second mode whirls are as follows:

$$\bar{\phi}_{1i} = 1, \quad \bar{\phi}_{2i} \approx \xi - (-1)^i \sqrt{\xi^2 + \frac{M_1}{M_2}}, \quad \bar{\phi}_{3i} \approx \bar{\phi}_{2i} \frac{K_3}{K_B+K_3+K_4}, \quad i=1,2 \tag{13}$$

where

$$\xi = \frac{1}{2}\left[\frac{K_1}{K_2} + 1 - \frac{M_1}{M_2} - \frac{K_3 M_1 (K_B+K_4)}{K_2 M_2 (K_B+K_3+K_4)}\right]$$

The modal functions of the first and second mode whips are as follows:

$$\bar{\phi}_{1i+2} = 1, \qquad \bar{\phi}_{2i+2} \approx 1 + \frac{K_1 - M_1\omega_{ni}^2}{K_2},$$

$$\bar{\phi}_{3i+2} \approx \frac{\bar{\phi}_{2i+2} K_3}{\sqrt{(K_B+K_3+K_4)^2 + D^2(\omega_{ni}-\lambda\Omega_{ST\,i+2})^2}} e^{-j\frac{D(\omega_{n\,i}-\lambda\Omega_{ST\,i+2})}{K_B+K_3+K_4}}, \quad i=1,2 \tag{14}$$

where ω_{ni} are given by Eq. (7) and $\Omega_{ST\,i+2}$ by Eq. (11).

During the whirl of the first mode, the entire shaft vibrates in phase. During the second mode whirl, the modal masses M_1, M_2 are 180° out of phase (when damping is neglected). During the first and second mode whips, two rotor masses vibrate in phase, and 180° out of phase, respectively, but the seal location leads the vibration of the second mass by an angle which depends on the system parameters (Eq. (14)).

2.3 Self–Excited Vibrations

After the onsets of instability, the rotor self–excited vibrations occur. Eqs. (1) have exact periodic solutions of the circular form:

$$z_1 = A_1 e^{j(\omega t+\alpha_1)}, \quad z_2 = A_2 e^{j(\omega t+\alpha_2)}, \quad z_3 = A_3 e^{j\omega t} \tag{15}$$

with frequency (or frequencies) ω, and corresponding amplitudes A_i, and phases α_i, i=1,2 relative to the phase of the fluid instability source location. Eqs. (15) describe rotor self–excited vibrations, known as whirl and whip. They occur as steady–state limit cycles after the onsets of instability and some transient process.

The frequencies, amplitudes, and phases of Eqs. (15) can be calculated from the set of nonlinear algebraic equations obtained by substituting (15) into Eqs. (1), and dividing all terms by $e^{j\omega t}$.

Note that the argument of the only nonlinear function ψ becomes now A_3. The final algebraic equations are as follows:

$$A_3 = \psi^{-1}\left[\frac{K_3^2\omega D_1 - D(\omega-\lambda\Omega)(\kappa_1\kappa_2 - K_3^2 - \omega^2 D_1 D_2)}{\omega(\kappa_1 D_2 + \kappa_2 D_1)} - K_B - K_3 - K_4\right] \tag{16}$$

$$A_1 e^{j\alpha_1} = \frac{K_2 K_3}{\bar{\kappa}_1\bar{\kappa}_2 - K_3^2} A_3\,, \qquad A_2 e^{j\alpha_2} = \frac{K_3\bar{\kappa}_1}{\bar{\kappa}_1\bar{\kappa}_2 - K_3^2} A_3 \tag{17}$$

where $\bar{\kappa}_i$, κ_i, i=1,2 are dynamic stiffnesses (3) and their real parts, respectively, and ψ^{-1} denotes the inverse function ψ. The frequency ω in Eq. (16) should be substituted by the frequencies obtained from the equation which differs from the characteristic equation (2) only by one nonlinear term. The approximate values for the self–excited vibration frequencies are, therefore, very close to the fluid whirl and whip frequencies. In Eqs. (6) and (7) the fluid radial stiffness K_B should read $[K_B+\psi(A)]$. Since the second terms in Eqs. (6) and (7) are proportional to rotor damping, and thus are relatively small, the above–discussed nonlinear function adjustment will, therefore, bring very little change to the approximate frequencies (6), (7). The reverse mode frequencies (8) do not satisfy Eq. (16).

For the whip frequencies $\omega = \omega_{n1}$ or $\omega = \omega_{n2}$, the denominators of Eqs. (17) are controlled only by damping, thus, independently of the amplitude A_3, the rotor with masses M_1, M_2 is in "resonant" conditions corresponding to its two lateral modes.

It is easy to show that for the first mode whirl and whip frequencies, the phase angles α_1 and α_2 are negative, thus the mass locations are lagging the instability source at the bearing or seal. For the second mode, the phase lag also occurs additionally to the relative 180° phase change of the modal mass locations. The instability source phase leading of the whirl or whip vibrations is well recognized in the field, and has become the basis of the identification method for the instability source axial location on machinery trains [18].

3. MULTI–MODE ROTOR WITH ONE SOURCE OF INSTABILITY

An analysis similar to that presented in the previous chapter can be performed for the multi–mode rotor (Fig. 4). The rotor characteristic equation now has the following form:

$$[Dj(\omega-\lambda\Omega) + K_B + K_{n-1} + K_n]\bar{\kappa} - K_{n-1}^2 = 0 \tag{18}$$

where

$$\bar{\kappa} = \left\{ \bar{\kappa}_{n-2} - \frac{K_{n-2}^2}{\bar{\kappa}_{n-3} - \frac{K_{n-3}^2}{\bar{\kappa}_{n-4} - \frac{K_{n-4}^2}{\bar{\kappa}_{n-5} - \cdots \bar{\kappa}_4 - \frac{K_4^2}{\bar{\kappa}_3 - \frac{K_3^2}{\bar{\kappa}_2 - \frac{K_2^2}{\bar{\kappa}_1}}}}}} \right\}$$

and

$$\bar{\kappa}_i = K_i + K_{i+1} + j\omega D_i - M_i\omega^2, \qquad i=1,...,n-2$$

are rotor partial complex dynamic stiffnesses. The stiffness $\bar{\kappa}$ represents the dynamic stiffness of the rotor, except its last section at the right side (Fig. 4). The real part of $\bar{\kappa}$, when equalized to zero, will provide the zero—th approximation to whip frequencies $\omega \approx \omega_{ni}$, i=1,...,n—2.

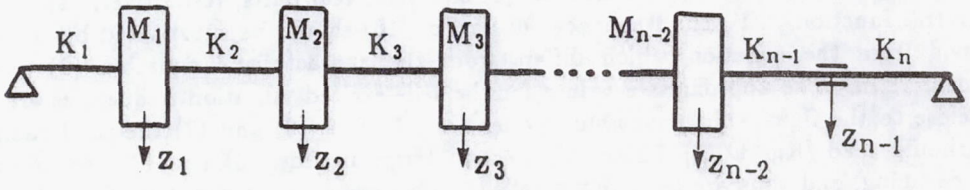

Fig. 4 Multi—mode rotor/bearing/seal model.

The zero—th approximation to the whirl frequency is still $\omega \approx \lambda\Omega$. The further terms in approximations to whirl and whip frequencies, which can be calculated from the imaginary part of Eq. (18), are proportional to the external damping, and except for the regions when $\Omega = \omega_{ni}/\lambda$, they are small.

Similarly to Eq. (4), the real part of Eq. (18) provides the stability thresholds.

The corresponding graphical analysis that is discussed in Section 2.1 can also be performed for Eq. (18). The result indicates virtually the same features: the instability onsets occur at rotative speeds lower than $1/\lambda$ fraction of natural frequencies, and can be controlled by the similar parameters, namely, λ, K_{n-1}, K_n, and K_B.

4. EXPERIMENTAL RESULTS

4.1 Experimental Rig

The experimental rotor, which was made of steel, consisted of a 0.375" diameter shaft with two disks of the mass 4.637×10^{-3} lb.s^2/in (inboard) and 4.643×10^{-3} lb.s^2/in (outboard). The rotor was supported inboard by a relatively rigid sliding bearing bushing, and outboard by a 360° oil—lubricated, cylindrical bearing with 1.5" diameter and 6—mil radial clearance. The lubricant was T10 oil with 5 psi inlet pressure. The rotor was driven by 0.5 hp electric motor through a flexible coupling. Four orthogonal springs supported the outboard end of the shaft, in order to maintain concentric position of the journal inside the bearing at rest. The rotor carried some amount of unbalance.

The sets of XY proximity transducers were located at the fluid—lubricated bearing and at four other axial locations of the shaft (Figs. 5 and 6). The vibrational data from these transducers, as well as from the Keyphasor® (once per rotation pulse) transducer, were collected by the computerized data acquisition and processing system.

4.2 Experimental Results

Two cases with different positions of the disks on the shaft were investigated (Figs. 5 and 6). The rotor vibrational responses at specific rotative speeds were filtered to whirl or to whip

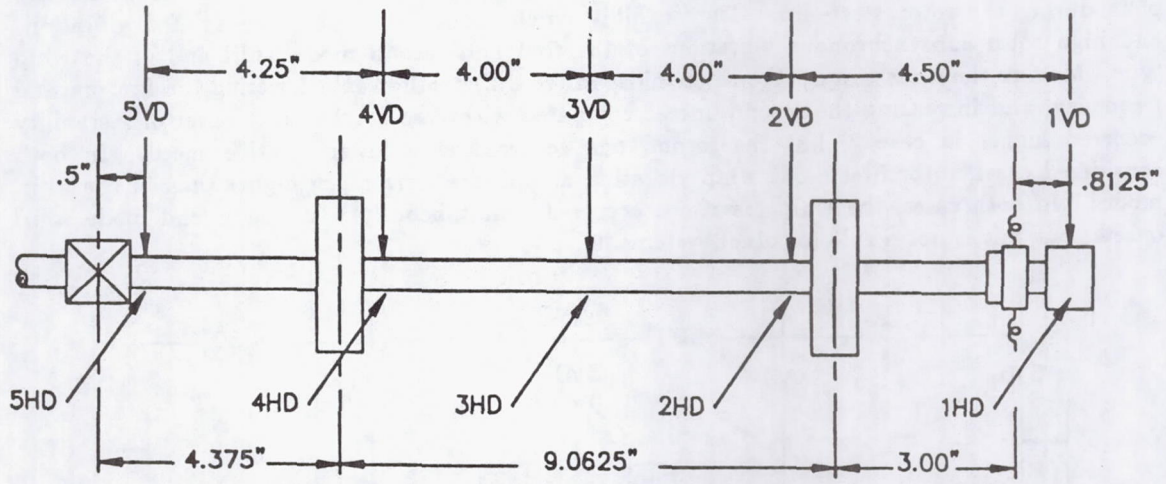

FIRST MODE WHIRL: Ω = 2440 rpm, ω_1 = 1170 cpm

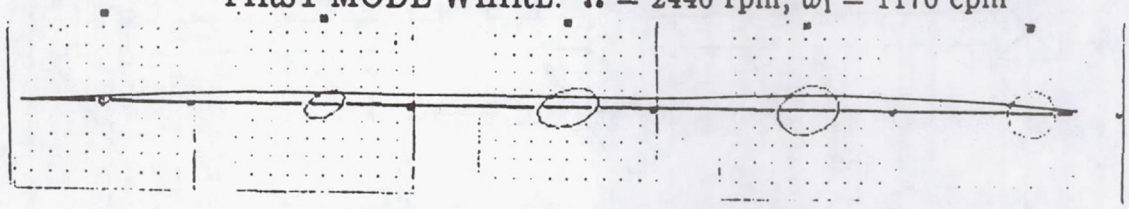

FIRST MODE WHIP: Ω = 3800 rpm, ω_2 = 1700 cpm

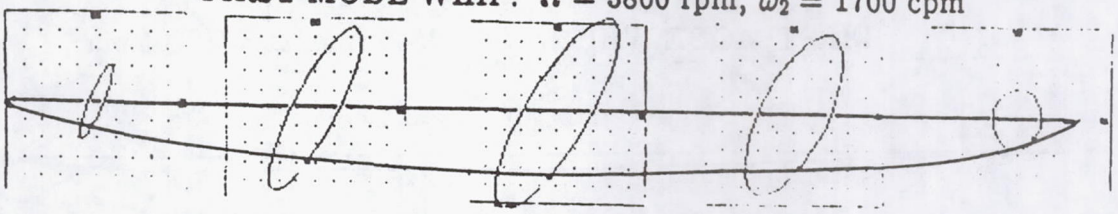

SECOND MODE WHIRL: Ω = 8800 rpm, ω_1 = 4200 cpm

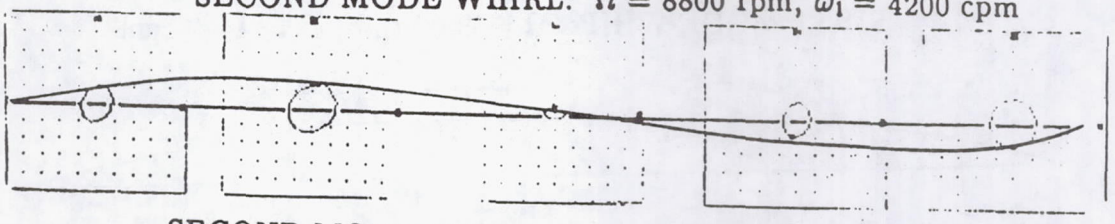

SECOND MODE WHIRL: Ω = 9200 rpm, ω_1 = 4220 cpm
(TRANSITION TO SECOND MODE WHIP)

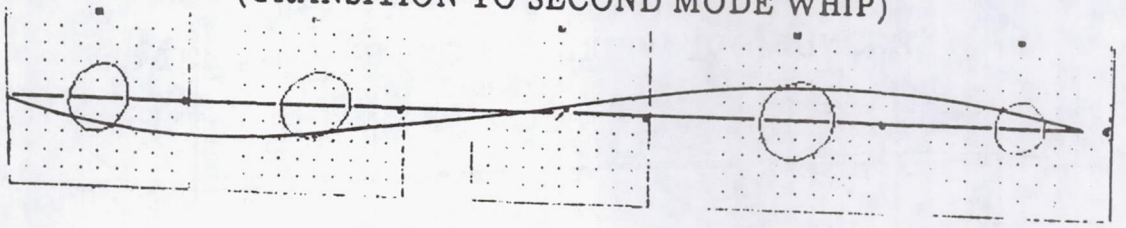

Fig. 5 Rotor sketch and rotor modal centerlines at the first and second mode whirl, the first mode whip, and at the transition from the second mode whirl to the second mode whip at specific rotative speeds. The orbits are filtered to whirl or whip frequencies ω_i, i=1,2. Orbit scale: 5 mil/div. Case 1: disks apart.

frequencies. The artificial Keyphasor marker positions were used to plot rotor centerline deflections for particular modes (Figs. 5 and 6). Figures 7 to 10 present the spectrum cascade plots during the rotor start–up. They exhibit synchronous (1×) unbalance–related vibrations and high rotor subsynchronous vibrations of the first and second mode whirl and of the whip type. Moving the disks toward the rotor midspan (case 2) resulted in a lowering the first natural frequency, and increasing the second one as compared with case 1. The first onset of instability occurred higher in case 2, but the second one occurred at a lower rotative speed. In both considered cases, rotor first mode whip vibration amplitudes were much higher than in the whirl modes. In both cases, the whip cessations occurred simultaneously with the second mode whirl onsets, but this is not a rule for other systems [9].

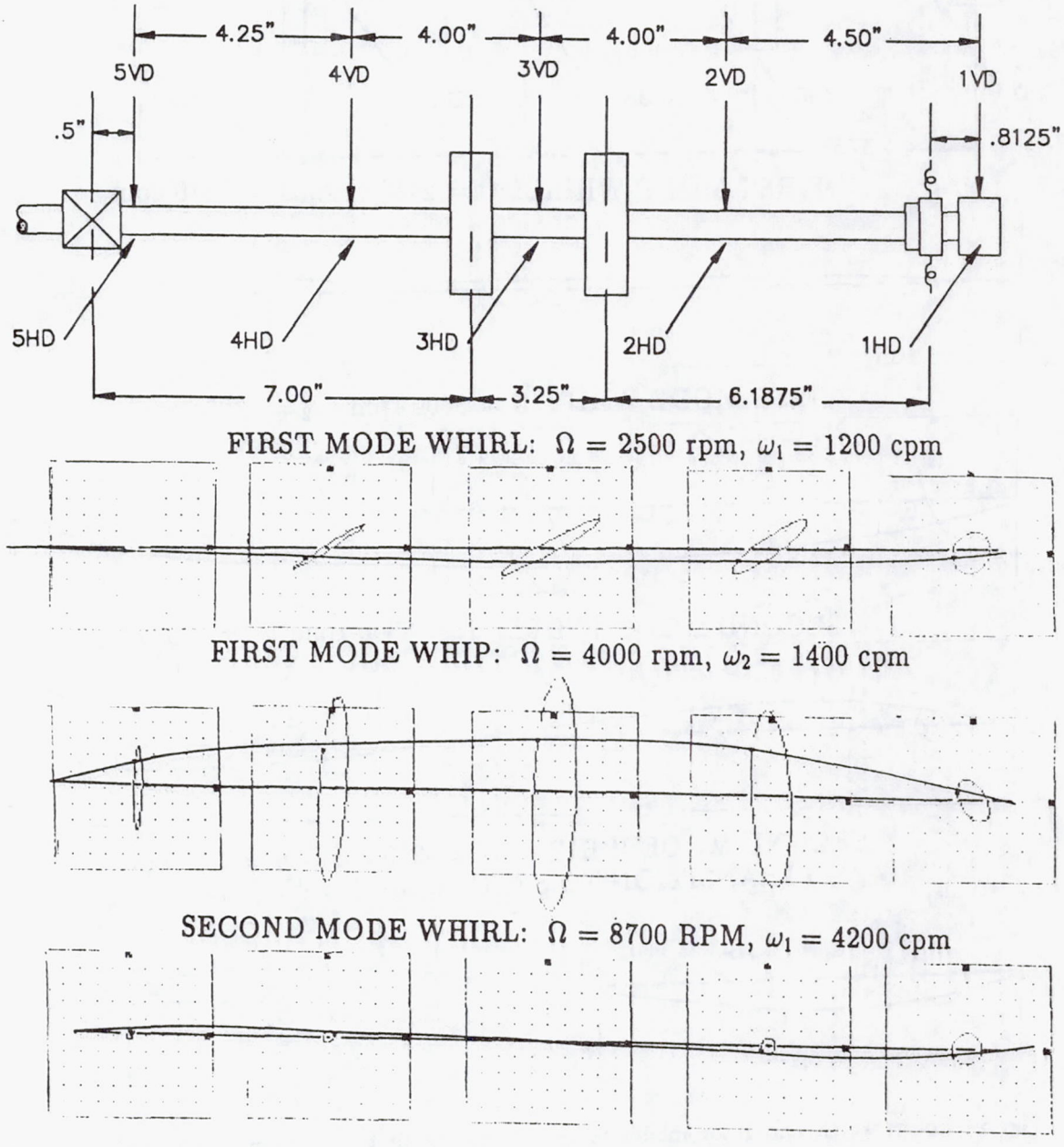

Fig. 6 Rotor sketch and rotor modal centerlines at the first and second mode whirl and at whip at specific rotative speeds. The orbits are filtered to whirl or whip frequencies ω_i, i=1,2. Orbit scale: 5 mil/div. Case 2: disks close to mid-span.

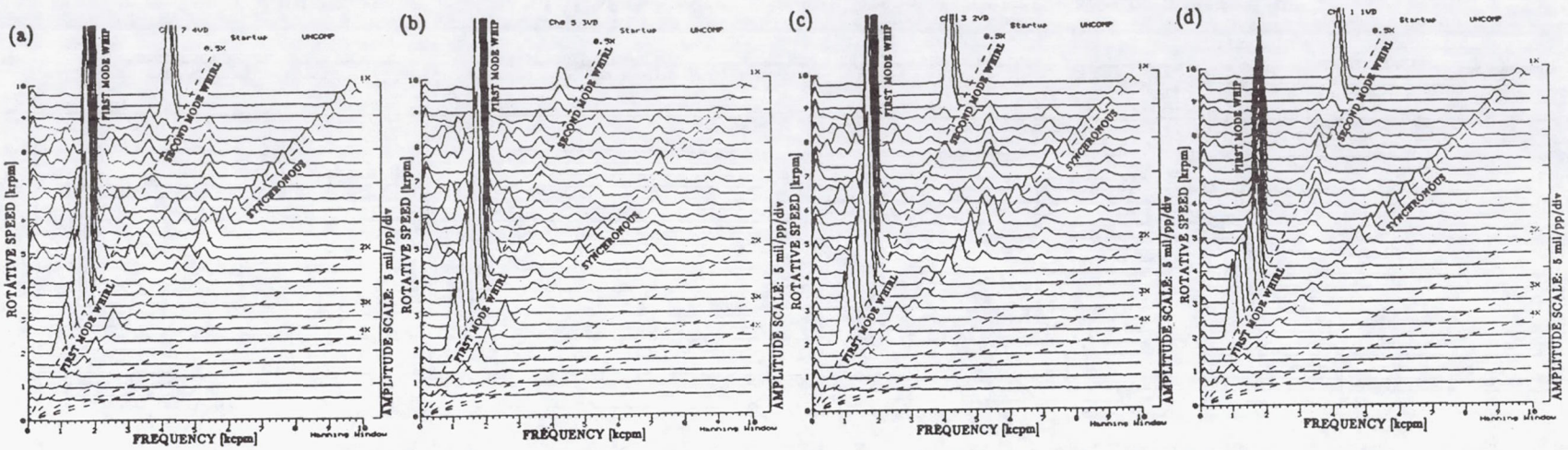

Fig. 7 Spectrum cascade plots of the rotor vertical responses during start-up, measured by the probes at axial locations 4(a), 3(b), 2(c), and 1 (journal) (d). Case 1.

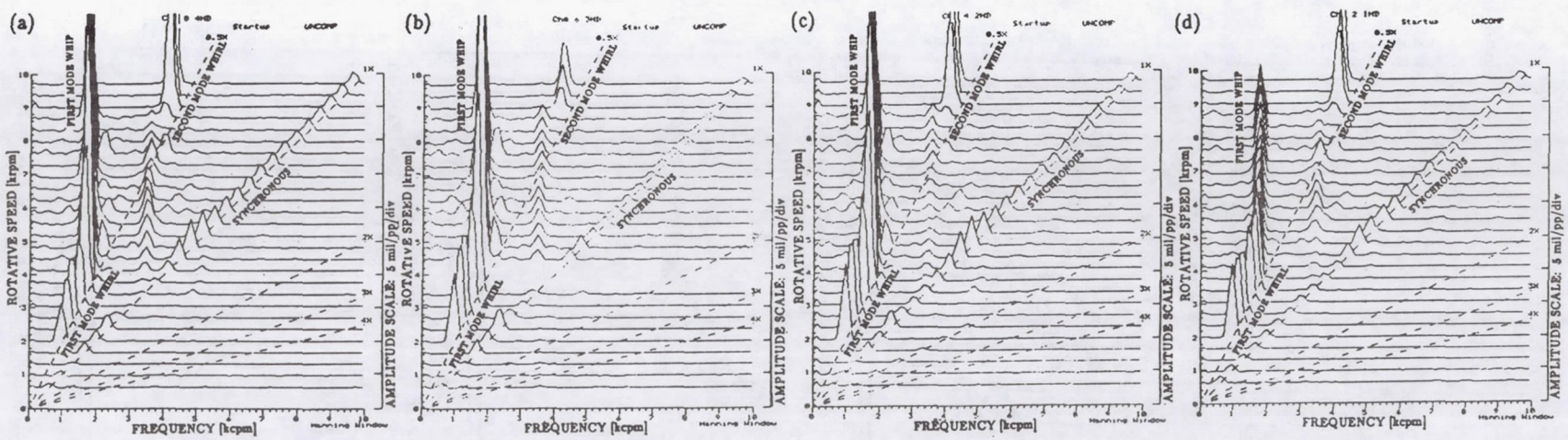

Fig. 8 Spectrum cascade plots of the rotor horizontal responses during start-up, measured by the probes at axial locations 4(a), 3(b), 2(c), and 1 (journal) (d). Case 1.

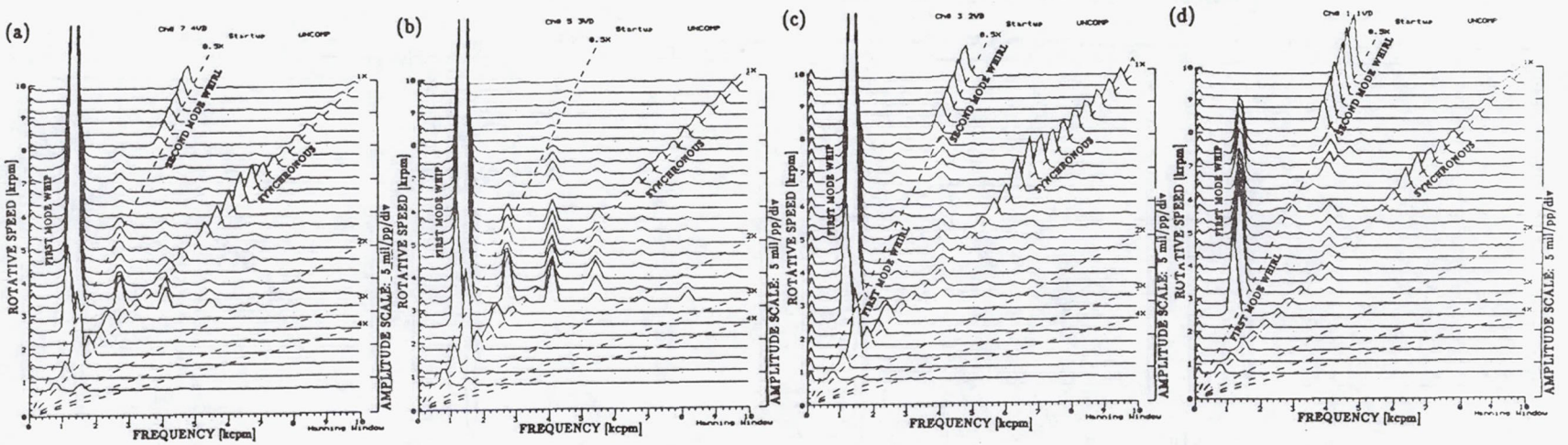

Fig. 9 Spectrum cascade plots of the rotor vertical responses during start-up, measured by the probes at vertical locations 4(a), 3(b), 2(c), and 1 (journal) (d). Case 2.

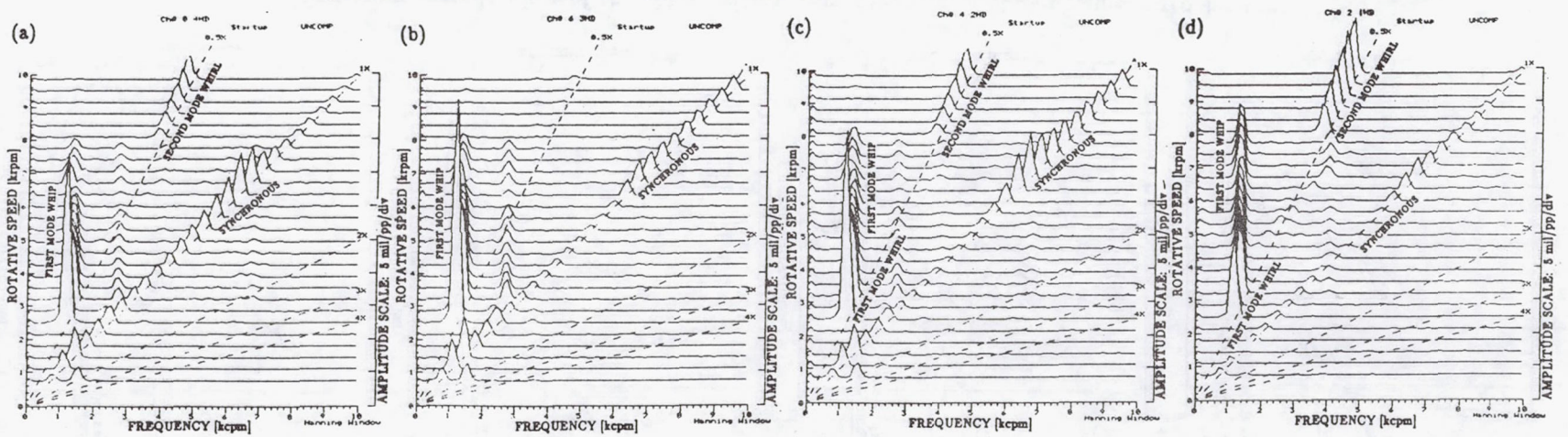

Fig. 10 Spectrum cascade plots of the rotor horizontal responses during start-up, measured by the probes at horizontal locations 4(a), 3(b), 2(c), and 1 (journal) (d). Case 2.

The modal parameter ratios as functions of the square root of mass ratio calculated from Eqs. (20) are presented in Figure 11. Since the modal parameter ratios must be positive, there exist limited ranges of mass ratios which satisfy this condition. It can be seen in Figure 11 that for case 1: $1.92 < \mu < 10.8$, and for case 2: $1.98 < \mu < 19.9$.

Perturbation testing should provide more reliable identification data [17].

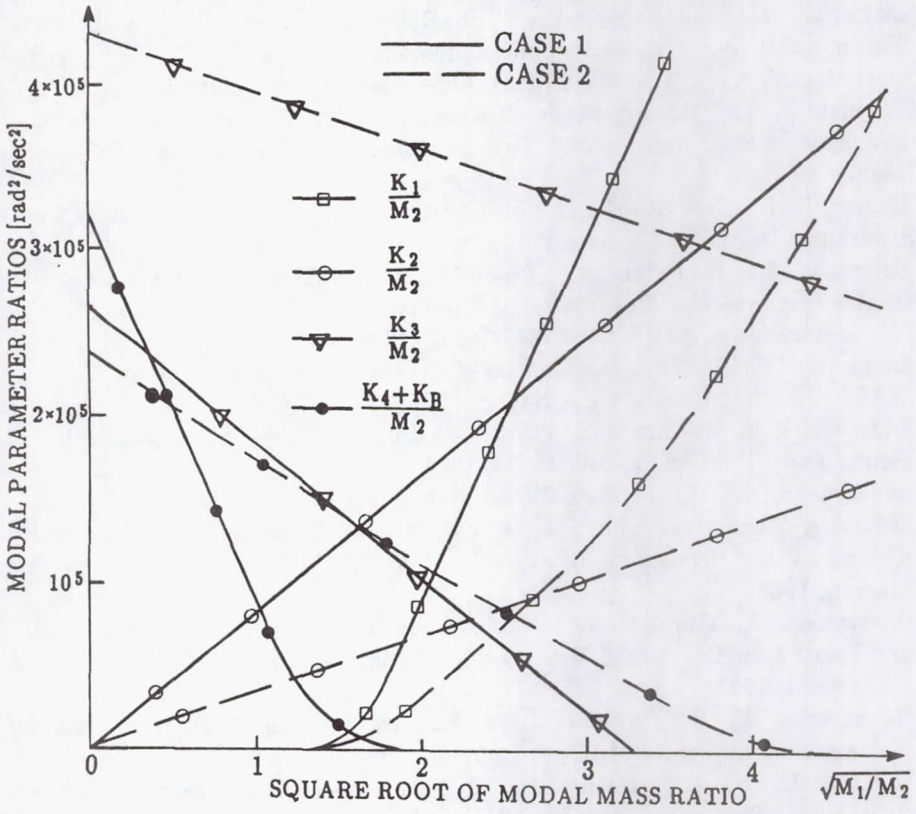

Fig. 11 Rotor modal parameter ratios as functions of the square foot of modal mass ratio.

NOTATION

A_i, α_i	Amplitudes and phases of rotor self-excited vibrations, respectively
D, K_B	Fluid radial damping and radial stiffness, respectively
$z_i, \lvert z_i \rvert$	Rotor complex lateral displacements and their absolute values
D_i, M_i	Rotor modal damping coefficients and modal masses, respectively
K_i	Rotor modal stiffnesses
i, ν	Integers
$j=\sqrt{-1}$	
t	Time
x_i, y_i	Rotor horizontal and vertical displacements, respectively
$\bar{\kappa}_i, \kappa_i$	Rotor complex dynamic stiffnesses and their real parts, respectively
λ	Fluid circumferential average velocity ratio
$\mu=M_1/M_2$	Modal mass ratio
$\bar{\phi}_{i\nu}$	Rotor complex modal functions
ψ	Fluid nonlinear stiffness function
ω	Complex eigenvalue; also self-excited vibration frequency
ω_i	Approximate natural frequencies of the rotor system
ω_{ni}	Rotor natural frequencies
Ω	Rotative speed
Ω_{STi}	Thresholds of stability

REFERENCES

1. Kirk, R. G., Nicholas, J. C., Donald, G. H., and Murphy, R. C., Analysis and Identification of Synchronous Vibration for a High Pressure Parallel Flow Centrifugal Compressor, Rotordynamic Instability Problems in High Performance Turbomachinery, NASA CP 2133, College Station, Texas, 1980.
2. Doyle, H. E., Field Experiences With Rotor Dynamic Instability in High Performance Turbomachinery, Rotordynamic Instability Problems in High—Performance Turbomachinery, NASA CP 2133, College Station, Texas, 1980.
3. Wachel, J. C., Rotordynamic Instability Field Problems, Rotordynamic Instability Problems in High Performance Turbomachinery, NASA CP 2250, College Station, Texas, 1982.
4. Baxter, N. L., Case Studies of Rotor Instability in the Utility Industry, Rotor Dynamical Instability, AMD, v. 55, New York, 1983.
5. Schmied, J., Rotordynamic Stability Problems and Solutions in High Pressure Turbocompressors, Rotordynamic Instability Problems in High Performance Turbomachinery, NASA CP 3026, College Station, Texas, 1988.
6. Laws, C. W., Turbine Instabilities—Case Histories, Instability in Rotating Machinery, NASA CP 2409, Carson City, Nevada, 1985.
7. Muszynska, A., Whirl and Whip —— Rotor/Bearing Stability Problems, Journal of Sound and Vibration, v. 110, No. 3, 1986.
8. Muszynska, A., Multi—Mode Whirl and Whip in Rotor/Bearing Systems, Dynamics of Rotating Machinery, The Second International Symposium on Transport Phenomena, Dynamics, and Design of Rotating Machinery, v. 2, Hemisphere Publ. Corp., Honolulu, Hawaii, 1988.
9. Muszynska, A., Grant, J. W., Stability and Instability of a Two—Mode Rotor Supported by Two Fluid—Lubricated Bearings, Trans. ASME Journ. of Vibration and Acoustics, v. 113, No. 3, 1991.
10. Muszynska, A., The Role of Flow—Related Tangential Forces in Rotor/Bearing Seal System Stability, ISROMAC—3, Honolulu, Hawaii, 1990.
11. Bently, D. E. and Muszynska, A., Anti—Swirl Arrangements Prevent Rotor/Seal Instability, Trans. ASME Journal of Vibration, Acoustics, Stress and Reliability in Design, v. 111, No. 2, 1989.
12. Bolotin, V. V., Nonconservative Problems in Theory of Elastic Stability, The MacMillan Company, New York, 1963.
13. Black, H. G., Effects of Hydraulic Forces in Annular Pressure Seals on the Vibrations of Centrifugal Pump Rotors, Journal of Mechanical Engineering Science, v. II, No. 2, 1969.
14. Black, H. F., Jensen, D. N., Dynamic Hybrid Bearing Characteristics of Annular Controlled Leakage Seals, Proceedings Journal of Mechanical Engineering, v. 184, 1970.
15. Muszynska, A., Improvements in Lightly Loaded Rotor/Bearing and Rotor/Seal Models, Trans. ASME, Journal of Vibration, Acoustics, Stress and Reliability in Design, v. 110, No. 2., pp. 129—136, 1988.
16. Muszynska, A., Modal Testing of Rotor/Bearing Systems, The International Journal of Analytical and Experimental Modal Analysis, v. 1, No. 3, 1986.
17. Muszynska, A., Perturbation Technique for Identification of the Lowest Modes of Rotors With Fluid Interaction, Proc. of the Course on "Rotor Dynamics and Vibration in Turbomachinery," von Karman Institute for Fluid Dynamics, Belgium, September 1992.
18. Bently, D. E., Bosmans, R. F., A Method to Locate the Source of a Rotor Fluid—Induced Instability Along the Rotor, ISROMAC—3, Honolulu, Hawaii, 1990.

During whip conditions the whip frequency filtered orbits are elliptical, reflecting rotor system anisotropic features. During whirl conditions the orbits are circular (except the first-mode whirl in case 2), and much smaller than at whips (Figs. 5, 6). There exist higher harmonic and combinational components in the spectra (Figs. 7 to 10), especially when amplitudes of whip vibrations are high (Figs. 7, 8) causing involvement of geometric nonlinearities.

The first instability onset in case 2 (Figs. 9, 10) occurs at relatively high rotative speed, in the range of the transition to whip rather than at whirl, as in case 1 (Figs. 7, 8). The phases and amplitudes of these self-excited vibrations change considerably just after the onset: first the horizontal amplitudes are large, then, at higher rotative speed, in whip conditions, the vertical amplitudes become dominant (Fig. 9).

4.3 Identification of Rotor Modal Parameters From Experimental Results

In this section a method of partial (incomplete) identification of the rotor two-mode modal parameters will be outlined. This method does not pretend to be general; the identification results show only that the modal modelling is feasible, simple, and reflects major dynamic features of the rotor behavior.

The data for identification is taken from the start-up runs (Figs. 7 to 10): rotor natural frequencies of the first two modes, ω_{n1}, ω_{n2}, and the onsets of instability for the first and second mode whirls, $\Omega_{ST\,1}$, $\Omega_{ST\,2}$. From Eqs. (9) and (10), the rotor parameters are calculated as follows:

$$\frac{K_2}{M_2} = [b(\omega_{n1}^2 + \omega_{n2}^2 - b) - \omega_{n1}^2\omega_{n2}^2]\sqrt{\mu}\,, \qquad \frac{K_1}{M_2} = b\mu - \frac{K_2}{M_2}$$

$$\frac{K_3}{M_2} = \omega_{n1}^2 + \omega_{n2}^2 - b - \frac{K_2}{M_2}\,, \qquad \frac{K_B+K_4}{M_2} = \frac{K_3}{M_2}\left[\frac{K_3/M_2}{\omega_{n1}^2+\omega_{n2}^2-\lambda^2(\Omega_{ST\,1}^2+\Omega_{ST\,2}^2)} - 1\right] \tag{20}$$

where

$$b = \frac{\omega_{n\,1}^2\omega_{n2}^2 - \lambda^4\,\Omega_{ST\,1}^2\,\Omega_{ST\,2}^2}{\omega_{n1}^2 + \omega_{n2}^2 - \lambda^2(\Omega_{ST\,1}^2 + \Omega_{ST\,2}^2)}\,, \qquad \mu = \frac{M_1}{M_2}$$

Since there are only four equations, (9) and (10), and seven unknown parameters, the stiffness-to-mass ratios are expressed as functions of the modal mass ratio μ.

The data for the cases 1 and 2 are given in Table 1.

TABLE 1. Experimental Data

	ω_{n1}	ω_{n2}	$\Omega_{ST\,1}$	$\Omega_{ST\,2}$	λ
	rpm				—
Case 1	1677	5200	2000	8800	0.48
Case 2	1400	6300	2500	8000	0.48

AN INVESTIGATION OF ANGULAR STIFFNESS AND DAMPING COEFFICIENTS OF AN AXIAL SPLINE COUPLING IN HIGH-SPEED ROTATING MACHINERY

C.-P. Roger Ku and James F. Walton, Jr.
Mechanical Technology Incorporated
Latham, New York

and

Jorgen W. Lund
The Technical University of Denmark
Lyngby, Denmark

ABSTRACT

This paper provided the first opportunity to quantify the angular stiffness and equivalent viscous damping coefficients of an axial spline coupling used in high-speed turbomachinery. A unique test methodology and data reduction procedures were developed. The bending moments and angular deflections transmitted across an axial spline coupling were measured while a non-rotating shaft was excited by an external shaker. A rotordynamics computer program was used to simulate the test conditions and to correlate the angular stiffness and damping coefficients. In addition, sensitivity analyses were performed to show that the accuracy of the dynamic coefficients do not rely on the accuracy of the data reduction procedures.

INTRODUCTION

Internal friction as a problem in rotor-bearing systems was first recognized in the mid-1920s when manufacturers began shrinking disks onto supercritical rotors. Newkirk [1] observed that at speeds above the first critical speed, the rotor would enter into a violent whirling in which the rotor centerline precessed at a rate equal to the first critical speed. Kimball [2] suggested that internal shaft friction could be responsible for the whirling. Since then, numerous contributors [3-6] have provided additional insight into the effects of internal friction.

Today, with the increased power densities of advanced turbopumps and the resultant increased rotor flexibility, internal friction is seen to be a potential source of problems. Turbopumps such as the Space Shuttle Main Engine (SSME) High-Pressure Oxidizer Turbopump (HPOTP) are of built-up design with many joints, fits and areas for friction-induced excitation if slippage takes place. These rotors operate above flexible bending critical speeds and the forces on the rotors are very large, which tends to encourage joint slippage and friction force generation. The rotor instability resulting from this type of vibration is usually cured by adding special dampers, redesigning rotor fits, or modifying the bearings, which does not allow the development of a true understanding of the mechanisms of internal friction. In addition, the practicing design engineer finds very little readily available information on how to model the various couplings which make up the complete rotor system. Often, a rotordynamicist must make an intelligent guess on the dynamic properties of the coupling in order to perform the analysis.

In the design charts of flanged and curvic couplings provided by Bannister [7], flexural stiffness values were provided but no damping data were available. Marmol et. al. [8] developed a

Preceding Page Blank

mathematical model to predict the lateral and angular stiffness and damping coefficients of spline couplings. Based on these coefficients, they calculated the natural frequencies of a rotor system and compared them to the experimental data. Recently, Walton et. al. [9] developed three nonlinear analytical models representing interference fits and axial and curvic spline couplings, and integrated them with a transient rotordynamics computer program analysis. Results from this work show the predictability of rotor system instability due to internal friction, which has been experimentally observed, especially for axial splines.

It has been shown that measuring only the natural frequencies of a rotor system cannot accurately verify models predicting angular stiffness and damping coefficients of axial spline couplings [10]. However, no direct measurement has been reported, such as measuring the angular displacement and moment. This paper describe a unique test methodology and data reduction procedures that have been developed determining the angular stiffness and damping coefficients of an axial spline coupling. The bending moments and angular deflections transmitted across the axial spline coupling were measured while a non-rotating shaft was excited by an external shaker. The angular stiffness and equivalent viscous damping coefficient were determined by the interactive use of rotordynamics computer program simulations and experimental measurements. In addition, sensitivity analyses were performed to demonstrate that the accuracy of the data reduction procedures does not affect the accuracy of the results.

EXPERIMENTAL TEST SETUP

The test facility was built to simulate an SSME HPOTP preburner spline. Figure 1 shows the overall test setup and Figure 2 is a functional block diagram of the test setup. The shaft consists of two offset male axial splines and an external female spline sleeve. The shaft was excited by an external dynamic force which was driven by an MTS hydraulic force control system in the X-direction (horizontal). An external damper was installed but was not active while the bending moment and angular deflection were measured. The damper was used to limit the shaft orbit while the system was traveling through its unstable natural frequencies. The shaft total length was 1.524 m, supported on two deep-groove ball bearings 1.357 m apart. Total shaft weight was 155.4 N without the spline sleeve installed and 222.4 N with the sleeve installed. The shaft diameter outboard of the splines was 37.34 mm, while the center section between the two splines was 29.97 mm in diameter and 57.15 mm in length. The active length of each shaft external spline was 38.1 mm while the spline sleeve active length was 133.4 mm in order to span both of the shaft external splines. A close-up of the axial spline coupling is shown in Figure 3. Both shaft splines were identical but were machined 0° 18' (±15") offset from each other. The static torque preload that resulted was approximately 678 N-m. This torque value is representative of the SSME HPOTP preburner spline. The two shaft splines and the mating internal spline sleeve were fabricated according to the following criteria:

Type	Fillet root side fit
Number of Teeth	42
Pressure Angle	30°
Pitch	20/40
Pitch Diameter	53.3 mm
Base Diameter	46.1937 mm
Surface Finish	32√
Coating	MoS_2

Kulite ADP-350-300 semiconductor strain gages and specially fabricated high-resolution capacitance displacement probes were used to measure the bending moments and angular displacements, respectively. Four pairs of strain gages were installed on the shaft surface at two axial locations (see Figure 3). At each location, one pair of strain gages was located at $0^{o}/180^{o}$ with respect to the key phase, and another pair was located at $90^{o}/270^{o}$. Eight capacitance probes were installed to measure the angular deflection of the shaft and spline sleeve at four axial locations, where a disc was attached to each end of the spline sleeve and two discs were attached to the shaft outboard of the spline sleeve. At these four axial planes, axial motion was measured in line with the shaker stinger and at 90° to the stinger, and was converted to the angular deflections of that plane. In all cases, precise angular position of the instrumentation is required to ensure the integrity of the data. Circumferential alignment of the bending moment strain gage bridges was maintained to within 0.125^{o}. Likewise, the angular deflection capacitance probes were positioned to the same accuracy from the shaft centerline plane. In addition to the bending moment and angular deflection instrumentation, shaft lateral motion in two orthogonal directions, input force, and acceleration of the input force ram head were measured. While the testing discussed herein relates to nonrotating testing, the instrumentation setup is capable of being used as the shaft is rotated and excited nonsynchronously by the shaker [11].

As shown in Figure 2, the data was acquired by a computer digital data acquisition system. For each test condition, the input force, input acceleration, frequency, shaft motions, axial capacitance probe displacements, and bending moments were measured. To ensure a clear reference signal for all of the data, the oscillator used to drive the MTS hydraulic actuator was run through a synchronous tracking filter and subsequently converted to a square wave signal with a sharp leading edge. This square wave signal was then used as the reference excitation timing signal for all data acquisition.

Prior to conducting the shaker testing, system qualification included a series of low-frequency tests where hysteresis loops of the input strain were plotted against the bending moment beneath the spline sleeve [11]. Once the data instrumentation was qualified, a series of tests was run to acquire bending moment and spline angular deflection data. During the test, data was taken with the shaft oriented so that the $0^{o}/180^{o}$ strain gage pair was directly in line with the shaker stinger. Then, the orientation of the shaft was rotated so that the $90^{o}/270^{o}$ strain gage pair was in line with the stinger, the data was retaken under the same conditions. During the data taking, the off-axis (orthogonal to the stinger plane) bending strain gage data was reviewed and the system alignment was adjusted by rotating the orientation of the shaft manually 1° or 2° to minimize the magnitude of the signal in that plane. Once the out-of-plane bending strain signal was minimized, it was judged that the system was properly aligned.

DATA REDUCTION PROCEDURES

A multi-level rotordynamics model of the test system was developed for a finite-element-based, steady-state linear rotordynamics computer program [12]. The main shaft was divided into 41 elements, and each element was connected by two stations. The axial spline sleeve was modeled as the second level and had 13 elements. The connections between the main shaft and spline sleeve were modeled as two identical bearings. Figure 3 defines the station numbers in this region and shows the locations where the instruments were installed. Each bearing was assumed to have non-zero lateral stiffness, angular stiffness and angular damping, but with zero lateral damping. To simplify the test data reduction procedures, all stiffness and damping were assumed isotropic, and cross-coupling terms were neglected. Introducing anisotropic terms would lead the dynamic

coefficients to be time dependent [10]. Lateral stiffness value was determined by a model developed earlier [9]. The rotordynamics model was tuned to match natural frequencies and mode shapes obtained during impact tests as closed as possible [10].

In the linear rotordynamics computer program, the change in the bending moments, ΔM, and angular deflections, $\Delta\phi$, across the axial spline can be represented by the following equation in terms of the angular stiffness, K_A, and equivalent viscous damping coefficient, B_A [6].

$$\Delta M_i = K_A \Delta\phi_i + B_A \Delta\dot{\phi}_i, \qquad i = x, y \tag{1}$$

Physically, it is very difficult to measure the bending moments and angular deflections at the spline coupling locations (stations 25 and 61). Therefore, to approximate the bending moments and angular deflections between stations 25 and 61 (61-25), the original test procedure called for subtracting the bending moments at stations 23 from the bending moment at station 29 (29-23) to arrive at an approximation of the bending moment at the spline coupling. Similarly, the angular deflection at the spline coupling was determined by subtracting the angular deflection at station 30 from that at station 65 (65-30). The initial approximated angular stiffness and damping coefficients were computed by Equation (1). Then, the bending moments and angular deflections at those stations were calculated by the rotordynamics computer program based on the approximated coefficients. An iterative procedure was developed to use both the rotordynamics computer program and Equation (1) interactively until results of the coefficients converged.

Table 1 displays the calculated relative bending moments and angular deflections, both amplitudes and phases, across the spline coupling, stations 61-25, and at the locations to be measured, stations 29-23 and 65-30, for a wide range of angular stiffness and damping coefficients as the shaft was shaking with 222 N at 50 Hz. We found that the coefficients were very sensitive to the accuracy of the phase of the relative angular deflection to be measured. The same phenomenon was found at a lower frequency. This is due to the fact that the shaft is much easier to bend near the outboard of the spline; therefore, the angular deflection of the shaft changes dramatically from station 25 to station 30 (see Figure 4). At the same time, the spline sleeve responded like a rigid body, and the angular deflections of the spline sleeve had almost the same values at both stations 61 and 65. Unfortunately, the change of the shaft angular deflection compensated for the change of the angular deflection across the spline coupling caused by the damping, especially the phase. Therefore, an alternative data reduction procedure was required to determine the dynamic coefficients.

Table 2 shows the calculated absolute bending moments and angular deflections, both amplitudes and phases, at stations 23, 29, 30 and 65, for the same range of angular stiffness and damping coefficients as shown on Table 1, but with an applied load of 222 N at 5 Hz. We found that the absolute amplitude of the bending moment at station 23, the neck section between two splines, decreased as the angular stiffness increased, and the phase, with respect to the phase of a key location, of the bending moment at station 23 increased as the damping decreased. As the frequency increased, the amount of the change in both amplitude and phase due to the change in angular stiffness and damping increased. The amount of change was both measurable and distinguishable, providing an opportunity to use only the bending moment at station 23 to determine the angular stiffness and equivalent viscous damping coefficient. Other measured data act as checking points against which to compare the calculated data.

The revised data reduction procedure is: (i) measure the bending moments at both stations 23 and 29, and angular deflections at both stations 30 and 65; (ii) calculate these bending moments and

angular deflections by a rotordynamics computer program based on guessing values of K_A and B_A; (iii) adjust K_A and B_A until the amplitude and phase of the bending moment at station 23 match the measured data; (iv) perform minor adjustment of K_A and B_A to minimize the sum of the relative errors due to the difference between the calculated and measured data at stations 29, 30 and 65.

RESULTS AND DISCUSSION

The tests were conducted at three levels of external shaking forces: 80.4, 162.6, and 221.1 N at 5 Hz while the shaft was not rotated. At each force level, three data sets were taken, and we found that the variations of all measured data were within 1% in amplitude and 0.2° in phase. As the orientation of the shaft was rotated 90°, the same accuracy was achieved.

Table 3 displays the calculated angular stiffness and damping coefficients of the three force levels using the revised data reduction procedures. The comparisons of the measured data and predicted values at those four stations are also shown in the same table. For all three force levels, the errors between measured data and predicted values are all within 5%. However, we expect that the errors may increase as the shaking force frequency increases.

Note that for these three test cases, the angular stiffness decreases and damping increases as the force increases. This may be due to the fact that the relative motion between contact surfaces of the spline and sleeve increases as the shaking force increases. To determine the source and the mechanism of damping of the spline coupling, more studies are required, especially testing at different static preload torque levels of the spline coupling; however, this requires a permanent change of the hardware.

The sensitivity analyses were performed for the case with 222 N shaking force at 5 Hz to study the effects of the accuracy of both the rotordynamics model as well as the measured geometrical configurations. On Table 4, which shows the results of the sensitivity analyses, it can be seen that the values of the various parameters were changed somewhat from the baseline values. The change occurred in ball bearing stiffness, K_B; spline lateral stiffness, K_R; the shaft diameters, D_{23} and D_{29}, at station 23 and 29, respectively; the length between two splines, $L_{22\text{-}24}$; the installed bending strain gage locations at both station 23 and station 29; the orientation of the shaft, ϕ_{Key}; and the misalignment of the external shaking force stinger. We found that all the parameters have little effect on the accuracy of predicting bending moments and angular deflections at stations 23, 29, 30 and 65. The biggest error is caused by the misalignment of the orientation of the shaft; however, in our experiment, we were able to reduce the misalignment to within 2°. After the sensitivity analyses were performed, we were able to conclude that the accuracy of the angular stiffness and damping coefficient determination relied on the accuracy of the measured amplitudes and phases at all four stations, but was unaffected by the revised data reduction procedures.

CONCLUSIONS

A unique test methodology and data reduction procedures were developed in order to measure the bending moments and angular deflections transmitted across an axial spline coupling while the nonrotating shaft was excited by an external shaker. The angular stiffness and equivalent viscous damping coefficients were determined by the interactive use of rotordynamics computer program simulations and experimental measurements. Sensitivity analyses were performed to demonstrate that the proposed data reduction procedure has little effect on the accuracy of the results.

For the three shaking force levels tested at 5 Hz, the errors between the measured data and the predicted values are all within 5%. In addition, we found that for these three test cases the angular stiffness decreases and damping increases as the force increases. However, more tests are required to determine the source and the mechanism of damping of the spline coupling, such as the measurements for different static preload torque levels of the spline coupling.

ACKNOWLEDGMENTS

The authors express their appreciation to the NASA Marshall Space Flight Center, the principal supporter of the work reported in this paper, for their generous support. The authors would also like to thank Messrs. D. Buesing, L. Hoogenboom, P. Quantock, and D. Smith of Mechanical Technology Incorporated for their help in preparing the test facilities.

REFERENCES

1. Newkirk, B. L., 1924, "Shaft Whipping," General Electric Review, Vol. 27, No. 3, March, pp. 169-178.
2. Kimball, A. L. Jr., 1924, "Internal Friction Theory of Shaft Whirling," General Electric Review, Vol. 27, No. 4, April, pp. 244-251.
3. Robertson, D., 1935, "Hysteretic Influences on The Whirling of Rotors," Proc. of Inst. Mech. Engr., Vol. 131, pp. 513-537.
4. Gunter, E. J. Jr., 1967, "The Influence of Internal Friction on The Stability of High Speed Rotors," ASME, J. of Engineering for Industry, Vol. 89, No. 4, pp. 683-688.
5. Williams, R. Jr., and Trent, R., 1970, "The Effects of Nonlinear Asymmetric Supports on Turbine Engine Rotor Stability," SAE 700320.
6. Lund, J. W., 1986, "Destabilization of Rotors from Friction in Internal Joints with Micro-Slip," Proc. of The International Conference on Rotordynamics, September 14-17, Tokyo, pp. 487-491.
7. Bannister, R. H., 1980, "Methods for Modeling Flanged and Curvic Couplings for Dynamic Analysis of Complex Rotor Constructions," ASME, J. of Mechanical Design, Vol. 102, No. 1, pp. 130-139.
8. Marmol, R. A., Smalley, A. J., and Tecza, J. A., 1980, "Spline Coupling Induced Nonsynchronous Rotor Vibrations," ASME, J. of Mechanical Design, Vol. 102, No. 1, pp. 168-176.
9. Walton, J. F. Jr., Artiles, A., Lund, J. W., Dill J., and Zorzi, E., 1990, "Internal Rotor Friction Instability," Mechanical Technology Incorporated, Latham, New York, 88TR39.
10. Ku, C.-P. R., Walton, J. F. Jr., and Lund, J. W., 1993, "A Theoretical Approach to Determine Angular Stiffness and Damping Coefficients of An Axial Spline Coupling in High Speed Rotating Machinery," submitted to the 14th Biennial Conference on Mechanical Vibration and Noise, September 19-22, Albuquerque, New Mexico.
11. Walton, J. F. Jr., Ku, C.-P. R., and Lund, J. W., 1993, "An Experimental Investigation of the Dynamic Characteristics of An Axial Spline Coupling in High Speed Rotating Machinery," submitted to the 14th Biennial Conference on Mechanical Vibration and Noise, September 19-22, Albuquerque, New Mexico.
12. Tecza, J. A., Malanoski, S. B., and Ku, C.-P. R., 1991, Rotordynamics and Modeling Workshop, Electric Power Research Institute, Eddystone, Pennsylvania, June 4-6.

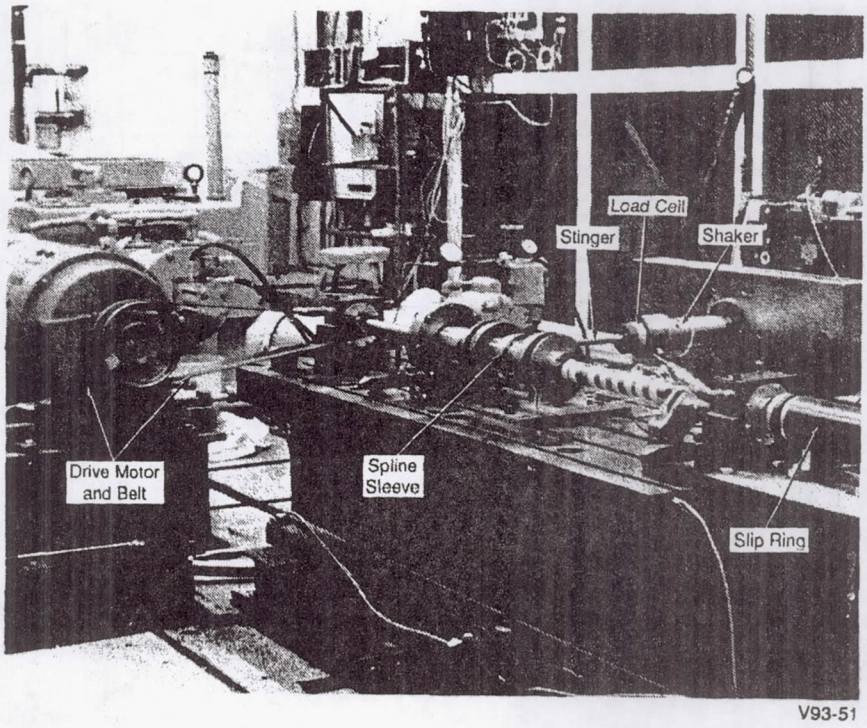

Figure 1 Experimental setup.

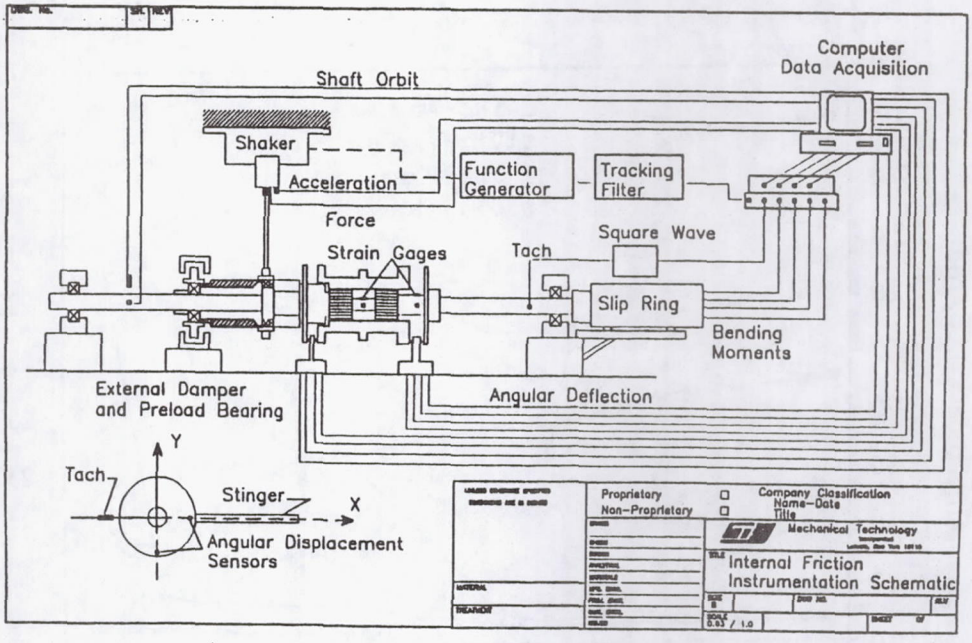

Figure 2 Experimental test setup functional diagram.

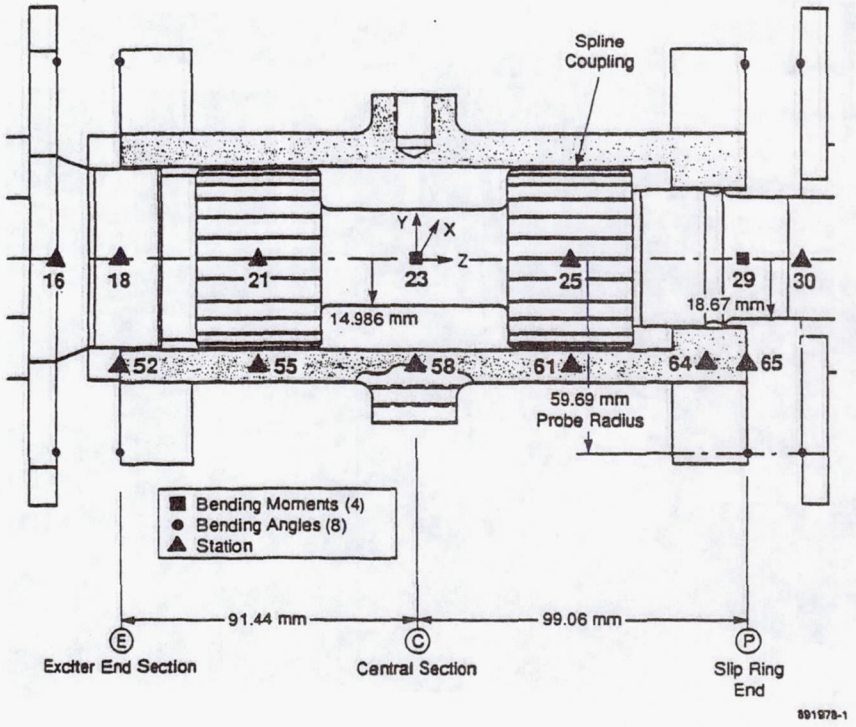

Figure 3 Close-up of the axial spline coupling and instrumentation installed locations

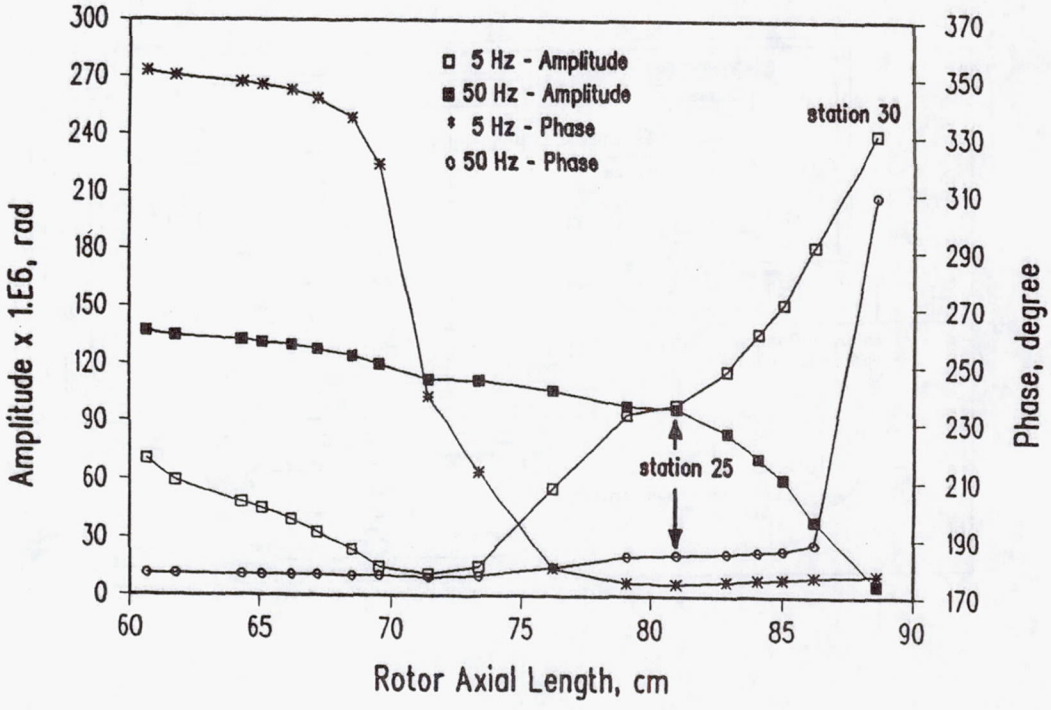

Figure 4 Predicted angular displacements at 225 N external force (K_A=1.13x10^6 N-m/rad, B_A=1.13x10^4 N-m-s/rad)

Table 1 Predicted relative bending moments and angular deflections
(222 N horizontal external shaking force at 50 Hz)

K_A	B_A	M_Y (29-23)		M_Y (61-25)		ϕ_Y (65-30)		ϕ_Y (61-25)	
		Amp.	Phase	Amp.	Phase	Amp.	Phase	Amp.	Phase
N-m/rad	N-m-s/rad	N-m	deg.	N-m	deg.	rad	deg.	rad	deg.
1.13E6	1.13E2	27.89	0.4	25.78	0.5	1.167E-4	-0.2	2.281E-5	-1.3
	1.13E3	28.36	3.7	26.32	4.4	1.160E-4	-1.6	2.223E-5	-13.0
	1.13E4	34.94	4.9	33.78	5.8	1.046E-4	-2.9	0.907E-5	-66.6
1.13E7	1.13E2	35.03	0.0	33.85	0.0	1.040E-4	0.0	2.997E-6	-0.2
	1.13E3	35.03	0.1	33.85	0.1	1.040E-4	0.0	2.995E-6	-1.7
	1.13E4	35.12	0.5	33.96	0.6	1.039E-4	-0.3	2.868E-6	-16.9
	1.13E5	35.99	0.5	34.96	0.6	1.023E-4	-0.3	0.939E-6	-71.7
1.13E8	1.13E2	35.99	0.0	34.95	0.0	1.023E-4	0.0	3.094E-7	0.0
	1.13E3	35.99	0.0	34.95	0.0	1.023E-4	0.0	3.094E-7	-0.2
	1.13E4	35.99	0.0	34.95	0.0	1.023E-4	0.0	3.093E-7	-1.8
	1.13E5	35.99	0.1	34.96	0.1	1.023E-4	0.0	2.953E-7	-18.4

Table 2 Predicted absolute bending moments and angular deflections
(222 N horizontal external shaking force at 5 Hz)

K_A	B_A	M_Y (23)		M_Y (29)		ϕ_Y (30)		ϕ_Y (65)	
		Amp.	Phase	Amp.	Phase	Amp.	Phase	Amp.	Phase
N-m/rad	N-m-s/rad	N-m	deg.	N-m	deg.	rad	deg.*	rad	deg.*
1.13E6	1.13E2	12.78	-0.1	51.45	0.0	2.434E-4	0.0	6.097E-5	0.0
	1.13E3	12.78	-0.2	51.45	0.0	2.434E-4	-0.2	6.098E-5	0.0
	1.13E4	12.40	-11.8	51.44	0.0	2.411E-4	-2.3	6.102E-5	0.1
1.13E7	1.13E2	3.51	0.0	51.34	0.0	2.077E-4	0.0	6.117E-5	0.0
	1.13E3	3.51	-0.1	51.34	0.0	2.077E-4	0.0	6.117E-5	0.0
	1.13E4	3.51	-0.6	51.34	0.0	2.077E-4	0.0	6.117E-5	0.0
	1.13E5	3.42	-5.9	51.34	0.0	2.073E-4	-0.4	6.117E-5	0.0
1.13E8	1.13E2	2.38	0.0	51.32	0.0	2.033E-4	0.0	6.116E-5	0.0
	1.13E3	2.38	0.0	51.32	0.0	2.033E-4	0.0	6.116E-5	0.0
	1.13E4	2.38	0.0	51.32	0.0	2.033E-4	0.0	6.116E-5	0.0
	1.13E5	2.38	-0.1	51.32	0.0	2.033E-4	0.0	6.116E-5	0.0

* With respect to 180°

Table 3 Test cases with horizontal external shaking force at 5 Hz

	Unit	F=80.4 N*	F=162.6 N*	F=221.1 N*
K_A - calculated	N-m/rad	2.79 E6	2.52 E6	2.31 E6
B_A - calculated	N-m-s/rad	3.7 E3	6.0 E3	6.9 E3
$M_Y(29)$ - measured	N-m	19.10	38.61	52.58
$M_Y(29)$ - calculated	N-m	18.58 (2.7%)$^{\$}$	37.61 (2.6%$^{\$}$)	51.13 (2.8%)$^{\$}$
$M_Y(23)$ - measured	N-m	2.83	6.06	8.71
$M_Y(23)$ - calculated	N-m	2.75 (2.8%)$^{\$}$	5.90 (2.7%)$^{\$}$	8.46 (2.8%)$^{\$}$
$M_X(29)$ - measured	N-m	0.39 (2.0%)@	0.75 (1.9%)@	1.59 (3.0%)@
$M_X(29)$ - calculated	N-m	0	0	0
$M_X(23)$ - measured	N-m	0.07 (2.5%)@	0.18 (3.0%)@	0.09 (1.1%)@
$M_X(23)$ - calculated	N-m	0	0	0
$M_Y(23)$ phase - measured	degree$^{\#}$	-1.43	-2.6	-3.2
$M_Y(23)$ phase - calculated	degree$^{\#}$	-1.4	-2.6	-3.2
$\phi_Y(30)$ - measured	μm	4.72	9.58	13.18
$\phi_Y(30)$ - calculated	μm	4.78 (1.1%)$^{\$}$	9.73 (1.6%)$^{\$}$	13.31 (1.0%)$^{\$}$
$\phi_Y(65)$ - measured	μm	1.30	2.59	3.48
$\phi_Y(65)$ - calculated	μm	1.32 (2.0%)$^{\$}$	2.67 (2.9%)$^{\$}$	3.63 (4.4%)$^{\$}$

* Data are average of 3 test cases, the deviations are: amplitude (±1%), phase (±0.2°)

With respect to $M_Y(29)$

$ Relative error with respect to measured data

@ Relative error with respect to measured data at M_Y

Table 4 Sensitivity analyses of 222 N horizontal external shaking force at 5 Hz

	$M_Y(23)$		$M_X(23)$	$M_Y(29)$	$M_X(29)$	$\phi_Y(30)$	$\phi_X(30)$	$\phi_Y(65)$	$\phi_X(65)$
	Amp.	Phase	Amp.	Amp.	Amp.	Amp.	Amp.	Amp.	Amp.
K_B=1.75E7 N/m	0.01%	—	—	0.07%	—	0.8%	—	3%	—
K_R ±7.01E8 N/m	—	—	—	—	—	—	—	0.3%	—
D_{23} ±0.51 mm	5%	—	—	—	—	0.1%	—	0.1%	—
$L_{22\text{-}24}$ ±0.25 mm	0.3%	—	—	—	—	—	—	—	—
D_{29} ±0.51 mm	0.01%	—	—	0.02%	—	1%	—	3%	—
M_{23} location ±2.5 mm	1.3%	0.03°	—	—	—	—	—	—	—
M_{29} location ±2.5 mm	—	—	—	0.4%	—	—	—	—	—
ϕ_{Key} ±5°#	0.4%	—	8.7%	0.4%	8.7%	0.4%	8.7%	0.4%	8.7%
Force Misalignment ±2.5 mm	0.01%	—	—	—	—	—	—	—	—
Combination	7%	< 0.1°	8.2%	0.1%	8.8%	0.6%	8.7%	6%	9.3%

The base line case uses the following parameters: K_A=2.03E6, B_A=5.65E3, K_B=1.23E8, K_R=1.21E8, D_{23}=29.97 mm, D_{29}=37.34 mm, $L_{22\text{-}24}$=57.15 mm, ϕ_{Key}=0°

Experiment is able to reduce the misalignment of the orientation of the shaft to within 2°

STABILITY AND STABILITY DEGREE OF A CRACKED FLEXIBLE ROTOR SUPPORTED ON JOURNAL BEARINGS

Meng Guang
Institute of Vibration Engineering
Northwestern Polytechnical University
Xian, Province of China

and

Robert Gasch
Institute of Aeronautics and Astronautics
Technical University Berlin, Germany

This paper investigates the stability and the stability degree of a flexible cracked rotor supported on different kinds of journal bearings. It is found that no matter what kind of bearings is used, the unstable zones caused by rotor crack locate always within the speed ratio $\frac{2}{N}\left(1-\frac{\triangle K_\xi}{4}\right)<\Omega<\frac{2}{N}$ when gravity parameter $W_g>1.0$; and locate always within the speed ratio $\frac{2\Omega_a}{N}\left(1-\frac{\triangle K_\xi}{4}\right)<\Omega<\frac{2\Omega_a}{N}$ when $W_g<0.1$, where $\triangle K_\xi$ is the crack stiffness ratio, $N=1, 2, 3, 4, 5\cdots$ and $\Omega_a=\left(\frac{1+2\alpha}{2\alpha}\right)^{1/2}$. When $0.1<W_g<1.0$, there is a region, where no unstable zones caused by rotor crack exist.

Outside the crack ridge zones, the rotor crack has almost no influence on system's stability and stability degree; while within the crack ridge zones, the stability and stability degree depend both on the crack and system's parameters. In some cases, the system may still be stable even the crack is very large. For small gravity parameter ($W_g<0.1$), the mass ratio α has large influence on the position of unstable region, but its influence on the stability degree is small. The influence of fixed Sommerfeld number S_0 on the crack stability degree is small although S_o has large influence on the stability degree of uncracked rotor.

NOMENCLATURES

$[A(\Phi)]$ = periodic state matrix

c_d = external damping

c_p = machined clearance of journal bearing

c_{ij}, $(i,j=x,y)$ = damping of journal bearing

C_{ij}, $(i,j=x,y)$ = dimensionless damping $\left(=\frac{c_p\omega c_{ij}}{W}\right)$

D_e = external damping ratio $\left(=\frac{c_d}{2m_d\omega_c}\right)$

e_u = unbalance eccentricity

f_x, f_y = fluid film forces

F_x, F_y = dimensionless fluid film forces $\left(=\frac{f_{x,y}}{m_d c_p \omega^2}\right)$

Preceding Page Blank

$g(t)$ or $g(\Phi)$ = periodic function, $0<g(t)<1$ and it has the form of Eq.5 for small crack.

k_c = complex stiffness of cracked shaft

k_s = stiffness of the uncracked shaft

k_ξ, k_η = stiffness of cracked shaft in ξ and η directions

$\triangle k_\xi$,$\triangle k_\eta$ = the largest stiffness change in ξ and η directions caused by crack

$\triangle K_\xi$ = stiffness change ratio in ξ (the crack) direction $\left(= \dfrac{\triangle k_\xi}{k_s} \right)$

$\triangle K_\eta$ = stiffness change ratio in η (the cross) direction $\left(= \dfrac{\triangle k_\eta}{k_s} \right)$

$$\triangle K_1 = \frac{\triangle k_\xi + \triangle k_\eta}{k_s}$$

$$\triangle K_2 = \frac{\triangle k_\xi - \triangle k_\eta}{k_s}$$

k_{ij} $(i,j = x,y)$ = stiffness of journal bearing

K_{ij} $(i,j = x,y)$ = dimensionless stiffness $\left(= \dfrac{c_p k_{ij}}{W} \right)$

m_b, m_d = mass lumped at bearing station and rotor mid-span

m_p = preload factor $\left(= 1 - \dfrac{c_b}{c_p}\right.$, where c_b *is the assembled clearance)*

S = Sommerfeld number $\left(= \dfrac{\mu\omega DL}{2\pi W}\left(\dfrac{R}{c_p}\right)^2 \right)$, where μ is the viscosity of lubricant

D is the bearing diameter, R is the bearing radius and L is the bearing width

S_o = fixed Sommerfeld number $\left(= S \cdot \left(\dfrac{\omega_c}{\omega}\right) = \dfrac{\mu\omega_c DL}{2\pi W}\left(\dfrac{R}{c_p}\right)^2 \right)$, it is a design parameter.

t = time

T = period

U = unbalance parameter $\left(= \dfrac{e_u}{c_p} \right)$

W = bearing load

W_g = gravity parameter $\left(= \dfrac{\delta_s}{c_p}, \text{ where } \delta_s = \dfrac{m_d g}{k_s} \right)$, it represents the elasticity of the shaft.

x, y = deflection in Cartesian coordinates

X, Y = dimensionless deflection $\left(= \dfrac{x}{c_p}, \dfrac{y}{c_p} \right)$

$z = x+iy$, complex deflection $= (\xi + i\eta)e^{i\Phi}$.

$Z = X+iY$

$\bar{Z} = X-iY$

Z_o = steady state response

$\triangle Z$ = perturbation deflection about the steady state response Z_o $(= \triangle X + iY)$

α = mass ratio $\left(= \dfrac{m_b}{m_d} \right)$

β = crack angle, it is the angle between crack and unbalance

$[\Gamma(T)]$ = transition matrix

ξ,η = body fixed rotating coordinates, ξ is in the direction of crack

μ_f = Floquet eigenvalue

$|\mu_f|$ = modulus of μ_f

τ = ωt, dimensionless time

φ = initial unbalance angle

Φ = $\omega t + \varphi + \beta$

ω = rotating speed

ω_c = rigid pin–pin critical speed $\left(= \left(\frac{k_s}{m_d} \right)^{1/2} \right)$

Ω = speed ratio $\left(= \frac{\omega}{\omega_c} \right)$

$(\cdot) = \frac{d}{dt}$

$(') = \frac{d}{d\tau}$ or $\frac{d}{d\Phi}$

[ ] = square matrix

{ } = column matrix

INTRODUCTION

Fatigue cracking of rotor shaft may cause a catastrophic damage to rotating machineries, an example was given by Jack and Patterson (1976). So that a detailed investigation into the behavior of a cracked rotor shaft is very important for diagnosing and preventing rotor cracks.

There are two major research field in cracked rotor analysis, one is the modeling and another is the detecting of the rotor crack. Gasch (1976) considered in body–fixed rotating coordinate the stiffness change due to open and closed cracks and solved the equations of motion of a cracked Jeffcott rotor by an analogue computer. Mays et al (1984) gave an approximate method of estimating the reduction of a section diameter required to model a crack. Nelson and Nataraj (1986) analysed the dynamics of a rotor system with a cracked shaft by the finite element method; Collins et al (1991) considered a rotating Timoshenko shaft with a single transvers crack and analysed the free vibrations and the responses to a single axial impulse and periodic axial impulses. Gasch (1988) et al analysed the dynamic behaviour of a Jeffcott rotor with a cracked hollow shaft and Bernasconi (1986) considered the vibrations of a stepped shaft by using singularity functions. Muszynska (1982) developed a solution for a gaping crack and concluded that the increase in the primary vibration is more than that in the subharmonic vibrations. Papadopoulos and Dimarogonas (1980) pointed out that the informations of subharmonic resonances and the frequency shifting are important for crack identification. Imam et al (1989) presented a very successful on–line crack diagnosis method which can detect cracks of the order of 1 to 2 percent of the shaft diameter deep. Most of the early research results on cracked rotor have been summarized in the book by Dimarogonas and Paipetis (1983) and more literatures on the dynamics of cracked rotors can be found in a reviewing paper by Wauer (1990).

Although more than 100 papers have been published in this field, there are still many problems to be solved. Up till now, only few papers, for example Tamura (1988) and Gasch (1992), analysed the stability of a cracked rotor supported on rigid bearings and it was found that the unstable zones caused by rotor crack are

near the speed ratio $\frac{\omega}{\omega_c}=\frac{2}{1},\ \frac{2}{2},\ \frac{2}{3},\ \frac{2}{4},\cdots$ and the unstable zone spreading out from $\frac{\omega}{\omega_c}=2$ is the broadest, where ω_c is the first rigid critical speed. Up till now, no papers about the stability of a cracked flexible rotor supported on fluid film bearings have been published, but the stability and dynamic characteristics of this kind of system are very important as dangerous cracks were mainly reported in rotors running in fluid film bearings.

EQUATIONS OF MOTION AND PERIODIC STATE MATRIX FOR STABILITY ANALYSIS

Considering a simple flexible Jeffcott rotor with a cracked shaft supported on journal bearings (see Fig.1), the equations of motion of the system can be written as:

$$\begin{cases} m_d\ddot{z}_d + c_d\dot{z}_d + k_c[(z_d-z_b),t]\cdot(z_d-z_b) = m_d g + m_d e_u\cdot\omega^2 e^{i(\omega t+\varphi)} \\ m_b\ddot{z}_b + \frac{1}{2}k_c[(z_d-z_b),t]\cdot(z_b-z_d) = m_b g - (f_x+if_y) \end{cases} \tag{1}$$

where m_b and m_d are the mass lumped at bearing station and rotor mid-span, z_d and z_b are the complex deflections of disk and bearing centers; ω is the rotating speed; $k_c[(z_d-z_b),t]$ is the stiffness coefficient which is a function of z_d–z_b *and changes with time* t due to the openning and closing of the rotor crack and, f_x and f_y are fluid film forces of journal bearing. There are

$$\begin{cases} z_d = x_d + iy_d \\ z_b = x_b + iy_b \end{cases}$$

(1) Stiffness Forces

Supposing that the vibration deflection is small enough and the influence of deflection difference z_d–z_b on shaft stiffness k_c can be omitted, then the shaft stiffness k_c changes only with time t and

$$k_c[(z_d-z_b),t]\approx k_c(t) \tag{2}$$

Supposing further that the weight deflection is dominant, then $k_c(t)$ changes periodically with time and can be written in ξ and η directions as:

$$\begin{cases} k_\xi = k_s - g(t)\triangle k_\xi \\ k_\eta = k_s - g(t)\triangle k_\eta \end{cases} \tag{3}$$

where $g(t)$ is a periodic function of time and $0<g(t)<1$. $\triangle k_\xi$ and $\triangle k_\eta$ are constant and represent the stiffness change caused by rotor crack. There is

$$z = x+iy = (\xi+i\eta)e^{i\Phi}$$

where $\Phi=\omega t+\varphi+\beta$, z is z_d or z_b. The stiffness force $k_c(t)\cdot z$ can be written as:

$$\begin{aligned} k_c(t)\cdot z &= \frac{1}{2}[(k_\xi+k_\eta)\cdot z + (k_\xi-k_\eta)\cdot\bar{z}e^{2i\Phi}] \\ &= [k_s - \frac{1}{2}g(t)(\triangle k_\xi+\triangle k_\eta)]\cdot z - \frac{1}{2}g(t)(\triangle k_\xi-\triangle k_\eta)]\cdot\bar{z}\cdot e^{2i\Phi} \end{aligned} \tag{4}$$

For small crack, the openning and closing of the crack can be represented by a rectangular function $g(t)$, and $g(t)$ can be written in a Fourier series of Φ as:

$$g(t)=g(\Phi)=\left(\frac{2}{\pi}\right)\left[\frac{\pi}{4}+\cos\Phi-\frac{1}{3}\cos 3\Phi+\frac{1}{5}\cos 5\Phi-\cdots\right] \tag{5}$$

where $\Phi=\omega t+\varphi+\beta$.

(2) Linearised Fluid Film Forces and Coefficients

The vibration response of the system can be split to

$$\begin{cases} z_d = z_{do} + \triangle z_d \\ z_b = z_{bo} + \triangle z_b \end{cases}$$

where z_{do} and z_{bo} are the steady state response of the system, $\triangle z_d$ and $\triangle z_b$ are the perturbation deflections.

For small dynamic perturbation, the nonlinear fluid film forces f_x and f_y can be linearised about the steady state response (x_{bo}, y_{bo}) as:

$$\begin{bmatrix} f_x \\ f_y \end{bmatrix} = \begin{bmatrix} f_{xo} \\ f_{yo} \end{bmatrix} + \begin{bmatrix} k_{xx} & k_{xy} \\ k_{yx} & k_{yy} \end{bmatrix} \begin{bmatrix} \triangle x_b \\ \triangle y_b \end{bmatrix} + \begin{bmatrix} c_{xx} & c_{xy} \\ c_{yx} & c_{yy} \end{bmatrix} \begin{bmatrix} \triangle \dot{x}_b \\ \triangle \dot{y}_b \end{bmatrix} \tag{6}$$

The nondimensional forms of f_x and f_y can be written as

$$\begin{bmatrix} F_x \\ F_y \end{bmatrix} = \frac{1}{m_d c_p \omega^2} \begin{bmatrix} f_x \\ f_y \end{bmatrix} = \frac{W}{m_d c_p \omega^2} \left\{ \frac{1}{W} \begin{bmatrix} f_{xo} \\ f_{yo} \end{bmatrix} + \begin{bmatrix} K_{xx} & K_{xy} \\ K_{yx} & K_{yy} \end{bmatrix} \begin{bmatrix} \triangle X_b \\ \triangle Y_b \end{bmatrix} + \begin{bmatrix} C_{xx} & C_{xy} \\ C_{yx} & C_{yy} \end{bmatrix} \begin{bmatrix} \triangle X'_b \\ \triangle Y'_b \end{bmatrix} \right\} \tag{7}$$

The nondimensional stiffness and damping coefficients K_{ij} and C_{ij} $(i,j = x,y)$ are

$$K_{ij} = \frac{c_p}{W} k_{ij}, \quad C_{ij} = \frac{c_p \omega}{W} c_{ij}$$

and they can be obtained from the book by Someya (1989) and the book by Vance (1988). These coefficients are only functions of Sommerfeld number S or eccentricity ratio $\varepsilon_o = \frac{e_w}{c_p}$ for a given set of bearing parameters, where the Sommerfeld number is

$$S = \frac{\mu \omega D L}{2\pi W} \left(\frac{R}{c_p} \right)^2 \tag{8}$$

As the rotating speed ω and the bearing parameters are mixed up in the Sommerfeld number S, it is difficult to seperate in the stability analysis the influences of rotating speed and bearing parameters on the nondimensional stiffness and damping coefficients. In order to solve this problem, the fixed Sommerfeld number S_o is introduced and it is defined as

$$S_o = S \cdot \left(\frac{\omega_c}{\omega} \right) = \frac{\mu \omega_c D L}{2\pi W} \left(\frac{R}{c_p} \right)^2 \tag{9}$$

That is, the rotating speed ω in Sommerfeld number S (see Eq.8) is replaced with the rigid pin–pin critical speed $\omega_c \left(= \left(\frac{k_s}{m_d} \right)^{1/2} \right)$. S_o is thus the Sommerfeld number in the rigid pin–pin critical speed and does not change with the rotating speed. Now the stiffness and damping coefficients are functions of the fixed Sommerfeld number S_o and the rotating speed ratio $\Omega \left(= \frac{\omega}{\omega_c} \right)$.

In this paper, three tapes of journal bearings are used for stability analysis, the 2 Axial Grooved Cylindrical Bearing, the 4 Lobe Bearing and the 5 Pad Tilting Pad Bearing. Fig.2 shows the diagrams of these journal bearings and the stiffness and damping coefficients of these three bearings are taken from Someya's book (1989).

For the simple Jeffcott rotor considered here, there is

$$W = \frac{m_d g}{2} + m_b g = m_d g \cdot \left(\frac{1}{2} + \alpha \right)$$

So that

$$\frac{W}{m_d c_p \omega^2} = \frac{W_g}{\Omega^2}\left(\frac{1}{2} + \alpha\right) \tag{10}$$

where $W_g = \dfrac{g}{c_p \omega_c^2} = \dfrac{\delta_s}{c_p}$ is the gravity parameter.

(3) Nondimensional Equations of Motion of the System

Substituting Eq.4 and Eq.6 into Eq.1, dividing both sides by $m_d c_p \omega^2$ and then substituting into Eq.7 and Eq.10, we can get at last the nondimensional forms of Eq.1 as

$$\begin{cases} Z''_d + \dfrac{2D_e}{\Omega} Z'_d + \dfrac{1}{\Omega^2}\left\{[1 - \dfrac{1}{2}g(t)\triangle K_1](Z_d - Z_b) - \right. \\ \quad \left. -\dfrac{1}{2}g(t)\triangle K_2 \cdot (\bar{Z}_d - \bar{Z}_b) \cdot e^{2i\Phi}\right\} = \dfrac{W_g}{\Omega^2} + Ue^{i(\tau+\varphi)} \\ Z''_b + \dfrac{1}{2\alpha\Omega^2}\left\{[1 - \dfrac{1}{2}g(t)\triangle K_1](Z_b - Z_d) - \dfrac{1}{2}g(t)\triangle K_2 \cdot (\bar{Z}_b - \bar{Z}_d) \cdot e^{2i\Phi}\right\} + \\ \quad + \dfrac{W_g(1+2\alpha)}{2\alpha\Omega^2}\left[\left(\dfrac{f_{xo}}{W} + K_{xx}\triangle X_b + K_{xy}\triangle Y_b + C_{xx}\triangle X'_b + C_{xy}\triangle Y'_b\right) + \right. \\ \quad \left. i\left(\dfrac{f_{yo}}{W} + K_{yx}\triangle X_b + K_{yy}\triangle Y_b + C_{yx}\triangle X'_b + C_{yy}\triangle Y'_b\right)\right] = \dfrac{W_g}{\Omega^2} \end{cases} \tag{11}$$

where $(') = \dfrac{\mathrm{d}}{\mathrm{d}\tau}$ and $\triangle K_1 = \dfrac{\triangle K_\xi + \triangle K_\eta}{k_s}$, $\triangle K_2 = \dfrac{\triangle k_\xi - \triangle k_\eta}{k_s}$.

In the steady state case, there are

$$Z_d = Z_{do},\ Z_b = Z_{bo},\ Z''_d = Z'_d = 0,\ Z''_b = Z'_b = 0,\ f_x = f_{xo} \text{ and } f_y = f_{yo}$$

As Z_{do} and Z_{bo} are also solutions of Eq.(11) and

$$Z_d = Z_{do} + \triangle Z_d,\quad Z_b = Z_{bo} + \triangle Z_b$$

the perturbation equations of motion of the system can be got from Eq.(11) as:

$$\begin{cases} \triangle Z''_d + \dfrac{2D_e}{\Omega}\triangle Z'_d + \dfrac{1}{\Omega^2}\left\{[1 - \dfrac{1}{2}\triangle K_1 g(t)] \cdot (\triangle Z_d - \triangle Z_b) - \right. \\ \quad \left. -\dfrac{1}{2}\triangle K_2 g(t)(\triangle \bar{Z}_d - \triangle \bar{Z}_b) \cdot e^{2i\Phi}\right\} = 0 \\ \triangle Z''_b + \dfrac{1}{2\alpha\Omega^2}\left\{[1 - \dfrac{1}{2}\triangle K_1 g(t)](\triangle Z_b - \triangle Z_d) - \dfrac{1}{2}\triangle K_2 g(t)(\triangle \bar{Z}_b - \triangle \bar{Z}_d)e^{2i\Phi}\right\} + \\ \quad \dfrac{W_g(1+2\alpha)}{2\alpha\Omega^2}\left[(K_{xx}\triangle X_b + K_{xy}\triangle Y_b + C_{xx}\triangle X'_b + C_{xy}\triangle Y'_b) + \right. \\ \quad \left. i(K_{yx}\triangle X_b + K_{yy}\triangle Y_b + C_{yx}\triangle X'_b + C_{yy}\triangle Y'_b)\right] = 0 \end{cases}$$

The above equations can be written in Cartesian coordinates as ($g(t)$ is written in th form of $g(\Phi)$):
rotor:

$$\begin{bmatrix} 1 & 0 \\ 0 & 1 \end{bmatrix}\begin{bmatrix} \triangle X''_d \\ \triangle Y''_d \end{bmatrix} + \begin{bmatrix} \dfrac{2D_e}{\Omega} & 0 \\ 0 & \dfrac{2D_e}{\Omega} \end{bmatrix}\begin{bmatrix} \triangle X'_d \\ \triangle Y'_d \end{bmatrix} + \frac{1}{\Omega^2}\left\{\begin{bmatrix} 1 & 0 \\ 0 & 1 \end{bmatrix} - \right.$$

$$\frac{1}{2}g(\Phi)\cdot\begin{bmatrix}\Delta K_1+\Delta K_2\cos 2\Phi & \Delta K_2\sin 2\Phi\\ \Delta K_2\sin 2\Phi & \Delta K_1-\Delta K_2\cos 2\Phi\end{bmatrix}\begin{bmatrix}\Delta X_d-\Delta X_b\\ \Delta Y_d-\Delta Y_b\end{bmatrix}=0$$

bearing:

(12)

$$\begin{bmatrix}1 & 0\\ 0 & 1\end{bmatrix}\begin{bmatrix}\Delta X''_b\\ \Delta Y''_b\end{bmatrix}+\frac{1}{2\alpha\Omega^2}\left\{\begin{bmatrix}1 & 0\\ 0 & 1\end{bmatrix}-\frac{1}{2}g(\Phi)\cdot\begin{bmatrix}\Delta K_1+\Delta K_2\cos 2\Phi & \Delta K_2\sin 2\Phi\\ \Delta K_2\sin 2\Phi & \Delta K_1-\Delta K_2\cos 2\Phi\end{bmatrix}\right\}\begin{bmatrix}\Delta X_b-\Delta X_d\\ \Delta Y_b-\Delta Y_d\end{bmatrix}+\frac{W_g(1+2\alpha)}{2\alpha\Omega^2}\left\{\begin{bmatrix}K_{xx} & K_{xy}\\ K_{yx} & K_{yy}\end{bmatrix}\begin{bmatrix}\Delta X_b\\ \Delta Y_b\end{bmatrix}+\begin{bmatrix}C_{xx} & C_{xy}\\ C_{yx} & C_{yy}\end{bmatrix}\begin{bmatrix}\Delta X'_b\\ \Delta Y'_b\end{bmatrix}\right\}=0$$

(4) Periodic State Matrix of the System

Taking the notes of

$$X_1=\Delta X_d\ ,\ X_2=\Delta Y_d\ ,\ X_3=\Delta X_b\ ,\ X_4=\Delta Y_b$$
$$X_5=\Delta X'_d\ ,\ X_6=\Delta Y'_d\ ,\ X_7=\Delta X'_b\ ,\ X_8=\Delta Y'_b$$

supposing that φ and β do not change with time, and renoting $(')=\mathrm{d}/\mathrm{d}\Phi$, the first order state equations of motion of the system can be obtained from Eq.12 and then can be written in matrix form as

$$\{X\}' = [A(\Phi)]\{X\} \tag{14}$$

where the vector $\{X\}$ is defined as $\{X\}=(X_1, X_2,\cdots,X_8)^T$

and $[A(\Phi)]$ is the periodic state matrix and has a period of 2π.

$$[A(\Phi)=\begin{bmatrix}0 & 0 & 0 & 0 & 1 & 0 & 0 & 0\\ 0 & 0 & 0 & 0 & 0 & 1 & 0 & 0\\ 0 & 0 & 0 & 0 & 0 & 0 & 1 & 0\\ 0 & 0 & 0 & 0 & 0 & 0 & 0 & 1\\ \frac{P_1(\Phi)}{\Omega^2} & \frac{Q_1(\Phi)}{\Omega^2} & \frac{P_1(\Phi)}{\Omega^2} & \frac{Q_1(\Phi)}{\Omega^2} & \frac{2\mu}{\Omega} & 0 & 0 & 0\\ \frac{Q_1(\Phi)}{\Omega^2} & \frac{P_2(\Phi)}{\Omega^2} & \frac{Q_1(\Phi)}{\Omega^2} & \frac{P_2(\Phi)}{\Omega^2} & 0 & \frac{2\mu}{\Omega} & 0 & 0\\ \frac{P_1(\Phi)}{2\alpha\Omega^2} & \frac{Q_1(\Phi)}{2\alpha\Omega^2} & \frac{K_{xx}+P_1(\Phi)}{2\alpha\Omega^2} & \frac{K_{xy}-Q_1(\Phi)}{2\alpha\Omega^2} & 0 & 0 & \frac{C_{xx}}{2\alpha\Omega^2} & \frac{C_{xy}}{2\alpha\Omega^2}\\ \frac{Q_1(\Phi)}{2\alpha\Omega^2} & \frac{P_2(\Phi)}{2\alpha\Omega^2} & \frac{K_{yx}-Q_1(\Phi)}{2\alpha\Omega^2} & \frac{K_{yy}+P_2(\Phi)}{2\alpha\Omega^2} & 0 & 0 & \frac{C_{yx}}{2\alpha\Omega^2} & \frac{C_{yy}}{2\alpha\Omega^2}\end{bmatrix} \tag{15}$$

where

$$\begin{cases}P_1(\Phi)=1-\frac{1}{2}\Delta K_1 g(\Phi)-\frac{1}{2}\Delta K_2 g(\Phi)\cos 2\Phi\\ P_2(\Phi)=1-\frac{1}{2}\Delta K_1 g(\Phi)+\frac{1}{2}\Delta K_2 g(\Phi)\cos 2\Phi\\ Q_1(\Phi)=\frac{1}{2}\Delta K_2 g(\Phi)\cdot\sin 2\Phi\end{cases} \tag{16}$$

The stability of the periodically time-variant system of Eq.14 can be analysed by the well known

Floquet's method.

FLOQUET'S THEORETICAL AND NUMERICAL METHODS USED FOR STABILITY ANALYSIS

The most straightfoward method for dealing with the stability of a periodic system is perhaps the Floquet's method (see eg., Caesari, 1970), which states that the knowledge of the state transition matrix over one period is sufficient for determining the stability of the equilibrium position $\{X\}=0$ of a periodic system

$$\{X\}'=[A(\Phi)]\{X\} \tag{17}$$

where $[A(\Phi)]=[A(\Phi+T)]$ and T is the period. The transition matrix $[\Gamma(T)]$ is defined by

$$\{X(T)\}=[\Gamma(T)]\{X(0)\}$$

When the transition matrix $[\Gamma(T)]$ has been obtained, the Floquet's eigenvalues of the system can be calculated from the following eigen–function

$$\left|[\Gamma(T)]-\mu_f[I]\right|=0 \tag{18}$$

where μ_f is the Floquet eigenvalue and $[I]$ is the unit matrix.

The stability of the equilibrium position $\{X\}=0$ of the periodic system (17) can be determined by the value of the Floquet eigenvalue μ_f that is, if all $|\mu_f|<1$, the $\{X\}=0$ position is stable; if one or more $|\mu_f|>1$, the $\{X\}=0$ position is unstable and the $\{X\}=0$ position is the critical case if one or more $|\mu_f|=1$. The physic meaning of the Floquet eigenvalue μ_f is clear, it shows the factor by which a given initial amplitude increases or decreases after one period of motion.

Although the stability of the equlibrium position $\{X\}=0$ of system (17) can be determined from the transition matrix $[\Gamma(T)]$ of the system, unfortunately, there is no general analytical method for calculating $[\Gamma(T)]$. But there are several efficient numerical methods although they take too much computer time (Fridemann, 1977). One of them is the so called Hsu's method and the essential aspects of this method are given in Fridemann's paper (1977), the following is the result of this method.

The period T is divided into K intervals denoted by Φ_k $(k=1,2,\cdots,K)$ with $0=\Phi_0<\Phi_1<\cdots<\Phi_K=T$. The kth interval $(\Phi_{k-1},\ \Phi_k)$ *is denoted by* τ_k. In the kth interval, a constant matrix $[B_k]$ is defined by

$$[B_k]=\int_{\Phi_{k-1}}^{\Phi_k}[A(\Phi)]d\Phi \qquad \Phi\in\tau_k \tag{19}$$

and the final approximation for the transition matrix $[\Gamma(T)]$ at the end of one period can be calculated by

$$[\Gamma(T)]=\prod_{i=1}^{K}\exp[B_i]\approx\prod_{i=1}^{K}\left\{[I]+\sum_{j=1}^{J}\frac{[B_i]^j}{j!}\right\} \tag{20}$$

STABILITY AND STABILITY DEGREE OF A CRACKED FLEXIBLE ROTOR SUPPORTED ON JOURNAL BEARINGS

Based on the Floquet's theorem and the Hsu's numerical method, the Floquet eigenvalues of Eq.15 are calculated numerically for speed ratio $0.2<\Omega<5.0$, crack stiffness ratio $0.0<\triangle K_\xi<0.8$, gravity parameter $0.001<W_g<10.0$, fixed Sommerfeld number $0.1<S_o<2.3$ and mass ratio $0.05<\alpha<0.45$. The stability and the stability degree of a cracked flexible rotor supported on journal bearings are analysed. At first, the following phraseologies are defined with Fig.5 as an example.

crack ridge: a protruding ridge of Floquet eigenvalue caused by rotor crack.

crack ridge zone: the zone where the crack ridge locates, for example from A to B in Fig.5. The position

and extent of the crack ridge zone is given by Eq.(21) and Eq.(22).

crack unstable zone: unstable zone caused by the crack, it is the zone where $|\mu_f| > 1.0$. It locates within the crack ridge zone.

stability degree: the degree of stability which is determined by the largest Floquet eigenvalue $|\mu_f|_m$, the larger the $|\mu_f|_m$ is, the smaller the stability degree. When $|\mu_f|_m < 1$, the equilibrium position of the system is stable, when $|\mu_f|_m > 1$, the equilibrium position of the system is unstable and the equilibrium position of the system is the critical case when $|\mu_f|_m = 1$.

diagram of stability degree: the 3–D diagram of Floquet eigenvalue. Its Z–axis is the largest Floquet eigenvalue $|\mu_f|_m$, Y–axis is the speed ratio Ω and X–axis is the system parameter (the fixed Sommerfeld number S_o, the gravity parameter W_R, the mass ratio α or the stiffness change ratio $\triangle K_\xi$).

1.0–Level: The level of the Floquet eigenvalue $|\mu_f|_m = 1$, it is the limit of stability. Above this leval, the system is unstable.

(1) The Stability and Stability Degree of Uncracked Rotor Shaft

It should be noticed that now the periodic system (17) is simplified to a time–invariant one and the Floquet's method is also simplified to the normal eigenvalue problem.

Journal bearings are superior to rolling element bearings in high–speed operation. They have high damping ability, high load–carrying capacity and low friction. In addition, silent operation and long life can be attained. Therefore, journal bearings of various types are widely used in high–speed rotating machineries. But an inappropriately designed journal bearing may not only increase the vibration amplitude, but bring also the oil whirl or oil whip, that is, a self–excited lateral vibration of rotating shaft caused by oil film in journal bearings. Generally, multilobe bearings are more stable than circular bearings. A tilting–pad bearing is always stable, because it has no cross–coupling terms of oil film coefficients.

The gravity parameter W_R is a very heavy parameter in the stability analysis. Fig.3 shows the influences of gravity parameter on the stability degree. It is found that there is a valley of Floquet eigenvalue for gravity parameter of mid–value ($0.05 < W_R < 1.0$) and small speed ratio Ω. As Ω increases, this valley becomes more narrow and more shallow. The tilting pad bearing has the longest valley and the cylindrical bearing has the shortest one. The system will be the most stable if the parameters are selected in the bottom of the valley. In the left side (the small gravity parameter side) of the valley, there is a hill of Floquet eigenvalue for cylindrical and multilobe bearings. This hill is very important for system's stability as it determines the stability limit. Besides, the hill of the cylindrical bearing is much higher and wider than the multilobe bearing, that is why the cylindrical bearing is more unstable than the multilobe bearing. The tilting pad bearing is always stable as it has no such a hill.

Although the multilobe bearing is generally more stable than the cylindrical bearing, it may be more unstable than the cylindrical bearing in the case of small fixed Sommerfeld number S_o and small gravlty parameter W_R.

Another heavy parameter in the stability analysis is the fixed Sommerfeld number S_o. Fig.4 shows the influences of $S_o$on the stability degree in different gravity parameter W_R. For multilobe bearing and for cylindrical bearing, when $S_o > 0.4$ or $W_R > 0.1$, it is found that the threshold speed ratio of stability increases as W_R increases.

The variation of stability degree with fixed Sommerfeld number S_o depends largely on the value of gravity parameter W_R. For small W_R, the stability degree decreases as S_o increases; while for large W_R, the variation of stability degree with S_o is very small.

(2) The Stability and Stability Degree of Cracked Rotor Shaft

It is well known that the stability and stability degree of an uncracked flexible rotor supported on journal bearing change greatly for different types of journal bearings. What will happen if the rotor has a small crack? Of course, the crack will have influence on the stability of the uncracked system and will cause new unstable regions, but how large is the influence and where are these new unstable regions? These questions are important for detecting the crack and preventing the system from an accident. In order to answer these questions, the Floquet eigenvalues of Eq.15 are calculated. For the reason of simple, the cross stiffness change caused by crack is omitted in the following analysis, that is $\triangle K_{\eta}=0$ is assumed, because $\triangle K_{\eta}$ is very small compared with $\triangle K_{\xi}$.

Based on the large quantities of numerical results, it is found that the position of crack ridge zones and then the position of crack unstable zones have no relation with the type of journal bearings, that is, they do not depend on the fixed Sommerfeld number S_o. The position of crack ridge zones depend only on the speed ratio and the stiffness change ratio for large gravity parameter ($W_g>1.0$), and depend also on the mass ratio for small gravity parameter ($W_g<0.05$).

Fig.5 to Fig.7 show the positions and the extents of the crack ridge zones. When $W_g>1.0$, the mass ratio has no influence and the crack ridge zones locate always within the two lines of $\Omega=\frac{2}{N}$ and $\Omega=\frac{2}{N}\left(1-\frac{\triangle K_{\xi}}{4}\right)$, where $N=1,2,3,4,5,\cdots$. The widthes of the crack ridge zones are seperately equal to or less than $\frac{\triangle K_{\xi}}{2N}$ (see Fig.5). So that the crack unstable zones locate within

$$\frac{2}{N}\left(1-\frac{1}{4}\triangle K_{\xi}\right)<\Omega<\frac{2}{N}\quad(N=1,2,3,4,5,\cdots) \tag{21}$$

When $W_g<0.05$, the crack ridge zones depend largely on mass ratio and they locate always within the two lines of $\Omega=\frac{2\Omega_{\alpha}}{N}$ and $\Omega=\frac{2\Omega_{\alpha}}{N}\left(1-\frac{1}{4}\triangle K_{\xi}\right)$, where $\Omega_{\alpha}=\left(\frac{1+2\alpha}{2\alpha}\right)^{1/2}$ and $N=1,2,3,4,5,\cdots$. The widthes of the crack ridge zones are seperately equal to or less than $\frac{\triangle K_{\xi}}{2N}\Omega_{\alpha}$ (see Fig.6). So that the crack unstable zones locate within

$$\frac{2\Omega_{\alpha}}{N}\left(1-\frac{1}{4}\triangle K_{\xi}\right)<\Omega<\frac{2\Omega_{\alpha}}{N}\qquad(N=1,2,3,4,5,\cdots) \tag{22}$$

In this paper, the shaft stiffness is supposed to change linearly with crack depth, so that the width of the crack ridge zone increases also linearly with crack stiffness change ratio due to the reduction of shaft stiffness. Besides, the larger the speed ratio and the stiffness change ratio are, the wider the crack ridge zone is (see Fig.7). Therefore, the instability caused by crack in larger speed ratio is more dangerous and should be payed more attention to.

It is known that the gravity parameter W_g is a very heavy parameter in the stability analysis of uncracked rotor shaft and it is found in the above discussions that when $W_g<0.05$, the mass ratio α has large influence on the crack ridge zone, while when $W_g>1.0$, α has almost no influence on the crack ridge zone. What will happen if $0.05<W_g<1.0$? Fig.8 shows the influence of gravity parameter W_g on the stability and stability degree (please compare Fig.8 with Fig.3). It is found that in a region of Wg within $0.05<W_g<1.0$, the crack has almost no influence on the stability degree no matter how large the crack is. This is because that in this region, the diagram of stability degree has either a valley or a hill. The cylindrical bearing and multilobe bearing have generally a valley at small speed ratio and a hill at large speed ratio, while the tilting pad bearing has always a

valley although this valley becomes smaller as the speed ratio increases.

It is found that the position of crack ridge zones almost do not change with the fixed Sommerfeld number S_o, but the extent of crack ridge zones decrease with the increasing of S_o when the gravity parameter is small ($W_g < 0.05$) and has almost no change or increase a little with the increasing of S_o when the gravity parameter is large ($W_g > 1.0$) (see Fig.9). When comparing with the uncracked rotor case, it is found that the change of crack ridge zone with S_o is not due to the crack itself, but due mainly to the influence of S_o on the stability degree of uncracked system.

Although the crack ridge zones almost do not change with the fixed Sommerfeld number S_o, the crack unstable zones become a little bit larger as S_o increases. This is also due to the change of the stability degree of uncracked system with S_o.

Fig.10 shows the influences of crack stiffness change ratio on the stability and stability degree. It is found again that the position of the crack ridge zones depend not on the types of journal bearings and, the crack unstable zones locate always within the crack ridge zones, but the stability outside the crack ridge zones depends mainly on the type of bearings used. Although the positions of crack ridge zones do not change with gravity parameter W_g and mass ratio α, the crack unstable zones depend both on the stiffness change ratio and the system parameters. When W_g is small, there is an extra crack unstable zones in high speed ratio due to the influence of mass ratio. When $W_g = 0.1$, almost no crack ridge zones exist, because the system is now in the valley of the Floquet eigenvalue. So that, as it is mentioned before, the crack has almost no influence on system's stablity in some combinations of system parameters. As W_g increases, the crack ridge zones appear again, but the crack ridge zone in high speed ratio is disappeared because now the mass ratio has no more influence on the crack ridge zones.

It is found that for tilting pad bearing, the crack ridge in small gravity parameter case is much higher and therefore is more unstable than in large gravity parameter case.

CONCLUSIONS

This paper investigates the stability and the stability degree of a flexible cracked rotor supported on different kinds of journal bearings. The influences of the crack stiffness ratio $\triangle K_\xi$, the fixed Sommerfeld number S_o, the gravity parameter W_g and the mass ratio α are analysed. It is found that no matter what kind of journal bearings is used, the position of crack ridge zones and then the position of crack unstable zones depend only on the speed ratio and the stiffness change ratio for large gravity parameter ($W_g > 1.0$), and depend also on the mass ratio for small gravity parameter ($W_g < 0.05$). The position and extent of the crack ridge zones are given by Eq.21 for $W_g > 1.0$ and by Eq.22 for $W_g < 0.05$. When $0.1 < W_g < 1.0$, there is a region, where no unstable zones caused by rotor crack exist.

The larger the speed ratio and the stiffness change ratio are, the wider the crack ridge zone is. Therefore, the instability caused by crack in larger speed ratio is more dangerous.

Outside the crack ridge zones, the stability and stability degree of the cracked system are almost the same with those of the uncracked system, that is, they have almost no relation with the crack and depend mainly on system's parameters; while within the crack ridge zones, they depend mainly on crack stiffness change ratio, but also on system's parameters. In some cases, the system may still be stable even the crack is very large.

ACKNOWLEDGEMENTS

The supports of the Alexander von Humboldt Foundation of Germany and the Huo Ying–Dong Youth Teachers Foundation of China are gratefully acknowledged. The authors also wish to thank Dr–Ing. M.

Wiedemann, Dipl–Ing. B. Weitz, Dipl–Ing. J. M. Xu and Dipl–Ing. M. F. Liao for their useful suggestions and fruitful discussions.

REFERENCES

[1] Bernasconi, O., *"Solution for Torsional Vibrations of Stepped Shafts Using Singularity Functions"*, Intl. J. Mech. Sci. Vol.28, 1986, pp31–39.

[2] Caesari, L., *"Asymptotic Behavior and Stability Problems in Ordinary Differential Equations"*, 3nd edn., Springer–Verlag, Germany, 1970.

[3] Collins, K. R., Plaut, R. H. and Wauer, J., *"Detection of Crack in Rotating Timoshenko Shafts Using Axial Impulses"*, ASME J. of Vibrations and Acoutics, Vol.113, 1991, pp74–78.

[4] Dimarogonas, A. D. and Paipetis, S. A., *"Analytical Methods in Rotor Dynamics"*, Applied Science, London, 1983.

[5] Fridemann, P. et al, *"Efficient Numerical Treatment of Periodic Systems with Application to Stability Problems"*, Intl. J. for Numerical Methods in Engineering, Vol. 11, 1977, pp1117–1136.

[6] Gasch, R., *"Dynamic Behavior of a Simple Rotor with a Cross Sectional Crack"*, Conf. on Vibrations in Rotating Machinery, IMechE., London, 1976, pp123–128.

[7] Gasch, R. et al, *"Dynamic Behaviour of the Laval Rotor with a Cracked Hollow Shaft––a Comparison of Crack Models"*, IMechE Conf. of Vibrations in Rotating Machinery, Sept, 1988, UK, C314 / 88.

[8] Gasch R., *" A Survey of the Dynamic Behaviour of a Simple Rotating Shaft with a Transverse Crack"*, J. of Vibration and Shock, No.4, Oct. 1992.

[9] Imam, I. et al, *"Development of an On–Line Rotor Crack Detection and Monitoring System"*, ASME J. of Vib. Acoustics, Stress, and Reliability in Design, Vol. 111, July 1989, pp241–250.

[10] Jack, A.R. and Patterson, A.N., *"Cracking in 500MW LP Rotor Shafts"*, 1st Mechanical Engineering Conference (The influence of the environment on fatigue), 1976.

[11] Mayes, I.W. and Davies, W. G.R., *"Analysis of the Response of a Multi–Rotor–Bearing System Containing a Transverse Crack in a Rotor"*, ASME, J. of Vib., Acoustics, Stress, and Reliability in Design, Vol. 106, 1984, pp139–145.

[12] Muszynska, A., *"Shaft Crack Detection"*, Proc. 7th Machinery Dynamics Seminar, Edmonton, Canada, 1982.

[13] Nelson, H. D. and Nataraj, C., *"The Dynamics of a Rotor System with a Cracked Shaft"*, ASME J. of Vib., Acoustics, Stress and Reliability in Design, Vol.108, 1986, pp189–196.

[14] Papadopoulos, C. A. and Dimarogonas, A. D., *"Coupled Longitudinal and Bending Vibrations of a Rotating Shaft with an Open Crack"*, J. of Sound and Vibration, Vol. 117, 1987, pp81–93.

[15] Someya, T., *"Journal–Bearing Databook"*, Springer–Verlag, 1989.

[16] Tamura, A. et al, *"Unstable Vibration of a Rotor with a Transverse Crack"*, IMechE Conf. of Vibrations in Rotating Machinery, Sept, 1988, UK, C322 / 88.

[17] Vance, J.M., *"Rotordynamics of Turbomachinery"*, John Wiley & Sons, New York, 1988.

[18] Wauer, J., *"On the Dynamics of Cracked Rotors: a Literature Survey"*, Appl Mech Rev. Vol.43, No.1, 1990, pp13–17.

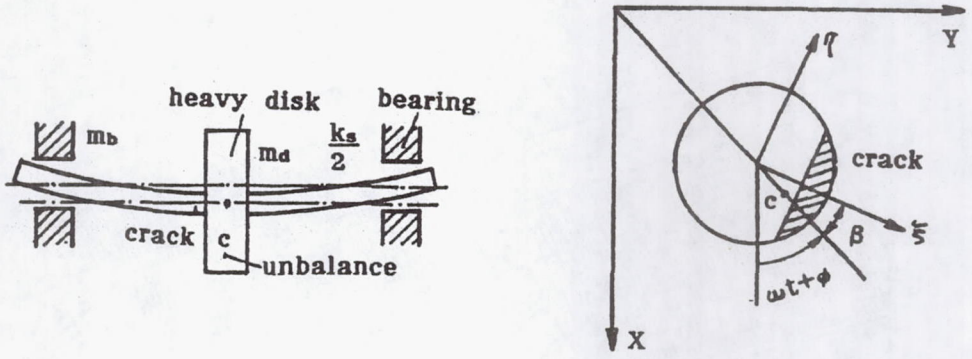

Fig.1 Schematic diagram of a cracked flexible rotor supported on journal bearings

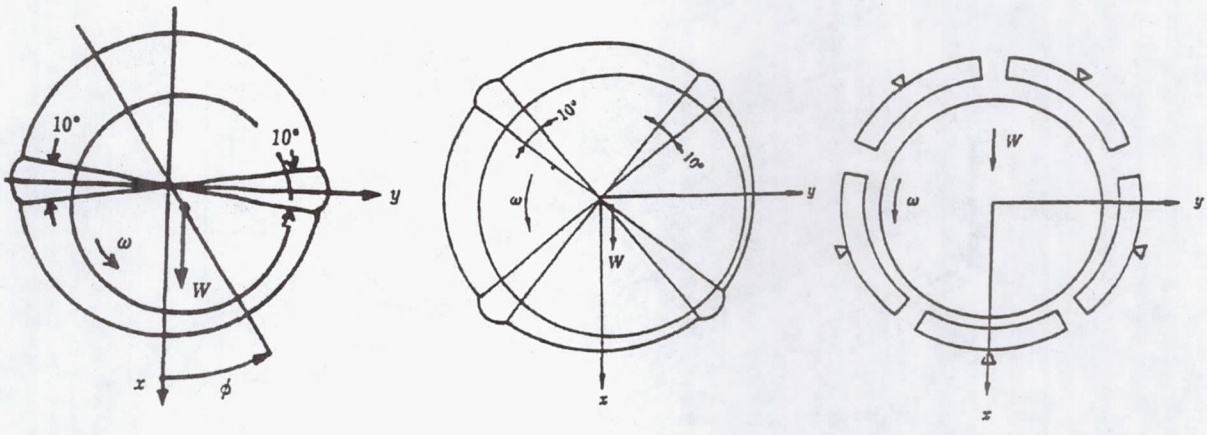

Cylindrical, with two axial grooves (L/D=0.5)

4 lobes (L/D=0.5, m_p=1/2)

Tilting pad, 5 pads (LOP, L/D=0.5, m_p=0)

Fig.2 Bearing geometry

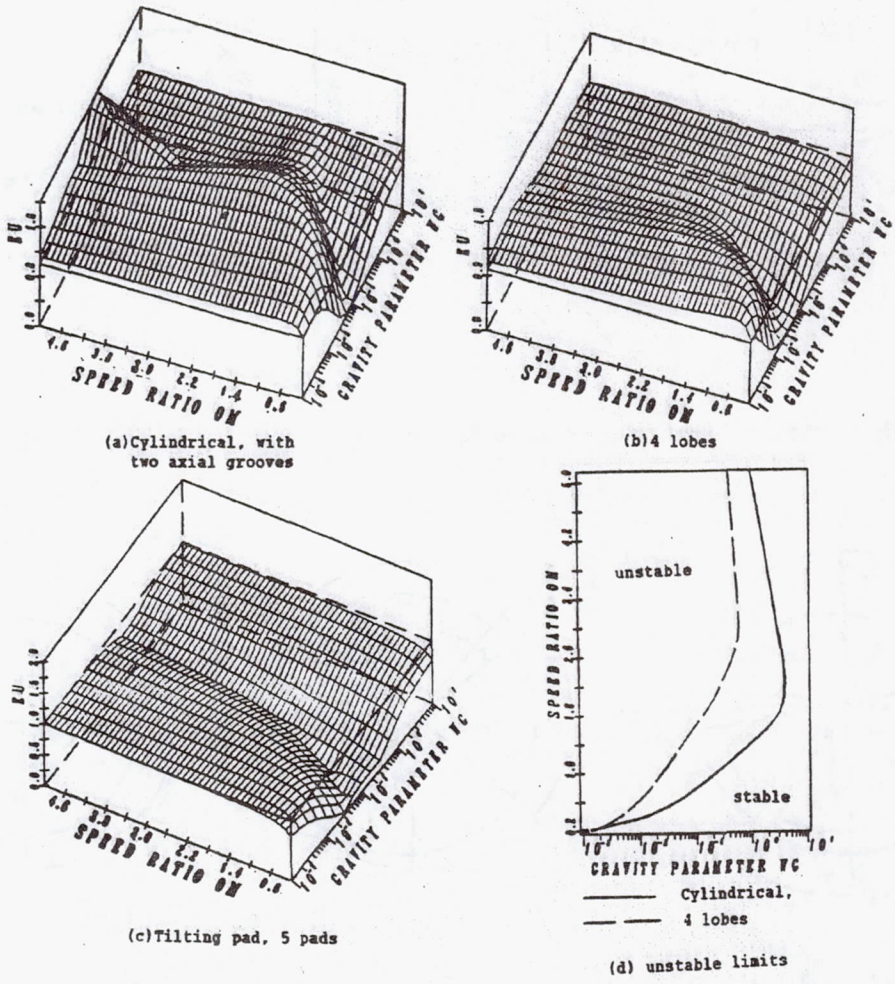

Fig.3 Influence of gravity parameter on the diagram of stability degree, without crack case ($\triangle K_\xi = 0.0$, $\triangle K_\eta = 0.0$, $D_e = 0.01$, $S_o = 2.0$, $\alpha = 0.2$)

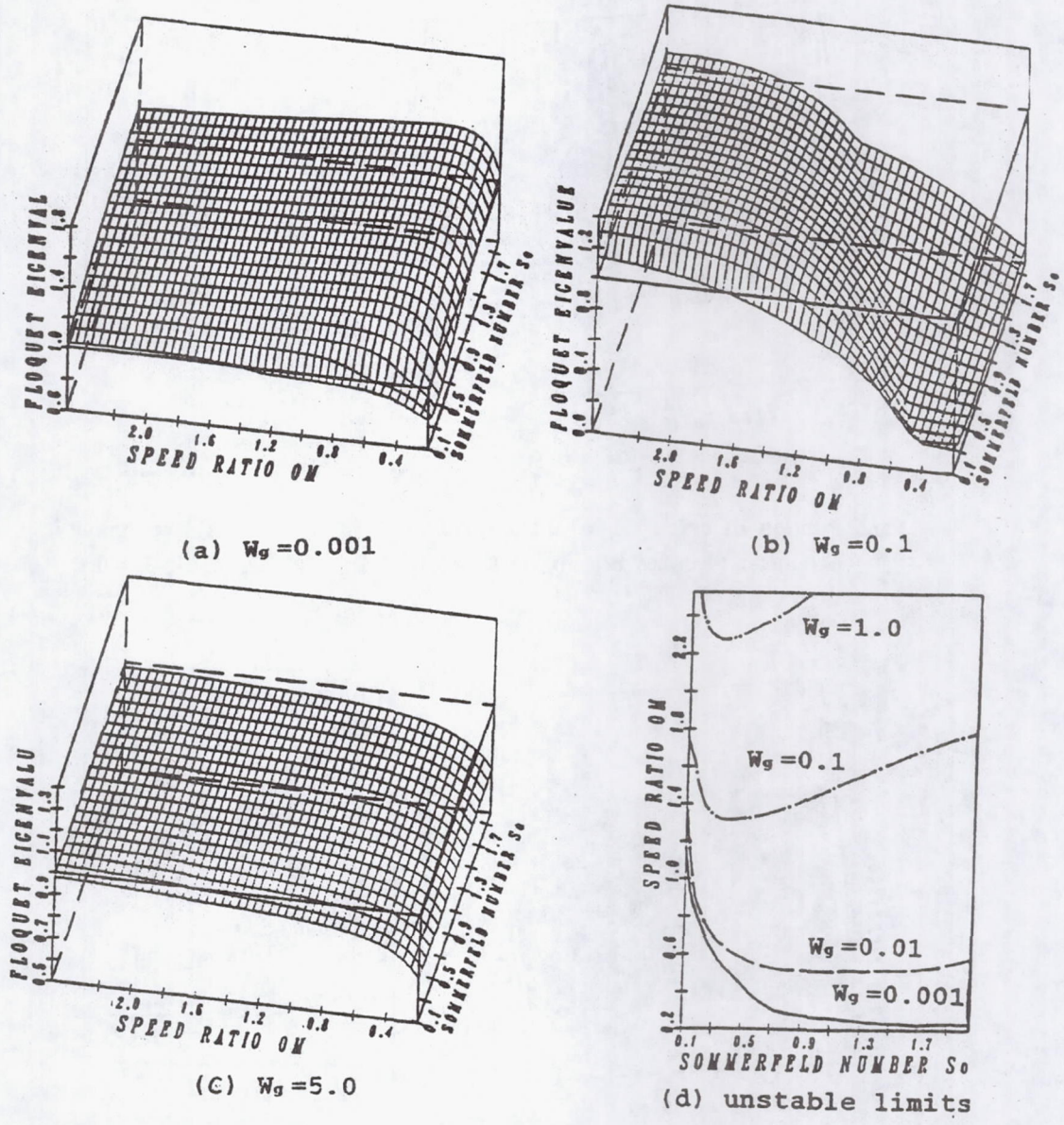

Fig.4 4–Lobes bearing, influence of gravity parameter and fixed Sommerfeld number on the diagram of stability degree, without crack case ($\triangle K_\zeta = 0.0$, $\triangle K_\eta = 0.0$, $D_e = 0.01$, $\alpha = 0.2$)

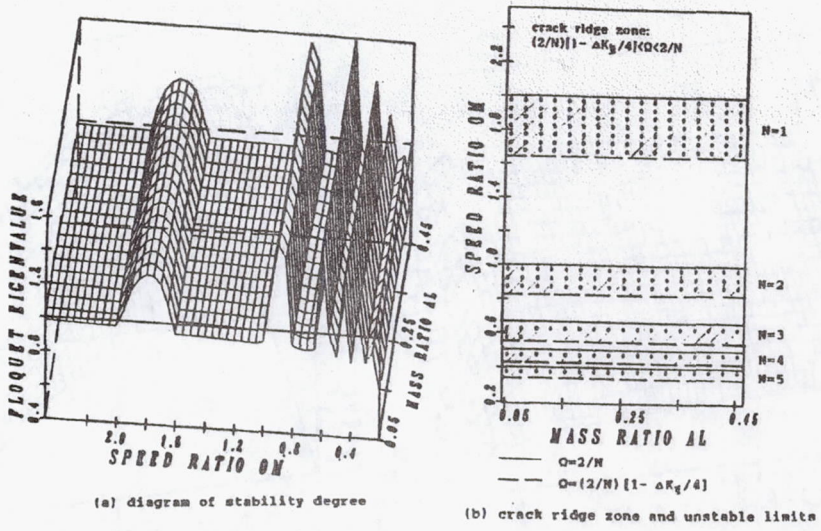

(a) diagram of stability degree

(b) crack ridge zone and unstable limits

Fig.5 Position of crack ridge zones, influence of mass ratio for large gravity parameter (4–lobes bearing, $\triangle K_\xi = 0.7$, $\triangle K_\eta = 0.0$, $D_e = 0.01$, $S_o = 0.1$, $W_g = 5.0$)

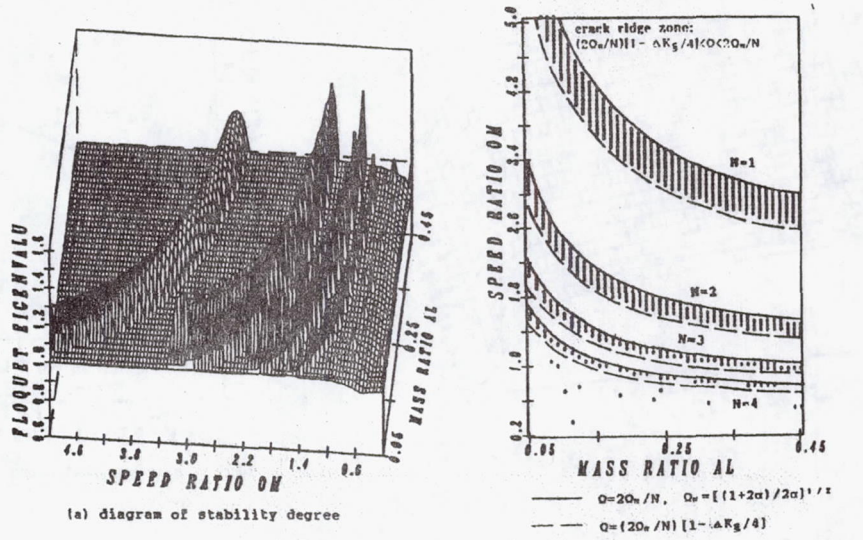

(a) diagram of stability degree

(b) crack ridge zone and unstable limits

Fig.6 Position of crack ridge zones, influence of mass ratio for small gravity parameter (Tilting pad bearing, $\triangle K_\xi = 0.5$, $\triangle K_\eta = 0.0$, $D_e = 0.01$, $S_o = 0.1$, $W_g = 0.001$)

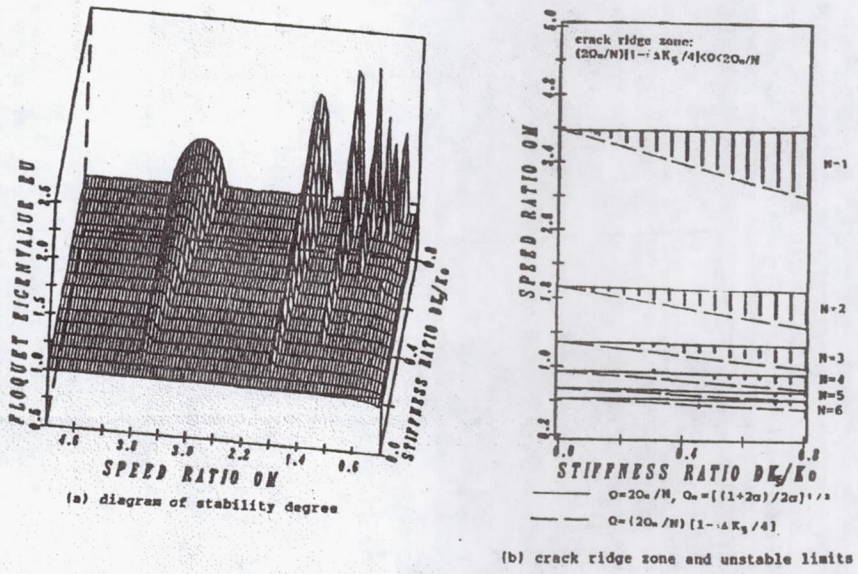

Fig.7 Position of crack ridge zones, influence of stiffness ratio (Tilting pad bearing, $\triangle K_\eta = 0.0$, $D_e = 0.01$, $S_o = 0.1$, $\alpha = 0.2$, $W_g = 0.001$)

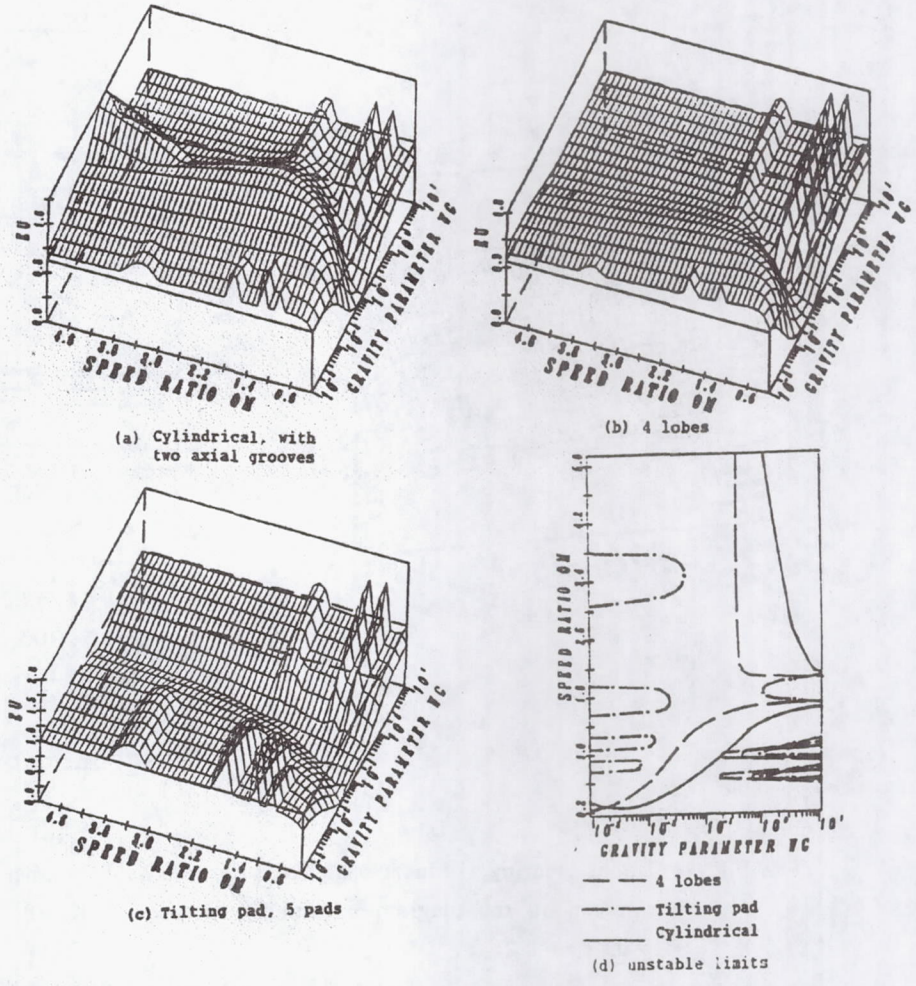

Fig.8 Influence of gravity parameter on the diagram of stability degree ($\triangle K_\xi = 0.7$, $\triangle K_\eta = 0.0$, $D_e = 0.01$, $S_o = 2.0$, $\alpha = 0.2$)

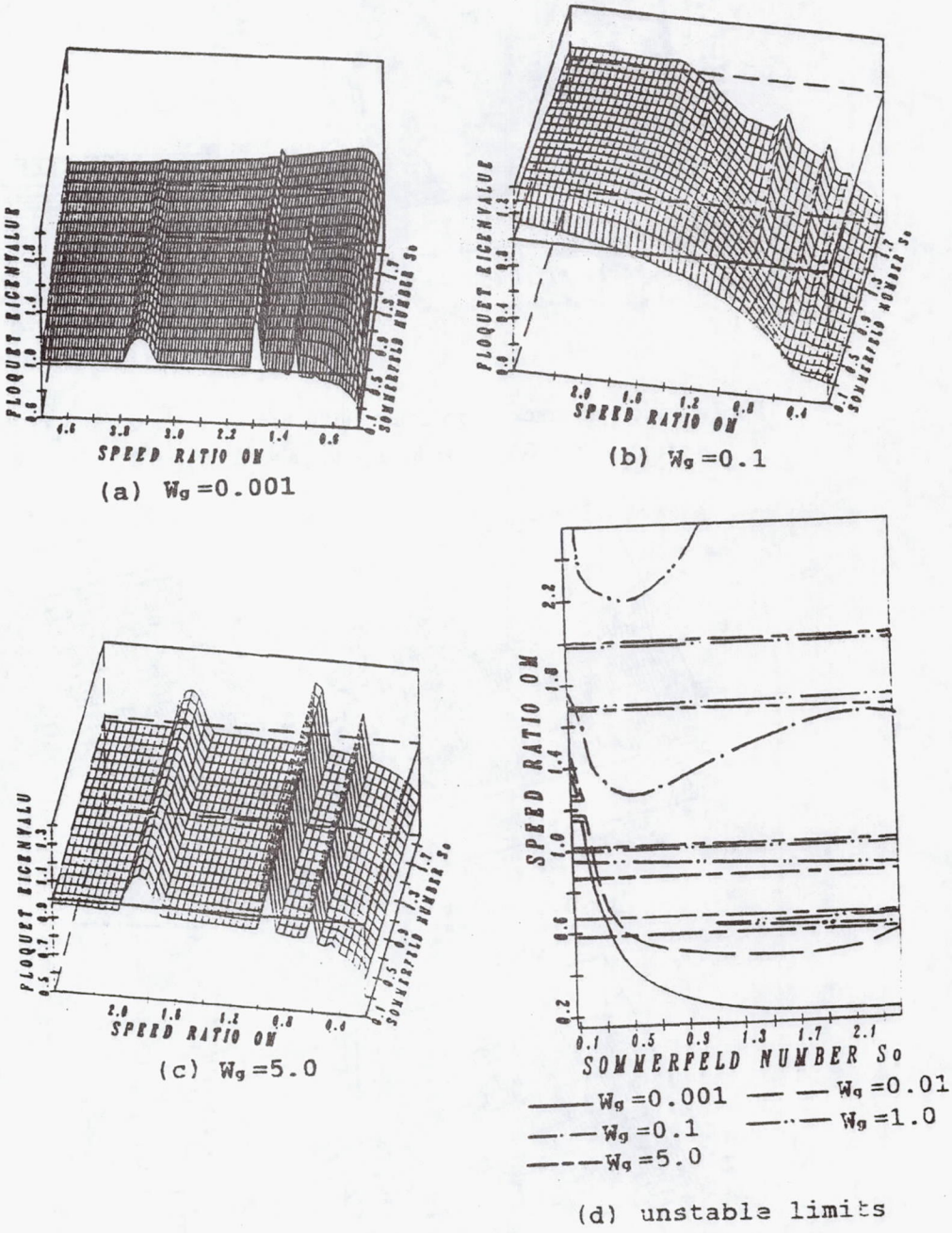

Fig.9 4-Lobes bearing, influence of fixed Sommerfeld number and gravity parameter on the diagram of stability degree ($\triangle K_\xi = 0.5$, $\triangle K_\eta = 0.0$, $D_c = 0.01, \alpha = 0.2$)

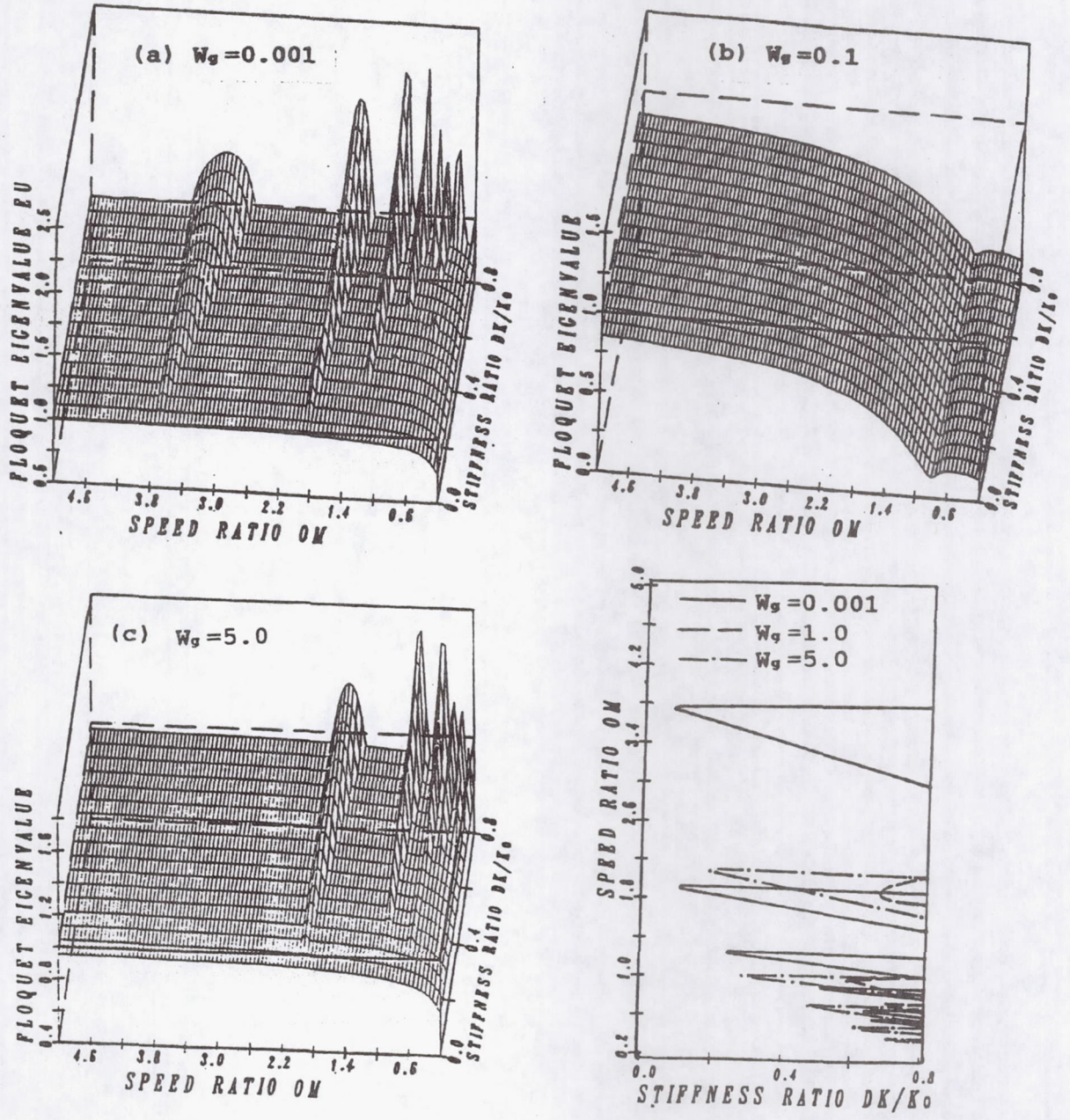

Fig.10 Tilting pad bearing, influence of stiffness change ratio and gravity parameter on the diagram of stability degree ($\triangle K_q = 0.0$, $D_e = 0.01$, $S_o = 2.0$, $\alpha = 0.2$)

Session IV

Bearings and Dampers

Preceding Page Blank

AN EXPERIMENTAL AND THEORETICAL STUDY OF STRUCTURAL DAMPING IN COMPLIANT FOIL BEARINGS

C.-P. Roger Ku
Mechanical Technology Incorporated
Latham, New York

ABSTRACT

This paper describes an experimental investigation into the dynamic characteristics of corrugated foil (bump foil) strips used in compliant surface foil bearings. This study provided the first opportunity to quantify the structural damping of bump foil strips. The experimental data were compared to results obtained by a theoretical model developed earlier. The effects of bearing design parameters, such as static loads, dynamic displacement amplitudes, bump configurations, pivot locations, surface coatings, and lubricant were also evaluated. An understanding of the dynamic characteristics of bump foil strips resulting from this work offers designers a means for enhancing the design of high-performance compliant foil bearings.

INTRODUCTION

Over the past 10 years, the ability of a conventional bearing to survive the rigors of today's advanced turbine engines and rocket propulsion systems has gradually declined. Extreme environments are pushing conventional liquid fluid-film bearings to, or perhaps beyond, their operating limits within high-temperature and cryogenic settings. In some turbine engines, bearing temperatures are expected to exceed the capabilities of conventional liquid lubricants completely; in rocket propulsion, bearing deficiencies persist in cryogenic turbopumps. On the other hand, compliant foil bearings, which can operate on either gas or liquid, have demonstrated good performance at elevated temperatures and high speeds, and are very attractive for use with cryogenic fluids.

The resilience offered by a compliant foil bearing stems from its construction of a smooth top foil, which provides the bearing surface, and a flexible, corrugated bump foil strip, which provides a resilient support to the top foil (see Figure 1). The bump foil strip is welded at one end to the bearing housing and is free at the other end. The advantages offered by the compliant foil bearing over conventional bearings include its adaptation to shaft misalignment, variations due to tolerance build-ups, centrifugal shaft growth, and differential thermal expansion. It has long life and reliability, higher load capacity, a lower power loss, and superior rotordynamic characteristics [1].

Existing analytical models of foil bearings are not as developed, however, as those of conventional-type fluid-film bearings. Walowit et al. [2] first introduced a theoretical model to determine the static structural stiffness of the resilient support. This model assumed that bumps do not interact with each other, thus neglecting local interactive forces between bumps as well as friction forces between the top foil and the bumps. According to this model, when the top foil is loaded, each bump has identical deflection and static stiffness.

Ku and Heshmat [3] recently developed a theoretical model to investigate the mechanism of deformation of a bump foil strip used in thrust foil bearings. This work was a first step toward

Preceding Page Blank

understanding the relationship between frictional and local interacting forces in bump foil strips. In this model, the friction forces between top foil and bumps, the friction forces between housing and bumps, and the local interactive forces between bumps are taken into consideration. These researchers predicted that the bumps near the fixed end would have higher static stiffness than the bumps near the free end, and that the load distribution profile would have a great effect on bump local static stiffness. More recently, Ku and Heshmat [4,5] extended their model to predict the dynamic structural stiffness and equivalent viscous damping coefficients of the resilient support, the bump foil strip, in a journal bearing or damper. The stiffness is calculated based on the perturbation of the journal center with respect to its static equilibrium position. The equivalent viscous damping coefficient is determined based on the area of a closed hysteresis loop of the journal center motion. With the introduction of this enhanced model, the analytical tools are now available for the design of compliant foil bearings.

In a follow-up experimental investigation [6,7], the two-dimensional deflections of bump foil strips were studied via an optical tracking system to verify the feasibility of the theoretical model. The static and dynamic structural stiffness of bump foil strips were measured and compared to theoretical predictions. The comparisons show very good agreement. The friction coefficients between the contact surfaces for different surface coatings were also determined empirically by matching the values of dynamic structural stiffness. It was reported that the dynamic structural stiffness is static load and/or dynamic amplitude dependent.

In this paper, the experimental study has been extended to quantify the equivalent viscous damping coefficients of bump foil strips. The results are compared to analytical predictions. The effects of static load, dynamic displacement amplitude, bump configurations, pivot locations and surface coatings are also investigated.

EXPERIMENTAL SETUP

The test apparatus and bump foil assembly are shown in Figures 2 and 3. Each pad is 41.1 mm by 24.6 mm and made of steel. The lower pad acts as a housing and the upper pad is supported by a bump foil strip. The bump foil strip is welded at one end of the lower pad; a smooth top foil is welded on the lower surface of the upper pad. As the lower pad moves or vibrates in the vertical direction, the bumps are deformed in both vertical and horizontal directions. The vertical deflections of the bumps determine load capacity, or stiffness, and the horizontal motions of the bumps yield damping.

A horizontal hard dowel, which acts as a pivot, is placed between a circular plate and the upper pad. The pivot can be located in any one of five grooves that are spaced 3.96 mm apart on the top surface of the upper pad. A vertical dowel, inserted tightly into the circular plate and loosely into the upper pad, prevents the horizontal motion of the upper pad. When the pivot location is changed, the upper and lower pads move as a unit.

The lower pad is mounted on the lower adaptor by two roll pins. The circular plate with a central groove is fixed on the upper adaptor. The upper and lower adaptors are mounted on an MTS hydraulic force control system. An extendsometer, which has a sensitivity of 25 μm/V, controls the relative distance between the adaptors. A force transducer (44.5 N/V) measures the load capacity of the bump foil strip. The optical tracking system used for the static deformation study [6] was removed. An Ono-Sokki two-channel analyzer and a plotter record the test data.

The bump foil strips and smooth top foils were made of Inconel X750; all the other parts were made of steel. Each bump foil strips is 24.1 mm wide and has six bumps. The surfaces of some of the foils were coated with either Teflon or copper. For the bump foil strip with one of these coatings, another smooth foil with the same coating was welded between the bump foil strip and the upper surface of the lower pad (see Figure 2, Surface 4). In this way, all contact surfaces had the same coating. For each coating, both dry contact surfaces and surfaces lubricated with light turbine oil were tested. Table 1 shows the configurations and coatings of the tested bump foils.

The detailed experimental procedures used to conduct the static load test were described in Reference 6. After a static load was applied, a dynamic force or displacement was imposed. In the current experiments, a dynamic displacement of the vertical deformation of the bump foil strip at the pivot location was controlled by the extendsometer, and the corresponding dynamic force was recorded. Dynamic load-deflection curves (hysteresis loops) were plotted with respect to the static equilibrium positions. For each bump foil strip specimen listed in Table 1, three most centrally located pivot positions were evaluated (see Figure 2). At each pivot location, two static loads (90 and 135 N) and two dynamic displacement amplitudes (~ 2.5 and 5.0 μm) at 1 Hz frequency were tested, respectively. The test parameters are shown in Table 2.

RESULTS AND DISCUSSIONS

The measured equivalent viscous damping coefficient was calculated based on the area of a hysteresis loop, A, of the pivot location and the following equation:

$$B = A/(\pi\Omega\delta^2) \tag{1}$$

The analytical result was calculated by the same equation but the hysteresis loop of the pivot location was determined by using the earlier developed theoretical model [3-5]. The experimental results are displayed in Figures 4 through 6. The resulting data points are represented by numbers, which are identical to the test number shown in the first column of Table 1. The dimensionless variables shown in the figures are defined as follows:

$$\text{Dimensionless displacement amplitude,}\quad \delta^* = \delta\frac{E_B}{2W_T(1-\nu_B^2)}\left(\frac{t_{Br}}{\ell_r}\right)^3 \tag{2}$$

$$\text{Dimensionless structural damping,}\quad B^* = \Omega B\frac{2(1-\nu_B^2)}{mu_B E_B}\left(\frac{\ell_r}{t_{Br}}\right)^3 \tag{3}$$

where E_B, ν_B, t_{Br}, ℓ_r, W_T, and m are known parameters (see Table 2 and Nomenclature).

Although it is very difficult to measure the friction coefficients accurately for different surface coatings, these coefficients are required as input parameters in the theoretical model. Therefore, the sum of the friction coefficients between Surfaces 1 and 2 and Surfaces 3 and 4 (Figure 2) was treated as unknown parameters, and the coefficients were determined empirically by matching the dynamic structural stiffness [7]. It was found that the Ni-Tef (or Tef-Ni) surface coating has a total friction coefficient near 0.4; the Ni-Ni surface coating has a total friction coefficient near 0.5; and the Ni-Cu (or Cu-Ni) surface coating has a total friction coefficient near 0.6. The results of structural damping for different total friction coefficients were plotted by the solid lines in Figures 4 through 6.

Figure 4 displays the effect of surface coatings and lubricant on structural damping at different static loads and dynamic displacement amplitudes. For each of the seven cases (1-7), the bump had a 4.6-mm pitch and a 76-μm thickness, and the pivot was in the center position. In general, the coating with a higher friction coefficient provides higher structural damping, however, there are exceptions when dynamic displacement amplitude is small. In comparing the experimental data with the theoretical results, the theoretical predictions always overestimate the structural damping, especially at the small dynamic displacement amplitudes. In detailed examination of both measured and calculated hysteresis loops, the measured loop does not follow the predicted one with a stick-slip condition [7]. Therefore, the area of the measured hysteresis loop is smaller than the predicted one.

Figure 5 displays the effect of three bump configurations on structural damping. For each configuration, the pivot was located in the center for a Ni-Ni surface coating with (cases 2 and 9) and without (cases 1, 8, and 10) lubricant. The theoretical results were calculated with total friction coefficients 0.6. At both static loads and dynamic displacement amplitudes, increasing the bump thickness and/or pitch would increase a small amount of structural damping. Again, the theoretical predictions overestimate the structural damping for all three bump configurations.

The effect of pivot location on structural damping is shown in Figure 6. For each pivot location, center or left, the bump had a 4.6-mm pitch, a 76-μm thickness, and a Ni-Ni surface coating with (cases C9 and L9) and without (cases C8 and L8) lubricant. The experimental data show that both pivot locations provide roughly the same amount of structural damping, which does not follow the trend of theoretical predictions. However, it is interesting to note that the theoretical results do have much better predictions for the left pivot location.

The effect of lubricant on structural damping is also shown in Figures 4 through 6. The addition of oil to the surfaces coated with nickel (cases 2 and 9) and copper (case 4) increases the damping, but not much, for most of the test conditions.

CONCLUSIONS

An experimental study was performed to quantify the structural damping of bump foil strips used in foil bearings. The results were compared to the analytical predictions by using the previously developed theoretical model. The effects of bump configurations, pivot locations, surface coatings, lubricant, static load, and dynamic displacement amplitude on the bump foil strip structural damping were also evaluated.

It was shown that the analytical predictions overestimate the structural damping for most of the test cases, especially at the small dynamic displacement amplitude. As the static load increases or dynamic displacement amplitude decreases, the structural damping does not change too much for all the test conditions. The bearing designer may use the coating with a higher friction coefficient, add the lubricant to the surfaces, and increase the bump thickness and/or pitch to achieve higher structural damping.

An understanding of the dynamic characteristics of bump foil strips resulting from this work offers designers a means for enhancing the design of high-performance compliant foil bearings. Recently, a rotor with 35 mm (1.375 in.) diameter and 15.2 N (3.4 lb) weight has been operated with two air

foil bearings to 132,000 rpm successfully. These bearings have demonstrated a load capacity to 0.67 MPa (97 psi) [8].

ACKNOWLEDGMENTS

The work was principally supported by Mechanical Technology Incorporated. The author express his appreciation to the organization for their support. The author would also like to thank his colleagues, Mr. M. Tomaszewski, for his help in preparing the test facilities, and Dr. H. Heshmat for his many valuable suggestions and discussions.

NOMENCLATURE

A	Hysteresis loop area of the pivot location
B	Bump foil strip structural damping
B^*	Dimensionless bump foil strip structural damping
E_B	Bump elastic modulus
W	Bearing static load
ΔW	Bearing dynamic load
W_T	Unit load along transverse direction = 175 N/m (1 lb/in.)
ℓ_r	Reference bump half length = 1.27 mm (0.050 in.)
m	Number of bumps in a bump foil strip
s	Bump pitch
t_B	Bump thickness
t_{Br}	Reference bump thickness = 76.2 μm (0.003 in.)
u_B	Bump transverse length
Ω	Dynamic displacement amplitude vibration frequency
δ	Dynamic displacement amplitude of bearing pivot location
δ^*	Dimensionless dynamic displacement amplitude of bearing pivot location
τ	Time
ν_B	Poisson's ratio of bump

REFERENCES

1. Gray, S., Heshmat, H., and Bhushan, B., 1981, "Technology Progress on Compliant Foil Air Bearing Systems for Commercial Applications," 8th International Gas Bearing Symposium, pp. 69-97.

2. Walowit, J. A., Murray, S. F., McCabe, J., Arwas, E. B., and Moyer, T., 1973, "Gas Lubricated Foil Bearing Technology Development for Propulsion and Power Systems," Air Force Aero Propulsion Laboratory, Wright-Patterson Air Force Base, Ohio, AFAPL-TR-73-92.

3. Ku, C.-P. R., and Heshmat, H., 1992, "Compliant Foil Bearing Structural Stiffness Analysis Part I: Theoretical Model - Including Strip and Variable Bump Foil Geometry," ASME, J. of Tribology, 114, 2, pp. 394-400.

4. Ku, C.-P. R., and Heshmat, H., 1993, "Structural Stiffness and Coulomb Damping in Compliant Foil Journal Bearings: Theoretical Considerations," accepted for publication in STLE Transactions and presentation at STLE Annual Meeting, May 17-20, Calgary, Canada.

5. Ku, C.-P. R., and Heshmat, H., 1993, "Structural Stiffness and Coulomb Damping in Compliant Foil Journal Bearings: Parametric Studies," accepted for publication in STLE Transactions and presentation at STLE Annual Meeting, May 17-20, Calgary, Canada.

6. Ku, C.-P. R., and Heshmat, H., 1993, "Compliant Foil Bearing Structural Stiffness Analysis Part II: Experimental Investigation," accepted for publishing in ASME, J. of Tribology, ASME paper 92-Trib-6.

7. Ku, C.-P. R., 1993, "Dynamic Structural Stiffness and Damping Coefficient in Compliant Foil Thrust Bearings - Comparison between Experimental and Theoretical Results," submitted to ASME J. of Tribology and ASME/STLE Joint Tribology Conference, Oct. 24-27, New Orleans, Louisiana.

8. Heshmat, H., 1993, "The Advancement in Performance of Aerodynamic Foil Journal Bearings: High Speed and Load Capability," submitted to ASME J. of Tribology and ASME/STLE Joint Tribology Conference, Oct. 24-27, New Orleans, Louisiana.

Table 1 Configurations and surface coatings of tested bumps

Test	Pitch	Thickness	Height	Material Combination		Lubricant
#	mm	μm	mm	Surfaces 1 & 2	Surfaces 3 & 4	
1	4.572	76.2	0.4953	Ni-Ni	Ni-Steel	Air
2	4.572	76.2	0.4953	Ni-Ni	Ni-Steel	Oil
3	4.572	76.2	0.4953	Ni-Ni	Cu-Cu*	Air
4	4.572	76.2	0.4953	Ni-Ni	Cu-Cu*	Oil
5	4.572	76.2	0.4953	Cu-Cu*	Ni-Steel	Air
6	4.572	76.2	0.4953	Tef-Tef#	Ni-Steel	Air
7	4.572	76.2	0.4953	Ni-Ni	Tef-Tef#	Air
8	4.572	63.5	0.4890	Ni-Ni	Ni-Steel	Air
9	4.572	63.5	0.4890	Ni-Ni	Ni-Steel	Oil
10	4.191	76.2	0.4699	Ni-Ni	Ni-Steel	Air

* INC-X750 Coated with Cu
\# INC-X750 Coated with PTFE

Table 2 Test parameters

Parameter	Symbol	English Unit	SI Unit
Static Load	W	20, 30 lb	90, 145 N
Perturbation Amplitude (Half)	δ	~0.0001-0.0002 in.	~2.5-5.0 μm
Perturbation Frequency	Ω	1 Hz	---
Number of Bumps	m	6	---
Bump Elastic Modulus	E_B	3.0×10^7 psi	2.07×10^5 MPa
Bump Poisson's Ratio	ν_B	0.25	---
Bump Transverse Length	u_B	0.95 in.	24.1 mm

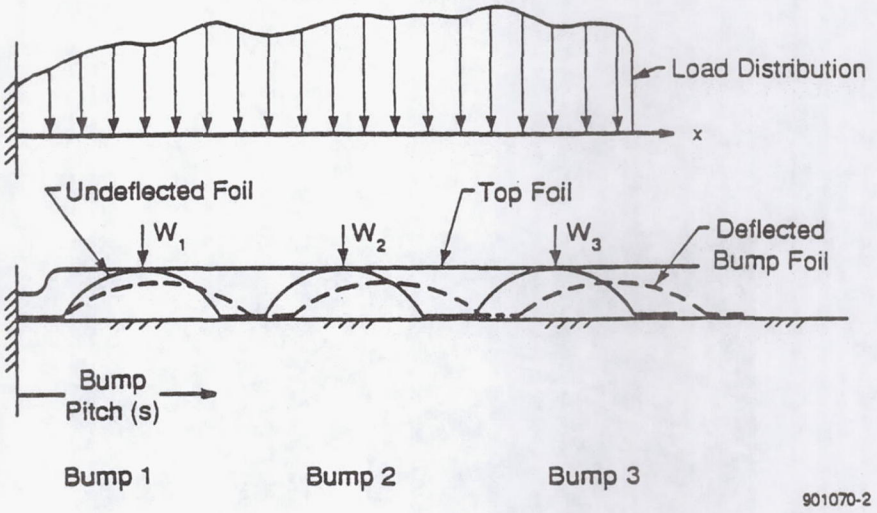

Figure 1 Bump foil strip with and without applied load

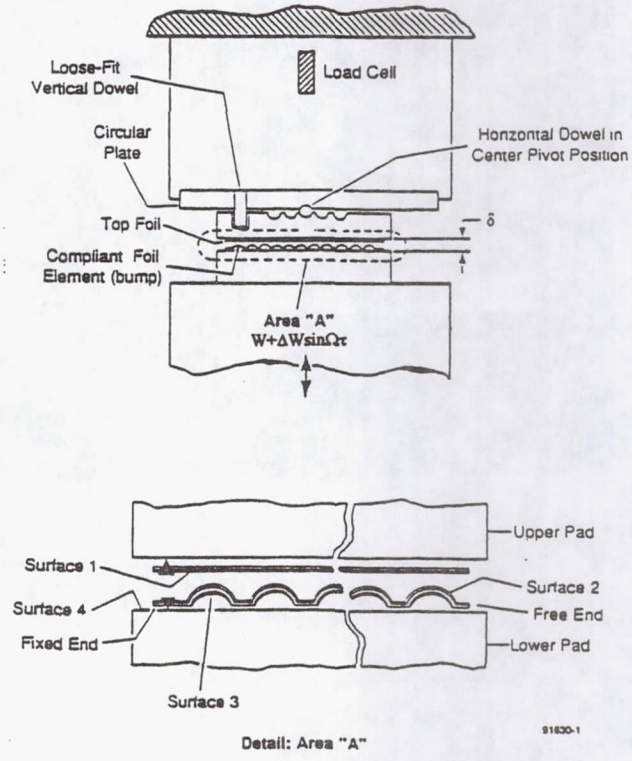

Figure 2 Bump foil pivot locations and identification of surface contacts

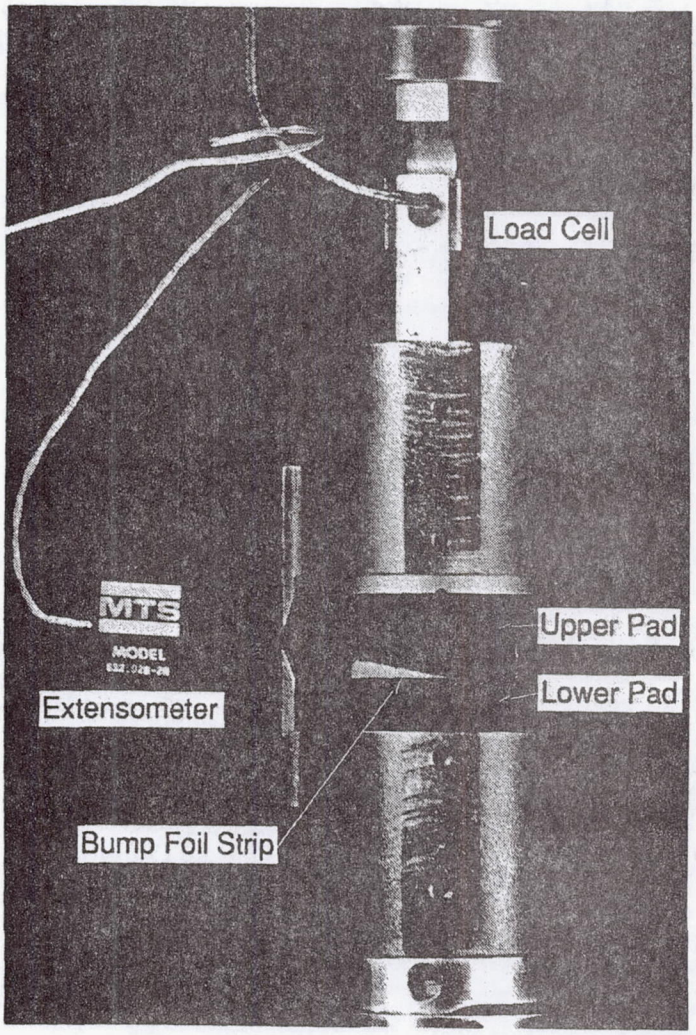

Figure 3 Close-up of bump foil assembly on test

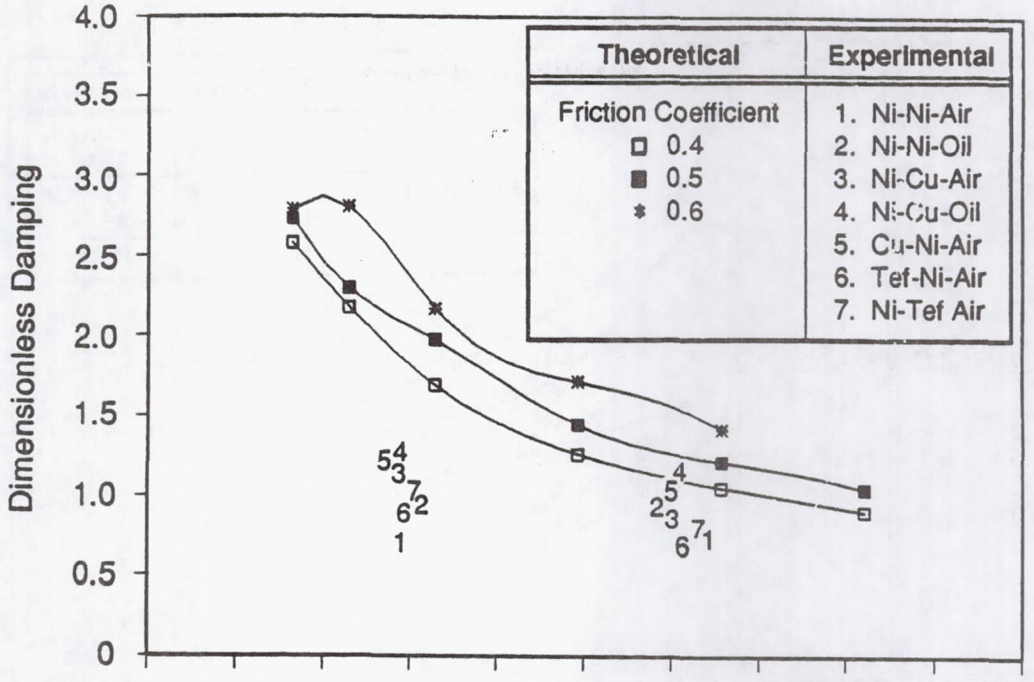

a) W = 90 N

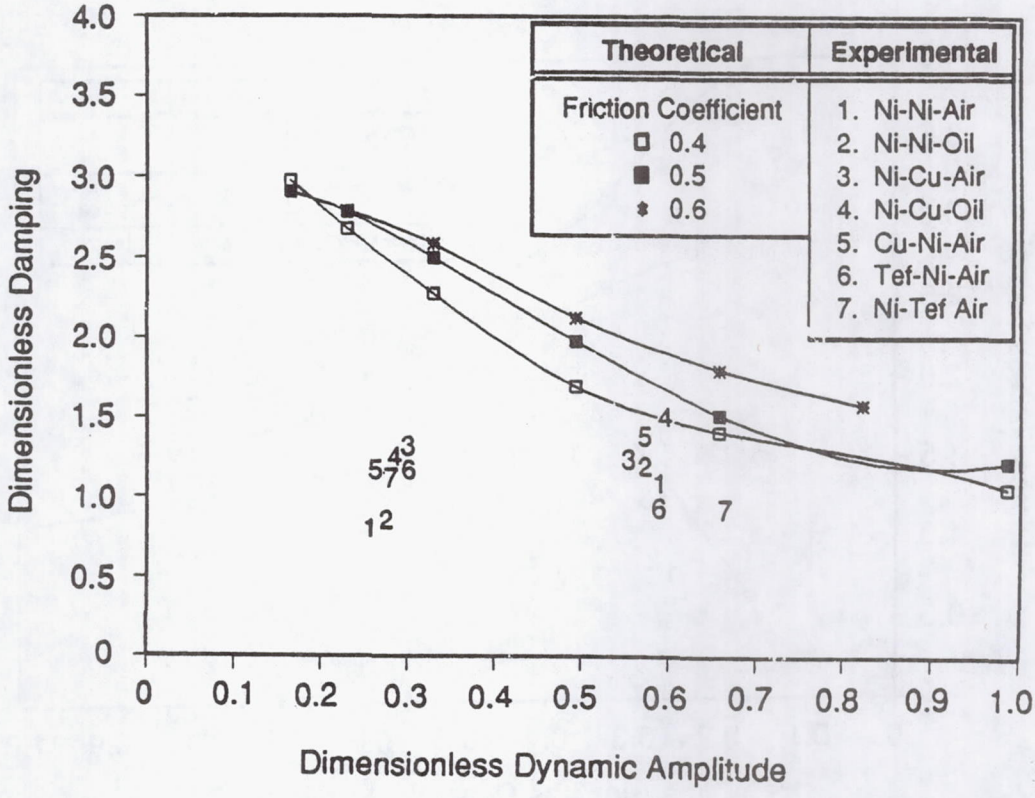

b) W = 135 N

Figure 4 Effect of surface coatings on structural damping
(s=4.6 mm, t_B=76 μm, center pivot)

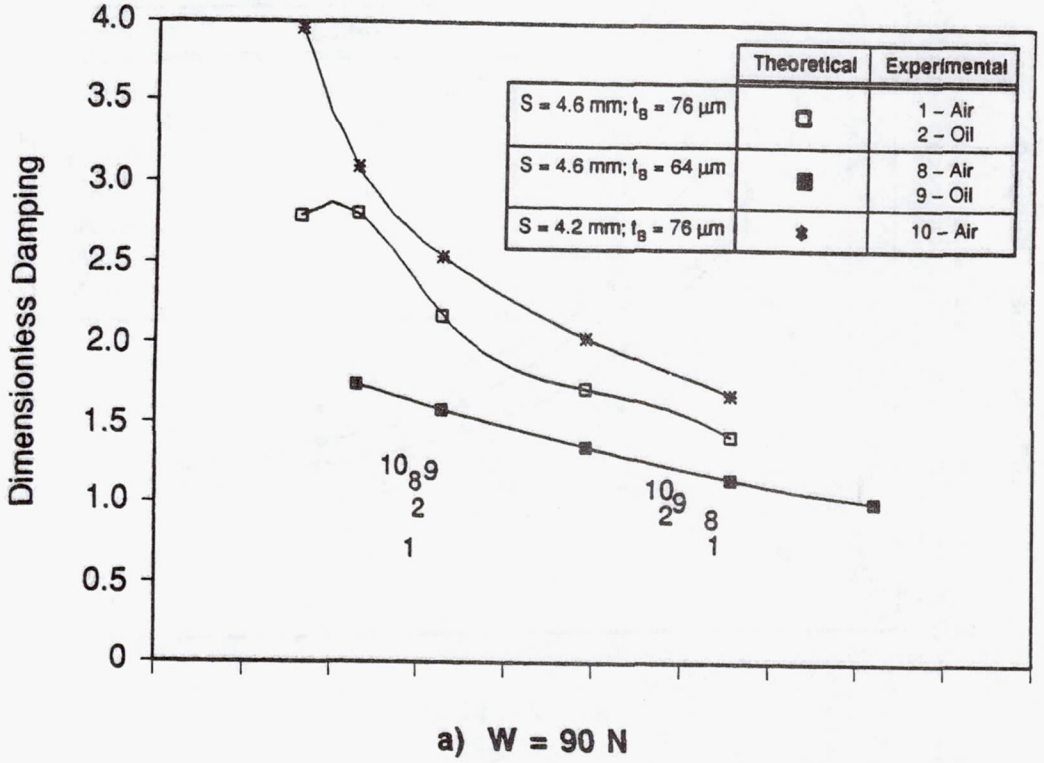

a) W = 90 N

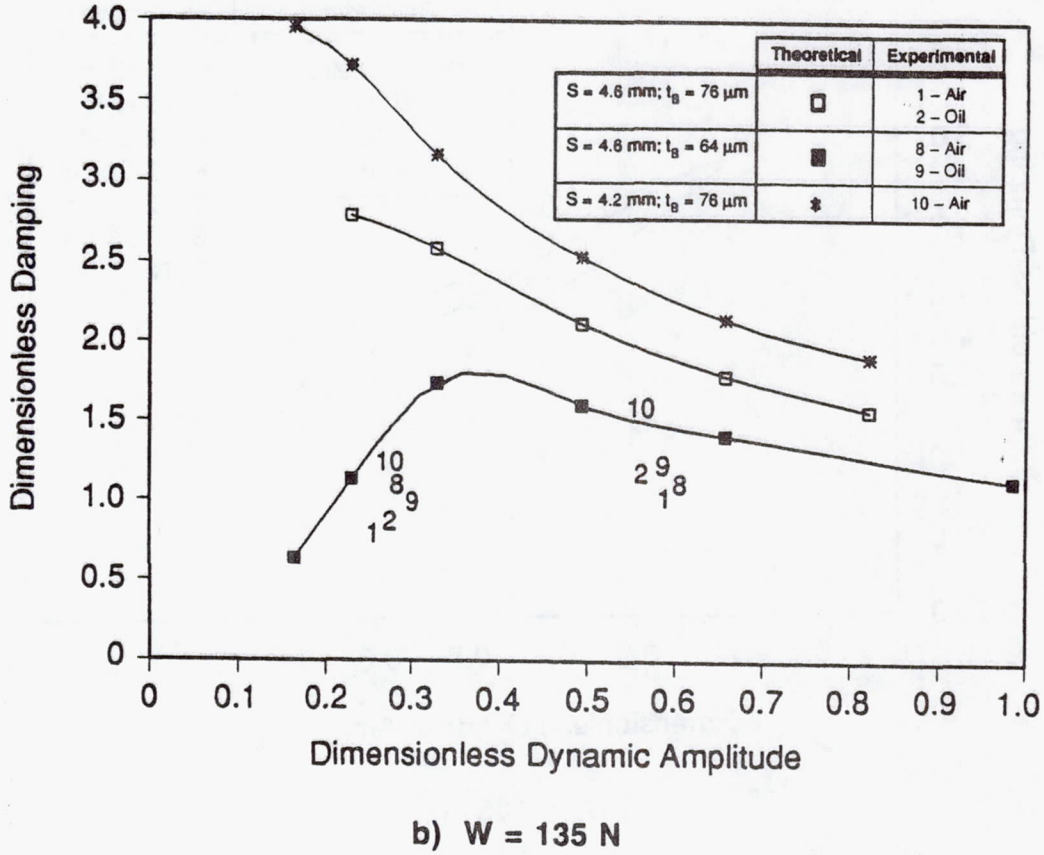

b) W = 135 N

Figure 5 Effect of bump configurations on structural damping (Ni-Ni surface coating, center pivot)

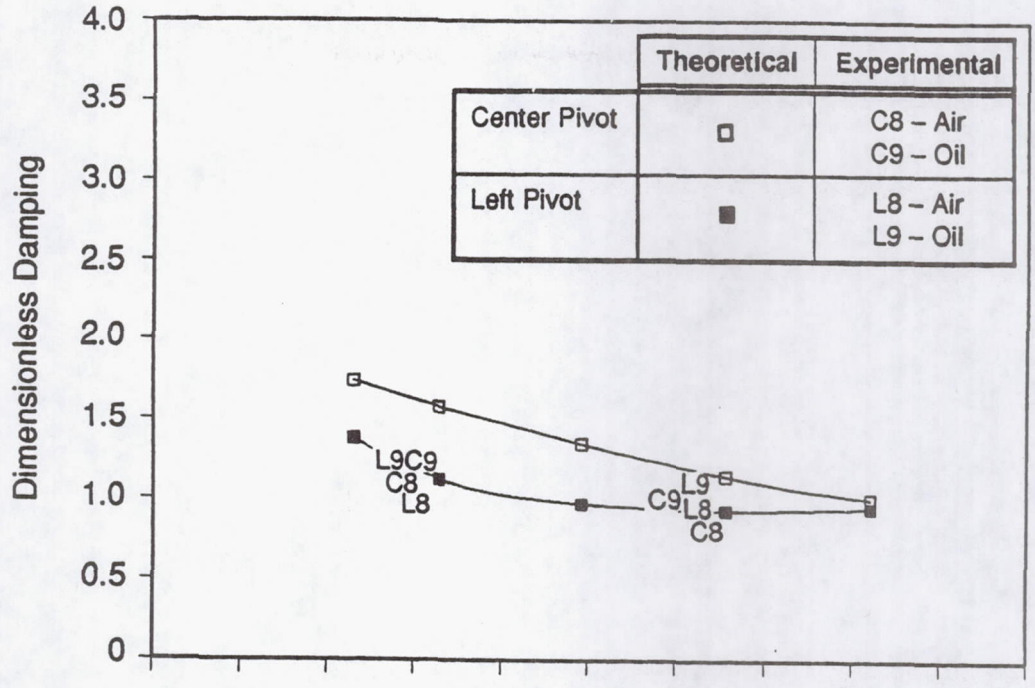

a) W = 90 N

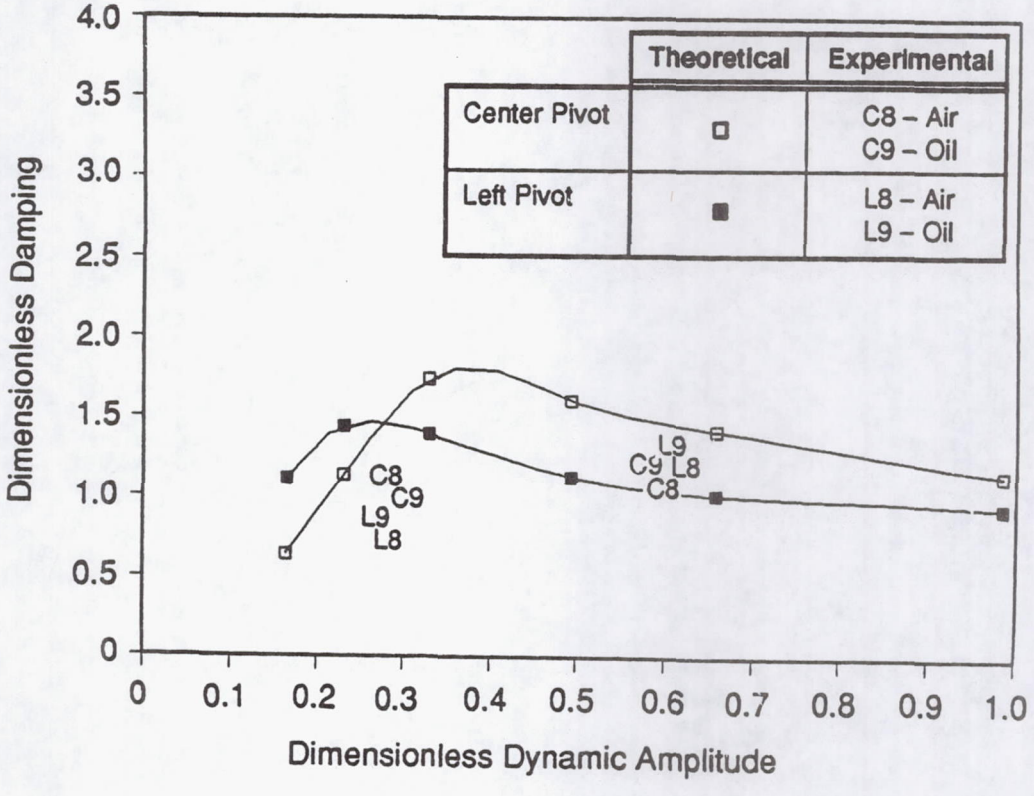

b) W = 135 N

Figure 6 Effect of pivot locations on structural damping
(s=4.6 mm, t_B=76 μm, Ni-Ni surface coating)

SQUEEZE FILM DAMPERS WITH OIL HOLE FEED*

P.Y.P. Chen and E.J. Hahn
The University of New South Wales
Kensington, Australia

To improve the damping capability of squeeze film dampers, oil hole feed rather than circumferential groove feed is a practical proposition. However, circular orbit response can no longer be assumed, significantly complicating the design analysis. This paper details a feasible transient solution procedure for such dampers, with particular emphasis on the additional difficulties due to the introduction of oil holes. It is shown how a cosine power series solution may be utilised to evaluate the oil hole pressure contributions, enabling appropriate tabular data to be compiled. The solution procedure is shown to be applicable even in the presence of flow restrictors, albeit at the expense of introducing an iteration at each time step. Though not of primary interest, the procedure is also applicable to dynamically loaded journal bearings with oil hole feed.

NOMENCLATURE

a_j	radius of j'th oil hole
C	radial clearance
D	bearing or journal diameter
d_j	diameter of j'th oil hole
h	film thickness; $H = h/C$
L	bearing land length
M, N	summation integers
n	number of oil holes
p	gauge pressure relative to cavitation pressure; $P = pC^2 / (12\mu\Omega L^2)$
P*	defined by eqn. (7)
p_i, p_o	inlet and outlet gauge pressures
P_S, P_C	solutions to eqns. (8) and (9) respectively
P_j	solution to eqn. (12)
P_{oj}	non-dimensional pressure at the j'th oil hole
P_{SS}	non-dimensional supply pressure
R	bearing or journal radius
r	non-dimensional radial coordinate; $r = \rho / a_j$
t	time; $\tau = \Omega t$
U, V	relative velocities of the bearing surfaces in the X, Y directions at angular location θ in Figure 1

* The work reported herein was supported by an Australian Research Council grant.

Preceding Page Blank

X, Y, Z	coordinates located in centre plane of bearing at intersection of the line of centres O_bO_j with the bearing surface as shown in Figure 1; $\bar{Z} = Z/L$
X_j	X coordinate of the j'th oil hole
α_{ij}	series coefficients defined by eqn. (20)
θ	angular location of the point A from the line of centres along the bearing surface as shown in Figure 1; $\theta = X/R$
θ_j	angular location of the j'th oil hole; $\theta_j = X_j / R$
μ	mean viscosity of lubricant
ρ, ψ	polar coordinates with origin at centre of j'th oil hole as shown in Figure 3
ρ	unbalance eccentricity in Figure 1
Δ_j	time dependent multiplier of P_j
χ_j	defined by eqn. (19)
ϕ	angular displacement of the line of centres from the vertical direction as shown in Figure 1.
η	a constant; $\eta = 1$ for journal bearings, $\eta = 0$ for dampers
Ω	$\omega_b + \omega_j$
$\omega_{b,j}$	angular velocity of bearing and journal respectively
λ_j	L/d_j
$\cdot$	denotes differentiation with respect to time τ

INTRODUCTION

Because of their compact size and wide range of damping capabiity, squeeze film dampers are frequently used for stabilisation and vibration attenuation of rotating machinery. Oil feed is generally via a central circumferential groove, effectively splitting the damper width L into two dampers, each with axial land length of L/2. However, such a design effectively reduces the damping capability of the damper by a factor of four. To recover this lost damping capability, one can dispense entirely with the circumferential groove feed and introduce all the lubricant from either of the bearing ends. Such a concept requires an axial seal to ensure that the lubricant does not bypass the damper clearance space. A practically more reliable alternative is to introduce the lubricant via one or more (usually two or four) oil holes in the central axial plane of the damper, i.e. replacing the circumferential groove with a number of oil holes. While this arrangement ensures that all the lubricant passes through the damper clearance, the unbalance response analysis for even the simplest case of a squeeze film damped centrally preloaded horizontal rigid rotor or a squeeze film damped vertical rotor has become significantly more complicated. Whereas with the end feed dampers, one can assume circular orbit response in the steady state, such is no longer the

case with oil hole feed dampers where the steady state response generally needs to be obtained by a transient solution. Transient analyses rely heavily on approximations such as the short bearing approximation or compilation of appropriate tabular data, to be computationally feasible, the latter approach being warranted at relatively high aspect ratios (L/D > 0.25) and eccentricity ratios (ε > 0.7) (Hahn, 1989). Such a tabular approach is expected to be necessary with oil hole feed, so the major emphasis of this paper centres on how to obtain satisfactory tabular data and thereby overcome the added complication due to the introduction of oil hole feed.

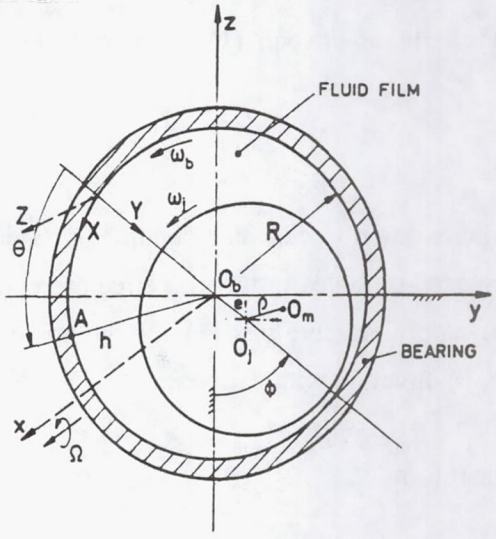

Figure 1: Simple circular bore hydrodynamic bearing or squeeze film damper.

SOLUTION STRATEGY

Figure 1 depicts a simple circular bore hydrodynamic journal bearing or squeeze film damper if the journal does not rotate (i.e. if $\omega_j = 0$). Figure 2 shows the journal oil feed pressure boundary conditions which now, in addition to specified inlet and outlet pressures p_i and p_o, allow for n oil feed holes at the centre plane of the bearing (i.e. along Z = 0). For the usual assumptions of laminar flow, Newtonian fluid, constant fluid properties, negligible inertia force, body force and curvature effects, no slip at bearing surfaces, no axial variation in film thickness, constant pressure across the film and validity of order of magnitude considerations, one can derive the Reynolds equation as (Pinkus and Sternlicht, 1961):

$$\frac{\partial}{\partial X}\left(h^3\frac{\partial p}{\partial X}\right)+h^3\frac{\partial p}{\partial Z^2}=-6\mu U\frac{\partial h}{\partial X}+12\mu V \quad , \tag{1}$$

where $h = (C + \varepsilon\cos\theta)$. (2)

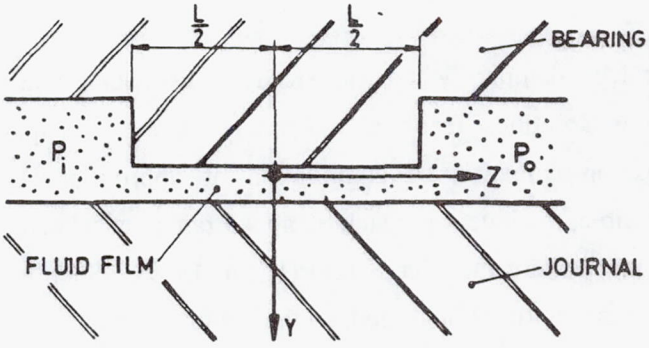

Figure 2: Bearing or damper with end feed and end drain pressure boundary conditions.

The boundary conditions pertaining to eqn. (1), as shown in Figure 2, are:

$$\begin{aligned} p &= p_i \text{ at } Z = -L/2 \\ p &= p_o \text{ at } Z = L/2 \quad . \end{aligned} \tag{3}$$

These boundary conditions describe end feed conditions. Additionally, there are now n circumferentially equispaced oil holes in the mid circumferential plane at Z = 0, supplied from an oil chamber at supply pressure p_S. Finally, the pressure distribution is periodic in the circumferential (i.e. θ) direction with period 2π.

Then, in non-dimensional form

$$\frac{L^2}{R^2}\frac{\partial}{\partial\theta}\left(H^3\frac{\partial P}{\partial\theta}\right)+H^3\frac{\partial^2 P}{\partial\bar{Z}^2}=\varepsilon\left(\dot{\phi}-\frac{\eta}{2}\right)\sin\theta+\dot{\varepsilon}\cos\theta \quad , \tag{4}$$

where $$H = (1 + \varepsilon\cos\theta) \quad . \tag{5}$$

Ignoring for the time being the problem of cavitation, the solution of eqn. (3) may be written as

$$P=\varepsilon\left(\dot{\phi}-\frac{\eta}{2}\right)P_s+\dot{\varepsilon}\,P_c+\left(\frac{P_o-P_i}{2}\right)\bar{Z}+\left(\frac{P_o+P_i}{2}\right)+\Delta_1P_1+\Delta_2P_2+\ldots.\Delta_nP_n \tag{6}$$

$$= P^*+\Delta_1P_1+\Delta_2P_2+\ldots.\Delta_nP_n \tag{7}$$

where P_S and P_C are the solutions of

$$\frac{L^2}{R^2}\frac{\partial}{\partial\theta}\left(H^3\frac{\partial P_s}{\partial\theta}\right)+H^3\frac{\partial^2 P_s}{\partial\bar{Z}^2}=\sin\theta \tag{8}$$

and

$$\frac{L^2}{R^2}\frac{\partial}{\partial\theta}\left(H^3\frac{\partial P_c}{\partial\theta}\right)+H^3\frac{\partial P_c}{\partial\bar{Z}^2}=\cos\theta \tag{9}$$

respectively, with boundary conditions $P_s = P_c = 0$ at $\bar{Z} = \pm 1/2$, (10)

and $$P_s(\theta) = P_s(\theta + 2\pi); P_c(\theta) = P_c(\theta + 2\pi);$$ (11)

and where $P_j (j = 1,2....n)$ are given by the solutions of:

$$\frac{L^2}{R^2}\frac{\partial}{\partial\theta}\left(H^3\frac{\partial P_j}{\partial\theta^2}\right) + H^3\frac{\partial^2 P_j}{\partial\bar{Z}^2} = 0,$$ (12)

with boundary conditions: $P_j = 0$ at $\bar{Z} = \pm 1/2$, (13)

and $$P_j = 1 \text{ at } \bar{Z} = 0, \theta = \theta_j.$$ (14)

In eqns. (6) and (7), the Δ_j's are time dependent multipliers so that at any instant of time, at $\bar{Z} = 0$ and $\theta = \theta_j$

$$\Delta_1 P_1 + \Delta_2 P_2 ..... + \Delta_n P_n = P - P^* = P_{oj} - P^*$$ (15)

Strictly speaking, this formulation implies that the pressure will be P_{oj} at the centre of the oil hole but may be somewhat different from this elsewhere; whereas in fact the pressure should equal P_{oj} everywhere within the oil hole region. The error due to this assumption will increase as the hole diameter d_j increases but owing to the near parabolic axial profiles of P_S and P_C, is expected to have insignificant effect for $\lambda \leq 6$.

If there is flow restriction between the supply pressure P_{SS} and the pressure at the hole at $\theta = \theta_j$, e.g. a capillary or orifice, one needs in general to balance the flow through the restrictor to the flow out of the oil hole. To cater for such an eventuality, an iteration is introduced whereby the hole pressures P_{oj} are guessed and subsequently modified until there is flow balance. Eqn. set (15) then constitutes a set of n simultaneous linear equations in the n unknowns $\Delta_1, ... \Delta_n$. If the restrictors offer sufficiently small resistance to the flows, the pressure drop across them will be negligible, whereupon all $P_{oj} = P_{SS}$ and the need for iteration is avoided. In any case, eqn. (6) gives, for this instant of time, the full pressure distribution around the damper. Such an approach allows for fluid to be pumped out as well as sucked in at the holes. Such pump out would in practice be avoided by using a check valve. In such a case, whereas the pressure can never fall below P_{SS} at any oil hole, any respective hole can be ignored once P^* exceeds P_{SS}, thereby reducing the number of 'effective' oil holes n.

The major computational problem involves obtaining the pressure distributions P_s, P_c and P_j at each instant of time. It is computationally prohibitive to solve numerically the partial differential equations (8), (9) and (12) at each instant of time, so a data tabulation/interpolation strategy is adopted. As may be seen from eqns. (8) – (11), P_s and P_c are, for a given aspect ratio L/R, functions of $\theta, \bar{Z}$ and ε. Three dimensional arrays for P_s and P_c with sufficient elements to allow accurate interpolation are both impractical and unnecessary for, as shown in Rezvani and Hahn (1992), by assuming a parabolic shape for the P_s and P_c in the axial direction, two dimensional arrays which are functions of θ and ε only will suffice with adequate accuracy for aspect ratios as high as L/D = 1, and eccentricity ratios as high as $\varepsilon = 0.9$, or even higher.

The same cannot, unfortunately, be said for any of the P_j pressure distributions, since they are a function of the j'th oil hole location θ_j with respect to the line of centres, which

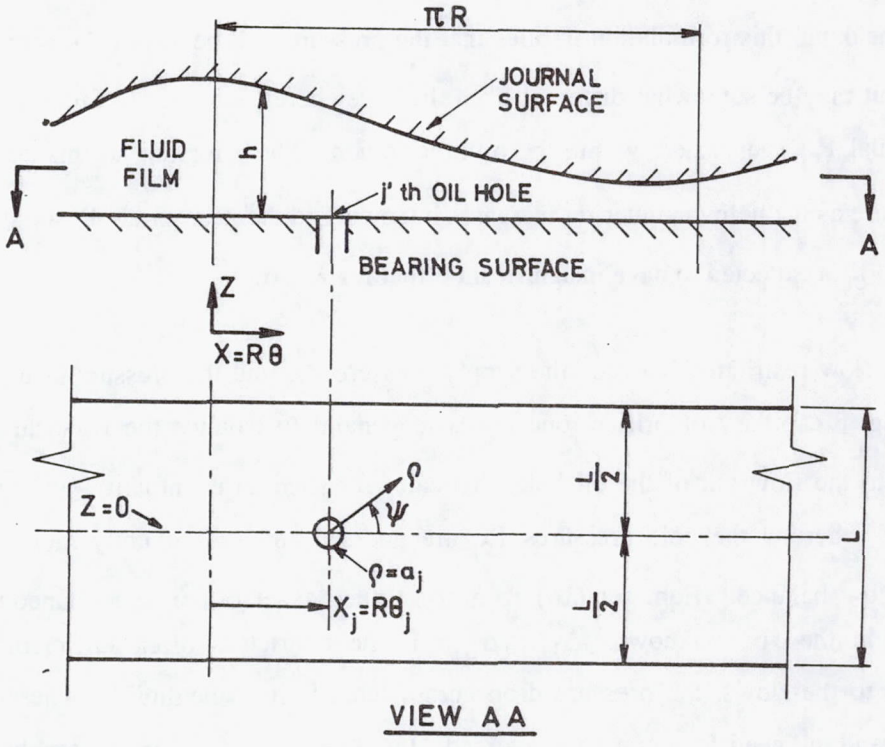

Figure 3: Laid out journal bearing or damper with oil hole at $\theta = \theta_j$.

location changes with time. Figure 3 depicts the laid out journal bearing or damper with the instantaneous location of the oil hole at θ_j. Attention can be restricted to the solution for P_j for a single oil hole, since the value of θ_j is arbitrary and can therefore apply to any of the

oil holes. Thus a sufficient number of P_j distributions need to be stored, to enable P_j to be found with sufficient accuracy at any time by interpolation. Additionally, the P_j are also functions of $\theta, \bar{Z}$ and ε suggesting the need for four dimensional arrays. Nor can they be found by approximate or numerical solution as easily as the P_S and P_C, owing to the finite size of the oil holes, and indeed the size of the axial width of the bearing land relative to the hole diameter λ_j is a parameter which is likely to have a significant effect. For finite sized oil holes, numerical solution of eqn. (12) using finite differences is awkward, owing to the mix of curved and straight boundaries. Thus, Marmol and Vance (1978) assume the oil holes to be smaller than the finite difference mesh. Not that a finite difference solution would solve the tabulation problem since at any instant of time, the P_j's would be functions not only of $\theta, \bar{Z}$ and ε but also of θ_j. Nor has a satisfactory approximate solution approach been found. Rather, a cosine power series solution approach, described below, has been found to be satisfactory and promises to provide manageable tabulation data.

Once all the pressure distribution components have been found, the full pressure distribution P can be found from eqn. (6). Cavitation can then be approximated by setting $P = 0$ when $P < 0$, a commonly adopted assumption in transient analysis, as the insistence of zero pressure gradient at the cavitation boundary would unduly prolong the time required to evaluate the pressure distribution, and hence, the fluid film forces, whereas the resulting gain in accuracy is expected to be minimal.

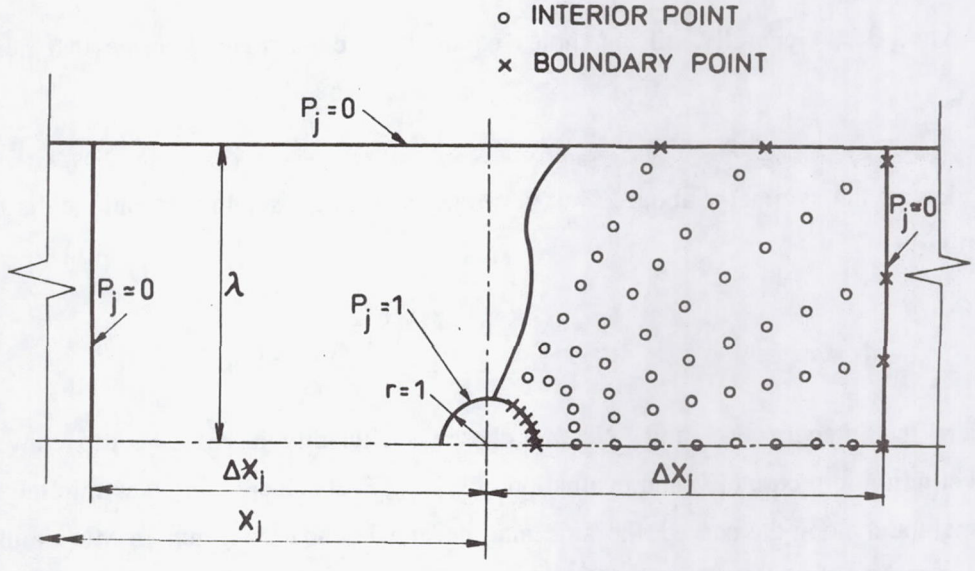

Figure 4: Solution domain for P_j $(M = 10, N = 16)$.

COSINE POWER SERIES SOLUTION FOR P_j

Required is the solution of

$$\frac{\partial}{\partial X}\left(H^3\frac{\partial P_j}{\partial X}\right)+\frac{\partial}{\partial Z}\left(H^3\frac{\partial P_j}{\partial Z}\right)=\nabla\cdot H^3\nabla P_j=0 \qquad (16)$$

over the domain in Figure 4, where $P_j=0$ at $Z=\pm L/2, P_j=1$ around the circumference of a circle of radius a_j centred at $Z=0,\theta=\theta_j$.

The circular boundary formed by the oil hole, suggests the reformulation of eqn. (16) in terms of polar coordinates (r, ψ). With origin of these coordinates at the centre of the oil hole, eqn. (16) may be written as:

$$\frac{\partial^2 P_j}{\partial r^2}+\frac{1}{r}\frac{\partial P_j}{\partial r}+\frac{1}{r^2}\frac{\partial^2 P_j}{\partial \psi^2}+3\left(\frac{\partial P_j}{\partial r}\frac{\partial \ell nH}{\partial r}+\frac{1}{r^2}\frac{\partial P_j}{\partial \psi}\frac{\partial \ell nH}{\partial \psi}\right)=0 \qquad (17)$$

where $$H=1+\varepsilon\cos\theta=1+\varepsilon\cos\chi_j \qquad (18)$$

and where $$\chi_j=\theta_j+\frac{a_j r}{R}\cos\psi=\theta_j+\frac{rL}{\lambda_j D}\cos\psi \qquad (19)$$

Thus, χ_j is a function of $r,\psi,\lambda_j,L/D$ and θ_j.

Hence, for a given bearing with given L/D and λ_j, the P_j at any instant of time will depend on ε and θ_j. Generally, all n holes would have equal diameters, so that henceforth $\lambda_j=\lambda$.

In view of the symmetry about Z = 0, a cosine power series solution approach is adopted. Letting

$$P_j=\sum_{i=1}^{M}\sum_{j=1}^{N}\alpha_{ij}\,r^{i-1}\cos(j-1)\psi \qquad (20)$$

where the integers M and N are chosen sufficiently large to assure convergence. Substitution into eqn. (17) and evaluation of eqn. (17) at selected points within the solution domain and along the curved, the 'side' and the 'end' boundaries results in MN simultaneous equations, for the MN unknowns α_{ij}.

RESULTS AND DISCUSSION

The points selected were along rays as shown in Fig. 4. Each ray was subdivided into 9 equal segments between the oil hole and an outer boundary, so that M = 10 in Eqn. (20). In this regard, since the precise boundaries to the left and right are unspecified and may be assumed to extend indefinitely, the solution is restricted to finite distances $\pm\Delta X_j$ on either side of X_j with the value of P_j set to 0 at these boundaries. To ensure that the solution was virtually asymptotic at $\pm\Delta X_j, \Delta X_j$ is increased until no readily discernible difference occurred in the respective solutions.

Using 16 such equispaced 'rays', so that N = 16 in eqn. (20), resulted in 160 linear simultaneous equations for the 160 values of α_{ij}. This was to give sufficient accuracy for the parameter combinations tested. Also, definition of the side boundaries by selecting a ΔX_j of four hole diameters was generally found to be adequate for $\lambda = 6$. Since eqn. (16) is simply Laplace's equation if H is constant, the accuracy of this solution procedure (for constant H) was able to be tested against an existing single series solution procedure described in the literature (Takeuti and Sekiya, 1968), and was found to be in agreement.

To illustrate the variation of the P_j with ε and θ_j, Figs. 5 to 10 give the solutions for $\varepsilon = 0.5$ and 0.9, with $\theta_j = 0°, 90°$ and $180°$ for a bearing with L/D = 0.5 and $\lambda = 6$. As expected, for $\theta_j = 0°$ and $180°$, (Figs. 5, 7, 8 and 10) the solution is symmetrical about the vertical centreline, but the pressure contours are skewed for the other θ_j. Maximum skewness would occur around $\theta_j = 90°$, and for $\varepsilon = 0.9$ (Fig. 9) one would probably need to further increase M, N and the ΔX_j to improve the accuracy of the small values of P_j.

Since θ_j is solution dependent, data for a sufficient number of discrete θ_j values will need to be provided to allow for interpolation in a transient programme. A comparison of Figs. 5 and 8, 6 and 9, and 7 and 10 illustrates the variability of the solutions with ε. Again, since ε is solution dependent, data for a sufficient number of discrete ε values will need to be provided to allow for interpolation. However, rather than store the P_j pressure distributions for a range of values of ε and θ_j, it will be sufficient to store the α_{ij} coefficients, thereby

significantly reducing data storage requirements, e.g. data for 10 discrete values of θ_j and 20 discrete values of ε would appear feasible.

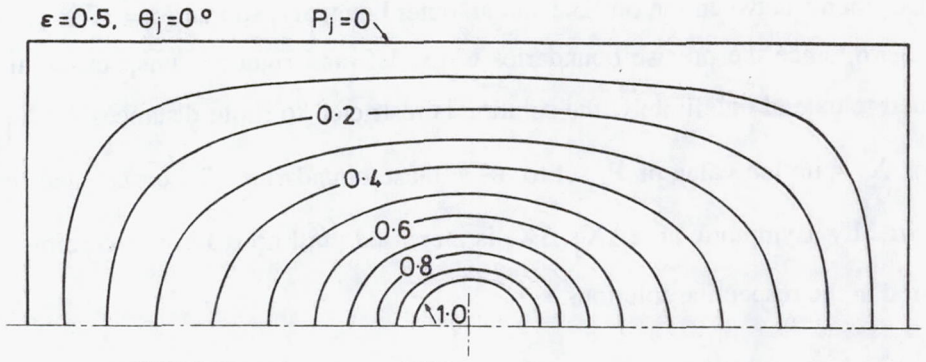

Figure 5: Solution for P_j for $\lambda = 6, \varepsilon = 0.5, \theta_j = 0°$.

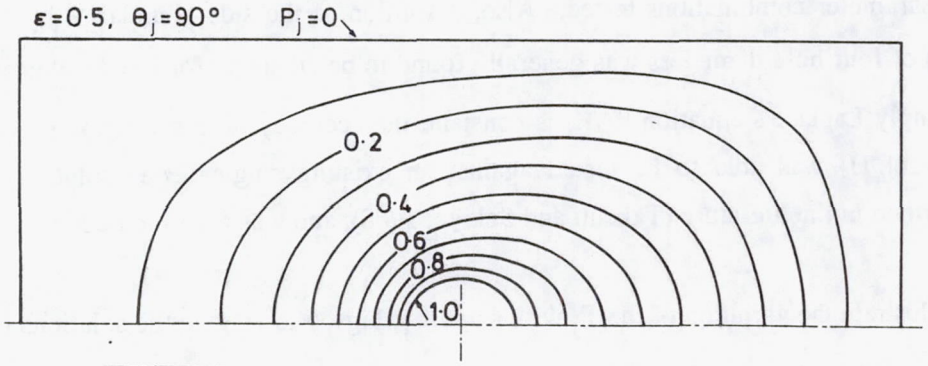

Figure 6: Solution for P_j for $\lambda = 6, \varepsilon = 0.5, \theta_j = 90°$.

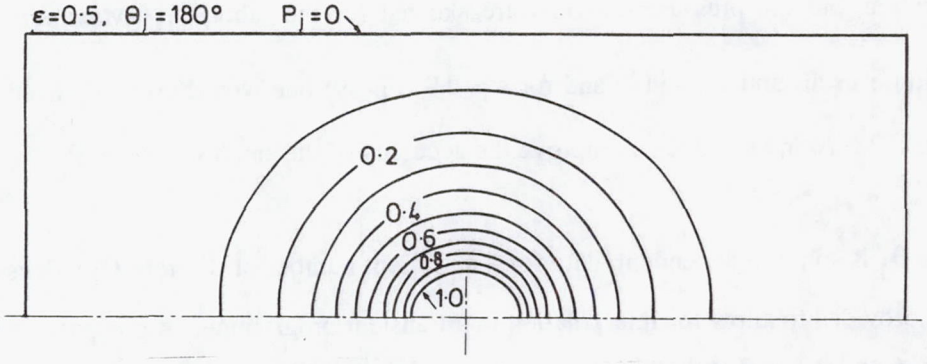

Figure 7: Solution for P_j for $\lambda = 6, \varepsilon = 0.5, \theta_j = 180°$.

Similar results were obtained for larger and smaller oil hole diameters (i.e. larger and smaller values of λ). Since the pressure drops relatively rapidly, interaction between the P_j

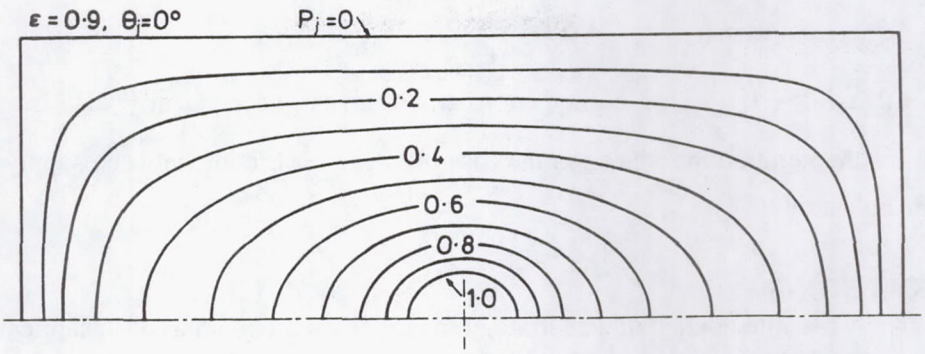

Figure 8: Solution for P_j for $\lambda = 6, \varepsilon = 0.9, \theta_j = 0°$.

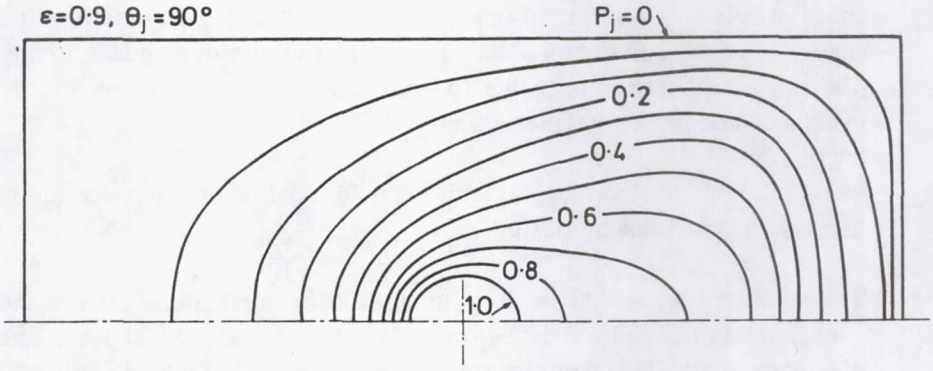

Figure 9: Solution for P_j for $\lambda = 6, \varepsilon = 0.9, \theta_j = 90°$.

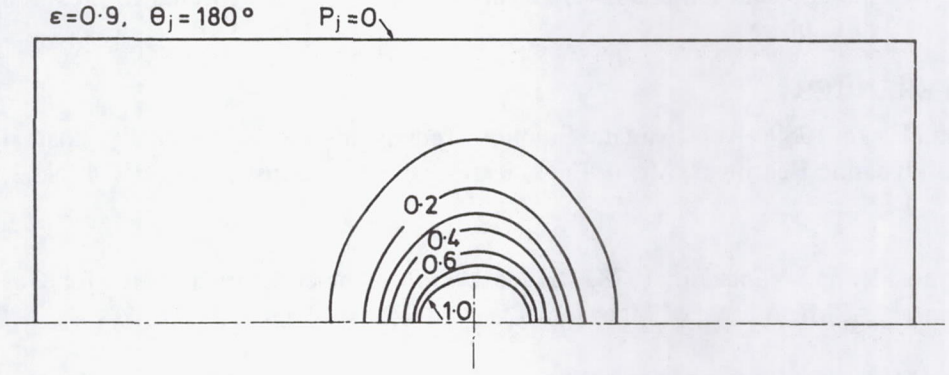

Figure 10: Solution for P_j for $\lambda = 6, \varepsilon = 0.9, \theta_j = 180°$.

pressure contributions from other oil holes is negligible until the number of oil holes is so large that neighbouring centres are within 5 oil hole diameters of each other, (e.g. for $\lambda = 6$ and L/D = 0.5, such interaction could be neglected provided there were fewer then about 8 oil holes). Hence, in most practical situations, it is expected that such interaction is negligible, so that eqn. (15) simplifies to:

$$\Delta_j P_j = P - P^* = P_{ss} \qquad (21)$$

at $\bar{Z} = 0$ and $\theta = \theta_j$. This ability to treat oil holes independently also considerably simplifies the iteration introduced in the case of a flow restriction between supply reservoir and the hole exit.

CONCLUSIONS

(a) A feasible computational strategy for the transient solution of dynamically loaded bearings or dampers with oil hole feed has been outlined, relying on interpolation from previously computed data.

(b) The procedure allows for any number of oil holes, allows for the provision of check valves to avoid pump out and allows for oil flow restriction between the supply reservoir and the oil hole, albeit at the expense of an added iteration.

(c) The pressure contributions due to the oil holes may be conveniently obtained using a cosine power series solution.

(d) Such solutions are eccentricity and oil hole location (relative to line of centres) dependent at any instant of time.

(e) The solutions prove that there is no significant interaction between the pressure contributions of adjacent holes, provided they are spaced at least four oil hole diameters apart. This would pertain in most if not all practical applications.

(f) The solution procedure is here restricted to the oil holes being located in the central circumferential plane. For off-centred oil holes, the series would need to include sine terms as well. This extension is not expected to create any undue difficulties.

REFERENCES

Hahn, E. J., 1989, Approximate Solution Techniques for Dynamically Loaded Narrow Hydrodynamic Bearings", Mech. Engg. Transactions, I.E.Aust., Vol. ME14, No.3, pp.134-140.

Marmol, R. and Vance, J., 1978, "Squeeze Film Damper Characteristics for Gas Turbine Engines", ASME Journal of Mechanical Design, Vol. 100, pp.139-146.

Pinkus, O. and Sternlicht, B., 1961, "Theory of Hydrodynamic Lubrication", McGraw Hill, N.Y.

Rezvani, M. and Hahn, E. J., 1992, "Limitations of the Short Bearing Approximation in Dynamically Loaded Narrow Hydrodynamic Bearings". Presented at 1992 ASME/STLE Tribology Conference. To be published in ASME Journal of Tribology, ≈ 7pp.

Takeuti, Y. and Sekiya, T., 1968, "Thermal Stresses in a Polygonal Cylinder with a Circular Hole Under Internal Heat Generation", Zeits. fur Angew. Mech. Math., Bd.48, Ht.4, pp237-246.

HOTFIRE TESTING OF A SSME HPOTP WITH AN ANNULAR HYDROSTATIC BEARING

Steven A. Nolan and Robert I. Hibbs
Rockwell International
Rocketdyne Division
Canoga Park, California

and

Gary G. Genge
NASA George C. Marshall Space Flight Center
Marshall Space Flight Center, Alabama

Abstract

A new fluid film bearing package has been tested in the Space Shuttle Main Engine (SSME) High Pressure Oxygen Turbopump (HPOTP). This fluid film element functions as both the pump end bearing and the preburner pump rear wear ring seal. Most importantly, it replaces a duplex ball bearing package which has been the primary life limiting component in the turbopump. The design and predicted performance of the turbopump are reviewed. Results are presented for measured pump and bearing performance during testing on the NASA Technology Test Bed (TTB) Engine located at Marshall Space Flight Center, Alabama. The most significant results were obtained from proximity probes located in the bearing bore which revealed large subsynchronous precession at ten percent of shaft speed during engine start which subsided prior to mainstage power levels and reappeared during engine shutdown at equivalent power levels below 65% of nominal. This phenomenon has been attributed to rotating stall in the diffuser. The proximity probes also revealed the location of the bearing in the bore for different operating speeds. Pump vibration characteristics were improved as compared to pumps tested with ball bearings. After seven starts and more than 700 seconds of testing, the pump showed no signs of performance degradation.

Introduction

Annular seals were developed and used as leakage control devices and in that capacity were designed for optimum pump efficiency. Lomakin[1] pointed out that annular seals develop significant direct stiffness while in the centered, zero-eccentricity position and can influence the rotordynamics of a pump. Later, Black[2], Jenssen[3], and Black and Jenssen[4,5] investigated and explained the influence of seal forces on the rotordynamic behavior of pumps.

The term damper seal was conceived to describe an annular seal which has been intentionally roughened. This definition grew out of the work by von Pragenau[6] who analytically predicted that roughness in an annular seal would increase damping and reduce leakage. This was subsequently supported by the test data and analysis of Childs and Kim[7,8,9], Childs and Garcia[10], and Kim and Childs[11]. Childs tested many different roughness patterns including hole, post, sawtooth, knurl, helically grooved, and circumferentially grooved. The test results showed that rough seals

produced more damping than smooth seals and that the hole pattern seal could be optimized for maximum damping.

The first intentional implementation of damping seal technology was in the SSME Phase II HPOTP shown in Figure 1. Wear ring labyrinth seals on the Phase I preburner pump impeller were replaced with damping seals. The knurl pattern and process were developed at Rocketdyne specifically for this purpose and were subsequently tested by Childs and Kim[7]. Significant reductions in pump dynamic loads and improvement in rotor stability resulted.

During SSME testing, ball bearing wear has been a recurring life limiting issue. Primarily, the wear of the pump end bearings has limited the life of the turbopump and has necessitated periodic refurbishment. Recently, there have been several events during the testing of the SSME HPOTP which resulted in reduced ball bearing stiffness indicating that the turbopump could operate safely on the damping seal alone. A subsequent review of component measurement and test data from previous testing showed that the turbopump had operated safely on the damping seal alone a minimum of six different times without significant degradation in performance. Based on this evidence, redesign of the turbopump without pump end ball bearings seemed feasible.

The design concept chosen is illustrated in Figure 2 (Scharrer et al.[12]). The figure shows that the pump end bearings could be eliminated in favor of a single damping seal located at approximately the same axial plane. Since the damping seal will now be the primary load carrying element, it has been renamed an annular hydrostatic bearing. This paper presents the predicted and experimentally measured performance of the bearing design. In addition, the rotordynamic and hydrodynamic performance of the hydrostatic bearing supported turbopump will be compared with that of the current ball bearing supported pump.

Requirements

The bearing design required substantial parametric evaluation before arriving at the current fully tapered, fully roughened annular hydrostatic bearing design. Parametric studies of geometry and configuration were considered to optimize the design in order to meet the hydrodynamic and rotordynamic requirements of the pump end bearing for the SSME HPOTP. Details of the design considerations are presented in Scharrrer et al.[12]. The final design is similar to the current Phase II SSME HPOTP preburner pump damping seal and its well documented performance in flight configuration SSME pumps.

The design objective was to increase the rotordynamic critical speed and stability margins as shown in Figure 3 as well as address the remaining turbine end bearings loads. It was also of particular interest to ensure the implementation of the pump end hydrostatic bearing did not result in detrimental loads on the remaining rolling element bearings. Based on these requirements the pump end bearing targets were 175 MN/m (1.0 E6 lbf/in) direct stiffness and 61.2 KN-s/m (350 lbf-s/in) direct damping. The geometry and clearance tolerances were optimized to meet this requirement. The rotordynamic coefficients of the bearing as a function of shaft speed and eccentricity were provided for the rotordynamic analysis. The analyses included coefficients for minimum, nominal, and maximum conditions resulting from potential variability of tolerances and pump operating conditions. Stability of the bearing was consistently good throughout the speed parametric as evidenced by the whirl frequency ratio (WFR) being constant at 0.30. The WFR is a ratio of the destabilizing forces, cross-coupled stiffness, over the stabilizing forces, damping times synchronous speed.

The impact of the pump end hydrostatic bearing on the turbine end ball bearing loads was evaluated with transient non-linear rotordynamic analyses performed over the entire pump operating speed range. The results of these analyses for the nominal predicted hydrostatic bearing coefficients are shown in Figure 4. It is evident from this data that the dynamic loads are significantly reduced for pump speeds above 27,000 RPM, which is the primary operating range of this pump. These reductions in alternating loads are a result of the increased critical speed margins on the second mode as well as the additional damping derived from the optimized bearing configuration. Alternating load reductions in excess of 30% are predicted for FPL operation, 30,000 RPM, and nominal hydrostatic bearing coefficients.

An additional important consideration was the start transient and the potential for substantial wear. Several configurations were considered which attempted to provide for both hydrodynamic performance during the start transient and hydrostatic performance at Full Power Level (FPL). The configurations considered were straight, tapered, partially tapered, rough, and partially rough. Although the configurations studied, as discussed in Scharrer et al.[12], did show some slight advantages to having a partially roughened or partially tapered configuration, the benefits were not substantial enough to justify the added complexity and cost.

In addition to the load impact issue, the transient analysis was utilized to predict rotor deflections for all pump operating conditions. The deflection at the hydrostatic bearing was identified as a control point for the design. Specifically, a 0.0254 mm (.001 in.) margin against rubbing, between the rotor and stator at the hydrostatic bearing location, was the guideline for all bearing design ranges. This guideline ensured adequate rub margins at all other axial locations along the rotor. The maximum deflection of the rotor, fixed and alternating deflections combined, was used to identify this margin as shown in the sample rotor orbit prediction of Figure 5.

TTB Test Facility

The Technology Test Bed (TTB) facility at the Marshall Space Flight Center (MSFC) was designated choice for testing the axially fed hydrostatic bearing. The facility was developed to serve as an accessible platform with capability for testing new technology in large liquid rocket engines. The test stand, formally used for the first stage of the Saturn V, was reactivated in 1988 as a SSME facility. With run tank capacities of 89,000 liters (23,500 gallons) of liquid oxygen (LOX) and 284,000 liters (75,000 gallons) of liquid hydrogen, the TTB facility can operate an SSME over 200 seconds per test depending on the desired thrust profile. TTB can operate the SSME from the engine's upper limit of 111% of rated power level (RPL) to 80% of RPL while independently controlling the engine LOX and fuel inlet pressures. The facility can vary the LOX and fuel engine inlet net positive suction pressures (NPSP) over the acceptable range for the SSME. The facility actually operates from 137.9 to 1,034.2 KPa (20 to 150 psi) ullage pressure for LOX and 55.2 to 344.7 Kpa (8 to 50 psi) ullage pressure for fuel. Because of its technology advancement role, the data collection system has 750 digital channels, 50 samples per second, and 216 analog channels to measure pressure, temperature, vibrations, speed, proximity, and more.

Pump/Engine Instrumentation

The SSME HPOTP is equipped with pump and turbine end radial accelerometers as well as external strain gages which are typically used for high frequency data evaluation. The pump tested at TTB had five accelerometers on both the pump end and turbine flanges as well as four strain gages on the pump housing between the pump and turbine. The housing strain gages which are typically used for bearing generated frequency detection on Phase II HPOTPs were included on

the hydrostatic configuration as an additional redundant point of comparison. In addition to the standard instrumentation, the hydrostatic bearing HPOTP contained seven internal strain gages. These gages are located near bearing support locations and intended for qualitative comparison to existing Phase II pump data.

Proximity probes were installed in the bearing in order to provide data for the determination of bearing liftoff/touchdown, rotor position in the bore, rotor orbit size the overall health of the bearing. For this particular pump build, Kaman proximity probes were chosen. Two pressure and temperature measurement taps were included directly upstream of the bearing inlet and downstream of the bearing exit to asses the bearings performance. Additionally, two pressure sensors were located in the cavity downstream of the bearing to anchor overall pump performance.

Test Plan

Health monitoring of the entire turbopump was a major issue when the turbopump was tested at TTB. Not only was the operational rubbing of the hydrostatic bearing a concern, but since the rotor response was changed the turbine end bearing life was an issue. Therefore all available means were taken to ensure that both the hydrostatic pump end bearing and the turbine end duplex ball bearings were not degrading. In addition to all of the standard SSME HPOTP post test inspections (rotor break/run torque, and visual inspection of turbine section, main pump inducer, number three bearing, and the preburner pump inlet) two additional measurements were included. The normal shaft travel measurement used on a test stand was replaced with a more precise measurement for measuring turbine bearing wear called shaft micro-travel described by Genge[13] and currently used for all flight HPOTPs. To ensure safety, the micro-travel acceptance limit was set at the current flight limit. The second post test measurement added was a radial "micro-wiggle" test which determined the amount of wear in the hydrostatic bearing. The wear guideline imposed on this measurement was set as the maximum wear found on the test article which had been exposed to 60 start/stop cycles in a test rig simulator reported by Scharrer et al.[14]

Acceptance criteria also was set on all data obtained during the hot fire testing which directly related to the operation of either the hydrostatic bearing or the turbine end ball bearings. This included a requirement that the proximity probes show that the rotor lifts off the hydrostatic bearing surface prior to 1.51 seconds into the test, and that they show the rotor maintains a .0254 mm (.001 in.) radial clearance from the wall during operation. Limits were also placed on the minimum pressure drop across the hydrostatic bearing that would analytically show rotor stability, the temperature rise across the bearing that would indicate operational rubbing, and the pressures in the upstream or downstream cavities being greater than the structural analysis. The fluid exiting the hydrostatic bearing was also required to be a liquid, not two phase or gaseous. In addition, all of the standard SSME data limits were maintained for the testing of this turbopump. The TTB facility Optical Plume Anomaly Detector (OPAD) (Cooper et al.[15]) data was reviewed with a special emphasis on the presence of silver in the plume.

Initially, a four test series was planned which would characterize the performance of the hydrostatic bearing at all points in a test matrix containing four power levels and three LOX engine inlet NPSP values. During the test series, uncertainty with the proximity probes led to the addition of an additional test. The profiles and the test matrix which shows which test will evaluate that matrix condition are shown in Figures 6 through 11.

The primary objective of the first test was to demonstrate that the bearing had the capacity to lift off. However, due to thrust balance concerns with the HPOTP with tests between 1.5 seconds and

10 seconds, the test was planned for 10 seconds (Figure 6). With the complete 10 seconds, the immediate comparison of the predictions for 100% power level operations to results from the test also became an objective. The subsequent tests planned in the series were intended to asses the bearings capability at all power levels and engine inlet pressures available at TTB with bearing evaluation between each test.

Test two was intended to exercise all power levels without variations in inlet pressures to isolate any response due only to power level changes. With the confidence gained from the second test, the third test was meant to obtain as many of the combination of power level/LOX inlet pressure extremes as possible (Figure 8). From Figure 11, it can be seen that seven of the desired steady state conditions could be achieved. Once again, this test isolated all power level changes from LOX inlet pressure changes to allow the cause of any potential anomaly to be more easily understood. The fourth test profile was driven by four different factors. The main goals were to complete data collection for the test matrix and to start the pump with the lowest viscosity LOX allowed by the SSME Interface Control Document (or closest attainable by TTB). The low viscosity "hot LOX" would test the lift capability of the bearing in the worst possible fluid state that the bearing could undergo. Additionally a constant power level was maintained at the beginning of the test to evaluate proximity probe thermal characteristics. After completion of the fourth test, a fifth test was added to allow for the thermal stabilization of the proximity probes at all major power levels (Figure 10).

Test Run Summary

Testing began in March, 1992, with test TTB-029. In spite of a premature cut at 5.2 sec due to the High Pressure Fuel Turbopump (HPFTP) exceeding its turbine discharge temperature redline, examination of the test data showed the primary objective was achieved. Although the engine did not reach a steady state condition at 100% power level, rotor liftoff evaluation was possible. Additionally, this test did show an unexpected shaft orbit at low power levels which was determined to be caused by the rotating stall in the preburner pump impeller discussed later.

Because the primary objective had been achieved, it was decided to continue the series as originally planned. However the TTB-030 was also cut off prematurely only .32 seconds into the test. An engine oxidizer actuator position measurement showed that the valve was opening slower than is allowed during a normal start. Although the engine controller took action to correct the slow opening and was recovering, and the engine shut down as programmed.

With no objectives achieved in TTB-030, the next test profile was a repeat. The test went the full 85 second duration following the profile in Figure 7. All of the steady state data for the nominal engine inlet pressure were collected, and rotor stability was maintained throughout the 80% to 109% power level range. The next test followed the profile in Figure 8, and also went for its planned duration. This 205 second test acquired data at all but one of the remaining steady state operating points of interest. TTB-033 was initially meant to finish the series, but it was stopped prematurely due to a fire external to the engine not related to the pump. Post test inspections revealed a broken line had leaked hot gas. Repairs were performed, and TTB-034 ran the full 205 second duration as shown in Figure 9. This test successfully attained the 80% power level 827.4 KPa (120 psi) NPSP engine inlet condition, and warmer lox was used for the start transient without a change in performance. The final test in the series was performed in June, 1992. Unfortunately, the proximity probe output became highly erratic before the probes became thermally stable probe evaluation was not attained. This new design had performed well for a total of seven starts and 724.5 seconds.

Bearing Performance

Bearing performance data analysis of the hydrostatic bearing on the TTB consisted of a determination of the performance of the bearing which included a repeatability evaluation, centered coefficient calculation, and an estimate of the dynamic load on the bearing. The repeatability evaluation showed no appreciable difference in the pressures and temperatures across the bearing, or the speed for 80%, 100%, 104%, and 109% power levels. This lack of discrepancy in the operational characteristics led to the small band between the maximum and minimum rotordynamic coefficients across the bearing. Based on orbit plots, the dynamic load on the bearing was estimated to be between 490 to 2050 N (110 to 460 lbf) for the tests at power levels between 80% and 109%. Data show that the bearing operated without any anomaly and could withstand the load experienced at the bearing location. The hydrostatic bearing could be run indefinitely without any problems provided that the operational characteristics remain within the trends of the data that has been collected to date.

Data was collected to determine the repeatability in the operational characteristics of the hydrostatic bearing from test to test. If the bearing pressures and temperatures remain unchanged from test to test at different operating speeds, the bearing performance is judged to be essentially unchanged. Typical data from the upstream and downstream pressures and temperatures are summarized in Table I. The data reviewed indicate only the downstream pressure indicate appreciable variance from test to test. Downstream pressures were approximately 345 KPa (50 psi) lower during low NPSH testing. However, because this difference is only a fraction of the total pressure drop, the performance of the bearing was essentially unchanged. Resulting pressures were below the vapor pressure of liquid oxygen but in order to vaporize the fluid must be at that state longer than the fluid is in the bearing. The velocity of the fluid at that point is approximately 400 m/s (1300 ft/s) for about .025 m (0.1 in.) which is approximately 6 microseconds. Under these conditions,the fluid could be approximately 690 KPa (100 psi) below the vapor pressure without cavitation.

Since the bearing did not experience substantial deviation in its operational characteristics, the band between the maximum and minimum empirical rotordynamic coefficients of the bearing was small. Figures 12 contains the values for direct stiffness, cross-coupled stiffness, and the direct damping of the bearing during the testing. These coefficients, owing to the fact that the operating conditions were in the range of the design, compared well with the coefficients predicted during the design phase. Load capacity versus eccentricity of the bearing is depicted in Figure 13 at each of the power levels. The coefficients showed only small differences in the maximum and minimum values verify the robustness of the hydrodynamic and bearing design. Although error in the actual values of the coefficients could be as high as 50 %, the coefficients generally were predicted in such a manner to provide a conservative design.

Dynamic Data

The most significant dynamic data obtained from the hydrostatic bearing pump was provided by the proximity probes monitoring the rotor position at the hydrostatic bearing. No data observing actual rotor motion in the SSME HPOTP has previously been available. The major source of uncertainty relative to the proximity probe data was the probes calibration sensitivity to temperature changes. Due to the large thermal changes present when going from an ambient environment to a liquid oxygen environment absolute values of rotor position were difficult to determine. The most obvious indication of the probes temperature dependence is in the initial

"overshoot" seen in the proximity probe data,shown in Figure 14, after the pump reaches mainstage speed at approximately 4.2 sec. While some of the overshoot is due to pump thermal stabilization effects on the rotordynamic boundary conditions, a significant portion is due to the large temperature change experienced by the probe, approximately 40° R, during the start transient.

The proximity probe data obtained from this pump provided several interesting new insights into the operation of the SSME HPOTP, in addition to providing data that was directly comparable to the rotordynamic analytical predictions. The most readily identifiably phenomenon observed in the proximity probe data was a relatively low frequency large precession of the rotor during the start and cutoff transients. The precession is depicted in orbit plot of test TTB-029 in Figure 15 and clearly visible in the frequency domain data of Figure 16. Originally, this motion was thought to be synchronous shaft motion and that either the hydrostatic bearing stiffness was much less than predicted or the loads were much greater. However, further analysis showed that this motion actually occurs at 10% of synchronous speed during the start transient and did not track speed well during the shutdown transient. The precession started shortly after the initial pump rotations and dropped out at approximately 20,000 RPM. The amplitude remained relatively constant at a level between 0.12 and 0.14 mm (.005 and .006 in.) An investigation into possible excitation sources for this phenomena led to rotating stall in either the preburner or main pump.

The identification of rotor motion associated with the rotating stall was considered a significant revelation. This phenomena had been measured in the laboratory in water for both the main pump and preburner pump. However, the magnitude and duration of the resulting forces were never fully understood or appreciated. The pump speed for the measured stall limit for both the preburner and main pumps correspond to the speed at which the large motion ceased during start-up.

The discovery of this phenomenon in the rotor motion has been attributed to the fact that the proximity probe data was the first good data defining rotor orbit motion. As mentioned previously, the significance of the presence of the phenomenon in the hydrostatic bearing configuration led to a greater appreciation of its existence. Previous isolator strain gage data was only viewed from a bearing load standpoint with frequency content during the transient being difficult to observe. The characteristics associated with rotor motion during stall were quite consistent from test to test. A tabulation of several characteristics associated with the precession for all the tests are listed in Table II.

A comparison of data, obtained from Phase II pump isolator strain gage data and the hydrostatic bearing proximity probes, exhibiting this phenomenon is shown in Figures 17 and 18. Figure 17 is a comparison of the time history data during the start transient which clearly shows the same characteristics for both sets of data. Figure 18 contains an estimate of the dynamic loads calculated from both sets of data. The isolator strain gage loads were calculated with standard load reduction technique developed for these gages, while the hydrostatic bearing loads were estimated from the displacement and predicted bearing stiffness. It is evident that the loads are comparable and the deflections present are not unique to the hydrostatic bearing configuration.

Another interesting phenomenon discovered in the proximity probe data was that the rotor appeared to "center" itself in the bearing when the propellants filled the pump while the engine was being prepared for test. This occurred due to propellent pressure forces lifting the rotating assembly, which is almost vertical while attached to the engine, and bottoming the rotor on an axial stop which is perpendicular to the pump centerline resulting in the "straightening" the rotor assembly in the pump. The most attractive feature of this phenomenon was that although the shaft may not have been exactly "centered", it did not contact the journal when pump rotation began.

With no contact present there was no indication of liftoff during the start transient. This is significant since it indicates the rotor runs on a fluid film during the start transient and removes the opportunity for wear during engine start. Additionally, there appeared to be little indication of contact during the shutdown transient. No obvious indication of contact appears in the proximity probe data until at least 10 sec. after engine shutdown at which time the pump speed had dropped to very low levels. These rub characteristics appeared to be relatively benign in all tests. The time history data from a typical rub indication where the rotor deflections reach a limit or flat spot is shown in Figure 19. Indications of rub characteristics during the shutdown transients are tabulated in Table III.

While not as spectacular, the proximity probes also provided excellent data of rotor orbits and synchronous amplitudes during mainstage operation. Although, as previously mentioned, temperature dependant probe calibrations made it difficult to determine with great accuracy the absolute position of the rotor, the dynamic amplitudes, which are a much smaller portion of full scale, were more easily assessed for rotor orbit size. The significant conclusion with respect to this data is that the rotor orbits are very well behaved and comparable in magnitude for all mainstage power levels.

Synchronous RMS amplitude time histories from the proximity probe data over a test with significant power level and inlet conditions variations contain little variation in rotor orbit amplitude. An example of the RMS amplitude throughout a test which included operation at 80% RPL as well as 109% RPL with minimum inlet pressure, worst case conditions, is provided in Figure 20. The amplitudes presented in this example include the maximum and minimum values observed during all tests. Based on this data, the synchronous amplitudes of the rotating assembly were between 2.5 and 7 mV RMS, which corresponds to a peak to peak amplitude of between 0.005 and 0.015 mm (0.0002 and 0.0006 in.). Due to these small amplitudes, the potential error in the absolute value of the orbit size, due to calibration uncertainties, is believed to be less than .002 mm (0.0001 in.). Additionally, no significant harmonics of synchronous, other than those caused by blade wake forces as would be expected, were present in the data.

Although the absolute rotor position was difficult to discern due to probe calibration uncertainties, a fairly simple method was used in an attempt to anchor the rotor position with respect to the bearing bore. The alternative method used rotor orbits believed to be indicative of rub during shutdown as a means of locating the bearing bore and subsequently obtaining rotor positions relative to that point. It is believed that this method produced absolute rotor orbit positions representative of values for comparison to the analytical predictions. Using the data in this manner rotor orbit positions at various power level and vent conditions were predicted. A typical set of these results for test TTB-032 are shown in Figure 21.

The rotor positions and orbit amplitudes obtained from the proximity probe data compared favorably with orbit predictions from the rotordynamic analysis. To maintain the rub margins desired, the rotordynamic analyses predicted the fixed displacement at the hydrostatic bearing would be less than approximately 0.10 mm (0.004 in.) with peak to peak synchronous amplitudes in the range of approximately .025 mm (0.001 in.). Based on the results similar to those presented in Figure 21, the fixed displacements were between .051 and .10 mm (.002 and .004 in.) with the synchronous amplitudes somewhat less than 0.025 mm (.001 in.).

The data obtained from the standard external accelerometers and strain gages was evaluated on the same level as a typical Phase II HPOTP hotfire test for comparative purposes. The review consists of frequency domain data as well as time history data. All the data reviewed compared

favorably with a typical pump.The frequency domain data contained no significant anomalies or indications of detrimental conditions occurring during testing.Very slight indications of the low frequency precession phenomenon, which is atypical of external instrumentation, were present in the data. Harmonics of synchronous present in the data are comparable to those seen in the Phase II configuration.

The time history data for all instrumentation reviewed was nominal. Synchronous amplitudes were below 2 Grms on all accelerometers and below nominal Phase II pump values on a majority of the accelerometers. No significant amplitude changes were identified during power level excursions or inlet condition excursions. Additionally, composite RMS values and synchronous harmonic values were well within the Phase II database. A typical RMS amplitude time history of the synchronous amplitude from the accelerometer data is presented in Figure 22.

The turbine cartridge strain gages which,primarily intended for axial displacement measurements, were also reviewed for high frequency characteristics. Although low amplitude intermittent bearing cage harmonics were identified on these strain gages, this activity at a low amplitude is considered typical for this instrumentation which is so closely coupled with the bearing carrier, and is not considered to be detrimental. Additionally, the synchronous amplitudes were comparable to previously measured data from SSME pumps The significance of this data is the confirmation that the implementation of the hydrostatic bearing did not result in any detrimental conditions at the turbine end bearings. This is of interest because the turbine bearing package contained separate modifications which have been demonstrated in other development pumps to resolve turbine bearing wear issues occasionally present in Phase II HPOTPS.

Plume Spectroscopy Information

The Optical Plume Anomaly Detector (OPAD) showed no conclusive evidence of silver during any test in this series. However, the OPAD system had not been calibrated for silver by plume seeding, and the NASA SP-273 chemical equilibrium code did not contain a complete set of reactants data for silver. Therefore, the system was limited to using primarily statistical methods with comparison to data collected on TTB tests 20 through 28, which had standard HPOTP bearing configurations. Because of this difficulty and the micro-wiggle measurements minimal silver, if any, was believed to have been ingested by the main injector.

Conclusions

The implementation of the hydrostatic bearing met or exceeded the rotordynamic requirements set forth. The data indicated no significant wear occurred due to rubbing during the transients and the rotor displacements were well behaved during all operating conditions. No rotordynamic issues resulted during the testing to 109% rated power levels and minimum NPSH, and the test program provided new insight into the operation of the SSME HPOTP.

References

[1]Lomakin, A., "Calculation of Critical Speed and Securing of Dynamic Stability of the Rotor of Hydraulic High Pressure Machines with Reference to Forces Arising in the Seal Gaps," Energomashinostroenie, Vol. 4, No. 4, pp. 1-5, April 1958.

[2]Black, H.F., "Effects of Hydraulic Forces in Annular Pressure Seals on the Vibration of Centrifugal Pump Rotors," Journal of Mechanical Engineering Science, Vol. 11, No. 2, pp. 206-213,1969.

[3]Jensen, D.N., "Dynamics of Rotor Systems Embodying High Pressure Ring Seals," Phd.Dissertation, Heriot-Watt University, Edinburgh,Scotland, July 1970.

[4]Black, H.F. and Jenssen, D.N., "Dynamic Hybrid Properties of Annular Pressure Seals," Proc.Journal of Mechanical Engineering, Vol. 184, pp.92-100, 1970.

[5]Black, H.F. and Jenssen, D.N., "Effects of High Pressure Ring Seals on Pump Rotor Vibrations."ASME paper No. 71-WA/FE-38, 1971.

[6]von Pragenau, G., "Damping Seals for Turbomachinery,* NASA TP-1987, March 1982.

[7]Childs, D.W. and Kim, C.-H., "Analysis and Testing for Rotordynamic Coefficients of Turbulent Annular Seals with Directionally Homogeneous Surface-Roughness Treatment for Rotor and Stator Elements," Trans. ASME Journal of Tribology, Vol. 107, July 1985, pp. 296-306.

[8]Childs, D.W. and Kim, C.-H., "Testing for Rotordynamic Coefficients and Leakage: Circumferentially-Grooved Turbulent Annular Seals," proceeding of the IFToMM International Conference on Rotordynamics, Tokyo, Japan, Sept. 1986, pp. 609-618.

[9]Childs, D., and Kim, Chang-Ho, "Test Results for Round-Hole Pattern Damper Seals: Optimum Configurations and Dimensions for Maximum Net Damping, ASME Transactions, Journal of Tribology, Vol. 108, October 1986, pp. 605-611.

[10]Childs, D.W. and Garcia, F., "Test Results for Sawtooth Pattern Damper Seals: Leakage and Rotordynamic Coefficients," ASME Journal of Tribology, Vol. 109, January 1987, pp. 124-128.

[11]Kim, C-H, and Childs, D., "Analysis for Rotordynamic Coefficients of Helically-Grooved Turbulent Annular Seals," ASME Transaction Journal of Tribology, Vol. 109, January 1987, pp. 136-143.

[12]Scharrer, J.K., Hibbs, R.I., Nolan, S.A., and Nolan, S.A., "Extending the Life of the SSMe HPOTP Through the Use of Annular Hydrostatic Bearings", AIAA paper no. 92-3401, July 1992.

[13]Genge, Gary G., "Developing Acceptance Limits for Measured Bearing Wear of the Space Shuttle Main Engine High Pressure Oxidizer Turbopump". AIAA 91-2412, 27th Annual Joint Propulsion Conference, June 24 to 26, 1991.

[14]Scharrer, J.K., Tellier, J.G. and Hibbs, R.I., "Start Transient Testing of an Annular Hydrostatic Bearing in Liquid Oxygen". AIAA 92-3404, 28th Annual Join Propulsion Conference, July 6 to 8, 1992.

[15]Cooper, A.E., Powers, W.T., and Wallace,T.L. "OPAD Status Report: Investigation of SSME Component Erosion". SAE 921030, 1992 Society of Automotive Engineers Aerospace Atlantic Conference in Dayton, Ohio, April 7 to 10.

Table I: TTB Engine 4404 LOX Bearing Tests.

Power Level	Speed (rpm)	U/S Pr (psia)	D/S Pr (psia)	U/S Temp (R)	D/S Temp (R)
80	23,400	4150	210	199	212
100	27,700	5450	230	212	230
104	28,500	5700	250	216	233
109	29,700	6100	250	220	237

Table II: Precession Characteristics

	Start Dropout		Cutoff Resumption	
	Time	Speed	Time	Speed
Test	E/S+sec	RPM	C/O+sec	RPM
801-029	3.05	20,400	0.5	16,800
801-030	N/A			
801-031	3.1	21,500	0.4	16,500
801-032	3.1	21,000	0.25	17,500
801-033	3.1	21,000	0.5	18,000
801-034	3.05	21,500	0.3	16,800
801-035	2.952	20,500	0.5	18,000

Table III: Rub Indications

	Time of Rub	Speed @Rub
Test	C/O+sec	RPM
TTB-029	11.0	550
TTB-030	None Obvious	
TTB-031	10.7	750
TTB-032	15.2	700
TTB-033	15.0	650
TTB-034	None Obvious	
TTB-035	14.0	700

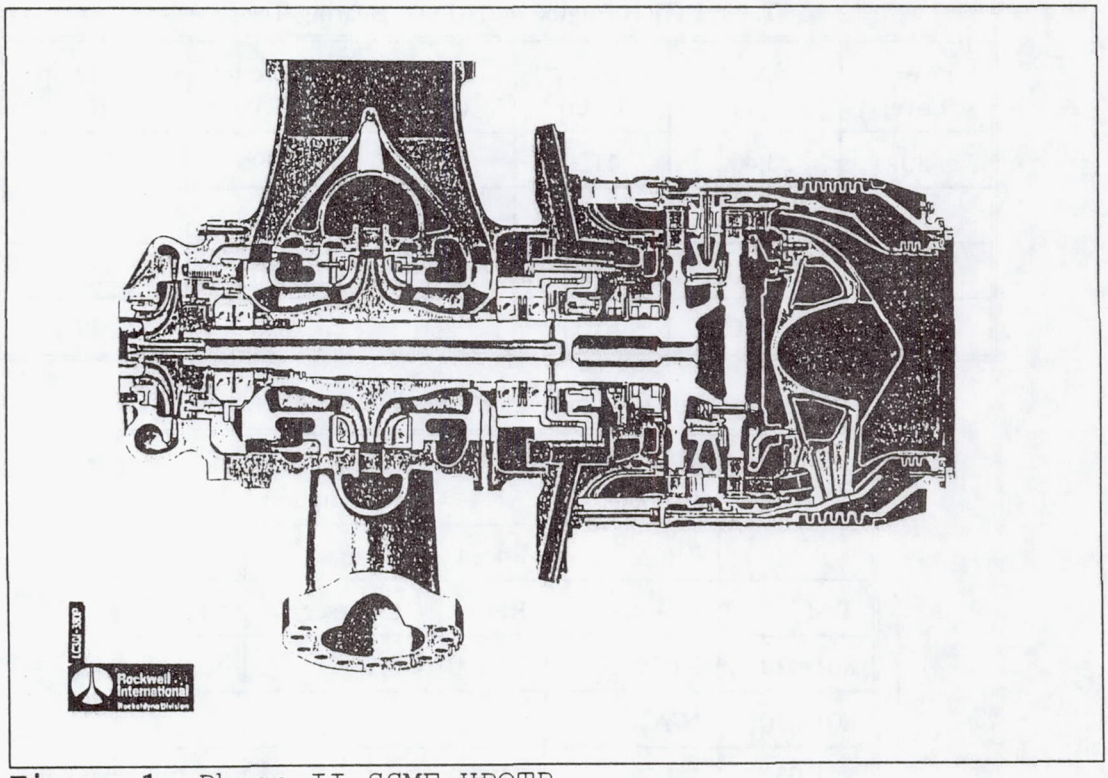

Figure 1. Phase II SSME HPOTP.

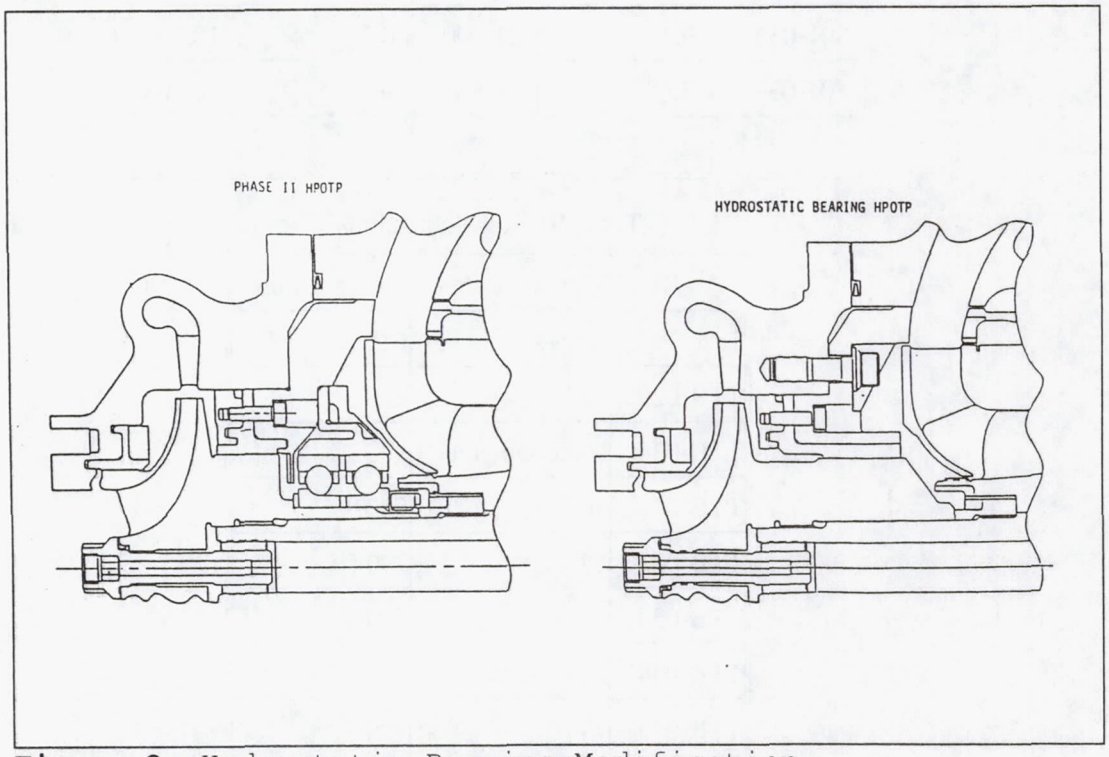

Figure 2. Hydrostatic Bearing Modification.

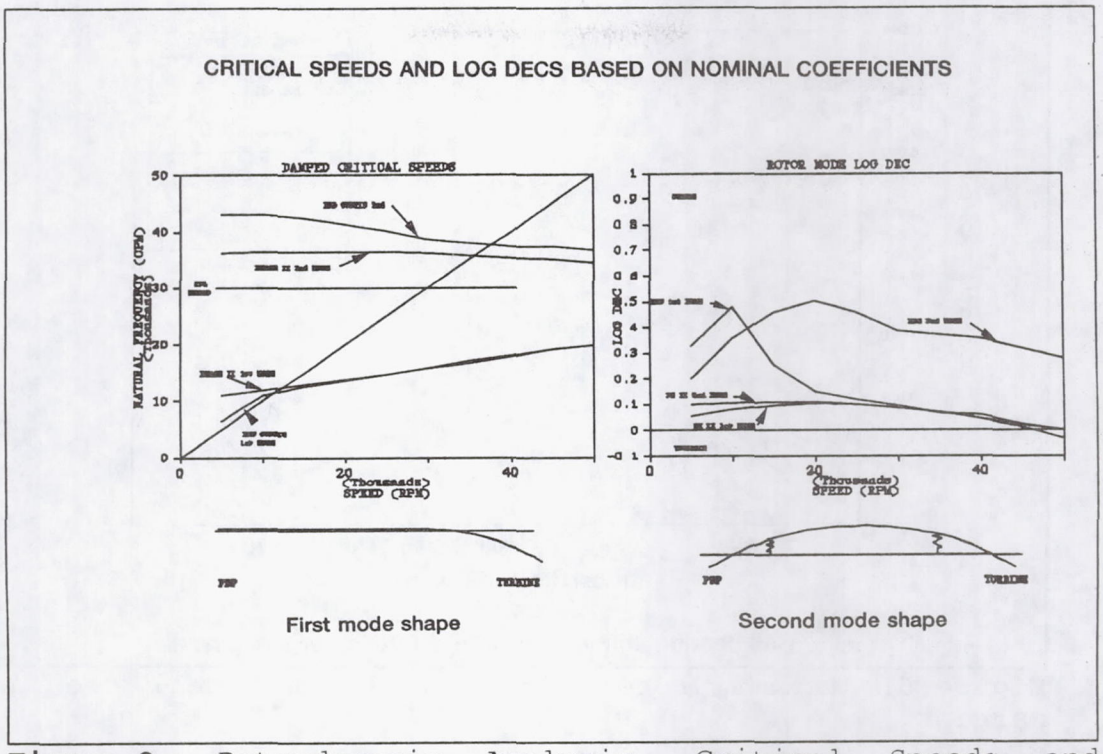

Figure 3. Rotordynamic Analysis- Critical Speeds and Stability.

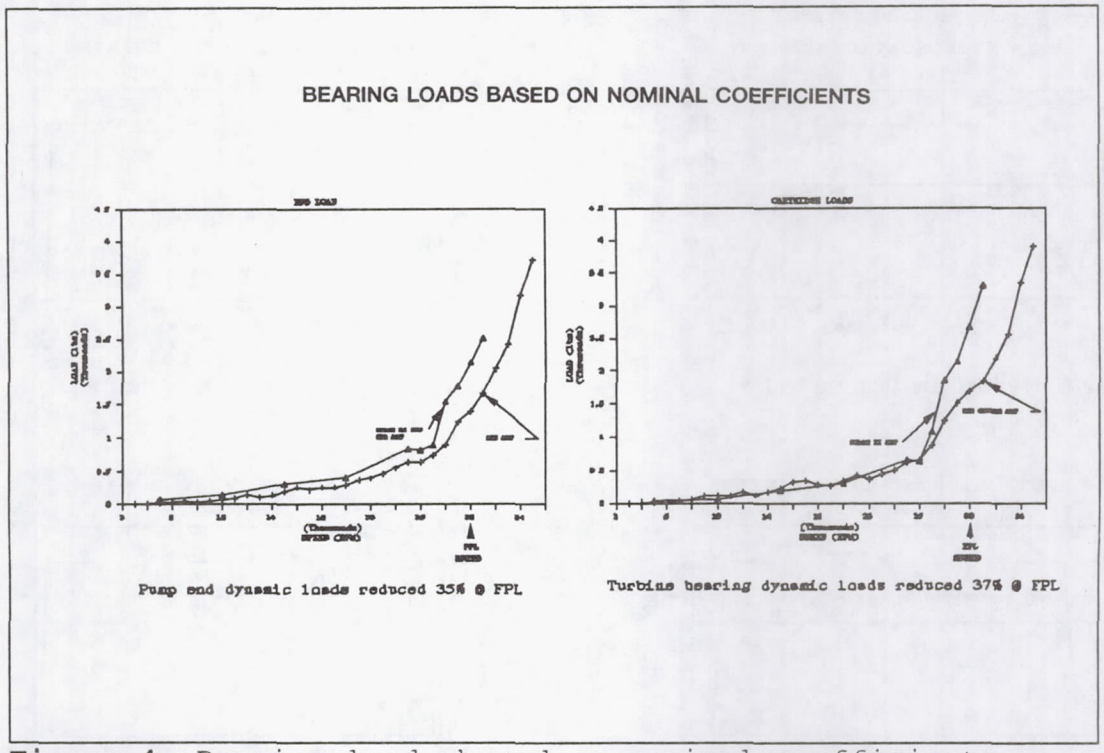

Figure 4. Bearing loads based on nominal coefficients.

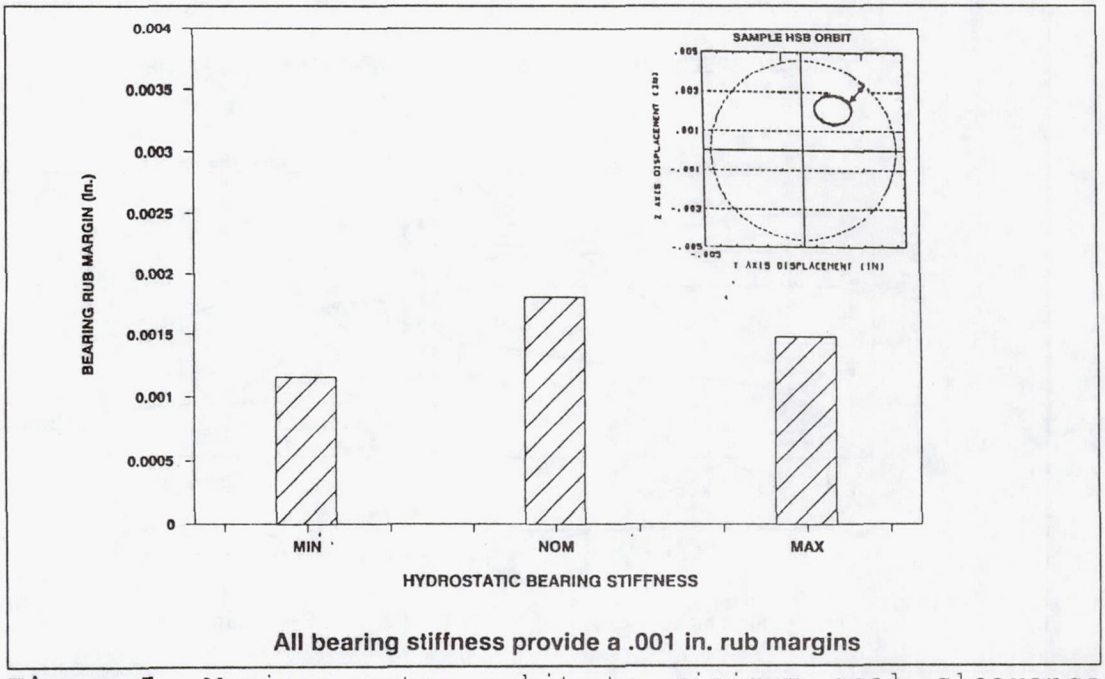

Figure 5. Maximum rotor orbit to minimum seal clearance margins.

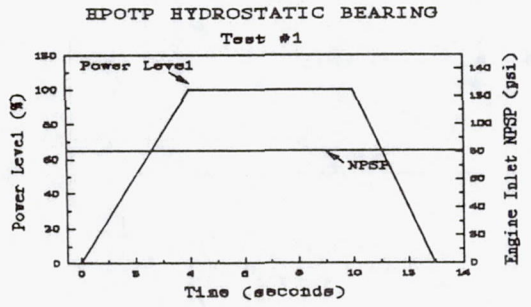

Figure 6. Hydrostatic bearing test #1.

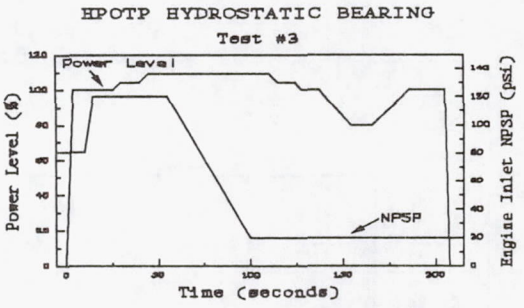

Figure 8. Hydrostatic bearing test #3.

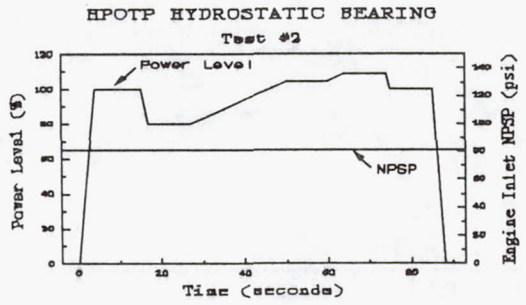

Figure 7. Hydrostatic bearing test #2.

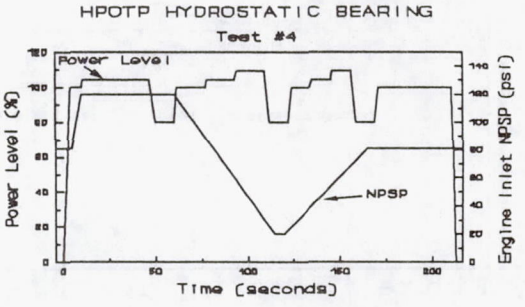

Figure 9. Hydrostatic bearing test #4.

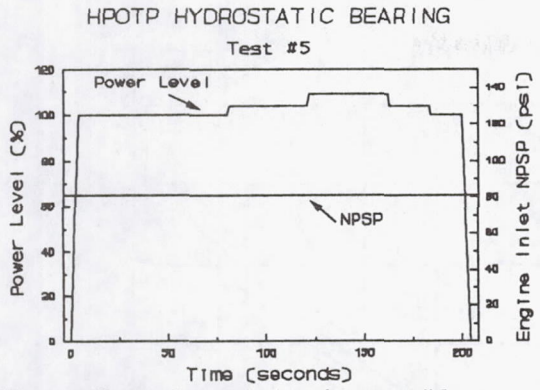

Figure 10. Hydrostatic bearing test #5.

Power Level (%)	Engine Inlet NPSP (psi) 20	81	120
80	#3	#2	#4
100	#3	#2	#3
104	#3	#2	#3
109	#3	#2	#3

Figure 11. Test condition matrix.

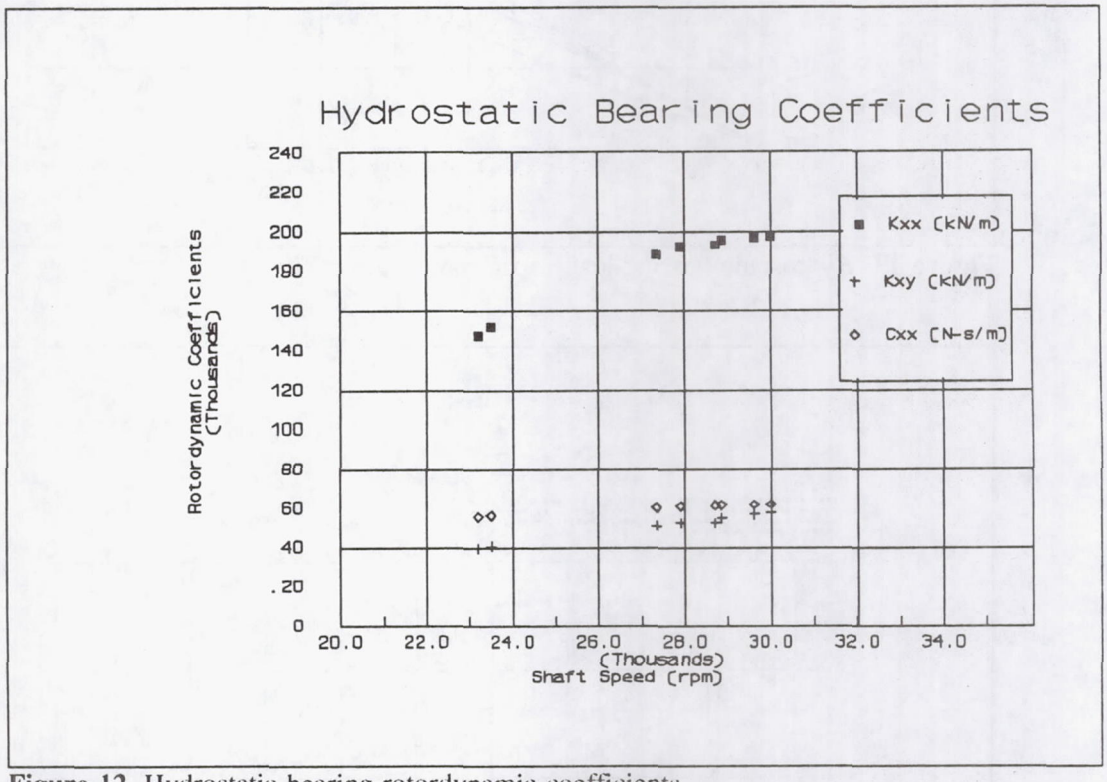

Figure 12. Hydrostatic bearing rotordynamic coefficients.

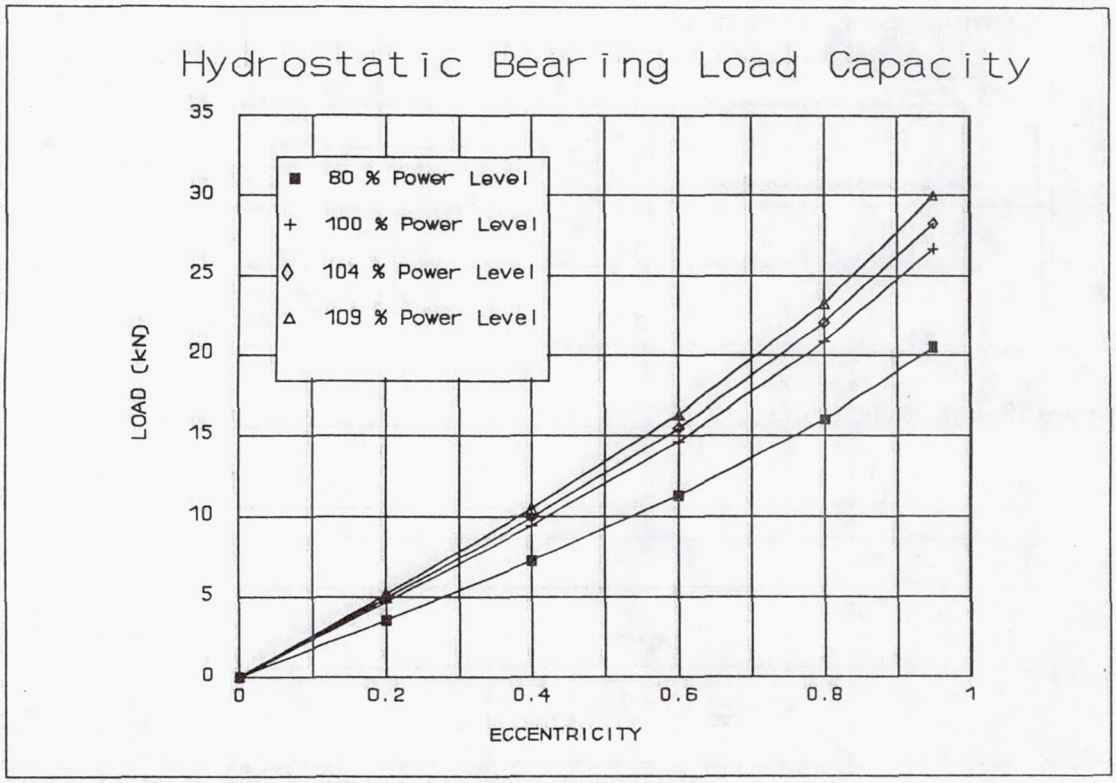

Figure 13. Hydrostatic bearing load capacity vs. eccentricity.

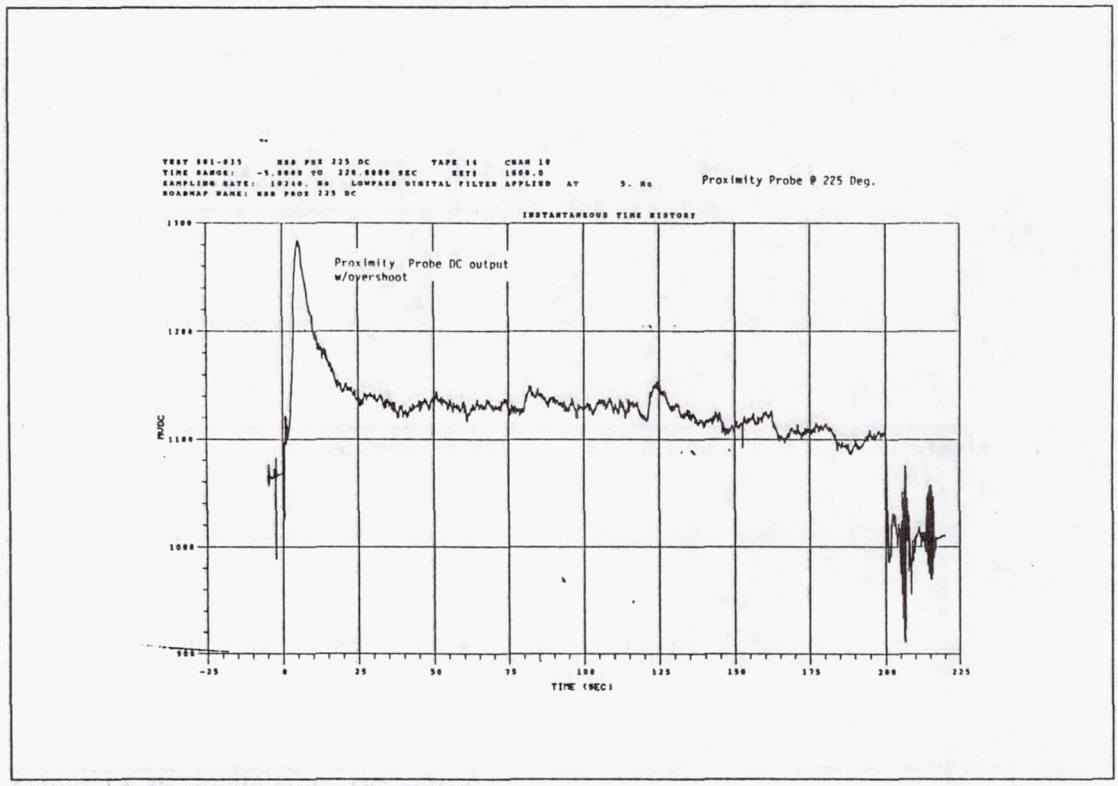

Figure 14. Proximity probe DC output.

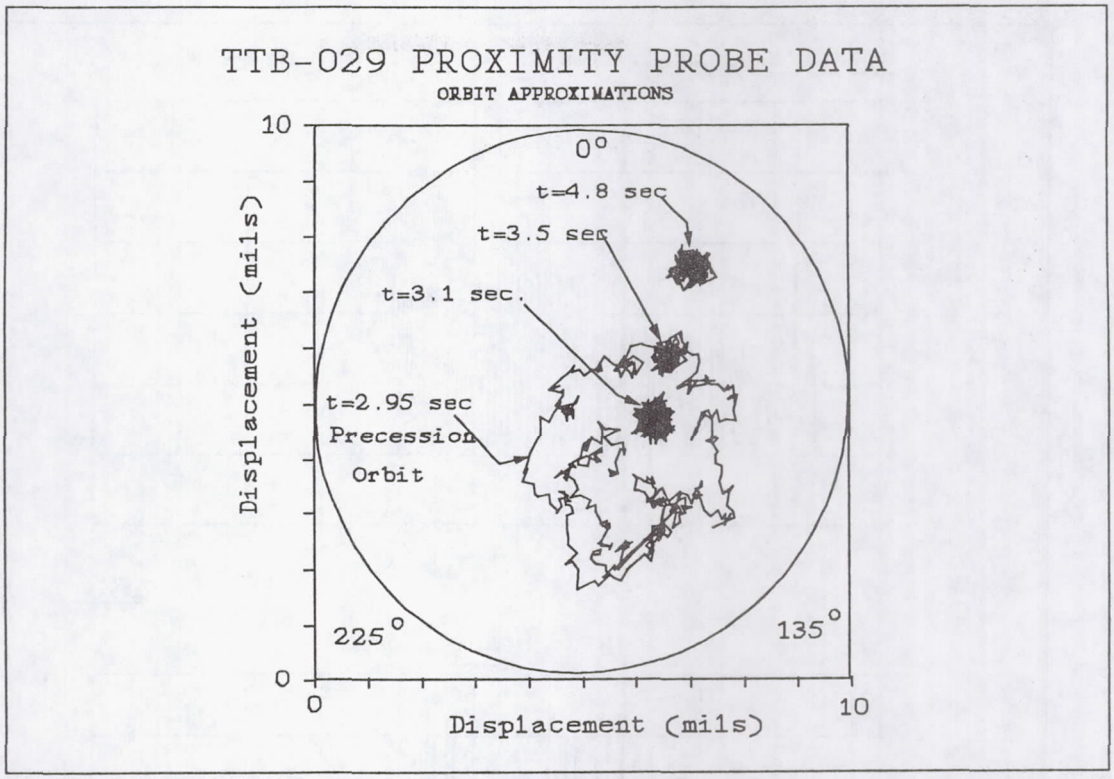

Figure 15. Test #1 Hydrostatic bearing orbit data.

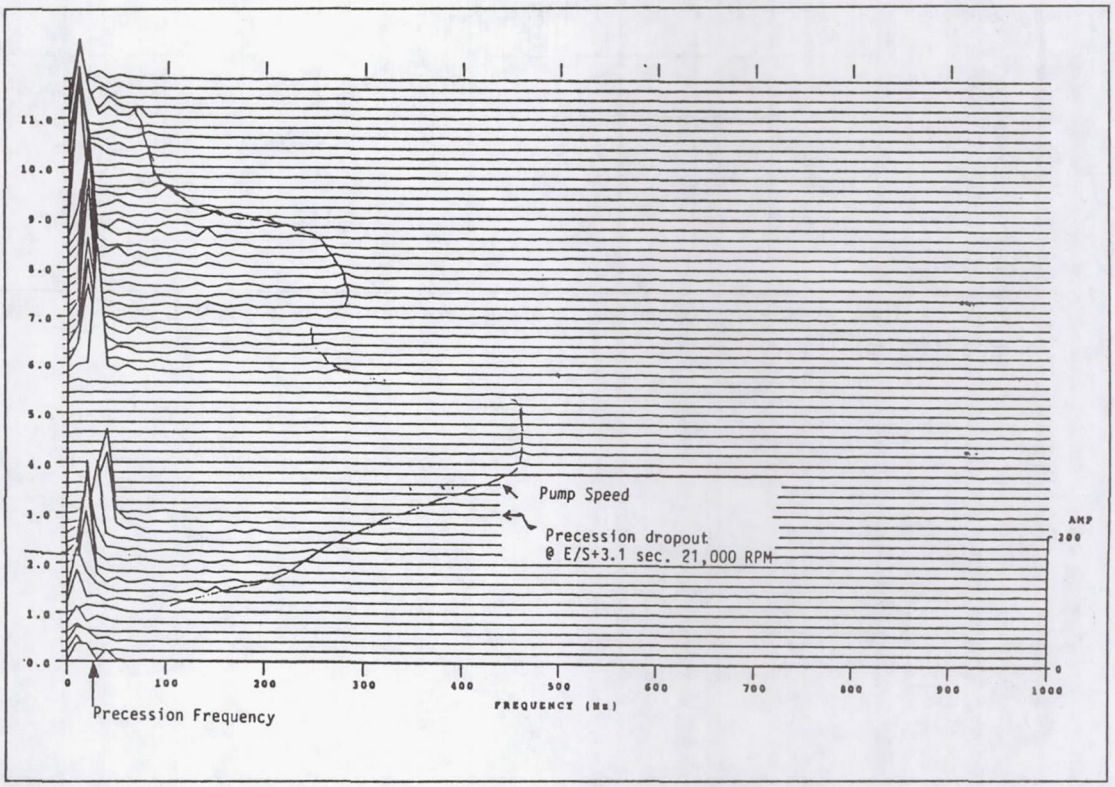

Figure 16. Test #1 proximity probe waterfall data.

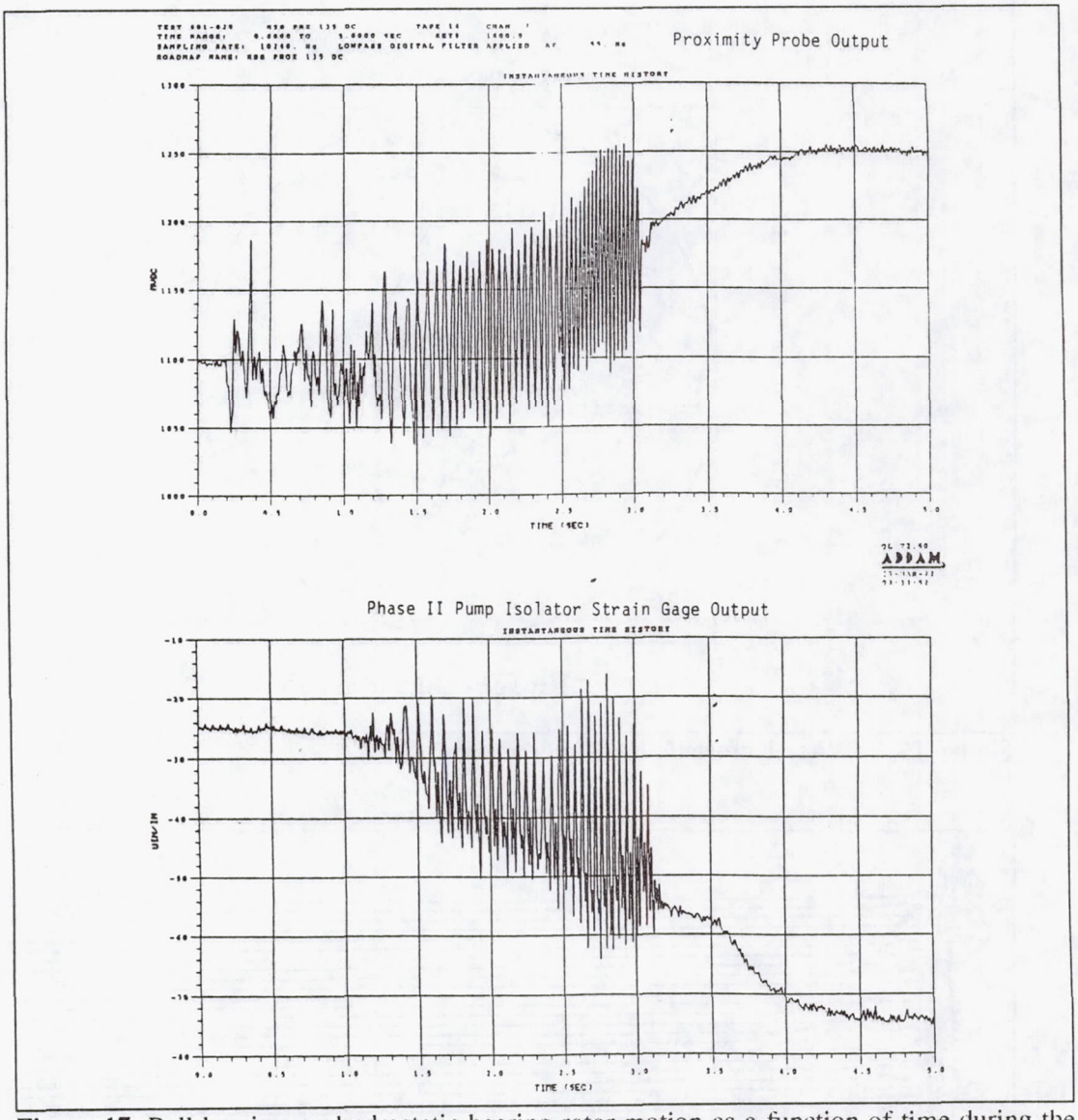

Figure 17. Ball bearing vs. hydrostatic bearing rotor motion as a function of time during the engine start transient.

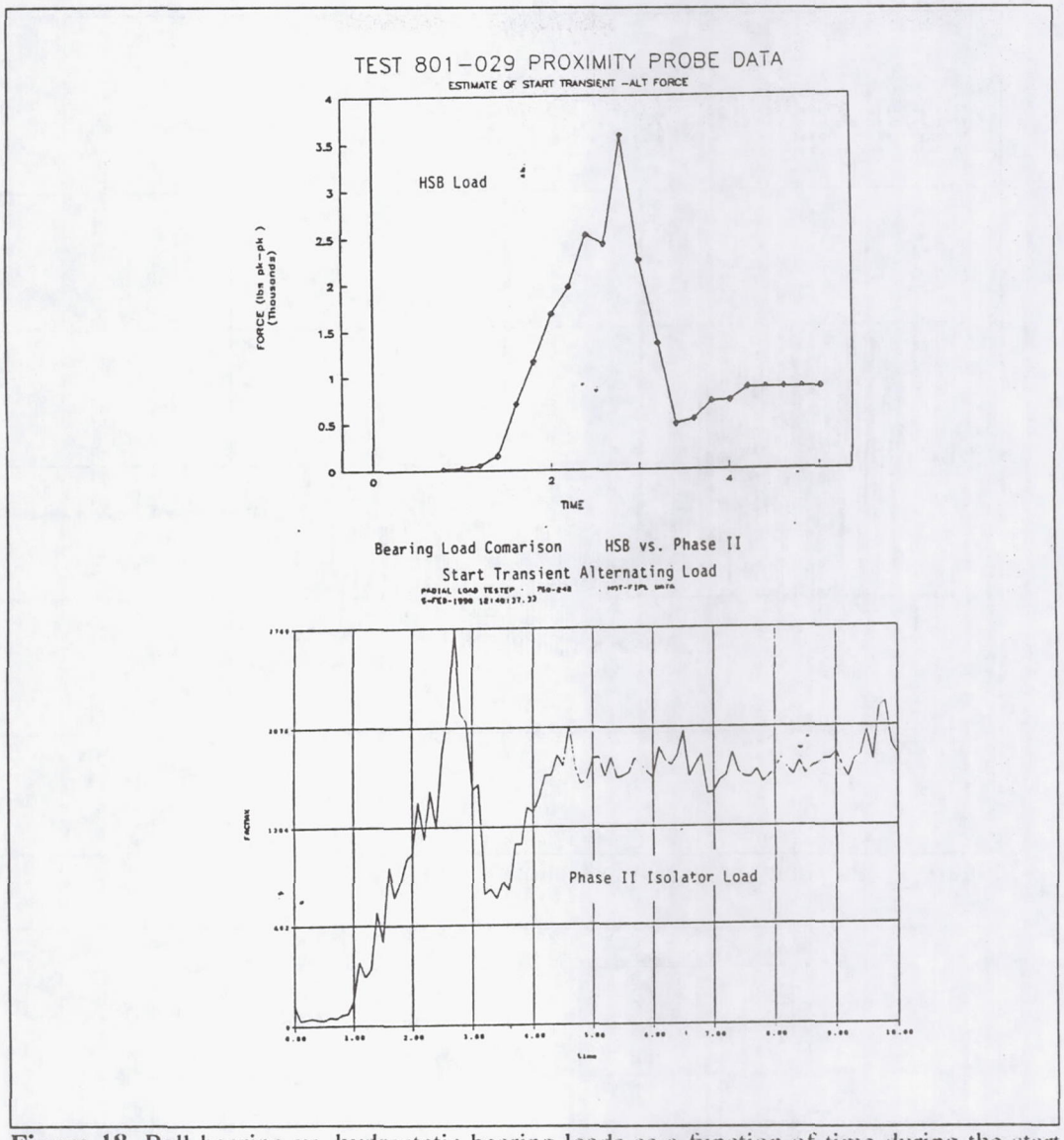

Figure 18. Ball bearing vs. hydrostatic bearing loads as a function of time during the start transient

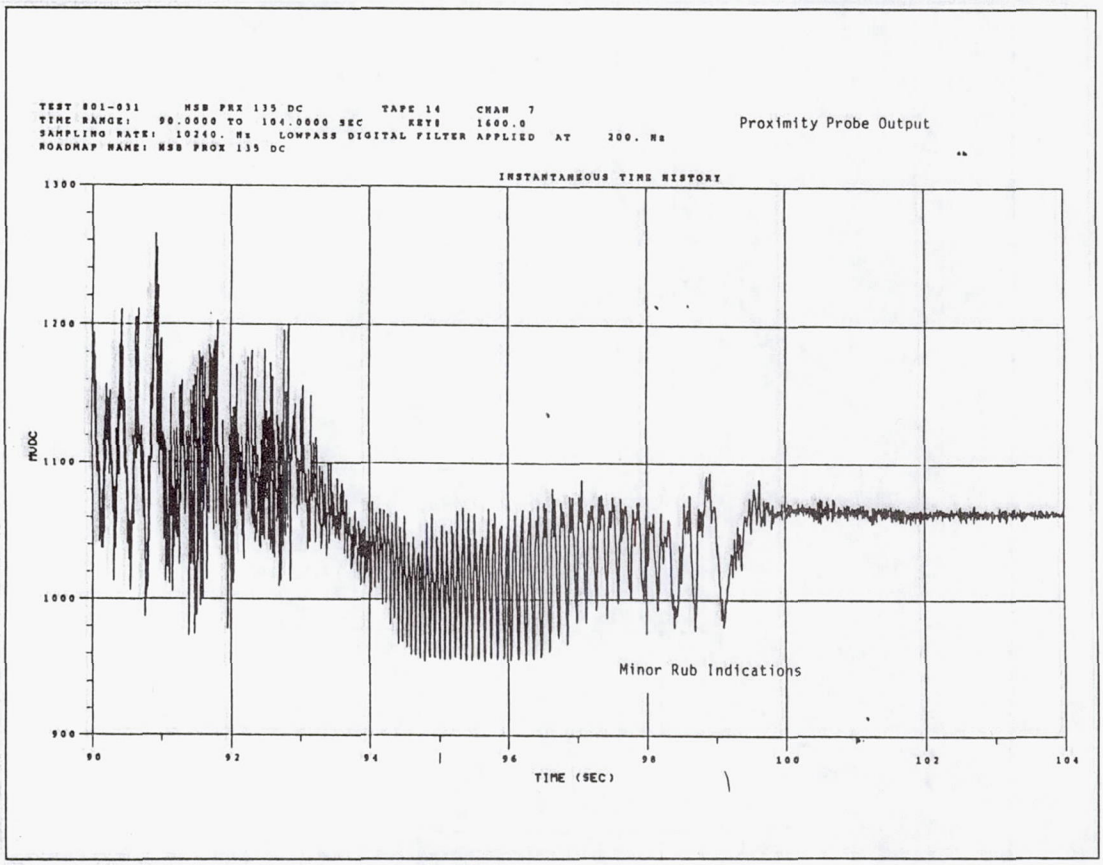

Figure 19. Proximity probe rub indications.

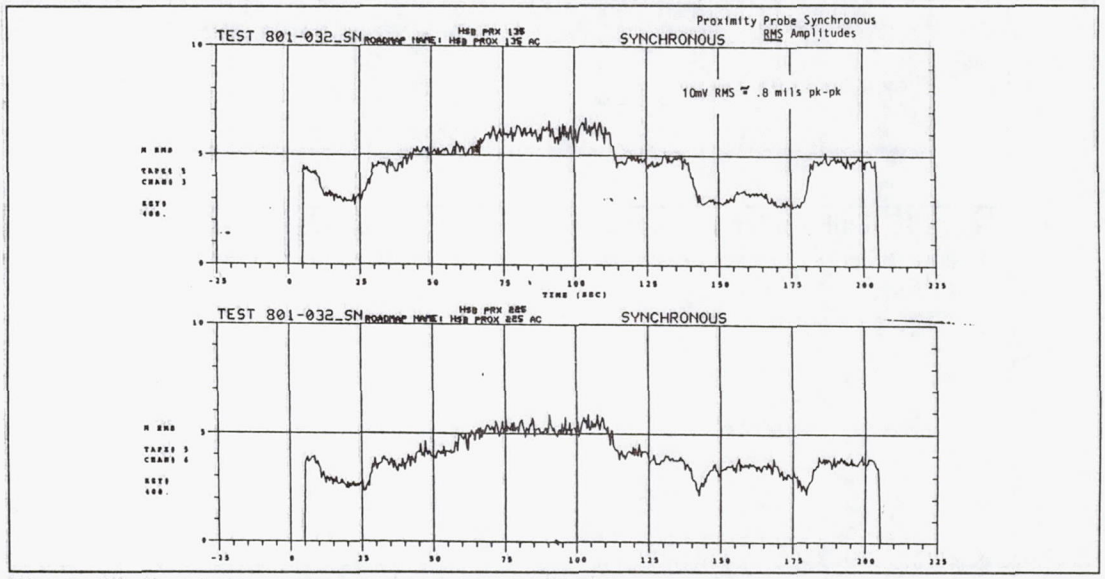

Figure 20. Proximity probe synchronous amplitudes.

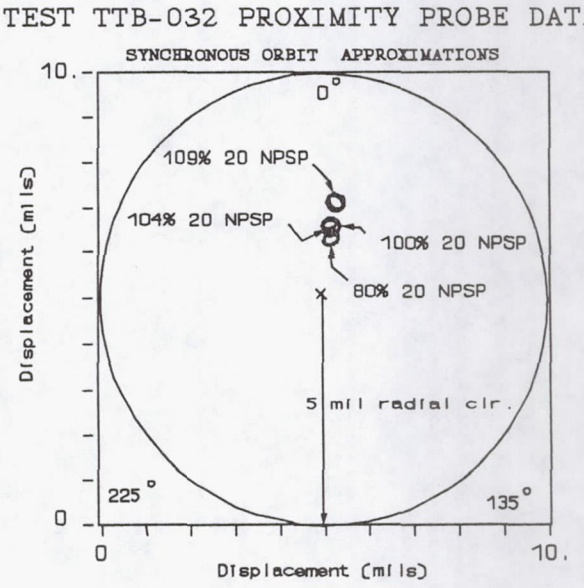

Figure 21. Rotor synchronous orbit amplitudes.

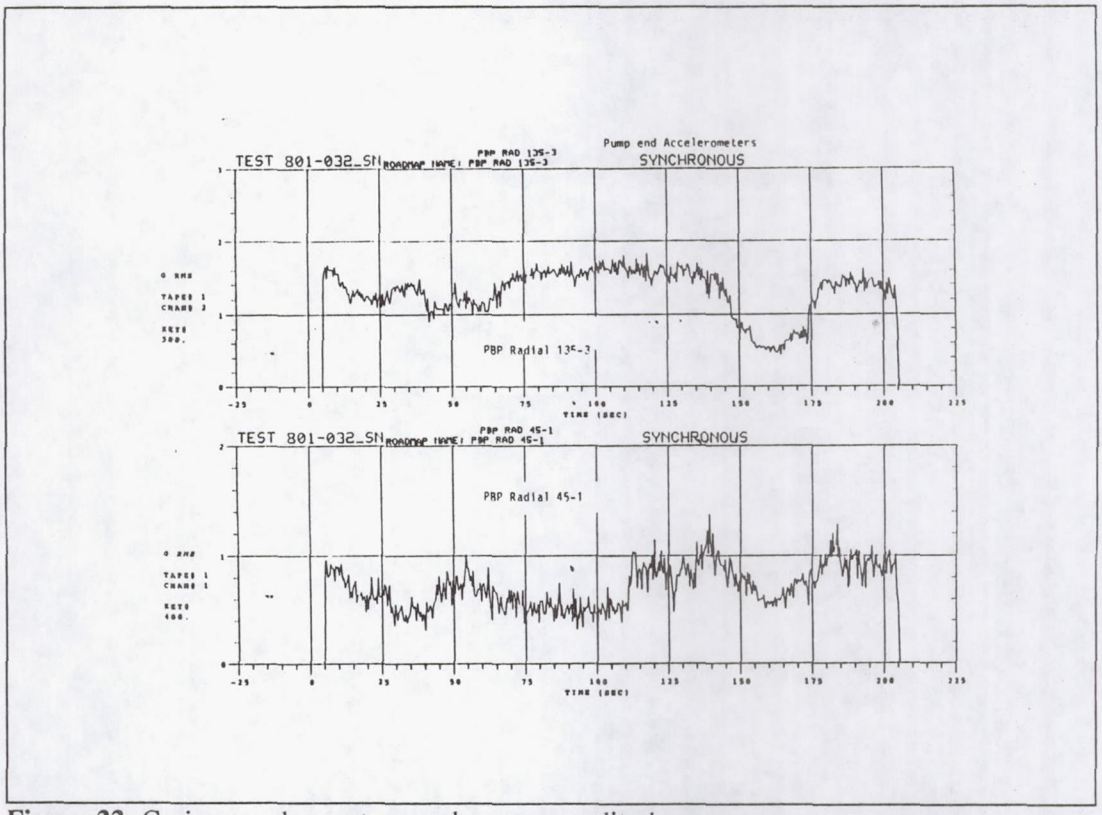

Figure 22. Casing accelerometer synchronous amplitudes.

PARAMETER IDENTIFICATION OF A ROTOR SUPPORTED IN A PRESSURIZED BEARING LUBRICATED WITH WATER

John W. Grant, Agnes Muszynska, and Donald E. Bently
Bently Rotor Dynamics Research Corporation
Minden, Nevada

ABSTRACT

A rig for testing an externally pressurized (hydrostatic), water—lubricated bearing was developed. Applying a nonsynchronous sweep frequency, rotating perturbation force with a constant amplitude as an input, rotor vibration response data was acquired in Bode and Dynamic Stiffness formats. Using this data, the parameters of the rotor/bearing system were identified. The rotor/bearing model was represented by the generalized (modal) parameters of the first lateral mode, with the rotational character of the fluid force taken into account.

1. INTRODUCTION

Experimental modal testing is a popular method for studying vibration problems of mechanical structures. The application of modal testing to a structure containing rotating elements requires a specialized approach [1]. The experimental testing provides data for identification of the system parameters which can be further used in the evaluation to the stability of the system, and in numerical modelling or engineer assist (expert system) programs. This paper presents results of perturbation testing and parameter identification of a rotor supported in one rigid and one externally pressurized water—lubricated bearing. The mathematical model used for the rotor system identification was developed in references [1—11]. The method of relating the applied input force to measured output response (henceforth known as the dynamic stiffness technique) serves very well for the parameter identification [1]. A new tool was developed for the experimental testing of the rotor/bearing system. This tool consists of a constant force amplitude perturbator used to apply the force to the system under test over a frequency range of ±3000 rpm (perturbation forward and backward). The unique feature of this perturbator is that the force has a constant amplitude, independent of frequency, unlike that of unbalance type perturbation. This feature enables one to obtain very clean (high signal to noise ratio) data in the low frequency range, therefore, it offers more accurate identification of the lowest modes of rotors with fluid interaction.

2. EXPERIMENTAL TEST RIG

The experimental rotor is shown in Figure 1. The system consists of a stainless steel shaft carrying a balanced, concentrated mass at the brass—sleeved, aluminum journal of 1.990 inch diameter and 10 mil diametrical clearance inside the bearing. The shaft is supported on one end by a relatively rigid, bronze (oilite) bearing, and the other by the water—lubricated, hydrostatic bearing. This cylindrical bearing has four equally spaced, canoe—shaped pockets, as shown in Figure 2. These pockets are fed through radial 0.135 inch diameter capillaries. The bearing contains, also, separately controlled tangential antiswirl ports. They will not be used, however, in the tests presented in this paper. The role of these ports is described in [12].

Preceding Page Blank

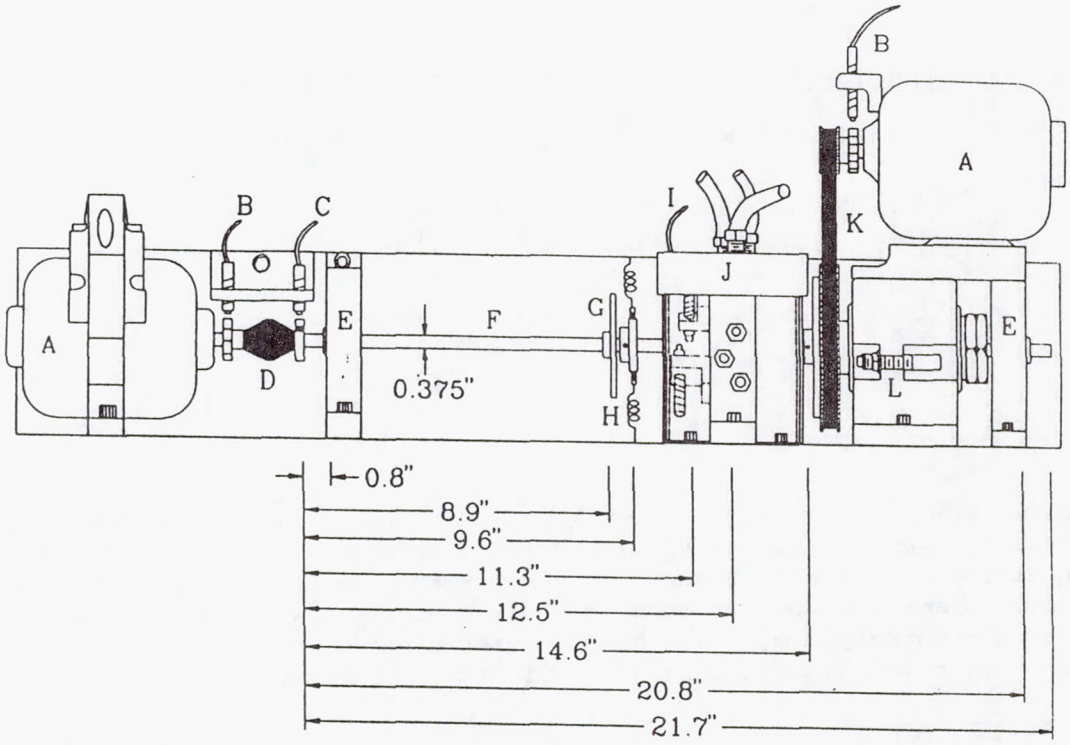

Fig. 1 Experimental rotor rig with constant force perturbator, A) 0.5 hp electric motor, B) speed control probe, C) Keyphasor® probe, D) flexible coupling, E) bronze sliding bearing, F) shaft, G) slim disk for balancing, H) spring support (with stiffness 38 lb/in), I) XY eddy current displacement probes, J) experimental pressurized bearing, K) constant force perturbator, L) optical Keyphasor.

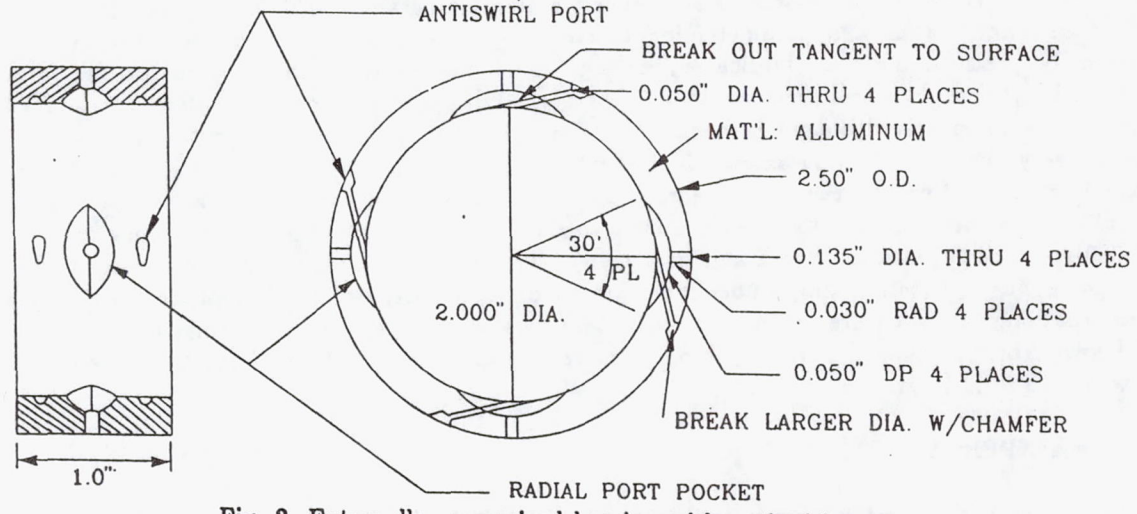

Fig. 2 Externally pressurized bearing with antiswirl ports.

The water temperature was monitored using a thermocouple that was located in a drain tube of the hydrostatic bearing. The rotative energy was derived from a 0.5 hp electric motor connected to the rotor through a flexible coupling. A speed controller was used to control rotative speed. The perturbation force was applied to the shaft rotating at a constant speed. Soft supporting springs installed near the test bearing allow for controlling journal eccentricity at rest: all tests were run with the journal concentrically located within the bearing. To obtain the shaft/journal lateral vibration data, one pair of XY eddy current displacement probes was mounted to

observe the shaft, next to the journal. A computerized data acquisition and processing system was used in the tests.

The right side of Figure 1 presents the system used to perturb the rotor/bearing system. The system consists of a stiff steel shaft connected to the journal within the hydrostatic bearing, using a sealed rolling element bearing. The shaft was supported on the other end by a bronze (oilite) bearing. A constant force perturbator was attached to the shaft next to the journal through a rolling element bearing (Fig. 3). The rotative energy for the perturbation was derived from a 0.5 hp bidirectional electric motor. Another speed controller was used to control perturbation speed and acceleration. The rotor response, to the input perturbation force, was filtered to the perturbation frequency. The response phase was measured in reference to an optical Keyphasor® that observed a reflective spot on the perturbator.

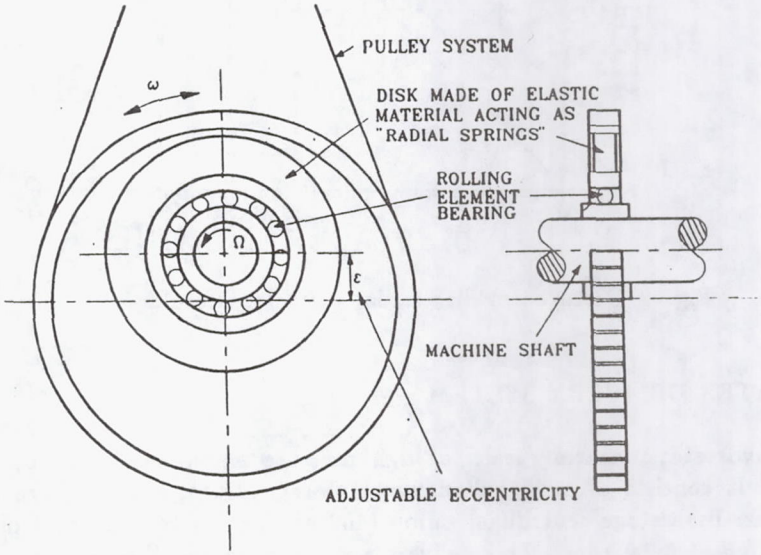

Fig. 3 Constant force perturbator (not to scale; eccentricity ϵ exaggerated).

3. CONSTANT FORCE AMPLITUDE PERTURBATOR

In previous experiments [1—12] the input perturbation force applied to the rotor was generated by an unbalance. Since unbalance centrifugal force is proportional to rotative speed squared, its amplitude becomes very small for low perturbation frequencies. A new device was designed that provides a constant force amplitude in order to increase the data accuracy in the low frequency range. The principle of the operation of this force perturbator is similar to the kinematic excitation, known in vibration theory: a calibrated rotating vector of displacement (ϵ) is exerted across a known radial stiffness (K) of the elastic material within the perturbator. This creates a known rotating force vector that is applied to the rotor under test. The known displacement is obtained by adjusting the eccentricity of an inner calibrated ring, as shown in Figure 3. To obtain the rotating force sweep frequency, the perturbation disk is rotated with very low acceleration in a direction the same as the rotor under test (forward perturbation), or opposite the direction (reverse perturbation). The elastic material used for the perturbator was Dow Corning® 3112 RTV silicon rubber. The stiffness, damping, and inertia of this material were separately identified by the use of dynamic stiffness testing of the perturbator itself. It was found that maximum inertia effect was 0.000209 lb sec^2/inch and maximum damping was 0.079 lb sec/inch. Using both static and dynamic testing, the perturbator radial stiffness was evaluated to be 374 lb sec/inch, as shown in Figure 4. Since the inertia and damping proved to be small compared to the stiffness, they were eventually neglected in the input force model.

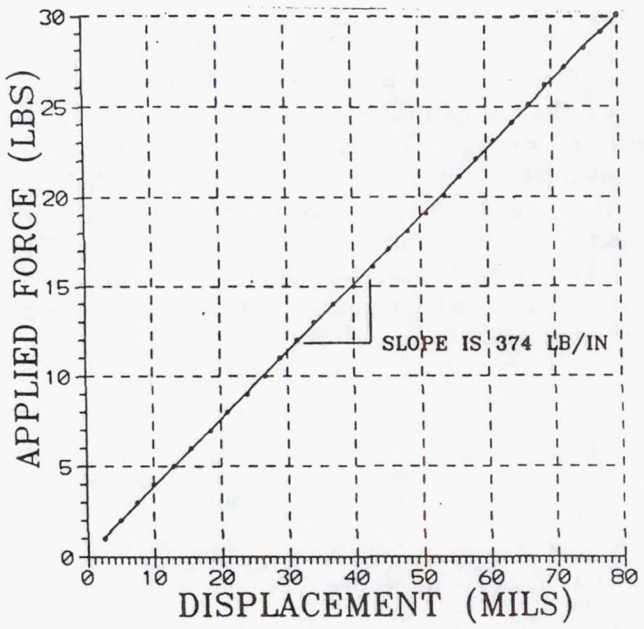

Fig. 4 Perturbator disk radial stiffness. Results from static tests.

4. WATER DELIVERY SYSTEM

To study hydrostatic bearing/seals, a high pressure water system (1000 psi @ 10 gpm) was developed. It consists of a 50 gallon water storage drum, low—pressure feed pump (100 psi), high—pressure multistage centrifugal pump (400 psi) driven by a 5 hp, 3 phase, 230 volt electric motor rotating at 3450 rpm. This delivers water through a pipeline which contains 80 mesh, 25 micron, and 1 micron filters, and several gauges and valves. Water is returned to the 50 gallon storage drum using a sump pump. Water temperature is openly controlled by using a submersion heater in the storage tank, with cooling provided by a fan blowing air at the storage tank surface.

The water is delivered to the hydrostatic bearing using three specially designed distribution manifolds. One manifold leads to the four radial ports, and the other two to the eight antiswirl ports of the test bearing. Each port is fed from the manifold to the port through a manually controlled flow valve, and a high—pressure hose. Each of the high—pressure feed lines is equipped with pressure gauges to measure the pressure drop at the bearing port. Pressure is also monitored at the manifold.

Flow is measured using the sump pump. The sump holds a calibrated 2.5 gallons before pumping, thus by timing this volume, the total flow rate is determined. Such calculation is only valid when testing one set of ports at a time, and when the journal rotates concentrically within the bearing.

5. MATHEMATICAL MODEL

The mathematical model of the fluid dynamic force and the corresponding dynamic stiffness components of the rotor/bearing system were developed in [1,3].

The model of the considered system is as follows:

$$M\ddot{z} + M_f(\ddot{z} - 2j\lambda\Omega\dot{z} - \lambda^2\Omega^2 z) + D(\dot{z} - j\lambda\Omega z) + (K_S + K_B + K)z = K\epsilon e^{j(\omega t+\delta)} \quad , \quad j=\sqrt{-1}$$

where $z = x+jy$ is the rotor lateral (x = horizontal, y = vertical) displacement, K_S and M are the rotor modal stiffness and mass, M_f is the fluid inertia effect, K_B and D are the fluid radial stiffness and damping respectively, and λ is the fluid average circumferential velocity ratio (the rate at which the fluid damping force rotates), with ω and Ω being perturbation frequency and rotative speed, respectively. K is the perturbator radial stiffness, ε and δ are the perturbator calibrated eccentricity parameters: its value and angular orientation, respectively. The rotor response is $z = Ae^{j(\omega t+\alpha)}$ where A and α are amplitude and phase respectively. The following relationships were further used in the identification procedure:

$$\text{Direct Dynamic Stiffness} = K_S+K_B+K-M_f(\omega-\lambda\Omega)^2 - M\omega^2 = \frac{K\varepsilon}{A}\cos(\delta-\alpha) \qquad (1)$$

$$\text{Quadrature Dynamic Stiffness} = D(\omega-\lambda\Omega) = \frac{K\varepsilon}{A}\sin(\delta-\alpha) \qquad (2)$$

Since Eqs. (1) and (2) are simple curves with respect to the perturbation frequency, it was possible to identify the parameters by using polynomial best fitting. The coefficients of the polynomial for these best fit curves can then be equated to the corresponding coefficients in Eqs. (1) and (2) to determine the value of each parameter.

6. EXPERIMENTAL TEST RESULTS

The set of tests was designed to determine the effects of pressurized water input through the radial inlets to the bearing (antiswirl ports shut off). The pressure at the radial port manifold was approximately 75 psi, and the drop across the bearing through the pocket was maintained constant at 20 psi. The water flow through the bearing varied from 3.9 to 4.6 gal/min for four consecutive tests. During four consecutive tests, the rotative speed was constant 0, 1000, 2000, and 3000 rpm respectively.

Figure 5 shows the rotor responses to a rotating sweep frequency perturbation force vector of $\varepsilon K = 1.535$ lbs at $\delta = -310°$. The responses to perturbation forward ($+\omega$) and backward ($-\omega$) were filtered to the perturbation frequencies and are presented in the Bode format (Fig. 5). Notice that the response amplitudes in the considered range of frequencies are rather flat, not the same as if the system was excited by an unbalance force. Note, also, that there is some disturbance in amplitudes and phases around the area when the perturbation and rotation frequency are equal. This is due to an interference of the rotative frequency vibrations in the filtering system.

Figure 6 presents the dynamic stiffness plots that were obtained using Eqs. (1) and (2), and the rotor response shown in Figure 5. Each plot consists of 570 data points. To identify the system's modal parameters, the plots were best fitted by polynomials. Interesting enough, the coefficients of higher power than the second for the direct stiffness, and first for the quadrature stiffness, were more than five orders smaller than those of lower powers. Therefore, a parabola was adopted for the direct, and a straight line for the quadrature dynamic stiffness. They are shown as solid lines in the plots of Figure 6. The coefficients of the best fit equations are summarized in Table 1.

If the best fit coefficients are equated to that of the dynamic stiffness model (1), (2), and converted to the proper angular frequency units, the system parameters can be identified, as shown in Table 2.

When calculating the rotor modal mass M at rotative speed of 0 rpm, the fluid inertia effect and the mass cannot be readily separated ($M_f + M = 7.37 \times 10^{-3}$). To obtain reasonable data for zero speed, the modal mass was obtained by averaging the values at all other rotative speeds.

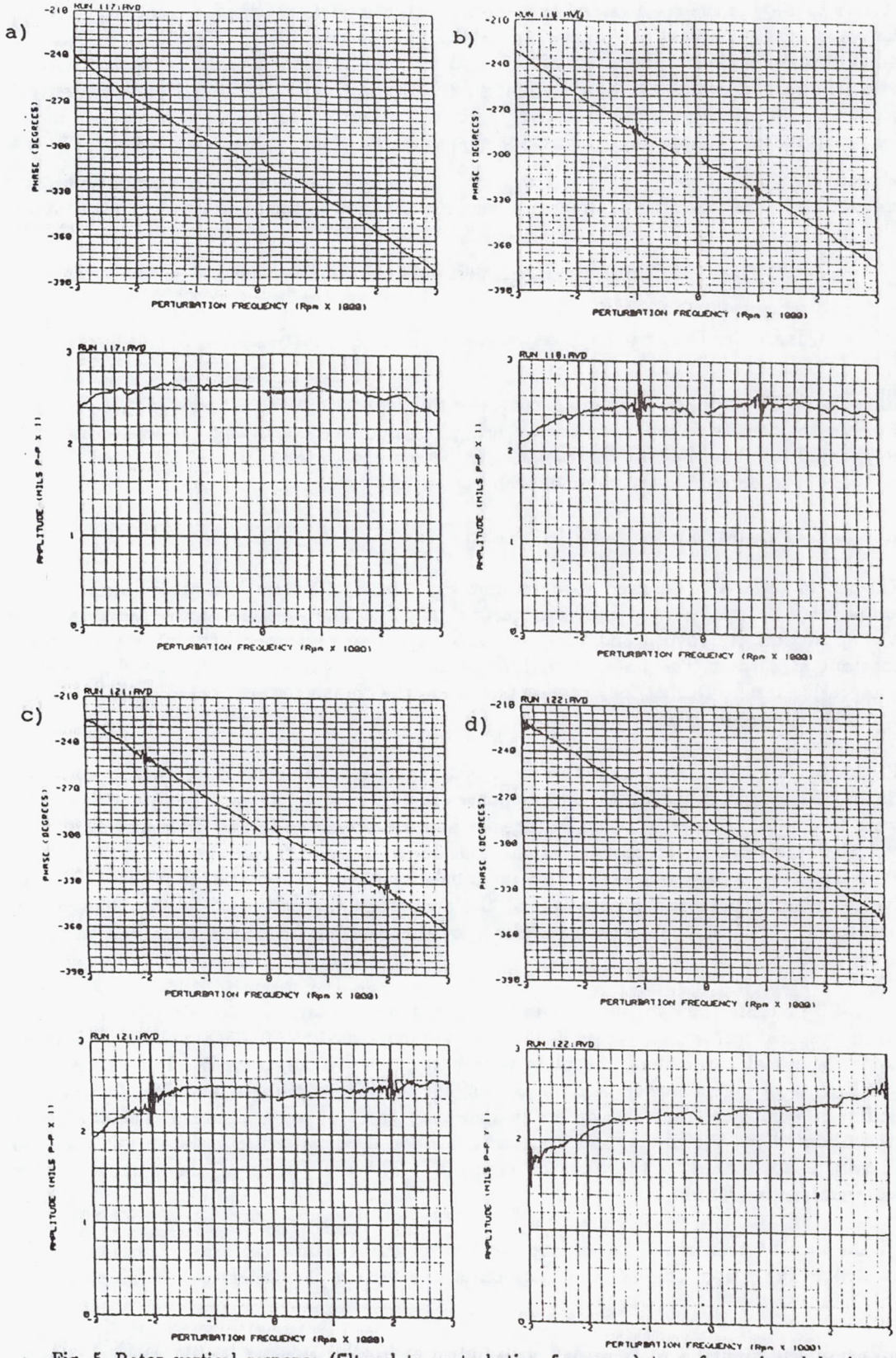

Fig. 5 Rotor vertical response (filtered to perturbation frequency) to a forward and backward perturbation force rotating vector of $K\epsilon$ = 1.535 lbs at δ = -310°, with the water-lubricated bearing radial port pocket pressure of 20 psi and a rotative speed of (a) 0 rpm, (b) 1000 rpm, (c) 2000 rpm, and (d) 3000 rpm. The horizontal responses which were very similar are not shown. Response amplitude measured peak to peak.

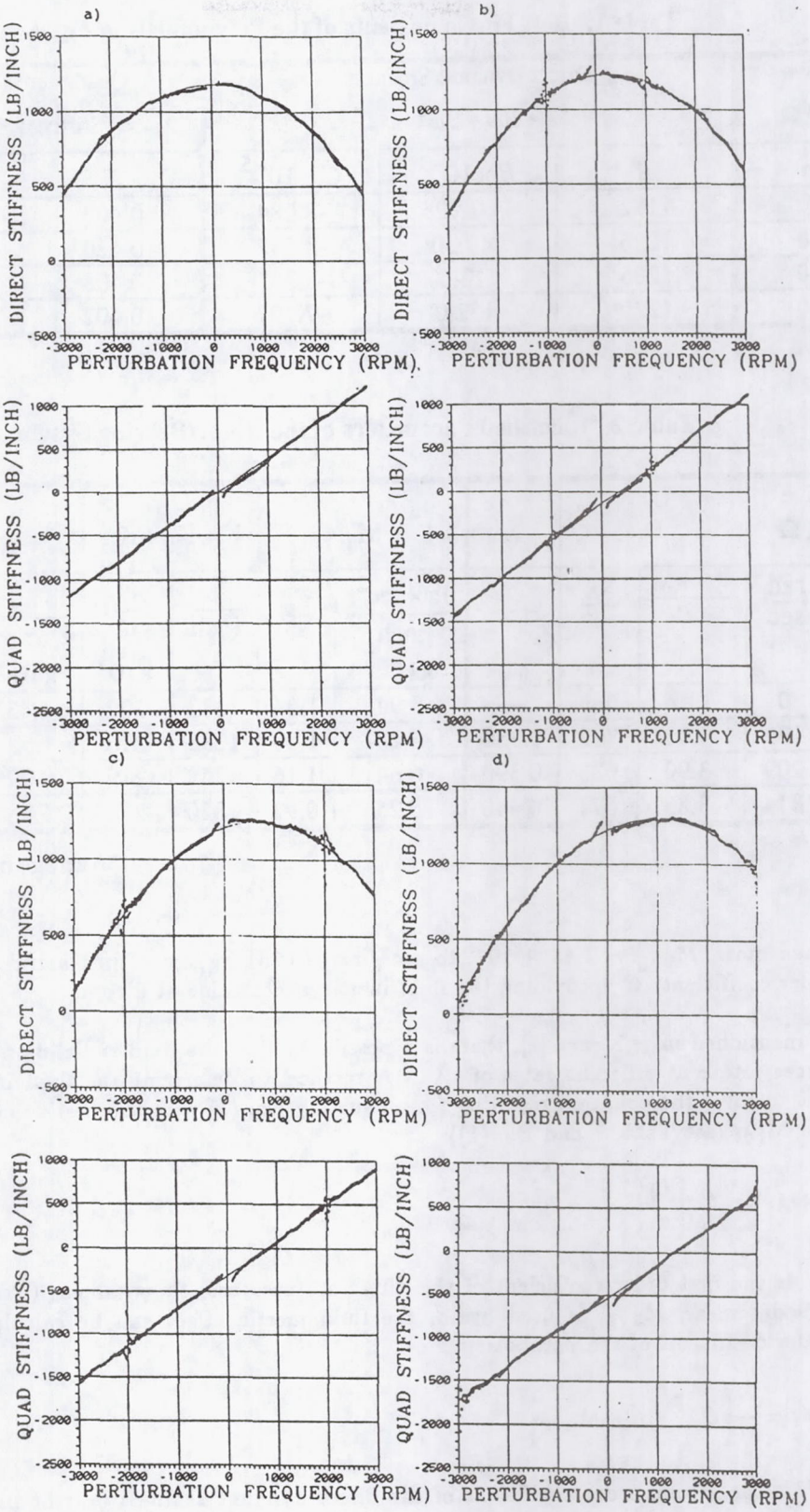

Fig. 6 Direct and quadrature dynamic stiffness plots based on Eqs. (1), (2) and on the system responses presented in Figure 5 for four rotative speeds: (a) 0 rpm, (b) 1000 rpm, (c) 2000 rpm, and (d) 3000 rpm.

Table 1. Best Fit Coefficients of the Polynomials in Fig. 6

Rotative Speed Ω	Direct Dynamic Stiffness $A+B\omega+C\omega^2$			Quadrature Dynamic Stiffness $E\omega+F$	
rpm	A	$B\times10^{-3}$	$C\times10^{-5}$	E	F
0	1182	2.126	-8.084	0.400	3.424
1000	1226	49.30	-8.557	0.420	-150.5
2000	1205	113.6	-8.363	0.408	-318.9
3000	1220	152.0	-7.707	0.402	-530.2

Table 2. Identified Parameters of the Rotor/Bearing System

Rotative Speed, Ω		D		λ	M_f		$K+K_s+K_B$		M	
rpm	$\frac{rad}{sec}$	$\frac{lb\times sec}{inch}$	$\frac{kg}{sec}$	---	$\frac{lb\times sec^2}{inch}\times10^{-3}$	kg	$\frac{lb}{inch}$	$\frac{N}{m}\times10^3$	$\frac{lb\times sec^2}{inch}\times10^{-3}$	kg
0	0	3.82	669	---	5.94	1.04	1182	207	1.43*	0.251*
1000	105	4.01	702	0.358	6.28	1.10	1235	216	1.52	0.267
2000	209	3.90	683	0.390	6.64	1.16	1249	219	0.99	0.173
3000	314	3.83	671	0.440	5.25	0.92	1320	231	1.78	0.312

*Average of the column

The average mass, $M_{avg} = 1.43 \times 10^{-3}$ lb sec^2/inch (0.251 kg), was then subtracted from the second order coefficient C, providing the fluid inertia effect value at 0 rpm.

As it was mentioned in reference [2], there is a possibility that the fluid radial damping and fluid inertia forces rotate at different rates of λ. A method to determine the fluid inertia rotation rate, λ_f, is to solve the equation resulting from equating Eq. (1) with the best fit coefficients and solve it for $M_f\lambda_f$ (see Table 1 and Eq. (1)):

$$M_f\lambda_f = \frac{B}{2\Omega}\left[\frac{30}{\pi}\right]^2 \tag{3}$$

where B is the first order coefficient of the direct stiffness best fit parabolas (Table 1). If the average modal mass, M_{avg}, is used again, the fluid inertia effect can be calculated from the second order coefficient of the parabola:

$$M_f = -\left[C\,(\frac{30}{\pi})^2 + M_{avg}\right] \tag{4}$$

where C is the second order coefficient of the direct dynamic stiffness best fit parabola (Table 1). The ratio λ_f is calculated by dividing Eq. (3) by Eq. (4). The results are summarized in Table 3. They show that the values λ and λ_f are, actually, very close (maximum difference is 7.2%).

Table 3. Identification of the Fluid Inertia Average Circumferential Velocity Ratio

Rotative Speed Ω		$M_f\lambda$		M_f		λ_f
rpm	$\frac{rad}{sec}$	$\frac{lb \times sec^2}{inch} \times 10^{-3}$	kg	$\frac{lb \times sec}{inch} \times 10^{-3}$	kg	---
1000	105	2.25	0.394	6.37	1.12	0.353
2000	209	2.59	0.454	6.19	1.08	0.418
3000	314	2.31	0.405	5.60	0.98	0.413

Figure 7 presents the results from another set of perturbation tests in which the rotative speed varied, while the perturbation force was constant with $K\epsilon = 1.535$ lbs and $\delta = -310°$. The quadrature dynamic stiffness data were identified as parabolas or straight lines by best fitting polynomials (Table 4). The corresponding quadrature stiffness components D and λ that were calculated from the data are summarized in Table 5. Generally, D resulting from these tests is slightly higher, and λ slightly lower than obtained from the previous tests.

All test results were not compensated for the water temperature changes, which, within each test, varied from 0.3° F to 0.8° F within the range of 90.4° F to 96° F. The data acquisition system was set on the average value of the proximity transducer sensitivity, 0.2 v/mil. Due to slightly increasing temperature during the tests, the transducer output sensitivity varied from 0.198 v/mil to 0.199 v/mil, thus the amplitude readings were 0.5% to 1% higher than the actual ones, and, consequently, the dynamic stiffness values became from 0.5% to 1% lower.

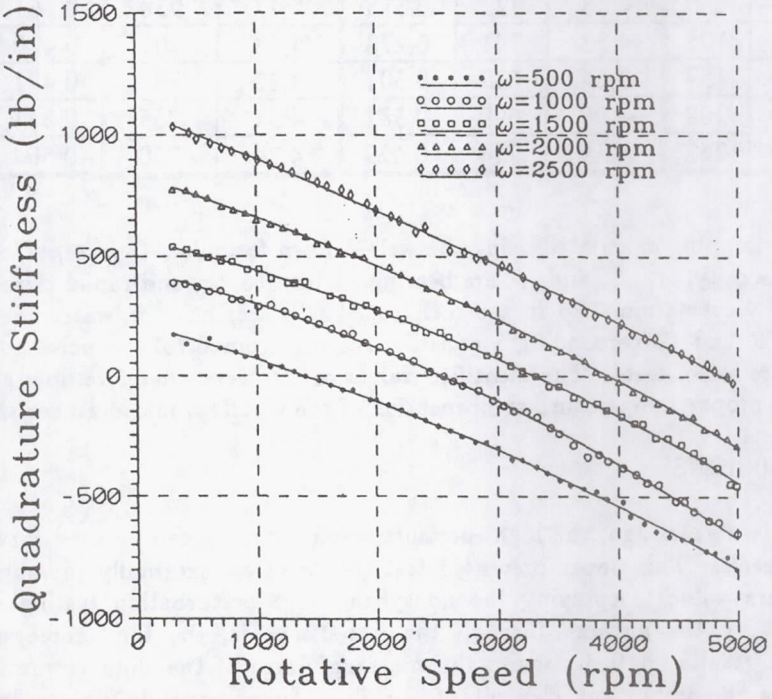

Fig. 7 Quadrature dynamic stiffness versus rotative speed for constant values of perturbation frequency. The solid lines are best fits using second order polynomials.

Table 4. Best Fit Coefficients for the Polynomials of the Quadrature Dynamic Stiffness From Fig. 6 Versus Rotative Speed.

Perturbation Speed ω, rpm	Second Order Fit $G+H\Omega+I\Omega^2$			First Order Fit $J\Omega+L$	
	G	$H\times10^{-3}$	$I\times10^{-6}$	$J\times10^{-3}$	L
500	216	-136	-13	-207	287
1000	443	-123	-19	-228	543
1500	573	-115	-17	-208	662
2000	835	-159	-13	-231	904
2500	1097	-188	-8	-229	1137

Table 5. Identified Parameters for Quadrature Dynamic Stiffness Using Eq. (2) and Polynomial Fits From Table 4.

Perturbation Speed, ω		Second Order Fit Parameters			First Order Fit Parameters		
		D		λ	D		λ
rpm	rad/sec	lb*sec/inch	kg/sec	- - -	lb*sec/inch	kg/sec	- - -
500	52	4.13	723	0.315	5.47	958	0.361
1000	105	4.23	741	0.278	5.18	907	0.420
1500	157	3.64	637	0.301	4.22	739	0.471
2000	209	3.99	699	0.381	4.31	755	0.511
2500	262	4.19	734	0.429	4.34	760	0.504

The fluid radial damping calculated using the well–known formula: $D = \pi\eta r(\ell/c)^3$ (where η is fluid dynamic viscosity, r, ℓ, and c are bearing radius, length, and radial clearance respectively) provides the values from 3.45 lb sec/inch to 3.22 lb sec/inch for water temperatures from 90.4° F to 96.5° F and corresponding viscosities varying from 0.7577 c poise to 0.7076 c poise through the entire set of tests. The identified values of D were, therefore, lower than the calculated ones. The proper temperature compensation of the results would decrease the difference.

7. CONCLUSIONS

Developed over two years ago, the high–pressure water rotor rig can be used for dynamic testing of bearing and seals. This paper presented test results of an externally pressurized bearing for only one pressure value. Applying the nonsynchronous perturbation testing which has been extensively used by the authors through the last 12 years, the fluid force parameters were identified. The results confirm, again, the meaningfulness of the fluid circumferential average velocity ratio as the important element of the fluid force model in lightly loaded lubricated bearings and seals. The results also indicate the existence of the fluid inertia effect which is relatively high, about five times larger than the rotor modal mass.

The use of the constant force perturbator has enabled the acquisition of very clean vibration data (higher signal, thus better signal to noise ratio) in the low frequency range, and hence clean dynamic stiffness data was produced. This data makes the identification procedure more accurate, and allows for advancements in adjustments of the mathematical model of the rotor/bearing system.

NOMENCLATURE

A,B,C,E,F,G,H,I,J,L	Best fit polynomial coefficients
A,α	Rotor response amplitude and phase respectively
D,K_B,M_f	Fluid radial damping, radial stiffness, and inertia effect respectively
$j=\sqrt{-1}$	
K_s,M	Rotor modal stiffness and mass respectively
K	Perturbator radial stiffness
$z=x+jy$	Rotor lateral (x=horizontal, y=vertical) displacement
δ,ε	Perturbator angular orientation and eccentricity respectively
λ	Fluid circumferential average velocity ratio at which fluid damping force rotates
λ_f	Ratio of the fluid inertia force rotation
ω	Perturbation frequency
Ω	Rotative speed

REFERENCES

1. Muszynska, A., Perturbation Technique for Identification of the Lowest Modes of Rotors With Fluid Interaction, Course on "Rotor Dynamics and Vibration in Turbomachinery," von Karman Institute for Fluid Dynamics, Belgium, 21—25 September 1992.

2. Muszynska, A., Bently, D. E., Frequency Swept Rotating Input Perturbation Techniques and Identification of the Fluid Force Models in Rotor/Bearing Seal Systems and Fluid Handling Machines, Journal of Sound and Vibration, v. 143, No. 1, pp. 103—124, 1990.

3. Muszynska, A., Improvements in Lightly Loaded Rotor/Bearing and Rotor/Seal Models, Transaction of the ASME Journal of Vibration Acoustics, Stress and Reliability in Design, v. 110, No. 2, April 1988.

4. Muszynska, A., Whirl and Whip —— Rotor/Bearing Stability Problems, Journal of Sound and Vibration, v. 110, No. 3, 1986.

5. Bently, D. E., Muszynska, A., Stability Evaluation of Rotor/Bearing System by Perturbation Tests, Rotor Dynamic Instability Problems in High Performance Turbomachinery, NASA CP 2250, The Second Workshop at Texas A&M University, College Station, Texas, 1982.

6. Bently, D. E., Muszynska, A., Oil Whirl Identification by Perturbation Test, Advances in Computer—Aided Bearing Design, 82—72978, ASME/ASLE Lubrication Conference, Washington, D.C., October 1982.

7. Bently, D. E., Muszynska, A., Perturbation Tests of Bearing/Seal for Evaluation of Dynamic Coefficients, Symposium on Rotor Dynamical Instability, Summer Annual Conference of the ASME Applied Mechanics Division, AMD —— Vol. 55, Houston, Texas, June 1983.

8. Bently, D. E., Muszynska, A., Perturbation Study of Rotor/Bearing System: Identification of the Oil Whirl and Oil Whip Resonances, Tenth Biennial ASME Design Engineering Division Conference on Mechanical Vibration and Noise, 85—DET—142, Cincinnati, Ohio, September 1985.

9. Bently, D. E., Muszynska, A., Modal Testing and Parameter Identification of Rotating Shaft/Fluid Lubricated Bearing System, Proc. of the 4th International Modal Analysis Conference, Los Angeles, California, February 1986.

10. Muszynska, A., Grant, J. W., Stability and Instability of a Two—Mode Rotor Supported by Two Fluid—Lubricated Bearings, Trans. of the ASME Journal of Vibration and Acoustics, v. 113, No. 3, 1991.

11. Bently, D. E., Muszynska, A., Role of Circumferential Flow in the Stability of Fluid—Handling Machine Rotors, Texas A&M Fifth Workshop on Rotordynamics Instability Problems in High Performance Turbomachinery, College Station, Texas, 16—18 May 1988.

12. Muszynska, A., Bently, D. E., Franklin, W. D., Grant, J. W., Goldman, P., Applications of Sweep Frequency Rotating Force Perturbation Methodology in Rotating Machinery for Dynamic Stiffness Identification, 92—GT—176, ASME International Gas Turbine and Aeroengine Congress and Exposition, Cologne, Germany, June 1992, Trans. of the ASME, Journal of Engineering for Gas Turbines and Power, April 1993.

DYNAMIC FORCE RESPONSE OF SPHERICAL HYDROSTATIC JOURNAL BEARING FOR CRYOGENIC APPLICATIONS

Luis San Andres
Texas A&M University
College Station, Texas

ABSTRACT

Hydrostatic Journal Bearings (HJBs) are reliable and resilient fluid film rotor support elements ideal to replace roller bearings in cryogenic turbomachinery. HJBs will be used for primary space-power applications due to their long lifetime, low friction and wear, large load capacity, large direct stiffness, and damping force coefficients. An analysis for the performance characteristics of turbulent flow, orifice compensated, **spherical** hydrostatic journal bearings (HJBs) is presented. Spherical bearings allow tolerance for shaft misalignment without force performance degradation and have also the ability to support axial loads. The spherical HJB combines these advantages to provide a bearing design which could be used efficiently on high performance turbomachinery.

The motion of a barotropic liquid on the thin film bearing lands is described by bulk-flow mass and momentum equations. These equations are solved numerically using an efficient CFD method. Numerical predictions of load capacity and force coefficients for a 6 recess, spherical HJB in a LO_2 environment are presented. Fluid film axial forces and force coefficients of a magnitude about 20% of the radial load capacity are predicted for the case analyzed. Fluid inertia effects, advective and centrifugal, are found to affect greatly the static and dynamic force performance of the bearing studied.

NOMENCLATURE

A_o	$Cd\ \pi\ d_o^2/4$. Equivalent orifice area [m^2].
A_r	$l\ R_*\ \theta_r$. Recess area [m^2].
$C_o(S), C_*, \bar{C}_o$	Radial clearance function, characteristic clearance [m], C_o/C_*
$C_{\alpha,\beta}$	Force damping coefficients due to displacements [Ns/m], (α,β = X,Y,Z)
D_*	$2\ R_*$. Bearing diameter at midplane (S=0) [m]
d_o, C_d	Orifice diameter [m], Orifice discharge coefficient
$f_{J,B}$	$a_M\ [1 + (c_M\ r_{J,B}/H + b_M/R_{J,B})^{eM}]$; a_M = 0.001375, b_M = 500,000 e_M = 1/3.00, c_M = 10,000, r = surface roughness Turbulent flow friction factors at journal and bearing surfaces.
F_X, F_Y, F_Z	Film forces along {X,Y,Z} axes [N]
f_X, f_Y, f_Z	$\cos\gamma$, $\cos\gamma$, $-\sin\gamma$
h_o	$H_o/c_* = C_o(s) + \epsilon_{X_o} f_X h_X + \epsilon_{Y_o} f_Y h_Y + \epsilon_{Z_o} f_Z h_Z$ Dimensionless zeroth-order film thickness
h_1	$\Delta\epsilon_\alpha\ f_\alpha\ h_\alpha$. First-order film thickness function.
h_X, h_Y, h_Z	$\cos\theta$, $\sin\theta$, +1. Circumferential film thickness components.
H_r	Recess depth [m]
$K_{\alpha,\beta}$	Force stiffness coefficients due to displacements [N/m], (α,β = X,Y,Z)
L, L_R, L_L	Bearing axial length = $L_R + L_L$ [m], Right and left axial side lengths measured from recess center
l	Recess path length [m]
M	$U_\theta \cdot \sqrt{\beta \cdot \rho_r}$. Circumferential velocity Mach number
$M_{\alpha,\beta}$	Force inertia coefficients due to displacements [Ns^2/m], (α,β = X,Y,Z)

N_{recess}	Number of recesses on bearing
P,Ps,Pr	Fluid pressure, supply and recess pressures [N/m^2]
P^-_e,P^+_e	Pressures just before and after recess edge [N/m^2]
P_L,P_R	Discharge pressures on left and right sides of bearing [N/m^2]
P_*	Min{P_L,P_R}. Characteristic discharge pressure [N/m^2]
p	(P-P_*)/(P_s-P_*). Dimensionless fluid film pressure
p_X,p_Y,p_Z	Dimensionless dynamic (first-order) pressures
Q_{ro}	Orifice mass flow rate [kg/s].
R(s),R_*,r(s)	Bearing radius, Characteristic bearing radius [m], R(s)/R_*
Re_c	(ρ Ω C R/μ)$_*$. Nominal circumferential flow Reynolds number
Re^*_p	(ρ U C /μ)$_*$. (C/R)$_*$. Modified pressure flow Reynolds number
Re_s	(ρ ω C^2 /μ)$_*$. Nominal Squeeze film Reynolds number
R_{ea}	(ρ U_s C /μ)$_*$. Path flow Reynolds number
R_J, R_B	$(\rho/\mu)H\sqrt{[U_\theta-\Omega\cdot R)^2 + U_s^2}$ $(\rho/\mu)\ H\sqrt{[U_\theta^2+U_s^2]}$ Flow Reynolds numbers relative to journal and bearing surfaces
S,s	Path coordinate on plane of bearing surface [m], S/R_*
S_R,S_L	Bearing path lengths on right and left sides of bearing [m]
T_*	Fluid mean operating temperature [°K]
U_*	C^2_*(P_s-P_*)/(μ_*R_*). Characteristic pressure flow speed [m/s]
u_s,u_θ	(U_s,U_θ)/U_*. Dimensionless mean flow velocities in path (s) and circumferential (θ) directions
V_r,V_s	(H_r+H)A_r+V_s. Total recess volume, Volume of orifice supply line [m^3]
{X,Y,Z}	Inertial coordinate system
z	Z(s)/R_*. Dimensionless axial coordinate
β	(1/ρ)($\partial\rho/\partial$P). Liquid compressibility coefficient [m^2/N]
ϵ_X,ϵ_Y, ϵ_Z	(e_X,e_Y,e_Z)/C_*. Dimensionless journal eccentricities in X, Y, Z directions
$\Delta\epsilon_X$,$\Delta\epsilon_Y$,$\Delta\epsilon_Z$	Dimensionless dynamic (perturbed) eccentricities
γ	Local slope of path coordinate (S) relative to Z axis
η	H/(H_r+H). Ratio of land film thickness to recess depth
θ	Circumferential or angular coordinate
Θ_r	Recess angular length [rad]
$\kappa_s=\kappa_\theta$	1/2(κ_J+κ_B). Turbulence shear factors in (s,θ) flow directions
κ_J,κ_B	f_J R_J, f_B R_B. Turbulent shear parameters at journal and bearing surfaces
κ_r	(Re h_r)$^{0.681}$/7.753. Turbulent shear flow parameter at recess
ρ,ρ_*	Fluid density [kg/m^3], characteristic density [kg/m^3]
μ,μ_*	Fluid viscosity [Ns/m^2], characteristic viscosity [Ns/m^2]
$\xi_{\theta u}$,$\xi_{\theta d}$	Empirical recess-edge entrance loss coefficients in circumferential (upstream,downstream) direction
ξ_{sL},ξ_{sR}	Empirical recess-edge entrance loss coefficients in path direction (left and right of recess)
Ω,ω	Rotational speed of journal, excitation or whirl frequency [1/s]
τ	ωt. Dimensionless time coordinate
Γ_r	Recess boundary with outward normal $\vec{n}$.

INTRODUCTION

Hydrostatic Journal Bearings (HJBs) are the ideal candidates to replace roller bearings as support elements in cryogenic turbomachinery. These bearings will be used for primary space-power applications due to their mechanical simplicity, long lifetime, low friction and wear, significant load capacity, and large direct stiffness as well as damping force coefficients. HJBs, unlike rolling element bearings, have no limit on a DN constraint, and shaft speeds can be allowed to increase to a level more suitable for high operating efficiency with reduced overall turbomachinery weight and size. Durability in HJBs is assured by the absence of contact between static and moving parts during steady-state operation, while long life reduces the frequency of required overhauls. Despite these attractive features, fluid film bearing stability considerations due to hydrodynamic and liquid compressibility effects are a primary concern for operation at high rotational speeds along with large pressure differentials. The present technological needs call for reliable and resilient fluid film bearing designs which provide maximum operating life with optimum - controllable rotordynamic characteristics at the lowest cost (Scharrer, 1991, 1992a).

The analysis of the flow and force response in turbulent flow hydrostatic bearings is of complex nature and confined within the realm of classical lubrication theory until recently, see for example Redecliff and Vohr (1969), Artiles et al. (1982), Chaomleffel et al. (1986). HJBs for process liquid applications present unique flow conditions, requiring for low viscosity liquids large levels of external pressurization to provide adequate load capacity and radial stiffness support. Typical pressure drops across a HJB can be as large as 30MPa and determine a fully inertial - turbulent fluid flow with significant variation of the liquid material properties across the flow region.

San Andres (1990,1992a) introduced turbulent - inertial bulk-flow models for the analysis of compressible liquid (**barotropic**) HJBs. Extensive numerical predictions have revealed the importance of fluid inertia at the film lands and at the recess boundaries of typical high speed HJBs. San Andres (1991a) shows that moderate to large journal eccentricities have a pronounced effect on the force coefficients of HJBs with large hydrodynamic effects (high rotational speeds). Furthermore, orifice back-flow along with a sudden drop on direct stiffness are likely to occur at large eccentricity operation.

Kurtin et al. (1991), Franchek (1992), and Mosher (1993) present relevant experimental data for the static and dynamic force characteristics of water lubricated, turbulent flow, hydrostatic bearings. Experimental measurements are routinely performed for hydrostatic bearings of different geometries and at journal speeds ranging from 10,200 to 24,600 rpm and pressure supplies from 4 to 7 MPa. These references also present extensive comparisons of test results with numerical predictions based on the models of San Andres (1990, 1992a). In general the correlation between experimental and theoretical results is very good for conventional HJB geometries. It is noted that accurate theoretical results depended greatly on the knowledge of the bearing operating clearance, and most importantly, on the orifice discharge coefficients.

Adams et al. (1992) have also presented test results for the rotordynamic force coefficients of a four pad, one recess/pad, laminar flow, hydrostatic bearing. The experiments were performed with SAE 30 oil and at low rotational speeds (1000 and 2000 rpm) and low pressure supplies (max. 2.6 MPa, 375psig). Force stiffnesses and direct damping coefficients seem to be well identified while cross-coupled damping and inertia force coefficients show a rather unexpected behavior.

The threshold speed of instability and the whirl frequency ratio (WFR) define the stability characteristics of a simple rotor-bearing system. This instability is of the hydrodynamic type and solely due to the effect of journal rotational speed on the flow field. Incompressible liquid hydrostatic bearings present a whirl frequency ratio identical to that of plain journal bearings (WFR ~ 0.5). This condition,

as also verified experimentally by Mosher (1993), then limits severely the application of HJBs to high speed, light weight turbomachinery. HJBs handling highly compressible liquids, such as LH_2 for example, are prone to show a self-excited type instability of the pneumatic hammer type and can produce negative damping force coefficients for low frequency excitations. Dynamic operation under these conditions will then result in a poor stability indicator (WFR) greater than 0.50. This important result, although first reported by Redecliff and Vohr (1969), has been largely overlooked until recently.

Recommended fixes to improve the limited dynamic stability of turbulent flow hydrostatic bearings are:

- Use of large scale roughened bearing surfaces to reduce the cross-coupled stiffness coefficients directly promoting hydrodynamic bearing instability (Franchek,1992).
- Use of end seal restrictions or wear end-rings (Scharrer et al., 1992b) to control bearing leakage, increase the damping coefficients, and add a degree of safety for start-up and shut-down transient operation.
- Use of liquid injection opposing journal rotation to reduce the development of the circumferential flow velocity and eliminate the cross-coupled stiffness coefficient (Franchek, 1992).

The development of a leading technology in HJBs calls also for a bearing geometry not only able to provide radial load support but also with the capability to handle axial loads accompanied by shaft dynamic axial excurtions (Sutton et al., 1991). Spherical bearings offer this advantage along with the capability to tolerate large levels of static and dynamic misalignment (from journal and bearing) without alteration of the bearing performance. Furthermore, the recent developments in CNC manufacturing processes allow to machine spherical surfaces almost as quickly and economically as cylindrical surfaces (Craighead, 1992).

Goenka et al. (1980) and Craighead et al. (1992) have provided analysis of spherical journal bearings for laminar/turbulent flow applications. However, in high-speed, turbulent flow applications with process liquids of low viscosity, fluid inertia effects need to be accounted. Most notably, centrifugal flow acceleration terms are of particular importance for these operating conditions. The present study considers the analysis of hemispherical hydrostatic bearings with a barotropic liquid. Turbulent bulk-flow equations of motion are derived and solved numerically using an efficient CFD algorithm. Numerical predictions for the load capacity (radial and axial) and dynamic force coefficients for a LO_2 HJB are presented and discussed in detail.

ANALYSIS

Consider, as shown in Figure 1, the flow of a variable properties liquid in the thin film region between an inner rotating journal and a stationary bearing. Cryogenic liquids are characterized by low viscosities, and thermal (energy transport) effects due to friction heating and kinetic energy variations are expected to be of minor importance in the performance of hydrostatic bearings. This assertion is not fully justified for especial operating conditions (see for example Yang et al., 1992a). On the other hand, due to the large levels of pressure differential required to provide substantial load capacity, the effects of pressure on the liquid properties, and ultimately on bearing performance, are thought to be of primary importance.

Figure 2 shows the journal outer surface as a surface of revolution formed by rotating the curve R(Z) about the axis Z. The path (S) and circumferential (θ) coordinates are used as independent spatial variables. The coordinates {Z,R} defining the journal surface are expressed as parametric functions of the path coordinate S. Trigonometric function of the angle γ defining the local slope of the path relative to the axis (Z) are given by:

$$\tan\gamma = -\frac{dR}{dZ}; \qquad \sin\gamma = -\frac{dR}{dS}; \qquad \cos\gamma = \frac{dZ}{dS} \tag{1}$$

where the coordinate relationships for journal/bearing spherical surfaces are:

$$\gamma = \frac{S}{R_*}; \qquad R(S) = R_* \cos\gamma, \qquad Z(S) = R_* \sin\gamma \tag{2}$$

and $R_*(=D_*/2)$ corresponds to the journal radius at the bearing axial midplane.

At operating conditions, the journal position relative to the bearing housing is described with reference to the inertial axes {X,Y,Z} by the journal center displacements ($e_X(t)$, $e_Y(t)$, $e_Z(t)$). Simple geometrical relationships determine the film thickness in the flow region to be given by the following expression (Goenka et al., 1980, Childs,1989):

$$H(S,\theta,t) = C(S) + e_X \cos\gamma\cos\theta + e_Y \cos\gamma \sin\theta - e_Z \sin\gamma \tag{3}$$

In a spherical bearing, journal axis rotations or misalignment provide no film thickness variation on the flow region. C(S) in (3) above is a general function describing the radial clearance variation along the path coordinate for the journal centered position.

The equations of motion

The turbulent bulk-flow equations for a variable properties (**barotropic**) liquid on the thin film lands of the spherical bearing are given as (Childs, 1989):

Equation of continuity:

$$\frac{\partial}{\partial t}(\rho H) + \frac{\partial}{R\partial S}(\rho H U_S R) + \frac{\partial}{R\partial\theta}(\rho H U_\theta) = 0 \tag{4}$$

Path momentum equation

$$-H\frac{\partial P}{\partial S} = \frac{\mu}{H}(k_s U_s) + \frac{\partial(\rho H U_S)}{\partial t} + \frac{1}{R}\left\{\frac{\partial(\rho H U_S U_S R)}{\partial S} + \frac{\partial(\rho H U_\theta U_S)}{\partial\theta} - \rho H U_\theta^2 \frac{dR}{dS}\right\} \tag{5}$$

Circumferential momentum equation:

$$-H\frac{\partial P}{R\partial\theta} = \frac{\mu}{H}\left\{k_\theta U_\theta - k_J \frac{\Omega R}{2}\right\} + \frac{\partial(\rho H U_\theta)}{\partial t} + \frac{1}{R}\left\{\frac{\partial(\rho H U_S U_\theta R)}{\partial S} + \frac{\partial(\rho H U_\theta U_\theta)}{\partial\theta} + \rho H U_S U_\theta \frac{dR}{dS}\right\} \tag{6}$$

on the region $\{-S_L \le S \le S_R;\ 0 \le \theta \le 2\pi\}$; and where, $k_s = k_\theta = (k_J + k_B)$ are the wall shear stress difference coefficients taken as local functions of the turbulent friction factors, Reynolds numbers and surface conditions, i.e, $k_J = f_J R_J$, $k_B = f_B R_B$ (Hirs, 1973, San Andres,1992a). For inertialess-laminar fluid flows the equations above reduce to the classical form given by Goenka and Booker (1980) for spherical bearing geometries.

For cryogenic liquids such as LH2, LO2, LN2, and LCH4, the fluid properties are calculated from the Benedict-Web-Rubin equation of state as given in the standard computer program and data base of McCarty(1986).

Recess Flow and Pressure equations:

A mass conservation equation at each bearing recess of area (1. $R_*.\theta_r$) and depth H_r is defined by the global balance between the mass flow through the orifice restrictor (Q_{ro}), the mass flow into the film lands and the time rate of change of liquid mass within the recess volume V_r. This equation is given as:

$$Q_{ro} = A_o\sqrt{2\rho_r(P_S - P_R)} = \int_{\Gamma_r} \rho H(\vec{U}\cdot\vec{n})d\Gamma_r + \rho_r\frac{\partial V_r}{\partial t} + \rho_r V_r\beta\frac{\partial P_r}{\partial t} \qquad (7)$$

$$for\ r = 1,2,\ldots,Nrecess$$

where $\beta=(1/\rho)\partial\rho/\partial P$ represents the fluid compressibility material coefficient at the recess volume, and Γ_r is the closure of the recess volume with the film lands and with normal n along the boundary line. Note that the orifice flow equation is valid only for small changes of the liquid density (Hall et al., 1986).

The fluid edge pressure at the entrance to the film lands is given by the superposition of viscous shear effects on the recess extent and an entrance drop due to fluid inertia. On the circumferential direction, the pressure rise (P_e) downstream of the recess orifice is given by (Constantinescu et al., 1987, San Andres, 1992a):

$$P_e^- = P_r - \mu_r k_r\frac{R_*\Theta_r}{2H_r^2}\left[U_\theta(\rho_e^-/\rho_r)\eta - \frac{\Omega R(s)}{2}\right]\frac{1}{(1-M^2)} \qquad (8)$$

where M is the circumferential flow local Mach number at the orifice discharge.

The entrance pressures (P_e) to the film lands in the circumferential and axial directions are given by:

$$P_e^+ = P_e^- - \frac{\rho_e^+}{2}(1+\xi_\theta)\left\{1 - \left(\rho_e^+/\rho_e^-\right)^2\eta^2\right\}U_\theta^2, \qquad (9)$$

$$P_e^+ = P_r - \frac{\rho_e^+}{2}(1+\xi_s)\left\{1 - (\rho_e^+/\rho_e^-)^2\eta^2\right\}U_s^2 \qquad (10)$$

$$for\ r = 1,2\ldots,Nrecess$$

The Bernoulli like pressure drop in equations (10) is considered only if the fluid leaves the recess towards the film lands. If on the contrary, fluid enters from the film lands into the bearing recess, then the edge pressure takes the value of the recess pressure (P_r). This consideration is based on momentum conservation for turbulent shear flows in sudden expansions and also on the fundamental measurements of Chaomleffel et al.(1986). The inertial pressure drop given above does not account for centrifugal flow effects in the spherical bearing geometry since the change in the bearing radial coordinate from recess edge to film lands is small.

Boundary Conditions:

Due to periodicity, the pressure and velocities are continuous and single-valued in the circumferential direction Θ; i.e.,

$$P, U_s, U_\theta(S,\Theta,t) = P, U_s, U_\theta(S,\Theta + 2\pi,t) \tag{11}$$

At the bearing side discharge planes, the fluid pressure is equal to specified values of discharge or sump pressures, i.e.:

$$\begin{aligned} &\textit{at the right plane,}\ Z = +L_R \quad P(+S_R,\theta) = P_R(\theta) \\ &\textit{at the left plane,}\ Z = -L_L \quad P(-S_L,\theta = P_R(\theta) \end{aligned} \tag{12}$$

In general the discharge pressures are uniform and constant. However, in some cryogenic turbopump applications the bearing may be located close to the pump-impeller discharge. In this case, the sump pressures are non-uniform though rotationally symmetric and expressed by a Fourier series. The boundary conditions described are valid for fluid flows well below sonic conditions.

Perturbation Analysis

Consider the journal center to describe small amplitude harmonic motions about an equilibrium static position. That is, let the journal center displacements be given as

$$e_X(t) = e_{Xo} + \Delta e_X e^{iwt},\quad e_Y(t) = e_{Yo} + \Delta e_Y e^{iwt},\quad e_Z(t) = e_{Zo} + \Delta e_Z e^{iwt};\quad i = \sqrt{-1} \tag{13}$$

where ω denotes the frequency of the whirl motion. The magnitudes of the dynamic perturbations in journal displacements, $|\{\Delta e_X, \Delta e_Y, \Delta e_Z\}/C_*|$ are very small (i.e. $<<<$ 1). Then, the film thickness is given by the superposition of steady-state (h_o) and dynamic (h_1) components given by the real part of the expression:

$$h = h_0 + h_1 e^{iwt} \tag{14a}$$

$$\textit{where}\ h_0 = \overline{C}_0(s) + \{\varepsilon_{Xo}\cos\theta + e_{Yo}\sin\theta\}\cos\gamma - \varepsilon_{Zo}\sin\gamma \tag{14b}$$

$$h_1 = \Delta\epsilon_\alpha f_\alpha h_\alpha = \Delta\epsilon_X f_X h_X + \Delta\epsilon_Y f_Y h_Y + \Delta\epsilon_Z f_Z h_Z \tag{14c}$$

$$\textit{with}\quad f_x(s) = f_Y(s) = \cos\gamma;\quad f_Z = -\sin\gamma,\quad \textit{and}\quad h_X = \cos\theta;\quad h_Y = \sin\theta,\ h_Z = 1 \tag{15}$$

are the film thickness perturbed functions along the path and circumferential coordinates, respectively. These functions greatly facilitate the comprehension of the perturbed flow field equations and the resulting rotordynamic force coefficients given latter.

The flow field variables (U_s,U_Θ,P), as well as the fluid properties (ρ,μ) and the shear parameters (k_Θ,k_s) are also formulated as the superposition of zeroth-order and first-order complex fields describing the static equilibrium condition and the perturbed dynamic motion, respectively. In general, these fields are expressed as:

$$\Psi = \Psi_o + e^{i\tau}\{\Delta\varepsilon_X\Psi_X + \Delta\varepsilon_Y\Psi_Y + \Delta\varepsilon_z\Psi_Z\} = \Psi_o + e^{i\tau}\,\Delta\varepsilon_\alpha\,\Psi_\alpha \quad , \qquad \alpha = X, Y, Z \tag{16}$$

San Andres (1990,1992a) and Yang (1992b) discuss the procedure for the numerical solution of the non-linear flow equations. The differential equations of motion are integrated on staggered control volumes for each primitive variable. Program computing time is relatively small since the code uses accurate approximate analytical solutions to initiate the computational procedure and accelerate convergence to a solution defined by the operating parameters and bearing geometry.

Fluid Film Forces and Dynamic Force Coefficients

Fluid film forces are calculated by integration of the zeroth-order pressure field on the journal surface,

$$\begin{bmatrix} F_{Xo} \\ F_{Yo} \\ F_{Zo} \end{bmatrix} = (P_s - P_*)R_*^2 \int_{-s_L}^{s_R} \int_{\theta_i}^{\Theta_i + 2\pi} P_o \cdot \begin{bmatrix} f_X \cdot \cos\theta \\ f_Y \cdot \sin\theta \\ f_Z \cdot 1 \end{bmatrix} r \cdot ds \cdot d\theta \tag{17}$$

The perturbation analysis allows the dynamic force coefficients due to journal center displacements to be obtained from the general expression for dynamic forces given as:

$$\begin{bmatrix} \Delta F_x \\ \Delta F_Y \\ \Delta F_Z \end{bmatrix} = - \begin{bmatrix} K_{XX} & K_{XY} & K_{XZ} \\ K_{YX} & K_{YY} & K_{YZ} \\ K_{ZX} & K_{ZY} & K_{ZZ} \end{bmatrix} \begin{bmatrix} \Delta e_X \\ \Delta e_Y \\ \Delta e_Z \end{bmatrix} - \begin{bmatrix} C_{XX} & C_{XY} & C_{XZ} \\ C_{YX} & C_{YY} & C_{YZ} \\ C_{ZX} & C_{ZY} & C_{ZZ} \end{bmatrix} \begin{bmatrix} \Delta \dot{e}_X \\ \Delta \dot{e}_Y \\ \Delta \dot{e}_Z \end{bmatrix} - \begin{bmatrix} M_{XX} & M_{XY} & M_{XZ} \\ M_{YX} & M_{YY} & M_{YZ} \\ M_{ZX} & M_{ZY} & M_{ZZ} \end{bmatrix} \begin{bmatrix} \Delta \ddot{e}_X \\ \Delta \ddot{e}_Y \\ \Delta \ddot{e}_Z \end{bmatrix} \tag{18}$$

where the force coefficients due to journal center displacements are given by:

$$K_{\alpha\beta} - \omega^2 \cdot M_{\alpha\beta} + i\,\omega \cdot C_{\alpha\beta} = - \frac{(P_s - P_*)R_*^2}{C_*} \int_{-s_L}^{s_R} \int_{\theta_i}^{\theta_i + 2\pi} p_\beta f_\alpha \cdot h_\alpha r \cdot ds\, d\theta \tag{19}$$

$$\alpha, \beta = X, Y, Z$$

RESULTS AND DISCUSSION

Experimental results for the steady state and dynamic force response characteristics of turbulent flow HJBs for process liquid applications are given by Kurtin et.al (1991), Adams et.al (1992), Franchek (1992), and Mosher (1993). These studies are relevant to the investigation of cylindrical bearing geometries with large pressure drops and high rotational speeds similar to those found in high performance turbomachinery components. Correlation of test measurements with predictions based on the present flow model are very favorable for smooth surface HJBs (Franchek,1992, Yang,1992b, Mosher,1993).

Spherical hydrostatic bearings may provide a unique alternative for radial load support in cryogenic liquid turbopumps (Sutton et.al, 1991) since they also offer the distinct advantages of tolerance to journal misalignment and ability to withstand shaft axial motions by providing axial thrust. In the following, the static and dynamic performance characteristics of a spherical HJB geometry handling LO_2 are presented and discussed. Normalization of results and extensive parametric studies accounting for variations in the bearing geometrical and operating parameters would be impractical due to the complex nature of the flow field and force response in turbulent hydrostatic bearings. It suffices to say that the example presented corresponds to a bearing element designed for optimal radial support at the rated operating conditions.

Table 1 shows the geometry and operating conditions of a 6 recess, LO_2 hydrostatic bearing with a fixed pressure drop across the bearing (2,000 psi) and a rotational speed equal to 22.5 Kcpm. The spherical bearing diameter (D_*) and axial length (L) are equal to 91.036 mm and 64.37 mm, respectively. The exit diameter of this bearing is equal to 64.37 mm and the arc described by the spherical path between the bearing middle and discharge planes is equal to $\gamma^*=45°$. At the rated conditions, a recess pressure ration (P_r) equal to 0.55 provides maximum direct stiffness coefficients and requires orifices of diameter equal to 2.37 mm. Table 1 also includes values for the empirical recess-edge non - isentropic loss parameters (ξ) and orifice discharge coefficients (C_d) used in the analysis. The values chosen are representative from those used in the extensive experimental - theoretical studies of Kurtin et al. (1991) and Franchek (1992). The regime of operations of the bearings is fully turbulent with circumferencial (R_{cc}) and axial flow (R_{ca}) Reynolds numbers equal to 56,900 and 35,857, respectively. A comprehensive study and comparison between the performance characteristics of equivalent cylindrical and spherical HJBs can be found in the work of San Andres (1992b).

Numerical predictions are presented for the static and dynamic force characteristics of the bearing for increasing values of the axial journal eccentricity (e_Z) while the journal center is displaced radially towards the middle of the bottom recess, i.e. e_X varies and $e_Y=0$. From equation (3), the maximum axial journal displacement is equal to $\varepsilon_Z = (1- \varepsilon_X \cos \gamma^*)/\sin \gamma^*$, where γ^* corresponds to the spherical angle at the bearing discharge, that is 45° for the example presented.

Figure 3 shows the radial load of the bearing as the static eccentricity (e_X) increases and for values of axial journal displacement (e_Z) equal to 0.0 and 0.60, respectively. The results show the load to increase linearly with the journal lateral displacement denoting a bearing with uniform stiffness characteristics for most eccentricities. The effect of the axial journal motion is relatively small on the total bearing load. Figure 4 shows the restoring force ($-F_Z$) as the axial journal is displaced towards the bearing shell and for increasing values of the static lateral eccentricity (ε_X). The axial force appears to be linear with displacement and increases with the radial journal displacement. Note that the thrust load (F_Z) is about 1/5 of the radial load, and shows the spherical bearing to have a limited axial load capacity in comparison with its radial load support.

Figures 5 and 6 show the direct (K_{XX},K_{YY}) and cross-coupled (K_{XY}, K_{YX}) radial force stiffness coefficients, and Figure 7 presents the direct damping coefficients (C_{XX},C_{YY}) for increasing values of the journal eccentricity e_X. The figures show the axial journal center displacements (e_Z) not to affect these coefficients except at large lateral eccentricities (ε_X). Note that the radial force coefficients are relatively constant for radial eccentricities as large as 50% of the bearing clearance and show clearly the major benefit of a hydrostatic bearing. A lucid discussion on the effect of these radial coefficients on the rotordynamic lateral force response can be found elsewhere (San Andres, 1991a).

Figures 8 and 9 show the direct axial stiffness (K_{ZZ}) and direct damping (C_{ZZ}) coefficients for dynamic journal axial motions as the lateral eccentricity (ε_X) increases. These coefficients increase with the journal axial position and show a significant rise at moderately large radial eccentricities. At the

concentric position ($\varepsilon_X = \varepsilon_Y = 0$), the axial stiffness is about 1/5 of the radial stiffness (K_{XX}), and the axial damping C_{ZZ} is approximately 11% of the direct lateral damping (C_{XX}). Thus, the axial force coefficients are relatively small when compared to the radial force coefficients. On the other hand, the magnitudes of the axial force coefficients are still significant in terms of their ability to sustain limited dynamic axial load conditions. For example, from Figure 4 it is inferred that the spherical HJB can tolerate safely an axial load as large as 5,000 N (1,125 lbs).

Cross-coupled axial force coefficients (K_{ZX},K_{ZY},C_{ZX},C_{ZY}) due to journal lateral motions, and radial force coefficients (K_{XZ},K_{YZ},C_{XZ},C_{YZ}) due to journal axial motions are not reproduced here for brevity. The radial force coefficients are very small except for large journal center displacements and provide a measure in uncoupling between axial dynamic motions and lateral dynamic force response. The axial force stiffness (K_{ZX},K_{ZY}) are approximately 1/2 of the direct stiffness (K_{ZZ}) at ε_Z=0.80, ε_X=0, and decrease rapidly as the lateral eccentricity (ε_X) increases.

For completeness in the analysis, calculations were performed to determine whether fluid inertia effects, both advective and centrifugal, are of importance on the static and dynamic force performance characteristics of the spherical hydrostatic bearing. Table 2 presents a summary of the results for increasing values of the journal rotational speed at the bearing concentric position ($\varepsilon_X = \varepsilon_y = \varepsilon_Z = 0$). The orifice diameter and loss coefficients are identical for the simulations. A comparison of results shows large differences on the recess pressure ratio (P_r) and the force coefficients. Fluid inertia acts as an additional flow resistance and then determines larger recess pressures with a reduced flow rate. The most notable effect is related to the reduced magnitude of the direct radial stiffnesses ($K_{XX} = K_{YY}$). At the rated operating point, 22.5 Kcpm, the values of direct stiffness are equal to 240.9 and 308.5 MN/m for the bearing with and without fluid inertia effects. This corresponds to a net reduction in hydrostatic load capacity of 22% and it is a direct consequence of the increased flow resistance due to centrifugal effects on the curved flow path and also due to the larger recess pressures. It is evident from the results presented that fluid inertia effects need to be included in the analysis of high speed, turbulent flow HJBs.

CONCLUSIONS

An analysis for the performance characteristics of turbulent flow, orifice compensated, **spherical** hydrostatic journal bearing (HJBs) is presented. Hydrostatic bearings offer a substantial radial load capacity and can be used with process liquids of low viscosity if large pressure differentials across the bearing are available. On the other hand, the spherical bearing geometry allows tolerance for shaft misalignment without force performance degradation and it also has the ability to support thrust loads. The spherical HJB combines these advantages to provide a bearing design which could be used efficiently on high performance turbomachinery.

The motion of a barotropic liquid on the thin film bearing lands is described by bulk-flow mass and momentum equations. Zeroth-order equations describe the fluid flow field for a journal equilibrium position, while first-order linear equations govern the fluid flow for small amplitude journal center radial and axial motions. Solution to the zeroth-order flow field equations provides the bearing flow rate, radial/axial film forces and drag torque. Solutions to the first-order equations determine the rotordynamic force coefficients due to journal lateral and axial motions. Numerical predictions of load capacity and force coefficients for a 6 recess, spherical HJB in a LO_2 environment are presented for increasing values of the journal center radial and axial displacements. The results show that axial journal motions do not alter significantly the radial load capacity of the bearing. On the other hand, the spherical bearing geometry provides fluid film axial forces of a magnitude about 20% of the radial load capacity for the example analyzed. Fluid inertia effects, advective and centrifugal, are found to affect greatly the static and dynamic force performance of the bearing studied.

ACKNOWLEDGEMENTS

The generous support of the Rocketdyne Division of Rockwell International is gratefully acknowledged.

REFERENCES:

Adams, M., J.T. Sawicki, and R. Capaldi, 1992, "Experimental Determination of Hydrostatic Journal Bearing Coefficients," *Proceedings of the Institution of Mechanical Engineers*, Paper C432/145, International Conference in Vibrations in Rotating Machinery, IMechE 1992-6.

Artiles, A., Walowit, J., and W. Shapiro, 1982, "Analysis of Hybrid Fluid Film Journal Bearings with Turbulence and Inertia Effects," *Advances in Computer Aided Bearing Design*, ASME Publication No. G0020, pp. 25-51.

Chaomleffel, J, D. Nicholas, 1986, "Experimental Investigation of Hybrid Journal Bearings," *Tribology International*, Vol. 19, No. 5, pp. 253-259.

Childs, D., 1989, "Fluid-Structure Interaction Forces at Pump-Impeller-Shroud Surfaces for Rotordynamic Calculations," *ASME Journal of Vibration, Acoustics, Stress and Reliability in Design*, Vol.111, pp.216-225.

Constantinescu, V.N., and F. DiMofte, 1987, "On the Influence of the Mach Number on Pressure Distribution in Gas Lubricated Step Bearings," Rev. Roum. Sci. Tech. - Mec. Appl., *Tome* 32, No 1, pp. 51-56.

Craighead, I.A., and P.S. Leung, 1992, "An Analysis of the Steady State and Dynamic Characteristics of a Spherical Journal Bearing with Axial Loading," *Proceedings of the Institution of Mechanical Engineers*, Paper C432/016, International Conference in Vibrations in Rotating Machinery, IMechE 1992-6, September, pp. 337-343.

Franchek, N., 1992, "Theory Versus Experimental Results and Comparisons for Five Recessed, Orifice Compensated, Hybrid Bearing Configurations," Texas A&M University, M.S. Thesis, TAMU Turbomachinery Laboratories.

Goenka, P.K., and J. Booker, 1980, "Spherical Bearings, Static and Dynamic Analysis Via the Finite Element Method," *ASME Journal of Lubrication Technology*, Vol. 102, 3, pp. 308-319.

Hall, K.R., P. Eubank, J. Holste, and K. Marsh, 1986, "Performance Equations for Compressible Flow Through Orifices and Other ΔP Devices: A Thermodynamics Approach," *AIChe Journal*, Vol.32, No. 3, pp. 517-519.

Hirs, G.G., 1973, "A Bulk-Flow Theory For Turbulence in Lubricating Films," *ASME Journal of Lubrication Technology*, pp. 135-146.

Kurtin, K., Childs, D., San Andres, L.A., and K. Hale, 1991, "Experimental versus Theoretical Characteristics of a High Speed Hybrid (combination Hydrostatic and Hydrodynamic) Bearing," *ASME Transactions*, Paper No. 91-Trib-35.

Mosher, P., 1993, "Experimental versus Experimental and Theoretical Characteristics of Five Hybrid (Combination Hydrostatic and Hydrodynamic) Bearing Designs for Use in High Speed Turbomachinery,"

M.S. Thesis, Texas A&M University.

McCarty, R.D., 1986, NBS Standard Reference Data Base 12, Thermophysical Properties of Fluids, MIPROPS 86, Thermophysics Division, Center for Chemical Engineering, National Bureau of Standards, Colorado.

Redecliff, J.M. and J.H. Vohr, 1969, "Hydrostatic Bearings for Cryogenic Rocket Engine Pumps," *ASME Journal of Lubrication Technology*, pp. 557-575.

San Andres, L.A., 1990, "Turbulent Hybrid Bearings with Fluid Inertia Effects", *ASME Journal of Tribology*, Vol. 112, pp. 699-707.

San Andres, L.A., 1991a, "Effect of Eccentricity on the Force Response of a Hybrid Bearing," *STLE Tribology Transactions*, Vol. 34, 4, pp.537, 544.

San Andres, L.A., 1992a, "Analysis of Turbulent Hydrostatic Bearings with a Barotropic Fluid," *ASME Journal of Tribology*, Vol. 112, 4, pp. 755-765.

San Andres, L.A., 1992b, "Analysis of Turbulent Bulk-Flow Hydrostatic Pad Bearings with a Barotropic Liquid, Cylindrical and Spherical Bearings," Turbomachinery Laboratory, Texas A&M University.

Scharrer, J.K., J. Tellier, R. Hibbs, 1991, "A Study of the Transient Performance of Hydrostatic Journal Bearings: Part I-Test Apparatus and Facility, Part II-Experimental Results," *STLE Tribology Transactions*, Preprint 91-TC-3B-2.

Scharrer, J.K., and T.W. Henderson, 1992a, "Hydrostatic Bearing Selection for the STME Hydrogen Turbopump," AIAA Paper 92-3283, 28th AIAA/SAE/ASME/ASEE Joint Propulsion Conference, Tennessee.

Scharrer, J.K., and L. San Andres, 1992b, "The Axisymmetrically Stepped, Orifice Compensated Hydrostatic Bearing," AIAA Paper 92-3405.

Sutton, R., J. Scharrer, and R. Beatty, 1991, "Hydrostatic Bearing for Axial/Radial Support," Official Gazette, U.S. Patent 5,073,036.

Yang, Z., San Andres, L., and D. Childs, 1992a, "Thermal Effects in Cryogenic Liquid Annular Seals, I: Theory and Approximate Solutions; II: Numerical Solution and Results", *ASME Transactions*, Papers 92-TRIB-4, 92-TRIB-5.

Yang, Z., 1992b, "Thermohydrodynamic Analysis of Cryogenic Hydrostatic Bearings in the Turbulent Flow Regime," Ph.D. Dissertation, Texas A&M University.

Table 1. Geometry and Operating Conditions of 6 recess, LO_2 Spherical Hydrostatic Journal Bearing.

Dimensions : Number of recesses Nrec = 6.

clearance, c=101.6μm(0.004 in), recess depth, Hr=381μm(0.015in); Hr/c=3.75

Spherical: Diameter, D*=91.036mm (3.58in); Path Length, S=71.50mm (2.815in) ; D_R= 64.372mm (2.5534in);
Axial length, L= 64.372mm (2.5534in); L/D* = 0.707, R*/c=448.0
Spherical angle $\gamma/2$= 45 deg.

Recess: length l=31.74mm(1.25 in), circumferential length Θr=30.0 deg.

journal and bearing surface conditions: smooth

Orifice C_d=0.89, diameter d_o=2.377mm for concentric recess pressure ratio pr=0.55,

Recess edge (non-isentropic) coefficients ξ_{xo}=0.0; ξ_{xa}=0.50; ξ_r=0.0

Operating Parameters: rotational speed: 2.356 rad/s (22.5 Kcpm)
Pressure supply, Ps=15.16 MPa (2.200 psia)
exit, Pa= 1.38 MPa (200 psia)

Fluid: LO_2 at 90K (162 R), μ_s=0.22454E-3 Pa-s, ρ_s=1.172 Kg/m3
μ_a=0.19813E-3 Pa-s, ρ_a=1.144 Kg/m3
β =0.1696-8 1/Pa=1..(85.52 kpsi)..

TYP Reynolds numbers:
$Re_{circ}=\rho_s\Omega R^* c/\mu_s$=56.900 ;
$Re_{axial}=\dot{m}/(2\pi D_R \mu_a)$= 35.857. Mass flow rate concentric=2.8735 kg/s

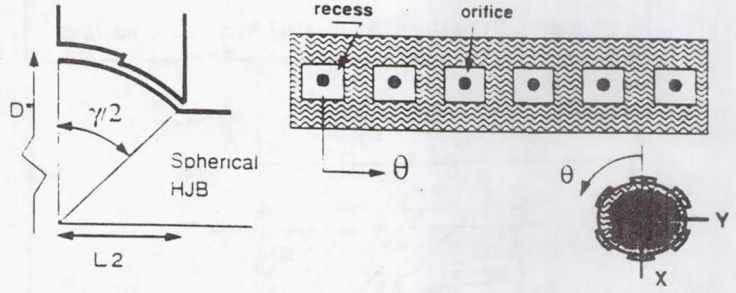

Table 2
Spherical hydrostatic bearing performance characteristics
Effect of Fluid Inertia

(a) Model with fluid inertia effects, d_o=2.37mm

Speed (Kcpm)	Pr-Pa / Ps-Pa	Mass flow (kg/s)	Torque (N·m)	$K_{XX}=K_{YY}$	$K_{XY}=-K_{YX}$ (MN/m)	K_{ZZ}	$C_{XX}=C_{YY}$	$C_{XY}=-C_{YX}$ (MN·s/m)	C_{ZZ}
0.00	0.4700	3.1314	0.000	179.32	0.00	6.82	151.90	0.00	19.30
12.50	0.4980	3.0160	2.833	229.20	112.30	6.74	153.60	16.86	19.50
22.50	0.5000	2.8735	5.980	240.90	198.90	6.43	165.30	25.50	19.70

(b) Model without fluid inertia effects, d_o=2.37mm

Speed (Kcpm)	Pr-Pa / Ps-Pa	Mass flow (kg/s)	Torque (N·m)	$K_{XX}=K_{YY}$	$K_{XY}=-K_{YX}$ (MN/m)	K_{ZZ}	$C_{XX}=C_{YY}$	$C_{XY}=-C_{YX}$ (MN·s/m)	C_{ZZ}
0.00	0.4157	3.2763	0.000	257.90	0.00	5.07	92.38	0.00	10.40
12.50	0.4302	3.2290	2.996	280.40	39.40	4.88	101.30	2.10	10.30
22.50	0.4632	3.1259	6.086	308.50	94.09	4.71	110.50	2.24	10.30

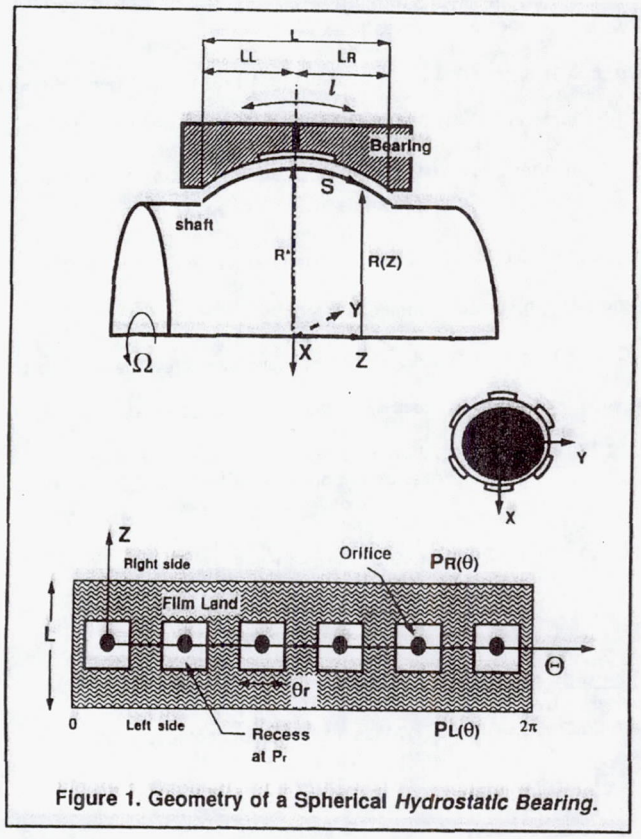

Figure 1. Geometry of a Spherical *Hydrostatic Bearing.*

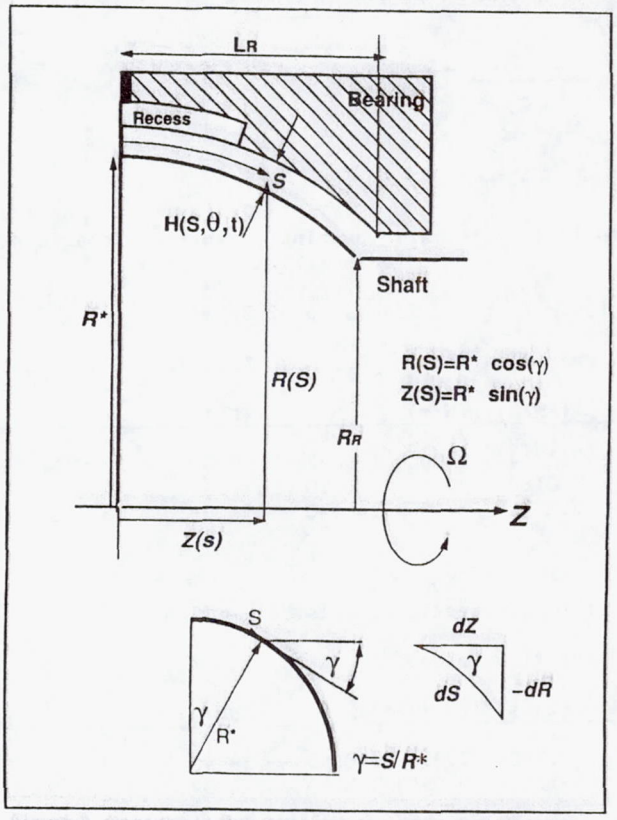

Figure 2. *Coordinate Relationships in a Spherical Bearing*

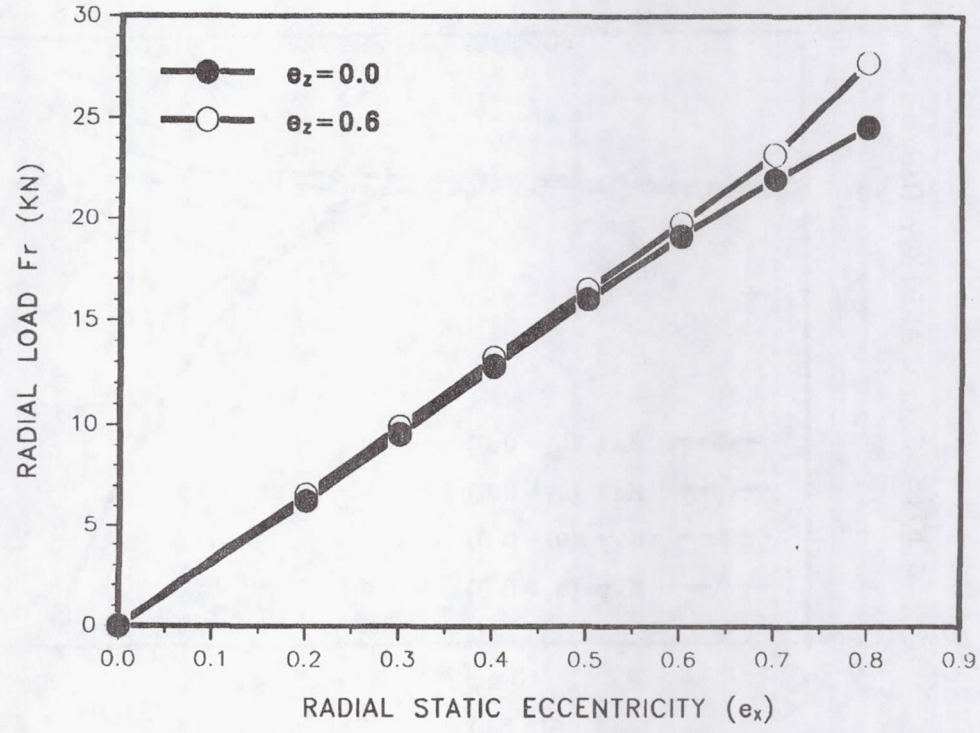

Figure 3. ***Radial Load vs. journal radial eccentricity (εx) for journal axial displacements εz=0.0 and 0.60***

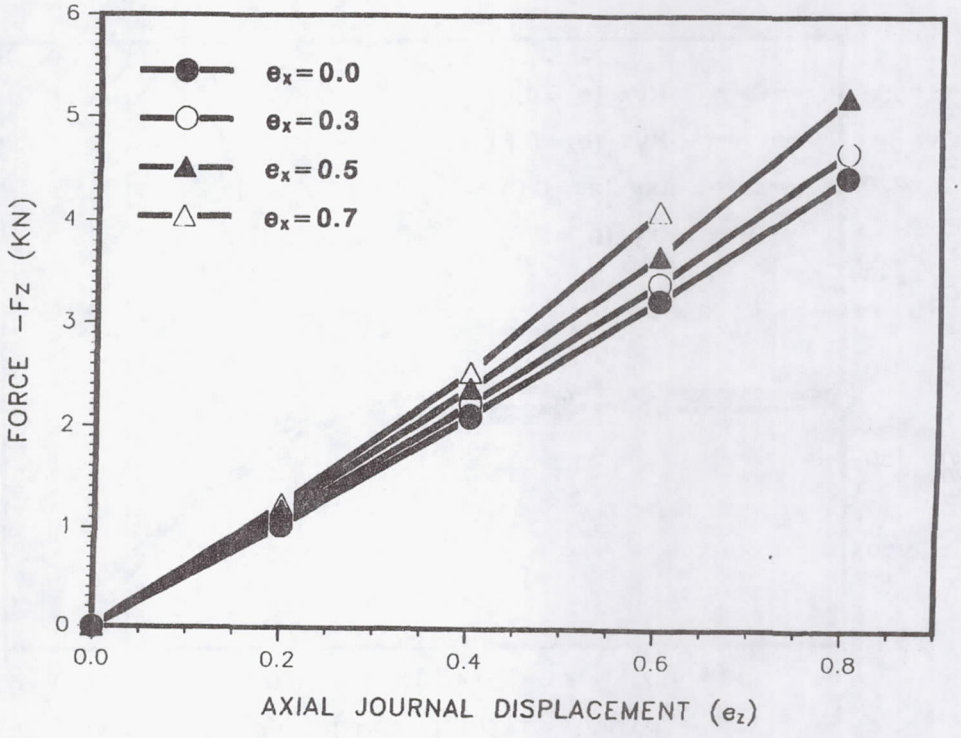

Figure 4. ***Axial force (−Fz) vs. journal axial eccentricity (εz) for increasing journal radial displacements εx.***

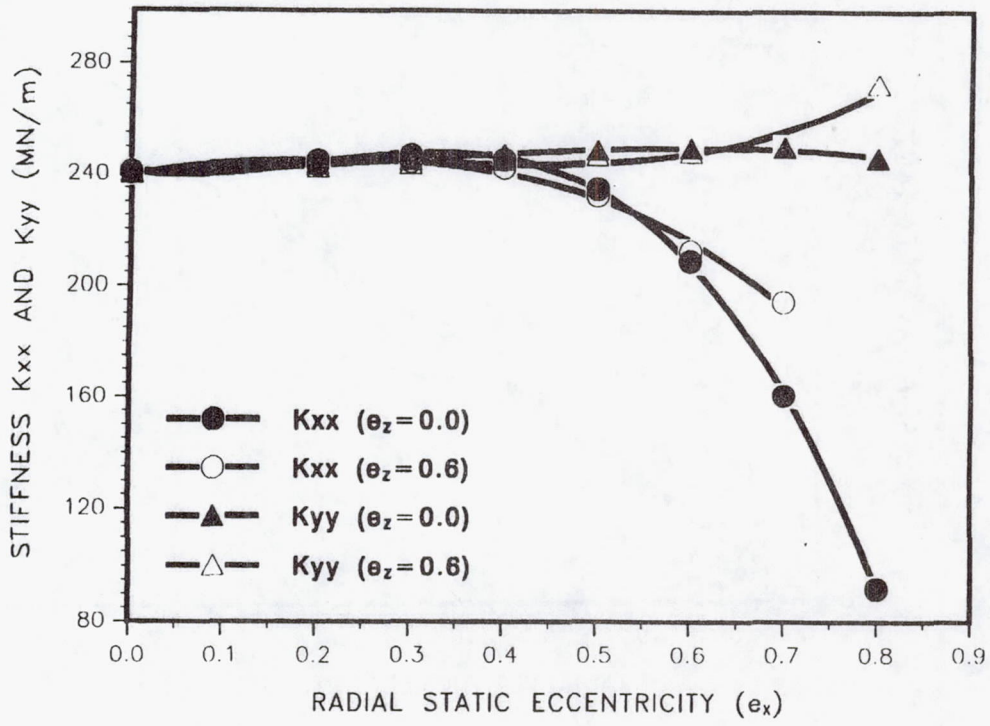

Figure 5. ***Lateral force stiffness coefficients (Kxx, Kyy) vs. journal radial eccentricity (εx) for journal axial displacements εz=0.0 and 0.60***

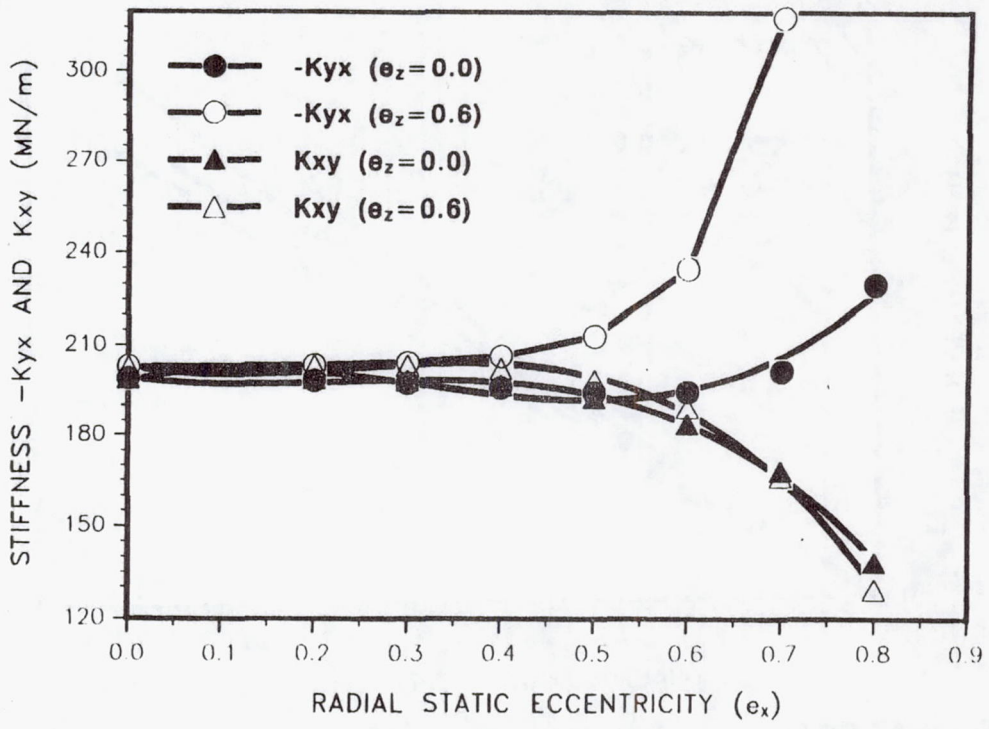

Figure 6. ***Lateral force stiffness coefficients (-Kxy, Kyx) vs. journal radial eccentricity (εx) for journal axial displacements εz=0.0 and 0.60***

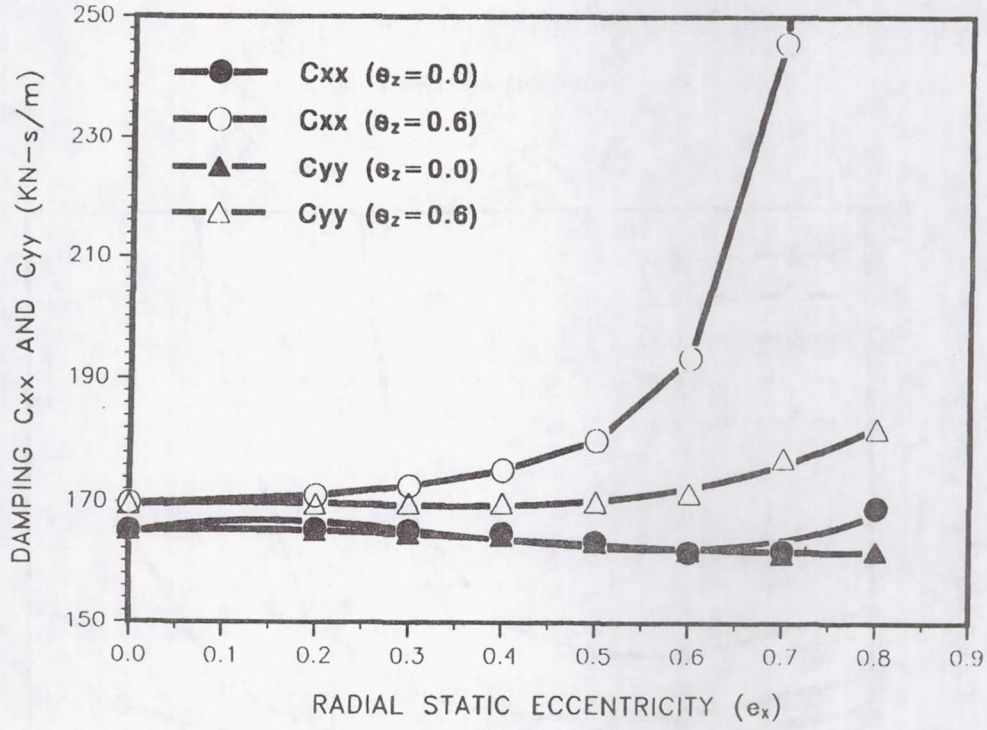

Figure 7. ***Lateral force damping coefficients (Cxx, Cyy) vs. journal radial eccentricity (εx) for journal axial displacements εz=0.0 and 0.60***

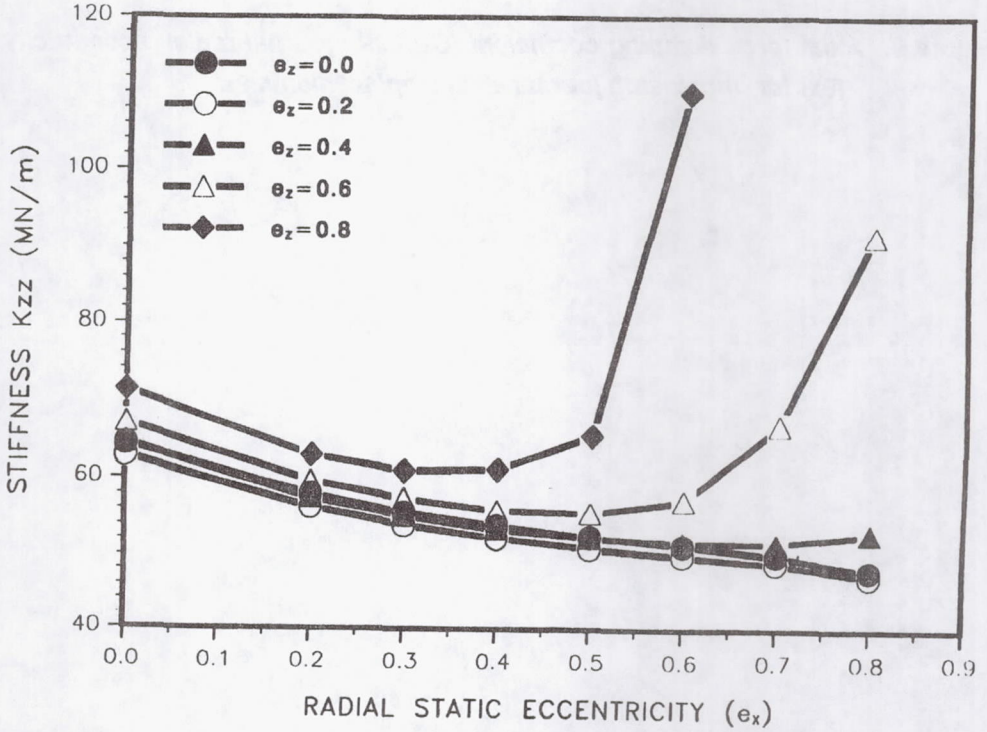

Figure 8. ***Axial force stiffness coefficient (Kzz) vs. journal radial eccentricity (εx) for increasing journal axial displacements εz***

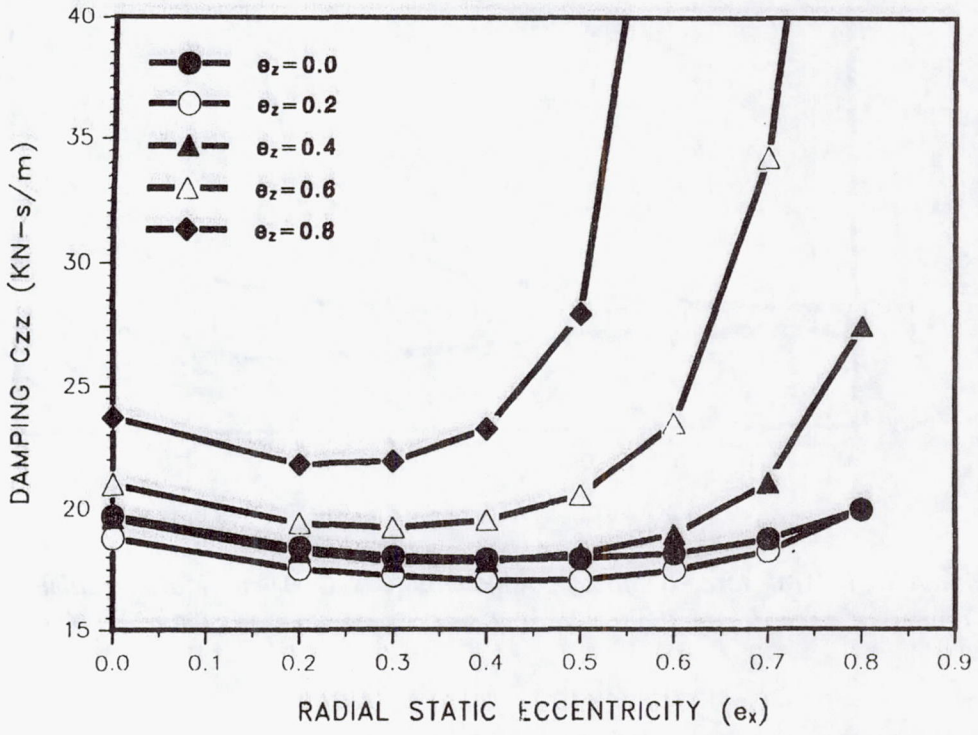

Figure 9. ***Axial force damping coefficient (Czz) vs. journal radial eccentricity (εx) for increasing journal axial displacements εz.***

A TEST APPARATUS AND FACILITY[1] TO IDENTIFY THE ROTORDYNAMIC COEFFICIENTS OF HIGH-SPEED HYDROSTATIC BEARINGS

Dara Childs and Keith Hale
Texas A&M University
College Station, Texas

Abstract

A facility and apparatus are described which determine stiffness, damping, and added-mass rotordynamic coefficients plus steady-state operating characteristics of high speed hydrostatic journal bearings. The apparatus has a current top speed of 29800 rpm with a bearing diameter of 7.62 cm (3 in.). Purified warm water, 55 °C (130 °F), is used as a test fluid to achieve elevated Reynolds numbers during operation. The test-fluid pump yields a bearing maximum inlet pressure of 6.9 Mpa (1000 psi). Static load on the bearing is independently controlled and measured. Orthogonally mounted external shakers are used to excite the test stator in the direction of, and perpendicular to, the static load. The apparatus can independently calculate all rotordynamic coefficients at a given operating condition.

Introduction

Experience with the SSME (Space Shuttle Main Engine) has demonstrated definite limits for the successful operation of ball bearings in liquid oxygen (LOX). Currently, bearings in the HPOTP (High Pressure Oxygen Turbopump) of the SSME experience accelerated wear at full power level. The balls in these bearings simply get smaller, rapidly. The problem has proven largely intractable. As a result, hydrostatic bearings have been proposed for many new turbopump applications because of their long lifetime, low friction factors, low wear, and their ability to use low-viscosity lubricants. For cryogenic applications, the bearings will be pressurized from pump-discharge flow. At zero speeds the bearings will be flooded but unpressurized. Rubbing will be experienced at start up and shut down as investigated by Scharrer et al. (1992 a, 1992 b). The present research concerns steady-state fully pressurized bearing operation.

The test apparatus and facility described here is used to develop **experimentally validated** tools to predict steady-state hydrostatic bearing operational data (resistance torque, static load, flowrate, temperature and pressure distributions, etc.) and rotordynamic coefficients for vibration analysis. By rotordynamic coefficients, we refer to the stiffness $\boldsymbol{K}$, damping $\boldsymbol{C}$, and added-mass $\boldsymbol{M}$ coefficients which are used in the following linearized force-displacement model for bearings

$$-\begin{Bmatrix} f_{bx} \\ f_{by} \end{Bmatrix} = \begin{bmatrix} K_{xx} & K_{xy} \\ K_{yx} & K_{yy} \end{bmatrix} \begin{Bmatrix} \Delta x \\ \Delta y \end{Bmatrix} + \begin{bmatrix} C_{xx} & C_{xy} \\ C_{yx} & C_{yy} \end{bmatrix} \begin{Bmatrix} \Delta \dot{x} \\ \Delta \dot{y} \end{Bmatrix} + \begin{bmatrix} M_{xx} & M_{xy} \\ M_{yx} & M_{yy} \end{bmatrix} \begin{Bmatrix} \Delta \ddot{x} \\ \Delta \ddot{y} \end{Bmatrix} \tag{1}$$

Here, $(\Delta x, \Delta y)$ define the motion of the bearing rotor relative to its stator, and (f_{bx}, f_{by}) are the components of the fluid film reaction force acting on the rotor. **Identification of the rotordynamic coefficients of Eq.(1) is a central objective of this research project.**

This paper describes the test-facility design requirements necessary to identify the rotordynamic coefficients and presents a sample of the resulting data for one bearing. The contents include results for a 7.62 cm (3 in.) diameter, square-recess, smooth-land, annular-fed and orifice-compensated hydrostatic journal bearing with an L/D ratio of 1 and a C_r/R ratio of 0.003. The design requirements and analysis techniques for determining the steady-state operational data are detailed thoroughly by Kurtin, et al.(1991) and will not be repeated here. Subsequent publications will provide test results for hydrostatic bearings with assorted recess shapes, distinct land patterns and roughness, varied area ratios, and tangential-injection against rotation.

[1] The research reported here was supported in part by Rocketdyne, Division of Rockwell International, under Contract No. R94QBA89-032182, NASA through the Texas A&M University Center for Space Power, Contract No. NAGW-1194, and The State of Texas Advanced Technology Research Program under Contract No. 4449.

Apparatus and Facility -- An Introduction and Overview

The Hydrostatic Bearing Test Stand illustrated in Figure 1 consists of the following major components. A base, fabricated from welded steel plates, supports the test section, gearbox, and drive motor. In the test section, two stainless steel pedestals spaced about 38 cm (15 inches) apart support a 7.62 cm (3 in.) diameter stainless steel high-speed rotor. The rotor is driven by a 93.2 Kw (125 HP) variable-speed electric motor through a 7:1 ratio speed-increasing gearbox via a disc-type coupling. The test-bearing stator supports itself on the rotor at a position midway between the support pedestals. A pneumatic cylinder provides a fixed-direction side load to the bearing.

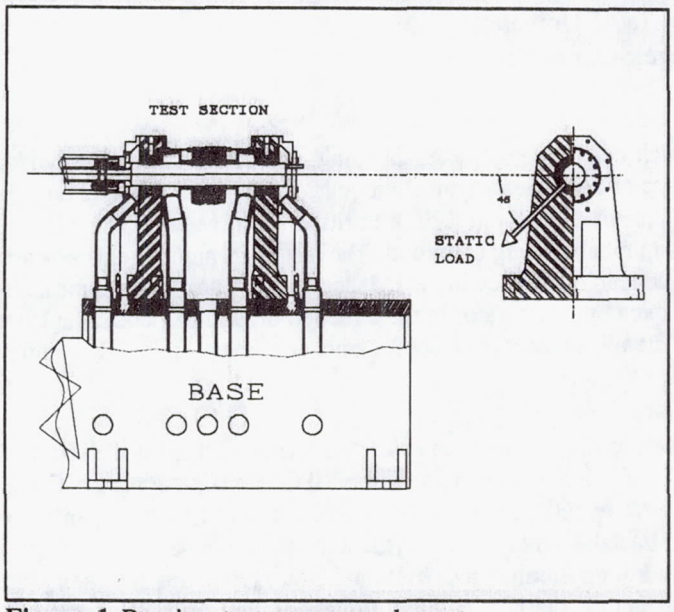

Figure 1 Bearing-test-apparatus layout

Two orthogonally mounted hydraulic shakers are attached to the stator through isolation stingers as illustrated in Figure 2. The shakers provide excitation parallel and perpendicular to the static side load along the X and Y directions, respectively. Each shaker can excite the stator with measured dynamic loads to 4450 N (1000 Lb) at frequencies to 1000 hz. The stingers were designed following guidelines by Mitchell and Elliott (1984). The static and dynamic loading arrangement of Figure 1 and Figure 2 is most closely related to that of Kanki and Kawakami (1984) who use orthogonal static loads from pneumatic cylinders in series with electromechanical shakers to excite the stator in a liquid-seal test rig. Glienicke (1966-67) is normally credited with the initial development of this rig type. Tonnesen and Hansen (1982) used this type of hydrostatic support bearings setup in static tests to investigate temperature effects of hydrodynamic bearings.

Preloaded axial cables arranged in an opposing trihedral configuration (Figure 3) constrain the shaft during static loading and dynamic excitation. A pitch mode instability of the stator with rotor onset speed around 17,000 rpm was also eliminated by these cables. This pitch restraint concept came from Nordmann and Massman (1984), who used a similar design on a liquid-seal test rig. The pitch-restraint cables have an additional advantage in insuring that the stator remains parallel to the rotor during excitation. Alternatively, they have been used to deliberately misalign a test bearing during excitation.

Returning to Figure 2, note that accelerometers are provided to measure the stator acceleration in the X and Y directions. Although not illustrated in Figure 2, the relative deflections $\Delta x(t),\Delta y(t)$ between the bearing rotor and stator are also measured with high-resolution eddy-current transducers. In summary, dynamic measurements at the bearing for rotordynamic coefficient identification include the dynamic excitation forces, the stator acceleration, and the relative rotor-stator deflections in the X and Y directions.

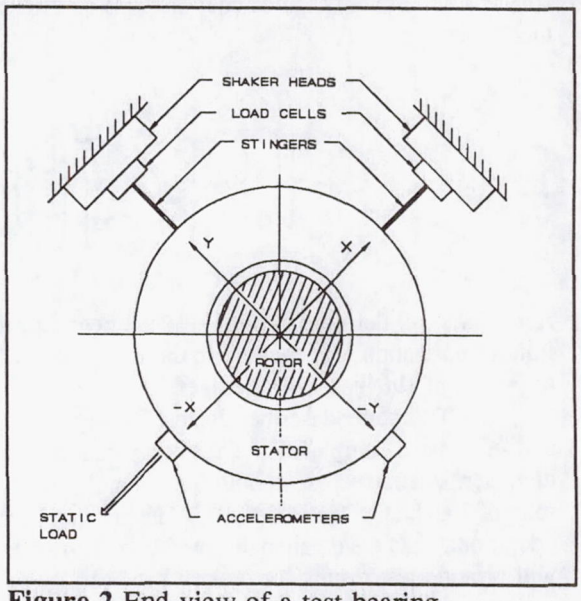

Figure 2 End view of a test bearing

Purified water at 55°C (130°F) is supplied to the

support and test bearings via a centrifugal pump with pressure and flow rate capacities of 6895 Kpa (1100 psi) and 303 liters/min (80 gpm), respectively. The main pump supplies the water to the test section through 10-micron absolute filters. The test-bearing flowrate is monitored by a turbine flowmeter and adjusted by a remotely-controlled valve. Nitrogen-backed accumulators provide a pressurized bearing coastdown in the event of a main pump failure. The water is elevated to test temperature by heat input from the main pump and test section. Two PID-controlled valves mix cooler water from a large 15,000 liter (4000 gallon) reservoir to maintain a constant fluid temperature at the test bearing inlet. The equipment is protected by an extensive logic-controlled monitoring and fault detection network capable of partially or totally unassisted safe shutdowns.

The test apparatus has been designed to facilitate rapid testing of multiple bearing configurations. The coupling design of Figure 1 allows rapid removal of a test rotor, followed by speedy replacement of a test bearing. A complete bearing test is accomplished in one week, including bearing and rotor installation, calibration, testing, and a computer-generated test report. Actual testing is computer driven and takes on the order of one-half day.

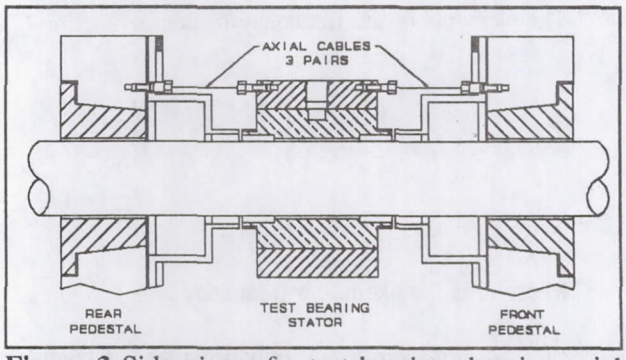

Figure 3 Side view of a test bearing showing axial tensioning cables

Rotordynamic-Coefficient Identification

The preceding section introduced the test apparatus and facility and explained the dynamic measurements taken at the bearing. The present section explains how the measurements are used to identify the rotordynamic coefficients.

The equations of motion for the stator mass M_s of Figure 2 can be written

$$M_s \begin{Bmatrix} \ddot{x}_s \\ \ddot{y}_s \end{Bmatrix} = \begin{Bmatrix} f_x \\ f_y \end{Bmatrix} + \begin{Bmatrix} f_{xb} \\ f_{yb} \end{Bmatrix} \tag{2}$$

Where $\ddot{x}_s, \ddot{y}_s$ are the (measured) components of the stator's acceleration, f_x , f_y are the (measured) components of the input excitation forces, and f_{xb} , f_{yb} are the bearing-reaction force components. The x and y subscripts in these equations identify the X and Y directions of Figure 2. Substituting from Eq.(1) and rearranging Eq.(2) gives

$$\begin{Bmatrix} f_x - M_s\ddot{x}_s \\ f_y - M_s\ddot{y}_s \end{Bmatrix} = \begin{bmatrix} K_{xx} & K_{xy} \\ K_{yx} & K_{yy} \end{bmatrix} \begin{Bmatrix} \Delta x \\ \Delta y \end{Bmatrix} + \begin{bmatrix} C_{xx} & C_{xy} \\ C_{yx} & C_{yy} \end{bmatrix} \begin{Bmatrix} \Delta\dot{x} \\ \Delta\dot{y} \end{Bmatrix} + \begin{bmatrix} M_{xx} & M_{xy} \\ M_{yx} & M_{yy} \end{bmatrix} \begin{Bmatrix} \Delta\ddot{x} \\ \Delta\ddot{y} \end{Bmatrix} \tag{3}$$

Since the mass M_s is known, the left-hand vector of Eq.(3) is a known function of time. On the right-hand side, $\Delta x(t)$ and $\Delta y(t)$ are measured functions of time. The rotordynamic coefficients are determined in the frequency domain via the Fourier Transform $\mathcal{F}$ which yields,

$$\begin{Bmatrix} F_x - M_s A_x \\ F_y - M_s A_y \end{Bmatrix} = \begin{bmatrix} H_{xx} & H_{xy} \\ H_{yx} & H_{yy} \end{bmatrix} \begin{Bmatrix} D_x \\ D_y \end{Bmatrix} \tag{4}$$

where

$$F_k=\mathcal{F}(f_k), \qquad A_k=\mathcal{F}(\ddot{k}_s), \qquad D_k=\mathcal{F}(\Delta k) \tag{5}$$

The elements of the frequency-response function (FRF) H are related to the coefficients defined in Eq. (3) by,

$$\begin{aligned} H_{xx} &= (K_{xx} - \omega^2 M_{xx}) + j(\omega C_{xx}) \\ H_{xy} &= (K_{xy} - \omega^2 M_{xy}) + j(\omega C_{xy}) \\ H_{yx} &= (K_{yx} - \omega^2 M_{yx}) + j(\omega C_{yx}) \\ H_{yy} &= (K_{yy} - \omega^2 M_{yy}) + j(\omega C_{yy}) \end{aligned} \tag{6}$$

where ω is the excitation frequency and $j = \sqrt{-1}$.

However, Eq.(4) only provides two complex equations for the four unknown H_{ij}'s. To get four independent equations, two independent orthogonal dynamic loads are applied to the stator by alternately exciting along the X and Y directions of Figure 2. Each of these "pseudo-random" dynamic loads contains 41 sinusoids. The superposition of these sinusoids is optimized to provide a composite loading that has a high $\mathcal{F}$ spectral-line energy to crest-factor ratio. The loadings are periodic and have energy only at 10 Hz frequency increments in the range from 40 to 440 Hz. The two independent loadings result in the four complex equations,

$$\begin{bmatrix} F_{xx} - M_s A_{xx} & F_{xy} - M_s A_{xy} \\ F_{yx} - M_s A_{yx} & F_{yy} - M_s A_{yy} \end{bmatrix} = \begin{bmatrix} H_{xx} & H_{xy} \\ H_{yx} & H_{yy} \end{bmatrix} \begin{bmatrix} D_{xx} & D_{xy} \\ D_{yx} & D_{yy} \end{bmatrix}, \tag{7}$$

where the subscripts ij of the force and displacement matrices correspond to response in the i direction due to dynamic loading in the j direction (Figure 2). Appendix A provides a complete discussion of the power-spectral density method used to calculate the $\mathbf{H}_{ij}$ functions.

Steady-State Operating Conditions

The test equipment varies the test bearing steady-state operating conditions by independently controlling the following four parameters:

1) Rotor speed,
2) Test fluid supply pressure,
3) Static bearing load, and
4) Test fluid supply temperature.

The normal operating-condition test matrix includes three running speeds from 10,000 to 25,000 rpm, three supply pressures from 4 to 7 Mpa (600 to 1000 psi), and six eccentricity ratios (determined by the static load) ranging from concentric to 0.5. Tests are conducted at a single temperature, usually 55°C (130 °F); however, the test apparatus has been operated to 29,800 rpm at 71°C (160°F).

Reynolds-numbers estimates for the test seal at 28,000 rpm, C_r/R=.0033, with 160°F water is

$$\begin{aligned} \mathbf{R}_\theta &= R_\omega C_r \rho/\mu = 37{,}400, \qquad \mathbf{R}_z = 2WC_r\rho/\mu = 20{,}600 \\ \mathbf{R} &= \sqrt{\mathbf{R}_\theta^2+\mathbf{R}^{2}_{z}} = 42{,}700, \qquad \mathbf{R}_\theta/\mathbf{R}_z = 1.82 \end{aligned} \tag{8}$$

For comparison, a typical liquid-oxygen turbopump bearing would have

$$\mathbb{R}_\theta = 91{,}300, \quad \mathbb{R}_z = 113{,}200, \quad \mathbb{R} = 145{,}400, \quad \mathbb{R}_\theta/\mathbb{R}_z = .81, \tag{9}$$

and a typical hydrogen bearing would give

$$\mathbb{R}_\theta = 121{,}300, \quad \mathbb{R}_z = 366{,}600, \quad \mathbb{R} = 386{,}200, \quad \mathbb{R}_\theta/\mathbb{R}_z = .33. \tag{10}$$

$\mathbb{R}$ for the LOX and H_2 bearings is seen to be about 3.5 and 9 times higher, respectively, than corresponding water values.

Test Bearing

As reviewed earlier, the test apparatus is used to identify rotordynamic coefficients of hydrostatic bearings with a variety of geometric configurations. The results presented here are for the 5-recess bearing of Figure 4, whose physical properties and dimensions are described in table 1. The bearing area ratio is the recess area divided by the total bearing area. The bearing's outer and inner shells are made, respectively, from aluminum and bronze. Shallow recess depths are typically required in cryogenic bearings to avoid "water hammer" by minimizing the recess volume. Because of the small depths, and the requirement of a smooth recess surface, recesses were manufactured by an Electrical Discharge Machining (EDM) process.

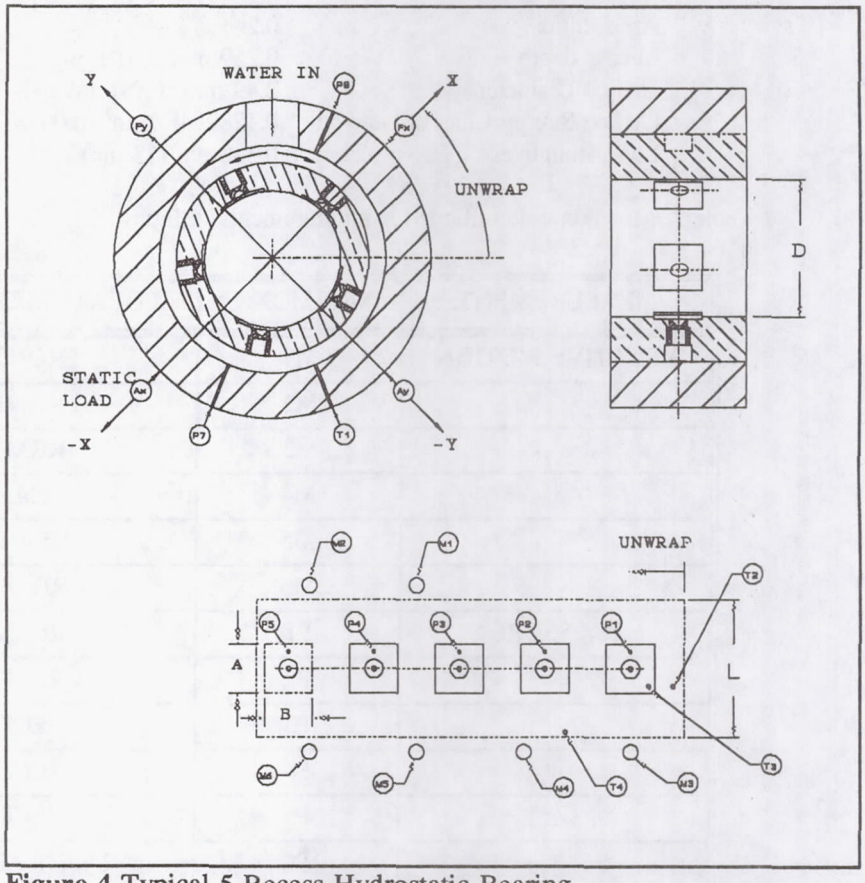

Figure 4 Typical 5-Recess Hydrostatic Bearing

Hot water enters as illustrated at the top left-hand element of figure 4, circulates through a 360° annulus and enters the recesses through orifices. Close-coupled, strain-gauge pressure transducers measure the static and dynamic pressures within each bearing recess. The unwrapped bearing view at the bottom of figure 4 and the end view at the left-hand side summarize the measurements made on a test bearing, with Ⓜ, Ⓕ, Ⓟ, Ⓣ, and Ⓐ denoting, respectively; relative motion, input force, pressures, temperatures, and accelerations. Table 2 documents the measurement mnemonics of figure 4.

Figure 5 provides a detailed view of the orifice and recess cross section. The apparatus design provides access and easy replacement of each orifice. Observe that there is a 90° expansion flow cone for a transition section from the orifice exit to the recess.

Table 1. Test-bearing physical parameters (Refer to figure 4 for dimension definitions.)

Mass	11.34 kg (25 lb)
Diameter (O.D.)	76.441 mm (3.0095 in)
Diameter (I.D.)	76.200 mm (3.0000 in)
Radial Clearance	0.12 mm (0.0048 in)
Length (L)	76.2 mm (3 in)
No. of Recesses	5
Recess dimension A	27.0 mm (1.064 in)
Recess dimension B	27.0 mm (1.064 in)
Recess Volume	0.184996E-6 m^3 (0.0112891 in^3)
Area Ratio	0.2
Recess depth	0.259 mm (0.010 in)
Orifice Diameter	2.49 mm (0.098 in)
Orifice Supply Line Volume	0.128994E-6 m^3 (0.00787173 in^3)
Land Roughness (peak-peak)	0.330 µm (13 µin)

Table 2. Mnemonic definitions for measurements in figure 4.

MEASUREMENT	MNEMONIC	LOCATION/DIRECTION
RELATIVE MOTION	M1	FRONT / X-
	M2	FRONT / Y-
	M3	REAR / X
	M4	REAR / Y
	M5	REAR / X-
	M6	REAR / Y-
PRESSURE	P1	RECESS 1
	P2	RECESS 2
	P3	RECESS 3
	P4	RECESS 4
	P5	RECESS 5
	P6	INLET ANNULUS
	P7	BACKSIDE ANNULUS
TEMPERATURE	T1	ANNULUS
	T2	LAND AT RECESSES
	T3	RECESS 1
	T4	LAND AT EXIT
ACCELERATION	Ax	CENTER / X
	Ay	CENTER / Y
FORCE	Fx	CENTER / X
	Fy	CENTER / Y

Representative Dynamic Test Data

Figure 6 illustrates the real and imaginary parts of H_{xx} and H_{xy} for a test case defined by zero eccentricity, 24600 rpm, and 6.9 Mpa (1000 psi) supply pressure. The dots in the figure are calculated transfer-function values resulting from an average (in the frequency domain) of 32 separate excitations. Note the discrepant data points at running speed (410Hz). Poor FRF accuracy can result at this frequency because rotor imbalance and runout can combine with the stator excited motion to result in very small relative displacements. This problem is fixable by phase locking the stator input excitation to the rotor angular position, but this fix has not been implemented. Hence, data points at or near the running speed were dropped in obtaining the curve-fitted lines shown in figure 6.

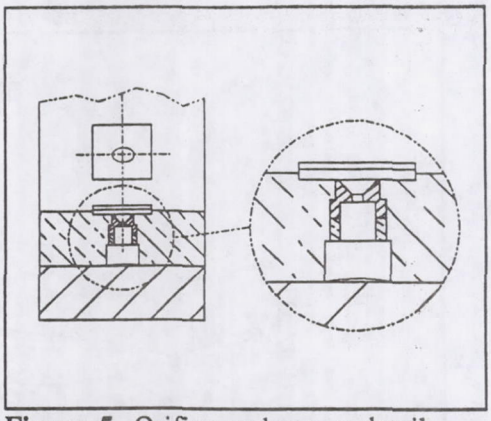

Figure 5 Orifice and recess detail

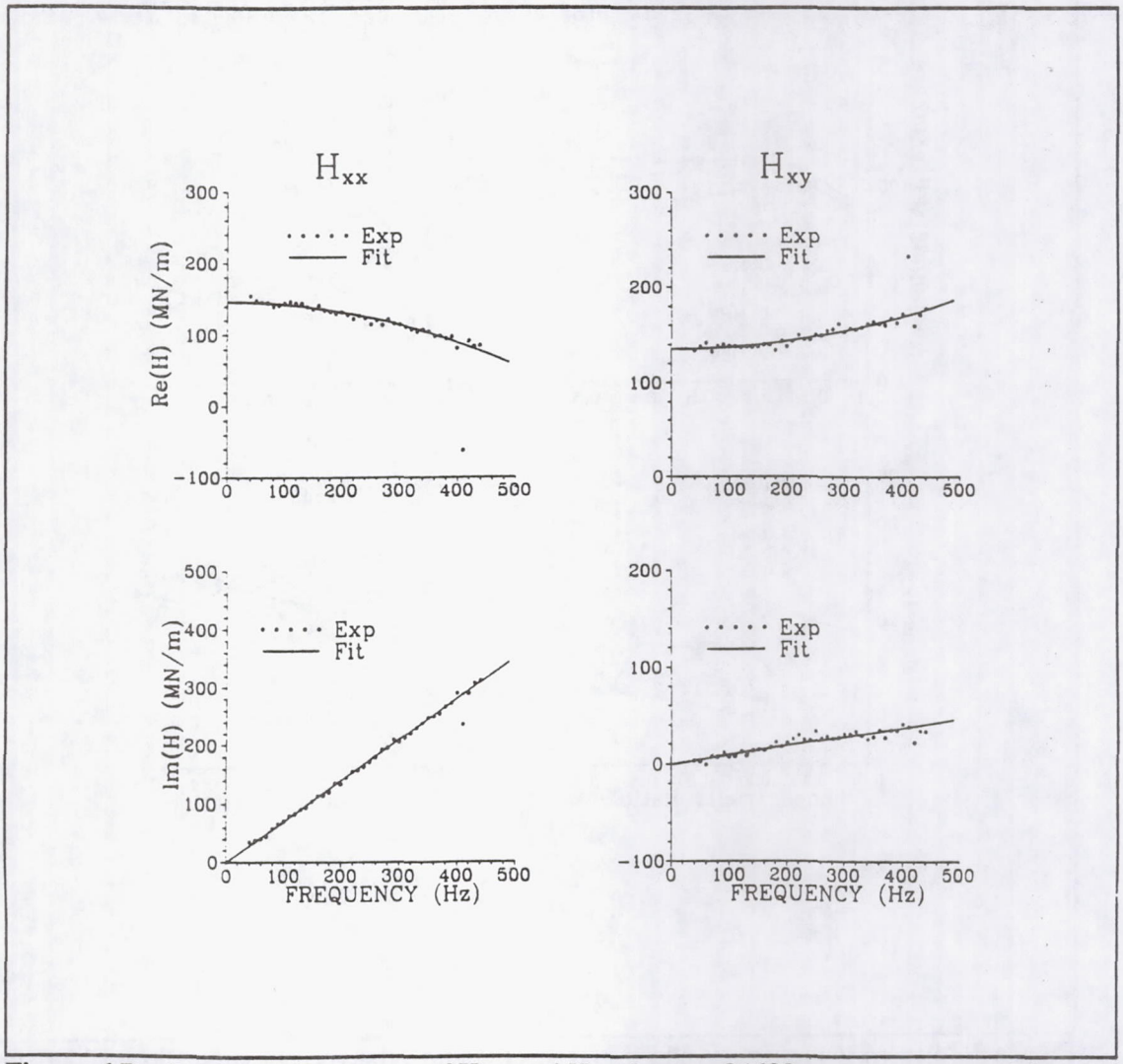

Figure 6 Real and imaginary parts of Hxx and Hxy for ω = 24600 rpm, zero eccentricity, and 6.9 Mpa (1000 psi) supply pressure

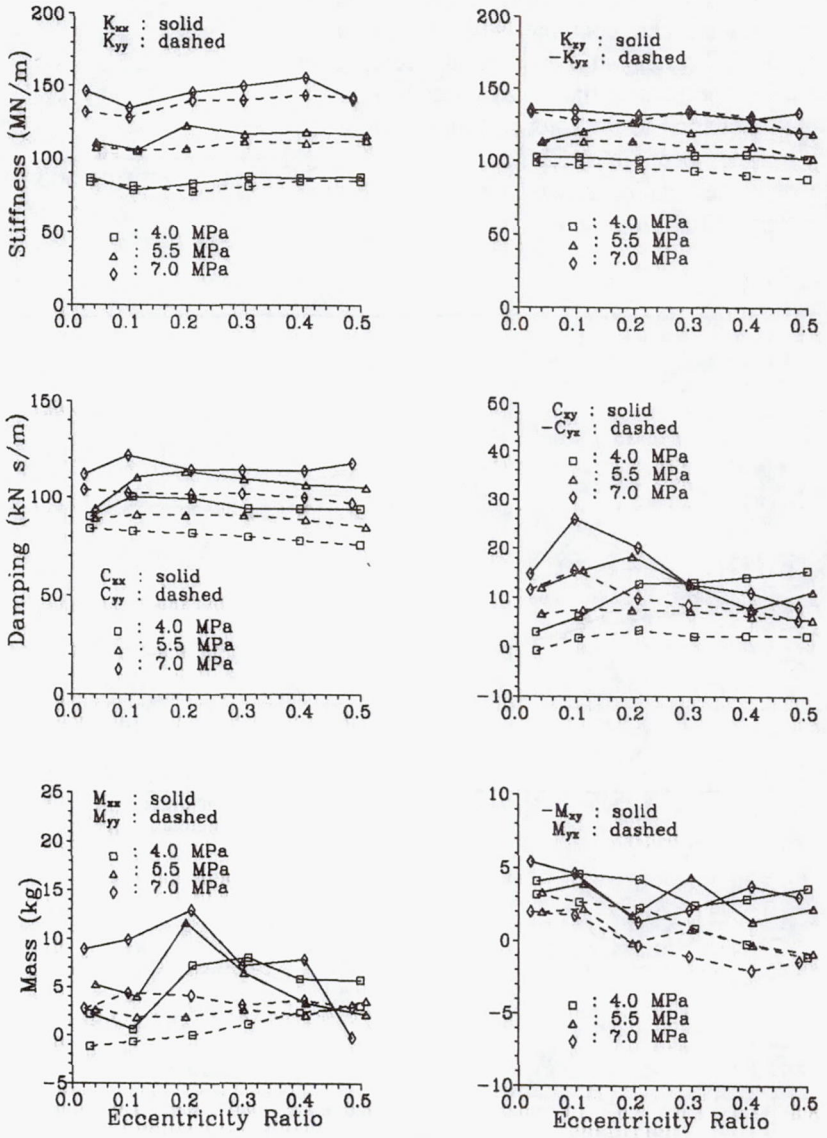

Figure 7 Stiffness, damping, and added-mass coefficients versus eccentricity ratio at 24600 rpm for three supply pressures

Recall from Eq.(6) that K_{xx} and M_{xx} come from the real part of H_{xx}, and C_{xx} is obtained from the imaginary part of H_{xx} , etc. Figure 7 illustrates the rotordynamic coefficients versus eccentricity ratio for a running speed of 24,600 rpm, a supply temperature of 54.4°C (130°F), and a range of supply pressures. The rotordynamic coefficients are seen to be generally insensitive to eccentricity ratio. Recall from figure 4 that the bearing is loaded toward the center of a recess, and the bearing is not symmetric. Hence, the direct coefficients (e.g. M_{xx} and M_{yy}) are not necessarily equal at zero eccentricity. Note the large value for direct and cross-coupled mass coefficients which arise because of the elevated Reynolds number.

Figure 8 illustrates whirl-frequency-ratio f_ω versus eccentricity ratio for three supply pressures at 24,600 rpm. The whirl-frequency ratio definition developed by San Andres (1991b) was used in these plots and depends on all the rotordynamic coefficients. Although not illustrated, f_ω increases slightly with decreasing running speed. In the absence of other rotordynamic forces, the onset speed of instability of a flexible rotor supported by plain journal bearings is approximately equal to the first critical speed divided by the whirl-frequency ratio, Lund (1966). Unfortunately, these test results show that $f_\omega \cong 0.5$ for the hydrostatic bearings which is no better than a plain journal bearing. Constaninescu (1969) predicts this outcome for hybrid gas bearings.

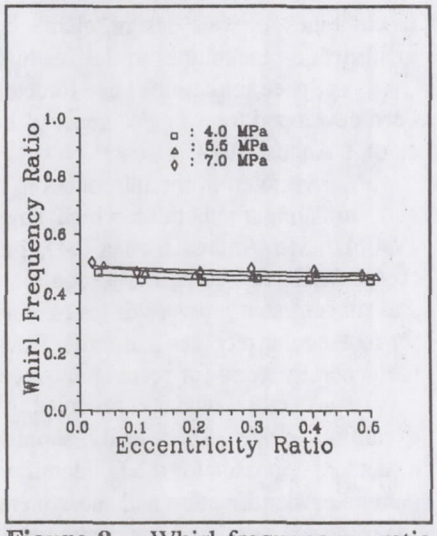

Figure 8 Whirl-frequency ratio versus eccentricity ratio for three supply pressures

Uncertainty Analysis

A "dry-shake" test (one in which the bearing fluid film consists only of air at atmospheric pressure) was conducted to examine the magnitude of the stiffness and damping imposed on the stator by the cable, stinger, and other attachments. These values are negligible compared to the stiffness and damping of all bearings tested so far.

Table 3 contains estimates of the upper limit bias errors B_{RSS} the precision indices S_{RSS} and the absolute uncertainties U_{RSS} of the coefficients for the test case of Figure 6. These are obtained by calculating bias and precision errors for each element of the force and displacement matrices of Eq.(7) then numerically propagating these errors through the functional relationship between the elements and the resulting coefficients. The method used conforms to the ANSI/ASME standard on Measurement Uncertainty (1986). The coefficients fall within **VALUE +/- U_{RSS}** for 95% coverage.

Table 3. Measurement Uncertainties for ω = 24600 rpm, zero eccentricity, and 6.9 MPa (1000 psi).

COEFFICIENT	VALUE	B_{RSS}	S_{RGS}	U_{RSS}	UNITS
K_{XX}	146	2.82	1.82	4.60	MN/m
K_{XY}	136	2.21	1.34	3.47	MN/m
K_{YX}	-133	2.11	1.86	4.27	MN/m
K_{YY}	132	2.46	1.30	3.59	MN/m
C_{XX}	112	2.26	0.74	2.71	kN/m
C_{XY}	14.4	2.60	1.42	3.85	kN/m
C_{YX}	-11.3	2.39	0.69	2.76	kN/m
C_{YY}	105	2.16	1.54	3.77	kN/m
M_{XX}	8.8	1.06	0.99	2.24	kg
M_{XY}	-5.1	0.50	0.79	1.66	kg
M_{YX}	2.2	0.44	1.00	2.04	kg
M_{YY}	2.9	1.06	0.59	1.58	kg

Summary, Conclusions, and Comments

The results and discussions included here present and explain the design of a new test system for hybrid (combined hydrostatic and hydrodynamic) bearings. The tester can measure static parameters including pressures, flowrate, temperatures, drag torque, etc plus a full complement of force/displacement rotordynamic coefficients. The test system expedites rapid and flexible testing of fluid-film bearings. It combines proven design elements of earlier experimenters and state-of-the-art excitation and identification techniques to deliver high-quality data.

Space limitations have forced us to present only a very limited selection of the data which have been developed for a single "generic" bearing. Tests have been completed for approximately 30 bearings as of 1 August 1992.

As noted in the introduction, this test program aims to produce test data to help in developing and validating predictions which have been under concurrent development by San Andres (1990a, 1990b). San Andres uses a 2-D, bulk-flow Navier-Stokes model for flow in the bearing land, a compressible flow continuity requirement for the recess, a discharge-coefficient model for the orifice, and concentrated pressure drops for flow leaving the recess and entering the lands. The analysis applies for rectangular recesses and radial flow injection. Comparisons between measurements and predictions are generally good for rectangular-recess bearings and are presently being prepared for publication.

A central question involved in the development of the present apparatus concerned the required excitation device. Specifically, should impulse devices or shakers be employed? Impulse excitation is a standard approach for modal identification, Ewins (1986), and was pioneered by Nordmann for bearing parameter identification and subsequently for annular seals, Nordmann and Massman (1984). Hydraulic shakers were first used for parameter identification of annular seals by Iino and Kaneko (1980).

Price is a central advantage of impulse devices over hydraulic shakers. The impulse "guns" which were initially purchased for this project cost less than one tenth the eventual cost of the hydraulic shakers. The decision to shift from impulse to shaker excitation, despite financial considerations, involved the quality and volume of data to be acquired. The hybrid bearings were extremely noisy. Pressure pulsations in their recesses generated unwanted relative bearing-rotor amplitudes of the same magnitude as that created by external excitation. As detailed by Rouvas et al. (1992), impulse excitation can be made to work, but only with many repetitions and averaging in the time domain. However, the FRF data developed by Rouvas et al. with impulse excitation never approaches the high quality shown in figure 6, despite averaging over 200 separate impulse excitations.

An additional practical problem with impulse excitation concerned tip selection for the impulse guns. Soft tips were required to deliver the required low-frequency force excitation, but they would not have survived testing a bearing over a large test matrix with 200-plus excitations per data point. A parallel identification concern involved the comparatively large **peak** rotor/stator amplitudes developed by impulse excitation which were necessary to give adequate amplitudes at discrete frequencies.

Having acquired and installed the hydraulic shakers, the nature of the excitation and identification procedures remained to be resolved. Pseudo-random excitation is used because it is fast, has no leakage in the analysis. The spectrum is shaped to only excite frequencies in the range of interest with energy only at each DFT analyzed spectral line, and only a few averages are needed due to its low crest factor and good signal-to-noise ratio (Herlufsen, 1985). This excitation technique, along with identification procedures as outlined by Bendat and Piersol (1986) and extended by Rouvas and Childs (1992)[4] eventually achieved the high-quality FRF's of figure 6..

The test results developed here show one principal limitation to the planned use of hybrid bearings in cryogenic turbopumps, specifically, a whirl-frequency ratio near 0.5. With this whirl-frequency ratio, running speeds above twice the rotor's first critical speed are likely to yield unstable motion. Hence, recent developments within this program have considered the following options for improving rotordynamic stability by reducing f_ω:

[4] See Appendix A

(a) **Directed injection against rotation.** Tondl (1967) initially proposed injecting the fluid against rotor rotation as compared to the radial injection of figure 4.

(b) **Roughened Stator.** Von Pragenau (1982) initially proposed roughened stators for annular seals to yield, "damper seals."

Both of these approaches act to reduce the average tangential velocity within the bearing. Favorable tests (reduced f_{ω}) have been completed for both types of improved bearing configurations and will be reported shortly.

The emphasis of this work has been on the application of hybrid bearings to cryogenic turbopumps. However, they present obvious alternatives as product-lubricated bearings for commercial pumps. Katayama and Okada (1992) have recently reported the results of a 6-year development program at Tokyo Gas Co. implementing hybrid bearings into vertical liquified-natural-gas pumps.

As noted by Kurtin et al. (1991), two practical problems have been encountered which might restrict the applications of hybrid bearings to commercial pumps. First, considerable cavitation erosion has been experienced in the divergent section downstream of the orifice in Figure 5 after a comparatively short test time (≈4 hrs). The eroded part is made from 17-4PH stainless steel with a high yield strength. Tests of a modified bearing with the orifice exit flush to the recess[5] showed no cavitation damage on the exit orifice surface but some roughening of the rotor. Given that the recess pressure is on the order of 3.5 MPa (500 psi), this damage could be resulting from air bubbles coming out of solution in the water versus an actual phase change of the water. Long-term testing to investigate potential cavitation damage is recommended before these bearings are selected for commercial pumps. Tests with the product fluid which will actually be used are advisable, since almost any fluid will be kinder from a cavitation viewpoint than water. Rocketdyne personnel report zero damage with liquid hydrogen.

The second problem concerns damage to the bearing due to fluid-borne debris. Our flow loop originally used a 10-micron nominal filter which was inadequate in removing particles from the flow stream. Particles entering the bearing would lodge at the corners of the recesses and then create circumferential damage grooves around the bronze stators. Switching to a 10-micron absolute filter eliminated the problem. None the less, care is suggested in providing adequate upstream filtration for this bearing type.

[5]The diverging transition section from the orifice exit to the recess is eliminated.

References

Bendat J. S. and Piersol A. G. (1986), *Random Data Analysis and Measurement Techniques, 2nd Edition,* Wiley Interscience.

Constantinescu, V. N. (1969), *Gas Lubrication*, ASME, New York.

Ewins, D. J. (1986), *Modal Testing: Theory and Practice*, Brüel & Kjær.

Glienicke, J. (1966-67), "Experimental Investigation of the Stiffness and Damping Coefficients of Turbine Bearing and Their Application to Instability Prediction," Proc. Mech. Engrs., Vol. 181 (pt 3B).

Iino, T. and Kaneko, H. (1980), "Hydraulic Forces Caused by Annular Pressure Seals in Centrifugal Pumps," proceedings of the 5th Rotordynamic Instability Workshop, Texas A&M University, pp. 213-225.

Herlufsen, H. (1985) "Digital Signal Analysis using Digital Filters and FFT Techniques", Selected reprints from "Technical Review", Brüel & Kjaer, pp.199-252.

Kanki, H. and Kawakami, T. (1984), "Experimental Study on the Dynamic Characteristics of Pump Annular Seals," *Vibrations in Rotating Machinery,* proceedings of the 3rd IMechE International Conference on Vibrations in Rotating Machinery, York, England, pp. 159-166.

Katayama, T. and Okada, A. (1992), "Liquified Natural Gas Pump with Hydrostatic Journal Bearings", proceedings of the 9th International Pump Users Symposium, Texas A&M University, pp. 39-50.

Kurtin, K., Childs D., San Andres L., and Hale K. (1991), "Experimental Versus Theoretical Characteristics of a High-Speed Hybrid (Combination Hydrostatic and Hydrodynamic) Bearing," accepted for publication in *ASME Trans., Journal of Tribology.*

Lund, J. (1966), "Self-Excited, Stationary Whirl Orbits of a Journal in a Sleeve Bearing," Ph.D. Thesis, Renselaer Polytechnic Institute, Troy, N.Y.

Measurement Uncertainty, ANSI/ASME PTC 19.1-1985 Part 1, 1986 (reaffirmed 1991).

Mitchell, L. and Elliott, K. (1984), "How To Design Stingers for Vibration Testing of Structures" April edition of the *Sound and Vibration* magazine, pp. 14-18.

Nordmann R., and Massman, H. (1984), "Identification of Dynamic Coefficients of Annular Turbulent Seals," Rotordynamic Instability Problems in High-Performance Turbomachinery - 1984, NASA CP-2338, Proceedings of a Workshop held at Texas A&M University, pp. 295-311.

Rouvas, C. and Childs, D. (1992), "A Parameter Identification Method for the Rotordynamic Coefficients of a High Reynolds Number Hydrostatic Bearing," accepted for publication in the *ASME Journal of Vibration and Acoustics.*

Rouvas, C., Murphy, B. and Hale K. (1992), "Bearing Parameter Identification Using Power Spectral Density Methods," proceedings of the Fifth International Conference of Vibrations in Rotating Machinery, Bath, England, pp. 297-303.

San Andres, L. (1991b), "Effect of Eccentricity on the Force Response of a Hybrid Bearing," *Tribology Transactions*, Vol. 34, No. 4, pp.537-544.

San Andres, L. (1990a), "Approximate Analysis of Turbulent Hybrid Bearings. Static and Dynamic Performance for Centered Operation," *ASME Journal of Tribology*, Vol. 112, pp. 692-698.

San Andres, L. (1990b), "Turbulent Hybrid Bearings with Fluid Inertia Effects," *ASME Journal of Tribology*, Vol 112, pp. 669-707.

Scharrer, J., Tellier, J., and Hibbs, R. (1991a), "A Study of the Transient Performance of Hydrostatic Journal Bearings. Part I: Test Apparatus and Facility," STLE Preprint 91-TC-3B-1, presented at the STLE/ASME Tribology Conference, St. Louis, Missouri.

Scharrer, J., Tellier, J., and Hibbs, R. (1992b), "A Study of the Transient Performance of Hydrostatic Journal Bearings. Part II: Experimental Results," STLE Preprint 91-TC-3B-2, presented at the STLE/ASME Tribology Conference, St. Louis, Missouri.

Tonnesen, J. and Hansen, P. (1982), "Some Experiments on the Steady State Characteristics of a Cylindrical Fluid Film Bearing Considering Thermal Effects," *J. Lub. Tech. Trans. ASME*, Vol. 103, pp. 107-114.

Tondl, A. (1967), "Bearings with a Tangential Gas Supply," University of Southampton, Department of Mechanical Engineering, Gas Bearing Symposium, United Kingdom, paper no. 4.

von Pragenau, G. (1982), "Damping Seals for Turbomachinery," NASA Technical Paper 1987.

Appendix A. Spectral-Density-Averaging for Rotordynamic-Coefficient Identification

Spectral density averaging techniques are used to obtain the frequency-response functions (FRF) of Eq.(7), which defines a multi-input multi-output (MIMO) system. The inputs are D_{xx}, D_{xy}, D_{yx}, and D_{yy}, and the outputs are $F_{xx} - M_s A_{xx}$, $F_{xy} - M_s A_{xy}$, $F_{yx} - M_s A_{yx}$, and $F_{yy} - M_s A_{yy}$.

Before calculating the FRF for this MIMO system, first consider the best solution for the FRF of a single-input single-output (SISO) system. A SISO system with a clean input a and a noise contaminated output b will be examined. According to Bendat and Peirsol, (1986) an unbiased estimate H, of the FRF for this type of SISO system is given by,

$$H = \frac{G_{ab}}{G_{aa}}, \tag{A.1}$$

with G_{ab} being the cross spectral density and G_{aa} the auto spectral density. For discrete data, (which we have) an FFT algorithm is used to calculate the Discrete Fourier Transforms (DFT's) of Eq.(A.1). In particular,the spectral densities are calculated by,

$$G_{ap} = \frac{2}{n_d N \Delta t} \sum_{i=1}^{n_d} A_i^*(\omega) P_i(\omega) \tag{A.2}$$

where n_d is the number of statistically independent blocks of data, N is the number of data points in each data block, Δt is the time increment between sampling of each data point, $A^*(\omega)$ = the complex conjugate of $\mathcal{F}\{a(t)\}$ and $P(\omega) = \mathcal{F}\{p(t)\}$ ($\mathcal{F}$ is used to represent the DFT here).

We wish to apply the unbiased estimator for the SISO system described above to the MIMO system of Eq. (7). First, recall that we have 32 statistically independent blocks of data ($n_d = 32$), each block containing 1024 ($N = 1024$) data points for each of the dynamic loads, accelerations, and relative motions whose $\mathcal{F}$ appear in Eq.(7). Next, we identify each independent dynamic load of Eq.(7) (F_{xx} and F_{yy}) as a clean input a, and each of the resulting elements of the force and displacement matrices as noise contaminated outputs b. Eq.(A.1) is then applied separately to each individual element of the force and displacement matrices, yielding an unbiased estimate for each input and output element contained in these matrices. The resulting equation,

$$\begin{bmatrix} 1 - M_s \dfrac{G_{f_{xx}a_{xx}}}{G_{f_{xx}f_{xx}}} & \dfrac{G_{f_{yy}f_{xy}}}{G_{f_{yy}f_{yy}}} - M_s \dfrac{G_{f_{yy}a_{xy}}}{G_{f_{yy}f_{yy}}} \\ \dfrac{G_{f_{xx}f_{yx}}}{G_{f_{xx}f_{xx}}} - M_s \dfrac{G_{f_{xx}a_{yx}}}{G_{f_{xx}f_{xx}}} & 1 - M_s \dfrac{G_{f_{yy}a_{yy}}}{G_{f_{yy}f_{yy}}} \end{bmatrix} = \begin{bmatrix} H_{xx} & H_{xy} \\ H_{yx} & H_{yy} \end{bmatrix} \begin{bmatrix} \dfrac{G_{f_{xx}d_{xx}}}{G_{f_{xx}f_{xx}}} & \dfrac{G_{f_{yy}d_{xy}}}{G_{f_{yy}f_{yy}}} \\ \dfrac{G_{f_{xx}d_{yx}}}{G_{f_{xx}f_{xx}}} & \dfrac{G_{f_{yy}d_{yy}}}{G_{f_{yy}f_{yy}}} \end{bmatrix}, \tag{A.3}$$

yields improved estimates for the FRF when solved.

Once Eq.(A.3) is solved, the rotordynamic coefficients are extracted from the FRF definitions of Eqs.(6) by performing a least-squares curve fit on the real and imaginary parts of each element of the FRF matrix. Plots of typical real and imaginary parts for Hxx are shown in Fig. 6. The stiffness, damping, and added-mass coefficients of Eqs. (1) and (3) have now been identified. A more detailed discussion is provided by Rouvas and Childs (1992).

Lists of Figures

1. Bearing-test-apparatus layout

2. End view of a test bearing

3. Side-view of a test bearing showing axial-tensioning cables

4. Test bearing

5. Orifice and recess detail

6. Real and imaginary parts of H_{xx} and H_{xy} for ω = 24,600 rpm, zero eccentricity, and 6.90 Mpa (1000 psi) supply pressure

7. Stiffness, Damping, and Added-mass coefficients versus eccentricity ratio at 24600 rpm for three supply pressures

8. Whirl-frequency ratio versus eccentricity ratio at 24600 rpm for three supply pressures

Lists of Tables

1. Test-bearing physical parameters (Refer to figure 4 for dimension definition).

2. Mnemonic definitions for measurements in figure 4.

3. Measurement Uncertainties for ω = 24600 rpm, zero eccentricity, and 6.90 MPa (1000 psi) supply pressure

A WAVED JOURNAL BEARING CONCEPT WITH IMPROVED STEADY-STATE AND DYNAMIC PERFORMANCE

Florin Dimofte*
NASA Lewis Research Center
Cleveland, Ohio

ABSTRACT

Analysis of the waved journal bearing concept featuring a waved inner bearing diameter for use with a compressible lubricant (gas) is presented. A three wave, waved journal bearing geometry is used to show the geometry of this concept. The performance of generic waved bearings having either three, four, six, or eight waves is predicted for air lubricated bearings. Steady-state performance is discussed in terms of bearing load capacity, while the dynamic performance is discussed in terms of dynamic coefficients and fluid film stability.

It was found that the bearing wave amplitude has an important influence on both steady-state and dynamic performance of the waved journal bearing. For a fixed eccentricity ratio, the bearing steady-state load capacity and direct dynamic stiffness coefficient increase as the wave amplitude increases. Also, the waved bearing becomes more stable as the wave amplitude increases. In addition, increasing the number of waves reduces the waved bearing's sensitivity to the direction of the applied load relative to the wave. However, the range in which the bearing performance can be varied decreases as the number of waves increases. Therefore, both the number and the amplitude of the waves must be properly selected to optimize the waved bearing design for a specific application. It is concluded that the, stiffness of an air bearing, due to hydrodynamic effect, could be doubled and made to run stably by using a six or eight wave geometry with a wave amplitude approximately half of the bearing radial clearance.

NOMENCLATURE

B_c = symbolic damping coefficient used in stability analysis
B_{ij} (i = x,y; j = x,y) = dimensionless dynamic damping coefficient
C = journal bearing radial clearance, m
D = journal bearing diameter, m
e = eccentricity, m
e_w = wave's amplitude, m
$F = \bar{F}/(p_a LD)$ dimensionless load capacity
$\bar{F}$ = load capacity, N (the resulting force of the pressure distribution)
$f = \nu/\Omega$ whirl frequency ratio
$f_0 = \nu_0/\Omega$ unstable whirl frequency ratio
$h = \bar{h}/C$ dimensionless film thickness
$\bar{h}$ = film thickness, m
$i = \sqrt{-1}$, the imaginary unit
K_{ij} (i = x,y; j = x,y) = dynamic stiffness coefficient, N/m (N/μm)
$\bar{K}_{ij}$ (i = x,y; j = x,y) = dimensionless dynamic stiffness coefficient
K_c, K_{c0} = symbolic stiffness coefficient used in stability analysis
L = bearing length, m
M = rotor mass allocated to one bearing; for a symmetric rotor M is half of the rotor mass, Kg
$\bar{M}_c$ = corresponding rotor mass, allocated to one bearing, required to make the bearing unstable, Kg (critical mass)
$M_c = \bar{M}_c(\nu_0^2 C)/(p_a LD)$ dimensionless critical mass
n_w = number of waves

*NASA Resident Research Associate at Lewis Research Center.

Preceding Page Blank

O = center of the bearing
O_1 = center of the shaft
p = dimensionless pressure
$\bar{p}$ = pressure, Pa
p_a = ambient pressure, Pa
p_0 = steady state component of the pressure p
p_1, p_2 = perturbation components of pressure p
R = journal bearing radius, m
t = time, s
W = bearing load, N
x = x-direction (direction of the load on bearing)
y = y-direction perpendicular to x
$x_{1,3}$ = fluid film coordinates
z = axial coordinate parallel to rotor axis
Z_{ij} (i = x,y; i = x,y) = impedance for translatory motion
α = angle between the starting point of the wave and the line of centers, dgrs
γ = wave position angle = angle between the starting point of the wave and the direction of the load, dgrs
ϵ = e/C, eccentricity ratio
ϵ_w = e_w/C, wave amplitude ratio
ϵ_0 = eccentricity ratio under static load
ϵ_1 = dimensionless radial whirl amplitude
$\epsilon_0\varphi_1$ = dimensionless tangential whirl amplitude
θ = angular coordinate originating at the line of centers
Λ = $(6\mu\Omega)(R/C)^2/p_a$, bearing number
μ = dynamic viscosity, Nsm^{-2}
ν = whirl frequency, rad/s
ν_0 = unstable whirl frequency, rad/s
τ = dimensionless time
Ω = rotation frequency, rad/s

INTRODUCTION

Hydrodynamic circular bearings can become unstable, generating a whirl motion whose frequency approximates half the rotation frequency of the shaft. However, hydrodynamic bearings can be made stable by changing the circular fluid film geometry to incorporate recesses, holes, steps, or lobes, although, these changes reduce the bearing's load capacity.

Recently, a new alternative to the plain circular hydrodynamic bearing, a waved journal bearing, was conceived [1]. The waved journal bearing features a waved inner bearing diameter. The numerical model of the waved journal bearing has shown significantly increased steady-state (stiffness) and dynamic (stability and dynamic coefficients) performance as compared to a circular bearing's performance.

The waved bearing concept is shown in figure 1 for a three wave journal bearing geometry. However, the waved bearing can have two, three, four, or more waves. Both three and four wave journal bearings are analyzed in order to show the influence of the number of waves. In addition, a truly circular bearing is analyzed and compared to a waved bearing, showing the performance improvements gained by the waved bearing. A compressible fluid (gas) is assumed as the lubricant. Both steady-state and dynamic bearing performance are predicted using a numerical code based on a perturbation solution of the complex form of the Reynolds equation [2, 3]. Waved bearing performance is computed assuming atmospheric air as the lubricant. The steady-state performance is discussed in terms of bearing load capacity, while the dynamic performance is discussed in terms of bearing stability and bearing dynamic coefficients. Both the wave amplitude ratio and the number of waves influence the waved journal bearing performance. Therefore, a waved bearing configuration (the number of waves and the wave amplitude) can be optimized for a specific

application. The type of load applied to the bearing (major side load or dynamic rotating load) and the bearing dynamic coefficient values required to control the rotor-bearing system behavior are important. Both the rotor-bearing system critical speed and amplitude can be changed by changing the bearing dynamic coefficients via the wave amplitude.

WAVED BEARING CONCEPT

A three wave, waved journal bearing geometry is shown in figure 1. The mean diameter of the waved bearing (the diameter of the mean circle of the waves) is also the diameter of the truly circular bearing to which that the waved bearing is compared. The radial clearance, C, is the difference between the mean circle radius and the radius, R, of the shaft. The clearance, C, and the wave's amplitude, e_w, are greatly exaggerated in figure 1 so that the concept may be visualized. The radial clearance, C, is typically less than one thousandth of the journal radius, R, and the wave amplitude, e_w, is typically a fraction, 0.2 - 0.6 typically, of the radial clearance, C. The waved bearing performance depends on the position of the waves relative to the direction of the applied load (W). This position can be defined by the wave position angle, γ, which is the angle between the starting point of the waves and the direction of the applied load. The wave amplitude, e_w, the number of waves, as well as the wave position angle, γ, are the basic design parameters of the waved journal bearing. The waved bearing performance is similar with the shaft rotating in either direction.

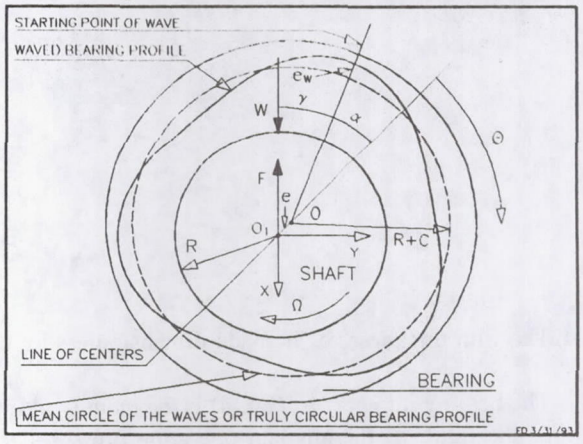

Fig.1 Three wave journal bearing geometry.

Any number of waves can be selected. In the present work the data for a three, four, six, and eight waves, waved journal bearing are compared to the data for a truly circular bearing.

ANALYSIS

When load, W (Fig. 1), is applied to the shaft, the shaft must find an equilibrium position at an eccentricity, e, such that the load capacity of the bearing, F, balances the applied load, W (Fig. 1). The load capacity, F, is a result of the pressure generated in the fluid film owing to both the rotation of the shaft and the variation in fluid film thickness along the circumference. This variation can be defined by:

$$\bar{h} = C + e \cos\theta + e_w \cos(n_w(\theta + \alpha)) \qquad (1)$$

where n_w is the number of waves, α is the angle between the starting point of the wave and the line of centers (Fig. 1), and θ is the angular coordinate starting from the line of centers.

The pressure generated in the fluid can be calculated by integrating the Reynolds equation. Assuming a compressible lubricant with isothermal behavior, the Reynolds equation has the following dimensionless form [4, 5, 6]:

$$\frac{\partial}{\partial\theta}\left(h^3\frac{\partial p^2}{\partial\theta}\right) + \frac{\partial}{\partial z}\left(h^3\frac{\partial p^2}{\partial z}\right) = 2\Lambda\frac{\partial(ph)}{\partial\theta} + \\ + i4f\Lambda\frac{\partial(ph)}{\partial\tau} \tag{2}$$

where:

$$p = \frac{\bar{p}}{p_a},\ \theta = \frac{x_1}{R},\ z = \frac{x_3}{R}, \\ \tau = i\,\nu t,\ (i = \sqrt{-1}) \tag{3}$$

$$\Lambda = \frac{6\ \mu\ \Omega}{p_a}\left(\frac{R}{C}\right)^2 \tag{4}$$

The film thickness, h, is made dimensionless by dividing equation 1 by the radial clearance, C.

The bearing number, Λ, (Eq. 4) is the main working parameter of the bearing. It reflects dynamic viscosity of the fluid, μ, the ambient operating pressure, p_a, the rotational speed of the shaft, Ω, and the bearing main geometry parameter, (R/C).

Bearing Steady-State and Dynamic Performance:

Both the steady-state and dynamic performance of the bearing can be determined using the small perturbation technique of the complex form of the Reynolds equation (Eq. 2) [2, 3]. Expanded in a Taylor series truncated to the first derivatives, the pressure can be written as:

$$p = p_0 + \epsilon_1\ \exp(\tau)\ p_1 + \epsilon_0\varphi_1\ \exp(\tau)\ p_2 \tag{5}$$

where p_0 is the steady-state component and p_1 and p_2 are the dynamic components of the pressure. Each component can be calculated by numerically integrating the corresponding differential equation derived from the Reynolds equation (Eq. 2), [2, 3].

The bearing steady-state and dynamic characteristics can be obtained by integrating the pressure components, p_0, p_1, and p_2, over the whole bearing fluid film. The steady-state load capacity, F, is calculated by integrating p_0, while both the dynamic stiffness, K_{ij}, and damping, B_{ij} (i =x,y; j = x,y), coefficients are calculated by integrating the dynamic pressure components, p_1 and p_2, respectively.

Under dynamic conditions, the journal (shaft) center whirls in an orbit around its static equilibrium position. The corresponding bearing dynamic reaction force is actually a nonlinear function of the whirl amplitude and depends implicitly on time. In a thorough analysis it is necessary to consider the rotor and the bearing simultaneously as is done, for example, in reference 7. In most practical situations, the amplitude of the shaft whirl is, of necessity, rather small. In these cases, a linearization of the bearing reaction is permissible [2]. Then it becomes possible to treat the bearing separately and represent the bearing reaction force components by means of bearing dynamic coefficients:

$$F_x = -K_{xx}x - B_{xx}\frac{dx}{dt} - K_{xy}y - B_{xy}\frac{dy}{dt}$$
$$F_y = -K_{yx}x - B_{yx}\frac{dx}{dt} - K_{yy}y - B_{yy}\frac{dy}{dt} \qquad (6)$$

Equation 6 is only valid when the journal motion is harmonic, and

$$x = \bar{x}\exp(i\nu t) = \bar{x}\exp(\tau)$$
$$y = \bar{y}\exp(i\nu t) = \bar{y}\exp(\tau) \qquad (7)$$

The equation 6 can be written in complex form as:

$$F_x = -Z_{xx}x - Z_{xy}y$$
$$F_y = -Z_{yx}x - Z_{yy}y \qquad (8)$$

where:

$$Z_{ij} = K_{ij} + i\,\nu\,B_{ij} \qquad (9)$$
$$i = x,y; \quad j = x,y$$

are the bearing impedance coefficients. For a given bearing geometry, the dynamic coefficients are functions of the static load on the bearing and the rotor speed. The dynamic coefficients also depend on the whirl frequency, and they are actually impedances of the gas film. Note, also, that the x-axis (Fig.1) was chosen along the direction of the steady-state load.

It is also important to note that the bearing's dynamic reaction force components, F_x, and F_y, are functions of the bearing dynamic coefficients, as equation 6 shows. Consequently, these bearing dynamic coefficients influence the rotor-bearing system dynamic behavior. It will be shown that these coefficients depend on the wave amplitude ratio. This means that the rotor-bearing system behavior could be controlled by varying the bearing wave amplitude ratio, e_w.

Bearing Stability:

In a bearing stability calculation, it is necessary to evaluate the bearing coefficients over a frequency range, usually around one half of the rotating frequency. On this basis, a stability analysis can be performed in order to calculate the critical mass. The critical mass, M_c is used to help determine whether the bearing will run free of "half frequency whirl" instability [2, 3]. Half frequency whirl is an instability of the fluid lubricant film of the bearing. It appears as a whirling, orbiting motion of the shaft and its frequency or speed, ν_0, is often close to one-half the running frequency or shaft speed. This phenomenon is more likely to occur when the shaft center is close to the center of the bearing (near zero eccentricity). This frequency,ν_0, can be much lower than one-half of the running frequency when the value of eccentricity is large [8]. To derive the equation for critical mass, in a simple manner, the rotor is considered rigid and symmetrical, and supported by two identical bearings [2, 3]. This means that each bearing carries one-half of the rotor mass. If M is the rotor mass supported by the each bearing (M = 1/2 of the rotor mass) and the bearing is represented by its four impedance coefficients, Z_{ij} (i = x,y; j = x,y), the motion equation can be written as:

$$\begin{bmatrix} (Z_{xx} - M\,\nu^2) & Z_{xy} \\ Z_{yx} & (Z_{yy} - M\,\nu^2) \end{bmatrix} \begin{bmatrix} x \\ y \end{bmatrix} = 0 \qquad (10)$$

The threshold of instability occurs when the determinant of the matrix is zero. Noting:

$$Z = K_c + i\,\nu\,B_c, \quad K_c = M\,\nu^2 \qquad (11)$$

the determinant equation can be solved to get:

$$Z = \frac{1}{2}\,(Z_{xx} + Z_{yy}) - \sqrt{\frac{1}{4}\,(Z_{xx} - Z_{yy})^2 + Z_{xy}\,Z_{yx}} \qquad (12)$$

For stability calculations, only the solution with a negative sign in front of the square root proves to be of interest [2]. At the threshold of instability, Z must be real. The imaginary part of Z can be evaluated over a range of frequencies to find the frequency value, ν_0, causing the imaginary part of Z to be zero. The corresponding mass is the mass required to make the bearing unstable under the selected working conditions and is:

$$M_c = \frac{K_{c0}}{\nu_0^2} \qquad (13)$$

If the calculated critical mass for the bearing (Eq. 13) is equal to or greater than one-half the actual rotor mass, then half-frequency whirl instability is likely to occur.

RESULTS AND DISCUSSION

In the present work, a generic bearing is used to better understand the waved bearing performance. The selected generic journal bearing has a mean diameter of 200 mm, a length of 100 mm, and a radial clearance of 0.080 mm. The bearing performance was determined at 5,000, 20,000, and 100,000 RPM (the corresponding bearing number, Λ, are 0.89, 3.56, and 17.38, respectively). However, the data of 20,000 RPM running regime is shown in here. The bearing is lubricated by atmospheric air. Generic bearings having three, four, six, and eight waves are considered; for each bearing the wave amplitude ratio, $\epsilon_w = e_w/C$, varies from 0 (truly circular journal bearing) to 0.5. Two eccentricity ratios ($\epsilon = e/C = 0.2$ and 0.4) are specified as input data to the numerical code. To evaluate the influence of the wave position angle, γ, on the bearing performance, the three, four, six and eight wave bearings are rotated over a range of angles from 0 to 120, 90, 60, and 45 degrees, respectively.

Bearing Load Capacity:

The waved journal bearing load capacity at each of the selected eccentricity ratios is strongly influenced by the wave amplitude ratio (Fig. 2). This remark is valid for all analyzed waved journal bearings. However, the three wave journal bearing's load capacity varies over a greater range (from 169 to 395 N at 0.2 eccentricity ratio, Fig. 2a, and from 380 to 1750 N at 0.4 eccentricity ratio, Fig. 2e), then do the other waved bearings(e.g. four waves from 169 to 315 N, Fig. 2b, and from 380 to 1275 N, Fig. 2f; the six waves from 169 to 255 N, Fig. 2c, and from 380 to 875 N, Fig. 2g; the eight waves from 169 to 223 N, Fig. 2d, and from 380 to 725 N, Fig. 2h; at both 0.2 and 0.4 eccentricity ratio, respectively).
Thus, a low number of waves such as three waves should be selected if the predominant load on the bearing is a steady-state side load and the bearing (waves) position can be properly fixed. As a direct

result, the influence of the wave amplitude on bearing performance can be maximized.Fig. 2 also shows that bearing load capacities are less sensitive to the orientation of applied load to the waves as the number of waves increase. Consequently, a large number of waves (four or more waves) is required if the direction of the steady-state load varies or a predominant rotating dynamic load is applied to the bearing.

Bearing Dynamic Coefficients:

Only the direct dynamic stiffness coefficient, $\bar{K}_{xx}$, of all analyzed bearings is strongly influenced by the wave amplitude ratio while the rest of the waved bearing dynamic coefficients are almost constant with respect to wave amplitude ratio. The direct dynamic stiffness, $\bar{K}_{xx}$, significantly increases with increasing wave amplitude ratio, especially at large amplitude ratios. Fig. 3 shows that the direct dynamic stiffness, $\bar{K}_{xx}$, could be up to 10 times greater than the truly circular bearing stiffness in the case of a three wave bearing with a wave amplitude ratio of 0.5, at a large eccentricity ratio such as 0.4. This effect decreases if the number of waves increase (e.g. the direct dynamic stiffness of an eight wave bearing could be only up to 4 times greater than the truly circular bearing). The remaining dynamic stiffness coefficients (Fig. 3) as well as the dynamic damping coefficients are less sensitive to the wave amplitude ratio than the direct dynamic stiffness coefficient. This physically explains the stabilizing effect of the waves. The shaft reaction forces align more closely with the applied load and the effects of the cross-coupling, destabilized forces become less important as the wave amplitude increases.

Fluid Film Bearing Stability:

The fluid film stability of the waved journal bearing will be discussed in terms of "critical mass" (Eq. 13). The numerical results show that the critical mass of all analyzed bearings is dependent on the wave amplitude ratio (Fig. 4). All waved bearings are unconditionally stable at large wave amplitude ratios (as 0.5) for an eccentricity ratio of 0.4. However, Fig. 4 shows also that the stability of a wave bearing with fewer waves is enhanced, exceeding the stability of a wave bearing with a large number of waves, if the orientation between the wave position and the applied load (the wave position angle) is properly selected. In addition, the waved bearing critical mass, as the other bearing performance, is less sensitive to the wave position angle, γ if the number of waves is increased.

Actively Controlled Waved Bearing:

The rotor-bearing system behavior can be controlled by the wave amplitude ratio. The wave amplitude ratio influences the wave bearing dynamic coefficients, especially the direct stiffness. As a direct result, the rotor-bearing system critical speed can be changed by changing the bearing stiffness via the wave amplitude. The dynamic forces (Eq. 6) that the bearing applies to the rotor also depend on the wave amplitude ratio. These bearing dynamic forces combined with rotor dynamic forces will determine the rotor-bearing system dynamic behavior. Consequently, the rotor-bearing system dynamics can potentially be actively controlled by actively controlling the wave amplitude of bearings which support the rotor.

Note: This analysis shows that a six or eight wave bearing geometry could increase the hydrodynamic effect and the bearing steady-state and dynamic performance is improved due to this effect. Thus, the bearing stiffness could be up to 4 or 5 times greater and is stable. Using six to eight waves the bearing reacts almost uniformly as the applied load changes, and as a consequence, the position of the bearing is not critical. However, the wave amplitude ratio must be greater than 0.2 to allow the bearing performance to be greater than that of the truly circular bearing. It is important to note that the manufacturing tolerance for the wave amplitude are critical in establishing the performance of wave bearings for any application, although this analysis was only done for a compressible lubricant. However, if due to manufacturing tolerances the wave amplitude ratio decrease below 0.2 the bearing performance can become less than that of the truly circular bearing.

SUMMARY OF RESULTS

An analysis was performed to demonstrate the performance improvements achieved by using a waved bearing concept. The waved bearing concept was depicted using a three wave journal bearing geometry. The performance of three, four, six, and eight wave journal bearings operating with air was numerically predicted and discussed. The main conclusions are:

1. The bearing wave amplitude has an important influence on both steady-state (load capacity) and dynamic performance (fluid film bearing stability and dynamic coefficients) of the waved journal bearing. Thus, the waved bearing load capacity could be from 2 to more than 4 times greater than the load capacity of a truly circular bearing, the direct dynamic stiffness could be increased from 4 to 10 times, and the bearing could be turned into an unconditionally stable bearing.

2. The waved bearing is less sensitive to the direction of the applied load relative to waves if a greater number of waves is used However, the range over which the bearing performance can be varied decreases as the number of waves increases. Therefore, the actual number of waves must be selected based on the actual rotor-bearing system particularities to optimize the bearing.

3. Stiffness of any air journal bearings, due to hydrodynamic effect, could be doubled and made to run stably by using a six or eight wave geometry with a wave amplitude approximately half of the bearing radial clearance. However, a small wave amplitude, less than 0.2 of the bearing radial clearance, the bearing performance can become less than that of the truly circular bearing, especially if the position of a three or four wave, bearing against the applied load is bad selected.

ACKNOWLEDGMENTS

The present paper reports work conducted at NASA Lewis Research Center, Cleveland, Ohio by the author, who is sponsored under grant NAG-1370 awarded to the University of Toledo. The author would like to express thanks to Sol Gorland and Jim Walker from NASA Lewis Research Center, who kindly reviewed this paper.

REFERENCES

1. Dimofte, F., "Waved Journal Bearing with Compressible Lubricant; Part I: The Waved Bearing Concept and a Comparison with a Plain Circular Journal Bearing and Part. II: A Comparison of the Waved Bearing with a Waved-Grooved and a Lobed Bearing," presented to STLE 1993 Annual Meeting, May 17-20, 1993, Calgary, Canada, in printing process to STLE Tribology Transactions.

2. Dimofte, F., "Fast Methods to Numerically Integrate the Reynolds Equation for Gas Fluid Films," NASA Technical Memorandum 105415 (1992).

3. Lund, J.W., "Calculation of Stiffness and Damping Properties of Gas Bearings," ASME Journal of Lubrication Technology, Series F, 90, 4, pp 793-808 (1968).

4. Constantinescu, V.N., "Gas Lubrication," ASME, New York (1969).

5. Szeri, A.Z., Fluid Film Lubrication," Hemisphere Publishing Corporation, Washington D.C. (1980).

6. Gross, W.A., "Fluid Film Lubrication," John Wiley & Sons, New York (1980).

7. Castelli, V., and McCabe, J. T., "Transient Dynamics of a Tilting Pad Gas Bearing System," ASME Journal of Lubrication Technology, Series F, Vol. 89, No. 4, Oct. 1967, pp. 499-509.

8. Dimofte, F., "Effect of Fluid Compressibility on Journal Bearing Performance," STLE Preprint No. 92-TC-1D-1 (1992). 11

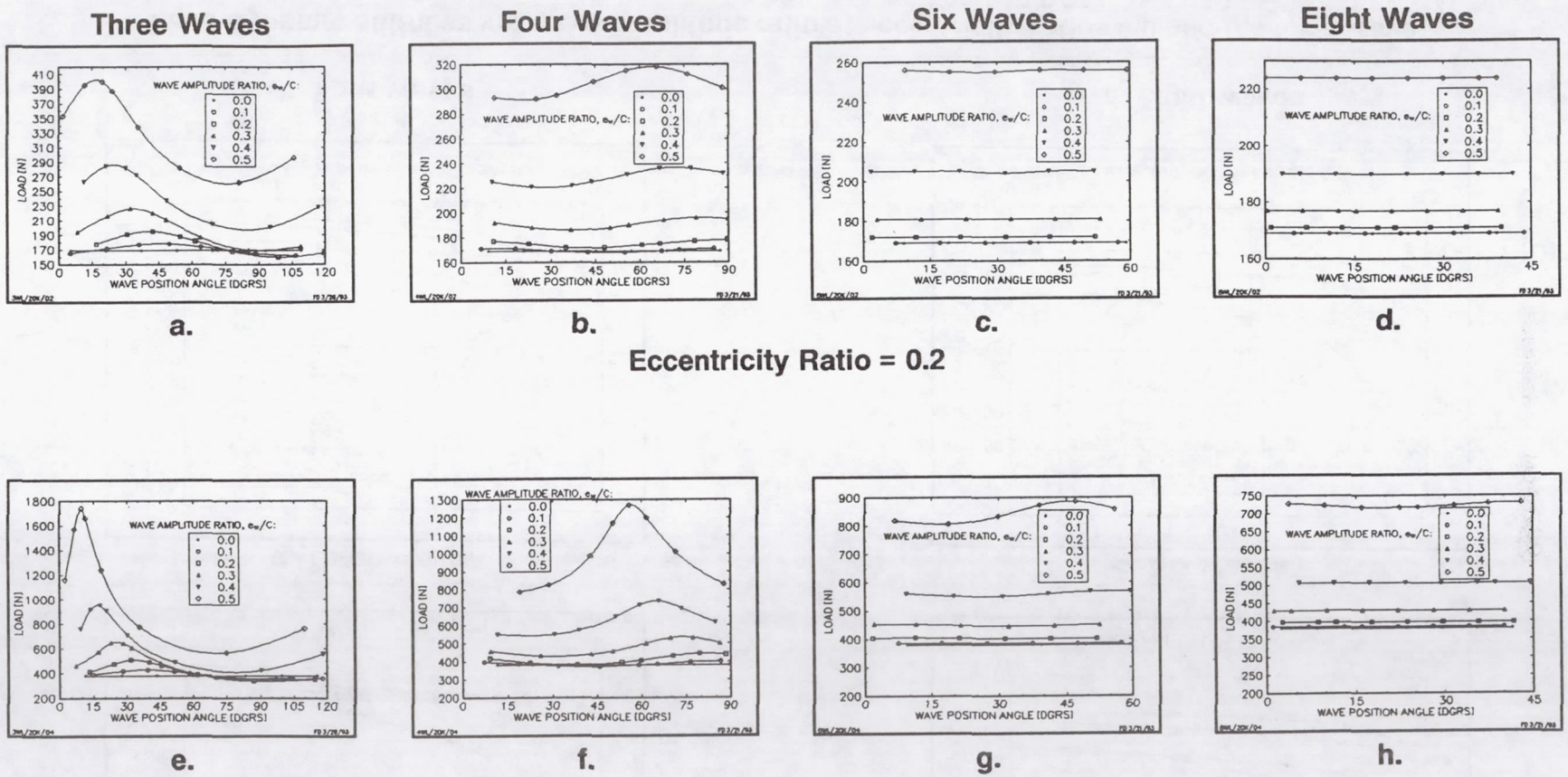

Fig. 2 Wave journal bearing load capacity vs. wave position angle; (D = 200 mm, L = 100 mm, C = 0.080 mm, N = 20,000 RPM)

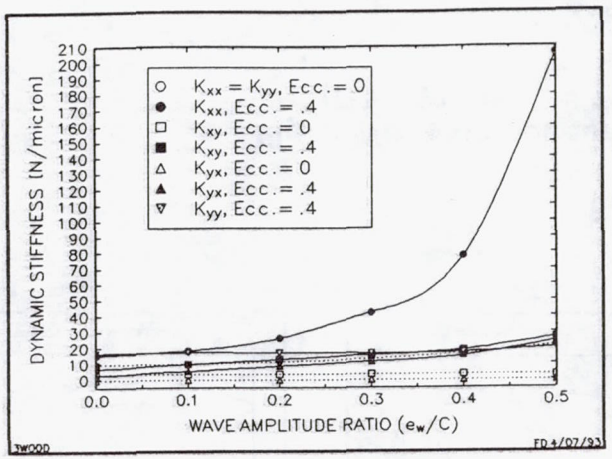

a. Three waves

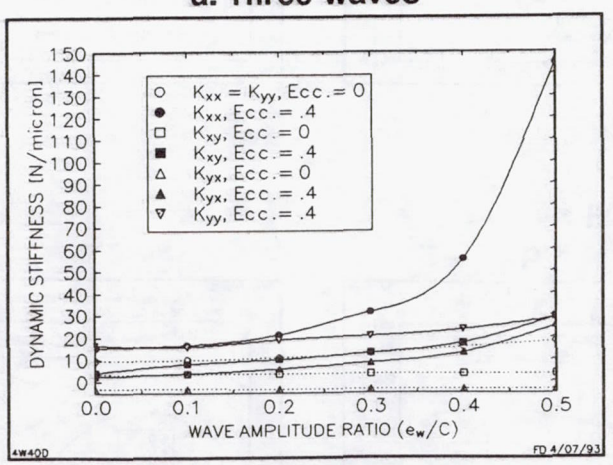

b. Four waves

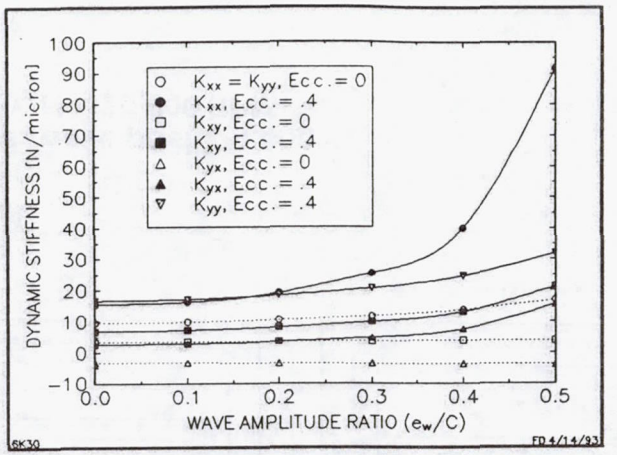

c. Six waves

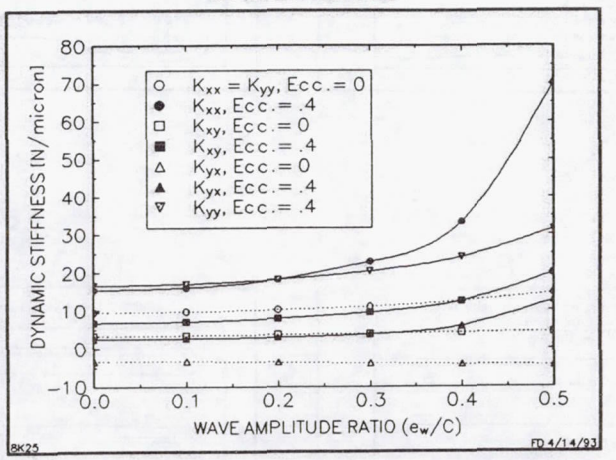

d. Eight waves

Fig.3 Dynamic stiffness vs. wave amplitude ratio at eccentricity ratios 0.0 and 0.4 for a wave journal bearing with:D = 200 mm, L = 100 mm, C = 0.080 mm, N = 20,000 RPM, and various number of waves.

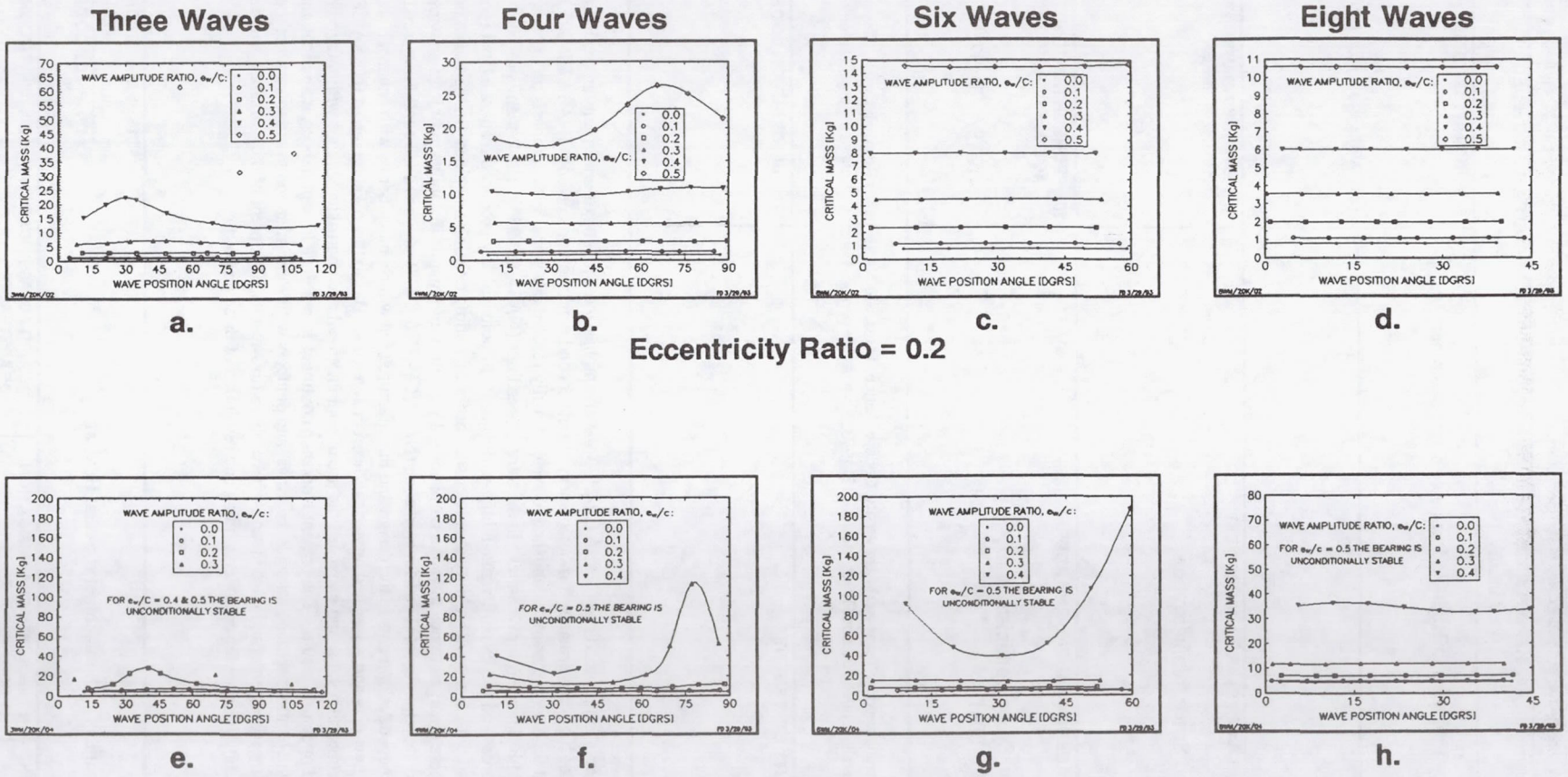

Fig. 4 Wave journal bearing critical mass vs. wave position angle; (D = 200 mm, L = 100 mm, C = 0.080 mm, N = 20,000 RPM)

REPORT DOCUMENTATION PAGE

Form Approved
OMB No. 0704-0188

Public reporting burden for this collection of information is estimated to average 1 hour per response, including the time for reviewing instructions, searching existing data sources, gathering and maintaining the data needed, and completing and reviewing the collection of information. Send comments regarding this burden estimate or any other aspect of this collection of information, including suggestions for reducing this burden, to Washington Headquarters Services, Directorate for Information Operations and Reports, 1215 Jefferson Davis Highway, Suite 1204, Arlington, VA 22202-4302, and to the Office of Management and Budget, Paperwork Reduction Project (0704-0188), Washington, DC 20503.

1. AGENCY USE ONLY (*Leave blank*)	2. REPORT DATE	3. REPORT TYPE AND DATES COVERED
	January 1994	Conference Publication

4. TITLE AND SUBTITLE
Rotordynamic Instability Problems in High-Performance Turbomachinery
1993

5. FUNDING NUMBERS
WU–584–03–11

6. AUTHOR(S)

7. PERFORMING ORGANIZATION NAME(S) AND ADDRESS(ES)
National Aeronautics and Space Administration
Lewis Research Center
Cleveland, Ohio 44135–3191

8. PERFORMING ORGANIZATION REPORT NUMBER
E–8199

9. SPONSORING/MONITORING AGENCY NAME(S) AND ADDRESS(ES)
National Aeronautics and Space Administration
Washington, D.C. 20546–0001

10. SPONSORING/MONITORING AGENCY REPORT NUMBER
NASA CP–3239

11. SUPPLEMENTARY NOTES
Proceedings of a workshop cosponsored by Texas A&M University, College Station, Texas, and NASA Lewis Research Center, Cleveland, Ohio, and held at Texas A&M University College Station, Texas May 10–12, 1993. Responsible person, Robert C. Hendricks, organization code 5300, (216) 433–7507.

12a. DISTRIBUTION/AVAILABILITY STATEMENT
Unclassified - Unlimited
Subject Category 37

12b. DISTRIBUTION CODE

13. ABSTRACT ***(Maximum 200 words)***

The first rotordynamics workshop proceedings (NASA CP-2133, 1980) emphasized a feeling of uncertainty in predicting the stability of characteristics of high-performance turbomachinery. In the second workshop proceedings (NASA CP-2250, 1982) these uncertainties were reduced through programs established to systematically resolve problems, with emphasis on experimental validation of the forces that influence rotordynamics. In the third proceedings (NASA CP-2338, 1984) many programs for predicting or measuring forces and force coefficients in high-performance turbomachinery produced results. Data became available for designing new machines with enhanced stability characteristics or for upgrading existing machines. In the fourth proceedings (NASA CP-2443, 1986) there emerged trends toward a more unified view of rotordynamic instability problems and several encouraging new analytical developments. The fifth workshop (NASA CP-3026, 1988) supported the continuing trend toward a unified view with several new developments in the design and manufacture of new turbomachineries with enhanced stability characteristics along with new data and associated numerical/theoretical results. The sixth workshop report (NASA CP-3122, 1990) field experience and experimental results, and expanded the use of computational and control techniques with integration of damper, bearing, and eccentric seal operation results. The present workshop continues to report field experiences, numerical, theoretical, and experimental results and control methods for seals, bearings, and dampers with some attention given to variable thermophysical properties and turbulence measurements, and introduction of two-phase flow results. The intent of the workshop and this proceedings is to provide a continuing impetus for an understanding and resolution of these problems.

14. SUBJECT TERMS
Instabilities, Rotordynamics; Turbomachinery; Seals; Bearings

15. NUMBER OF PAGES
442

16. PRICE CODE
A19

17. SECURITY CLASSIFICATION OF REPORT	18. SECURITY CLASSIFICATION OF THIS PAGE	19. SECURITY CLASSIFICATION OF ABSTRACT	20. LIMITATION OF ABSTRACT
Unclassified	Unclassified	Unclassified	